The University Of Sheffield.

Feasibility of using MAX phase materials in molten salt reactors

Daniel John Cooper

April 2019

Thesis submitted in partial fulfilment of the requirements for the degree of Doctor of Philosophy

Department of Materials Science and Engineering
The University of Sheffield

Contents

Abstract

The applicability of MAX phases in molten salt reactors has been investigated via their resistance to corrosion in chloride salts. High purity Ti_3AlC_2 (95wt.%) was synthesised by milling titanium and graphite for 2 h then sintering at 1350°C for 15 min with 1.0 parts aluminium. The milling time, aluminium fraction and sintering temperature were varied. Samples of Ti_3AlC_2, Maxthal 312 and TiC were exposed to molten LiCl-KCl (LKE) and KCl-$MgCl_2$ (KME) eutectics under argon with variation of the exposure time (125 h and 250 h), exposure temperature (600°C and 850°C) and salt processing. TiC performed best whereas Ti_3AlC_2 performed worst. In the absence of salt processing, Ti_3AlC_2 corroded by dissolution of aluminium and penetration of chlorine into the layers of the material. A Ti-C-Cl phase was observed which appeared to have a crystal structure similar to that of the original MAX phase. When salt processing was implemented, the extent of corrosion was minimal at 600°C but severe at 850°C. At 850°C, the sample exposed to LKE formed an oxide scale containing lithium aluminate and lithium titanate which underwent pitting corrosion, whereas the sample exposed to KME formed a stable magnesium aluminate scale by diffusion of aluminium from the underlying MAX phase. The samples of Maxthal 312 which were exposed to processed salts underwent minimal reaction at 600°C, forming a thin titanium oxide scale. At 850°C, more complex oxides formed such as lithium silicate and lithium titanium silicate in LKE and magnesium titanate in KME. Samples exposed to as-received KME formed magnesium silicate, but also underwent significant reaction with nickel wire which was used to suspend them. Corrosion of TiC was minimal. A thin coating of titanium oxide formed at 600°C, whereas lithium titanate and magnesium titanate formed in LKE and KME respectively at 850°C.

Dedication

This thesis is dedicated my grandfather, Charles Frank Cooper, who will henceforth be known as "the other Dr Cooper".

Acknowledgements

I would like to thank all of my supervisors, of which there have been many. To Karl Whittle, thank you for helping me to write a proposal to work on molten salt reactors for my project, and for suggesting that I study the corrosion of MAX phases. To Mark Rainforth, thank you for taking me on as another student. Your advice and support throughout the project has ensured I have made it to the end. To Tim Abram, thank you for being an encyclopaedia of nuclear knowledge, and for providing encouragement when I felt I was struggling. And to Mark Ogden, thank you for your advice and the many beers!

I would like to thank the people who I've worked with closely during this project, without whom I would have struggled to complete the work that I have. To Craig Jantzen, thank you for allowing me to work with you for the static corrosion tests. You have been a good friend along the way and have always supported me. To Hugues Lambert, thank you for teaching me the ways of molten salt chemistry, and for answering my many questions. To Tanagorn Kwamman, thank you for being a great desk buddy, for the discussions of our work, and for providing the samples of titanium carbide. To Carl Magnus, thank you for the discussions on MAX phase synthesis and for providing the samples of Maxthal 312.

I would like to thank the many friends I have made along the way. To Colleen Mann, your support has kept me going since the beginning, and you pushed me to carry on when things got tough. To Seb Lawson, thank you for aiding my understanding of physics and for all the good times at the pub! To the other members of Nuclear FiRST Cohort 5, on both sides of the Pennines, thanks for being awesome people. And to everyone else I've spent time with, thank you.

I would like to thank all the staff members who have supported me, particularly Kerry Abrams, Nik Reeves-McLaren, Martin Stennett, Michael Bell, Lisa Hollands, Andrew Mould, Dikai Guan and Mark Clegg. Without your training and advice, I would have struggled to get anything done.

Finally, I would like to thank the team at Seaborg Technologies, particularly Troels Schønfeldt, Eirik Eide Pettersen and Andreas Vigand Pedersen. The camaraderie during my secondment gave me the boost of energy I needed to finish my thesis.

List of Abbreviations

ARE	aircraft reactor experiment
BPR	ball-to-powder mass ratio
BSE	backscattered electron
EDS	energy dispersive X-ray spectroscopy
GAXRD	glancing angle X-ray diffraction
KME	KCl-$MgCl_2$ eutectic
LKE	LiCl-KCl eutectic
MA	mechanical alloying
MAX phase	$M_{n+1}AX_n$ phase
MSBR	molten salt breeder reactor
MSFR	molten salt fast reactor
MSR	molten salt reactor
MSRE	molten salt reactor experiment
ORNL	Oak Ridge National Laboratory
SE	secondary electron
SEM	scanning electron microscopy
SHS	self-propagating high temperature synthesis
SPS	spark plasma sintering
TEM	transmission electron microscopy
XPS	X-ray photoelectron spectroscopy
XRD	X-ray diffraction

1 Introduction

Molten salt reactors (MSRs, Figure 1) are a proposed class of Generation IV nuclear reactors and suggested for use as small modular reactors [1–9]. Unlike conventional reactors they use a liquid fuel comprised of fissile and fertile elements, with alkali metal and rare earth diluents in the form of molten halide salts acting as the coolant [2–8]. Fluoride salts are proposed in the designs for all thermal neutron reactors, whilst chloride salts have been proposed in some fast spectrum variants [4,10–12]. The use of liquid fuel offers many benefits for operation and safety [2,8]. However, the salts are potentially very corrosive at high temperature (typically 500-800°C), particularly with fission product impurities. Hence, significant material and reactor chemistry challenges exist in extending reactor lifetimes to 30-50 years and beyond whilst maintaining a high output temperature [5]. The materials must withstand a potentially corrosive halide environment, possess adequate strength and creep resistance, resistance to extensive radiation damage (100-200 dpa, *c.f.* 10-50 dpa for conventional reactors), and be manufacturable [5,13–16]. Formerly, nickel superalloys such as Hastelloy-N (Ni-Mo-Cr-Fe) were developed for experimental MSRs at Oak Ridge National Laboratory, USA [5]. In this project, carbide materials, particularly the MAX phases, have been investigated.

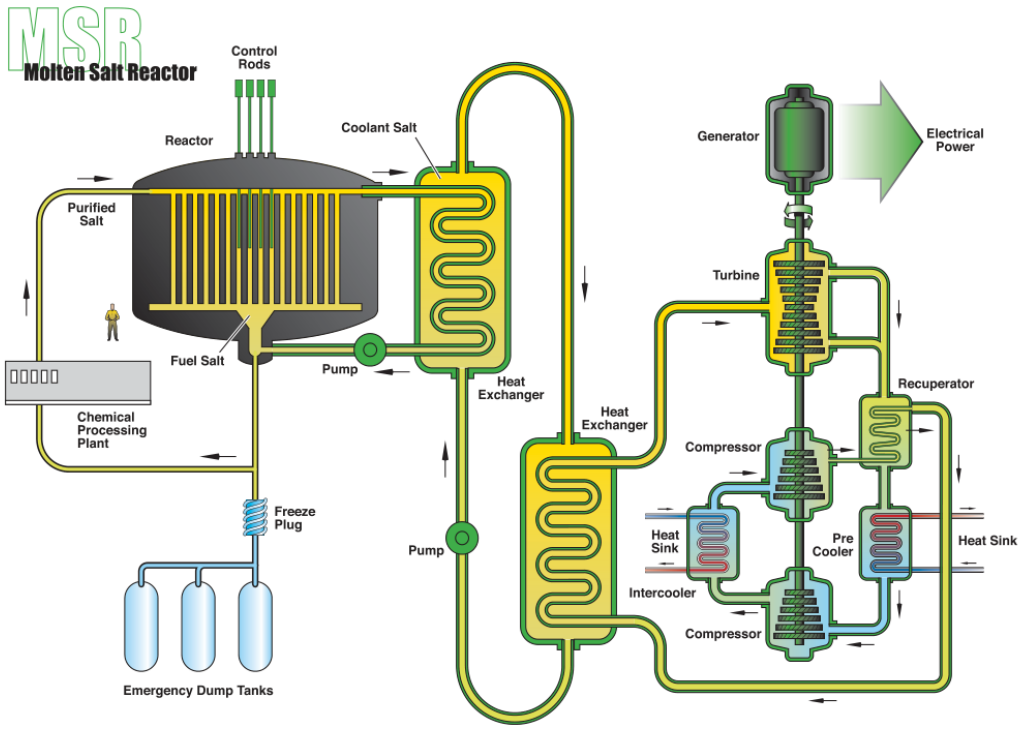

Figure 1 – Generalised schematic of an MSR based on the Molten Salt Breeder Reactor; reproduced from [1].

Two prototype MSRs have been successfully operated [6]. The Aircraft Reactor Experiment (ARE), operated during 1954, was commissioned by the United States Air Force to develop a nuclear reactor to power aircraft for continuous flight [17]. Molten salts were chosen as the coolant, achieving the high

temperature required for the jet engine without a pressure vessel. A successor named the Fireball was developed but not built as the project was cancelled upon development of air-to-air refuelling [2]. Later, development of a commercial power-producing MSR led to the Molten Salt Reactor Experiment (MSRE), a prototype reactor which operated between 1965 and 1969 [17]. A reactor for the next development stage, the Molten Salt Breeder Reactor (MSBR), was cancelled, in part due to the Liquid Metal Fast Breeder Reactor being more advanced in development [6]. Material compatibility was cited as a problem but was being solved at the time of cancellation [5]. Funding was obtained again in 1972-1974 and the Denatured Molten Salt Reactor was developed, a simplified design compared to the MSBR which did not require continuous reprocessing of the salt [2,18]. Concurrent to the MSBR research program, a Molten Salt Fast Reactor was researched in the UK and cancelled around the same time [10,11]. After these cancellations research continued in other countries including Russia, France and Japan [5].

Arguably the greatest advantage of MSRs over conventional solid-fuelled reactors is the use of liquid fuel. Solid fuel poses several challenges. In particular, solid fuel and the cladding which separates it from the coolant suffer extensive radiation damage. Consequently, the fuel must be removed after only a small fraction of fissionable material has been used, otherwise its mechanical integrity may be compromised, potentially causing contamination of the coolant and reactor shutdown. Furthermore, manufacturing fuel pellets with highly radioactive materials such as actinides other than uranium and plutonium is very challenging, whereas these are easier to handle with liquid fuel.

Liquid fuel reactors utilising various solvents, such as water, a number of different molten salts such as halides, carbonates and nitrates, and molten metals such as sodium have all been developed [19]. Halide salts in particular provide a range of benefits for commercial energy generation. Water boils at 100°C under ambient conditions; pressurisation introduces additional safety hazards and the coolant temperature is still limited to below 360°C. Mixtures of molten halide salts boil at temperatures greater than 1000°C at atmospheric pressure, enabling higher operating temperatures and more thermally efficient conversion to electricity. Molten metals, such as sodium and lead, also have high boiling points at atmospheric pressure. However, molten metals, particularly sodium, can be extremely reactive if they encounter water or oxygen. Furthermore, their opacity limits in-situ monitoring of the reactor.

Molten salts have been used as heat transfer media and solvents in numerous industrial processes for decades, a handful of which are summarised as follows [20]. Fluoride salts are used in the extraction of aluminium from bauxite, and chloride salts are used in the extraction of titanium and other metals from their ores. Similarly, chloride salts have been used extensively in the pyroprocessing of nuclear waste from fast reactors. Nitrate salts have been used as heat transfer media in chemical plants for over 60 years [5], and nitrate salts and carbonate salts are used for heat storage in concentrated solar power plants. Carbonate salts, along with hydroxide salts, have been used as electrolytes in fuel cells [21].

Halide salts are more stable than oxygen-containing salts as they do not decompose under irradiation and high temperatures. In particular, alkali and alkali-earth chlorides and fluorides solvate a wide range of species and fission products, forming stable products in the medium. Gaseous krypton and xenon simply bubble out and are collected, and noble fission products generally precipitate or plate-out of solution but can be separated using metal sponges [22]. Whilst not necessary for successful operation, online reprocessing of the fuel improves the neutron economy of the reactor and burn-ups much greater than conventional reactors can be achieved through rigorous management of the fuel composition, significantly reducing the volume of transuranics in the waste stream [22].

Further advantages of MSRs are outlined as follows. Designs typically run at temperatures greater than 600°C enabling high thermal efficiency using Brayton cycles (*e.g.* helium-nitrogen or super-critical CO_2), combined cycles and cogeneration [23–25]. Safety is greatly improved over existing reactor designs as the core is maintained near atmospheric pressure, eliminating the need for a pressure vessel. Increased passive safety such as a large negative temperature coefficient and freeze-plug minimise the requirement for redundant safety mechanisms [2]. The chain reaction is self-regulating due to the negative temperature coefficient: an increase in power and heat production causes an increase in temperature, which leads to thermal expansion of the fuel and reduction in density, decreasing the amount of fission and returning the reactor power to equilibrium. Most designs implement a freeze-plug of cooled material which leads to a vessel with geometry designed for subcritical reaction and heat dissipation [8]. In the event of an accident, the electrical power cuts and the plug melts, draining the reactor vessel and stopping the reaction. The majority of these advantages lead to significant cost reductions, with many proposing designs which would result in energy cheaper than coal [8,18,22].

A rigorous overview of the current state of international molten salt reactor development can be found in “Molten Salt Reactors and Thorium Energy”, edited by Thomas J. Dolan [26]. The key design options of molten salt reactors are summarised in Table 1. Due to the nature of development, many designs change with time, so a rigorous review here would not be worthwhile. However, of particular note are the organisations which have already begun pre-licencing. These are Moltex Energy in the UK and Terrestrial Energy in Canada, both of whom are working with the Canadian Nuclear Safety Commission with the intention to build a pilot reactor at the Canadian Nuclear Laboratories, Chalk River, Ontario [27,28]. Additionally, the Shanghai Institute of Nuclear and Applied Physics in China have support from the Chinese government to develop and build a prototype MSR, with an ambitious program employing over 500 staff [29]. There are also a few groups developing solid-fuelled fluoride salt cooled reactors which use Triso fuel, similar to Very High Temperature Reactors. Such reactors are a logical stepping stone to liquid-fuelled reactors whilst also having the potential for a higher temperature output relative to first-of-a-kind liquid-fuelled reactors.

Table 1 – Key design options for molten salt reactors.

Design Element	Options
Fuel	U-235, U238, Pu-239, Th-232, transuranics/spent fuel
Neutron spectrum	Thermal, epithermal, fast
Salt	Fluoride or chloride. Numerous cations and eutectic mixtures
Fuel geometry	Single fluid, dual fluid, or static fuel tubes
Power output	small (<300 MW_e), medium (300-700 MW_e) or large (>700 MW_e)
Reprocessing	online (continuous or batch) or post operation

The Moltex Energy "Stable Salt Fast Reactor" uses U-238 and Pu-239 from spent fuel in a fast spectrum [30]. The fuel is a chloride salt (60% NaCl-20% $PuCl_3$-20%(UCl_3/$LnCl_3$)) contained in numerous tubes which are suspended in the coolant. The coolant in the primary circuit is a fluoride salt (48% KF-10% NaF-40% ZrF_4-2% ZrF_2). The reactor is unique in its use of static fuel tubes containing molten salt, similar to the fuel rods used in conventional reactors. The reactor has a medium power output (750 MW_{th}) produced by two small modules (375 MW_{th} each). There is no online reprocessing, only periodic replacement of fuel tubes and reprocessing in the front and backend of the fuel cycle.

The Terrestrial Energy "Integral Molten Salt Reactor" is based heavily on the MSRE [31]. It uses denatured (slightly enriched) uranium in a thermal spectrum as the fuel, and fluoride salts are used in both the primary and secondary circuits (proprietary mixtures). It is a single fluid reactor (*i.e.* no secondary breeding fluid) and the power output per module is small (185-192 MW_e). They intend to replace the core-unit for reprocessing every 7 years.

The Chinese "Thorium Molten Salt Reactor – Liquid Fuel" is essentially a small modular version of the MSBR [32]. It uses thorium and uranium fluorides as fuel (LiF-BeF_2-UF_4-ThF_4) and operates in the thermal spectrum. The coolant salt in the secondary circuit is also a fluoride salt (NaF-BeF_2). It is a single fluid reactor and the power output per module is small at 168 MW_e. An online reprocessing scheme will be used.

There are numerous industrial processes where heat could be supplied by molten salt reactors. Furthermore, such applications can be coupled with electricity generation systems to enable energy efficient load following [23,24]. Low temperature applications of nuclear heat already exist, although use is not widespread. These include district heating, seawater desalination, paper and cardboard manufacture, heavy water distillation and salt refining [33]. Desalination is particularly important as it can provide water for irrigation and human consumption [34]. These existing applications use conventional light water reactors which are only capable of achieving temperatures of ~315°C (after considering tolerances). For higher temperature chemical processes, fossil fuels are still widely used as

the energy source. However, heat from an MSR could replace fossil fuels for intermediate temperatures (500-750°C) with currently available materials, and higher temperatures (750-1000°C) with further materials development.

From the range of possible chemical processes, hydrogen production (which requires temperatures >750°C to maximise efficiency) is perhaps the most significant. Hydrogen can be used in numerous chemical processes such as ammonia synthesis, methanol synthesis, direct reduction of iron ore, fossil fuel processing, and the Fischer-Tropsch process [35]. Currently, 96% of hydrogen production is from fossil fuels [36]. This is unsustainable and produces significant carbon dioxide. Thus, improvements to these chemical processes can be made if hydrogen can be mass-produced from water. It is also possible to produce synthesis gas, a mixture of carbon monoxide and hydrogen, by high temperature co-electrolysis of water and carbon dioxide [37]. This can then be used to sustainably produce numerous hydrocarbons for chemical feedstock and synthetic fuels [34].

Due to their use of a liquid-fuel, molten salt reactors are radically different to all reactors currently in operation worldwide. Thus, the key challenges to their implementation lie in the development of a supply chain and improvement in understanding by regulatory bodies [9]. As for technical challenges, improved understanding of the reactor chemistry is key, and can have a detrimental effect on materials corrosion if not handled appropriately. Online reprocessing is required to improve the neutron economy of most thermal spectrum reactors but can be avoided in some fast-spectrum designs. However, fast-spectrum reactors are exposed to greater radiation damage. Additionally, more components are exposed to radioactive material than for solid-fuelled reactors because the fuel is combined with the coolant, adding complexity to maintenance and decommissioning.

The development of novel materials is vital to improve performance of the reactor, enabling operation at the highest achievable temperature for the longest duration. Thus, the materials must have a suitable mix of high temperature mechanical strength and resistance to chemical attack and radiation damage. Most research to date has focused on metallic materials as they exhibit such properties. However, the best materials currently available, modified versions of Hastelloy N such as HN80MTY, can only be used to a maximum working temperature of 700-800°C [5].

Despite their refractoriness, resistance to chemical attack and resistance to radiation damage, limited research has been performed on the use of ceramic materials in MSRs. Bulk ceramics generally have unsuitable properties; their lack of ductility leads to poor fracture toughness and machinability. However, ceramics have the potential to be used as coatings or as components of composite materials such as cermets, of which MAX phases are an example. Depending upon cost and manufacturability, such materials may be more suitable for specialist components such as pumps, valves and heat exchangers as opposed to structural materials. However, corrosion testing in chloride and fluoride salts is required in order to test the viability of these materials in such an application.

MAX phases are ternary, layered, carbide or nitride materials consisting of alternating nanoscale metallic and covalent bonded layers. Interest in MAX phases has been growing since 1996, made popular by Michel Barsoum [38]. They have attributes of both metals and ceramics: high electrical and thermal conductivity, stiff yet easily machinable, resistant to thermal shock, oxidation and corrosion resistant, relatively lightweight, creep and fatigue resistant and able to maintain strength at high temperatures [38–40]. There has been limited research on the corrosion of MAX phases in molten halide environments [41], yet their nature and properties suggests they are ideal for such applications and may outperform the current modifications of Hastelloy-N [38]. The objective of this project was therefore to provide an initial assessment of MAX phase materials in high purity molten halide salts.

2 Aims

The key aim of this work was to produce a pure MAX phase material and investigate how it corrodes in molten halide salt in order to assess the feasibility of using MAX phases in molten salt reactors. Based on the available literature, it appears that the high temperature mechanical properties and irradiation damage resistance of these materials is suitable for the performance requirements of molten salt reactors, but their compatibility with molten halide salts is largely unknown. More specifically, the aims were as follows:

1. Determine a synthesis method to produce pure Ti_3AlC_2.

   This composition was chosen because its synthesis and properties have been studied significantly, including its radiation damage resistance. A pure MAX phase was desired in order to limit the effects of impurities on the corrosion mechanism. The implemented method was based on methods presented in the literature, but alternative equipment was used. Consequently, the results were interpreted with reference to synthesis mechanisms proposed in the literature, and the synthesis parameters were optimised based on this mechanism.

2. Perform corrosion tests in purified molten chloride salts.

   Methods of salt purification [42] and testing equipment [43] were developed by colleagues at the University of Manchester. Molten chloride salts were used as there are safety challenges with handling molten fluoride salts. Molten chloride salts are suitable fuel carrier salts for fast reactors and as secondary coolants.

3. Compare the corrosion of Ti_3AlC_2 to other materials.

   A commercial MAX phase called Maxthal 312, which is predominantly Ti_3SiC_2, was used for this purpose, as well as TiC. Furthermore, corrosion tests on alloys including the current standard for molten salt reactors, Hastelloy N, were tested under identical conditions by a colleague at the University of Manchester [43].

3 Literature Review

3.1 Properties of Binary Carbides

The term carbide is applied to compounds formed by carbon with elements of lower electronegativity. The binary carbides can be split into four categories dependent on the type of bonding they involve [44]. These are interstitial carbides, covalent carbides, ionic carbides and intermediate carbides. The differences are primarily due to the electronegativity and atomic radii of the atoms involved.

The covalent carbides include SiC and B_4C. Their bonding is mostly covalent due to the small difference in electronegativity between the two elements and their similar atomic radii.

The interstitial carbides are of primary interest to this work and are the only carbides which form MAX phases. They include the transition metal carbides of groups 4-6, with the exception of chromium. The larger difference in electronegativity decreases the extent of covalent bonding, and the large size of the metal atom relative to the carbon atom allows the latter to nest in the interstices. Their bonding is primarily metallic, with partial covalent and ionic character, and as such they behave chemically similar to metals.

The salt-like carbides include Al_4C_3 and their bonding is primarily ionic. In aluminium carbide, the two elements are ionised as Al^{3+} and C^{4-}. Upon exposure to water or acids they undergo hydrolysis. In the case of Al_4C_3, methane and aluminium hydroxide are formed.

Chromium carbide is an example of an intermediate carbide. Intermediate carbides are typically the carbides of group 7 and 8 transition metals (e.g. Mn, Fe). The metallic element is too small to accommodate carbon interstitials without lattice distortion. Overall, their bonding character is a mixture of the three types previously mentioned.

3.2 Properties of MAX phases

MAX phases are predominantly ternary carbides, or nitrides, consisting of nanoscale layers of carbides, $M_{n+1}X_n$, interleaved with a layer of atoms from the A-group of the periodic table, typically elements from groups 13-16 such as Al or Si (Figure 2 and Figure 3) [39]. The thickness of the $M_{n+1}X_n$ layer is determined by n, with n = 1, 2 or 3 named 211, 312 and 413 MAX phases respectively. They are cermet in nature, exhibiting properties of both metals and ceramics. Like ceramics they are refractory, resistant to chemical attack and oxidation, and creep resistant, whereas like metals they are ductile (above 1000°C), electrically and thermally conductive and readily machinable [38,39].

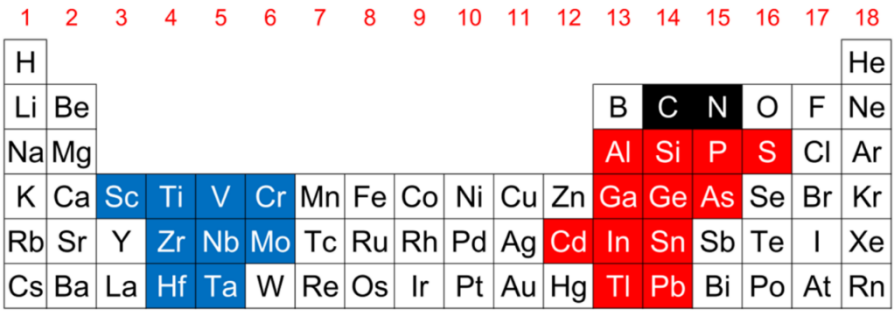

Figure 2 – A periodic table highlighting the common constituents of the MAX phases (blue = M, red = A and black = X).

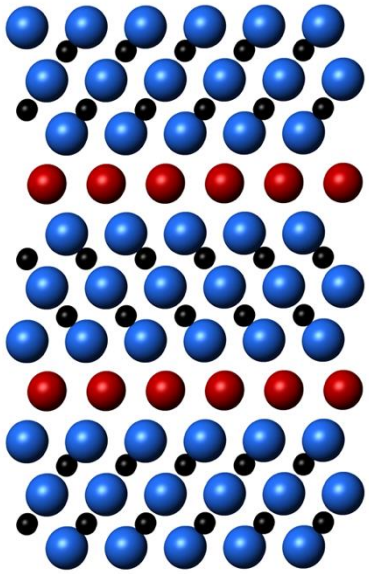

Figure 3 – The layered structure of a 312 MAX phase (blue = M, red = A, black = X).

The first MAX phases produced, referred to as the H-phases, were discovered by Nowotny and co-workers in Vienna in the 1960's and given the structure M_2BX [38], according to IUPAC classification of the periodic table. Barsoum and Houng managed a processing breakthrough involving hot pressing in 1993 which was later applied to MAX phase formation [45]. Impurities significantly hinder the properties of MAX phases, thus the production of pure, highly dense MAX phases using this method enabled identification of their unique properties, and the discovery of the 413 phases [38]. This distinguished the general formula $M_{n+1}AX_n$, and A was used instead of B due to changes in IUPAC classification of the periodic table.

3.2.1 Crystal Structural Properties of MAX Phases

There are two polymorphs of the 312 MAX phases, as shown in Figure 4, and three polymorphs, α, β and γ, exist for the 413 MAX phases [38]. In the *β* polymorph of 312 MAX phases, alternating layers of the A group element are shifted relative to the previous layer. This results in different intensities for the reflections observed by X-ray diffraction.

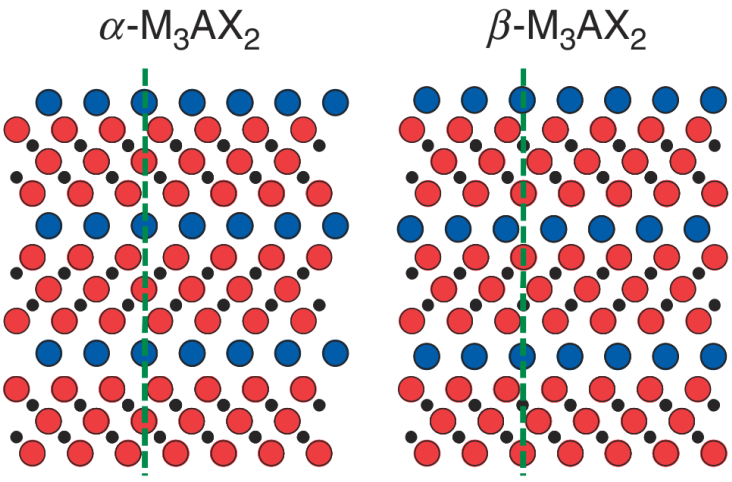

Figure 4 – Crystal structures of the two polymorphs of 312 MAX phases; reproduced from [38].

The simulated X-ray diffraction patterns for the polymorphs of Ti_3SiC_2 are shown in Figure 5 [38]. The symmetry and lattice parameters for each phase are identical, and therefore the peak positions are in the same locations [46]. The differences are for intensity of peaks only. Farber *et al.* observed the *β* polymorph after thinning samples for high-resolution transmission electron microscopy, whereas the bulk samples were determined as the *α* polymorph by X-ray and neutron diffraction.

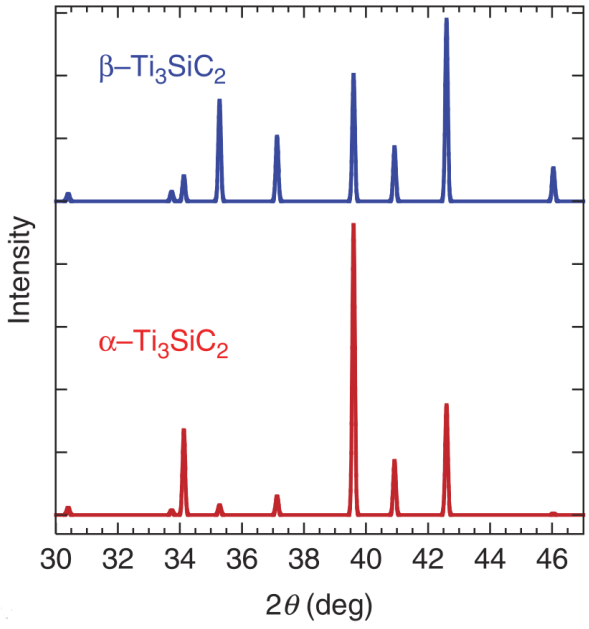

Figure 5 – Simulated X-ray diffraction patterns for the two polymorphs of Ti_3SiC_2; reproduced from [38].

3.2.2 Applications of MAX phases

MAX phases have been investigated for use in a number of applications, many of which have subsequently been awarded patents [38]. There is strong interest for their use within jet engines where

they can enable increased temperatures, improving fuel efficiency and cost savings [39]. This is due to their favourable high temperature mechanical properties and oxidation resistance, which has led to interest in their use in further high temperature structural applications [38]. Comparisons to existing alloys such as nickel-based superalloys are favourable, although the technology of such alloys is mature, and they have been optimised by small variations in composition. Further high temperature applications include heating elements, gas burner nozzles, and replacement of graphite in many high temperature applications.

The coefficients of friction of MAX phases are typically low, and the layered structure makes them self-lubricating like graphite [38]. This leads to a number of applications such as high temperature foil bearings, non-stick cookware and casts for thin-walled products such as gloves. They are electrically conductive, enabling their use in a range of electronic applications such as ignition devices, electrical contacts, electrochemical processing components and magnetic components.

A number of MAX phases, particularly Ti_3AlC_2 and Ti_3SiC_2, are resistant to radiation damage [38]. There is continuing research on developing thin-film coatings of MAX phases for nuclear fuel in order to improve accident tolerance by preventing the zirconium-catalysed dissociation of water into hydrogen and oxygen [47]. Ti_3SiC_2 has been found unreactive with molten lead or lead-bismuth alloys leading to significant interest in its use for lead-cooled fast reactors [48–53].

3.3 Synthesis of MAX phases

3.3.1 Synthesis Methods

The synthesis of high-purity Ti_3AlC_2 was one of the primary aims of this work. The phases in the Ti-Al-C system have been reviewed extensively by Cornish *et al.* [54]. A number of synthesis methods have been employed for the production of MAX phases, including sintering cold-compacted powder mixtures under a reducing atmosphere, hot-pressing, hot-isostatic pressing, self-propagating high-temperature synthesis (SHS), spark plasma sintering (SPS, a.k.a. Pulsed Electric Current Sintering [55]) and mechanical alloying (MA). Nanometer or micrometer sized elemental powders and binary carbide or nitride powders are typically used as reagents, and reagents such as TiH_2 or TiO_2 can minimise production costs incurred during extraction from ores [38,56–58]. Powdered metals such as titanium and aluminium are pyrophoric so care must be taken during handling; hence, mixing is typically performed under an inert atmosphere or vacuum [55,57,59–67]. A combination of mechanical alloying and spark plasma sintering has been used in this work, so are described in more detail as follows.

3.3.1.1 Spark Plasma Sintering

A schematic of the SPS apparatus (left) and process (right) are shown in Figure 6. The powder is placed within a graphite die, typically lined with graphite paper, between two graphite punches. Pressure is applied uniaxially and a pulsed direct current is applied causing a rapid temperature rise through Joule

heating of the powder particles. Heating rates of 1000°C min^{-1} can be achieved with dwell times typically on the order of minutes, minimising grain coarsening. This produces bulk materials with fine microstructures which have interesting properties. Improved sintering typically prevents the need for the sintering aids required in conventional processes, increasing product purity.

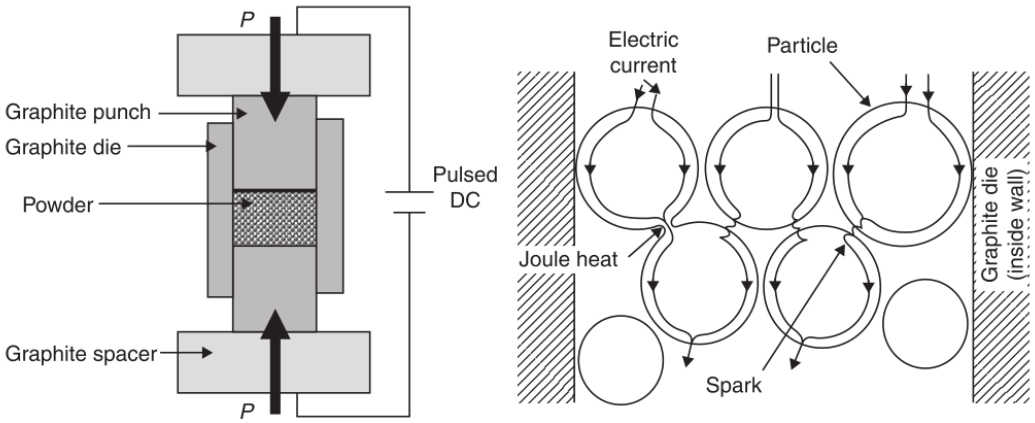

Figure 6 – Left: diagram of the apparatus used for SPS. Right: diagram of the Joule heating process by which powders are consolidated by SPS; reproduced from [55].

3.3.1.2 Mechanical Alloying

MA is a dry, solid-state powder processing technique used to mix compounds to create alloys or to perform chemical reactions (mechanochemical synthesis) [68–71]. The powders are repeatedly cold welded, fractured and re-welded in order to produce a homogeneous mixture whilst reducing the particle size and introducing defects. As well as increasing reaction kinetics, this facilitates the formation of both equilibrium and metastable phases such as supersaturated solid solutions and metallic glasses. The resultant powders are typically nanocrystalline and sinter easily due to increased surface area, grain boundary volume fraction and structural defect concentration [68].

A variety of milling equipment is available for MA such as high-energy ball mills, vibratory mills and attritor mills. Reactants are powdered, and the milling media is typically a number of balls of various sizes, with material composition dependent on the composition or hardness of the reagents. Mixing, welding and reaction occur due to continuous ball-ball and ball-vessel collisions. The rate of particle size reduction is proportional to the number of balls used as this increases the number of impacts. A mixture of ball sizes is desirable in order to prevent close-packing of balls and promote mixing, and the majority of developed milling equipment use batch processes. Commercial applications of MA have been limited as equipment capable of processing large quantities of material in a continuous fashion is required. However, in recent years a variety of new equipment capable of operation in semi-continuous or auto-batch modes, such as the Zoz horizontal attritor mill, have become available [71].

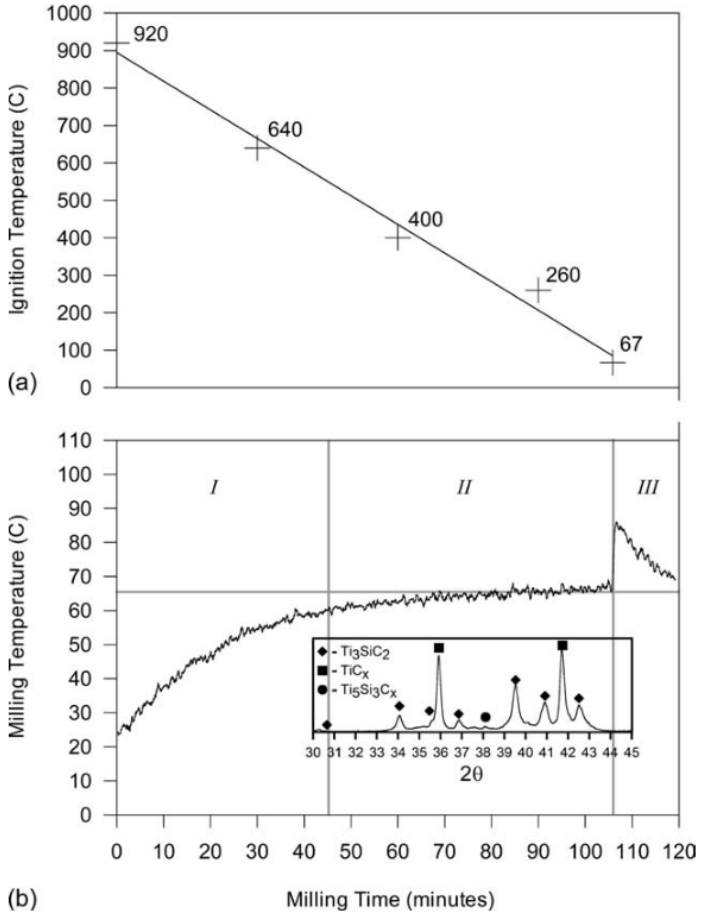

Figure 7 – (a) shows the reduction in ignition temperature for self-propagating synthesis with milling time for the synthesis of Ti_3SiC_2 from Ti, SiC and C; (b) the change in milling temperature with milling time, and the inset XRD pattern is representative of the product after 120 min milling; reproduced from [72].

Solid-state synthesis methods, like many processes, are kinetically limited in nature. Reactions such as TiC_x formation from Ti and C are strongly exothermic and thermodynamically favourable at room temperature but are kinetically limited as diffusion is required. MA improves reaction kinetics by repeatedly creating new surfaces for diffusion and reducing the particle size increases the surface area. The reaction progresses gradually as particles are repeatedly fractured. Self-propagating combustion reactions have been observed for numerous reactions when the reaction is sufficiently exothermic. The concentration of reactive surfaces increases by particle size reduction. When the particles reach a combination of critical size and temperature, a sharp temperature spike is observed indicative of a combustion reaction. The temperature of ignition, T_{ig}, is proportional to the particle size, whilst the milling time for ignition, t_{ig}, is dependent upon the MA conditions.

Riley *et al.* investigated the depression of the ignition temperature for self-propagating high-temperature synthesis (SHS) with MA for the reaction of Ti (-100 mesh), SiC (< 100 µm) and C (< 100 µm) to form Ti_3SiC_2 (Figure 7) [72]. In the absence of milling, SHS was initiated at 920°C

and T_{ig} was shown to decrease as milling progressed. In the primary milling phase, the temperature of the vessel increases due to the movement of milling media and gradual exothermic reaction, whilst in the secondary phase heat formation tends to equilibrate with the environment. Finally, in the third phase T_{ig} is equal to the temperature of the vessel and spontaneous combustion occurs.

3.3.2 Reactive Spark Plasma Sintering

Zou *et al.* carried out an extensive investigation of the synthesis of Ti_3AlC_2 by SPS from a number of reagents, including mixtures of Ti, Al, C, Al_4C_3, TiH_2 and TiC [56,58,73–75]. Powders were mixed for 24 h in a Turbula shaker mixer under argon. The use of TiH_2 was investigated to reduce production costs of MAX phases as TiH_2 is an intermediate in the extraction of titanium [56,58]. Single-phase Ti_3AlC_2 was obtained when a non-stoichiometric molar ratio of Ti (< 10 µm), Al (< 10 µm) and C (5 µm) powders (3:1.1:1.8) underwent SPS at 1250-1350°C for 15 min under vacuum [73]. Rapid quenching at a range of temperatures (800°C to 1300°C in 100°C intervals) was applied to determine the reaction mechanism. The proposed mechanism is shown by Equation 1 to Equation 5. TiAl and Ti_3Al were detected at 800°C, followed by TiC and Ti_3AlC at 900°C. Ti_2AlC peaks began to appear at 1000°C and were most intense at 1100°C. Ti_3AlC_2 first appeared at 1200°C accompanied by a decrease of TiC.

Equation 1

$$4Ti + 2Al \rightleftharpoons TiAl + Ti_3Al$$

Equation 2

$$Ti + C \rightleftharpoons TiC$$

Equation 3

$$Ti_3Al + C \rightleftharpoons Ti_3AlC$$

Equation 4

$$Ti_3AlC + AlTi + C \rightleftharpoons 2Ti_2AlC$$

Equation 5

$$Ti_2AlC + TiC \rightleftharpoons Ti_3AlC_2$$

Yoshida *et al.* carried out a similar experiment and found results in relatively good agreement with Zou *et al.* [76]. They mixed Ti (< 40 µm), Al (< 40 µm) and C (< 5 µm) in a molar ratio of 3:1:2 by mechanically stirring in ethanol for 1 h. They then cold-isostatically pressed pellets and sintered them in an argon atmosphere. In comparison to Zou *et al.*, Yoshida *et al.* used a larger powder particle size, a different molar ratio and a different sintering method.

Zou *et al.* also obtained fully dense, predominantly single phase Ti_3AlC_2 from Ti (< 10 µm), Al (< 10 µm) and TiC powders (2-5 µm) (molar ratio of 2:2:3) at 1300°C for 15 min [74]. The Ti_3AlC_2 grains were rectangular with a width of 3-5 µm and length of 20-50 µm. Using rapid quenching at a range of temperatures, the mechanism shown by Equation 6 to Equation 9 was proposed. As previously noted, TiAl and Ti_3Al intermetallics formed at 800°C. At 900°C, the intensity of Ti_3Al decreased whilst that of TiAl increased. At 1000°C, Ti_2AlC began to appear, and Ti_3AlC_2 began to appear at 1200°C.

Equation 6

$$4Ti + 2Al \rightleftharpoons TiAl + Ti_3Al$$

Equation 7

$$Ti_3Al + 2Al \rightleftharpoons 3TiAl$$

Equation 8

$$TiAl + TiC \rightleftharpoons Ti_2AlC$$

Equation 9

$$Ti_2AlC + TiC \rightleftharpoons Ti_3AlC_2$$

Kisi *et al.* argue that the use of post-reaction microstructural analyses to determine reaction mechanisms often results in incorrect or ambiguous conclusions, as determined by comparisons to in-situ neutron diffraction during synthesis [77–80]. The mechanisms described previously from rapid quenching methods used by Zou *et al.* may therefore be incorrect or inaccurate. Using in-situ neutron diffraction, patterns can be collected at much smaller temperature steps, *e.g.* 5 to 25°C, whereas Zou *et al.* collected diffraction patterns every 100°C, limiting the precision of the results [73,74,77]. Quenching may also result in the formation of phases different to those present at high temperature due to phase changes during cooling.

3.3.3 Combustion Synthesis

Ge *et al.* proposed a mechanism for the combustion synthesis of Ti_3AlC_2, shown in Figure 8, which proceeded via formation of a Ti-Al melt [81]. A Ti-Al melt forms, within which the TiC_x particles dissolve and precipitate as Ti_3AlC_2. Ge *et al.* note that the solubility of graphite in the melt is low, but a TiC_x layer which forms on the exterior of the particles facilitates its dissolution in a Ti-Al melt. Any excess TiC_x which is unable to react with the Ti-Al melt forms as equiaxed grains which are clustered together. The melt spreads via capillary action, which is affected by the compact density and consequently the application of uniaxial pressure (Figure 9) [82]. If the compact is not sufficiently dense, the melt will struggle to spread. It is likely that regions of quenched liquid would be observed in

the material in this scenario. Conversely, if the compact is too dense, the melt will be blocked from moving. Therefore, there is an optimal compact density where capillary action is maximised.

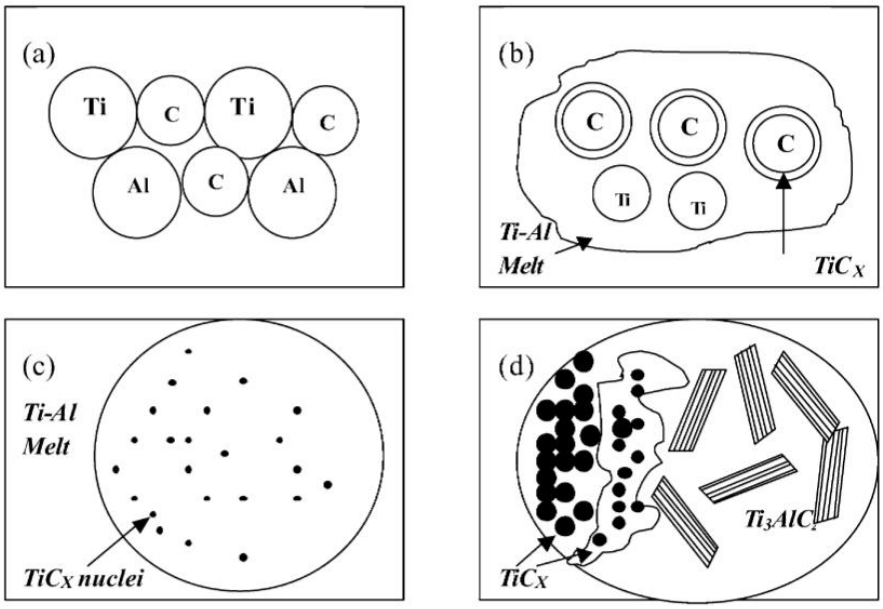

Figure 8 – Reaction mechanism proposed by Ge *et al.* for the combustion synthesis of Ti_3AlC_2 from Ti-Al-C: (a) the reagents are in contact; (b) a Ti-Al melt forms, within which C reacts with Ti to form TiC_x as an outer layer; (c) TiC_x nuclei form in the Ti-Al melt; (d) some TiC_x nuclei dissolve in the Ti-Al melt and precipitate as Ti_3AlC_2, while other TiC_x nuclei grow to form equiaxed TiC_x grains at the edge of the melt; reproduced from [81].

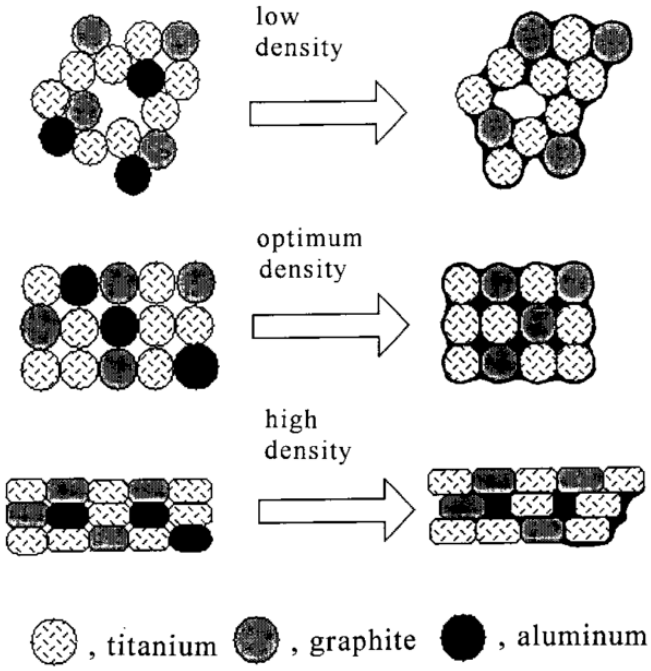

Figure 9 – Diagram showing the effect of compact density on capillary action; reproduced from [82].

3.3.4 Synthesis by Mechanical Alloying followed by Sintering

Li *et al*. synthesised Ti_3AlC_2 by MA of Ti, Al and C (molar ratio of 3:1:2) in a QM-1SP4 planetary ball mill with a stainless steel vessel and balls, using ball-to-powder mass ratios (BPRs) of 20, 50 and 100 and rotation speed of 500 rpm [83]. The vessel was evacuated prior to milling, and the powders were cold compacted then pressureless sintered under vacuum. The authors propose a possible reaction mechanism for the MA process based on XRD results and SEM investigation on samples removed between milling intervals. This mechanism concurs with that proposed by Ge *et al.* [81]. Firstly, the particle size decreases and the reagents homogenise. Secondly, Ti and Al react exothermically to form an intermetallic, and Al melts, coating the particles. Following this stage, Ti and C react exothermically, initiated by the exothermic reaction of Ti with Al, where the intermetallic melts and TiC_x precipitates, leading finally to Ti_3AlC_2 precipitation from the melt. A BPR of 50:1 caused faster reaction and particle size reduction than 20:1, but a BPR of 100 was unfavourable as the concentration of reagents was too low for reaction to occur.

3.3.5 Synthesis via an $M_{n+1}X_n$ Precursor

Kisi and Riley patented a method of MAX phase synthesis via a non-stoichiometric $M_{n+1}X_n$ precursor which they claim produces pure Ti_3AlC_2 and Ti_3SiC_2 [77,84,85]. A Ti_3C_2 precursor was formed then mixed separately with Al or Si and sintered. The precursor was formed by MA for an optimal time of approximately 109 minutes, as evidenced by a rapid temperature increase indicative of ignition [72,77,85]. A strength of mechanical alloying is the ability to produce non-equilibrium compounds, so the use of MA to form the precursor appears to be a key step in this method. The powders were handled in an argon atmosphere and milling performed in a SPEX 8000 Mixer/Mill in 15 min intervals between 15-120 min, with six 5 mm and three 10 mm steel ball bearings and a BPR of 10:1 [72]. The precursor was mixed with Al or Si by hand then sintered in a vacuum furnace at 1000°C. In-situ neutron diffraction was used to monitor the reaction mechanism. They proposed a four step reaction: formation of the non-stoichiometric binary carbide, vacancy ordering, twinning, and interdiffusion of the A element (Figure 10) [77].

Bei *et al.* synthesised Ti_3AlC_2 and $Ti_3Al_{0.8}Sn_{0.2}C_2$ from a number of reagents via hot isostatic pressing [86]. $TiC_{0.66}$ was synthesised according to the work of Dubois *et al.* and Liu *et al.* [87]. The reagents were mixed in a Turbula mixer with one steel ball (size or mass not given) for 1 h. HIPing was performed at 1450°C for 2 h under 50 MPa argon. When $3TiC_{0.66}$-Al was the reagent combination, the product was 64vol.% Ti_3AlC_2 and 36vol.% TiC; conversely, pure Ti_3AlC_2 was obtained when the reagent combination was Ti-Al-1.9TiC. The lattice parameter, *a*, of the TiC impurity was 4.3269 ± 0.0004 Å. Bei *et al.* argue that the impurity of the former was likely due to not using an excess of Al, whereas a slight excess of Al was used in the latter. Furthermore, it is not clear whether the

stoichiometry of the $TiC_{0.66}$ was confirmed prior to HIPing. The researchers also argue that use of TiC or $TiC_{0.66}$ is preferred to elemental powders because it avoids the highly exothermic reaction between Ti and C to form TiC, thus making the reaction pathway smoother.

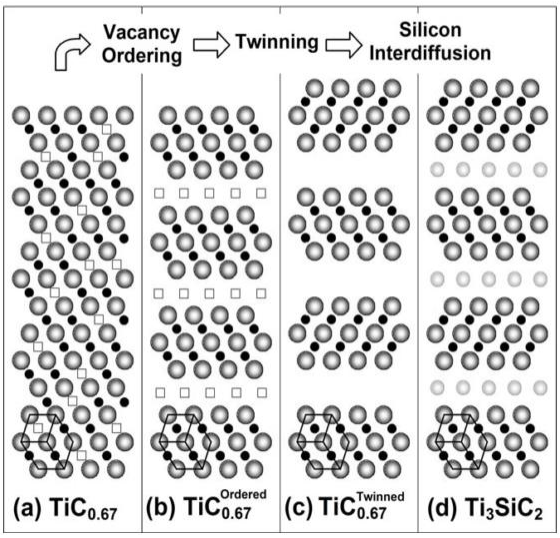

Figure 10 – Proposed mechanism of Ti_3SiC_2 formation via a Ti_3C_2 precursor; reproduced from [77].

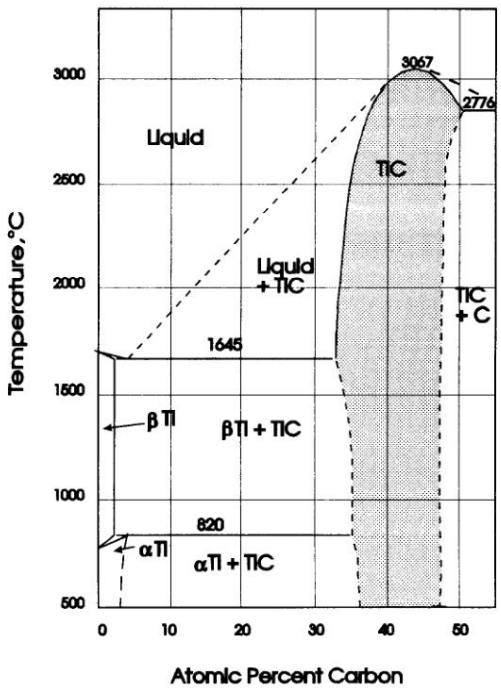

Figure 11 – Titanium-carbon phase diagram; reproduced from [88].

3.3.6 Synthesis of a Ti_3C_2 precursor

The titanium-carbon phase diagram is shown in Figure 11. Titanium carbide is more accurately presented as TiC_{1-x} as the stoichiometry can be < 1. This has been presented as "TiC_x" in the majority of this work when the stoichiometry is unclear, with TiC mostly being used when the phase is believed to be stoichiometric. A mixture of titanium and titanium carbide will be obtained if insufficient carbon is present.

The lattice parameters of TiC_x with varying values of x have been determined by Rudy for samples quenched from the melt slightly above the solidus temperature and for reannealed samples [89]. A graph of the variation of the lattice parameter with varying carbon stoichiometry is shown in Figure 12.

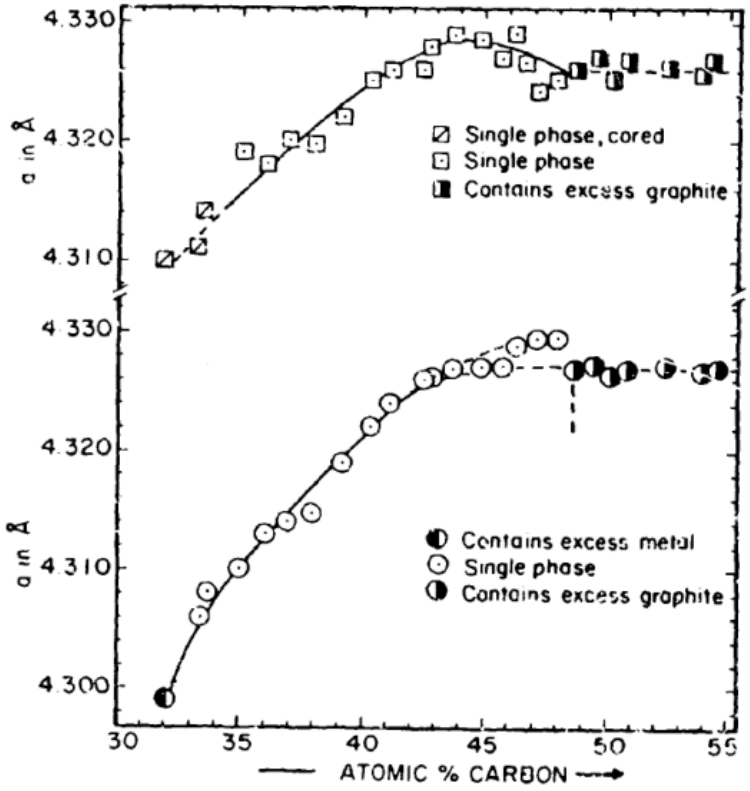

Figure III.B.1.3: Lattice Parameters of Titanium Monocarbide.

⊡ – Quenched from Slightly Above Solidus Temperatures.

⊙ – Melted Samples Reannealed for 40 hrs at 1350°C.

Maximum Concentration Uncertainty: ± 0.4 At.% C.
Maximum Uncertainty in Lattice Parameters: ± 0.0008 Å
Combined Content of Oxygen + Nitrogen: < 150 ppm

Figure 12 – Graph showing the variation of the lattice parameter, *a*, of TiC_x with change in stoichiometry of carbon relative to titanium; reproduced from [89].

Liu *et al.* produced $TiC_{0.5}$, $TiC_{0.75}$ and TiC by high-energy ball milling of Ti (74 µm) and C (250 µm) powders, where ignition was observed at 148 min, 178 min and 186 min respectively. Milling was performed in a SPEX 8000 mixer mill with a hardened steel vessel and balls with a BPR of 10:1 at 20 Hz.

Lohse *et al.* used Raman spectroscopy to study the formation of TiC_x by ball milling Ti and C [90]. A magneto ball mill with a stainless-steel vessel and multiple hardened steel balls was used under helium. There are no Raman-active vibrational modes for stoichiometric TiC but carbon vacancies induce disorder leading to Raman scattering [90]. The carbon peaks broadened with milling, indicative of loss of long-range structure. Raman results indicated the formation of TiC_x prior to ignition whereas XRD results did not [91]. Prior researchers relied solely on XRD to determine the formation of TiC_x. Lohse *et al.* suggest that TiC_x is present prior to ignition but the grain size or phase fraction may be too small to be detected by XRD, therefore the heat released at ignition may be due to production of TiC or recrystallisation of any TiC_x already formed.

Lohse *et al.* show that XRD alone does not provide sufficient information of the powder evolution process when milling Ti and C to form TiC_x [90]. The mass absorption coefficient for Cu $K\alpha$ is 208 $m^2\ g^{-1}$ for Ti and 4.6 $m^2\ g^{-1}$ for C [92]. As a result, graphite is difficult to detect both by itself and sandwiched between Ti particles during milling [90]. In the range observed, graphite is Raman active and Ti is not. Stoichiometric TiC is not Raman active, but the presence of carbon vacancies in non-stoichiometric TiC_x leads to inelastic scattering. The following is typically observed in the Raman spectra when milling Ti and C [90]. Initially, the graphite peaks at 1320 and 1590 cm^{-1} are strong. As milling progresses, these peaks broaden and weaken in intensity because the particle size of graphite is reduced, defects are introduced, and C is combined with Ti to form TiC_x. Concurrently, the TiC_x peaks at 260, 420 and 605 cm^{-1} increase in intensity. The ignition time was observed by measuring the temperature of the vessel with an infrared thermometer. Prior to ignition, only Ti peaks were observed in the XRD pattern, whereas the Raman spectra indicated the presence of TiC_x peaks. Post ignition, TiC_x peaks were observed in the XRD pattern with a small peak for Ti. Variation in the intensity of Raman spectra indicated that mixing was inhomogeneous.

3.4 Theory of Corrosion

Corrosion is defined as "the degradation of a metal by an electrochemical reaction with its environment" [93]. For the electrochemical reaction to occur, a cathodic process (reduction reaction) drives the anodic process (oxidation reaction). To determine whether corrosion is likely to occur, it is important to consider both the thermodynamics and the kinetics of the reaction. The thermodynamics refers to the tendency of the material to corrode. For a spontaneous reaction to occur, the products should be more stable than the reactants, and this is defined by a negative Gibbs free energy of reaction, $\Delta_r G$. However, there is an energy barrier for rearrangement of the atoms from one arrangement (*e.g.*

crystal structure) to another. This is the activation energy of the reaction, $\Delta G^{\neq}$, and defines the kinetics of the process.

Corrosion can occur in a number of different ways. When the material corrodes evenly across its entire surface it is referred to as uniform or general corrosion. Dissimilar metal corrosion (a.k.a. galvanic or bimetallic corrosion) occurs when the corroding metal is in contact with a metal which is significantly more stable than itself. The less stable metal provides electrons to the stable metal where a cathodic reaction occurs at its surface, providing the driving force for the less stable metal to corrode preferentially. In general, if the anodic component has a larger surface area than the cathodic component, it is usually stable to corrosion. However, if the anodic component has a smaller surface area than the cathodic component, significant dissimilar metal corrosion is likely to occur.

Selective attack occurs when corrosion is non-uniform or localised. Examples include grain boundary corrosion, intergranular corrosion, and selective leeching. These are also galvanic processes, but they occur due to differences within the metal itself. The grain boundaries of a metal are less stable than the grains, so can undergo an anodic reaction whilst a cathodic reaction occurs at the grains. Intergranular corrosion is a form of grain boundary corrosion which is driven by the presence of precipitates in the region where corrosion occurs. Precipitates in metals are typically intermetallics (*e.g.* $TiAl_3$) or compounds (*e.g.* TiC and $TiSi_2$). If the precipitate is anodic to the bulk then it will corrode preferentially, whereas if it is cathodic then the surrounding bulk material will corrode. Selective leeching (a.k.a. dealloying or demetallification) is the preferential removal of one element from the alloy, often resulting in a porous material.

Crevice and pitting corrosion are driven by concentration cells. Crevice corrosion occurs when a small volume of the electrolyte is trapped next to the corroding material. The concentration of reactive species in this volume becomes different to the bulk electrolyte, creating a potential difference which drives the reaction. Pitting corrosion is similar to crevice corrosion but is initiated differently. A pit forms at the surface of the material due to a defect and spreads radially outwards across the surface.

3.5 Corrosion of alloys in molten halides

3.5.1 Salt selection

The main categories of molten salts are halides, hydroxides, carbonates, nitrates and sulfates. Nitrates have been used extensively in the chemical industry for over 60 years as heat transfer media. However, MSRs require salts which are stable at > 700°C for most efficient operation; this rules out the use of nitrate, sulfate and carbonate salts, which decompose at ~600°C [5].

Fluorides, chlorides and fluoroborates are the only salts which are stable for the required operating conditions. All three categories are potential candidates for coolant salts. However, fluoroborates cannot be used in the fuel salt without isotopic separation of ^{11}B due to the high neutron absorption cross section

of ^{10}B. Furthermore, there is much greater experience with fluoride salts than chloride salts. This is mainly due to the fact the fluorides are better for thermal spectrum reactors due to their lower neutron absorption cross-section than chlorides. It is worth noting that chloride salts were considered in many early fast reactor designs, and are the chosen fuel salt for the Moltex Energy stable salt fast reactor [30,94]. The moderating ability of chlorine is significantly poorer than fluorine; the neutron scattering and absorption cross-sections (for thermal neutrons) of the two elements are shown in Table 2 [95]. Fluorine has a larger scattering cross section, a lower absorption cross section and greater moderating power (inversely proportional to the atomic mass) than chlorine, even when chlorine is enriched to Cl-37. However, both Cl-35 and Cl-37 pose additional difficulties for waste management due to the formation of the highly mobile activation product Cl-36 by neutron capture reactions.

Table 2 – Neutron absorption cross-sections for thermal neutrons of salt anion elements [95].

Element	**Natural abundance / %**	**Neutron scattering cross section, σ_s / barn**	**Neutron absorption cross section, σ_a / barn**
B-10	20	3.1	3835
B-11	80	5.77	0.0055
F-19	100	4.018	0.0096
Cl	-	16.8	33.5
Cl-35	75.77	21.8	44.1
Cl-37	24.23	1.19	0.433

For both chlorides and fluorides, the corrosion behaviour is mainly due to the impurities present in the melt. These impurities increase the redox potential of the melt, leading to oxidation of alloying elements by reaction with an oxidising species in the melt. However, when the melt chemistry is adequately controlled, it is generally considered that fluorides are less corrosive than chlorides [96]. Combined with the fact that fluoride salts are more difficult to handle in a laboratory setting due to the potential formation of HF and F_2 gases, chloride salts present an ideal choice for initial corrosion testing of new materials.

With regard to fluoride salts, salts containing 25-40mol.% BeF_2 or ZrF_4 have been found to exhibit the least corrosion [5,97]. Furthermore, salts which enable very reducing environments to be established, such as LiF-NaF-KF and BeF_2-containing salts, are favourable for corrosion prevention [5,97].

LiCl-KCl eutectic (LKE) is generally considered the lead candidate medium for possible future large scale pyroprocessing of spent nuclear fuel. Therefore, significant information can be found regarding its handling and use. KCl-$MgCl_2$ eutectic (KME) has the potential to have a very low-cost and is

therefore considered for use as a secondary coolant salt in molten salt reactors [5]. However, the melting point of KME is higher than that of LKE. The ternary salt LiCl(9mol%)-KCl(63mol%)-$MgCl_2$(28mol%) is a similarly likely candidate, with the best compromise between melting point, cost and performance.

3.5.2 Corrosion mechanisms in molten halides

The oxidation products in chloride and fluoride melts are generally soluble in the melt, preventing the formation of passivating oxide films [5]. Therefore, corrosion is driven by the presence of impurities which act as oxidants (e.g. H_2O, O_2, HF), thermal gradients, flow rates, and dissimilar materials corrosion [5]. Note that due to the high temperatures involved, reactions are considered kinetically fast and thermodynamic data gives an adequate prediction of corrosion behaviour [98].

In a pure salt, reactions occur in order of forming the most stable halide species. Table 3 shows the Gibbs free energy of formation per mole of halide for several elements of interest to a molten salt reactor [99]. It can be seen that the alloying components of Hastelloy N are more stable metals (and therefore less stable fluorides) in the order Cr < Fe < Ni < Mo. The fuel salt is composed of elements which form very stable fluorides, in particular the alkaline fluorides. As an example, lead fluoride, despite having favourable neutronic properties, cannot be used as a salt component because it is less stable than chromium fluoride and iron fluoride, so would react with chromium and iron in the structural materials.

The component of most concern in the fuel salt is UF_4, as this can react with alloying elements to form UF_3 as per Equation 10.

Equation 10

$$xUF_4 + M \rightleftharpoons xUF_3 + MF_x$$

Consequently, the ratio of UF_4/UF_3 is maintained at a particular value, most preferably 50-60, and can be used as a measure of the redox potential of the system [3,5]. The redox couple is shown by Equation 11, and the corresponding Nernst equation is shown in Equation 12. The latter shows that the ratio of UF_4/UF_3 directly affects the potential. As a result, UF_4/UF_3 is used as a redox buffer – any perturbations in the redox potential adjust the ratio of these two species. A similar redox couple can be envisaged between UCl_3 and UCl_4. A number of other elements have been considered for use as redox couples for coolant salts, including Sm(III)-Sm(II), Yb(III)-Yb(II), V(III)-V(II) and Eu(III)-Eu(II) [100]. Furthermore, Moltex Energy have proposed the use of Zr(IV)-Zr(II) as a redox buffer for their coolant salt [30]. The potential is typically made more reducing by adding a metallic species which is a major component of the salt to the melt, for example Be, Zr, Th or U.

Equation 11

$$UF_3 + F^- \rightleftharpoons \mathrm{UF}_4$$

Equation 12

$$E_{fuel\ salt} = E^o_{UF_4/UF_3} + \frac{2.303RT}{F}\log\left[\frac{a(UF_4)}{a(UF_3)}\right]$$

Table 3 – Gibbs free energy of formation per mole of halide atoms for several elements of interest to a molten salt reactor [99].

Halide	$\Delta_f G_{973}(MF_z)/z$ (kJ mol^{-1})	$\Delta_f G_{973}(MCl_z)/z$ (kJ mol^{-1})
$CX_{4(g)}$	-196	10
$MoX_{6(g)}$	-214	-30
$WX_{6(g)}$	-239	-38
NiX_2	-253	-80
PbX_2	-264	-112
FeX_2	-290	-111
CrX_2	-327	-138
TiX_4	-343	-144
$SiX_{4(g)}$	-369	-134
UX_4	-409	-187
AlX_3	-419	-170
UX_3	-431	-217
ThX_4	-452	-226
KX	-469	-344
NaX	-474	-321
MgX_2	-478	-245
LiX	-523	-331
CaX_2	-531	-324

From the relationship shown in Equation 12 it is clear that thermal gradients can also be a key driver for corrosion. It can be seen from the Nernst equation that a difference in temperature at two locations will lead to a potential difference. This potential difference can act as a driver for corrosion reactions. Consequently, material is dissolved from the hot section and deposited in the cold section.

When fission reactions are considered, the most obvious concern is the formation of F_2 from uranium fission. This can react with UF_3 in the salt to form UF_4, as per Equation 13. This raises the redox potential of the salt and can cause corrosion of the structural materials as per Equation 10. Alternatively, it can react with the fission products.

Equation 13

$$UF_3 + \frac{1}{2}F_2 \rightleftharpoons \mathrm{UF_4}$$

The fission products formed can cause significant corrosion issues. The formation of stable metal halides will also cause dissolution of elements in the structural material, as per Equation 14.

Equation 14

$$Cr + MF_2 \rightarrow CrF_2 + M$$

The group 16 elements in particular are detrimental to the structural materials [3,5,101,102]. S, Se, and Te can each exist in the (-I) and (-II) oxidation states. O and S can be present as impurities and Se and Te form as fission products. For example, metallic tellurium can react with alloy components such as Ni and Cr to form intermetallic telluride species. The formation of intermetallic telluride phases in the molten salt reactor experiment was found to cause significant corrosion and embrittlement of the structural material [3,5]. Figure 13 shows the cross section of a Ni-based alloy which has undergone intergranular corrosion by exposure to tellurium in fluoride salts at 700°C [3]. Tellurium embrittlement has been largely resolved for Ni-based alloys by the use of Nb as an alloying element [5,101,102]. An alternative method is to maintain a low redox potential so that metallic tellurium does not exist in the salt, for example by reacting with a ZrF_4 redox buffer to form $ZrTe_2$. A further method is to reprocess the salt by online reprocessing, where Te can undergo fluorination to a higher oxidation state whereby it forms a gaseous TeF_6 compound and is removed from the salt [103,104].

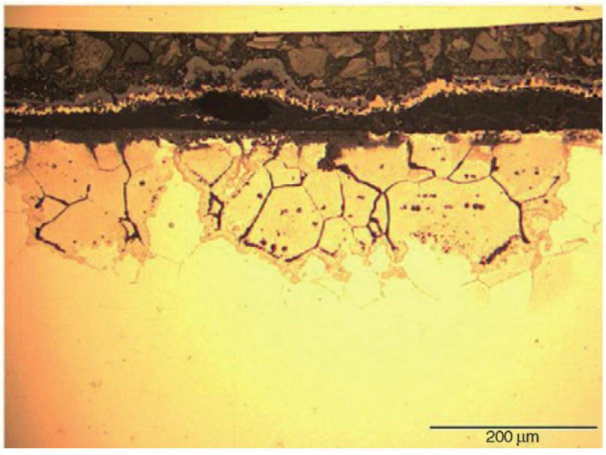

Figure 13 – Intergranular corrosion of a Ni-based alloy (Ni-21.5Cr-13.7Mo-3.8Fe-3W) by tellurium-containing fluoride salts at 700°C; reproduced from [3].

Impurities such as H_2O and O_2 are largely eliminated by processing the salt prior to use, but there is always the possibility that such impurities could be introduced during operation. Oxidants undergo cathodic reduction, removing electrons from the structural material to form soluble species. Furthermore, the potential formation of oxide films by reaction with H_2O or O_2 results in oxides, such as NiO, which react with the fuel or coolant salt to form soluble halides (Equation 15). Such reactions will continue until the most stable oxide species is formed. For example, the uranium dioxide formed in Equation 15 will react further in the presence of zirconium fluoride as per Equation 16.

Equation 15

$$2NiO + UF_4 \rightarrow NiF_2 + UO_2$$

Equation 16

$$UO_2 + ZrF_4 \rightarrow UF_4 + ZrO_2$$

It is also possible that corrosive hydrogen halide and dihalide gases can form due to the presence of impurities or by the formation of their tritium-based equivalents from neutron activation of lithium. These can be absorbed by the melt and react directly with the metallic species to form soluble halides, as per Equation 17 and Equation 18. In significant quantities, the formation of hydrogen gas could lead to embrittlement of the structural materials through the formation of hydrides.

Equation 17

$$Cr + 2HX \rightarrow CrX_2 + H_2 \uparrow$$

Equation 18

$$Cr + X_2 \rightarrow CrX_2$$

Overall, impurity driven reactions can lead to initially high corrosion rates if the salt has not been adequately purified, but eventually cease upon complete reaction. However, the redox potential increases gradually as uranium fissions leading to corrosion. Additionally, when fission products are considered, reactions with tellurium or noble species causes further corrosion.

Novikov stated a number of design constraints used in an earlier Russian molten salt reactor program to produce a reactor that can withstand 30 years of operation [105]. In particular, it was decided that the rate of corrosion should not exceed 10 μm y^{-1}. Additionally, corrosion should be uniform; methods of local corrosion such as pitting or intergranular corrosion are relatively unpredictable in their behaviour. It is also stated that the pressure on the walls due to salt is approximately 2 MPa, therefore if a ten-fold safety factor is used the material must be able to withstand 20 MPa of pressure at the operating temperature for the reactor lifetime.

3.5.3 Salt Purification Methods

Fluoride salts are typically purified by sparging with a mixture of HF/H_2 gas then adding a reactive metal which is part of the salt composition [3,5]. The ratio of HF/H_2 must be carefully controlled as HF is soluble in the salt. Fluoride salts are easier to purify than chlorides as fluorine more readily displaces oxygen due to its greater electronegativity, although from a safety perspective HF is much more challenging to use. The most common method for purification of chloride salts is to dry the solid salt under vacuum above the temperature at which water is removed, then sparge with HCl gas for an extended period of time. However, this method is incapable of completely removing oxygen from the melt, and typically a few wt.% of oxygen remains.

Carbochlorination has been shown to be a more effective method of sparging, reducing the oxygen content to ~3 ppm when LKE was sparged for 4 h at 800°C using nitrogen saturated with carbon tetrachloride [106]. The reactions by which this purifies the salt are shown in Equation 19 and Equation 20 [106,107]. However, the degree of purification was limited by the formation of carbonate salts by absorption of carbon dioxide. It is worth noting that the use of chlorofluorocarbons is highly regulated due to their effect on the ozone layer of the atmosphere.

Equation 19

$$CCl_4 \uparrow + 2O^{2-} \rightleftharpoons CO_2 \uparrow + 4Cl^-$$

Equation 20

$$CCl_4 \uparrow + O^{2-} \rightleftharpoons COCl_2 \uparrow + 2Cl^-$$

Further purification can be achieved by adding NH_4Cl to the melt. It removes residual oxide as water through the reaction shown in Equation 21.

Equation 21

$$2NH_4Cl + O^{2-} \rightleftharpoons 2NH_3 \uparrow + H_2O \uparrow + 2Cl^-$$

HCl and CCl_4 are both hazardous gases. A simpler purification method was therefore used by Lambert [42], and was adopted in this work. By applying a positive current to the melt, chlorine gas is produced at the working electrode and lithium metal is deposited at the counter electrode. The chlorine gas then reacts with any oxide impurities, liberating oxygen gas from the melt. The associated metallic impurities form chlorides and migrate to the counter electrode, where they react with metallic lithium and are deposited on the counter electrode and removed from the salt.

3.6 Materials development for molten salt reactors

3.6.1 Materials Requirements

The materials used in the primary circuit must maintain their performance when used up to 700-750°C [4]. They are the main limiting factor for the operating temperature of the reactor, so improved materials capable of operating at higher temperatures would be ideal. The outside of the materials will be exposed to nitrogen gas, but some air is expected to be present. Therefore, moderate oxidation resistance is necessary unless a coating can be used.

In a thermal spectrum the expected neutron fluence over 30-50 years is approximately 1-2 x 10^{20} neutrons cm^{-2}, and in a fast spectrum it is 5-8 x 10^{21} neutrons cm^{-2} [4]. The materials must be capable of withstanding high levels of irradiation damage. It is worth noting that resistance to irradiation may be improved at higher temperatures as the damage is annealed out of the microstructure; however, effects such as radiation-induced corrosion may be enhanced. In particular, radiation damage causes embrittlement of the materials, primarily by the neutron activation of Ni-58 which leads to alpha decay and formation of helium bubbles.[1]

The material must be fabricable into a variety of shapes and must be weldable or capable of joining. Tubing thickness will vary for different components, but some components may require thicknesses less than 1 mm. Depending on the component and the reactor design, these materials may need to withstand damage for up to 60 years.

The ideal maximum corrosion rate can be found by optimising the size and thickness of a component with consideration of the minimum thickness where it could maintain its structural properties. In general, <5 µm y^{-1} is a reasonable target (<300 µm after 60 years), and <2 µm y^{-1} (120 µm after 60 years) would be ideal.

3.6.2 Stainless Steels

Stainless steels have been tested in molten fluoride salts, but they are generally regarded as unsuitable for use [5]. This is primarily due to their high chromium content. Extensive experiments have been performed in the USA and Russia. 304SS and 316SS have been tested at ORNL. In closed loop systems at 600-650°C, a maximum uniform corrosion rate of 21 µm y^{-1} was observed for 304L and 25 µm y^{-1} for 316 [108]. Russian-made austenitic steels were tested at the RRC-Kurchatov Institute [5]. Comparable results with the 300-series stainless steels were observed for 12H18N10T (Fe, 18% Cr, 10% Ni, 1% Ti, 0.12% C) and AP-164 (Fe, 15% Cr, 24% Ni, 1.5% Ti, 4% W, 0.08% C). It

[1] Formation of Ni-59 is also highly probable, and Ni-59 can undergo reactions to form Fe-56 and an alpha particle in a thermal spectrum or Co-59 and a proton in a fast spectrum. These processes have been studied in a research project by Miles Alexander Stopher at the University of Cambridge [243].

may be possible to use these steels in very reducing conditions, but the tolerance would be much lower than for nickel-based superalloys, which are the primary choice for structural materials. However, it is worth noting that their radiation tolerance is regarded as significantly high and there are numerous materials which are already approved for use; for these reasons, Moltex Energy are considering the use of alloys such as HT9 [30]. Further references regarding the corrosion of steels can be found in the review by Ignatiev and Surenkov [5].

3.6.3 Nickel-Based Superalloys

A description of the microstructure of nickel-based superalloys can be found in the review by Pollock and Tin [109]. A description of the alloying elements and the role they play in the alloy chemistry is shown in Table 4 [110]. The compositions of numerous nickel-based superalloys which have been used in or developed for molten salt reactors are shown in Table 5 [5].

Table 4 – The effects of various alloying elements on the properties of nickel-based superalloys; reproduced from [110].

Effect		**Fe-Ni Base**	**Ni Base**
Solid Solution Strengthener		Cr, Mo	Co, Cr, Fe, Mo, W, Ta, Re
FCC Matrix Stabilizers		C, W, Ni	-
Carbides	MC	Ti	W, Ta, Ti, Mo, Nb, Hf
	M_7C_3	-	Cr
	$M_{23}C_6$	Cr	Cr, Mo, W
	M_6C	Mo	Mo, W, Nb
Carbonitrides		C, N	C, N
Promotes General Precipitation of Carbides		P	-
Forms γ' Ni_3(Al, Ti)		Al, Ni, Ti	Al, Ti
Retards Formation of Hexagonal η (Ni_3Ti)		Al, Zr	-
Raises Solvus Temperature		-	Co
Hardening Precipitates and/or Intermetallic		Al, Ti, Nb	Al, Ti, Nb
Oxidation Resistance		Cr	Al, Cr, Y, La, Ce
Improves Hot Corrosion Resistance		La, Y	La, Th
Sulfidation Resistance		Cr	Cr, Co, Si
Improves Creep Properties		B	B, Ta
Increases Rupture Strength		B	B
Grain-Boundary Refiners		-	B, C, Zr, Hf
Retards γ' Coarsening		-	Re

Table 5 – Compositions of numerous Ni-based superalloys which have been developed for use in molten salt reactors

Element	Inconel 600	Hastelloy B	Hastelloy W	Hastelloy N (INOR-8)	Ti-modified Hastelloy N (1972)	Nb-Modified Hastelloy (1976)	HN80M-VI	HN80MTY(EK-50)	MONICR
Ni	>72	67	>56	>70	>74	>76	>76	>77	>74
Cr	14-17	-	4.0-6.0	7.52	6–8	6–8	7.61	6.81	6.85
Mo	-	28	23-26	16.28	11–13	11–13	12.2	13.2	15.8
Ti	-	-	-	0.26	2	–	0.001	0.93	0.026
Fe	6-10	5	4.0-7.0	3.97	0.1	0.1	0.28	0.15	2.27
Mn	<1.00	-	<1.00	0.52	0.15–0.25	0.15–0.25	0.22	0.013	0.037
Nb	-	-	-	–	0–2	1–2	1.48	0.01	<0.01
Si	<0.50	-	<1.00	0.5	0.1	0.1	0.04	0.04	0.13
Al	-	-	-	0.26	–	–	0.038	1.12	0.02
W	-	-	-	0.06	–	–	0.21	0.072	0.16
Cu	<0.50	-	-	0.02	–	–	0.12	0.02	0.016
Co	-	-	<2.5	0.07	–	–	0.003	0.003	0.03
Ce	-	-	-	–	–	–	0.003	0.003	<0.003
Zr	-	-	-	–	–	–	–	–	0.075
B	-	-	-	<0.01	0.001	0.001	0.008	0.003	<0.003
S	<0.015	-	<0.03	0.004	0.01	0.01	0.002	0.001	0.003
P	-	-	<0.04	0.007	0.01	0.01	0.002	0.002	0.003
C	<0.015	-	<0.12	0.05	0.05	0.05	0.02	0.025	0.014

The first alloy to be used in a molten salt reactor was Inconel 600. This was used in the Aircraft Reactor Experiment and exposed to NaF-ZrF_4-UF_4-UF_3 at 850°C. The corrosion was too severe, and it possessed insufficient strength. Hastelloy B and Hastelloy W were pre-existing alloys which also underwent significant testing. The absence of chromium and high molybdenum content of Hastelloy B significantly improved the corrosion resistance in fluoride salts, even to temperatures exceeding 1000°C. However, the high molybdenum content of both alloys led to the formation of Ni-Mo

intermetallic species which increased the brittleness of the materials considerably. Ultimately, the brittleness and poor fabricability, and in the case of Hastelloy B the lack of oxidation resistance, mean that these alloys cannot be used.

Following this experience, Hastelloy N was developed and used successfully in the molten salt reactor experiment. Through extensive testing in loops containing Li,Be,Th,U/F the maximum corrosion rate was determined as 5 μm y^{-1}. Additionally, the corrosion rate in the MSRE, which used Li,Be,Zr,U/F up to 704°C for 3 y, was <20 μm y^{-1}. This higher rate was due to an increase in redox potential during operation and corrosion from fission products, particularly tellurium.

Two key materials issues were encountered with the use of Hastelloy N in the MSRE, neither of which were due to fluoride-based corrosion. The first issue was helium embrittlement from alpha-decay. Ni-58 undergoes a nuclear reaction under neutron bombardment to form Fe-55 by neutron capture and alpha-decay Equation 22 [3]. This produces helium, which is nucleated as discrete voids within the alloy matrix. This was resolved in future alloys by the use of fine carbide precipitates which retain the helium and prevent its accumulation at grain boundaries. Coarse carbide precipitates are present in Hastelloy N due to the presence of Mo and Si; however, reduction in the content of these elements (from 16% to 12% Mo and from 0.5% to 0.1% Si) and addition of a carbide former such as titanium resulted in the formation of fine carbide precipitates which prevent embrittlement.

Equation 22

$$^{58}_{28}Ni + ^{1}_{0}N \rightarrow ^{55}_{26}Fe + ^{4}_{2}\alpha$$

The second key issue was tellurium embrittlement, which results in the formation of microcracks and stress corrosion cracking. This can be resolved by maintaining the fuel under reducing conditions. Experiments were performed by exposing samples to gaseous tellurium. Comparison of Hastelloy N with Inconel 601 (Ni, 22% Cr, 12% Fe) revealed that the latter did not suffer the same effects, indicating that tellurium embrittlement can also be controlled by changing the alloy composition. ORNL identified Nb as an alloying element which could prevent tellurium embrittlement. It was later identified that the most representative experimental testing method was to create a slurry of metal tellurides such as Li_xTe_y and Cr_xTe_y in a stirred melt.

Following the identification of the use of Ti to prevent radiation embrittlement and Nb to prevent Te embrittlement, the issue was to find an alloy composition which could also retain the beneficial properties identified with Hastelloy N such as corrosion resistance and creep resistance. Upon cancellation of the research programs in the USA, much of the further alloy design work was carried out by Russian researchers. A review of this work has been written by Ignatiev and Surenkov [111]. The best composition they have found is HN80MTY, which has the composition shown in Table 5. There has also been research in the nuclear fusion field in order to produce FLiBe resistant materials; a

number of references are summarised by Delpech [3]. The European SAMOFAR project has also recently investigated the use of nickel alloys containing significant quantities of tungsten [3,112].

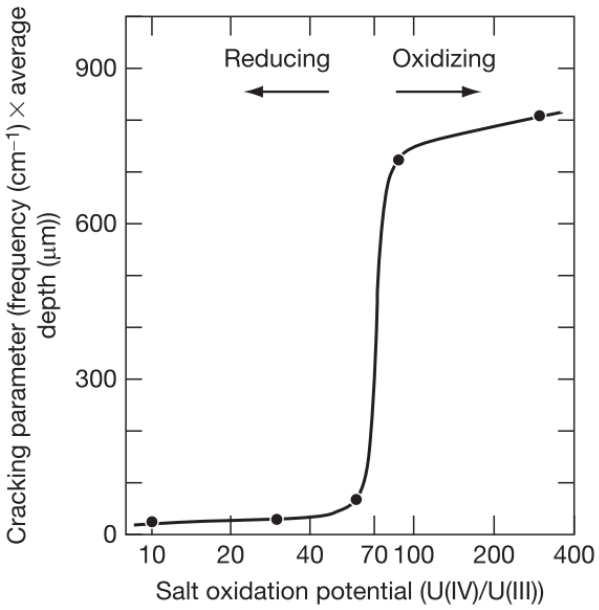

Figure 14 – Cracking behaviour as a function of redox potential for Hastelloy N exposed to MSBR fuel containing Cr_3Te_4 and Cr_5Te_6 at 700°C for 260 h; reproduced from [5].

3.6.4 Molybdenum Alloys

The development of a MSFR in the UK preferred the choice of molybdenum or alloys such as TZM as a structural material due to the use of lead as the primary coolant [4]. Based on strength requirements alone, the working temperature limit in molten chlorides was predicted to be 1000-1200°C for the initial UK MSFR design (relative to 600°C for stainless steel and 700°C for Hastelloy N) [11]. More recently, the corrosion resistance of these alloys has been investigated by Jantzen [43].

3.6.5 Alternative Materials

There has been some investigation of oxide-dispersion strengthened (ODS) alloys due to their improved mechanical properties at high temperatures [113]. Oxide particles pin grain boundaries, preventing growth and grain movement. The resistance of such alloys to corrosion in fluoride salts is questionable, as one would expect the oxide particles exposed at the surface to dissolve, increasing the oxoacidity of the melt and exacerbating corrosion.

NiMo-SiC alloys, referred to as dispersion and precipitation-strengthened (DPS) alloys have been prepared by Chinese and Australian researches via powder metallurgical routes [114]. The motivation for the work was based on the fact that ODS steels are unsuitable for use in molten fluorides due to the presence of oxygen [113], whereas nanoparticles of SiC, which are stable in molten fluorides to very

high temperatures, may provide the same high temperature dispersion strengthening. Ni-SiC alloys were prepared initially, and NiMo-SiC alloys were developed later [114,115]. Overall, there is a lot of promise for these materials, but they are still in the preliminary stages of development.

The use of coating technologies should not be ruled out. Nickel plating would be particularly useful for secondary loops and reprocessing components. The likelihood of He embrittlement from neutron capture and tellurium embrittlement would likely limit their usefulness in the primary circuit [3,5]. Mo and W would likely form similar corrosion resistant platings, which may be more resistant to these problems. There are also numerous techniques for coating materials such as steels or nickel alloys with carbides or nitrides. These would be expected to have significant resistance to both fluoride salt corrosion and irradiation damage. In particular, it has been observed that carbide precipitates prevent embrittlement from radiation damage, and niobium and titanium carbides in particular show resistance to tellurium embrittlement. For molybdenum carbide in particular, relatively simple methods exist to electroplate samples in molten fluoride salts [116,117].

3.7 Chemical reactivity of MAX phases

The MAX phases are, in general, resistant to chemical attack [38]; the $M_{n+1}X_n$ layers in particular are chemically stable, whilst the A layers are more weakly bound so tend to be the most reactive species. It has been found that the diffusivity of the A-group element is at least two orders of magnitude greater than that of the transition metal [38,118]. Particularly in the absence of an oxygen-containing environment, a common theme in the stability and corrosion mechanisms of MAX phases is loss of the A-group element to form an ordered, non-stoichiometric MX_n compound (named MXene when isolated), followed by de-twinning to form an ordered MX_n compound. This is essentially the opposite of the reaction observed by Riley and Kisi [77,85].

3.7.1 Reactivity with nickel

The reactivity of MAX phases with nickel has been investigated in order to determine whether they can be used in combination with superalloys [38,119–125]. In particular, Yin *et al.* investigated the diffusion bonding of Ti_3SiC_2 with Ni, and Lu *et al.* investigated brazing Ti_2AlC to Ni with a Ni-based filler [119,120].

Yin *et al.* found that a maximum shear strength (121 ± 7 MPa) close to that of Ti_3SiC_2 (130 ± 18 MPa) could be obtained, indicating that diffusion bonding is a suitable technique for joining Ti_3SiC_2 and nickel [119]. Two reaction layers formed between the two materials, and the rate of reaction was controlled by diffusion of Ni through the reaction layers. As the thickness of the reaction layers increased, the rate of reaction slowed due to resistance to the diffusion of Ni.

Lu *et al.* obtained an even greater maximum shear strength (193 MPa) when brazing Ti_2AlC to Ni with a Ni-based filler alloy, BNi-2 (melting point 1000°C) [120]. The shear strength of Ti_2AlC is

223 MPa. Ni diffused along the grain boundaries of Ti_2AlC (as with Ti_3SiC_2). Al then dissolved in Ni via a solid-state reaction to form Ni_3Al, leaving behind ordered TiC_x nanolaminates. There were further reaction zones and phases along the braze to the Ni substrate, including a TiB phase formed from TiC_x, with four zones between the Ti_2AlC and Ni substrates. As with Ti_3SiC_2, the thickness and rate of growth of the reaction zone was determined by the diffusion of Ni. They also note that based on the binary phase diagrams, the solid solubilities of Ti and Si in Ni are ~9% and ~12% respectively.

3.7.2 Reactivity in molten metals

When exposed to liquid metals, the rate of reaction is directly proportional to the solubility of the A-group element in the melt. For example, the solubility of Al and Si in Cu is high, therefore Ti_2AlC and Ti_3SiC_2 react readily with molten Cu, whereas solubility in molten Mg is low and they do not react even at 850°C.

El-Raghy *et al.* investigated the reaction of Ti_3SiC_2 with molten aluminium [126]. They observed dissolution of Si leaving behind TiC_x. By measuring the variation of reaction layer thickness with time at different temperatures, the activation energy and rate constant of reaction was determined.

MAX phases such as Ti_3SiC_2 and Ti_3AlC_2 show promise for use in lead-cooled fast reactors because of the low solubility of Al and Si in molten Pb and Pb-Bi alloys [38,48–53,127]. Furthermore, the materials are tolerant to small quantities of oxygen in the melt due to the formation of protective surface oxide layers. Exposure tests have been performed at the entire range of operating temperatures for significant durations, and under both static and dynamic conditions with little, if any, corrosion observed.

3.7.3 Reactivity in molten salts

Limited research has been performed on the corrosion of MAX phases in molten chloride and fluoride salts. Mroz was the first to expose MAX phases to molten salts, exposing samples of Ti_3SiC_2 to molten cryolite [128]. Barsoum *et al.* repeated their experiments [129]. Later, Naguib *et al.* exposed Ti_2AlC to LiF [41]. In all these experiments there was no attempt to control the oxygen content of the melt, so it is no surprise that significant corrosion was observed. Li *et al.* exposed Ti_3SiC_2 and Ti_3AlC_2 to molten LiF-NaF-KF under an argon atmosphere, but access to the full paper has not been obtained [130]. MAX phases have also been exposed to other molten salts such as carbonates [131], hydroxides [132] and sulfates [133,134], as well as chloride-containing sulfate salts [135,136]. Liu *et al.* exposed Ti_3SiC_2 to NaCl at 850°C in air as a control for comparison to chloride-containing sulfate salt and observed a slight mass gain [135]. Furthermore, various researchers have successfully produced MAX phases in molten chloride salts [137–142].

Mroz exposed Ti_3SiC_2-TiC composites to cryolite at 900-1000°C for up to 100 h [128]. It was concluded that the samples showed reasonable corrosion resistance, but the results were mixed. Three

of the five samples showed a total mass loss of < 5%, whereas the other two samples lost 15-20% of their mass. In particular, heavily corroded samples showed severe corrosion at the cryolite-air interface, suggesting that corrosion was exacerbated by oxygen.

Barsoum *et al.* exposed samples of Ti_3SiC_2 to molten cryolite at 960°C for 100 h to validate the results of Mroz and concluded that it was not stable [129]. Air was bubbled through the melt (which also contained 5% Al_2O_3), which agrees with the fact that Mroz observed severe corrosion at the cryolite-air interface and clarifies why the results of Barsoum *et al.* conclusively showed that Ti_3SiC_2 was unstable. They observed loss of Si, forming partially-ordered cubic $Ti(C_{0.67},Si_{0.06})$. Si was removed from the basal planes and diffused to the Ti_3SiC_2-cryolite interface via the grain boundaries, and residual Si could be observed in the centre of the grains (Figure 15). Characterisation by XRD revealed that the (111) peaks of the $Ti(C_{0.67},Si_{0.06})$ phase were more intense than the (200) peaks and the intensity switched after the sample was annealed, indicating an order-disorder transition.

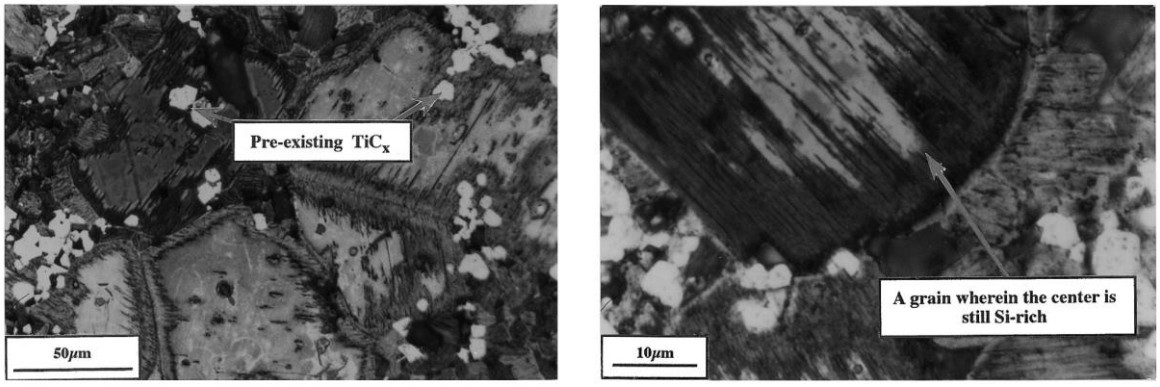

Figure 15 – Micrographs of Ti_3SiC_2 after exposure to molten cryolite at 960°C for 100 h; reproduced from [129]. Left: intergranular corrosion is clearly visible. Right: the grain centres contain residual Si after removal along the basal planes.

Naguib *et al.* attempted removal of the Al layer in powdered Ti_2AlC by exposure to LiF at 900°C in air for 2 h to obtain TiC_x with ordered vacancies, otherwise known as MXenes, for use as anodes in lithium-ion batteries [41]. They found that Al diffused out of the structure to react with LiF and form Li_3AlF_6. The change in molar volume to TiC_x was small (~-2%), suggesting that minimal cracking would occur in bulk samples, potentially maintaining mechanical properties and preventing further corrosion. They showed that oxygen is crucial for the reaction to occur as the reaction rate was significantly greater in air than in vacuum, thus corrosion may be hindered in a non-oxidising atmosphere. Presence of oxygen led to the formation of an A_xO_y layer which readily dissolved in the molten salt. This is consistent with observations of alloy corrosion in molten halides, where presence of oxygen in the salt exacerbates the rate of corrosion via formation of a soluble metal oxide [3,5]. A

non-oxidising atmosphere is maintained in MSRs in order to prevent the formation of UO_2 from UF_4, the precipitation of which is a criticality concern [143].

Li *et al.* exposed Ti_3SiC_2 and Ti_3AlC_2 to molten LiF-NaF-KF at 850°C for 144 h in airtight graphite crucibles under an argon atmosphere [130]. They observed loss of the A element in both materials, leaving TiC_x as the product. Aluminium was completely removed from the structure, whereas Si was only partially lost to a depth of 150 µm. Consequently, Ti_3SiC_2 was much more corrosion resistant than Ti_3AlC_2, although the severe depth of corrosion suggests neither MAX phase composition is resistant to corrosion in molten fluorides.

Liu *et al.* exposed Ti_3SiC_2 to NaCl at 850°C in air for up to 100 h [135]. A slight mass gain of 2 mg cm^{-2} was observed, and the same result was obtained for a sample exposed to 25wt.% Na_2SO_4-75wt.% NaCl. As the Na_2SO_4 content was increased further, severe corrosion and spalling was observed. There was no evidence of chlorine-based corrosion products, and the corrosion layer consisted of oxides including titanium dioxide, sodium titanates, sodium silicate and silicon dioxide.

It is also worth noting that many researchers have successfully synthesised MAX phases in molten salts, particularly molten chlorides [137–142]. This suggests that MAX phases should be relatively stable in molten chloride salts under certain conditions. However, it is unclear whether leaving the reactions to occur over longer periods of time would form equilibrium products other than that of the pure MAX phase.

3.7.4 Reactivity with gaseous halogens

In the presence of $Cl_{2(g)}$, MAX phases typically undergo loss of both the M- and A-group elements to produce carbide-derived carbons [38,144–146]. The overall reactions for Ti_3AlC_2 and Ti_3SiC_2 are shown by Equation 23 and Equation 24 respectively. Yushin *et al.* note that $CCl_{4(g)}$ is stable at temperatures below ~600°C which can limit the formation of carbide-derived carbons [145]. Gogotsi *et al.* note that carbide-derived carbon can store $Cl_{2(g)}$ [144].

Equation 23

$$Ti_3AlC_{2(s)} + 7.5Cl_{2(g)} \rightleftharpoons 2C_{(s)} + 3TiCl_{4(g)} + AlCl_{3(g)}$$

Equation 24

$$Ti_3SiC_{2(s)} + 8Cl_{2(g)} \rightleftharpoons 2C_{(s)} + 3TiCl_{4(g)} + SiCl_{4(g)}$$

Naguib *et al.* exposed Ti_2AlC to anhydrous $HF_{(g)}$ at 55°C for 2 h [147]. Carbon was removed from the structure as methane and the remaining Ti_2Al reacted with fluorine to form small cuboids of Ti_2AlF_9 (Equation 25).

Equation 25

$$Ti_2AlC_{(s)} + 11HF_{(g)} \rightleftharpoons Ti_2AlF_{9(s)} + \frac{1}{2}CH_{4(g)} + \frac{1}{2}CF_{4(g)} + 4.5H_{2(g)}$$

3.7.5 Reactivity in aqueous solutions

Travaglini *et al.* exposed Ti_3SiC_2 to dilute HF for 6 months and observed minimal corrosion, with a corrosion rate of ~5 μm y^{-1} [148]. Naguib *et al.* exposed a number of Al-containing MAX phases, including Ti_3AlC_2, to HF of varying concentration [149,150]. Whilst some samples such as Ti_2AlC underwent complete dissolution in concentrated HF solutions, it was possible to selective leech Al below a certain concentration [150]. The reaction was summarised by Equation 26 to Equation 28, producing $M_{n+1}X_n$ sheets which underwent further reaction to incorporate fluoride and hydroxide ions on the faces of the sheets (Figure 16). The $M_{n+1}C_nT_2$ phase has the same space group as Ti_3AlC_2. The *c*-axis lattice parameters for $Ti_3C_2(OH)_2$ and $Ti_3C_2F_2$ were determined by DFT as 19.494 Å and 21.541 Å respectively (*c.f.* 18.554 Å for Ti_3AlC_2), and the value determined by XRD was 20.51 Å (*c.f.* 18.42 Å for Ti_3AlC_2) [149,150]. When separated by sonication, the sheets have properties similar to graphene and consequently have been named MXenes. The same process has since been achieved with milder reagents such as NH_4F [151,152].

Equation 26

$$M_{n+1}AlX_n + 3HF_{(aq)} \rightleftharpoons AlF_3 + \frac{3}{2}H_2 + M_{n+1}X_n$$

Equation 27

$$M_{n+1}X_n + 2H_2O \rightleftharpoons M_{n+1}X_n(OH)_2 + H_2$$

Equation 28

$$M_{n+1}X_n + 2HF \rightleftharpoons M_{n+1}X_nF_2 + H_2$$

Lukatskaya *et al.* selectively etched the M and A elements from Ti_3AlC_2, Ti_2AlC and Ti_3SiC_2 in dilute aqueous solutions of HF (5wt.%), HCl (10wt.%) and NaCl (5wt.%) by anodic dissolution [153]. The results were similar to those obtained by exposure to chlorine gas, producing predominantly amorphous carbide derived carbon, but without the necessity of elevated temperatures. The carbide derived carbons presented as black films and were confirmed by Raman spectroscopy; they were amorphous and therefore not detected XRD. Pitting corrosion occurred with Ti_3SiC_2 in HCl, and gas evolution was observed > 2.0 V (vs. Ag/AgCl). Peaks were observed in the cyclic voltammograms of Ti_3AlC_2 and Ti_2AlC, indicating that dissolution occurred in a two-step process. Aluminium was removed in the first step, and both aluminium and titanium were removed in the second step.

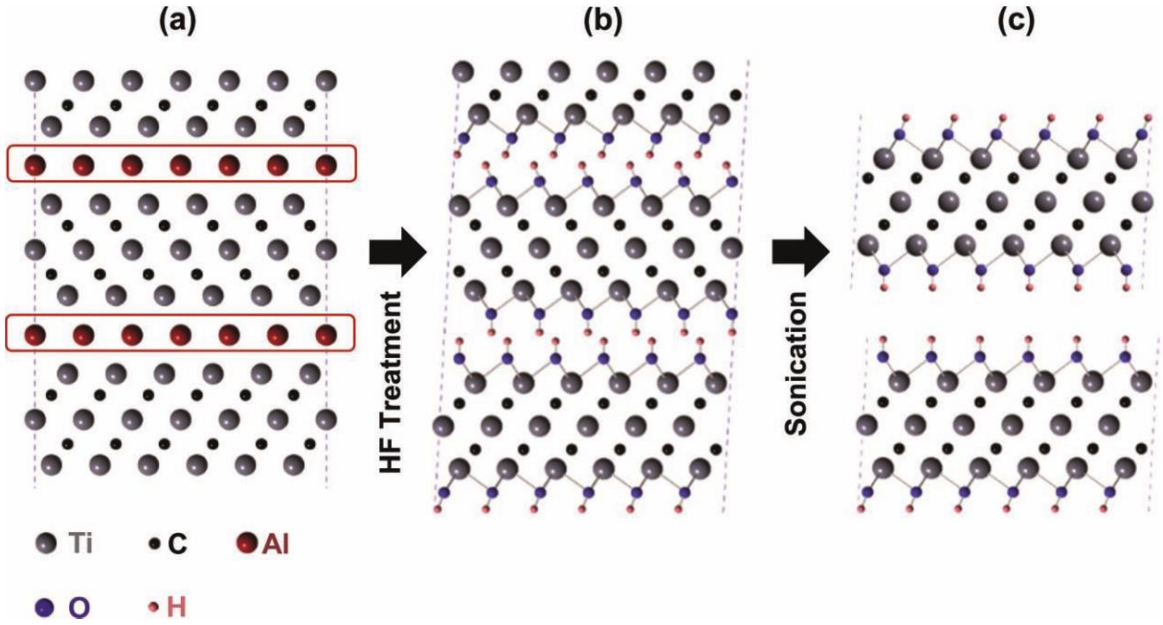

Figure 16 – Diagram showing the reaction of Ti_3AlC_2 with aqueous HF: (a) the original TI_3AlC_2 structure; (b) removal of Al by reaction with HF to form Ti_3C_2 sheets which subsequently react with H_2O to incorporate hydroxyl end-groups (or HF to incorporate fluoride end-groups); (c) separation of the $Ti_3C_2T_2$ sheets after sonication, resulting in a two-dimensional material with similar properties to graphene; reproduced from [149].

Li *et al.* investigated the corrosion resistance of Ti_3AlC_2 in 1 M NaOH and 1 M H_2SO_4 [154]. A passive TiO_2 film formed in NaOH, but in H_2SO_4 a sufficient passivation layer did not form, and intergranular corrosion of the material occurred. This latter case may be similar to corrosion in molten halides where a stable passivation layer does not form. In both solutions it is suggested that dissolution of titanium as a metallic species occurs during the cathodic process, followed by oxidation to oxides of titanium during the anodic process. Furthermore, it is suggested that the same occurs for aluminium in H_2SO_4, whereas in NaOH the aluminium in Ti_3AlC_2 is oxidised to Al_2O_3 during the cathodic process, following which it dissolves by reaction with hydroxide anions.

3.7.6 Anisotropy

Du *et al.* investigated the effect of texture on corrosion of Ti_2AlC and Ti_3AlC_2 in supercritical water at 500°C [155]. The grains were aligned with the (00*l*) planes perpendicular to the hot-forge direction. The (00*l*) planes, which consist of layers of Ti_2C and Ti_3C_2, were more corrosion resistant than the sides, where Al atoms were exposed and could be easily removed. Of further note, the corrosion mechanism occurred via formation of an anatase phase followed by a transition to a rutile phase, resulting in cracking due to volume changes.

3.8 Chemical Reactivity of Titanium Carbide

Pierson states that TiC is susceptible to attack by HNO_3, HF, and the halogens [88]. Limited research has been found on the corrosion of titanium carbide in molten halide salts. However, various researchers have successfully produced TiC coatings in molten chloride and fluoride salts, indicating that it is relatively stable in such media [156–158].

Popov *et al.* investigated the electrochemical behaviour of Ti and TiC in molten LKE [159]. Anodic dissolution of TiC in LKE produced stable Ti(III) species, whereas that of Ti produced stable Ti(II) species. A cyclic voltammogram of TiC in LKE containing a small concentration of $TiCl_3$ is shown in Figure 17.

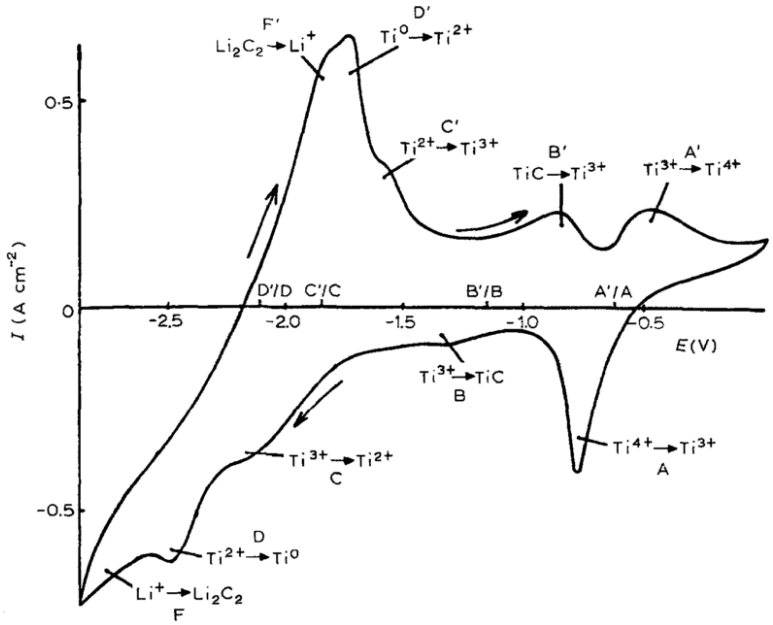

Figure 17 – Cyclic voltammogram of TiC in 450°C LKE containing 6.3 x 10^{-2} M $TiCl_3$ at a scan rate of 0.05 V s^{-1}; reproduced from [159].

Gu *et al.* studied the corrosion of TiC, SiC and TiC-SiC composites in molten LiF-NaF-KF at 800°C under argon for 25-200 h to determine their compatibility for use in molten salt reactors [160]. Intergranular corrosion was observed for all TiC-containing samples due to diffusion of Ti along the grain boundaries. SiC and the SiC-containing samples performed better than TiC due to formation of a carbon-rich protective layer on the surface from uniform depletion of Si. The mass loss of TiC after 200 h exposure was < 5 mg cm^{-2}, and that of SiC was ~2 mg cm^{-2}. Additionally, earlier work by Wang *et al.* investigated the properties of ZrC-SiC composites and observed significantly greater weight loss due to selective attack of zirconium [161].

4 Materials and Methods

This chapter summarises the parameters used for synthesis and characterisation techniques and the materials which were used for synthesis and corrosion testing. All materials and methods used in this work are as described in this chapter unless otherwise stated. Further details of the theory of these techniques can be found in Appendix A.

4.1 Materials

Samples of MAX phases were prepared using the following reagents. Titanium powder (-100 mesh, 99.7% purity, Aldrich), aluminium powder (-200 mesh, 99% purity, Acros Organics) and titanium carbide powder (2 µm, 99.5% purity, Alfa Aesar) were used for initial samples prepared by a non-precursor method. Later, titanium powder (-200 mesh, 99.5% purity, Alfa Aesar) and graphite powder (general purpose grade, Fisher Chemical) were used to prepare TiC_x precursors. An additional sample was prepared using silicon powder (-325 mesh, 99% purity, Aldrich) in place of aluminium. All powder handling operations were carried out in an argon atmosphere with < 0.1 ppm O_2 and < 0.1 ppm H_2O.

Samples of Maxthal 312 were prepared using fine-grade powder (2.5 µm, 92wt.% Ti_3SiC_2, 8wt.% TiC) from Kanthal – see Appendix D. Samples of titanium carbide were prepared from titanium carbide powder (2 µm, 99.5% purity, Alfa Aesar) – see Appendix E. Both powders were used on a benchtop with exposure to atmosphere.

LiCl (Alfa Aesar, >99%), KCl (Sigma Aldrich, >99%) and $MgCl_2$ (Alfa Aesar, >99%) were used in the preparation of eutectic mixtures for electrochemical experiments and corrosion testing.

4.2 Synthesis Techniques

4.2.1 Mechanical Alloying

Initially, milling was performed using a Retsch CryoMill and a hardened steel milling vial. Milling parameters are described in further detail in the relevant sections. For samples prepared from TiC, liquid nitrogen cooling was used, and a 25 mm diameter hardened steel ball was used as milling media in a later sample. Milling was conducted for 30 min at 22 Hz in 5 min intervals with 2:40 min intercooling stages. A further sample was prepared from a TiC_x precursor by milling for 4 h at room temperature in 30 min intervals with no intercooling stages. The precursor was mixed with Al by milling without milling media at room temperature for 30 min.

Later samples were prepared using a SPEX 8000M Mixer/Mill with a tungsten carbide vial set and two 11.2 mm diameter tungsten carbide balls. Milling was performed in 1 h intervals. The precursor was mixed with aluminium by milling with a single 11.2 mm diameter tungsten carbide ball for 10 min.

4.2.2 Spark Plasma Sintering

Sintering was achieved via spark plasma sintering (SPS), in an FCT HD P 1050 Systeme GmbH SPS. The sintering parameters for each material are summarised in Table 6. Heating was carried out under vacuum for all samples, and a 20 mm diameter graphite die lined with graphite paper was used. The majority of samples of Ti_3AlC_2 were prepared with boron nitride coated graphite paper and boron nitride coated graphite punches.

Table 6 – SPS parameters for all target materials.

Target Material	Reagent Mass / g	Maximum Uniaxial Pressure / MPa (kN)	Ramp Rate / °C min^{-1}	Holding Temperature / °C	Dwell Time / min	On/Off Pulse Time / s
Ti_3AlC_2	6-7.5	50 (16)	50	1000-1400	15-30	12/2
Ti_3SiC_2	7.5	50 (16)	50	1350	15	12/2
Ti_2AlC	7.5	30 (10)	80	1100	8	12/2
Maxthal 312	7	50 (16)	100	1400	10	12/2
TiC	7.5	50 (16)	200	2000	15	15/5

4.2.3 Synthesis Parameters of Static Corrosion Test Samples

Samples of Ti_3AlC_2 used for static corrosion tests were prepared by milling titanium and graphite powders for 2 h in a SPEX 8000M Mixer/Mill, mixed with 1.0 parts aluminium then reactively sintered by SPS at 1350°C for 15 min (see 5.1). The phase fractions from Rietveld refinement were 95±1wt.% Ti_3AlC_2 and >99% relative density. Samples of Maxthal 312 (Appendix D, § 14.2) and TiC (Appendix E, § 15) were prepared using the parameters in Table 6.

4.3 Characterisation Methods

4.3.1 Micropreparation

Micropreparation of samples was performed in several stages using a Buehler Automet. Initial grinding was performed with a grit P120 (142 µm [162]) MetPrep Matrix diamond grinding disc until all external graphite and titanium carbide was removed and the sample was plane. This was followed by grinding with grit P600 (14 µm [162]) MetPrep Matrix and 3 µm Buehler Apex diamond grinding discs, and polishing with a 1 µm Buehler MetaDi™ Combo Monocrystalline Diamond Suspension + Extender diamond suspension on an Microcloth. Samples for image analysis and nanoindentation hardness testing also underwent an additional polishing stage with colloidal silica on a Chemomet pad. Each stage was performed in 3 min cycles with 15 N force, 141 rpm platen speed, 60 rpm head speed

and complimentary rotation until the appropriate sized scratches were removed. The samples were then sonicated in isopropanol.

Samples of MAX phases for corrosion tests were prepared by polishing both faces of the circular samples to 1 µm as above, then cutting the samples into bars. Cutting was achieved with a Buehler IsoMet™ Low Speed Precision Cutter using a 0.5 mm thick 20 LC Buehler IsoMet™ Diamond Wafering Blade at a speed of 4-8 rpm. The sides of the samples were then polished by hand to grit P1200 (6 µm [162]), although the sides of some earlier samples were polished to 3 µm. Samples of TiC were polished to 1 µm on both faces and an attempt was made to remove graphite from the sides, but the samples were difficult to cut and the sides were difficult to polish well. After rinsing with water and isopropanol and drying, the samples were weighed to 4 d.p. and the dimensions were measured with a micrometer.

Cross-sections were prepared by cutting samples with a diamond slow saw then mounting in a conductive thermosetting resin. Cutting was performed as above, then mounting was carried out with a Buehler SimpliMet 3000 Mounting Press using conductive Bakelite (Konductomet, Buehler). Samples then underwent grinding and polishing as described previously.

4.3.2 Density

Densities were determined using Archimedes' principle. Relative densities were calculated from the weight fractions determined by Rietveld refinement using Equation 29, where ρ is the density measured by Archimedes' principle, f_i is the weight fraction of phase i determined by Rietveld refinement, and ρ_i (in g cm^{-3}) is the theoretical density of phase i.

Equation 29

$$Relative\ Density = \frac{\rho}{\sum_i f_i \rho_i} \times 100$$

4.3.3 X-ray Diffraction

X-ray diffraction (CuK_α) was mainly performed using a Panalytical X'Pert^3 Powder diffractometer (45 kV, 40 mA) with a 0.25° divergence slit and a step size of 0.01° 2θ. Earlier X-ray diffraction work was performed on a Bruker D2 Phaser (30 kV, 10 mA), typically with a 0.6 mm divergence slit and a step size of 0.02° 2θ and is explicitly stated where relevant. In most cases, the diffraction patterns shown in this work cover a shortened range showing all phases present to aid visibility.

Glancing angle X-ray diffraction was performed using a Panalytical X'Pert^3 diffractometer. Typical settings were a 0.25° divergence slit with a 4 mm mask with no rotation for bars of MAX phase, and a 20 mm mask with rotation for pellets of TiC. Scans were performed between 5-80° 2θ with a step size

of 0.04° 2θ and 6.6 s per step. The glancing angle, ω (in °), was varied between the limits of 0.5° and 10°, with the largest angle used only when the depth of corrosion was significant. Again, in most cases the diffraction patterns cover a shortened range showing all phases present to aid visibility.

4.3.3.1 Rietveld refinement

Rietveld refinement is a procedure whereby a calculated X-ray diffraction pattern is fitted to an experimental diffraction pattern in order to determine various properties of the sample [163–166]. The complexity of the calculated pattern is built up in stages until eventually a good fit is obtained and the calculated parameters are approximately equal to the observed values. The parameters of the instrument are also factored into the calculated pattern, measured using a standard material to account for discrepancies. In this work, the main objective of Rietveld refinement was to determine the weight fractions of phases present in bulk samples.

Rietveld refinement was conducted using GSAS and EXPGUI on data collected from 5° to 120° 2θ [167,168]. A generalised refinement strategy was applied to all samples. The difference plot and fit were checked visually at all stages of refinement, and refinements were abandoned if the goodness of fit increased at any step. First, the scale factor for each phase was refined, and the background was fitted using a shifted Chebyshev polynomial with 6 terms. Next, the zero parameter was refined to account for peak shift due to discrepancies such as sample height displacement. At this stage, data below 18° 2θ was cut in most cases because the irradiated sample length gave incorrect intensities at lower angles. Next, the unit cell was refined. The peak shape parameters were then refined, starting with the Gaussian parameters (GU, GV, GW) then the Lorentzian parameters (LX, LY). Following this, the lattice parameters were refined. The thermal parameters were then refined, and any change to negative values was rejected. The peak shape parameters were then refined again, after which the refinement was abandoned provided the fit was visually good and the R factors (*i.e.* residual factors, a measure of the agreement between observed and calculated data; see [169]) were ≤ 0.1.

4.3.3.2 Crystallite Size

The crystallite size of milled powders was determined using the Scherrer equation, although instrumental broadening was unaccounted for. Peak breadth was measured by Pearson VII curve fitting using the TOPAS software suite (Bruker).

4.3.4 Scanning Electron Microscopy and Electron Dispersive X-ray Spectroscopy

Scanning electron microscopy images were obtained primarily using an FEI Inspect F50 scanning electron microscope at 5-20 kV, equipped with an Oxford Instruments X-Max 80 mm^2 silicon drift detector for EDS. An accelerating voltage of 5 kV was found to give the best image resolution, whereas 20 kV was required for energy dispersive X-ray spectroscopy. Some earlier images were obtained using

a Hitachi TM3030 at 15 kV, equipped with a Bruker Nano XFlash® Detector 430 H for energy dispersive X-ray spectroscopy.

4.3.4.1 Image Analysis

Particle and grain size measurements were conducted on SEM images using the ImageJ image processing program [170]. The volume fraction of particles (*e.g.* aluminium oxide) was obtained by adjusting the colour threshold until the particles were black and the rest of the image was white, then measuring the fraction of the image which was black. The particles were assumed to be spherical, such that the area fraction was assumed equivalent to the volume fraction.

The grain size of a material is typically measured using an intercept method, such as those described by the ASTM E112-13 standard [171]. However, these methods are more suited to equiaxed grains; for rectangular grains such as those of MAX phases, the result would be an average of both the length and width. Therefore, a simpler method of measuring the lengths and widths of individual grains was used in order to obtain an estimate of the grain size.

4.3.5 X-ray Photoelectron Spectroscopy

X-ray photoelectron spectra were collected at the Sheffield Surface Analysis Centre using a Kratos Axis Supra DLD with an aluminium source. The data were collected and analysed by Deborah Hammond. Analysis of pristine material was performed on a 110 µm diameter area: survey scans were collected with a 160 eV pass energy between 1200 to 0 eV binding energy with a 1.0 eV interval; high resolution scans were collected in the same range with 40 eV pass energy and 0.1 eV intervals. Analysis of the corroded sample was performed in four locations which were 700 µm by 300 µm: survey scans were collected with a 160 eV pass energy between 1200 to 0 eV binding energy with a 1.0 eV interval; high resolution scans were collected in the same range with 20 eV pass energy and 0.1 eV intervals. A gas cluster ion source (Ar^+, 5 keV) was used to etch samples under vacuum.

4.3.6 Raman spectroscopy

Raman spectra were collected using a Renishaw inVia Raman microscope with a 514.5 nm laser. Spectra were obtained from 10 accumulations, with an exposure time of 60 s. The peak centres were determined by curve fitting with a Voigt peak profile.

4.3.7 Thermal Analysis

Simultaneous thermal analysis was performed using a Netzsch STA 449 F3 Jupiter equipped with a Netzsch QMS 403 D Aëolos mass spectrometer. Samples were placed in alumina crucibles in a glovebox, and exposure to atmosphere was limited as much as possible during transport from the glovebox to the instrument. Heating was performed under an argon atmosphere at a rate of 20°C min^{-1} to a maximum temperature of 1400°C.

4.3.8 Indentation Hardness Testing

Vickers microhardness testing was performed using two instruments. A Mitutoyo HM-101 Hardness Testing Machine was used at a force of 10 kN initially. Later samples were measured using a Struers DuraScan-70 Hardness Tester at 4.9 N for a duration of 10 s. The mean of twelve measurements was used. The HV value was converted to GPa by multiplying by 0.009807 [172].

Nanoindentation hardness testing was performed using an atomic force microscope equipped with a Hysitron TriboScope Nanoindenter and Berkovich diamond tip. A maximum load of 1 kN was used and the area of the resultant indent was measured by atomic force microscopy.

4.3.9 Profilometry

Contact profilometry was performed in order to observe the change in roughness of samples after exposure to molten chloride salts. Profilometry measurements were taken using a Dektak 150 (Veeco) contact profilometer. The parameters were as follows: 3 mm scan length; 0.333 μm resolution; 30 s per scan; 3.00 mg stylus force; and 12.5 μm stylus radius. The mean roughness was determined from five scans.

4.4 Electrochemical Methods

4.4.1 Apparatus

Further details of the electrochemical apparatus used in this work can be found in the PhD thesis by Hugues Lambert [42]. A brief description is provided here. In summary, the system consisted of a sealed vessel which could maintain a controlled atmosphere, allowed for insertion and removal of electrodes, and was heated by a well furnace.

The vessel used is detailed in Figure 18. A custom designed quartz vessel and borosilicate lid were used to maintain a controlled atmosphere (argon or vacuum) whilst conducting experiments. This vessel was placed inside a well furnace as the heat source. The molten salt was contained in an alumina crucible which was placed at the bottom of the quartz vessel. The borosilicate lid was separated from the quartz vessel using a ring of mica, and the two parts were sealed together using a stainless-steel clamp. Ports on the borosilicate lid allowed gas lines to be connected to the vessel and electrodes or thermocouples to be inserted.

A diagram of the gas system is shown in Figure 19. The gas inlet was connected to a Schlenk line, which enabled switching between argon gas and vacuum. The argon gas passed through a drying column before entering the vessel. The gas outlet was connected to a drying column and bubblers to prevent gases such as HCl or Cl_2 escaping.

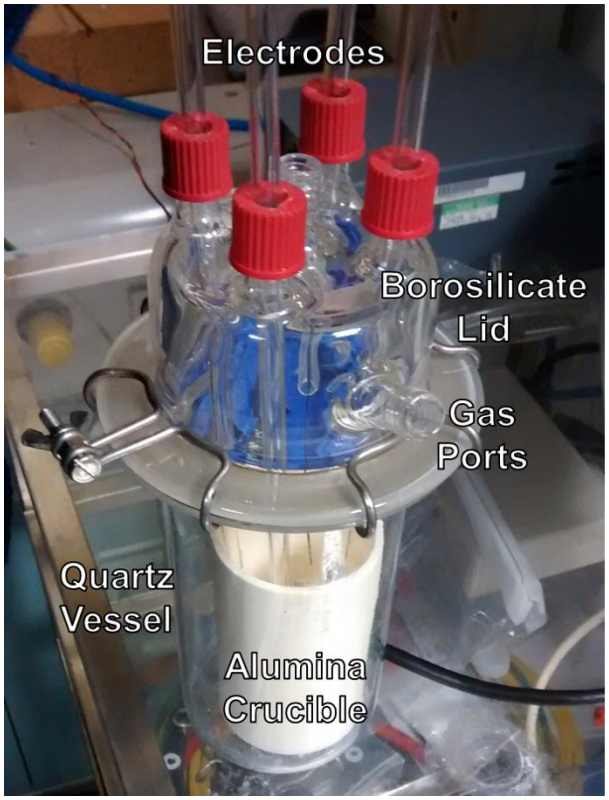

Figure 18 – Labelled photograph of vessel used for electrochemical experiments.

The potentiostat was an Autolab PGSTAT101. A coil of 0.5 mm diameter molybdenum wire was used as the counter electrode. A 1.0 mm diameter tungsten wire was used as the working electrode for electrochemical processes regarding the salt. For electrochemical processes regarding a sample of material, the sample was wrapped in 0.5 mm diameter molybdenum wire and suspended in the salt.

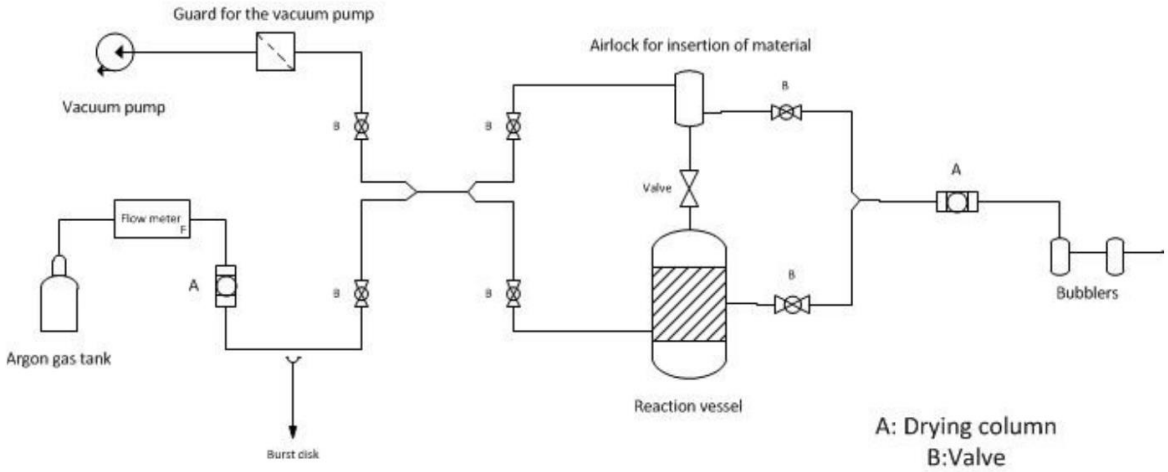

Figure 19 – Diagram of the gas system used for electrochemical work; reproduced from [42].

The reference electrode used an Ag/AgCl redox couple [42,173]. A dilute solution of AgCl in LKE was prepared with a concentration of AgCl of 1wt.% in some earlier experiments then 1.5wt.% in all later experiments. This was then placed at the bottom of a mullite sheath. The ionic conductivity of the mullite sheath acts as a salt bridge between the reference electrode and the system of interest. The very high resistance ensures the potential difference across the sheath is negligible. A 2 mm diameter silver rod was placed within the sheath (with sealant used at the top) to complete the redox couple and enable its connection to the potentiostat.

The potential of the system at a given temperature can be converted to that of the Cl_2 reference electrode by calculating the potential of the Ag/AgCl couple using the Nernst equation and adding this to the potential measured. The Nernst equation for this system is represented by Equation 30, where E_{AgCl} (in V) is the observed potential of the couple, E^o_{AgCl} (in V) is the standard potential of the couple, R (equal to 8.314 J K^{-1} mol^{-1}) is the universal gas constant, T (in K) is the temperature of the system, z (no units) is the number of electrons transferred in the redox reaction, F (equal to 96485 C mol^{-1}) is the Faraday constant, and x_{AgCl} (between 0 and 1) is the mole fraction of AgCl in the system. The mole fraction for 1wt.% AgCl is 0.0039, and that for 1.5wt.% AgCl is 0.0059. The standard potential for AgCl can be calculated at a given temperature using Equation 31 [174].

Equation 30

$$E_{AgCl} = E^0_{AgCl} + \frac{RT}{zF} \ln x_{AgCl}$$

Equation 31

$$E^0_{AgCl} = -1.0910 + 0.0002924 \cdot T$$

4.4.2 Salt Cleaning Procedure

Two compositions of salt were used in this work, an LiCl-KCl eutectic (59.5:40.5mol.%) and a KCl-$MgCl_2$ eutectic (68:32mol.%). Initial experiments used the salts, LiCl, KCl and $MgCl_2$, as purchased – these salts are referred to as as-received salts. Later experiments used salts which were cleaned and dried via the method used by Hugues Lambert [42], and are referred to as processed salts. Both as-received and processed salts were used for corrosion tests to understand the effectiveness of the cleaning procedure. The cleaning and drying procedure is described as follows.

After weighing (total mass ~200 g), the salts were placed in an alumina crucible inside the electrochemical cell. The cell was sealed and purged, then heated under vacuum to 200°C for LKE or 300°C for KME overnight to evaporate moisture (temperatures were determined from DTA

measurements, see [43]). Following this, the cell was heated under vacuum to 550°C for LKE and 650°C for KME. Electrolysis was performed by applying a positive current of 99 mA for 60 min to produce chlorine at the working electrode and deposit lithium (in LKE) or potassium (in KME) at the counter electrode. Chlorine reacts with oxides and hydroxides causing evolution of oxygen gas and dissolving metallic impurities as chloride salts. Lithium and potassium then react with any metallic impurities causing them to plate-out on the counter electrode, although the process occurs over the course of an hour or so. Cyclic voltammetry was used before and after cleaning to determine the presence and absence of impurities. If impurities were still observed after leaving the system to equilibrate, current was applied for longer.

Figure 20 shows a cyclic voltammogram for clean LKE at a scan rate of 200 mV s^{-1}. The potential window is formed by LiCl: at negative potentials, the cathodic and anodic processes represent reduction and oxidation of lithium respectively. The anodic process at the positive potential is oxidation of chloride ions. The absence of peaks within this window indicates that the salt is clean.

Figure 21 shows a cyclic voltammogram of KME after cleaning. The scan rate was 200 mV s^{-1}. The electrochemical window is formed by the electrolysis of KCl: at negative potentials, the cathodic and anodic processes represent reduction and oxidation of potassium respectively. Note that these processes occur at more negative potentials relative to lithium. At positive potentials, the anodic process is oxidation of chloride ions, the same as with LKE. The small anodic peak at ~0.3 V is dissolution of tungsten and the cross-over indicates tungsten deposition [42].

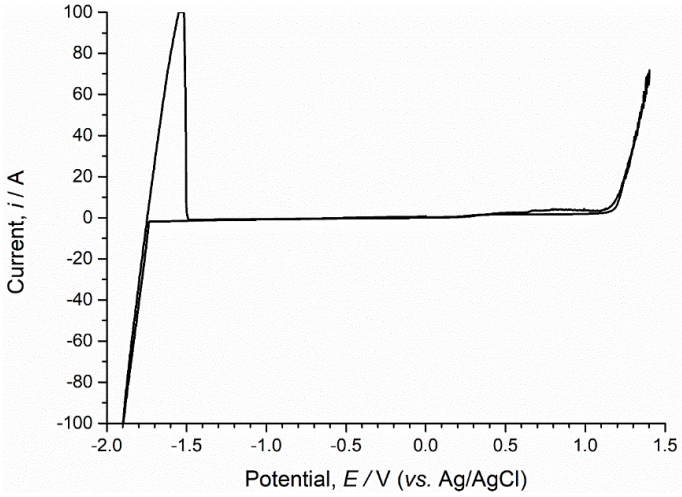

Figure 20 – Cyclic voltammogram of LiCl-KCl eutectic after cleaning procedure.

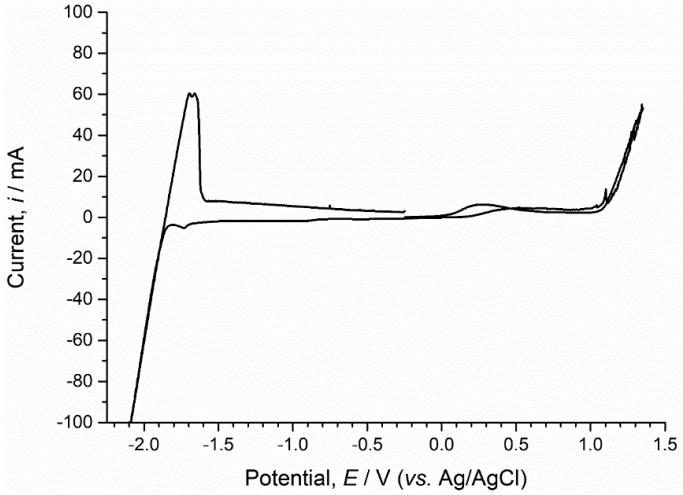

Figure 21 – Cyclic voltammogram of KCl-$MgCl_2$ eutectic after salt cleaning procedure, taken at a scan rate of 200 mV S^{-1}.

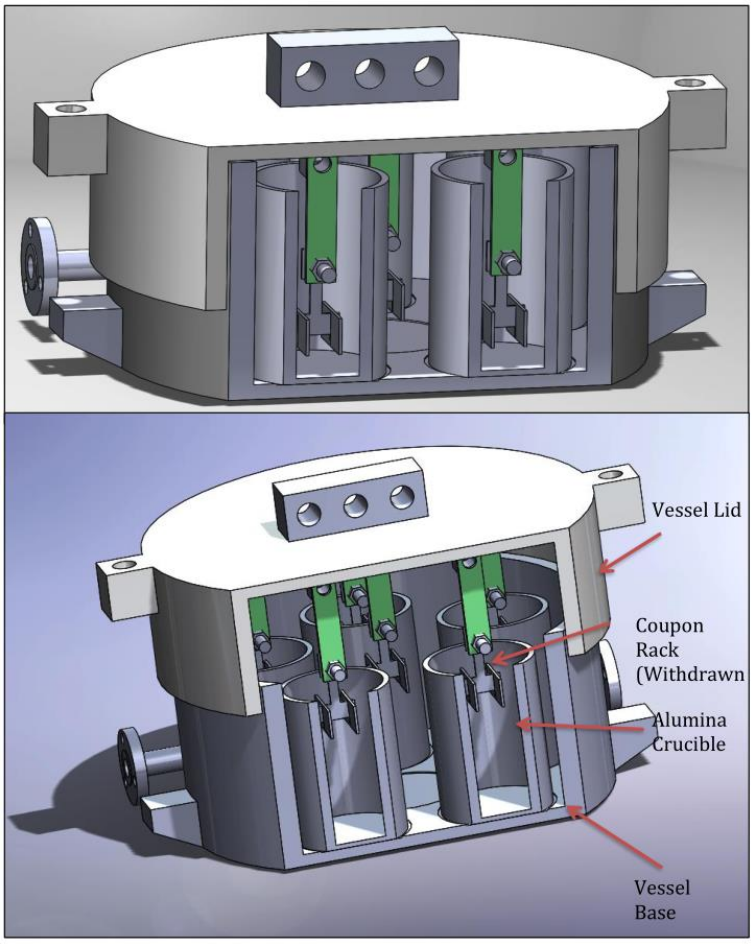

Figure 22 – Diagram of vessel used for static corrosion tests; reproduced from [43].

4.5 Static Corrosion Testing

Static corrosion tests were conducted predominantly in alumina crucibles (an initial test used a nickel crucible) inside the vessel depicted in Figure 22, designed by Craig Jantzen at the University of Manchester [43]. An inlet and outlet valve on the vessel enabled use of an argon gas flow, limiting the presence of air and moisture. The vessel was designed to be able to open the furnace at 500°C to raise the lid and suspend the samples above the salt for the duration of cooling. However, due to greater oxidation of the vessel than expected this was not possible.

Samples were removed from their crucibles by dissolving the salt in warm water. They were then cleaned in distilled water for 5 min in an ultrasonic bath, then isopropanol for 5 min in an ultrasonic bath to aid drying. However, in many cases corrosion products began to dissociate from the samples: in such cases, sonication was stopped, and the sample was left in distilled water for 5 min for salt to dissolve. In other words, retention of corrosion products for chemical and microstructural analysis was favoured over accurate gravimetric analysis. When dry, the samples were weighed, and the mass loss was calculated with respect to the initial surface area.

The parameters of all static corrosion tests are presented in Table 7. Ti_3AlC_2 was studied most extensively. For the test in as-received salt, the sample of Ti_3AlC_2 in KME was accidentally switched with the sample of Maxthal 312 in LKE.

A single sample of Ti_3AlC_2 also underwent an initial experiment in as-received LKE at 600°C for 116 h. The sample was suspended from the vessel by molybdenum wire to expose as much of the surface area to the salt as possible and to enable the sample to be raised from the salt during cooling. However, a nickel crucible was used which caused an electrical circuit to form, accelerating corrosion by dissimilar materials corrosion. Additionally, due to degradation of the vessel it was not possible to raise the lid during cooling.

Table 7 – Matrix of static corrosion test conditions.

Salt	**Ti_3AlC_2**	**Maxthal 312**	**TiC**
LKE, as-received	600°C – 125 h	-	600°C – 125 h
LKE, processed	600°C – 125 h, 250 h	600°C – 125 h	600°C – 125 h
	850°C – 125 h	850°C – 125 h	850°C – 125 h
KME, as-received	-	600°C – 125 h	600°C – 125 h
KME, processed	600°C – 125 h, 250 h	600°C – 125 h	600°C – 125 h
	850°C – 125 h	850°C – 125 h	850°C – 125 h

Figure 23 – Samples suspended by nickel wire in as-received salts.

Following this, samples of all three materials were exposed to as-received LKE and KME at 600°C for 125 h. The samples were suspended from a stainless-steel bar using nickel wire. Mica was placed between the bar and the wire to provide electrical insulation (Figure 23). Alumina crucibles were used for the Ti_3AlC_2 and Ti_3SiC_2 samples and nickel crucibles were used for the TiC samples due to lack of availability of alumina crucibles. The heating profile is described as follows. The temperature was raised to 200°C at a rate of 5°C min^{-1}. The temperature was held at 200°C for 2 h to dry the salt. The temperature was then raised further to 600°C at a rate of 5°C min^{-1}. The temperature was held at 600°C for 125 h. The furnace was then cooled to room temperature naturally.

Following this, all experiments used processed salts and were conducted in alumina crucibles with alumina lids and without suspension of samples. All three materials were exposed to both eutectics at 600°C and 850°C for 125 h. Samples of Ti_3AlC_2 were also exposed to both eutectics at 600°C for 250 h. For the test at 850°C, one end of each sample was raised on an alumina nut to try to expose as much of the surface area as possible.

5 Synthesis and Characterisation

A synthesis method was developed to produce samples of MAX phase materials of the highest possible purity and minimise the influence of impurity phases during corrosion. It is well known that pure MAX phases are currently difficult to produce, and commercial materials are typically less than 90% pure [52]. A summary of samples of Ti_3AlC_2 which were produced and characterised can be found in Table 8.

Ti_3AlC_2 was chosen as the initial composition for corrosion testing. Its synthesis has undergone significant study, so data is readily available for comparison. Ti_3SiC_2 and Ti_2AlC have also undergone significant study and would have been the next logical steps for synthesis.

Synthesis was initially performed using TiC as the carbon-containing reagent using variables suggested by Zou *et al*. [74], albeit with a different milling method. Their research indicated that TiC forms as an intermediate in the reaction between Ti, Al and C, so it was understood that using TiC as a reagent would eliminate this reaction step. However, replication of work in the literature proved unsuccessful, and product purity was low with the variables used. These results are summarised in Appendix B.

A further review of the literature suggested that TiC hinders the formation of a pure product as it is thermodynamically stable and must decompose to form Ti_3AlC_2. A precursor method was adopted based on the work of Riley and Kisi (see Literature Review) [77,84,85]. A non-stoichiometric binary carbide precursor was formed by milling titanium and graphite, which then underwent reactive sintering in the presence of the A-group element to form a pure MAX phase. The milling equipment and parameters in this work differed to those used by Riley and Kisi, and SPS was used for the reactive sintering step as opposed to pressureless sintering.

The reagents were handled under an inert argon atmosphere due to their pyrophoric nature. Thus, options for milling were limited to equipment with vials which could be sealed in a glovebox. Initially, a Retsch cryomill was used at room temperature to produce a TiC_x precursor, and reactive sintering with aluminium via SPS resulted in >98% pure Ti_3AlC_2 (see Appendix B). However, this mill was later deemed unsuitable for further work due to loosening of the vial during milling.

Consequently, access to a SPEX 8000M Mixer/Mill was obtained to produce precursors for further samples. However, this mill operates at significantly higher energy and the results were not directly transferable; a tungsten carbide vial and milling media were used instead of hardened steel, and the ball-to-powder mass ratio was lower, with two 11.2 mm diameter balls being used instead of one 25 mm diameter ball. This resulted in an increase in the number of balls, which is preferable for more efficient milling, but lowered the BPR from 8.4 to 3.3. Furthermore, the milling media differed to that used by

Riley and Kisi, who used a hardened steel vial with six 5 mm and three 10 mm hardened steel ball bearings and a BPR of 10:1 [72]. The effects of several variables were investigated; most significantly, the effects of milling time, sintering temperature and aluminium content were studied to understand the reaction mechanism better. Synthesis with a non-precursor method confirmed the precursor method was superior. The method was also applied to the synthesis of Ti_3SiC_2 with promising results (see Appendix B), but further optimisation of parameters is required to improve purity.

It is clear that milling is a key step in the production of pure MAX phases via this method. As such, the milled powders have been characterised by XRD and thermal analysis.[2] However, further study is required to fully determine how milling can be optimised to produce pure MAX phase materials and to replicate the work with further MAX phase compositions.

The following reaction mechanism has been proposed for this synthesis method, and the results which follow provide evidence for this mechanism. Milling titanium and graphite caused diffusion of graphite into the titanium structure without spontaneous, exothermic recrystallisation to titanium carbide. In the presence of aluminium, when the temperature was raised above 642°C, titanium and aluminium reacted exothermically to form Ti_3Al. Further temperature rise caused Al and Ti_3Al to melt, quickly followed by formation of TiC_x and intercalation of Al into the non-stoichiometric titanium carbide structure. The molten Ti-Al continued to fill gaps between particles, aiding densification and mass transport and enabling any remaining Ti-C to dissolve in the melt and recrystallise in the presence of aluminium to TiC_x, followed by intercalation of aluminium to form Ti_3AlC_2.

[2] A key challenge of such research is handling the pyrophoric materials appropriately, limiting the possibilities for characterisation with standard equipment.

Table 8 – Summary of Ti_3AlC_2 synthesis and characterisation.

Variation	Composition	Milling Parameters		Sintering Parameters		Al Content	Percentage by Mass / wt.%			Lattice Parameters / Å			Rietveld Fitting Statistics			Density	
		Milling Time (min)	BPR	Temperature (°C)	Dwell Time (min)		Ti_3AlC_2	TiC_x	$TiAl_3$	Ti_3AlC_2 a	Ti_3AlC_2 c	TiC_x a	χ^2	R_p	wR_p	Observed (g cm^{-2})	Relative (%)
milling time	Ti-C, Al	60	3.3	1350	15	1.0	88	12	-	3.080	18.610	4.332	3.011	0.081	0.105	4.292 ± 0.006	99
milling time	Ti-C, Al	120	3.3	1350	15	1.0	95	5	-	3.078	18.594	4.331	3.357	0.082	0.109	4.276 ± 0.002	100
milling time	Ti-C, Al	180	3.3	1350	15	1.0	85	15	-	3.079	18.607	4.332	2.900	0.078	0.102	4.208 ± 0.005	97
milling time	Ti-C, Al	(continuous) 240	3.6	1350	15	1.0	30	70	-	3.081	18.624	4.331	2.508	0.073	0.095	4.396 ± 0.011	99
non-precursor	Ti-Al-C	120	3.3	1350	15	1.0	87	13	-	3.080	18.612	4.333	2.614	0.075	0.097	4.243 ± 0.005	98
temperature	Ti-C, Al	120	3.3	1250	15	1.0	85	9	6	3.079	18.607	4.335	2.829	0.078	0.100	4.196 ± 0.010	98
temperature	Ti-C, Al	120	3.3	1300	15	1.0	89	11	-	3.081	18.622	4.333	2.700	0.076	0.098	4.283 ± 0.003	99
temperature	Ti-C, Al	120	3.3	1400	15	1.0	81	19	-	3.080	18.608	4.332	3.835	0.089	0.117	4.336 ± 0.002	99
Al content	Ti-C, Al	120	3.3	1350	15	1.1	89	11	-	3.081	18.615	4.333	2.269	0.069	0.090	4.158 ± 0.006	97
Al content	Ti-C, Al	120	3.3	1350	15	1.2	87	13	-	3.082	18.626	4.333	2.391	0.071	0.092	4.165 ± 0.004	96
Al content	Ti-C, Al	120	3.3	1350	15	1.3	85	15	-	3.081	18.622	4.333	2.378	0.071	0.092	4.222 ± 0.005	97
Al content	Ti-C, Al	120	3.3	1350	15	1.4	85	15	-	3.082	18.626	4.333	3.198	0.081	0.107	4.181 ± 0.005	96

5.1 Variation of milling conditions

The following samples were prepared by varying the milling time when producing the precursor. Titanium powder and graphite were milled between 1 h and 4 h to produce a precursor, which was then mixed with aluminium and reactively sintered by SPS at 1350°C for 15 min. The molar ratio of reagents was Ti:Al:C 3:1:2. A bulk sample of TiC_x was also produced and characterised, and the effect of milling Ti-Al-C together in one-step for 2 h was investigated in order to verify the effectiveness of the precursor method. Additionally, characterisation of a sample prepared with a hardened steel vial set can be found in Appendix B.

The powders were characterised by XRD (including estimation of crystallite size and lattice strain) and differential thermal analysis. The bulk samples were characterised by XRD and density measurements, and their phase compositions were determined by Rietveld refinement. The microstructure was examined by SEM. Certain samples also underwent micro-indentation hardness testing.

5.1.1 Characterisation of reagents

The reagents used were characterised by XRD and indexed using standards from the ICSD database (Figure 24) [175–177]. All patterns were collected on samples covered with Kapton® polyimide film for comparison with patterns from the air-sensitive milled powders. The film has distinctive amorphous humps at < 30° 2θ.

5.1.2 X-ray diffraction of milled powders

Indexed XRD patterns for the powders milled from 1 h to 4 h are shown in Figure 25. Titanium (5.53 g) and graphite (0.93 g) were used for each sample, with a ball-to-powder mass ratio of 3.3. The powders were milled in 1 h intervals with a pause of at least 10 min between intervals. As the milling time increased, the graphite (200) peak height decreased and the titanium peaks shifted to lower angles. This indicates the dissolution of carbon into titanium as the presence of carbon interstitials increases the d-spacings in the titanium crystal structure, leading to diffraction at lower angles of 2θ. However, sample height displacement errors also lead to shifts in 2θ, the error of which may distort results. The absence of titanium carbide peaks indicates that a spontaneous ignition reaction has not occurred.

The peaks have broadened significantly relative to those in the XRD patterns of the reagent powders due to the reduction in crystallite size and the introduction of carbon interstitials upon milling [90,91]. The crystallite size and lattice strain were calculated after plotting $B\cos\theta$ against $\sin\theta$ as per Figure 26. Note that B is the breadth of peaks determined without subtracting instrumental broadening.

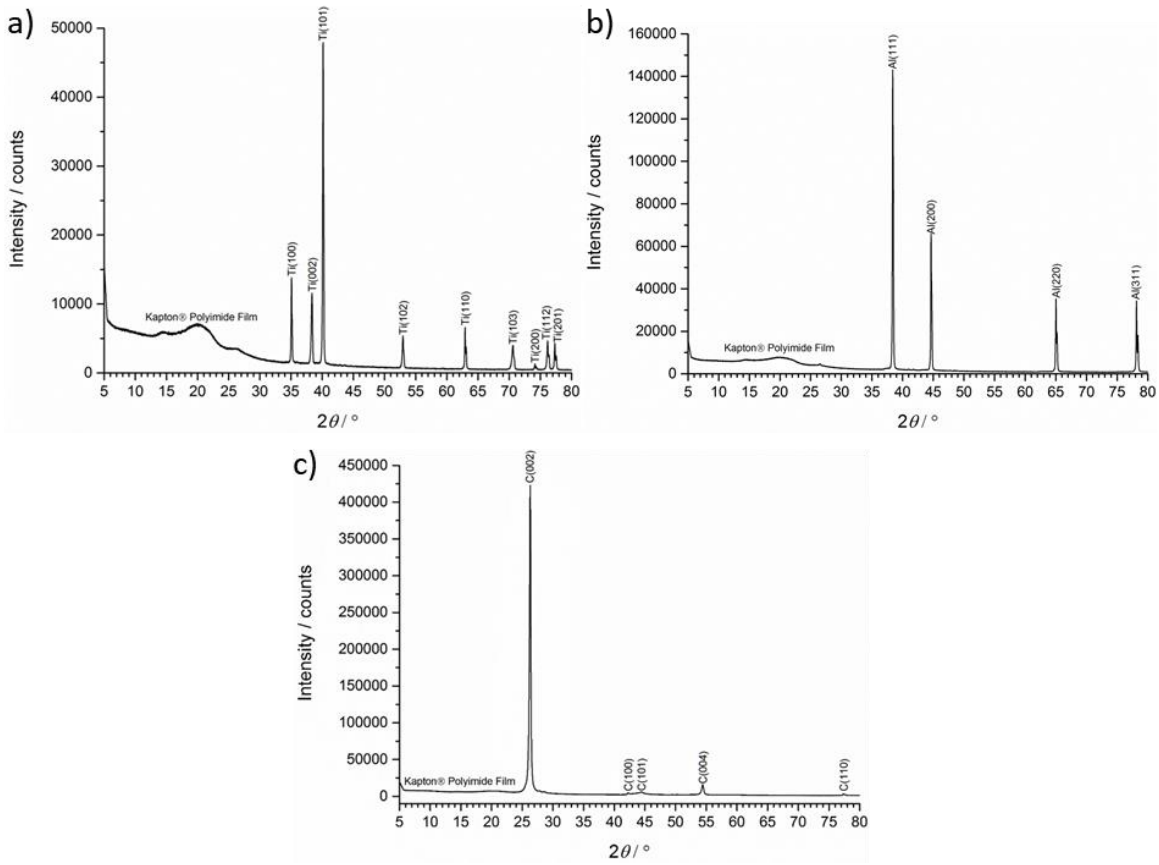

Figure 24 – Indexed XRD patterns of reagent powders under Kapton® polyimide film [175–177]: a) 200 mesh titanium powder¸ 99.5% purity, Alfa Aesar; b) 200 mesh aluminium powder, 99% purity, Acros Organics; c) general purpose grade graphite powder, 99% purity, Acros Organics.

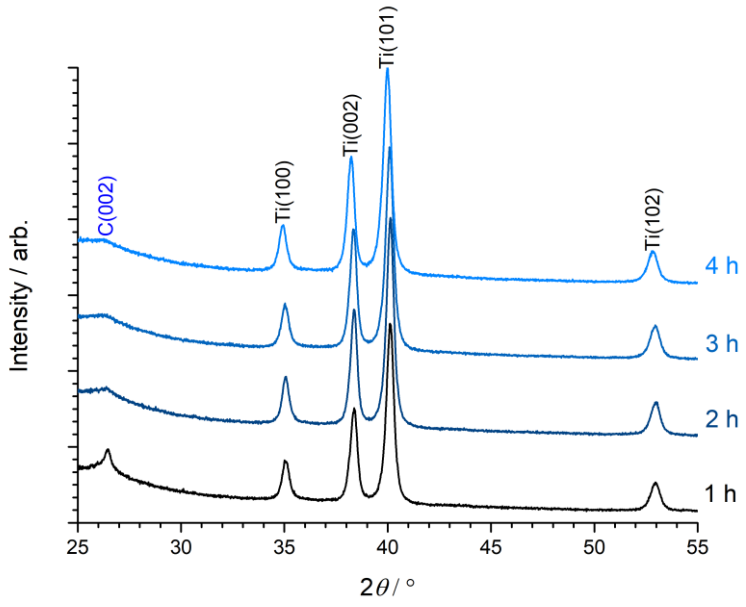

Figure 25 – Indexed XRD patterns for titanium and graphite powders milled for 1 h to 4 h. With increased milling time the graphite peak height decreases, and the titanium peaks shift to lower angles.

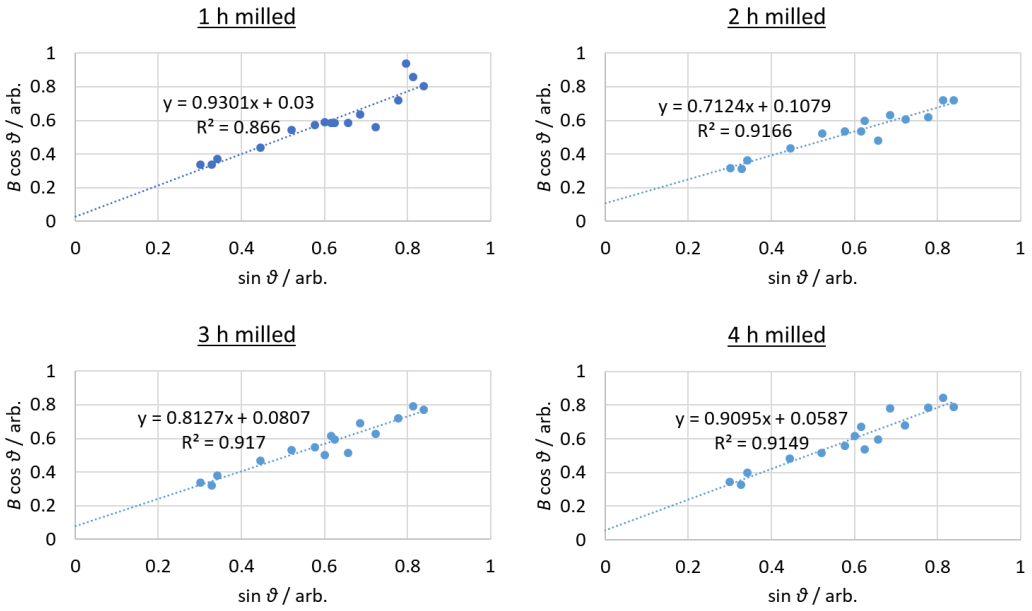

Figure 26 – Plots of $B \cos \theta$ versus $\sin \theta$ used to determine the crystallite size and lattice strain of Ti-C powders milled from 1 h to 4 h.

The variation of crystallite size and lattice strain with milling time is shown in Figure 27; these results are summarised in Table 9 along with their fitting statistics. Both the crystallite size and lattice strain are relatively large after 1 h milling, decreasing after 2 h and followed by an increase. The large crystallite size and lattice strain for the sample milled for 1 h was due to insignificant reaction between Ti and C, as indicated by the presence of the graphite (002) peak in the XRD pattern. The graphite peak was hardly visible after 2 h, although it was obscured slightly by the Kapton film. The crystallite size and lattice strain also decreased to the lowest values observed. Milling for 2 h also resulted in the greatest fraction of Ti_3AlC_2 in the product, suggesting these factors affect the synthesis process. The increase of crystallite size and lattice strain at 3 h and 4 h are likely due to increased Ti and C interdiffusion with milling time, leading to greater agglomeration of crystallites and formation of defects. The increase in crystallite size was not due to the formation of TiC_x by ignition, which would likely be accompanied by grain growth, because the peaks in the XRD patterns remained as Ti peaks.

Table 9 – Fitting statistics for variation of crystallite size and strain with milling time.

Milling Time / h	Crystallite Size / nm	Lattice Strain / nm	Whole Powder Pattern Fit R_{wp}	Linear Fit R^2
1	51	0.93	3.95	0.886
2	14	0.71	4.05	0.9166
3	19	0.81	4.07	0.917
4	27	0.91	4.24	0.9149

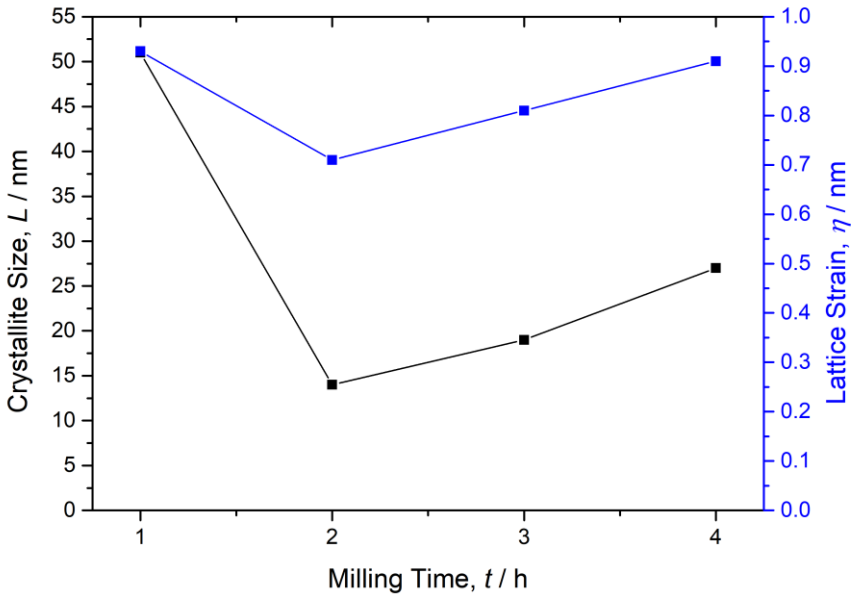

Figure 27 – Variation of crystallite size and lattice strain with milling time.

A sample was also prepared by milling titanium (5.14 g) with graphite (0.86 g) continuously for 4 h, rather than in 1 h intervals with cooling. The indexed XRD pattern is shown in Figure 28, collected on a Bruker D2 Phaser with a step size of 0.1° 2θ. The XRD pattern for titanium powder was also collected to distinguish which peaks were due to the sample holder. Titanium carbide formed upon milling as opposed to the broadened titanium peaks which were observed when milling for 4 h in 1 h intervals with 10 min cooling between intervals. The ball-to-powder mass ratio of 3.6 (*c.f.* 3.3) was slightly greater, suggesting the change was a combination of reduction of the ignition temperature, and the temperature being greater than the ignition temperature due to lack of cooling. The lattice parameter, *a*, was calculated for the four peaks shown, and the mean was 4.327 ± 0.002 Å. Note that this value has limited accuracy because instrumental shifts in 2θ have not been accounted for; however, the value is more consistent with that of stoichiometric TiC rather than $TiC_{0.67}$ [89].

The indexed XRD pattern of powder produced by milling Ti-Al-C for 2 h in one step is shown in Figure 29 [175–177]. The peaks have broadened relative to those in the XRD patterns for the reagent powders. This broadening is due to a reduction in crystallite size and the introduction of defects such as carbon interstitials [90,91]. The graphite peak at 26° 2θ is obscured by the Kapton® polyimide film and may or may not be present. No additional phases such as TiC_x or Ti-Al intermetallics are visible.

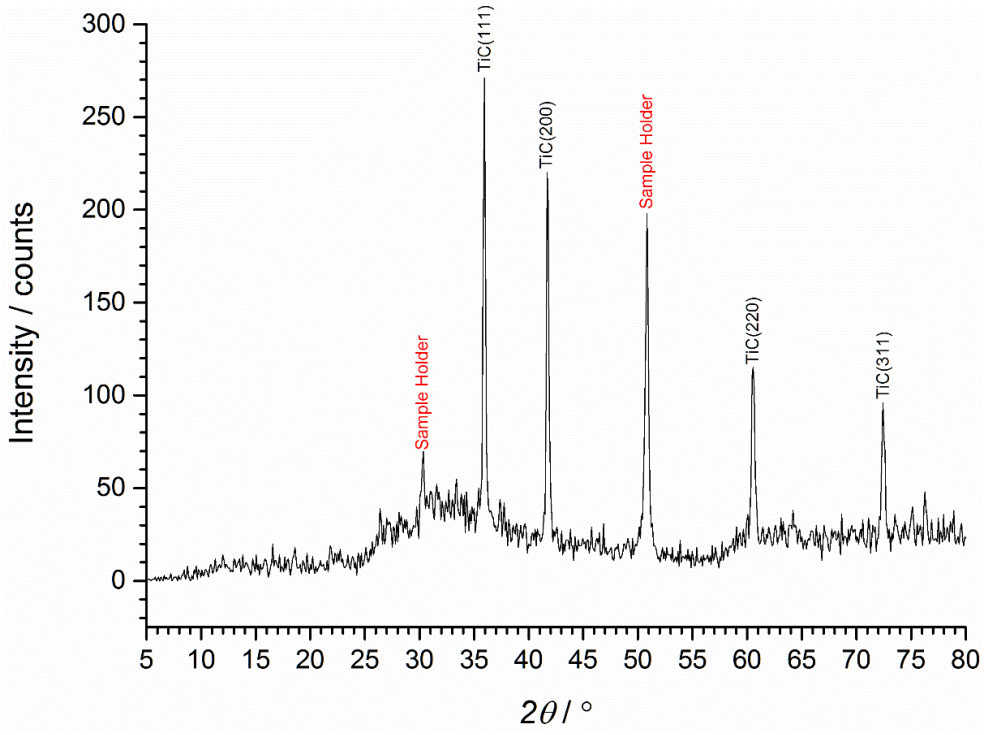

Figure 28 – XRD pattern of a powder sample prepared by milling Ti and C continuously for 4 h in a SPEX 8000M Mixer/Mill.

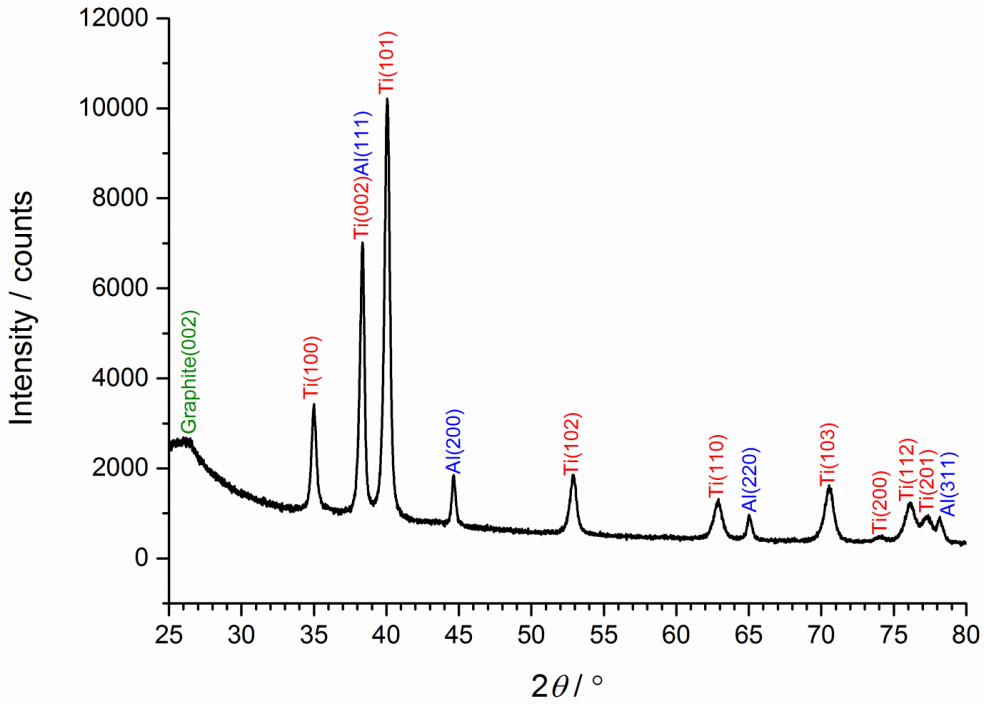

Figure 29 – XRD pattern of Ti, Al and C powders milled for 2 h.

5.1.3 Thermal analysis of milled powders

The differential thermal analysis results for powders milled from 1 h to 4 h are shown in Figure 30, and the temperatures of peak centres are summarised in Table 10. No significant changes were observed in the TG and mass spectroscopy data. Argon was used as the cover gas so reactions with the atmosphere were not expected, and the results show that no volatile phases formed during reaction. The DTA results show broad exothermic peaks for all four samples. However, with increased milling time the centres of these peaks shifted to lower temperatures and the peak areas and maximum heat flow increased. Two peaks are clearly observed for the sample which was milled for 1 h. Furthermore, there appear to be some shoulders, suggesting that curve fitting is required to determine the peak centres more accurately.

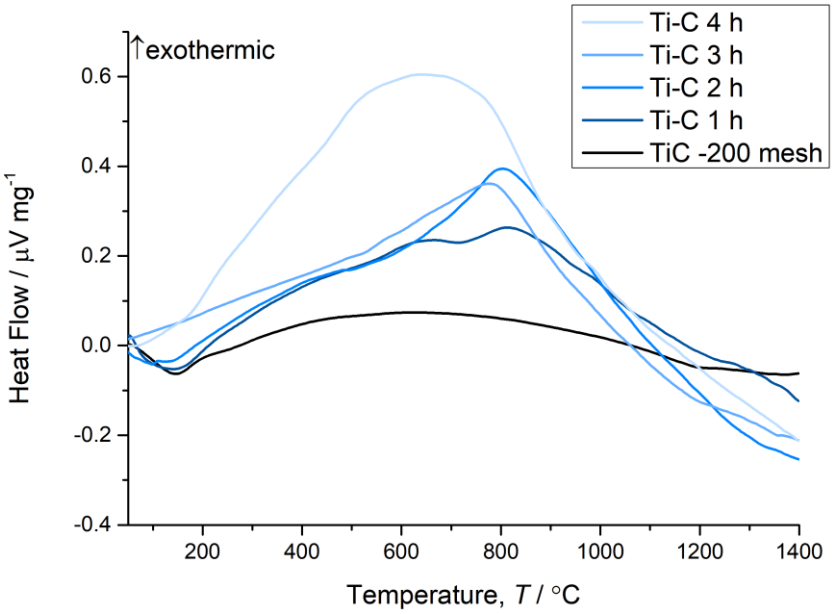

Figure 30 – Differential thermal analysis of powders of Ti and C milled from 1 h to 4 h.

Table 10 – Peak centres in DTA data shown in Figure 30 and Figure 32. The positions were determined from the highest points in the DTA curves.

Sample	Peak Centres / °C
Ti-C 4 h	642
Ti-C 3 h	775
Ti-C 2 h	805
Ti-C 1 h	666, 813
Ti-Al-C	641, 649 (trough), 685, 785, 874

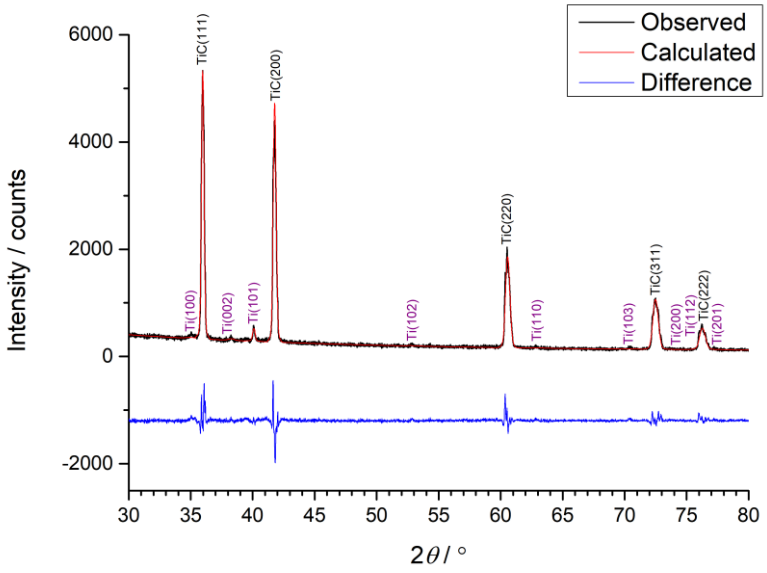

Figure 31 – Indexed XRD pattern and Rietveld refinement fit for a sample of Ti-C which was milled for 2 h then heated to 1400°C during STA. The major phase is TiC_x, with unreacted Ti as the minor phase.

Titanium carbide powder (2 µm) was also analysed for comparison. A broad exothermic peak with low peak height was observed, as well as some endothermic processes which overlap with those of the other powders. At 100-200°C, there is a small endothermic peak which was also observed for the 1 h and 2 h milled powders. This could represent volatilisation of an impurity such as water but should have been observed by mass spectroscopy. There is a steady decrease in heat flow at higher temperatures which most likely represents sintering.

The indexed XRD pattern for the Ti-C sample which was milled for 2 h after it was subject to thermal analysis is shown in Figure 31 along with the Rietveld refinement fit (χ^2 2.245, Rp 0.0762, wRp 0.0987) [178,179]. TiC_x was observed as the major phase, with a weight fraction of 97wt.% and a lattice parameter, a¸ of 4.325 Å. The secondary phase was unreacted Ti, with a weight fraction of 3wt.% and lattice parameters *a* and *c* of 2.957 Å and 4.701 Å respectively.

The exothermic reactions observed by DTA represent the formation of TiC_x, as confirmed by XRD of the 2 h milled powder after it underwent STA. Shift of the peak centres to lower temperatures is consistent with reduction in ignition temperature with milling time. However, it is interesting that the peaks are broad, as a self-sustaining ignition reaction would be expected to result in a spike. The increase in peak area with milling time is consistent with production of a broader range of particle sizes, including generation of smaller particles. The breadth of the peaks suggests that the smallest particles react first. It is likely that the peaks observed for the milled powders reveal the point at which the energy absorbed by sintering and reordering of vacancies and carbon interstitials exceeds that of the energy

released by formation of TiC_x. The height of the peak at 3 h was lower than that at 2 h, which is likely because more sintering occurred at lower temperature due to a greater number of smaller sized particles. The 1 h milled powder revealed multiple peaks, one of which represents formation of TiC_x. It is possible that the higher temperature peak represents an order-disorder transition of the carbon vacancies [180–182].

The differential thermal analysis results for a powder of Ti-C which was milled for 2 h then mixed with Al is shown in Figure 32, and the peak centres are summarised in Table 10. No significant changes were observed in the TG and mass spectroscopy data. Multiple peaks were observed for the sample due to the more complex reactions relative to reaction of Ti with C.

The indexed XRD pattern for the sample of Ti-C which was milled for 2 h, mixed with Al, then heated to 1400°C during STA is shown in Figure 33. Rietveld refinement was attempted, but the fit was poor due to significant preferred orientation on the (00*l*) plane. However, the best fit obtained suggested the presence of 91wt.% Ti_3AlC_2 and 9wt.% TiC_x. Furthermore, the best fit was obtained with stoichiometric TiC rather than $TiC_{0.67}$ [179,183].

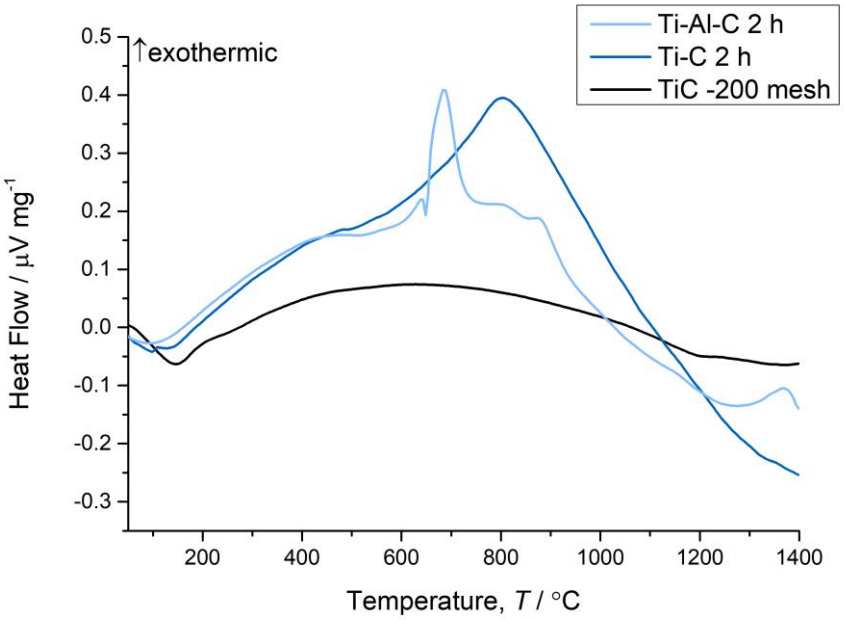

Figure 32 – Differential thermal analysis results for a powder sample of Ti-Al-C. Ti and C were milled for 2 h then mixed with Al. The result is compared to that of Ti-C milled for 2 h and -200 mesh TiC reagent.

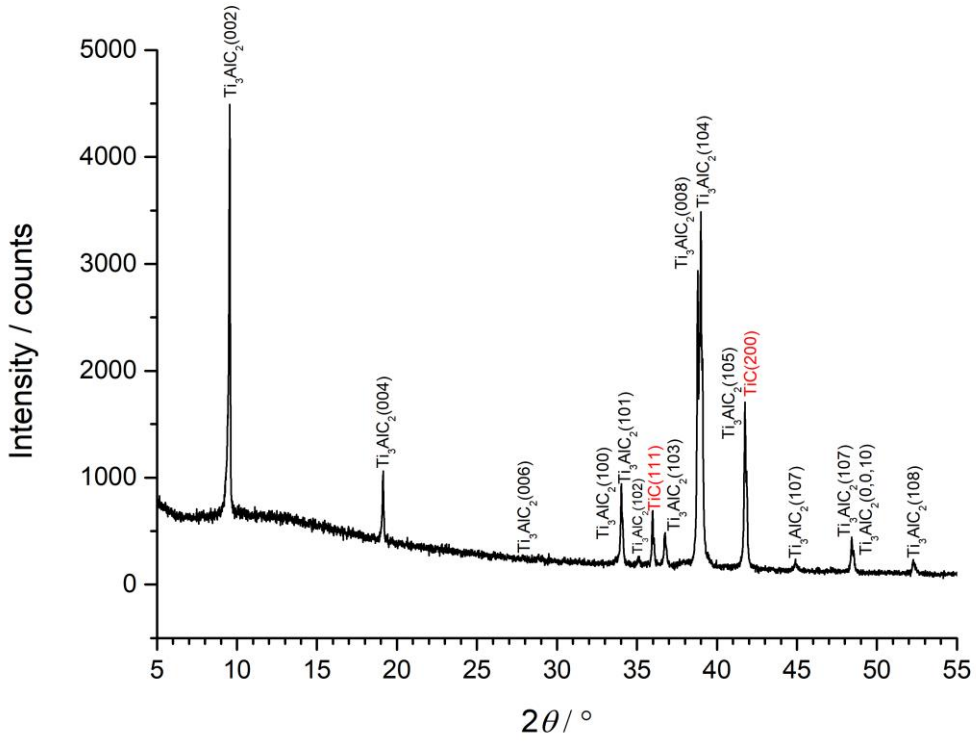

Figure 33 – Indexed XRD pattern of 2 h milled Ti-C which was mixed with Al then heated during STA to 1400°C. The major phase is Ti_3AlC_2, with preferred orientation on the (00*l*) plane, and the minor phase is TiC_x.

Up to ~500°C the heat flow in the DTA data matched that of the 2 h milled Ti-C powder. The heat flow was then slightly lower for the Ti-Al-C powder up to the first peak at 642°C, followed by a dip to 649°C, then a sharp rise to the largest peak at 685°C. Based on the results of Choi and Rhee, the first peak represented the exothermic reaction of Ti with Al to form $TiAl_3$, and the endothermic peak that followed was the melting of Al [184]. Choi and Rhee observed these processes at 656°C and 670°C for the Ti-Al system (molar ratio 1.0), and 654°C and 681°C for the Al-C system (molar ratio 1.0), and the melting point of pure Al is 660°C [184,185]. The impurities introduced by milling caused Al to melt at a lower temperature. The peak for the 2 h milled Ti-C powder was at 805°C, so this melting occurred significantly prior to the formation of TiC_x. The sharp peak for Ti-Al-C at 685°C represents the formation of TiC_x. The peak is sharp because the energy released by $TiAl_3$ formation is sufficient to cause a self-propagating high temperature reaction between Ti and C. The peaks for samples without Al are broad because there is insufficient energy for a self-propagating reaction to occur. Based on the findings of Riley and Kisi, the peaks at 785°C and 874°C most likely represent vacancy ordering and Al intercalation respectively [77,85]. The XRD data suggests that any remaining TiC_x is converted to stoichiometric TiC.

5.1.4 Sintering profiles

The sintering profile for a bulk sample of TiC_x which was prepared from Ti (5.53 g) and C (0.93 g) milled in a SPEX 8000M Mixer/Mill for 2 h then sintered at 1300°C for 15 min by SPS is shown in Figure 34. Most densification occurred as the temperature and uniaxial pressure were increased, with the rate slowing from ~900°C. The piston movement during cooling is due to thermal contraction.

The sintering profile for a sample prepared from 2 h milled powder is shown in Figure 35. The piston movement is significant initially as 10 kN force is applied, densifying the powder. Further piston movement is observed at a slower rate between 500-600°C. At 600°C, the piston movement halts slightly before slowly rising until another halt at around 1150°C. For all the samples of Ti_3AlC_2 produced from a TiC_x precursor, the rate of piston movement slows around 600°C. This is the approximate temperature that aluminium reacts with titanium and melts. The piston movement then slowly rises as TiC_x dissolves in the molten phase until another halt at around 1150°C. At this point, there is a steeper increase in piston movement which begins to slow around 1300°C, indicative of a reaction which causes rapid densification of the material, likely due to vacancy ordering of the TiC_x structure and intercalation of aluminium. This is observed for all Ti_3AlC_2 samples for which sintering profiles were obtained, with a variation in onset temperature up to up to ±100°C (*e.g.* ~1200°C for the 3 h milled sample). No further movement is observed during the dwell period at 1350°C and 16 kN force. There is some final piston movement due to thermal contraction as the sample is cooled.

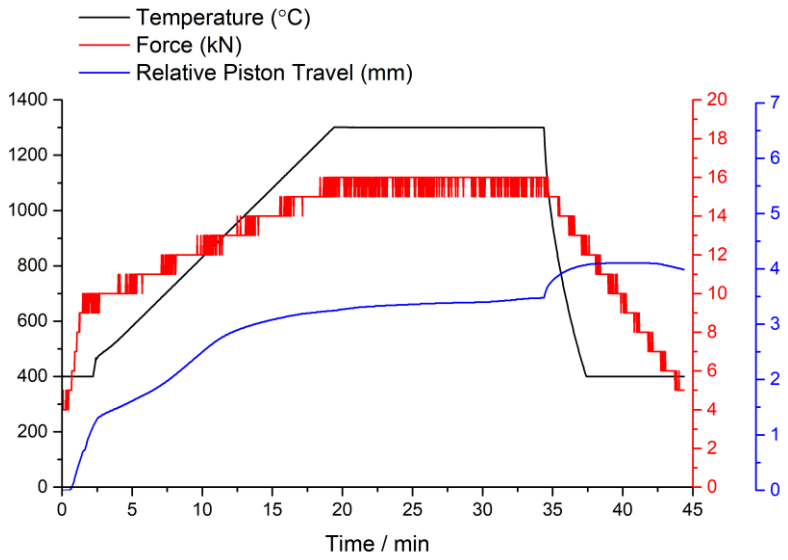

Figure 34 – Sintering profile of a bulk sample of TiC_x. Ti and C were milled for 2 h using a SPEX 8000M Mixer/Mill, then sintered at 1300°C for 15 min by SPS.

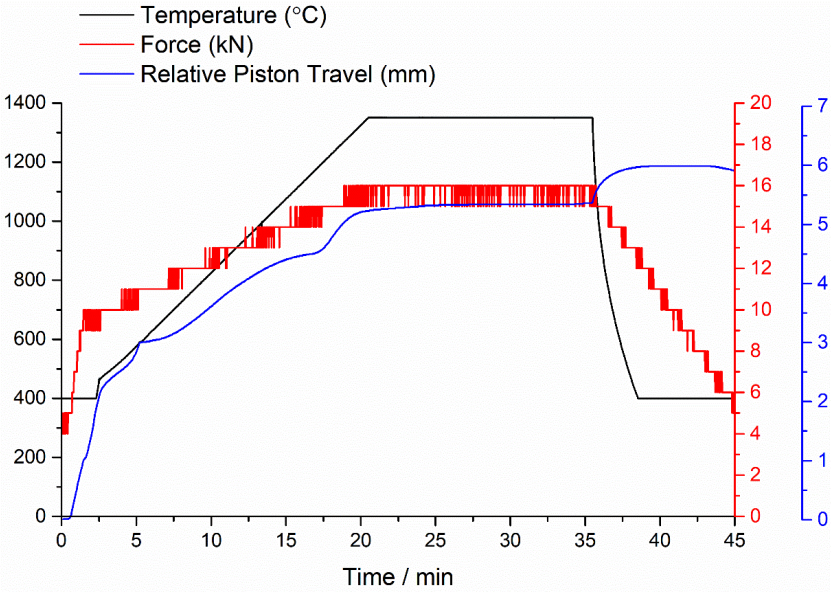

Figure 35 – Sintering profile for a sample which was prepared from a 2 h milled Ti-C precursor.

The sintering profile for a sample prepared from Ti-Al-C which was milled for 2 h in one step is shown in Figure 36. There is significant piston movement at the start as the uniaxial force was applied. Piston movement begins to slow from ~500°C, picks up speed again at ~700°C, slows again at ~1000°C, then speeds up significantly at ~1200°C. According to Zou *et al.* and Yoshida *et al.*, the movement observed at 700°C likely represents the movement of molten Al and Ti-Al, filling the pores of the material and aiding densification [73,76]. This slows around 1000°C as Ti_2AlC begins to form. From 1200°C, Ti_2AlC reacts with TiC to form Ti_3AlC_2, causing further densification.

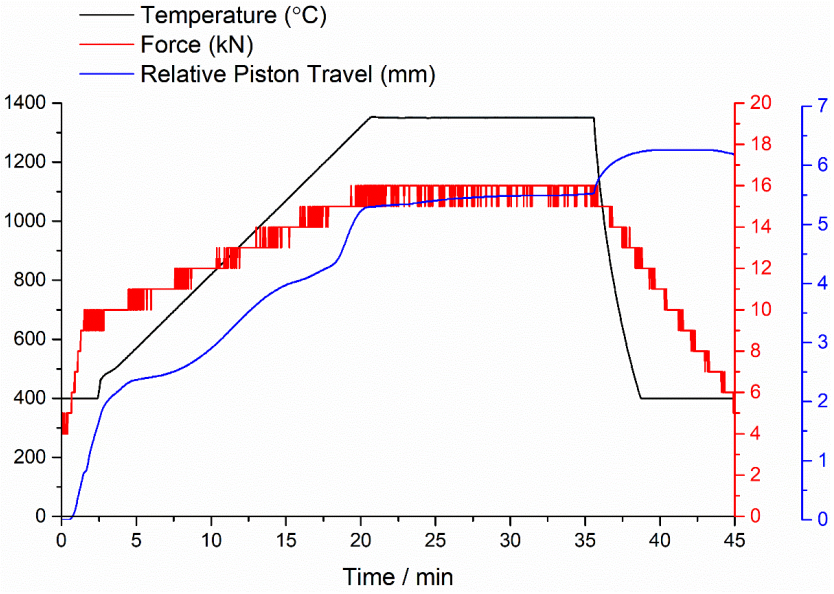

Figure 36 – Sintering profile for a sample prepared by milling Ti, Al and C for 2 h in a SPEX 8000M Mixer/Mill.

In all the samples of Ti_3AlC_2 produced from a TiC_x precursor, the rate of piston movement slows around 600°C. This is the approximate temperature that aluminium melts, so the decrease in piston movement is consistent with the proposed mechanism of Al melting and penetrating into the TiC_x structure. Furthermore, this drop in the rate of piston travel does not appear to be the same for the sample prepared from Ti-Al-C which was milled for 2 h, *i.e.* a non-precursor sample. However, there is a drop at around 550°C in the rate of piston movement which lasts for a longer period of time, which may indicate that aluminium is melting but reacting slower with Ti and C. The lower temperature observed could be due to a lower melting temperature for Ti-Al alloys or intermetallics. This change in piston travel is also not observed for the sample of Ti_3SiC_2 which was prepared from a TiC_x precursor (see Appendix D). It is likely that the reaction between TiC_x and Si occurs more slowly as Si does not melt until a much higher temperature (1414°C) than Al, so a molten Ti-Si phase must form first [185].

There appears to be a further reaction at higher temperature which leads to rapid densification of the material. This is observed for all Ti_3AlC_2 samples for which sintering profiles were obtained, and the Ti_3SiC_2 sample prepared from a TiC_x precursor. For the standard 2 h milled, 1350°C, 1.0 parts Al sample, this temperature is ~1150°C, but the temperature varies by up to ±100°C for other samples. Based on the microstructural examination of samples produced at various holding temperatures, it is likely that this is a reaction between TiC_x and $TiAl_3$ to form Ti_3AlC_2, or similarly $TiSi_2$ to Ti_3SiC_2, via intercalation into the ordered TiC_x structure.

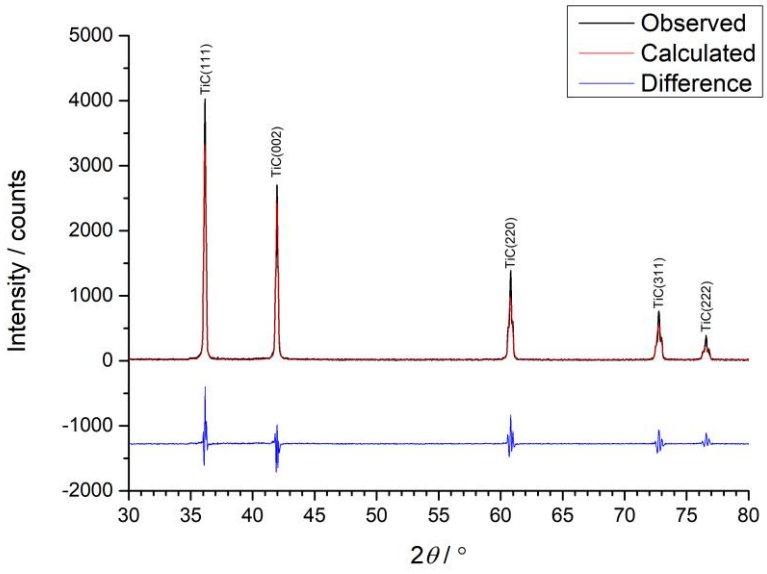

Figure 37 – Indexed XRD pattern with Rietveld refinement difference plot of a bulk sample of TiC_x. Ti and C were milled for 2 h using a SPEX 8000M Mixer/Mill, then sintered at 1300°C for 15 min by SPS.

5.1.5 X-ray diffraction of bulk samples

The indexed XRD pattern for a bulk sample of TiC_x, fitted by Rietveld refinement, is shown in Figure 37 (χ^2 2.389, R_p 0.1563, R_{wp} 0.1985). XRD was conducted on a Bruker D2 Phaser between 5-80° 2θ, with a step size of 0.02° per step and 36.8 s per step. The best match was $TiC_{0.67}$ with a space group of Fm-3m [183]. The lattice parameter, *a*, was 4.314 Å and the cell volume was 80.292 $Å^3$. The density was measured as 4.436 ± 0.010 g cm^{-3}, which is 96% of the calculated density of $TiC_{0.67}$ (4.628 g cm^{-3}).

The product was $TiC_{0.67}$, as expected based on the quantity of powder used. The Rietveld refinement fit was good but has limited accuracy due to the low counting statistics from the XRD data used. No superlattice reflections were observed, indicating the carbon vacancies were disordered, but the (111) peak was more intense than the (200) peak, which confirms the presence of vacancies [180–182]. Furthermore, the lattice parameter was 4.314 Å, which is lower than that typically observed for stoichiometric TiC (for example, the bulk samples of TiC (Appendix E) had a lattice parameter of 4.333 Å). This value corresponds approximately to $TiC_{0.67}$ on the graph of lattice parameter by atomic fraction of carbon produced by Rudy [89]. The lower fraction of carbon interstitials in the $TiC_{0.67}$ sample results in less expansion of the crystal lattice so the lattice parameter is smaller. The lattice parameter is smaller than that for the sample which underwent thermal analysis to 1400°C, but the difference is likely due to the lower heating rate and higher temperature reached for that sample, enabling reordering of vacancies and carbon interstitials.

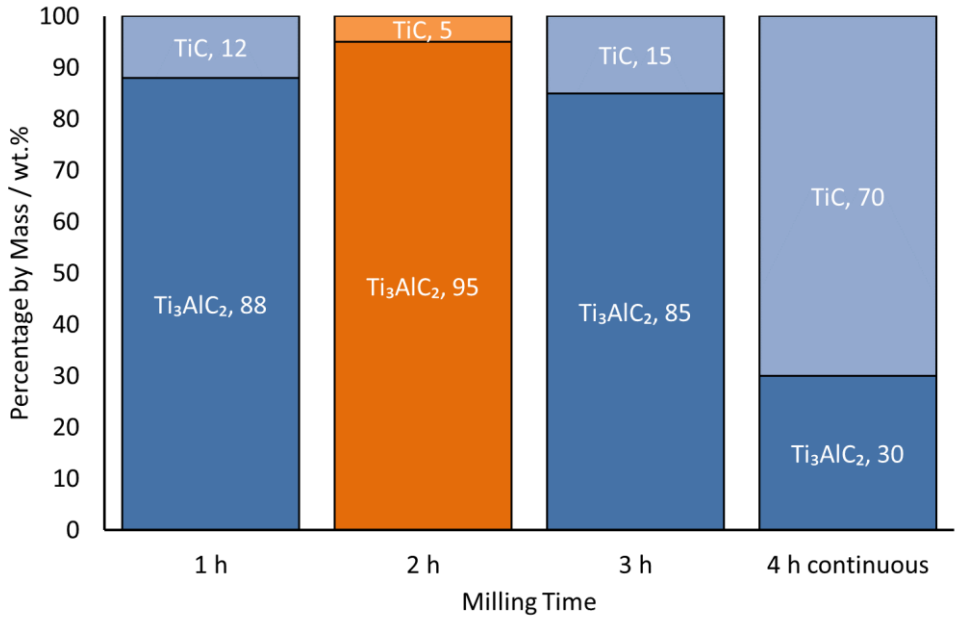

Figure 38 – Bar chart showing the phase compositions of samples formed from powder milled for different lengths of time.

Table 11 – Lattice parameters and fitting statistics from Rietveld refinement of XRD data for samples prepared with different Ti-C milling times.

Milling Time	Lattice Parameters / Å			Fitting Statistics		
	Ti_3AlC_2, *a*	Ti_3AlC_2, *c*	TiC_x, *a*	χ^2	Rp	wRp
1 h	3.080	18.610	4.332	3.011	0.081	0.105
2 h	3.078	18.594	4.331	3.357	0.082	0.109
3 h	3.079	18.607	4.332	2.900	0.078	0.102
4 h (continuous)	3.081	18.624	4.331	2.508	0.073	0.095

The weight fractions for bulk sample of Ti_3AlC_2 produced with different T-C precursor milling times are shown in Figure 38, and the lattice parameters and fitting statistics from Rietveld refinement are shown in

Table 11. The purest product was obtained with a milling time of 2 h. Milling for 4 h continuously significantly reduced the purity of the sintered product, with TiC being the major phase. The XRD patterns of the powders after milling showed only peaks for Ti for the 1 h, 2 h and 3 h sample, whereas only peaks for TiC were present after 4 h continuous milling. This highlights the difficulty of breaking down a stable TiC intermediate. The *a*-axis lattice parameters for Ti_3AlC_2 and TiC_x hardly change, but the *c*-axis lattice parameter for Ti_3AlC_2 contracts for the 2 h milled sample and is largest for the 4 h continuous milled sample.

The indexed XRD pattern for a sample milled for 2 h is shown in Figure 39 [178,186]. The patterns for the 1 h milled and 3 h milled samples were very similar but had more intense TiC_x peaks.

The XRD pattern for a bulk sample prepared from powder milled continuously for 4 h is shown in Figure 40. Before sintering, the XRD pattern of the powder showed the presence of TiC_x only. There is an unidentified peak at approximately 47° 2θ, suggesting the presence of a third phase in low quantity. This sample was prepared by milling Ti (5.14 g) with C (0.86 g), after which 0.83 g of the product was replaced with Al. As such, only 6 g of material was used during SPS, compared to 7.5 g for all other samples. The BPR during milling was approximately the same, albeit slightly greater (3.6 *c.f.* 3.3).

The XRD pattern of the bulk sample produced from Ti-Al-C which was milled for 2 h in one step is shown in Figure 41. The phase fractions were determined by Rietveld refinement indicating 87wt.% Ti_3AlC_2 and 13wt.% TiC (χ^2 2.614, R_p 0.0751, R_{wp} 0.0967). The lattice parameters were similar to those for previous samples. The *a*-axis lattice parameter of Ti_3AlC_2 was 3.080 Å, and that of the *c*-axis was 18.612 Å. The lattice parameter for TiC_x was 4.333 Å. The purity was lower than the sample prepared with equivalent parameters via a TiC_x precursor, indicating the precursor method was superior.

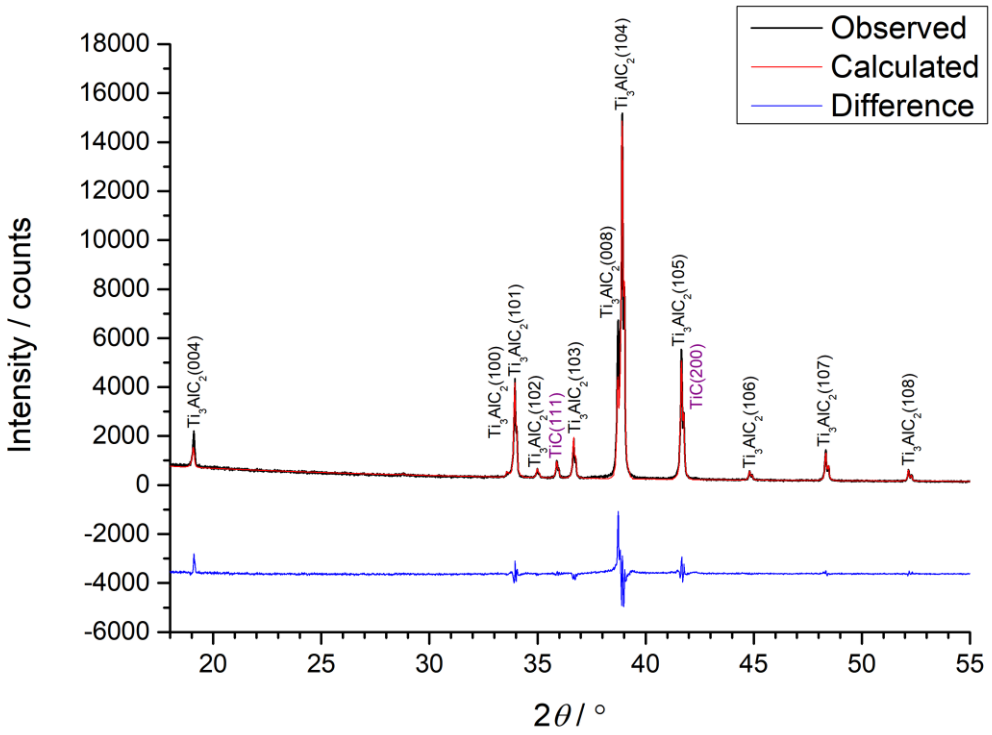

Figure 39 – XRD pattern of a bulk sample prepared from powder milled for 2 h.

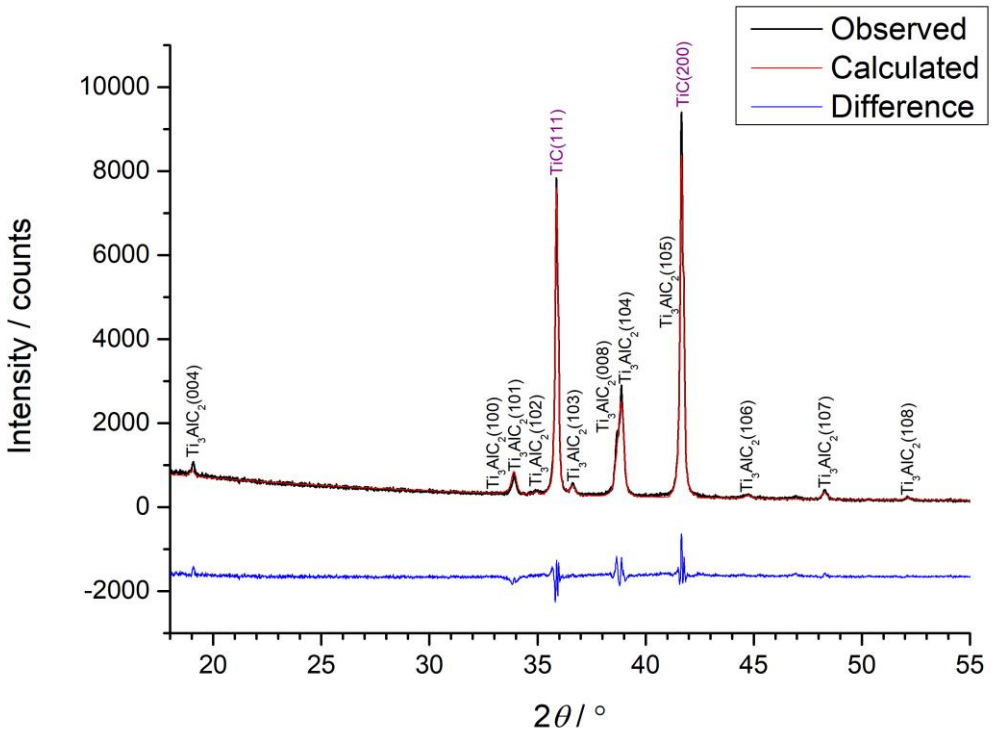

Figure 40 – XRD pattern of a bulk sample prepared from 4 h continuous milled Ti-C.

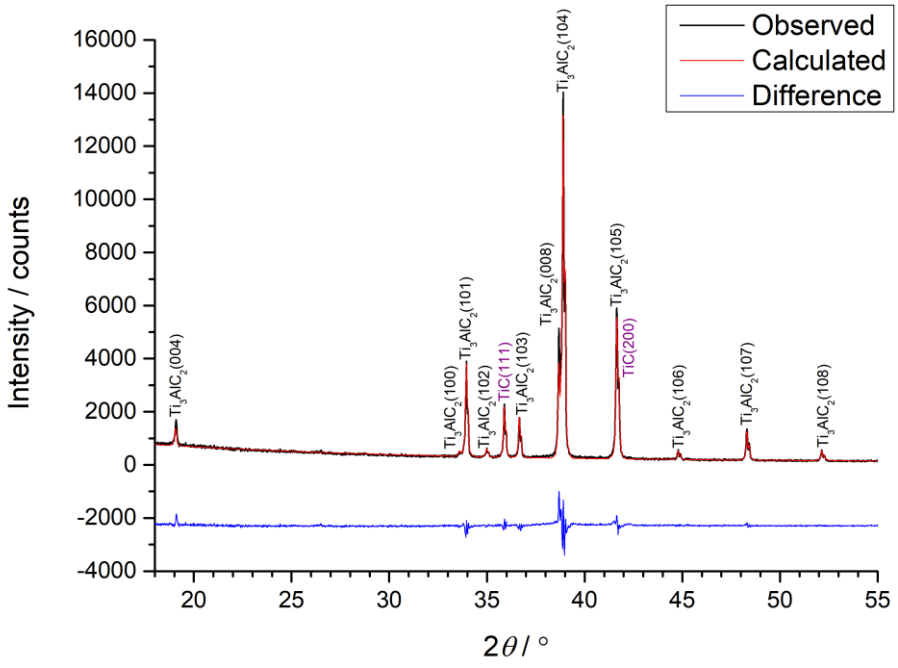

Figure 41 – XRD pattern of a sample prepared from Ti-Al-C milled for 2 h in a SPEX 8000M Mixer/Mill.

5.1.6 Density

The densities of samples prepared with different milling times are shown in Table 12. All samples are approximately fully dense, with a slightly lower relative density observed when milling was performed for 3 h.

Table 12 – Densities of samples prepared with different milling times.

Milling Time, t / h	Density, ρ / g cm^{-3}	Relative Density / %
1	4.292 ± 0.006	99
2	4.276 ± 0.002	100
3	4.208 ± 0.005	97
4 (continuous)	4.396 ± 0.011	99
2 (Ti-Al-C)	4.243 ± 0.005	98

5.1.7 Indentation hardness testing

The hardness of the samples prepared from powder milled for 2 h and the powder milled continuously for 4 h were measured using a DuraScan-70 hardness tester at 4.9 N with a dwell of 10 s. The Vickers hardness of the 2 h milled sample was 5.4 ± 1.0 GPa, and that of the 4 h continuously milled sample was 10.5 ± 0.6 GPa. The large difference reflects the difference in hardness between TiC and Ti_3AlC_2.

5.1.8 Microstructural examination

5.1.8.1 Milled for 2 h

Figure 42 is a BSE image of the surface of the sample prepared by milling for 2 h. This image, taken at an original magnification of 1,500x, provides a general overview of the phase distribution. Three distinct levels of contrast can be seen. The lightest contrast represents the major phase, which consists of layered, rectangular grains typical of MAX phase materials [187]. The medium contrast represents a phase with much smaller grains. These regions are heterogeneously distributed throughout the material. The darkest contrast may be due to grain pull-out or the presence of alumina, as observed in earlier samples.

Figure 43 is a BSE image of the sample prepared by milling for 2 h. Semi-quantitative elemental analyses were conducted at the annotated locations and are represented by the bar chart in Figure 44. The composition of the major phase is consistent with the stoichiometry of Ti_3AlC_2, while that of the minor phase is consistent with TiC. The grains of Ti_3AlC_2 are rectangular and vary significantly in size but are much larger than the grains of TiC which have a diameter < 1 μm. The jagged shape of the darkest contrast regions, similar in shape to the TiC grains, indicate the presence of pluckouts [162]. The SE image, Figure 45, taken at the same location as Figure 43, confirms that the regions of dark

contrast in the BSE image are due to grain pluckouts during micropreparation. Such pluckouts are consistent with the fact that TiC is harder than Ti_3AlC_2 so is more likely to be pulled out of the matrix.

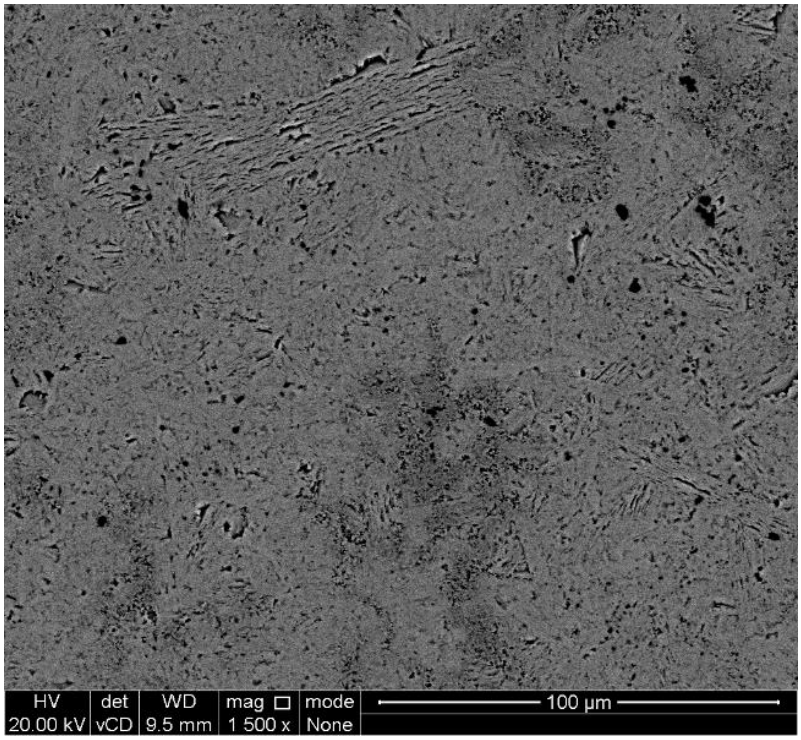

Figure 42 – BSE image of a sample prepared from powder milled for 2 h.

The clustering of TiC_x particles may be partly due to TiC_x formation prior to $TiAl_3$ formation and Al melting. This would limit the movement of molten Al through the material, causing the TiC_x particles to react further with each other and sinter into clusters. However, a more consistent explanation is their precipitation and sintering from the molten phase due to insufficient availability of aluminium, as shown by the following images of a cross-section of a sample.

A BSE image and associated EDS maps for a cross-section of a sample are shown in Figure 46. The graphite from the SPS process was retained; the sample was cut, mounted in conductive Bakelite (Konductomet) and only the cross-sectional surface was ground and polished. As observed for the surface of this composition, the lighter grey contrast is Ti_3AlC_2, whereas the darker grey contrast is TiC_x. The black contrast on the right-hand side of the image is the graphite and mounting material at the sample edge. The EDS maps indicate a lower concentration of Al in the dark grey region, with a much higher concentration present at the right-hand edge, indicating diffusion of Al to the edge of the sample. The Al-O layer at the edge of the sample is ~10 µm thick. The TiC_x region is >100 µm thick, extending further into the sample to ~160 µm at some locations. Such titanium carbide layers have been observed by other researchers [188]. The centre of the sample contains unevenly distributed regions of TiC_x as can be seen on the left side of Figure 46, albeit at much lower concentrations than at the surface of the sample.

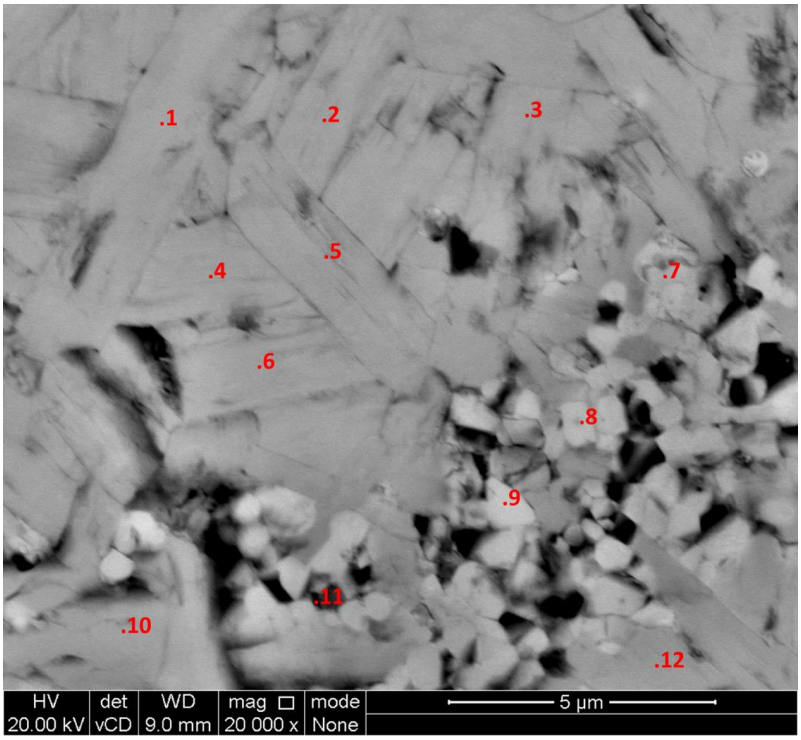

Figure 43 – BSE image of a sample prepared from powder milled for 2 h, annotated with locations of EDS point analyses.

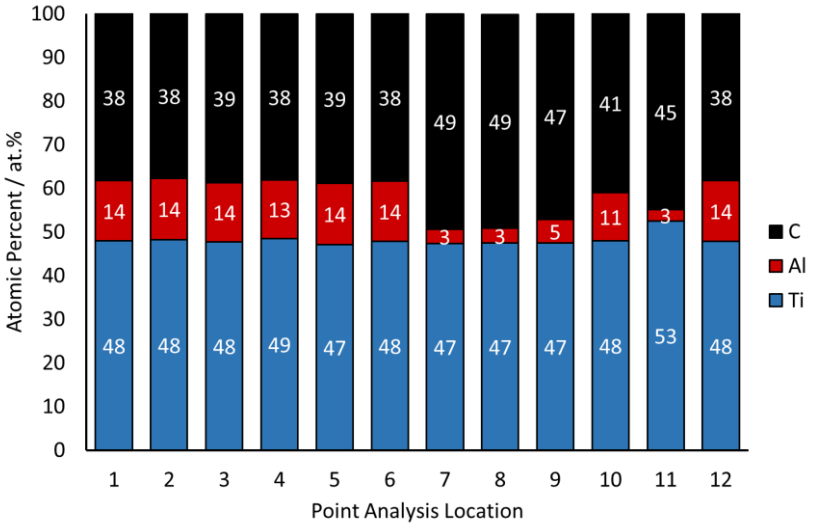

Figure 44 – Bar chart of the elemental compositions measured at the locations annotated in Figure 43.

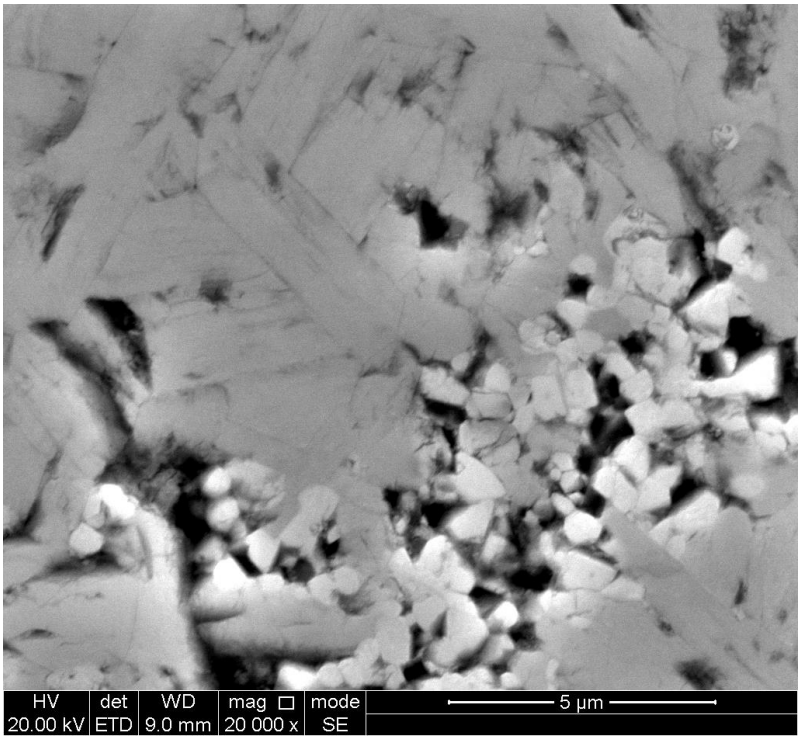

Figure 45 – SE image of the surface of a sample prepared from powder milled for 2 h.

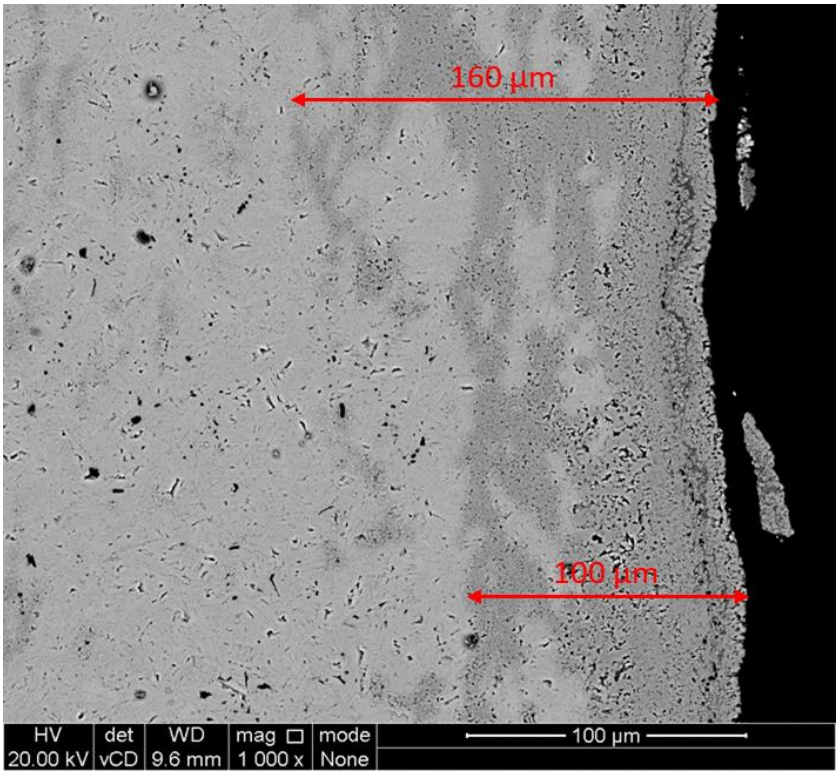

(a) BSE image

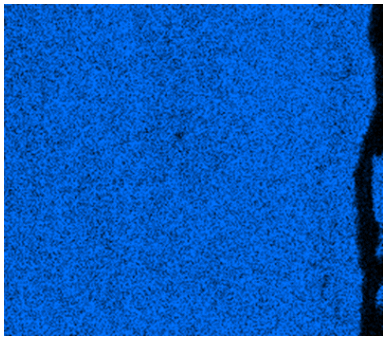

(b) Ti $K_{\alpha1}$

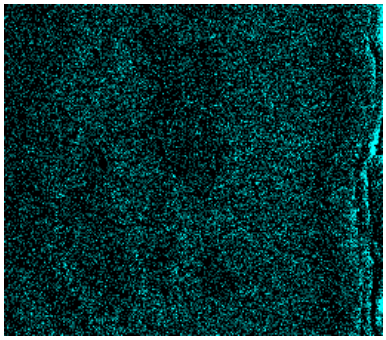

(c) C $K_{\alpha1}$ and $K_{\alpha2}$

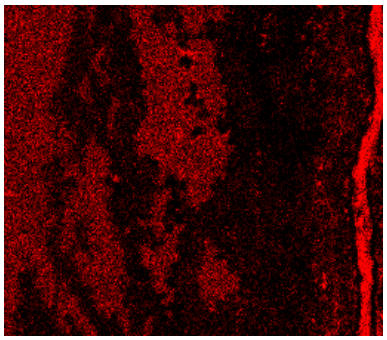

(d) Al $K_{\alpha1}$

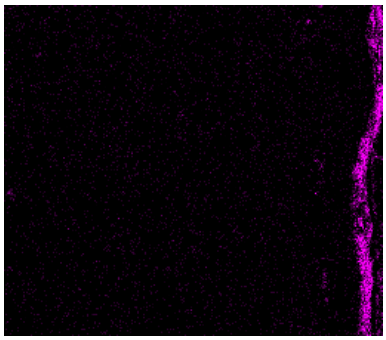

(e) O $K_{\alpha1}$

Figure 46 – (a) BSE image of the cross-section with graphite retained, (b)-(e) EDS maps for Ti, C, Al and O.

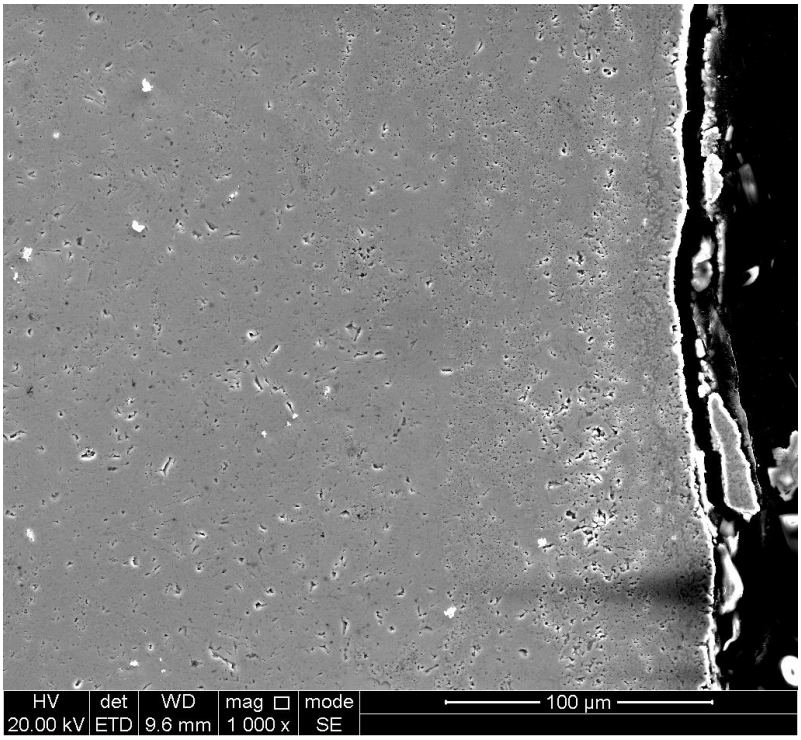

Figure 47 – Secondary electron image of the cross-section of a sample with the graphite from sintering retained, taken at the same location as Figure 46.

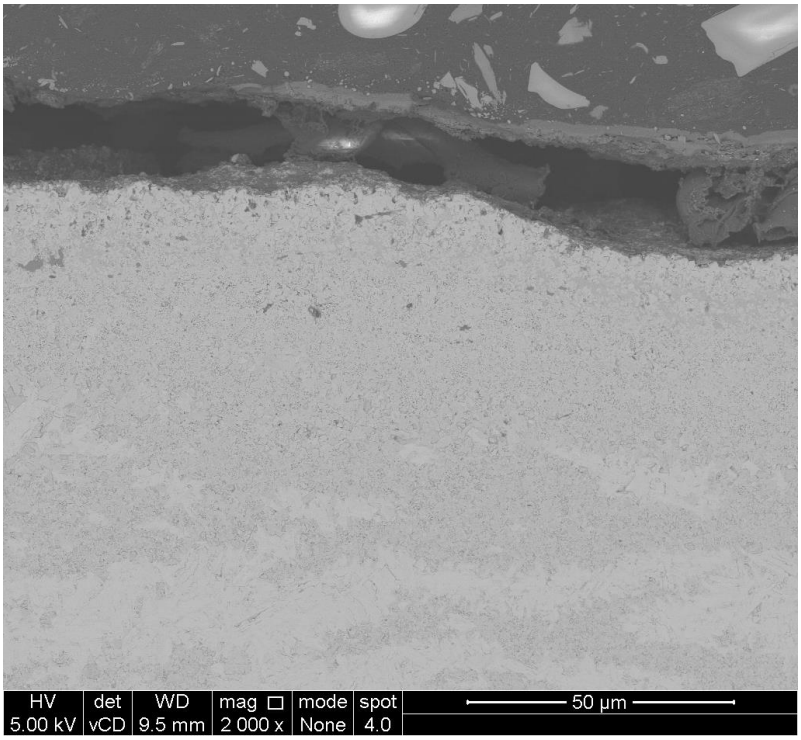

Figure 48 – BSE image of the cross-section of a sample with the graphite from SPS retained, taken a year after the sample was prepared. The band between the sample and the Bakelite containing aluminium and oxygen has disappeared.

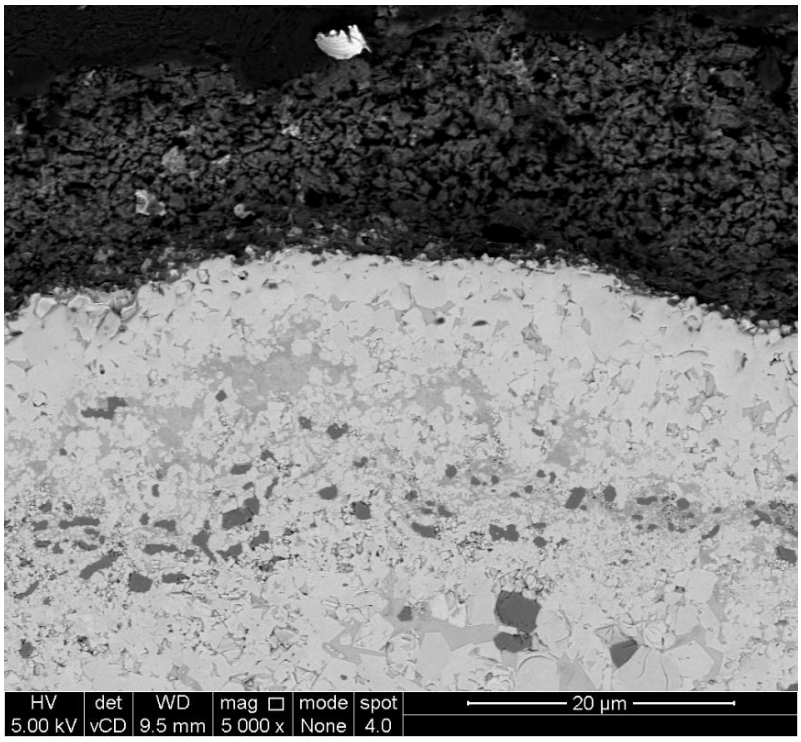

(a) BSE image

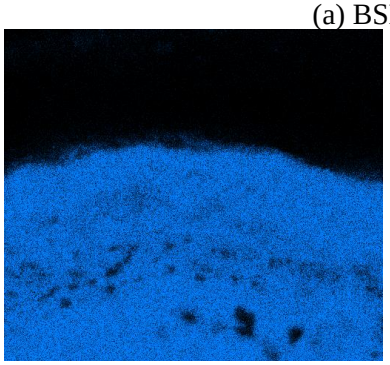

(b) Ti $K_{\alpha 1}$

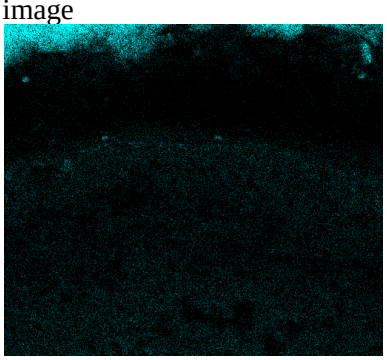

(c) C $K_{\alpha 1}$ and $K_{\alpha 2}$

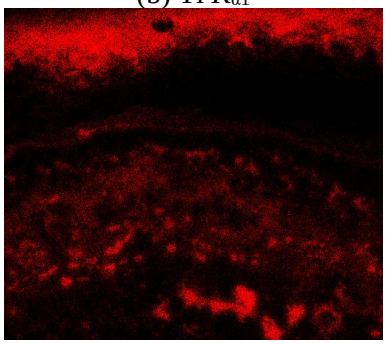

(d) Al $K_{\alpha 1}$

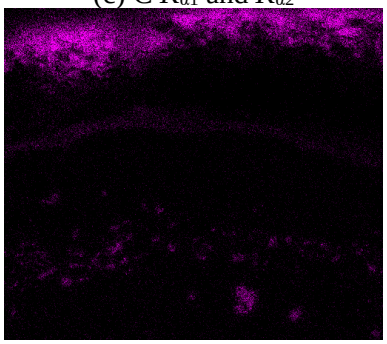

(e) O $K_{\alpha 1}$

Figure 49 – BSE image and EDS maps of a cross-section with the graphite from SPS retained. The images were taken after leaving the sample for a year. The gap at the top of the image contains aluminium and oxygen. Some alumina particles can be seen amongst the titanium carbide at the sample edge.

A secondary electron image, taken at the same location as Figure 46, is shown in Figure 47. This image highlights the band between the sample and the graphite which contains significant quantities of aluminium and oxygen, no titanium, and some carbon in the EDS maps. This band is likely $Al(OH)_3$ produced from the hydrolysis of Al_4C_3 [44]. Further evidence for this is the fact that graphite paper left on the samples fell off over time, consistent with dissolution of $Al(OH)_3$ in moisture.

The microstructural examination was repeated a year later, and the region containing aluminium and oxygen had disappeared, as shown in Figure 48. This is consistent with the product being Al_4C_3 then $Al(OH)_3$. Given extra time, the reaction proceeded to completion and the $Al(OH)_3$ was removed when the sample was cleaned for SEM.

A higher original magnification image of the sample after a year, with EDS maps, is shown in Figure 49. Aluminium and oxygen can be seen within the gap, which is likely due to hydrolysis of aluminium carbide which has been exposed due to the removal of the overlying aluminium hydroxide. The resolution of the image is improved relative to the earlier images, so the morphology in the TiC_x phase can be seen more clearly. EDS point analyses revealed that some of these phases contain boron from the boron nitride coating.

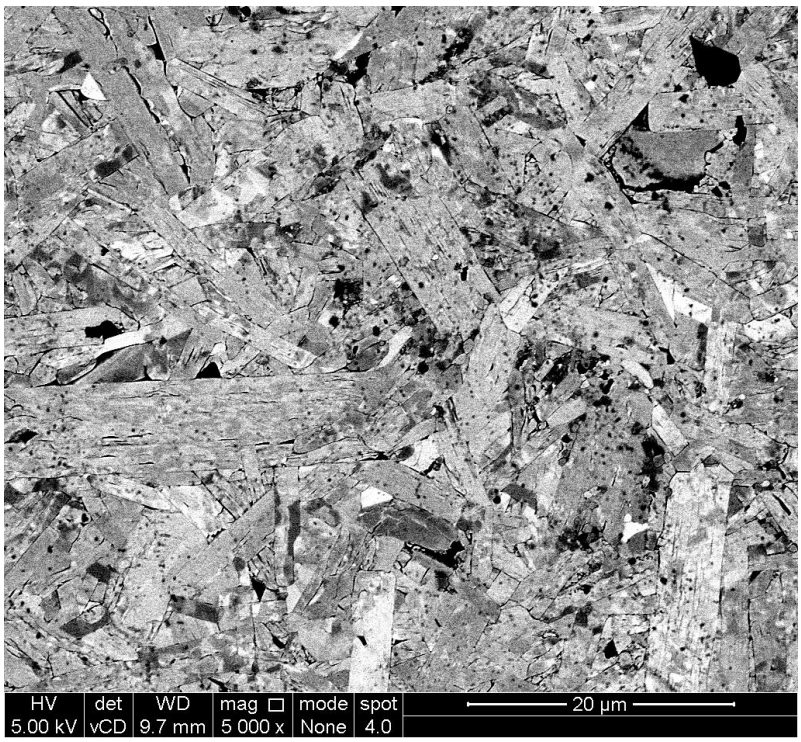

Figure 50 – BSE image of a sample of Ti_3AlC_2 which was prepared from 2 h milled Ti-C. The grain boundaries were revealed by polishing with colloidal silica then maximising the contrast of the SEM. Images such as this were used to determine the grain size of the sample.

The grain boundaries of the material were made visible by polishing with colloidal silica then maximising the contrast in the SEM. The grain size of the sample was determined approximately from four images taken at an original magnification of x5000, such as Figure 50.

The lengths and widths of individual grains were measured then used to calculate the aspect ratio. Four images taken at an original magnification of 5000x were used. Histograms and box plots of the results are shown in Figure 51. The mean values of length, width and aspect ratio for all 178 measurements were 8.2 ± 4.1 µm, 2.3 ± 1.1 µm and 3.8 ± 1.8 respectively.

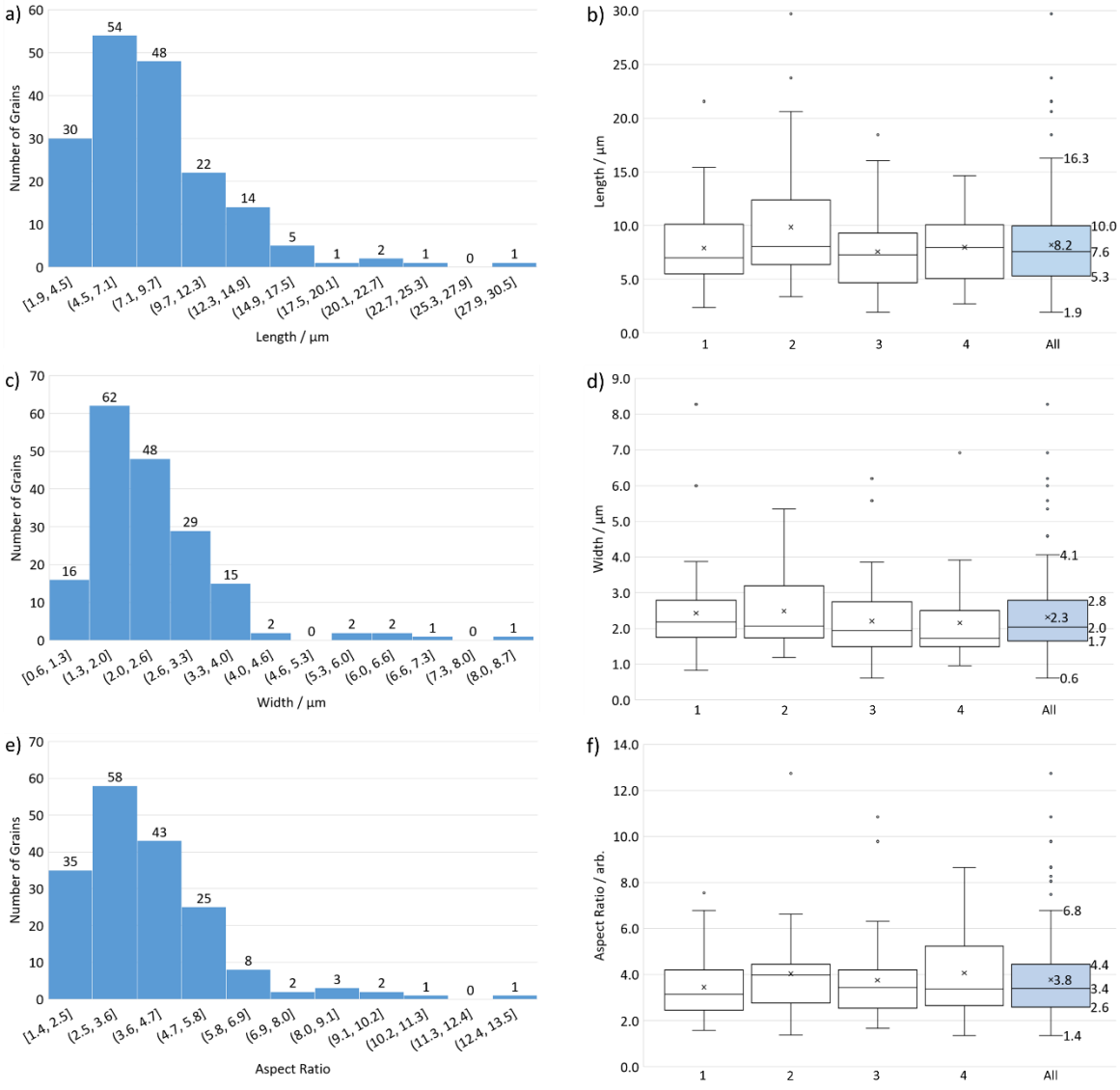

Figure 51 – Histograms and box plots of the length, width and aspect ratio of grains in a sample of Ti_3AlC_2 which was prepared from 2 h milled Ti-C powder. In the box plots, the lines represent the minimum, 1st quartile, median, 3rd quartile, and maximum. The X represents the mean after removing outliers, which are shown as circles above the maximum.

The grain size appears to be bimodal but skewed towards smaller grain sizes, with many smaller grains distributed in the space between significantly larger grains and many larger grains not being measured due to the magnification used; consequently, the standard deviation was large. Milling is known to result in a bimodal distribution of particles sizes with the two peaks of the distribution at the extremes of large and small particles, so the different sizes could be due to the distribution of TiC_x particle sizes [69]. Additionally, this distribution of larger and smaller grains may indicate that significant grain growth occurred due to the length of holding time, and it would be interesting to investigate the effects of holding time on the microstructure.

5.1.8.2 Milled for 3 h

Figure 52 is a BSE image showing the phases present in a sample formed by milling the precursor for 3 h. The lightest contrast is Ti_3AlC_2, the darker grey contrast is TiC, and the darkest contrast is Al_2O_3. The TiC regions appear to have grains of Ti_3AlC_2 distributed throughout them, which is consistent with the formation of Ti_3AlC_2 from TiC_x in an Al-containing melt. These Ti_3AlC_2 grains have a smaller grain size than those observed in the bulk of the sample. The Al_2O_3 forms round spots which are relatively evenly distributed throughout the material. These alumina spots are likely present throughout the material as aluminium but have oxidised upon exposure to the atmosphere at the surface. Such morphology is also observed in the samples produced with excess aluminium (see § 5.3)

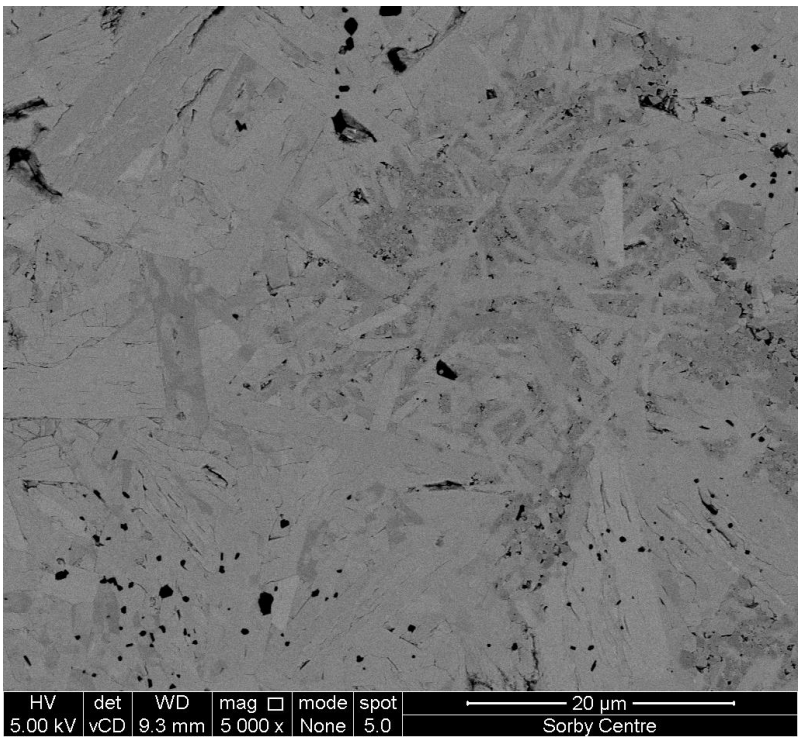

Figure 52 – BSE image showing the three phases observed in a sample produced from powder which was milled for 3 h. The lightest contrast represents Ti_3AlC_2, the darker grey contrast represents TiC, and the dark spots represent Al_2O_3.

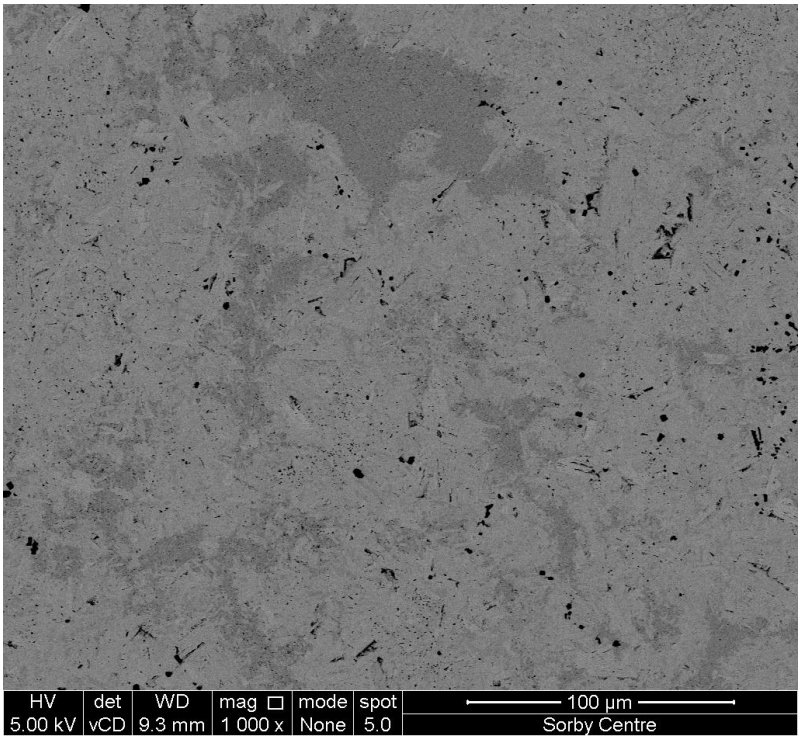

Figure 53 – BSE image taken at a relatively low original magnification of x1000. The image shows the distribution of the phases in a sample prepared from powder which was milled for 3 h.

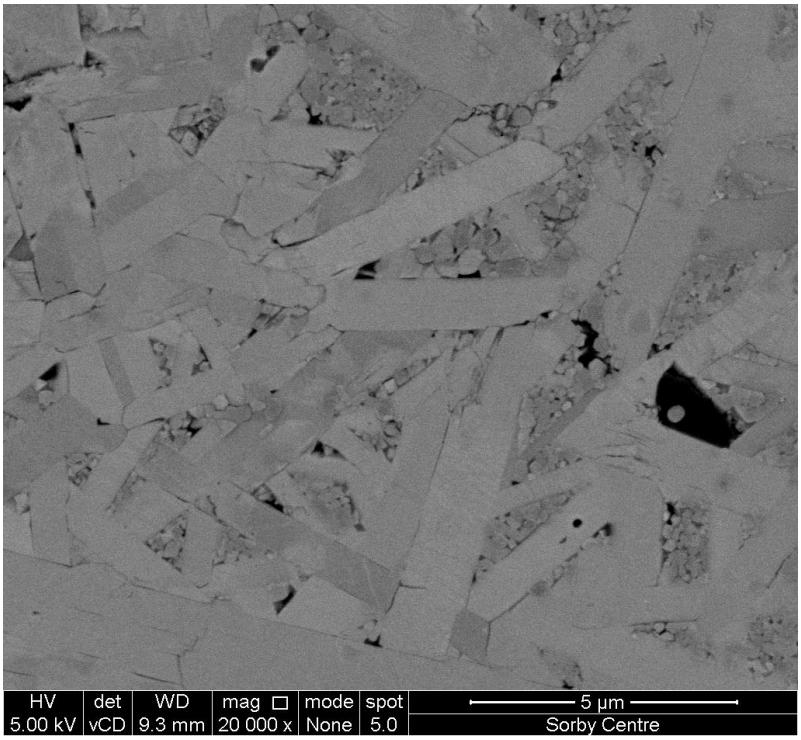

Figure 54 – BSE image showing the morphology of TiC grains amongst Ti_3AlC_2 grains.

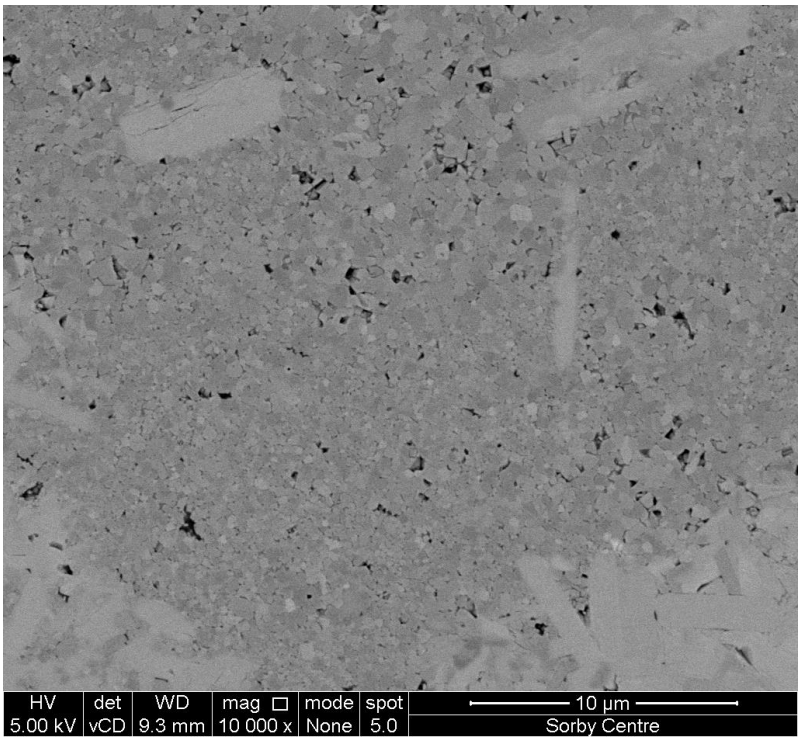

Figure 55 – BSE image showing a concentrated region of TiC_x.

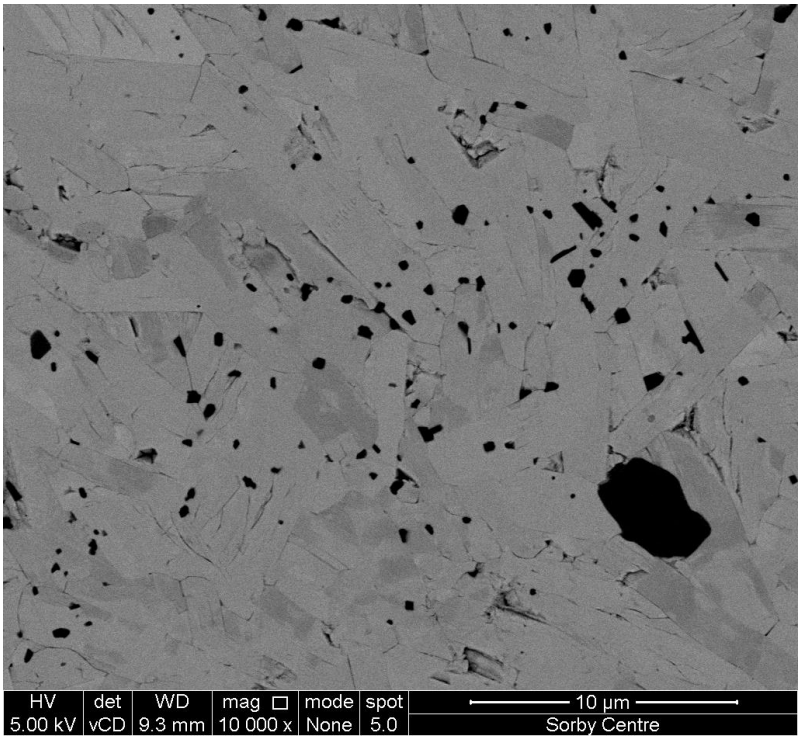

Figure 56 – BSE image of an area with a high concentration of Al_2O_3 (darkest contrast). Many of these particles appear to be present at the corners of Ti_3AlC_2 grains where several grains meet.

Figure 53 provides a general overview of the phase distribution. The TiC regions are heterogeneously distributed in concentrated regions throughout the material. Most of these regions contain rectangular grains of Ti_3AlC_2; however, there are several very large regions containing only grains of TiC. Spots of Al_2O_3 appear to be evenly distributed throughout the Ti_3AlC_2 regions of the material. The fact that Al and TiC_x form separate clusters suggests that the mobility of aluminium has been limited, most likely by the formation of stable TiC at lower temperatures than the formation of the molten phase, as indicated by differential thermal analysis of powder milled for 3 h.

Figure 54 is a BSE image showing the morphology of the TiC grains which are interspersed with Ti_3AlC_2. The grains of TiC are very small, with average diameters significantly less than 1 µm. The smaller grain size relative to the sample which was milled for 2 h appears to be due to the extended milling time.

Figure 55 shows a region of concentrated TiC_x. The particle size was smaller due to milling for longer and therefore has led to TiC_x particles sintering together much more readily, as shown by the thermal analysis results. It appears that once the clusters grow past a certain size they prevent aluminium diffusion and reaction with TiC_x during the 15 min holding time, resulting in such large concentrated regions.

Figure 56 is a BSE image focused on a region with many Al_2O_3 grains. These grains appear to be prevalent at the corners of Ti_3AlC_2 grains where several grains meet. However, some also appear to be present within the Ti_3AlC_2 grains themselves. Clearly there was insufficient TiC_x in these regions for the Al-containing melt to react with. The Al_2O_3 grains appear to be typically < 1 µm in diameter; however, a few significantly larger particles as in the bottom right of the image were observed throughout the material.

5.1.8.3 Milled for 4 h continuously

Figure 57 is a BSE image showing the morphology of the phases in a sample prepared from powder which was milled continuously for 4 h. The EDS maps aid identification of the phases. The darker contrast equiaxed grains are titanium carbide, which was the major phase identified by XRD, and is indicated by a lack of aluminium in the EDS map. As the particle size would have been very small after milling, these particles preferentially sintered, limiting the ability of Al to diffuse into the structure and form Ti_3AlC_2. Furthermore, if the powder was stoichiometric TiC rather than non-stoichiometric, the structure would need to be broken down first, as discussed by the work of Zou *et al.* and Riley and Kisi [73,77,85]. These grains contain black spots which look like pores, although the relative density was 99%. They could be spots of concentrated aluminium; the accelerating voltage may be too high to enable a sufficiently low resolution to be obtained in the EDS maps. The lighter contrast phase is Ti_3AlC_2. The TiC grains appear to be distributed throughout a matrix of Ti_3AlC_2.

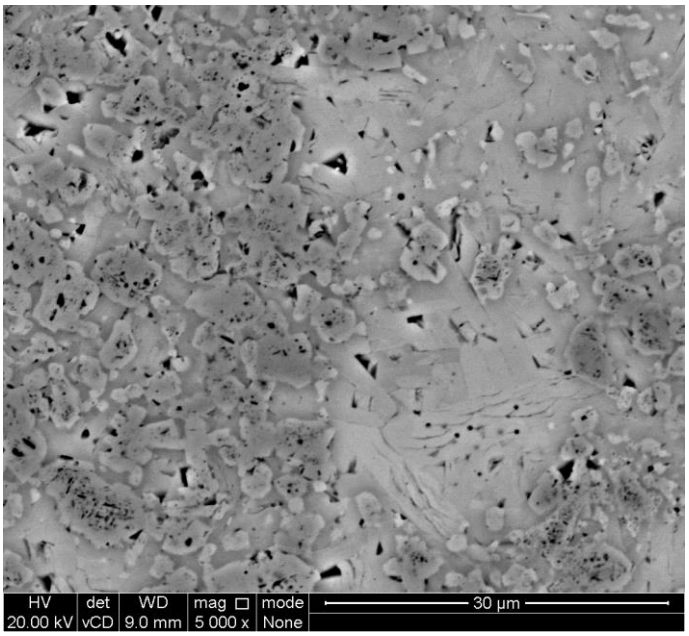

(a) BSE image

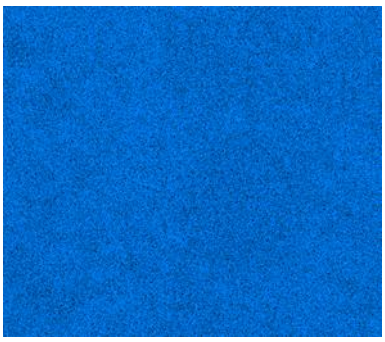

(b) Ti $K_{\alpha 1}$

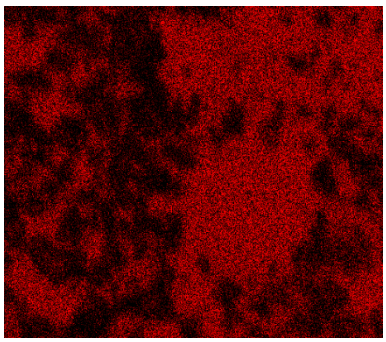

(c) Al $K_{\alpha 1}$

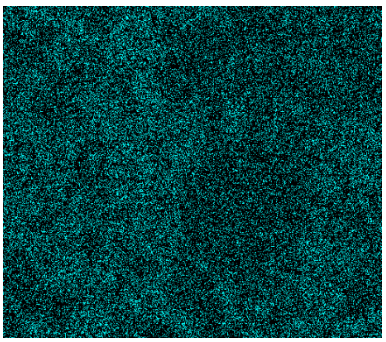

(d) C $K_{\alpha 1}$ and $K_{\alpha 2}$

Figure 57 – BSE image of a sample produced from powder milled continuously for 4 h in a SPEX 8000M Mixer/Mill. The major phase consists of darker contrast grains with black spots; the lack of aluminium confirms that this phase is titanium carbide. The lighter contrast phase is Ti_3AlC_2.

Figure 58 is an SE image taken at the same location and original magnification as Figure 57. The lighter contrast of the TiC_x grains shows that they are raised relative to the Ti_3AlC_2 matrix. This indicates greater removal of Ti_3AlC_2 during polishing because of its lower hardness relative to TiC_x. The hardness, 10.5 ± 0.6 GPa, was almost double that of the 2 h milled sample due to the hardness of TiC_x. In comparison, the hardness of bulk TiC was 22 ± 3 GPa [189]. Initial investigations of the wear behaviour of this material (by Carl Magnus) reveal that it has a very high resistance to wear, consistent with the high content of TiC_x [190].

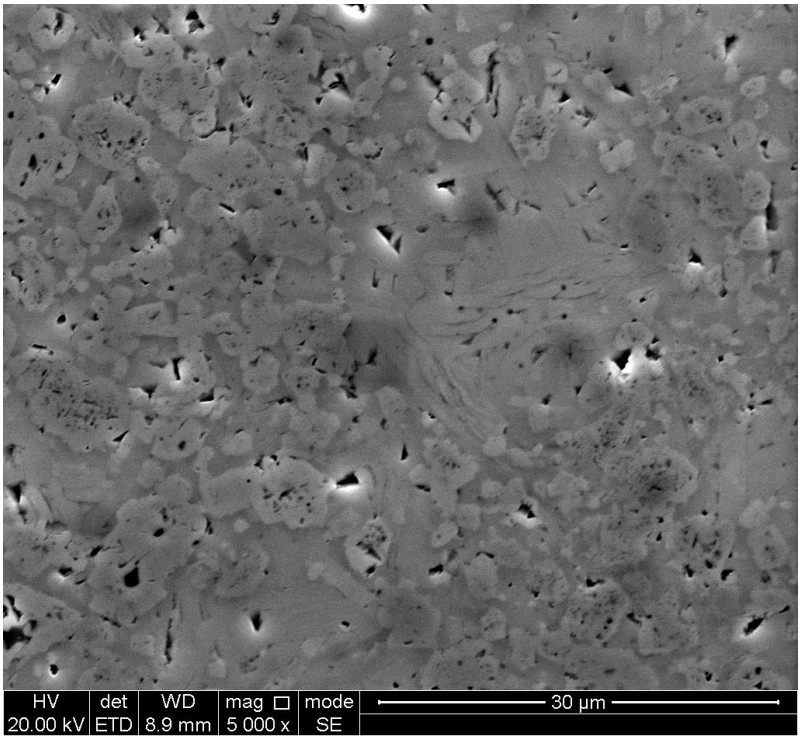

Figure 58 – SE image of a sample prepared from powder milled continuously for 4 h in a SPEX 8000M Mixer/Mill. The location and original magnification are the same as that in Figure 57.

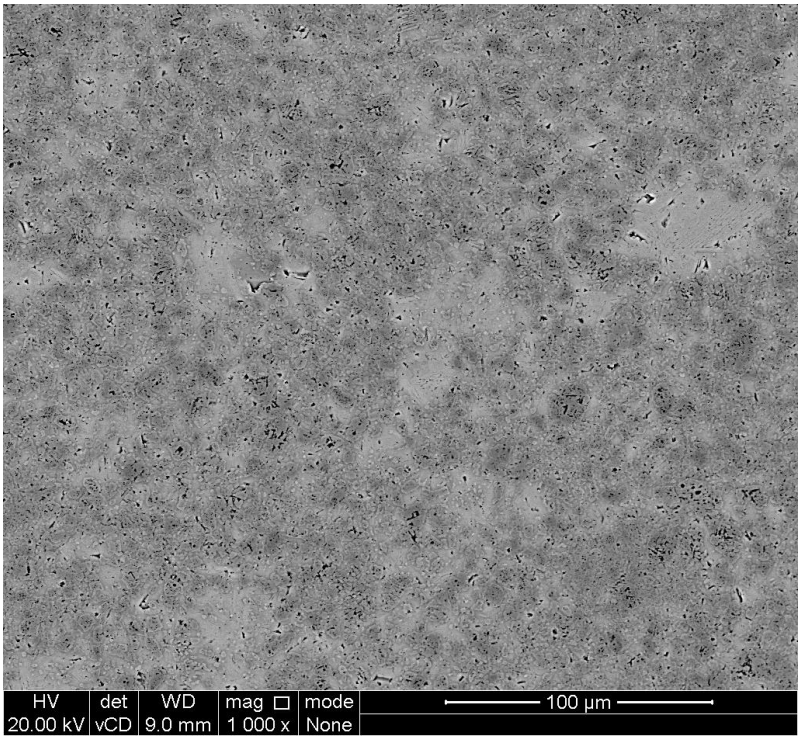

Figure 59 – BSE image providing a general overview of the surface morphology of a sample produced from powder which was milled continuously for 4 h in a SPEX 8000M Mixer/Mill.

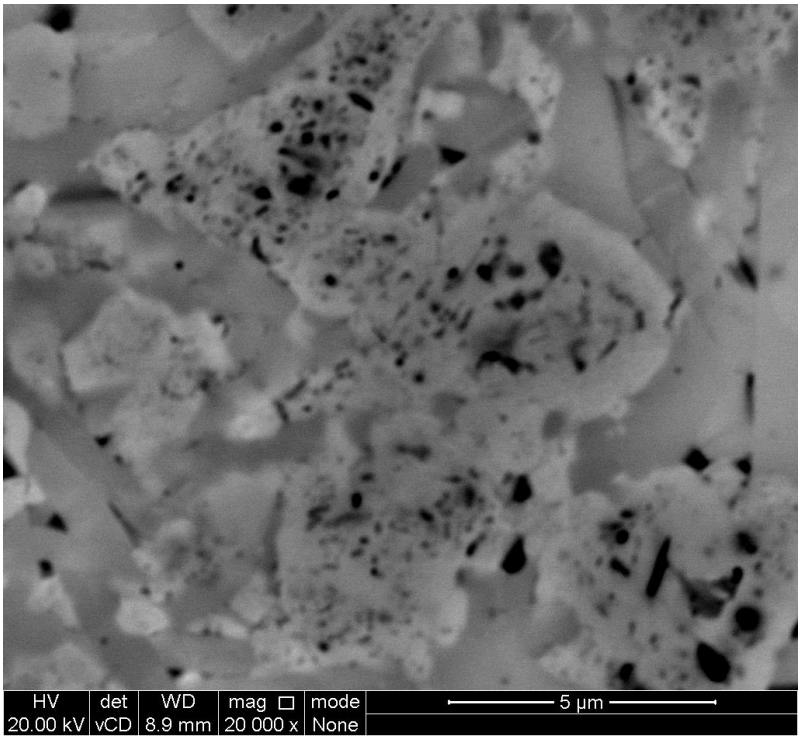

Figure 60 – BSE image of grains of TiC in a sample prepared from powder milled continuously for 4 h in a SPEX 8000M Mixer/Mill. The dark spots are round and look like they may be connected, indicative of porosity.

Figure 59 is a lower magnification BSE image. It indicates that the major phase is titanium carbide, with concentrated regions of Ti_3AlC_2 heterogeneously distributed throughout the material. Figure 60 is a higher magnification image of the grains of TiC. The dark contrast spots are round and appear interconnected, suggesting porosity. However, the relative density was approximately 99% and the XRD pattern suggests the presence of a third phase in minor quantities.

Further investigation is required to confirm that synthesis of this material with the same microstructure is repeatable, and to precisely determine its formation mechanism. It may prove to be a very useful composite material, especially given its high wear resistance [190]. Raman spectroscopy would be particularly useful to determine whether the TiC_x in both the powder and the bulk sample is stoichiometric or non-stoichiometric [90,92], although a method of maintaining the powder in an inert atmosphere is required to prevent any spontaneous reaction.

5.2 Variation of sintering temperature

It was decided to reinvestigate the effect of temperature on the synthesis method. It was suspected that a small fraction of TiC_x was always obtained because the sintering temperature was too high. Furthermore, the temperature used had been based on a different method, then was successful under different milling conditions, so it was suspected that a different sintering temperature may improve the product purity.

Four samples were prepared with SPS holding temperatures between 1250°C and 1400°C. Titanium and graphite powders were milled for 2 h in a SPEX 8000M Mixer/Mill then mixed with 1.0 parts aluminium powder. The results for the sample prepared at 1350°C can be found in § 5.1.

The sintering profiles have the same shape and similar onset temperatures for changes in piston movement as that shown for the sample which was milled for 2 h and sintered at 1350°C with 1.0 parts Al (§5.1.4). The sintering profiles for samples held at 1250°C, 1300°C and 1400°C can be found in Appendix B (§12.1.1)

5.2.1 XRD and Rietveld refinement

Figure 61 is a bar chart showing the phase compositions of samples formed at different holding temperatures. The Rietveld refinement statistics and key lattice parameters are shown in Table 13. The greatest fraction of Ti_3AlC_2 was obtained at 1350°C. At 1250°C it appears that the reaction was incomplete, as the intermediate phase Al_3Ti was present. At 1300°C, Al_3Ti had fully reacted, but a greater fraction of TiC was present. The smallest fraction of Ti_3AlC_2 was obtained at 1400°C, with a significant increase in TiC content compared to 1350°C.

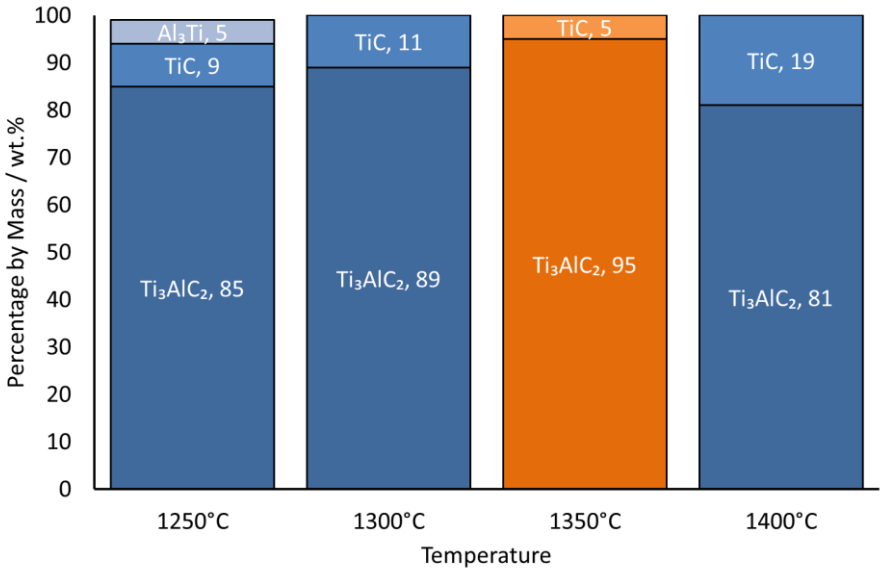

Figure 61 – Bar chart showing the phase compositions of samples formed at different holding temperatures.

Table 13 – Lattice parameters and fitting statistics from Rietveld refinement of XRD data for samples prepared with different SPS dwell temperatures.

Dwell Temperature / °C	Lattice Parameters / Å			Fitting Statistics		
	Ti_3AlC_2, *a*	Ti_3AlC_2, *c*	TiC_x, *a*	χ^2	Rp	wRp
1250	3.079	18.607	4.335	2.829	0.0778	0.1004
1300	3.081	18.622	4.333	2.700	0.076	0.098
1350	3.078	18.594	4.331	3.357	0.082	0.109
1400	3.080	18.608	4.332	3.835	0.089	0.117

5.2.2 Density

The densities of samples produced at different holding temperatures are shown in Table 14. The relative densities of all samples were close to 100%. A lower density was obtained for the sample produced at 1250°C due to the presence of Al_3Ti, and higher densities were obtained for the samples at 1300°C and 1400°C containing increased quantities of TiC_x.

Table 14 – Densities of samples produced at different holding temperatures.

Temperature, *T* / °C	Density, ρ / g cm^{-3}	Relative Density / %
1250	4.196 ± 0.010	98
1300	4.283 ± 0.003	99
1350	4.276 ± 0.002	100
1400	4.336 ± 0.002	99

5.2.3 Microstructural examination

5.2.3.1 Sintered at 1250°C

Figure 62 is a representative BSE image of a sample sintered at 1250°C showing the morphology of phases present. The EDS maps provide indications to the compositions of these phases. The lightest contrast is Ti_3AlC_2. The medium contrast regions are TiC_x, as indicated by the lack of aluminium. The large section of darkest contrast appears to contain a greater concentration of aluminium and lower concentration of titanium, connoting it is the Al_3Ti phase observed by XRD.

Figure 63 is an SE image taken at the same location and magnification as Figure 62. The Al_3Ti region has darker contrast, indicating that it has been removed more than the surrounding Ti_3AlC_2 due to it being softer. Numerous grain pluck-outs can be seen in the TiC_x phase due to it consisting of small grains and being a harder material than the surrounding Ti_3AlC_2.

Figure 64 is a BSE image taken at a much lower original magnification. It shows the distribution of phases throughout the material. Both the TiC_x and Al_3Ti phases are heterogeneously separated into concentrated regions with varying, relatively large volumes. Such separation of these two phases may indicate insufficient mixing of aluminium with the milled Ti-C precursor.

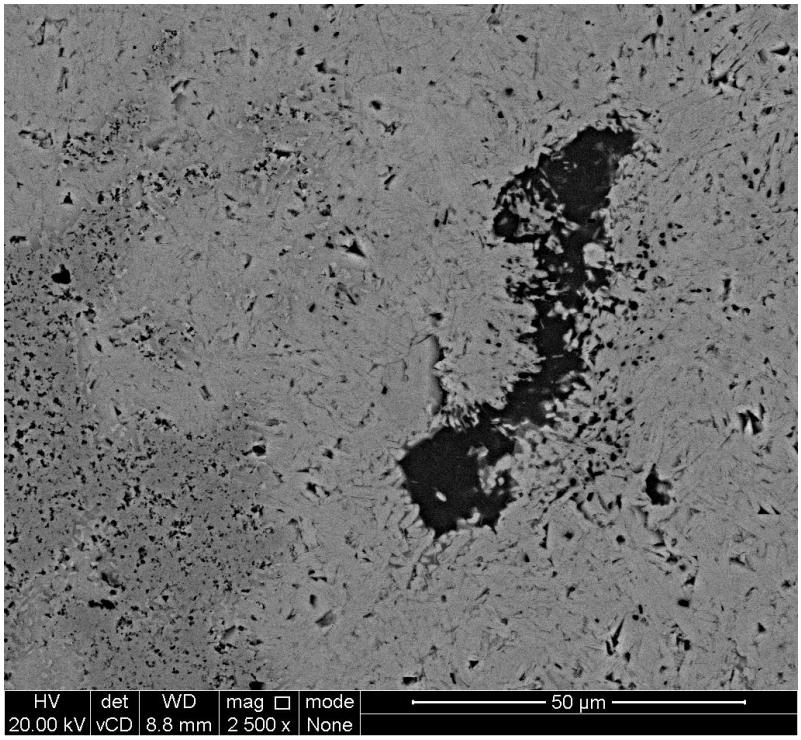

(a) BSE image

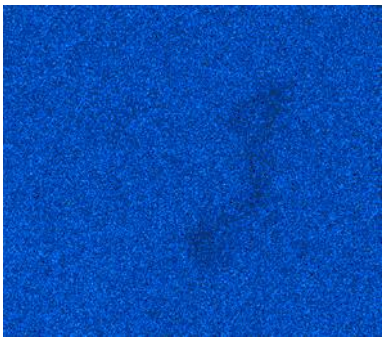

(b) Ti $K_{\alpha1}$

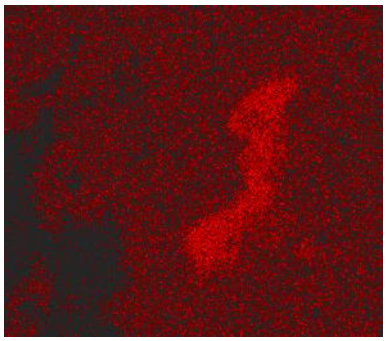

(c) Al $K_{\alpha1}$

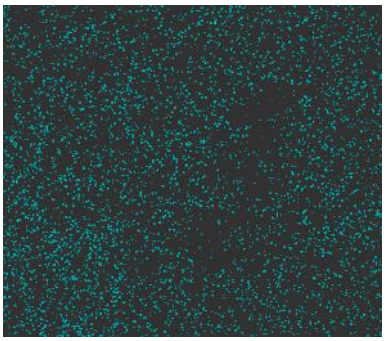

(d) C $K_{\alpha1}$ and $K_{\alpha2}$

Figure 62 – BSE image and EDS maps representative of the microstructure of a sample sintered at 1250°C. The lightest contrast phase, which has the greatest volume fraction, represents Ti_3AlC_2. The medium contrast phase on the left side of the image is TiC_x, as indicated by the lack of Al. The darkest contrast phase is Al_3Ti, as indicated by the lack of Ti and abundance of Al.

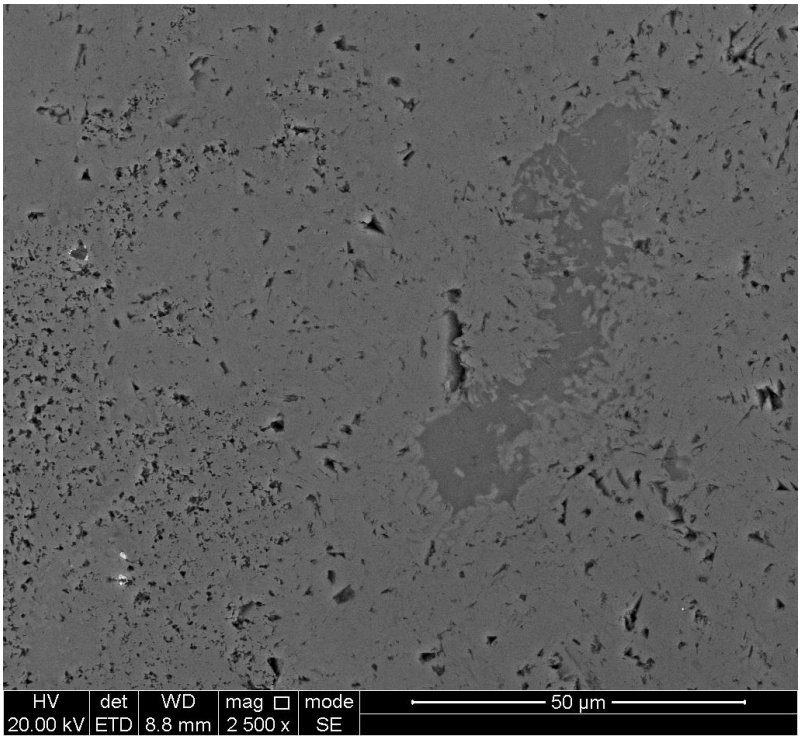

Figure 63 – SE image of a sample sintered at 1250°C, taken at the same location and magnification as Figure 62. The medium contrast region shows greater loss of Al_3Ti due to it being softer than the surrounding Ti_3AlC_2. The spots of dark contrast which are prevalent in the TiC_x region represent grain pull-outs.

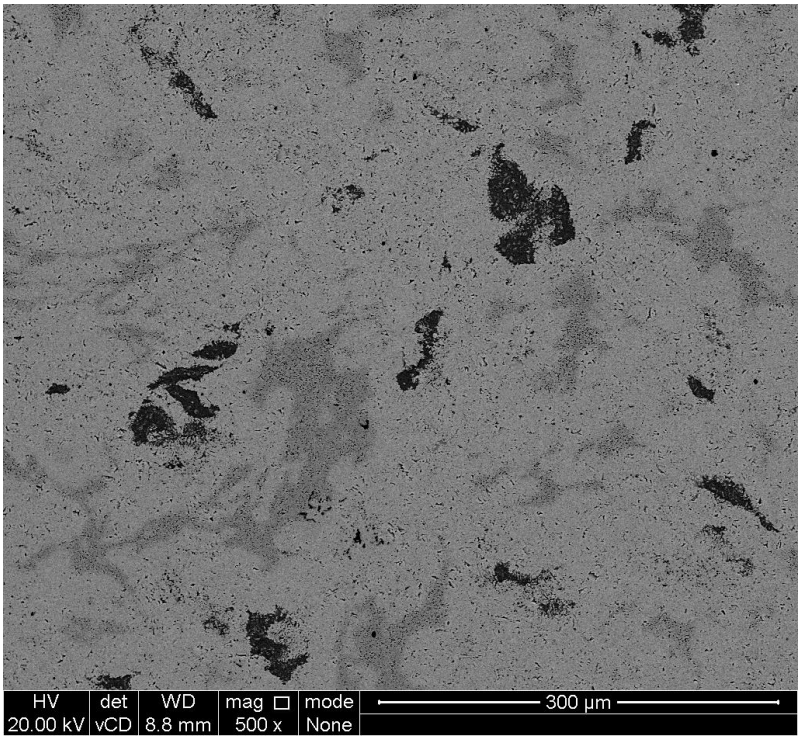

Figure 64 – BSE image of a sample sintered at 1250°C, taken at a relatively low original magnification to show the distribution of phases throughout the material. The TiC_x (medium grey contrast) and Al_3Ti (dark contrast) phases concentrate heterogeneously into relatively large volumes.

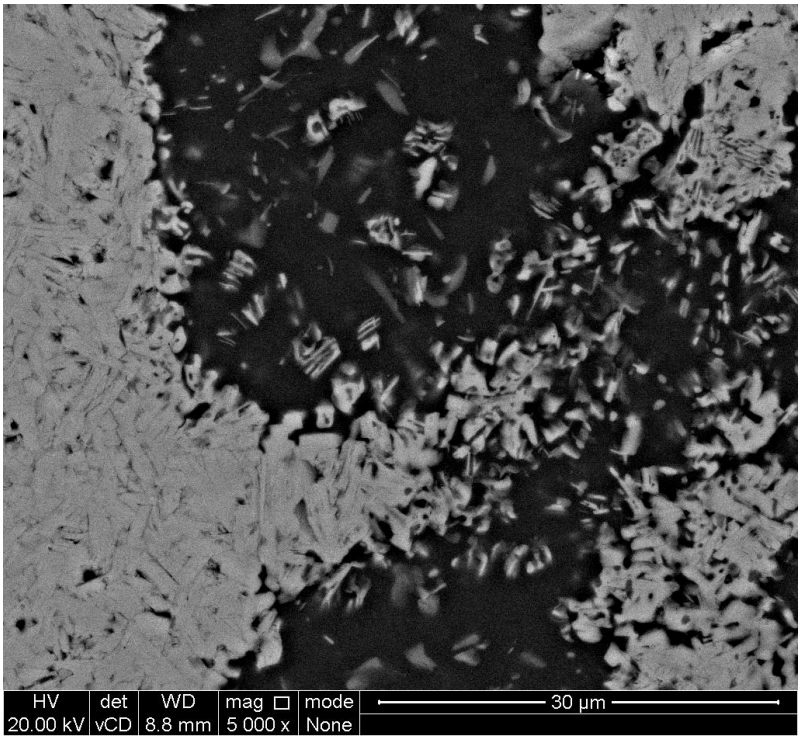

Figure 65 – BSE image showing the morphology of the Al_3Ti phase. No grains appear to be visible other than those of Ti_3AlC_2 in the process of forming.

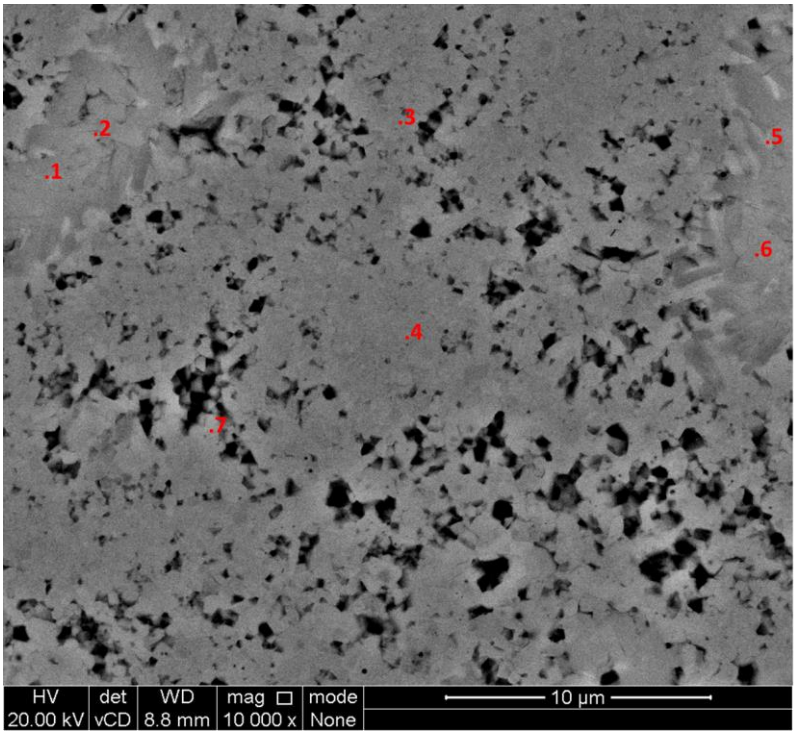

Figure 66 – BSE image of the TiC_x phase in a sample prepared at a sintering temperature of 1250°C. The annotations mark the locations of EDS point analyses, the compositions of which can be found in Figure 67.

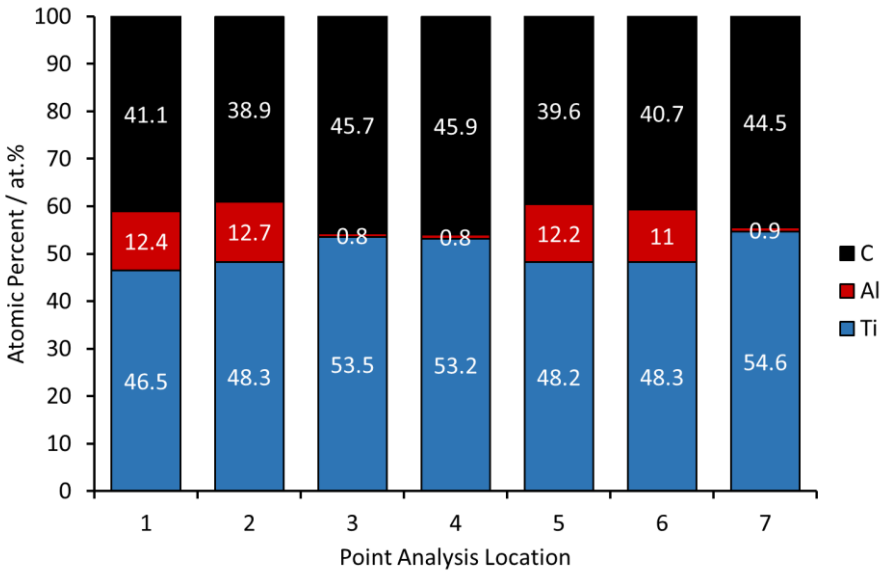

Figure 67 – Compositions of EDS point analyses at the annotated locations in Figure 66. Points 1, 2, 5 and 6 appear to be a mixture of Ti_3AlC_2 and TiC_x. Points 3, 4 and 7 appear to be mainly TiC_x.

Figure 65 is a BSE image showing the Al_3Ti phase at higher magnification. It is difficult to distinguish any grain structure in this region other than what appears to be Ti_3AlC_2 grains in the process of forming. This provides evidence that Ti_3AlC_2 forms from Al_3Ti and indicates that the reaction did not proceed to completion. The lack of Al_3Ti grain structure is likely a result of rapid quenching from the molten state. The Ti_3AlC_2 grains at the border between phases appear to have rounded as opposed to rectangular morphology.

Figure 66 is a BSE image centred on the TiC_x phase. EDS point analyses were conducted at the annotated locations, the compositions of which are summarised in Figure 67. The equiaxed shape of the grains is similar to that observed at 1350°C, but the grains are smaller ($\ll$ 1 µm), and overall the phase appears as though it has undergone densification. Such morphology is consistent the observations of Choi and Rhee, and agrees with the mechanism proposed by Ge *et al.* [81,184]. The sample which was milled for 3 h also had small TiC_x grains, but they were comparatively large and the boundaries were more clearly defined.

5.2.3.2 Sintered at 1300°C

Figure 24 is a BSE image of a sample which was sintered at 1300°C. The image is representative of the microstructure of the sample. Three distinct levels of contrast are visible. The lightest contrast represents the major phase, Ti_3AlC_2, as observed by XRD. The medium contrast represents the minor phase, TiC_x. The morphology of the larger regions of dark contrast does not appear to be solely due to grain pluck-outs, and it represents at least one further phase which was not identified via XRD, most likely Al_3Ti. Al_3Ti is known to decompose at 1340°C, so it is unsurprising that it is still present at 1300°C but disappears completely at 1350°C [184,191].

Figure 69 is a BSE image taken at greater magnification. The annotations note the locations of point analyses, the results of which are summarised in Figure 70. The high aluminium content of points 1 to 3, combined with the oxygen content, suggests this phase is Al_2O_3 or oxidised Al_3Ti. Further confirmation could be obtained through Raman spectroscopy, as it is likely that this phase is actually consists of Al-Ti-O. The compositions of points 4 to 8 and point 10 are representative of sub-stoichiometric TiC_x. The TiC_x phase occupies a larger volume fraction than the sample sintered at 1350°C, and the grain size appears smaller ($\ll$ 1 µm). Furthermore, while the majority of TiC_x is present in clusters, some grains appear to be located along the grain boundaries of Ti_3AlC_2. This indicates that TiC_x is observed due to incomplete reaction with Al_3Ti to form Ti_3AlC_2. The smaller grain size is likely representative of the particle size after milling, and the reduction in volume and increase in grain size at 1350°C suggests the reaction with aluminium has proceeded further and the remaining TiC_x has undergone sintering and grain growth. Although the composition of point 9 is representative of Ti_3AlC_2, the location has morphology closer to that of TiC_x; the location may have been undergoing reaction to Ti_3AlC_2 when the temperature began to decrease, or the penetration depth of the electron beam may be reaching an area below the grain.

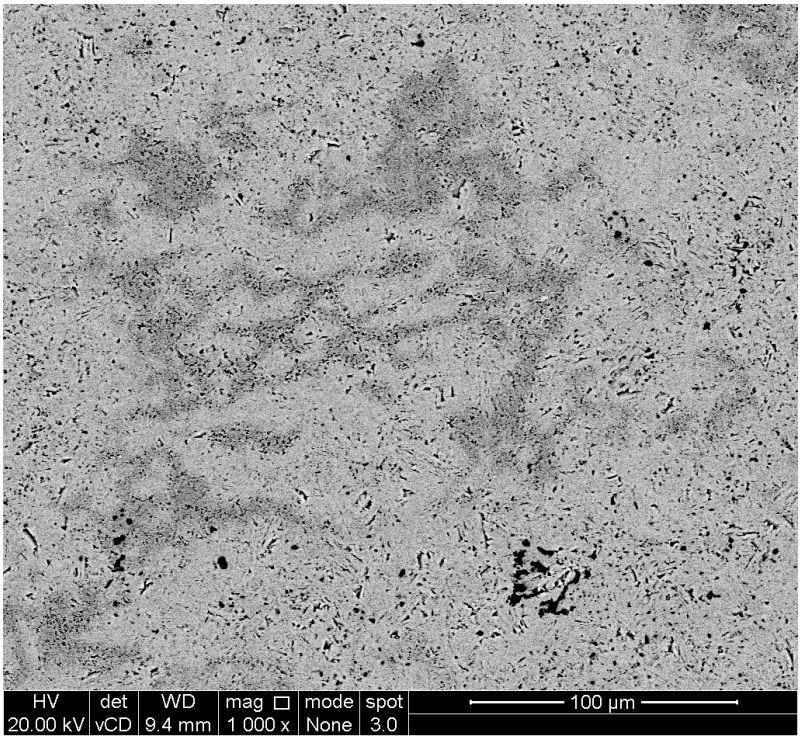

Figure 68 – BSE image of a sample sintered at 1300°C from titanium and graphite that was milled for 2 h. The image is representative of the general microstructure of this sample.

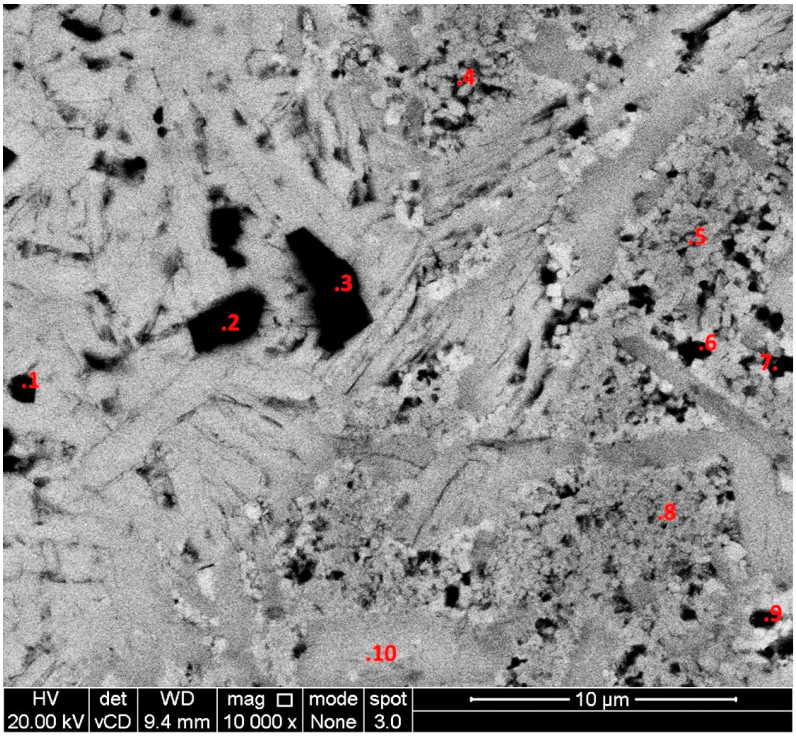

Figure 69 – BSE image of a sample sintered at 1300°C from Ti-C which was milled for 2 h. The annotations show the location of EDS point analysis, the elemental compositions of which are summarised in Figure 70.

Figure 71 is a similar BSE image which shows TiC_x distributed along the grain boundaries of Ti_3AlC_2. The close proximity of Al-O particles further suggests the morphology is indicative of unreacted TiC_x. The size of these alumina particles is much greater than the TiC_x grains. It is possible that use of aluminium of smaller particle size, improved mixing with aluminium, or a longer holding time during sintering may lead to a greater yield of Ti_3AlC_2.

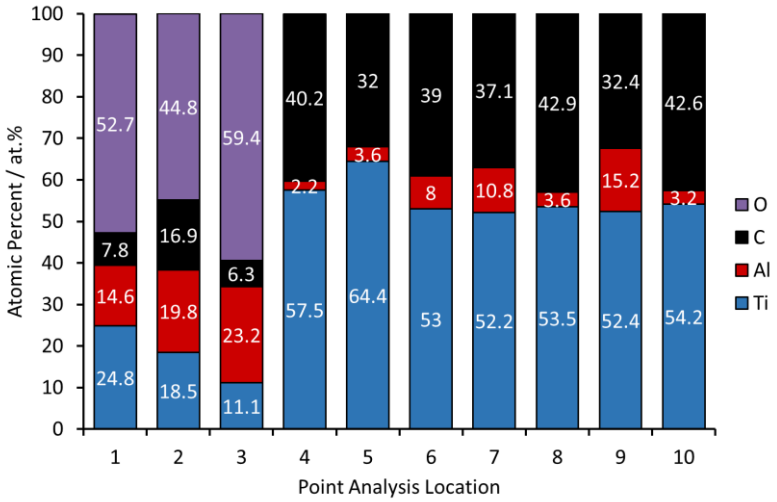

Figure 70 – Compositions of point analyses at the locations shown in the annotated BSE image, Figure 69.

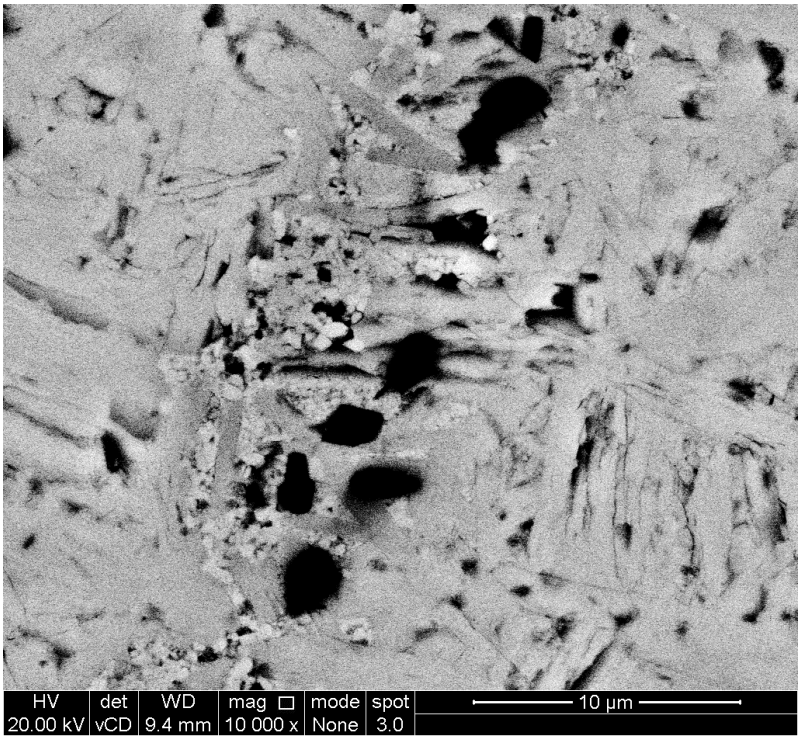

Figure 71 – BSE image showing the distribution of TiC_x around the grain boundaries of Ti_3AlC_2, and the close proximity of particles of alumina. The alumina particles are significantly larger than the TiC_x grains.

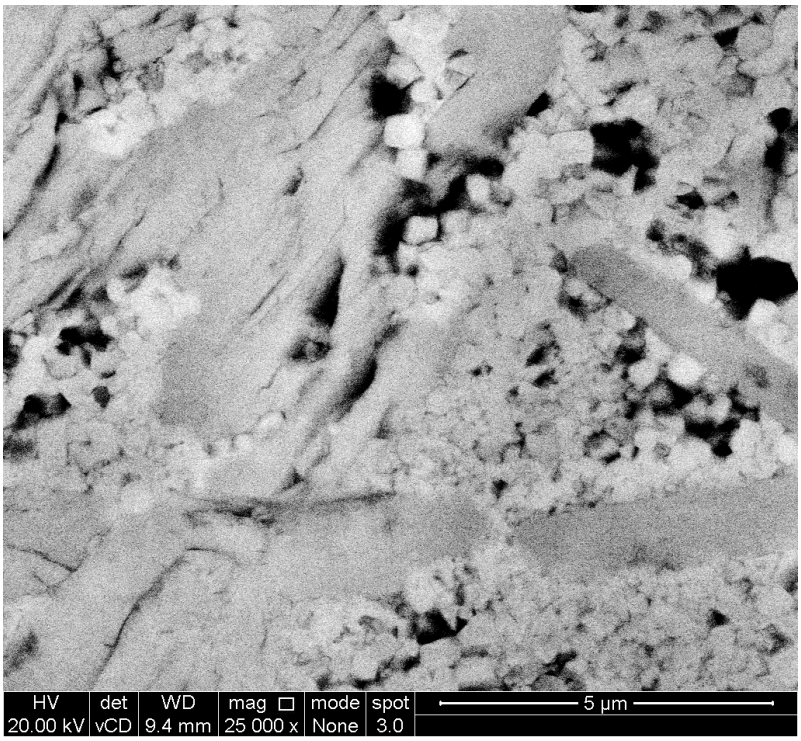

Figure 72 – BSE image showing the distribution and morphology of the TiC_x phase in a sample prepared at a holding temperature of 1300°C.

Figure 72 is a BSE image at a relatively high original magnification of ×25,000 which shows the morphology of the TiC_x phase. All grains appear < 1µm in size, with most grains much smaller than this. These grains appear to surround and separate the grains of Ti_3AlC_2. Figure 73 is an SE image taken at the same location and magnification. This image indicates the dark contrast observed in the TiC_x regions of the BSE images is due to grain pull-out.

Figure 74 is a BSE image of a region showing morphology similar to the Al_3Ti regions observed in the sample sintered at 1250°C. Observation at lower magnifications suggested such regions were infrequent, occupying a volume fraction < 1vol.%. Point spectra were obtained at the annotated locations, the compositions of which are summarised in Figure 75. By assuming that the carbon content in points 2 and 3 is associated with Ti_3AlC_2 and subtracting the relevant amounts from the overall composition, it can be confirmed that the composition of the dark contrast phase distributed amongst Ti_3AlC_2 grains in the top part of the image is Al_3Ti. Points 4 and 5 suggest the presence of a large particle of alumina.

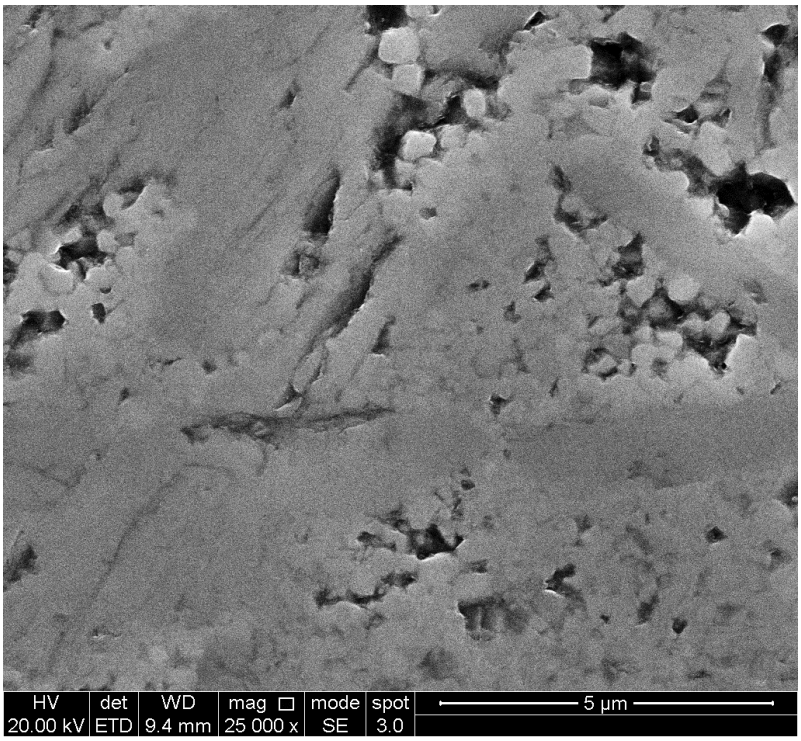

Figure 73 – SE image showing the distribution and morphology of the TiC_x phase in a sample prepared at a holding temperature of 1300°C. Grain pull-out of the TiC_x phase is evident.

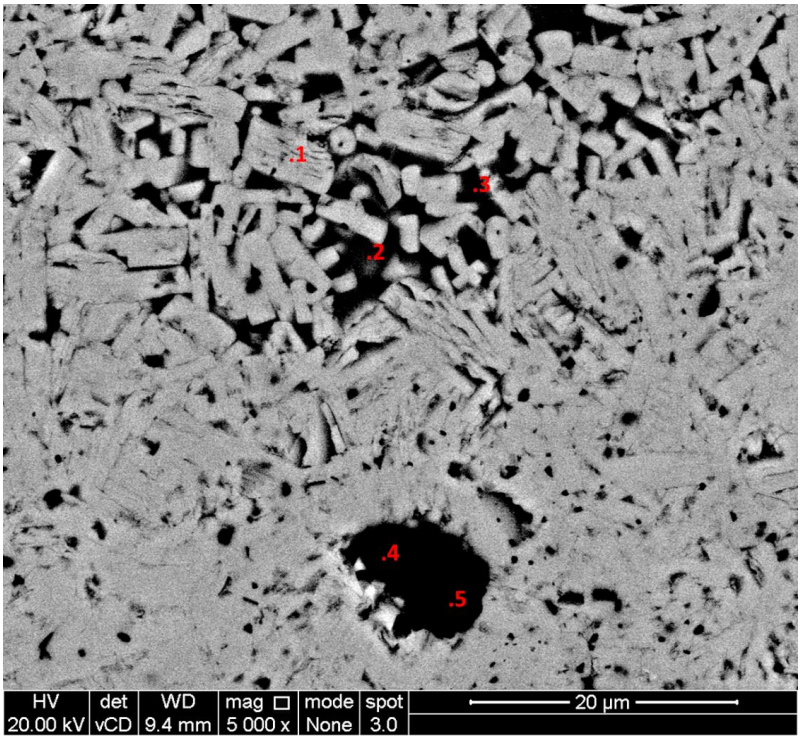

Figure 74 – BSE image of a sample prepared at a holding temperature of 1300°C showing a region with Al_3Ti and alumina present. The annotations mark the locations of EDS point analyses, the compositions of which can be found in Figure 75.

Figure 76 is an SE image taken at the same location and magnification as Figure 74. Al_3Ti is softer than Ti_3AlC_2, so the darker contrast in these regions shows greater loss of Al_3Ti from micropreparation. The morphology of the alumina particle may suggest cracking during oxidation.

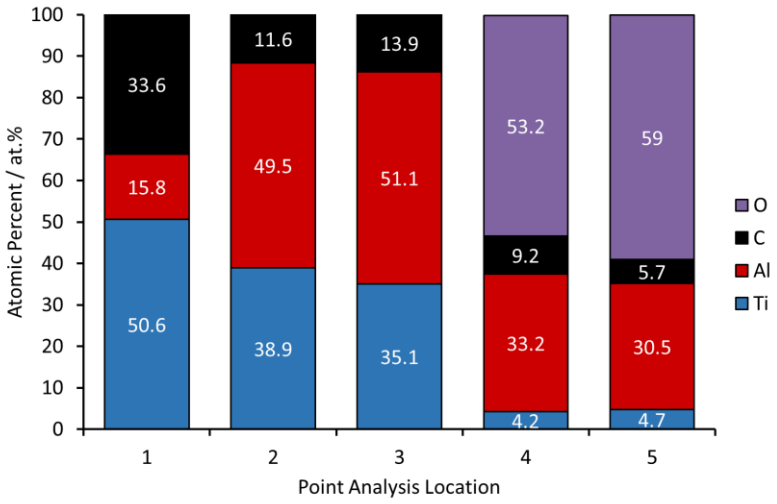

Figure 75 – Compositions of EDS point analyses obtained at the locations marked in Figure 74. Point 1 is consistent with the stoichiometry of Ti_3AlC_2. Points 2 and 3 represent a mixture of Ti_3AlC_2 and Al_3Ti. Points 4 and 5 suggest a mixture of Ti_3AlC_2 and Al_xO_y.

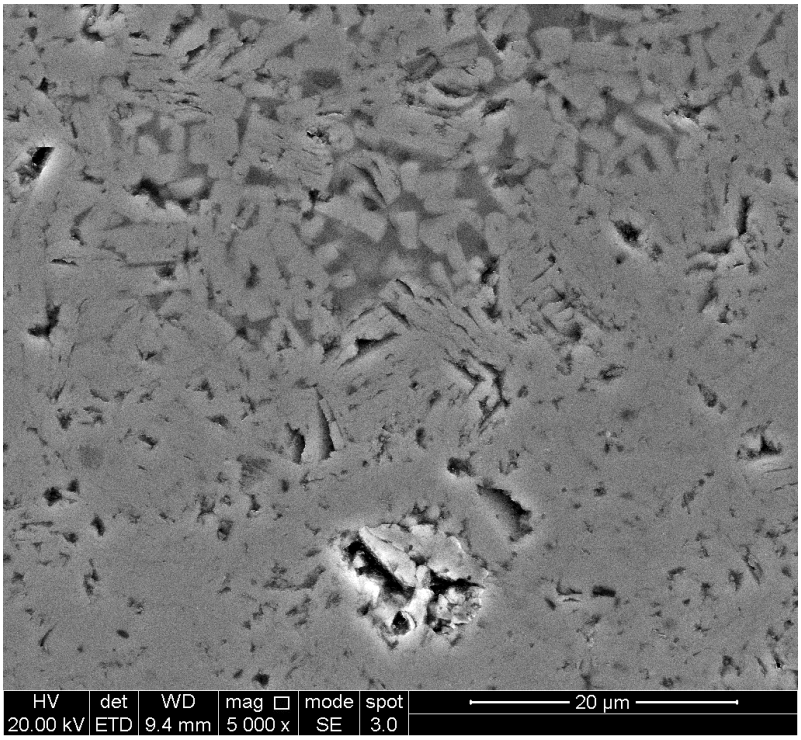

Figure 76 – SE image of a region containing Al_3Ti in a sample produced at a holding temperature of 1300°C. The image was taken at the same location and magnification as Figure 74.

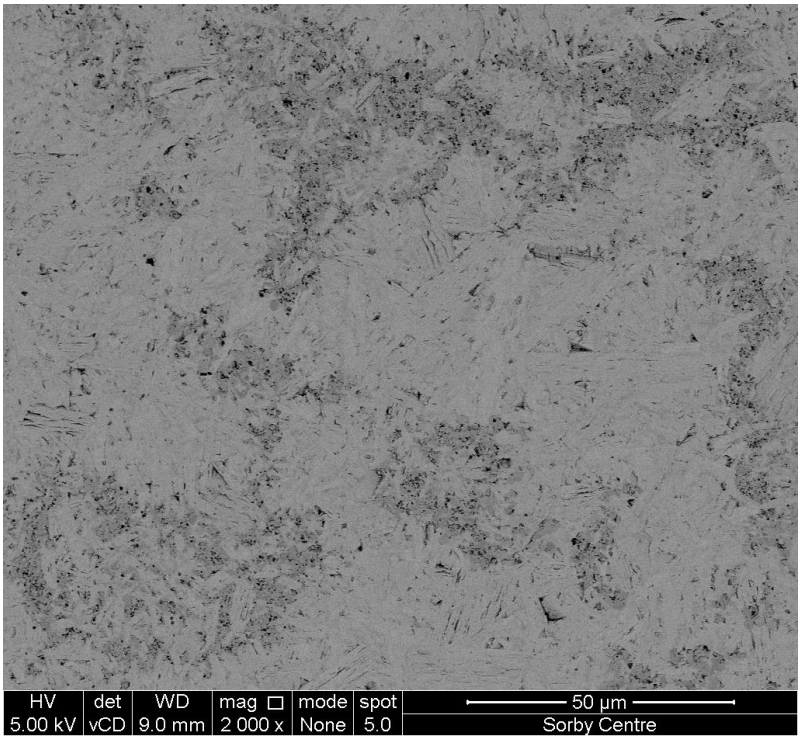

Figure 77 – BSE image of a sample sintered at 1400°C providing a general overview of the phase distribution. The lighter contrast phase is Ti_3AlC_2, and the darker contrast phase is TiC_x.

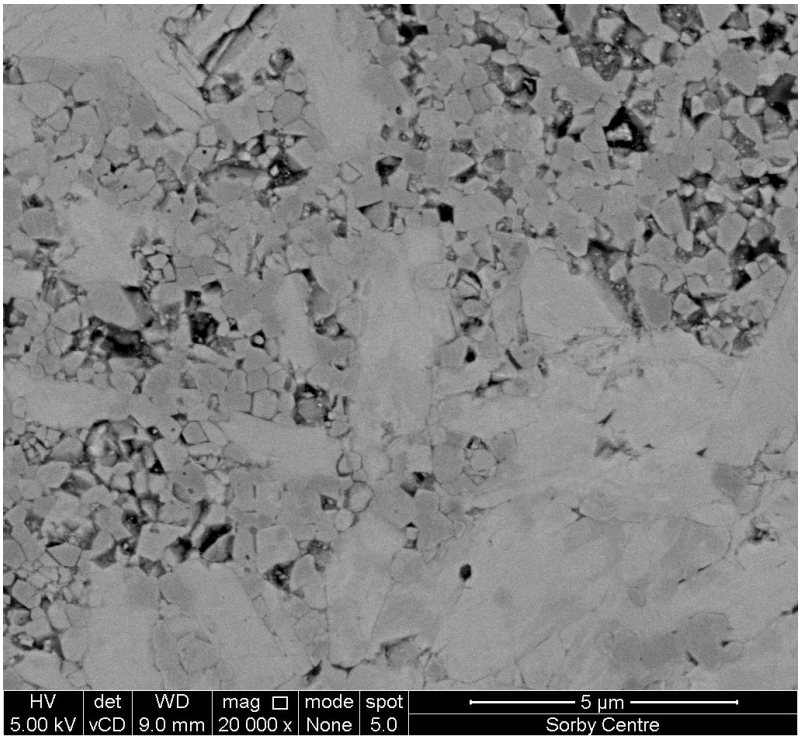

Figure 78 – BSE image showing the morphology of the TiC_x phase in a sample sintered at 1400°C. Rectangular grains of Ti_3AlC_2 can be found within the TiC_x phase. The TiC_x grains are < 1 µm in diameter.

5.2.3.3 Sintered at 1400°C

Figure 77 is a BSE image of a sample sintered at 1400°C. The image provides a general overview of the distribution of phases. The TiC_x phase (darker contrast) appears to be heterogeneously distributed in concentrated regions. Additionally, rectangular grains of Ti_3AlC_2 can be found within these regions of TiC_x.

Figure 78 is a BSE image taken at a much greater original magnification and shows the morphology of the TiC_x phase, which has a grains size of < 1 µm. Where the rectangular grains of Ti_3AlC_2 are present, the TiC_x grains form a straight line at the boundary and in many cases occupy a rectangular shape. This suggests much of the TiC_x has formed by decomposition of Ti_3AlC_2.

Ti_3AlC_2 is known to decompose to TiC_x and $Al_{(g)}$ from ~1300°C to 1400-1450°C [54,76,187,192]. Furthermore, aluminium volatilises at 1209°C at 1 Pa and 1359°C at 10 Pa [185]. The FCT Systeme SPS can achieve a vacuum pressure of 5 Pa. Thus, it is probable that aluminium evaporates and diffuses to the edge of the sample where it reacts rapidly with the graphite to form aluminium carbide. Overall, the morphology of the TiC_x particles at 1350°C seems to be most similar to those at 1400°C, suggesting TiC_x is forming by decomposition. It is possible that a slightly lower sintering temperature such as 1325°C may give superior results. Conversely, it is worth noting that Zhou *et al.* obtained pure

$Ti_3AlSi_{0.2}C$ at 1200°C and 1250°C, observing $TiAl_3$ and TiC_x at 1150°C and TiC_x at 1300°C [192]. However, the lower temperatures may be due to better mixing of the reagent powders, the use of a solid solution of Al and Si (silicon volatilises at 1635°C at 1 Pa and 1829°C at 10 Pa, so may lower the volatility of Al [185]), or more accurate measurement of the temperature during the SPS process.

5.3 Variation of aluminium stoichiometry

The effect of increasing the aluminium content was investigated next but did not improve the phase purity of the product. Many researchers suggest that an aluminium mole fraction greater than that of the stoichiometry (*i.e.* > 1) is required to produce pure Ti_3AlC_2 due to loss of aluminium through processes such as evaporation [54,76,187,192]. For example, Zhou *et al.* observed decomposition of Ti_3AlC_2 to TiC_x and $Al_{(g)}$ at 1300°C [192], and Yoshida *et al.*, observed Al evaporation when a sample of Ti_3AlC_2 was heated at 1400°C for extended dwell times [76]. In the present work, aluminium was observed to diffuse to the edges of the pellet where it reacted with the graphite paper to form aluminium carbide (§ 5.1.8.1). It was therefore decided to increase the aluminium content to account for such losses.

Samples were prepared with hyperstoichiometric quantities of Al to account for aluminium loss during SPS. Further detail of the sample prepared with 1.0 parts aluminium can be found in § 5.1. The sintering profiles, which can be found in Appendix B (§12.1.1), have the same shape and similar onset temperatures for changes in piston movement as that shown for the sample which was milled for 2 h and sintered at 1350°C with 1.0 parts Al (§5.1.4).

5.3.1 XRD and Rietveld refinement

The phase compositions are shown in the bar chart in Figure 79. The largest fraction of Ti_3AlC_2 was obtained with a stoichiometric aluminium content of 1.0. As the aluminium content increased above stoichiometric, the weight fraction of Ti_3AlC_2 decreased. At 1.1 Al the results were comparable to 1.0 Al, but at 1.2 Al and beyond the weight fraction of TiC_x was unacceptably large.

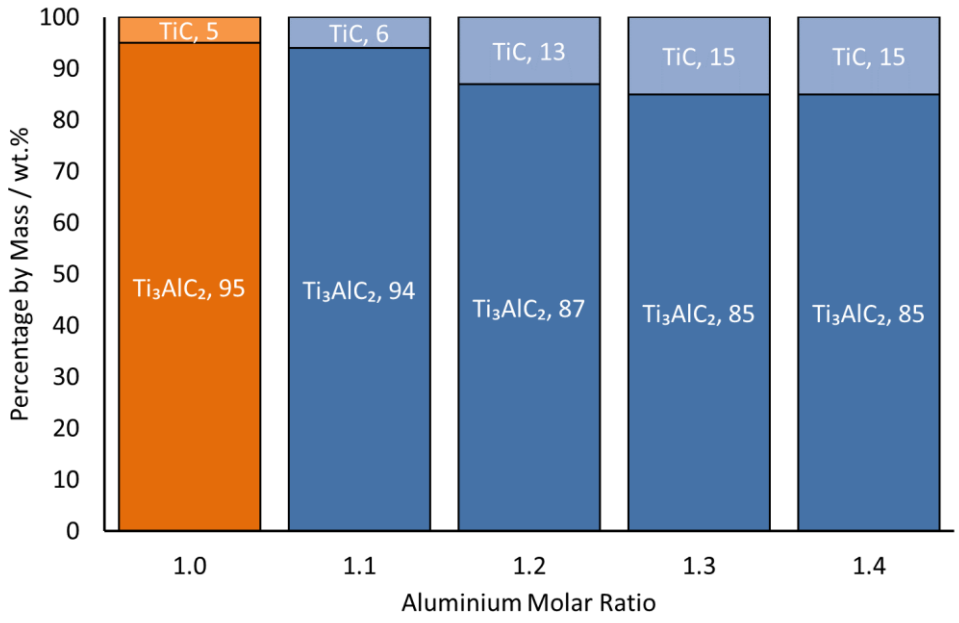

Figure 79 – Bar chart showing the phase compositions of samples produced with hyper-stoichiometric aluminium content. The purest sample was obtained with stoichiometric aluminium content, and the purity decreased as the stoichiometry increased.

Table 15 – Lattice parameters and fitting statistics from Rietveld refinement of XRD data for samples prepared with increasing aluminium content.

Milling Time	Lattice Parameters / Å			Fitting Statistics		
	Ti_3AlC_2, *a*	Ti_3AlC_2, *c*	TiC_x, *a*	χ^2	Rp	wRp
1.0	3.078	18.594	4.331	3.357	0.082	0.109
1.1	3.081	18.615	4.333	2.269	0.069	0.090
1.2	3.082	18.626	4.333	2.391	0.071	0.092
1.3	3.081	18.622	4.333	2.378	0.071	0.092
1.4	3.082	18.626	4.333	3.198	0.081	0.107

The lattice parameters and fitting statistics from Rietveld refinement are shown in Table 15. The *a*-axis lattice parameters for both Ti_3AlC_2 and TiC_x remain approximately constant, but the *c*-axis lattice parameter appears to increase with the aluminium content.

5.3.2 Density

The densities and relative densities of samples produced with variable aluminium content are shown in Table 16. The relative density decreased from 100% as the aluminium content increased, further indicating that a stoichiometric aluminium content gave the greatest quality of the product. However, as shown by the SEM images which follow, Al_2O_3 was observed as a third phase which was not detected by XRD. Al_2O_3 would be expected to lower the observed density, and not being detected by XRD would lower the calculated relative density.

Table 16 – Density and relative density of samples produced with variable aluminium content. The relative density decreased from fully dense as the aluminium stoichiometry was increased.

Aluminium Stoichiometry	Density, ρ / g cm^{-3}	Relative Density / %
1.0	4.276 ± 0.002	100
1.1	4.158 ± 0.006	97
1.2	4.165 ± 0.004	96
1.3	4.222 ± 0.005	97
1.4	4.181 ± 0.005	96

5.3.3 Microstructural examination

5.3.3.1 Prepared from 1.1 parts Al

Figure 80 is a BSE image which shows the general surface morphology of the material. The TiC_x regions all appear to have Ti_3AlC_2 grains interspersed throughout them. These regions are heterogeneously distributed in concentrated regions throughout the material. The spots of Al_2O_3 are evenly distributed throughout the Ti_3AlC_2 phase. According to Tzenov and Barsoum, these particles of

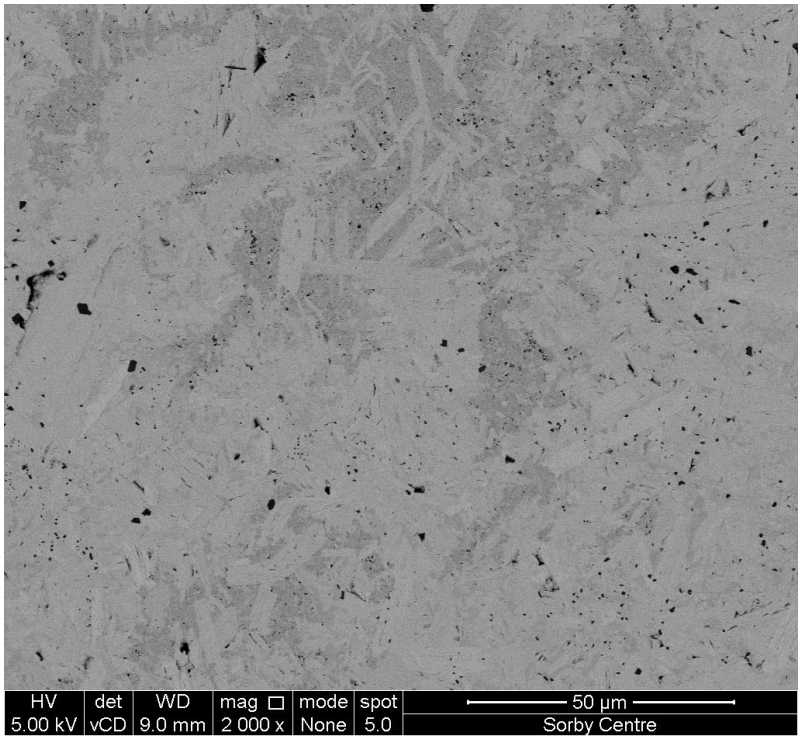

Figure 80 – BSE image which provides a general overview of the surface morphology of a sample prepared using 1.1 parts Al. The lightest contrast phase is Ti_3AlC_2, the medium grey contrast phase is TiC_x, and the dark contrast spots are Al_2O_3.

Al_2O_3 may be formed from Al_4C_3 as per Equation 32 [187]. Al_4C_3 forms from an equilibrium between the Al-containing melt, $TiAl_3$ and graphite [54].

Equation 32

$$Al_4C_3 + 6H_2O \rightleftharpoons 2Al_2O_3 + 3CH_4$$

Figure 81 shows the morphology of the TiC_x phase. There is a large variation in grain size, but most of the grains are $\ll 1$ µm in diameter. Some of the TiC_x grains are clustered in rectangular shapes, which may indicate partial formation of TiC_x by decomposition of Ti_3AlC_2, as observed for the sample sintered at 1400°C (§ 5.2.3.3). It is possible that excess Al forms a melt which aids removal of any Al released by decomposition of Ti_3AlC_2.

5.3.3.2 Prepared from 1.2 parts Al

Figure 82 is a BSE image taken at a relatively low original magnification which provides a general overview of the phases visible within the material. Spots of alumina are prevalent throughout, and TiC_x is heterogeneously distributed in concentrated regions. Overall, the microstructure is fairly similar to the sample prepared from 1.1 parts aluminium, but the TiC_x clusters appear to be larger (Figure 84), and some $TiAl_3$ was observed in some locations (Figure 85).

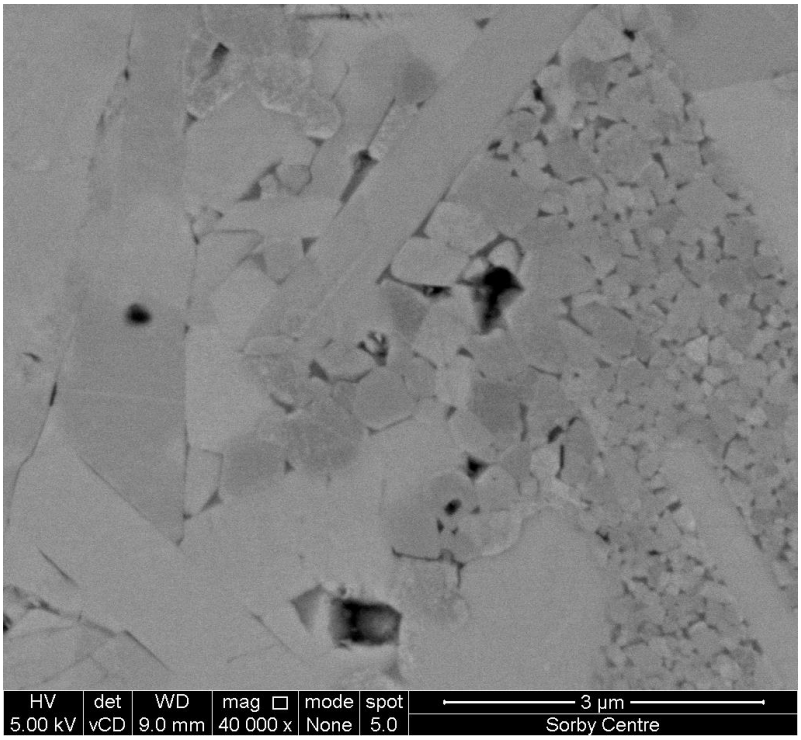

Figure 81 – BSE image showing the morphology of TiC_x in a sample prepared using 1.1 parts Al. The image was taken at a relatively high original magnification of x40,000 and shows grains with diameters significantly smaller than 1 µm.

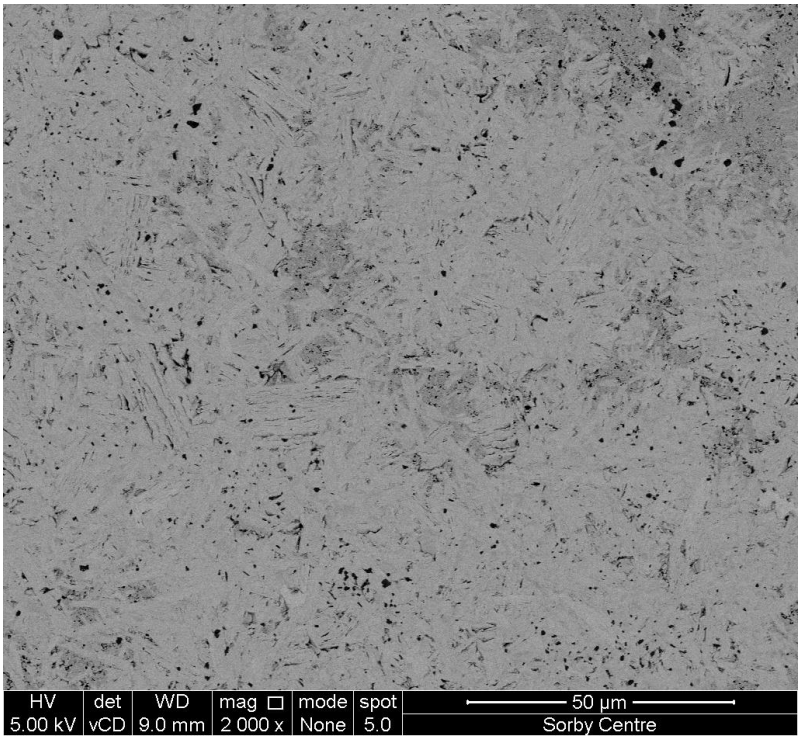

Figure 82 – BSE image providing a general overview of the surface microstructure of a sample prepared using 1.2 parts Al. Three key phases are visible: the lightest contrast is Ti_3AlC_2, the medium grey contrast is TiC_x, and the dark contrast is mainly aluminium oxide.

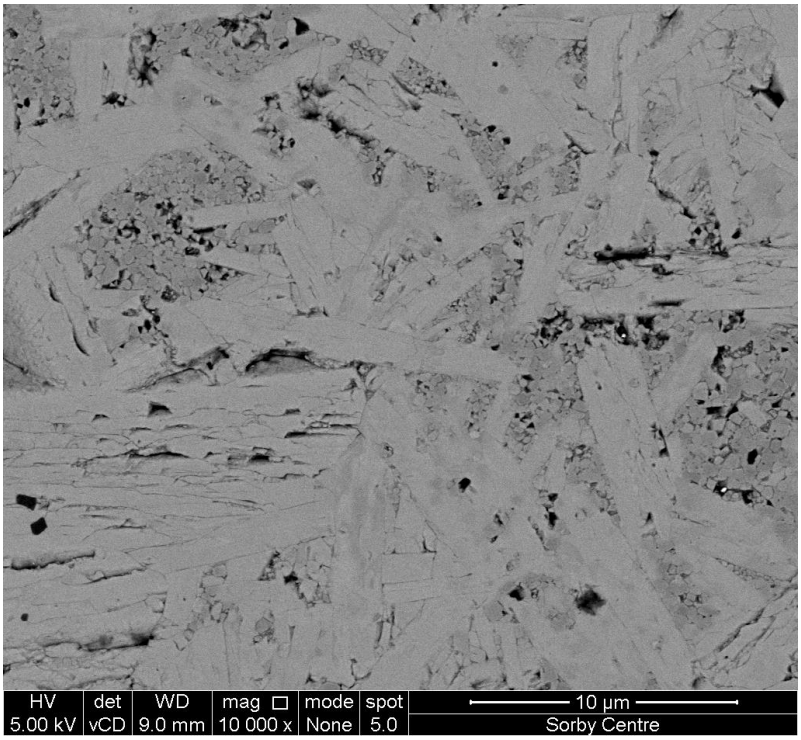

Figure 83 – BSE image of a region of high TiC_x concentration. The TiC_x particles are distributed amongst the grain boundaries of Ti_3AlC_2.

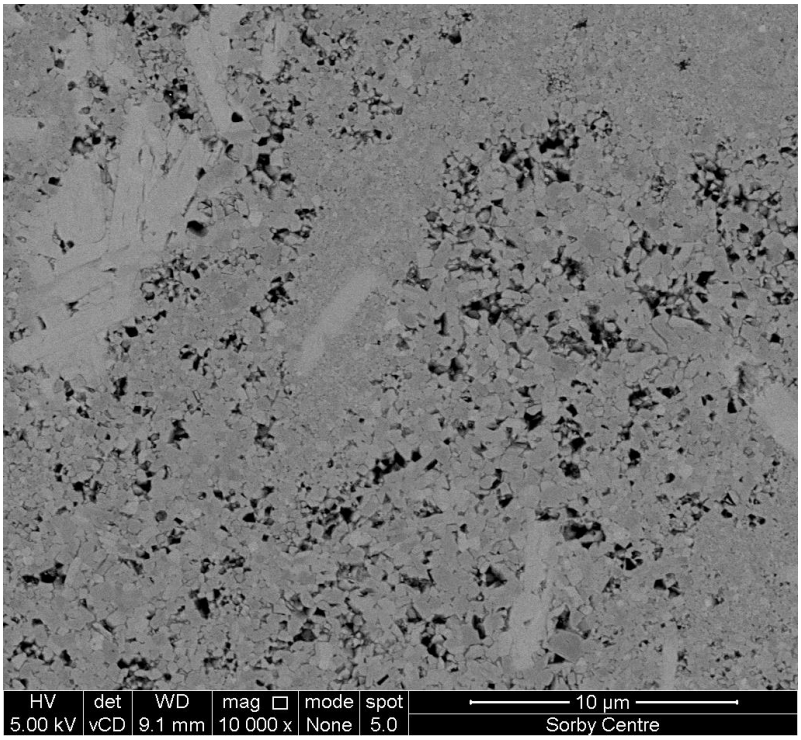

Figure 84 – BSE image of a large concentrated region of TiC_x. Such regions are infrequent but cover large areas with very small, dense TiC_x grains.

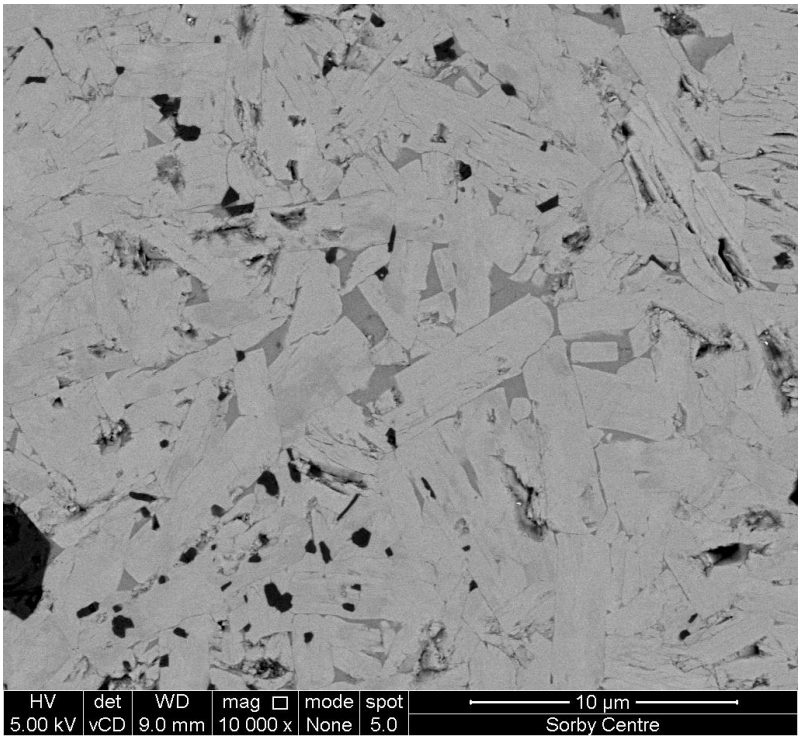

Figure 85 – BSE image showing a region containing Al_3Ti distributed around grains of Ti_3AlC_2. The Ti_3AlC_2 grains within this region are small, and no grain structure is visible within the Al_3Ti phase.

Figure 83 is a BSE image of a region containing significant amounts of TiC_x with a grain size < 1 µm. Here, the TiC_x is distributed between the grain boundaries of Ti_3AlC_2 grains. It may have precipitated from a melt containing insufficient aluminium, or some TiC_x formed and sintered before it was able to interact with Al.

Figure 84 is a BSE image of a large region of TiC_x particles. The morphology is very similar to that found for the sample prepared from a precursor which was milled for 3 h (§ 5.1.8.2), with a grain size ≪ 1 µm for most grains. It is possible that the increased quantity of Al increases the amount of $TiAl_3$ which forms exothermically, simultaneously reducing the quantity of Ti available to form non-stoichiometric TiC_x and causes Ti and C to react and sinter as particles of TiC. Additionally, it appears as if the embedded Ti_3AlC_2 particles are in the process of reacting, either decomposing to or forming from, TiC_x. In particular, in the bottom of the image is a grain which has the same contrast and rectangular shape as Ti_3AlC_2, but the equiaxed shape of TiC_x grains is visible within the grain. This is suggests decomposition of Ti_3AlC_2 grains, as observed for the sample sintered at 1400°C (§ 5.2.3.3).

Figure 85 is a BSE image showing a region containing Al_3Ti distributed among grains of Ti_3AlC_2. Such regions are uncommon within the material, in agreement with the XRD data which did not show Al_3Ti. The Ti_3AlC_2 grains within the Al_3Ti region are quite small. The data obtained for samples prepared with variable sintering temperatures (§ 5.2) indicates Al_3Ti is an intermediate in the reaction

mechanism to form Ti_3AlC_2. Therefore, the small size of these Ti_3AlC_2 grains is likely due to them being in the process of forming.

5.3.3.3 Prepared from 1.3 parts Al

Figure 86 is a BSE image providing a general overview of a sample prepared with 1.3 parts Al. There are two different regions of TiC_x, both of which are heterogeneously distributed in concentrated regions throughout the material and consist of very fine grains of TiC_x. Most of these regions are interspersed with rectangular grains of Ti_3AlC_2, but some are concentrated regions consisting solely of TiC_x. The concentrated TiC_x regions appear larger than those observed with 1.2 parts Al, which were in-turn larger than those with 1.1 parts Al. There is an unusual lack of Al_2O_3 visible throughout the material; dark contrast mostly represents indents into the surface or pluck-out of TiC_x grains.

Figure 87 is a BSE image of a large concentrated region of TiC_x grains. The grains are very small, with a grain size $\ll 1$ µm. Again, the morphology is similar to the sample prepared from a precursor which was milled for 3 h (§ 5.1.8.2) and suggests TiC formed and sintered before the molten Al-containing phase was able to distribute throughout the material and react with TiC_x.

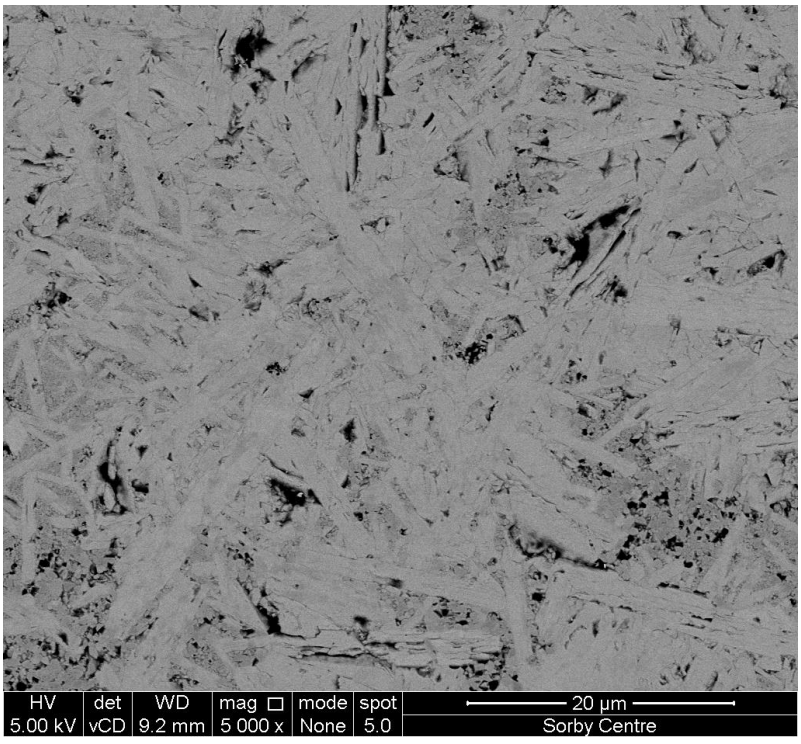

Figure 86 – BSE image providing a general overview of the microstructure of a sample prepared from 1.3 parts Al. The lightest contrast phase is Ti_3AlC_2, and the darker grey phase is TiC_x. The dark contrast shows mainly indents and grain pluck-outs.

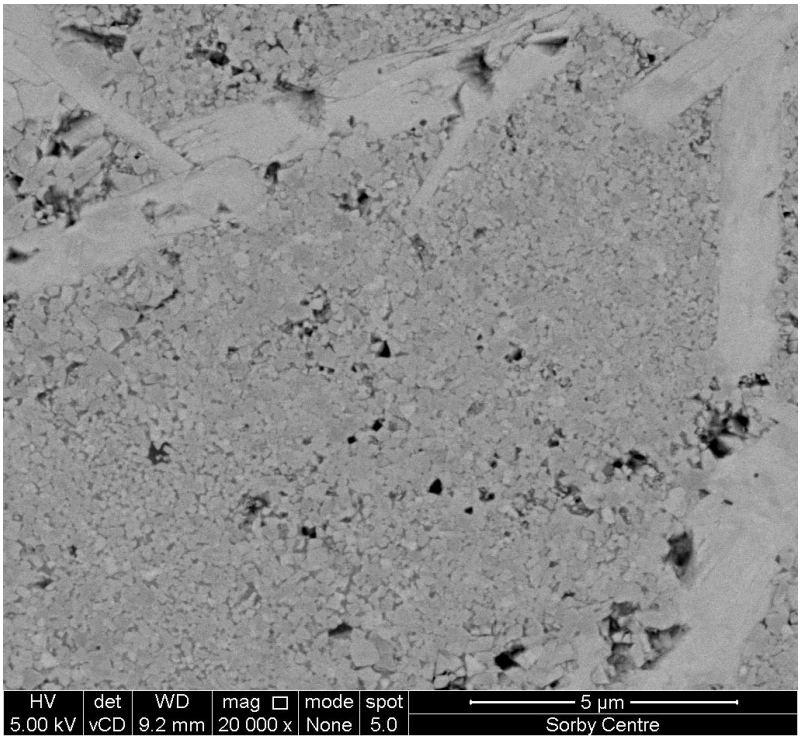

Figure 87 – BSE image of a large region of TiC_x. The particles are nanosized, with a grain size $\ll 1$ µm.

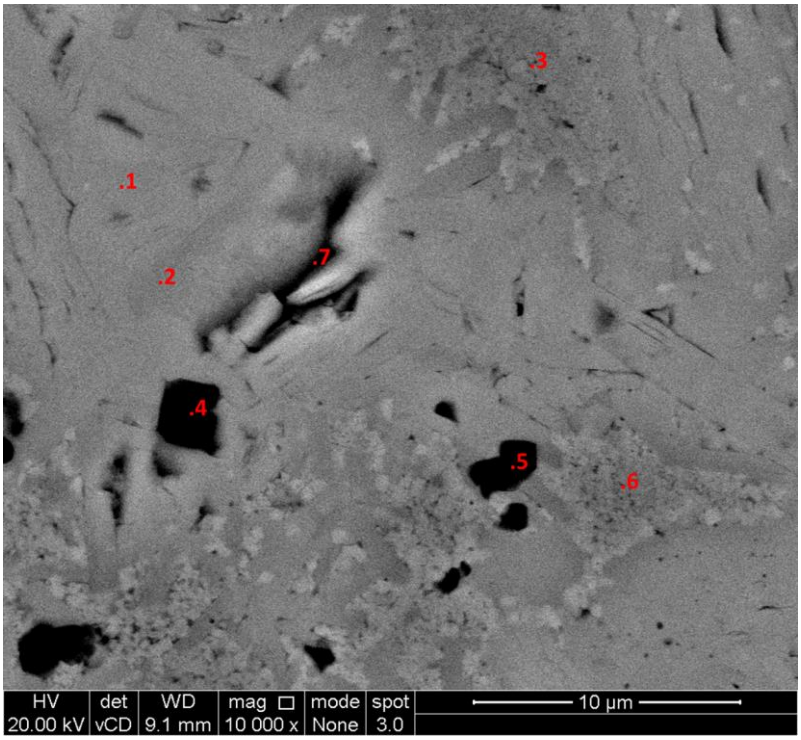

Figure 88 – BSE image showing the phases present in a sample prepared using 1.4 parts Al. The annotations mark the locations of point analyses, the compositions of which are shown in Figure 89. Points 1 and 2 represent the morphology of Ti_3AlC_2. Points 3 and 6 show the morphology of TiC_x. Points 4 and 5 show the morphology of Al_2O_3, which was not observed by XRD.

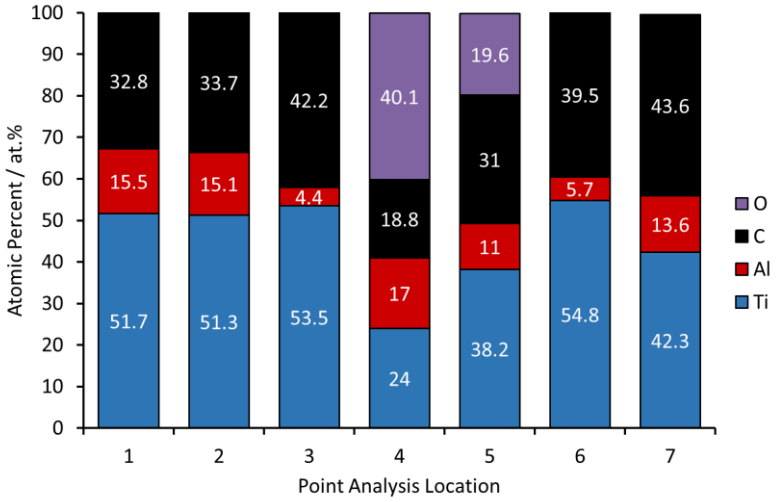

Figure 89 – Compositions of EDS point analyses conducted at the locations marked in Figure 88.

5.3.3.4 Prepared from 1.4 parts Al

Figure 88 is a BSE image with EDS point analyses at the annotated locations. Most of the material consists of Ti_3AlC_2. The fine-grained regions are TiC_x, the grains of which are ≪ 1 µm. The dark spots (*e.g.* points 4 and 5), approximately 1-4 µm in size, have a composition and morphology consistent with previously observed Al_2O_3 particles.

Figure 90 provides a general overview of the surface morphology. There is a significant fraction of Al_2O_3 distributed throughout the material which was not observed via XRD; Raman spectroscopy may further aid its identification. The TiC_x regions appear to be distributed at the grain boundaries of Ti_3AlC_2 which suggests an incomplete reaction, as observed in the sample sintered at 1300°C (§ 5.2.3.2).

Figure 91 is a higher magnification BSE image focused on the TiC_x region in the top of Figure 90. It shows clearly that the TiC_x particles are distributed at the grain boundaries of Ti_3AlC_2. Furthermore, this phase has a nanoscale grain size. Figure 92 is a BSE image which shows that there is a significant volume fraction of Al_2O_3 particles evenly distributed throughout the material.

The grain size of the TiC_x particles appears to decrease as the Al content increase; this was also observed by Choi and Rhee, who attribute the phenomenon to the reduction in combustion temperature as heat is used to decompose titanium aluminides [184]. Also, the presence of Al may limit diffusion of C along the grain boundaries, which is the reported mechanism of grain growth of TiC.

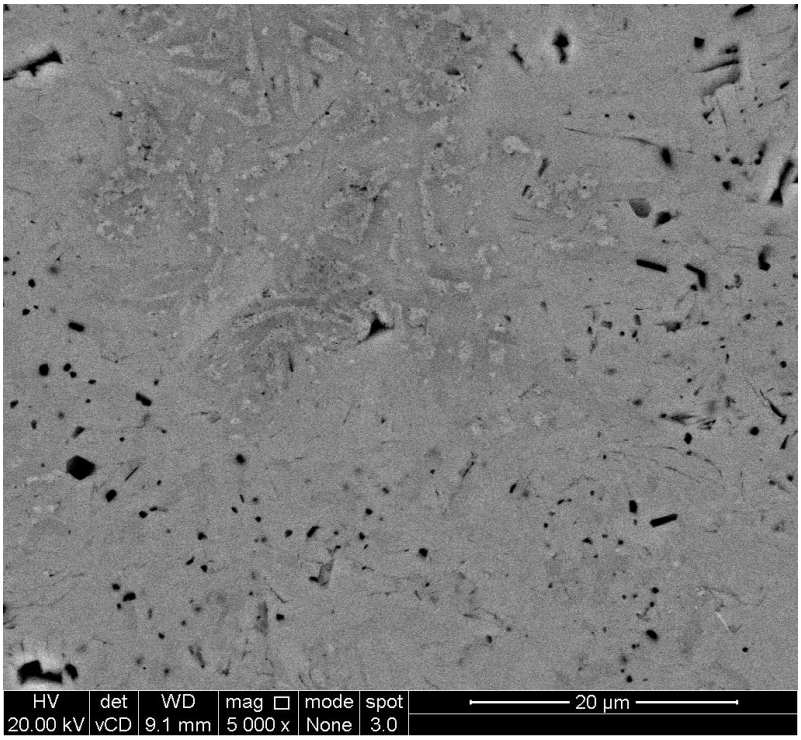

Figure 90 – BSE image showing the general surface morphology of a sample prepared using 1.4 parts Al. The dark contrast spots are Al_2O_3 and appear to occupy a significant fraction of the material. The TiC_x in the top of the image appears to be present at the grain boundaries of Ti_3AlC_2.

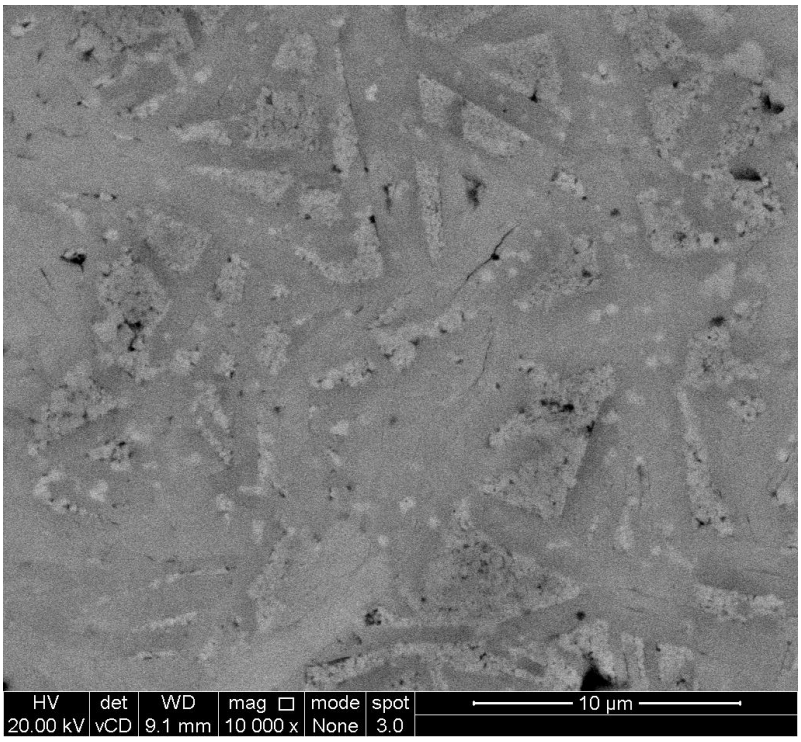

Figure 91 – A BSE image of a sample produced from 1.4 parts Al which shows the distribution of nanoscale TiC_x grains among the grain boundaries of Ti_3AlC_2.

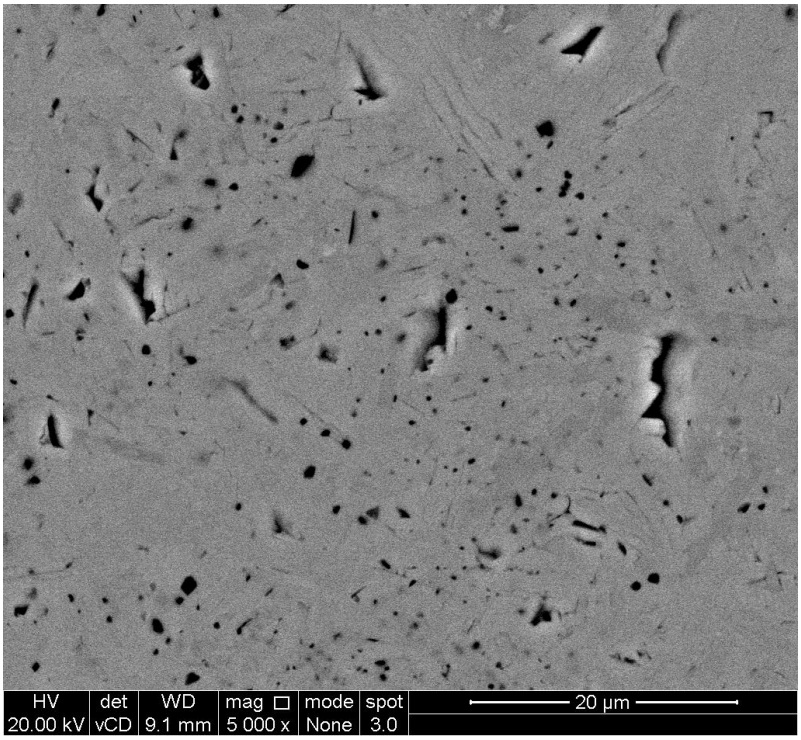

Figure 92 – BSE image of a sample prepared from 1.4 parts Al. A significant fraction of the aluminium is present as Al_2O_3 particles, evenly distributed throughout the material.

At greater aluminium content, *i.e.* 1.2 and 1.3 parts, the graphite punches became more difficult to remove from the sample after sintering. At 1.4 parts aluminium the punch broke significantly when removed from the sample. It appears that any excess aluminium is simply pushed out of the bulk sample as it densifies and reacts preferentially with the graphite liner. Furthermore, it is possible that titanium dissolved within the aluminium melt and was transported to the edge of the pellet, lowering the fraction of titanium in the pellet and favouring the formation of TiC_x with higher carbon stoichiometry over Ti_3AlC_2. Further characterisation of the diffusion layer would enable better understanding of this process.

5.4 Discussion

The following reaction mechanism is proposed. Milling Ti and C causes significant mixing of the two reagents and particle size reduction, with partial interdiffusion between Ti and C. The fraction of Ti_3AlC_2 is maximised when the temperature of ignition for this mixture is slightly greater than the melting point of Al. During SPS, the first reaction is between Ti and Al, which react exothermically to form $TiAl_3$. Al and $TiAl_3$ then begin to melt and spread throughout the material, aiding mass transfer and densification and enabling further reaction with Ti. This is closely followed by a self-propagating reaction between Ti and C to form $TiC_{0.67}$. Graphite itself has low solubility in the melt, whereas dissolution of TiC_x into the Ti-Al melt is relatively facile. The reaction between $TiC_{0.67}$ and the melt proceeds by the mechanism proposed by Riley and Kisi, with ordering of the carbon vacancies in the $TiC_{0.67}$ then infiltration of the predominantly Al-containing melt as the TiC_x particles dissolve [77,85]. This reaction was sustained by further temperature rise and dwelling in the SPS.

When milling was performed for just 1 h, the reaction between Ti and C was not self-propagating, so formation and reaction of $TiC_{0.67}$ occurred more slowly and more TiC_x was observed in the product. When milling was performed for 3 h or 4 h, Ti and C reacted exothermically before $TiAl_3$ formation and Al melting. The heat released caused partial evaporation of Al and limited Ti_3AlC_2 precipitation at higher temperature, maximising the formation of stable TiC_x. Furthermore, milling Ti and C continuously for 4 h caused ignition and formation of TiC_x during the milling step, which then preferentially sintered before Al melting could occur.

The reaction was incomplete when the temperature rise was stopped at 1250°C, with precipitation of TiC_x and regions of $TiAl_3$ observed. This confirmed that the mechanism proposed by Ge *et al.* for the combustion synthesis of Ti_3AlC_2, with an intermediate step of Ti-Al melt formation, is relevant to the mechanism observed in this work, except the production of TiC_x is more facile due to the milling process used [81]. At 1300°C the reaction was closer to completion but some $TiAl_3$ remained. At 1350°C, the reaction proceeded to completion, but Al evaporation led to some impurity of TiC_x. At 1400°C, decomposition of Ti_3AlC_2 formed significant quantities of TiC_x.

When Si was used instead of Al, a Ti-Si melt formed, and the reaction proceeded by the same mechanism, but the temperature was too low, or the holding time was too short, for complete reaction to occur (see Appendix D). Using an excess of Al changed the position within the phase diagram, leading to the preferential formation of TiC_x, and may have aided removal of Al upon decomposition of Ti_3AlC_2 [54]. It is worth noting that Tzenov and Barsoum obtained the purest product with 1.1 parts Al and 1.8 parts C, so it may be necessary to also reduce C to stay in the thermodynamically most stable region for phase formation [187].

The ignition temperature for the reaction between Ti and C is affected by the rate of reaction, which is proportional to the contact surface area between Ti and C particles [82]. This contact surface area is increased significantly by milling. The ignition temperature for the Ti-C mixture would have differed when milling was performed with the Retsch Cryomill compared to when milled in the SPEX 8000M Mixer/Mill, and was a contributing factor to the increased purity of this sample (see Appendix B). Therefore, it would be useful in the future to investigate the effect of slight variations in milling time around 2 h in the SPEX 8000M Mixer/Mill. It is also possible that the morphology of Ti-C was more equiaxed in the Retsch Cryomill due to the higher BPR, but more flake-like in the SPEX 8000M Mixer/Mill due to the lower BPR [69]. It would therefore be interesting to investigate the effect of milling time at different BPRs.

The work of Lee *et al.* (1997) indicates that clusters of aluminium or TiC_x would likely be observed if the compact density is not optimal (see Figure 9, § 3.3.3) [82]. This suggests that the effect of uniaxial force should be investigated, including its magnitude, rate of application, and temperature at which it is applied. While the relative density of samples was high, the formation of TiC_x clusters may be due to application of too much force.

Evaporation of Al contributes significantly to the presence of TiC_x in all of the samples. In order to minimise this, synthesis should be performed in argon rather than vacuum in order to lower the vapour pressure of Al. Additionally, the holding time at maximum temperature should be reduced, and the ramp rate should perhaps be increased after Al has melted and spread through the material. It may be necessary to investigate changes to holding temperature and Al content with these changes.

6 Corrosion of Ti_3AlC_2

Table 17 summarises the results from corrosion experiments of Ti_3AlC_2. Results for the majority of these samples follow, and additional results can be found in Appendix F. Ti_3AlC_2 was tested because it is one of the most well studied MAX phase compositions available and there is evidence that it performs well under irradiation damage and has low neutron absorption. Samples were exposed to LiCl-KCl eutectic (LKE) because it is generally considered the lead candidate medium for possible future large scale pyroprocessing of spent nuclear fuel (there is a wealth of data available for the chemistry of elements in this solvent) and KCl-$MgCl_2$ eutectic (KME) because it has been proposed as a very low-cost solvent for the secondary coolant loop of molten salt reactors. The samples in this section were prepared from a Ti-C precursor which was milled from titanium and graphite in a SPEX 8000M Mixer/Mill for 2 h using a tungsten carbide vial set. The precursor was then mixed with 1.0 parts aluminium and heated in an SPS to 1350°C at a rate of 50°C min^{-1} then held for 15 min. The synthesis and characterisation of these samples is discussed in detail in § 5.1.

Many of the experiments with relatively pure salts (*i.e.* low metallic and oxide impurities) resulted in loss of Al and formation of TiC_x and a Ti-C-Cl phase. These results show some resemblance to samples of Ti_3AlC_2 which were exposed to $Cl_{2(g)}$. The reaction of MAX phases with chlorine gas has been investigated by numerous researchers [144–146], and found to result in loss of the A-group element and formation of a layered MX_n compound. This appears to be consistent with the observations in this work. Furthermore, it appears that a Ti-C-Cl phase may form as an intermediate, similar to the $Ti_3C_2T_2$ compounds (e.g. $Ti_3C_2F_2$ and $Ti_3C_2(OH)_2$) observed by researchers such as Naguib *et al.* [149–151].

In processed salts, the samples generally show reaction with impurities, primarily W and O. In LKE at 600°C, some uniform corrosion occurred with deposition of W and MgO impurities on the surface. At 850°C, the extent of corrosion was much more severe; oxides such as lithium aluminate formed at the surface which subsequently underwent pitting corrosion, and the underlying reaction layer resembled that of reaction with $Cl_{2(g)}$. The samples exposed to KME formed relatively stable W and oxide deposits with relatively little corrosion of the underlying substrate.

The mass loss for samples exposed to processed LKE at 600°C was negligible, but increased when the temperature was raised to 850°C. The mass loss was much greater in as-received LKE but may be due to dissimilar materials corrosion. In processed KME, mass gain was observed, which increased when the temperature was raised to 850°C. The roughness of a pristine sample polished to 1 µm was 0.15 ± 0.01 µm. A slight increase in roughness was observed for all samples exposed to processed LKE, but the increase was significant for all samples exposed to processed KME and the sample exposed to as-received LKE. Furthermore, an increase in exposure time resulted in a greater increase in roughness than an increase in exposure temperature.

Table 17 – Summary of corrosion results for samples of Ti_3AlC_2.

Experiment	Salt	Temperature / °C	Duration / h	Mass loss / mg cm^{-2}	Reaction Layer Thickness / µm	Roughness / µm	Reaction Products	Type of reaction	Type of corrosion	Main Impurities	Relation to MSR Operation
OCP	LKE, processed	550	16	N/A	40 + deposition layer	N/A	TiC_x, $LiAl_5O_8$ or $LiAl_2O_{3.5}$	Reaction with Cl_2	Intergranular and intragranular	O (limited quantity)	Pure conditions, no redox control, highlights corrosion greatest at start-up
Anodic dissolution	LKE, processed	550	1	N/A	125-185	N/A	TiCx	Reaction with Cl_2	Galvanic (50 mA)	O (limited quantity)	Accelerated testing. Shows what would occur with significant deviation from reducing conditions
Static corrosion (initial)	LKE, processed	600	125	5.54	170-270	N/A	TiCx, Ti-C-Cl	Reaction with Cl_2	Galvanic (intergranular and intragranular)	Fe, Ni	Suggests incompatibility with steel and possibly nickel alloys
Static corrosion (sample A)	LKE, as-received	600	125	1.32	80-120	N/A	TiC_x, Ti-C-Cl (Ti_2C_3Cl)	Reaction with Cl_2	Intergranular and intragranular	O, Fe, Cu, P, S	Operation in impure conditions with air ingress
Static corrosion (sample B)	LKE, as-received	600	125	0.34	60-400	4.04 ± 0.35	TiC_x, Ti-C-Cl	Reaction with Cl_2	Intergranular and intragranular	O	Operation in impure conditions with air ingress
Static corrosion	LKE, processed	600	125	0.00	< 3	0.24 ± 0.04	TiC_x, MgO, Mg_2TiO_4	General corrosion and surface oxidation	Uniform corrosion	Mg, O, Fe	Operation in slightly impure conditions.
Static corrosion	LKE, processed	600	250	0.06	< 3	0.46 ± 0.04	TiC_x, α-W, β-W, ε-W_2C	General corrosion and deposition of W	Uniform corrosion	W, O, Fe	Effect of noble metal fission products
Static corrosion	LKE, processed	850	125	0.47	15-20 on one side, 7 on opposite	0.33 ± 0.07	TiC_x, γ-$LiAlO_2$, $Al_{0.95}Ti_{1.05}$, γ-$Al_{2.67}O_4$, $Li_4Ti_5O_{12}$	Oxidation and pitting	Oxide formation, pitting	W, O, Fe	Highlights limited stability of oxide reaction layers at higher temperature
Static corrosion	KME, processed	600	125	-0.54	25 on one side, 5-8 on opposite	2.90 ± 0.41	α-W, β-W, MgO	Deposition of W and oxides	Deposition	W	Effect of noble metal fission products with air ingress
Static corrosion	KME, processed	600	250	N/A	15-25	4.85 ± 0.64	α-W, β-W, MgO	Deposition of W and oxides	Deposition	W	Effect of noble metal fission products with air ingress
Static corrosion	KME, processed	850	125	-1.99	4-15	2.25 ± 0.12	TiC_x, $MgAl_2O_4$, MgO, α-W, Al	Deposition of W and oxides	Deposition	W, Ag	Effect of noble metal fission products with air ingress. Suggests tungsten or tungsten carbide coating could be very protective at higher temperatures.

6.1 Corrosion in LiCl-KCl Eutectic

6.1.1 As-received salt, 600°C, 125 h, sample A

6.1.1.1 Glancing angle X-ray diffraction

GAXRD patterns are shown in Figure 93, normalised relative to the TiC (200) peak [178,179]. TiC_x was the most intense phase at all glancing angles. The Ti_3AlC_2 peaks are relatively weak, and many of these peaks disappear when the glancing angle is decreased to < 5° ω. The peaks which appear at < 10° ω, most notable at 7.9° and 16.0° 2θ, are postulated to be the (002) and (004) peaks of a Ti-C-Cl phase based upon the original 312 MAX phase crystal structure. Based on this assumption, the *c*-axis lattice parameter would be 22.3 ± 0.2 Å, an expansion from that of the original Ti_3AlC_2 (18.557 Å) [178]. Further evidence for formation of such a phase was found by microstructural examination of the cross-section.

6.1.1.2 Microstructural examination of the surface

Figure 94 is a BSE image of the sample surface prior to cleaning in distilled water in an ultrasonic bath. EDS was performed, and the elemental composition data is summarised in Table 18. The fraction

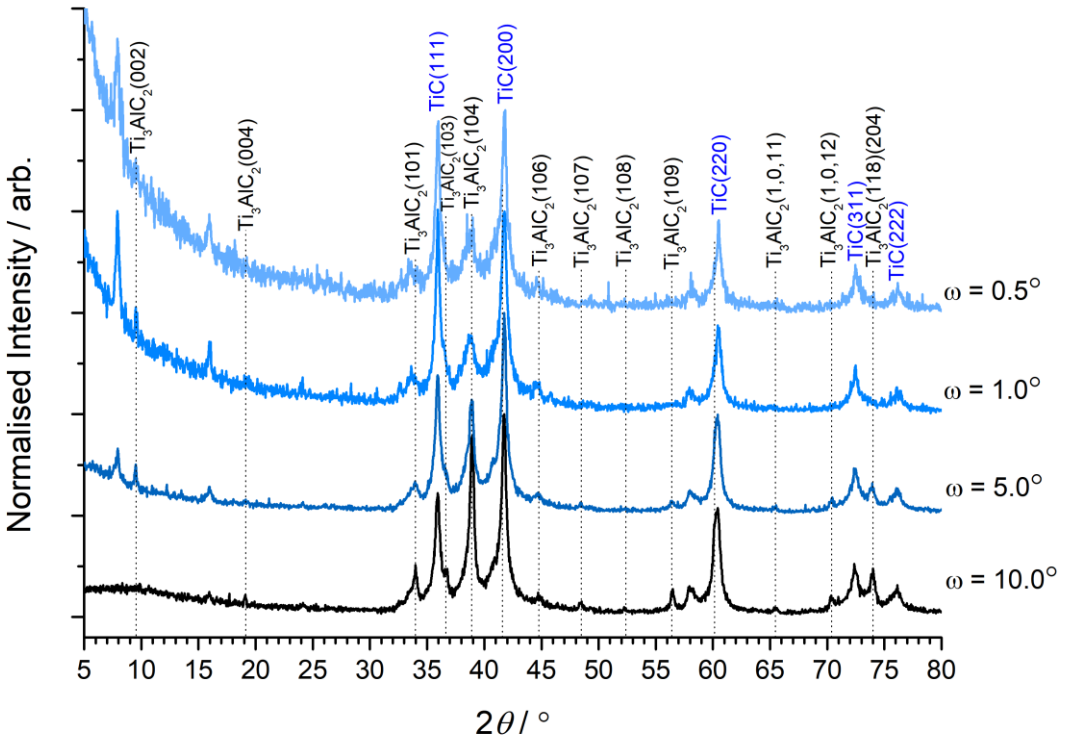

Figure 93 – GAXRD patterns for the first of two samples which were exposed to as-received LKE at 600°C for 125 h. TiC_x was the most intense phase at all glancing angles, and the patterns were normalised relative to the TiC (200) peak. There are unidentified peaks, notably those at 7.9° and 16.0° 2θ which are postulated to belong to a Ti-C-Cl phase based upon the original 312 MAX phase structure.

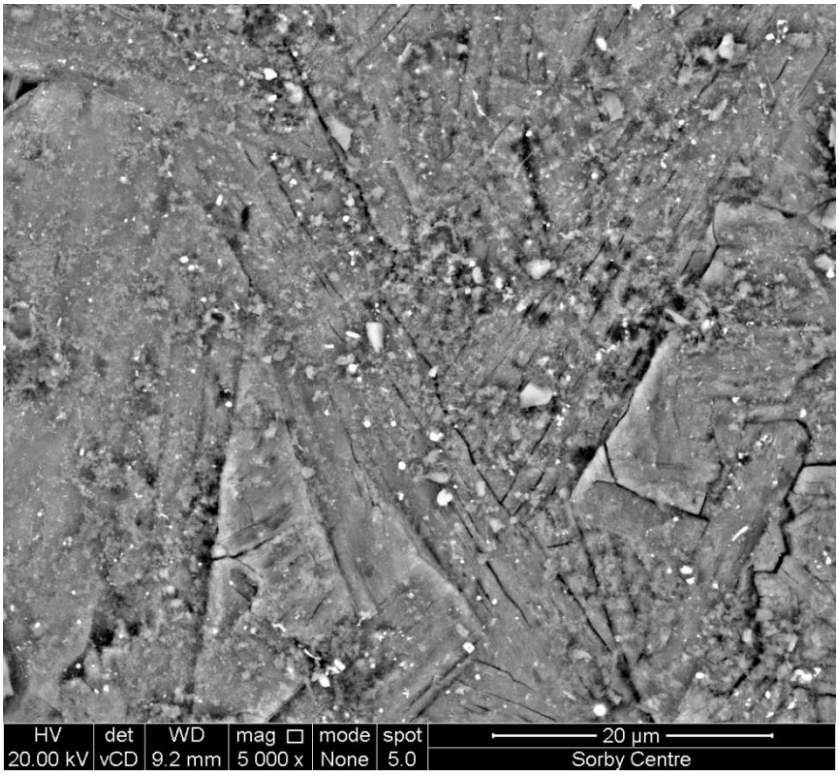

Figure 94 – BSE image of the surface of Ti_3AlC_2 after exposure to as-received LKE at 600°C for 125 h.

Table 18 – Elemental composition data (in at.%) for the map sum spectrum of Figure 94.

O	Ti	C	Fe	Cl	Al	Other	Other Elements
37.7	33.4	18.3	4.5	4.2	0.9	0.8	S, Si, K, P, Cu

of aluminium is very low, indicating significant loss from the surface of the material. The oxygen fraction is quite high, although this may be due to absorbed water in the remaining salt which is still visible on the surface. The iron fraction is also quite high and is most likely due to material from the vessel lid falling into the crucible during the experiment. The absence of nickel indicates there were no issues of interdiffusion with the nickel wire used to suspend the sample.

6.1.1.3 Microstructural examination of the cross-section

Figure 95 is a BSE image of the cross-section, with the surface which was exposed to molten salt facing towards the top of the image. The reaction layer was ~80-120 µm thick.

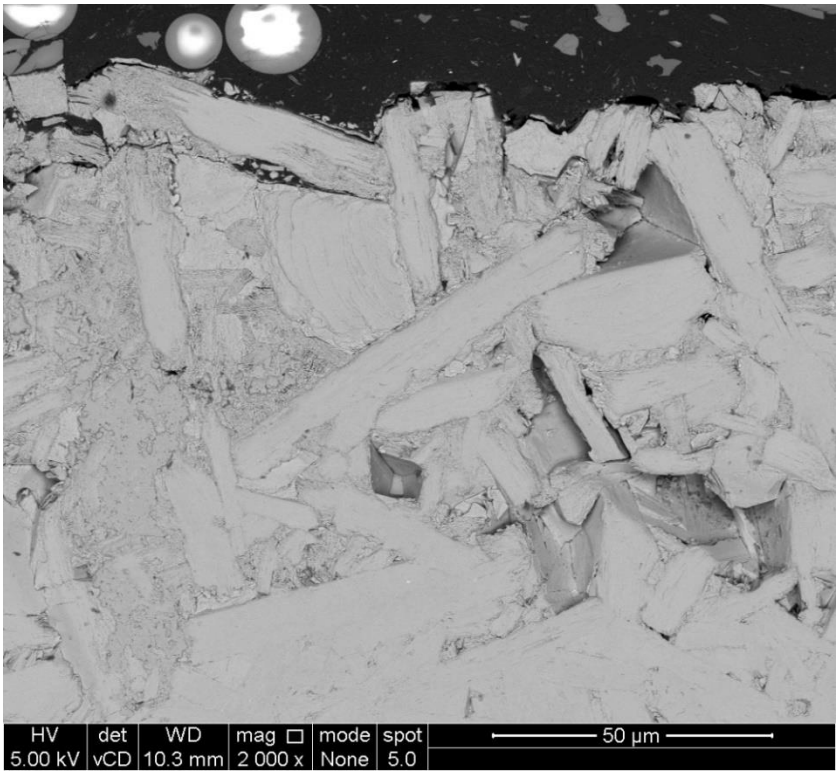

Figure 95 – BSE image showing the thickness of the reaction layer. The top of the image is the corrosion surface. The reaction layer extends to a depth of ~80-120 µm.

The EDS maps in Figure 96 were collected at the same location as Figure 95. The annotations mark the locations of point analyses, the compositions of which are shown in Table 19. Three distinct phases are present. The first is that of the underlying substrate, Ti_3AlC_2, which is clearly visible from the aluminium map. The second is TiC_x, which is distinguishable from a lack of aluminium and chlorine. The third is the Ti-C-Cl phase, which is most easily distinguished by the presence of chlorine. The EDS point analyses suggest that this phase has an approximate stoichiometry of Ti_2C_3Cl.

Table 19 – Elemental compositions (in at.%) of the point analyses shown in Figure 96.

Spectrum	Ti	Al	C	Cl	Other	Other Elements
1	32.4	0.2	48.0	18.8	0.6	Fe, Ca, K, Si
2	34.5	0.7	47.4	16.7	0.7	Fe, K, Si
3	54.4	0.1	45.2	0.2	0.1	Fe, K, Zn, Si, Ca
4	55.6	0.2	43.8	0.1	0.3	Si
5	48.2	14.6	36.3	0.2	0.7	Ni, W
6	49.2	14.8	35.7	0.2	0.1	Fe, Cu, Ca

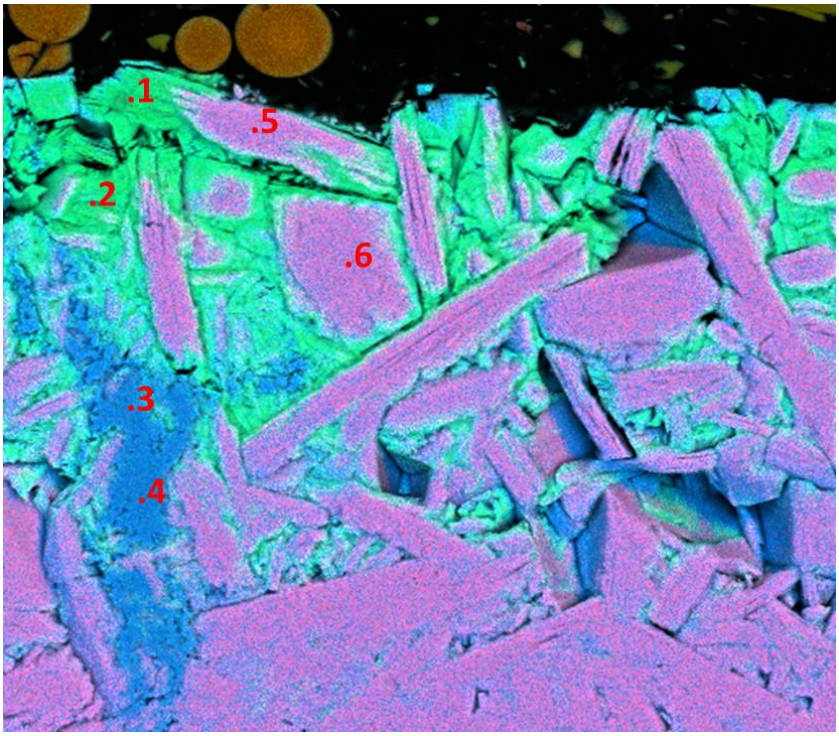

(a) EDS layered image

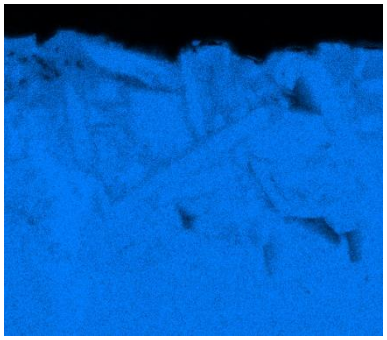

(b) Ti $K\alpha_1$

(c) Al $K\alpha_1$

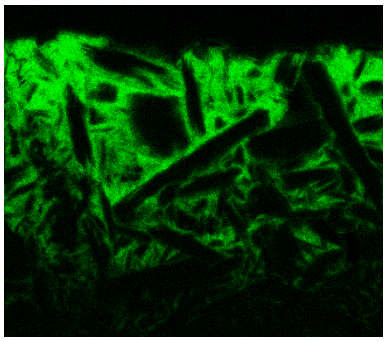

(d) Cl $K\alpha_1$

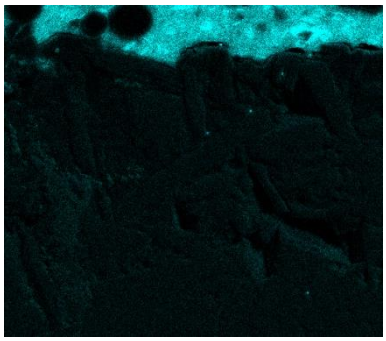

(e) C $K\alpha_1$ and $K\alpha_2$

Figure 96 – EDS maps (image width ~150 µm) of the cross-section. The top of the image is the sample surface. The layered map shows three distinct morphologies: Ti_3AlC_2, TiC_x and a Ti-C-Cl phase. The annotations mark the locations of point analyses, the elemental compositions of which are shown in Table 19.

Figure 97 is a BSE image showing a grain of Ti_3AlC_2 undergoing decomposition to the Ti-C-Cl phase. The layers of the former MAX phase material can be seen as they exfoliate. The composition of the Ti-C-Cl phase shows a greater fraction of carbon than titanium. This suggests that after aluminium loss, chlorine reacts with the exposed titanium which then dissolves into the melt. Eventually, this likely leaves behind a carbide-derived carbon [144–146]. This carbide-derived carbon may have been lost during sample cleaning and therefore the actual depth of corrosion may have been greater than observed.

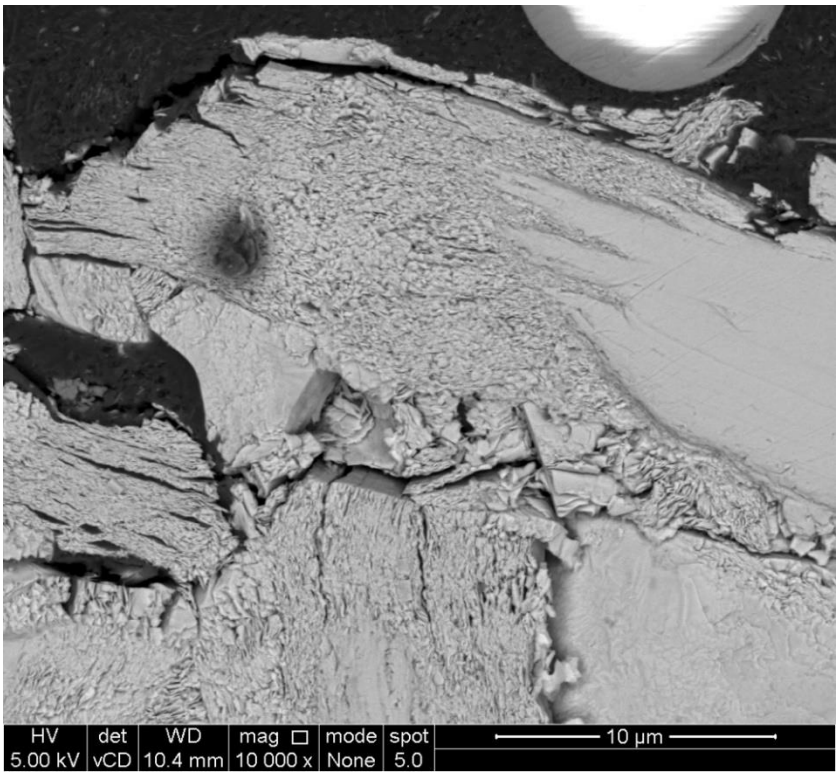

Figure 97 – BSE image of a Ti_3AlC_2 grain undergoing decomposition to form a Ti-C-Cl phase which has the morphology of exfoliated MAX phase grains.

Figure 98 is a BSE image showing greater detail of the TiC_x and Ti-C-Cl phases. The TiC_x particles appear to have sintered and there is significantly less grain pull-out than in the pristine samples.

Figure 99 is a BSE image taken at a greater magnification which shows more detail of the morphology of the Ti-C-Cl and TiC_x phases. The layers of the Ti-C-Cl phase clearly resemble the layers in MAX phase materials. The TiC_x phase has a grain size < 1 µm. It is unclear whether this is a product of corrosion or a region of TiC_x which was present during formation of the sample.

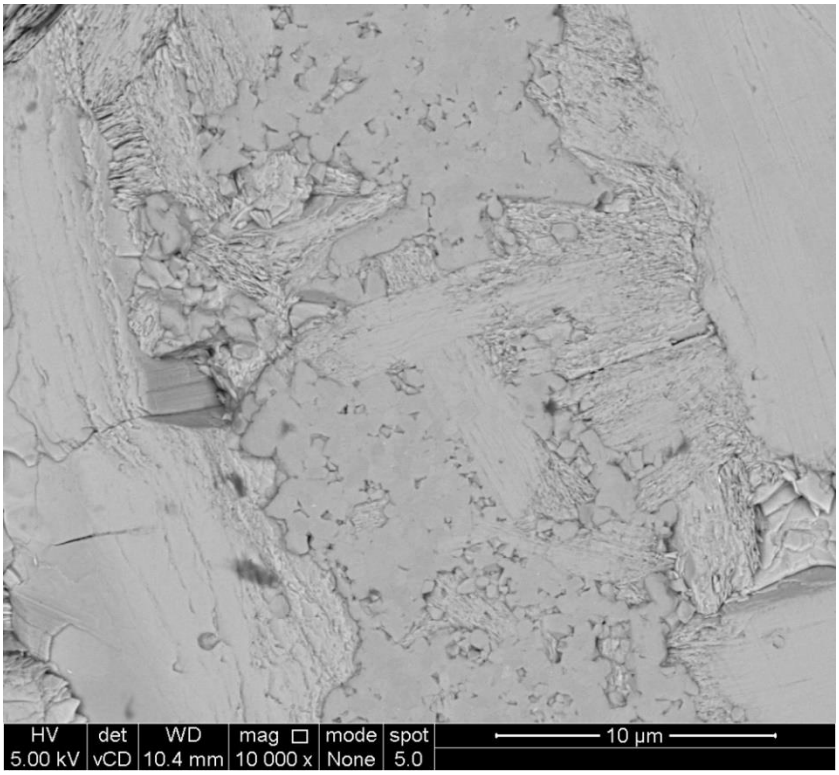

Figure 98 – BSE image showing the TiC_x and Ti-C-Cl phases in greater detail.

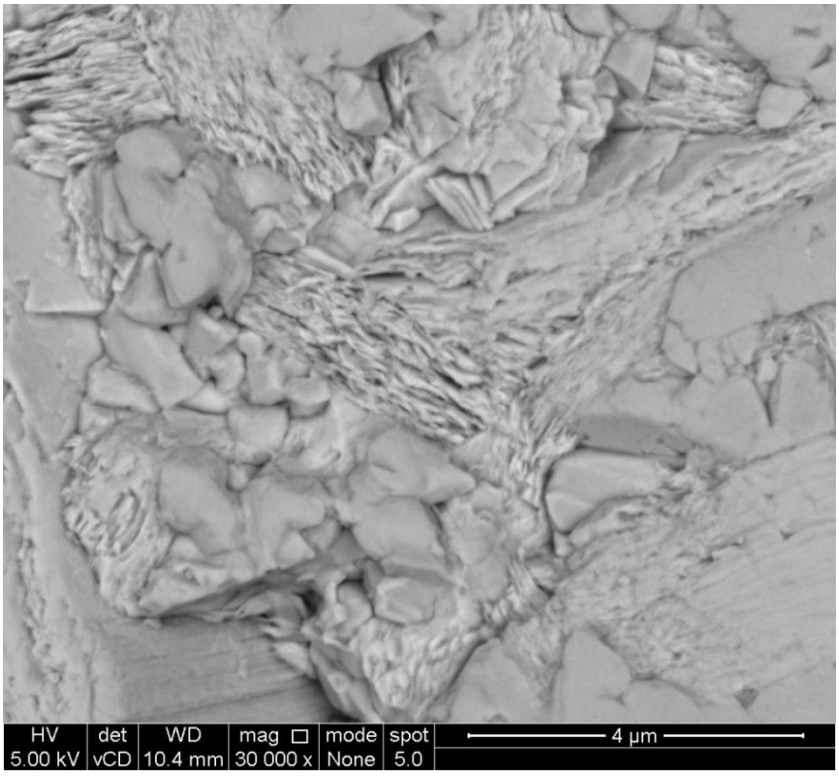

Figure 99 – BSE image showing the morphologies of the Ti-C-Cl and TiC_x phases in greater detail. The exfoliated layers of the Ti-C-Cl phase are clearly visible. The TiC_x grains have similar morphology to those observed during synthesis and have a grain size < 1 µm.

6.1.2 Processed salt, 600°C, 125 h

6.1.2.1 Glancing-angle X-ray diffraction

The GAXRD patterns are shown in Figure 100, normalised relative to the Ti_3AlC_2 (104) peak [178,179,195]. Ti_3AlC_2 was the dominant phase at all glancing angles, indicating minimal corrosion occurred. Small peaks of TiC_x are present at all glancing angles, as in the pristine material. MgO is also present at all glancing angles, with its concentration increasing as the glancing angle decreased, indicating its presence at the surface of the material. The MgO peaks appear relatively broad; it is possible that an additional phase with similar peak positions such as Mg_2TiO_4 is also present [196]. There is also a small unidentified peak at ~42.2° 2θ at low glancing angles.

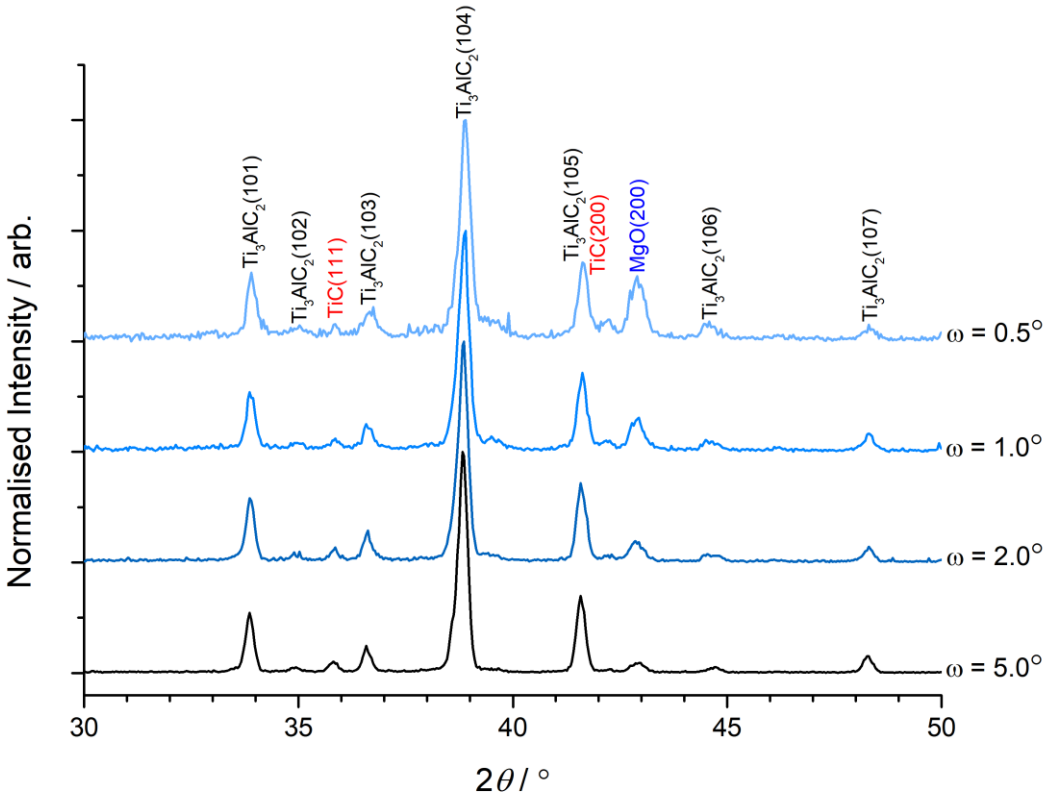

Figure 100 – GAXRD patterns for a sample of Ti_3AlC_2 which was exposed to processed LKE at 600°C for 125 h. The patterns were normalised relative to the Ti_3AlC_2 (104) peak. Ti_3AlC_2 was the dominant phase at all angles. MgO was the only other phase observed. There is a small unidentified peak at ~42.2° 2θ at low glancing angles.

6.1.2.2 Microstructural examination of the surface

Figure 101 is a BSE image showing the general morphology observed on the surface of the sample. The cubic particles appear to contain a mixture of magnesium, titanium and oxygen, which confirm the presence of Mg_2TiO_4 in the GAXRD patterns. The surface was slightly rougher after exposure and a bumpy coating of spherical oxide particles formed. Such morphology is observed in samples exposed to air at high temperatures [38]. The SE image in Figure 102 provides a better view of the topography,

and the cubic oxide particles have deposited or grown on top of the underlying surface. Magnesium was present in the salt due to insufficient cleaning of the reference electrode between preparation of batches of salt.

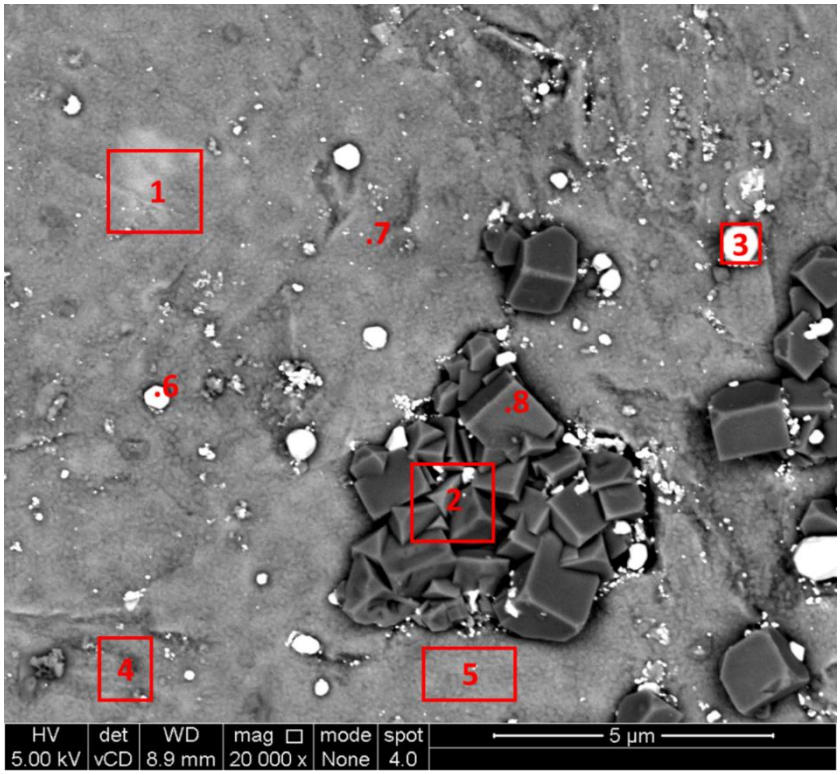

Figure 101 – BSE image of the surface of a sample of Ti_3AlC_2 which was exposed to LKE at 600°C for 125 h. The image shows the general morphology of corrosion products observed. The annotations mark the locations of point analyses, the compositions of which are summarised in Table 20.

Table 20 – Elemental compositions (in at.%) of the point analyses shown in Figure 101.

Point	Ti	Al	Mg	O	Fe	Other	Other elements
Map	36.2	10.4	5.5	47.1	0.2	0.6	Si, S
1	48.6	16.2	0.4	34.2	-	0.6	Si
2	13.8	0.5	22.8	61.6	0.4	1.0	Cr, Mo, Si
3	24.2	11.3	5.5	43.9	13.7	1.4	Si, Mo, Ni
4	47.4	13.9	0.3	37.8	-	0.7	Si
5	49.5	8.6	2.2	39.0	-	0.7	Si
6	34.5	14.0	0.9	34.4	14.8	1.4	Si, Ni, Mo
7	48.1	15.1	0.3	35.7	-	0.8	Si
8	9.1	2.2	25.9	61.6	0.3	0.9	Cr, Si, Mo

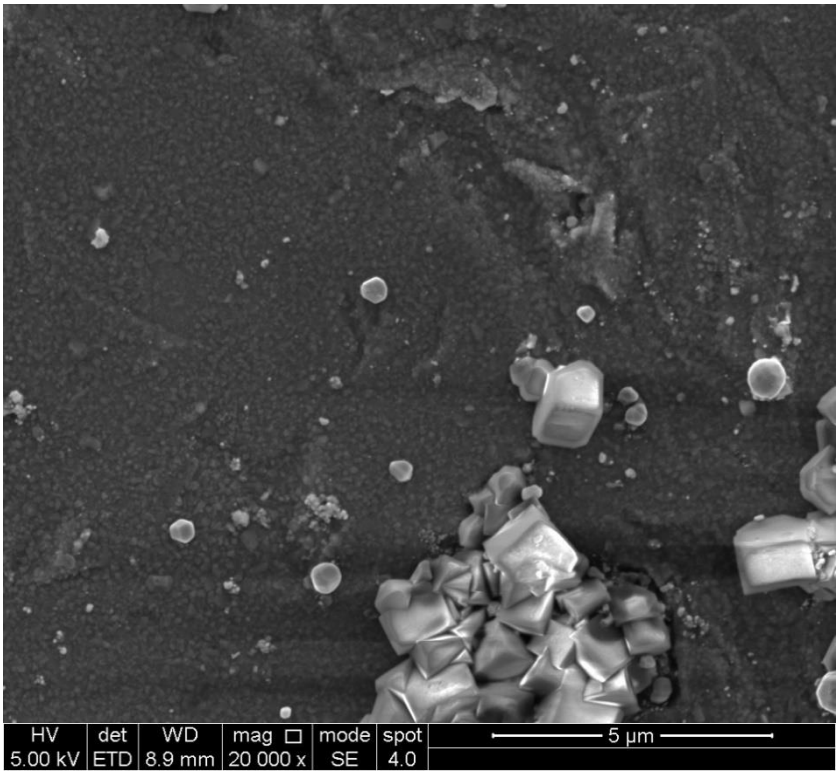

Figure 102 – SE image showing the general morphology of corrosion products on the surface of a sample of Ti_3AlC_2 which was exposed to LKE at 600°C for 125 h.

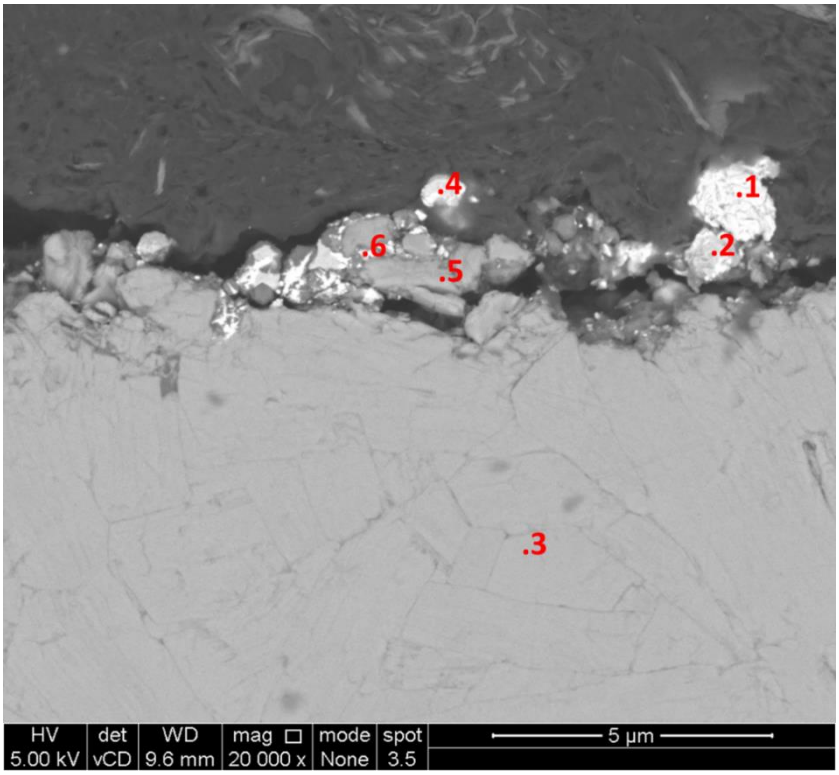

Figure 103 – BSE image showing the morphology of the corrosion products. The annotations mark the locations of point analyses, the elemental compositions of which are shown in Table **21**.

Table 21 – Elemental compositions (in at.%) of the point analyses shown in Figure 103.

Point	Ti	Al	C	Cu	Fe	O	Zn	Mg	Mo	Other	Other Elements
1	0.7	0.2	71.3	20.3	3.8	1.9	1.5	-	-	0.3	Ni
2	2.8	1.1	65.5	6.1	18.1	3.7	0.5	1.0	-	1.2	Ni, S, Cr, Si
3	45.8	13.3	40.8	-	-	-	-	-	-	0.1	Ca
4	1.0	0.5	73.1	13.8	3.7	4.6	1.1	0.8	0.9	0.7	Ni, Si, Ca, Cr
5	12.6	5.0	62.2	1.1	2.3	7.4	0.2	5.6	2.6	1.1	Cr, Si, W, Ca
6	3.8	1.5	66.1	0.5	4.1	13.5	0.1	7.5	2.1	0.9	Cr, Si, W

6.1.2.1 Microstructural examination of the cross-section

Figure 103 is a BSE image showing the morphology of the corrosion products in the sample. In general, small depositions could be seen across the entire surface with a thickness of ~2 μm and an underlying roughened surface. Point 3 shows the composition of a Ti_3AlC_2 grain in the bulk. The high fraction of carbon suggests the sample was likely contaminated with adventitious carbon and therefore the carbon results should be considered inaccurate. Significant fractions of Cu and Zn are present, particularly at points 1 and 4, likely due to contamination from the brass tools used during micropreparation. Mg is also present, particularly at points 5 and 6. The presence of Mo may be due to preparing this particular batch of salt using molybdenum electrodes. The presence of Fe and Ni suggest contamination during the corrosion tests.

6.1.3 Processed salt, 600°C, 250 h

6.1.3.1 Glancing angle X-ray diffraction

The GAXRD patterns from 0.5-10.0° ω are shown in Figure 104 [178,179,197–199]. The observed reaction products are all W-based phases, although there are unassigned peaks at ~35°, 42.1°, 43.1° and 44.5° 2θ. The W-based phases may contain additional elements such as Ti, Al or C [200,201].

6.1.3.2 Microstructural examination of the surface

Figure 105 is an SE image of the surface. A variety of phases are clearly visible, indicating that the surface morphology of this material post-corrosion is relatively complex.

Figure 106 is a BSE image of the surface. The annotations mark the locations of EDS analyses, the results of which are summarised in Table 22. Oxygen is present in all spectra. Mg is present, particularly at point 4, which indicates that the salt for this batch was also contaminated, although it seems to a

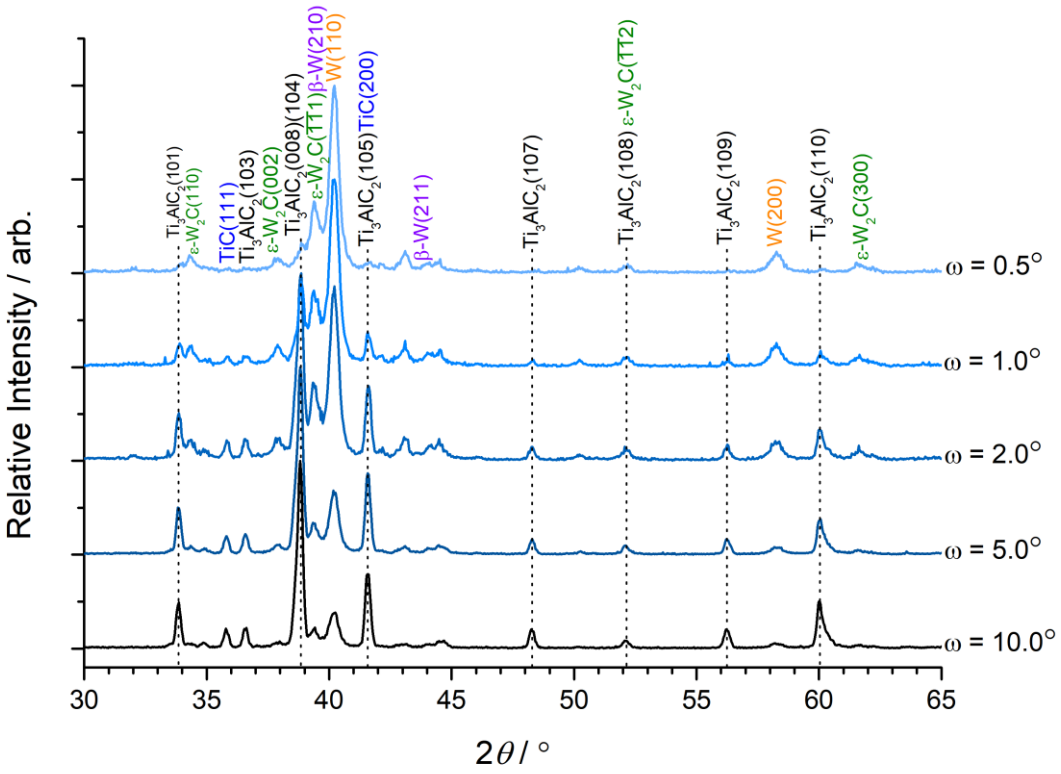

Figure 104 – GAXRD patterns for a sample of Ti_3AlC_2 which was exposed to processed LKE at 600°C for 125 h. The intensity of each pattern was normalised to 100% based on the highest peak. Between 0.5-1.0° ω the patterns are normalised relative to the W (110) peak, and from 2.0° ω the patterns are normalised relative to the Ti_3AlC_2 (104) peak.

lesser extent than that used for 125 h exposure. The presence of copper is unusual, but it was observed multiple times, confirming its presence as an impurity. As previously, this was likely due to the brass tools used during micropreparation, although no zinc was observed on this sample.

6.1.3.3 Microstructural examination of the cross-section

Figure 107 is a BSE image of the cross-section. Roughening of the surface indicates some uniform corrosion occurred, consistent with the slight mass loss observed (Table 17). The annotations mark the locations of point analyses, the results of which are summarised in Table 23. The ratios of Ti, Al and C in points 1 and 2 do not match those of Ti_3AlC_2. This may be due to the presence of adventitious carbon on the sample. The ratio of Ti to Al is about 3.4, indicating there may have been slight loss of Al. Points 3 and 4 show that the brightness of the spot on the surface is due to the presence of W. Oxygen is also present in this region, along with Ti and C and a small amount of Al. Fe and Cu appear to be present as impurities at the surface, which was also indicated by microstructural examination of the surface.

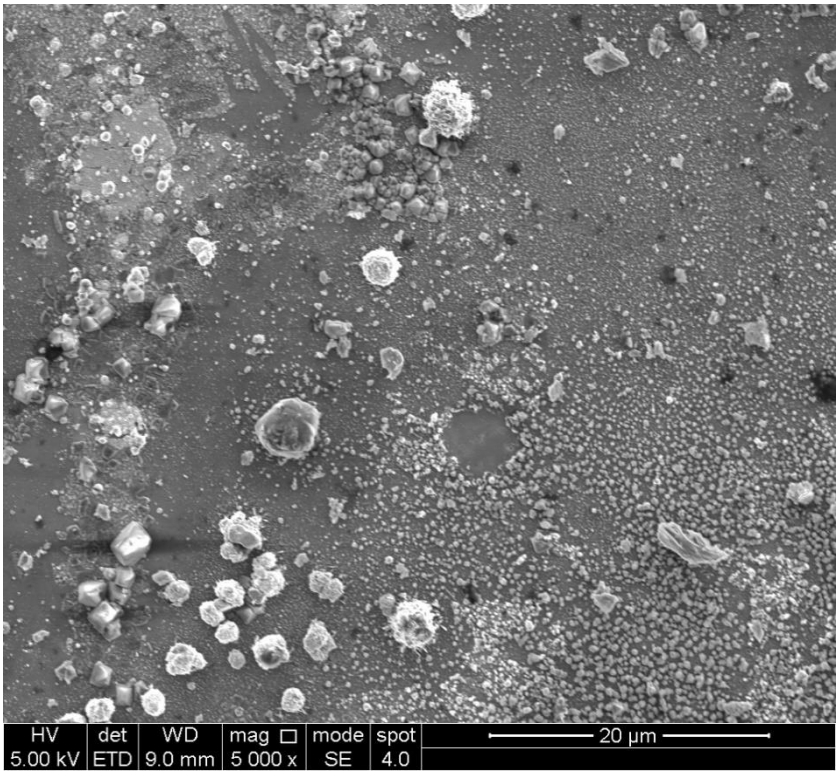

Figure 105 – SE image of the surface of a sample of Ti_3AlC_2 which was exposed to LKE for 250 h at 600°C.

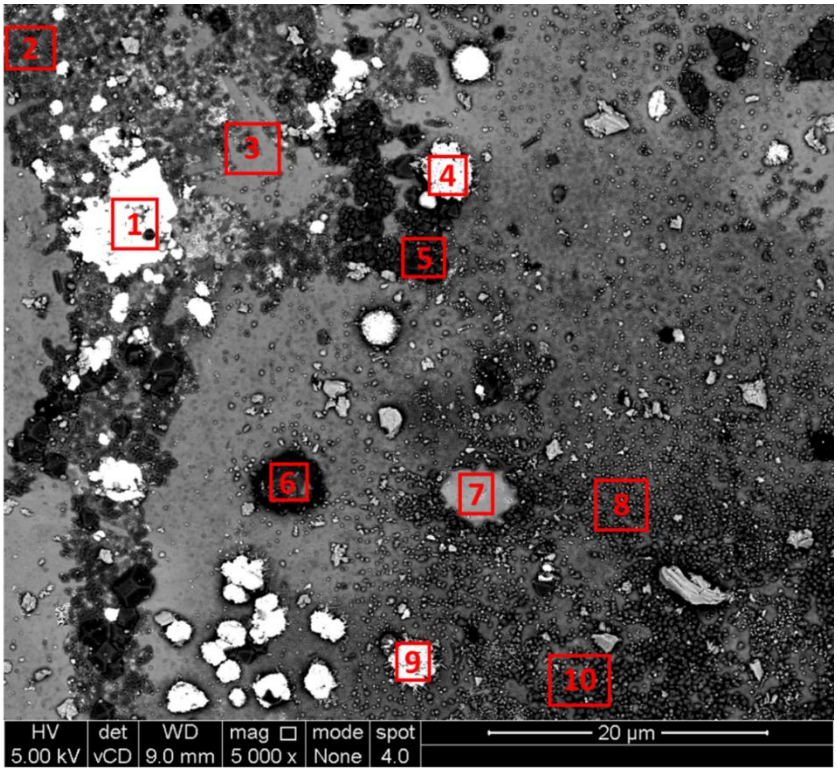

Figure 106 – BSE image of the surface of a sample of Ti_3AlC_2 which was exposed to LKE for 250 h at 600°C. The annotated locations mark the positions of EDS analyses, the elemental compositions of which are summarised in Table 22.

Table 22 – Elemental compositions (in at.%) of the point analyses shown in Figure 106.

Point	Ti	C	O	W	Al	Cu	Fe	Mg
1	45.8	32.2	12.2	5.9	2.5	0.6	0.5	0.4
2	43.1	20.1	25.2	-	11.0	-	-	0.6
3	40.2	18.6	33.2	-	5.9	-	-	2.0
4	24.4	9.0	51.4	-	4.1	-	-	11.0
5	28.8	10.6	47.8	-	3.0	-	0.1	9.6
6	41.8	21.2	23.8	-	13.2	-	-	-
7	35.9	15.0	39.1	-	8.2	0.3	0.5	1.0
8	33.2	13.7	40.2	-	11.9	0.4	0.5	-
9	26.4	30.1	26.4	7.4	8.6	-	0.3	0.4
10	33.2	12.6	44.4	0.1	6.8	0.2	1.4	1.3

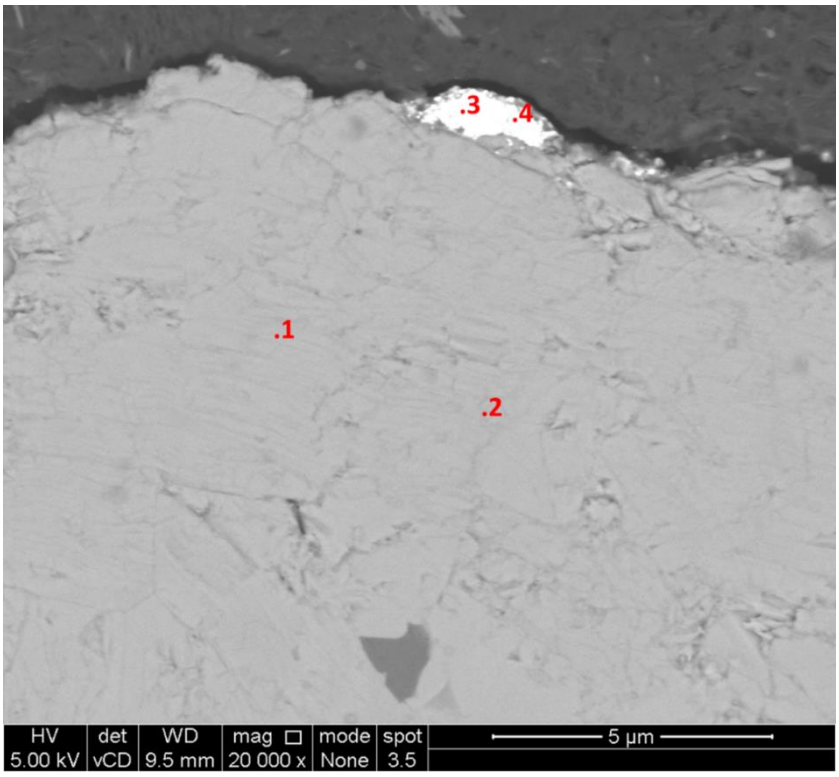

Figure 107 – BSE image of the cross-section of a sample of Ti_3AlC_2 which was exposed to LKE for 250 h at 600°C. The annotations mark the locations of EDS point analyses, the compositions of which are summarised in Table 23.

Table 23 – Elemental compositions (in at.%) of the point analyses shown in Figure 107.

Point	Ti	Al	C	W	O	Fe	Cu
1	43.0	12.6	44.4	-	-	-	-
2	44.0	13.0	43.0	-	-	-	-
3	31.1	3.0	46.0	9.1	8.5	1.1	0.7
4	30.1	1.1	49.8	9.3	9.0	0.4	-

6.1.4 Processed salt, 850°C, 125 h

6.1.4.1 Glancing-angle X-ray diffraction

The GAXRD patterns are shown in Figure 108, normalised relative to the Ti_3AlC_2 (104) peak [178,179,198,202–205]. A pattern was also collected at 0.5° ω but the counts were too low for accurate determination of phases. The Ti_3AlC_2 (004) peak disappears at 1.0° ω. This peak represents diffraction from the Al basal planes, indicating loss of Al from the structure at the surface. Conversely, the (002) peak, which is associated with diffraction from the plane running through the Ti atoms which are bonded to carbon only, increases in intensity at lower glancing angles. Numerous reaction products form after Al loss, the majority of which are oxides. The most notable reaction product is γ-$LiAlO_2$ due to its clearly defined peaks. The presence of $Al_{0.95}Ti_{1.05}$, γ-$Al_{2.67}O_4$ and $Li_4Ti_5O_{12}$ are harder to determine, but their most intense peaks appear to fit. As with other samples, TiC_x is present, either as a starting impurity or a corrosion product from Al loss, and W has been introduced to the melt during salt processing.

6.1.4.1 Microstructural examination of the surface

The sample retained a metallic lustre but had some green and pink iridescence, most likely due to refraction from thin oxide layers. Several large pits, ~3 mm diameter, were also observed on the surface. Figure 109 is a BSE image of the edge of a pit. An oxide layer which covered most of the surface is present in the top left, and the rest of the image shows the pitted region. The SE image in Figure 110 shows the oxide layer is raised relative to the pitted region. Al is concentrated in the oxide layer and is diminished in the pitted region. Fe seems to be present at the edge of the pit, which may indicate it is involved with the pit formation mechanism. Point 3 has morphology and elemental composition approximately consistent with Ti_3AlC_2, so appears to be an exposed grain of Ti_3AlC_2 which is undergoing reaction.

Figure 111 is a BSE image which appears to show the initial stages of pit formation. Figure 112 is a higher magnification image showing the rectangular shape of the underlying MAX phase grains in the centre of the pit. The surrounding material contains Al and O, which could be γ-$Al_{2.67}O_4$ or γ-$LiAlO_2$. Some tungsten and some particles of iron, most likely iron oxide, can also be seen on the sample.

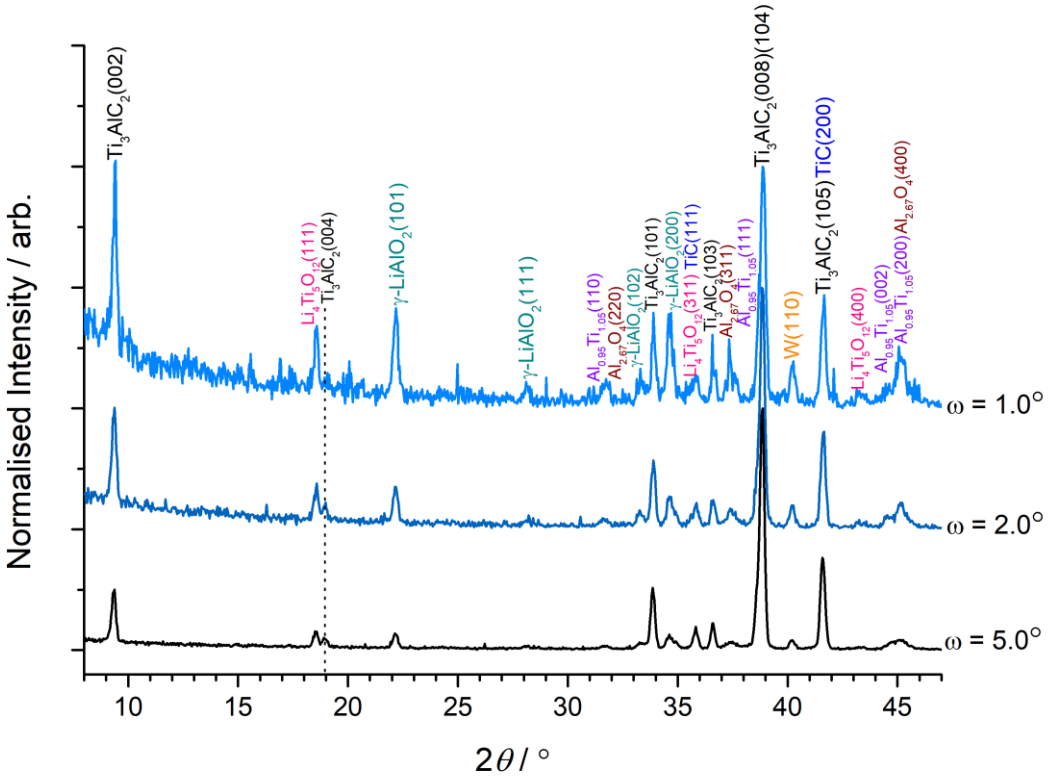

Figure 108 – GAXRD patterns for a sample of Ti_3AlC_2 which was exposed to processed LKE at 850°C for 125 h. The patterns were normalised relative to the Ti_3AlC_2 (104) peak, which also has the (008) peak slightly to the left of it.

Table 24 – Elemental compositions (in at.%) of the EDS map and point analyses show in Figure 109.

Spectrum	Ti	Al	O	Cl	C	Fe	N	Fe	W	Cu	Other	Other Elements
Map	28.3	7.9	39.4	1.0	21.3	-	-	0.6	0.4	0.7	0.6	Si, Sr, P, Ni Pb
1	27.9	14.0	46.0	2.8	8.3	0.2	-	-	0.1	0.7	-	-
2	6.3	12.7	47.2	0.4	22.0	1.0	9.6	-	0.4	0.3	0.2	P, K
3	36.3	10.3	22.2	0.2	28.6	0.2	-	-	0.0	2.1	0.1	Pb
4	28.5	3.3	19.9	5.6	40.9	0.2	-	-	0.2	1.2	0.1	Pb

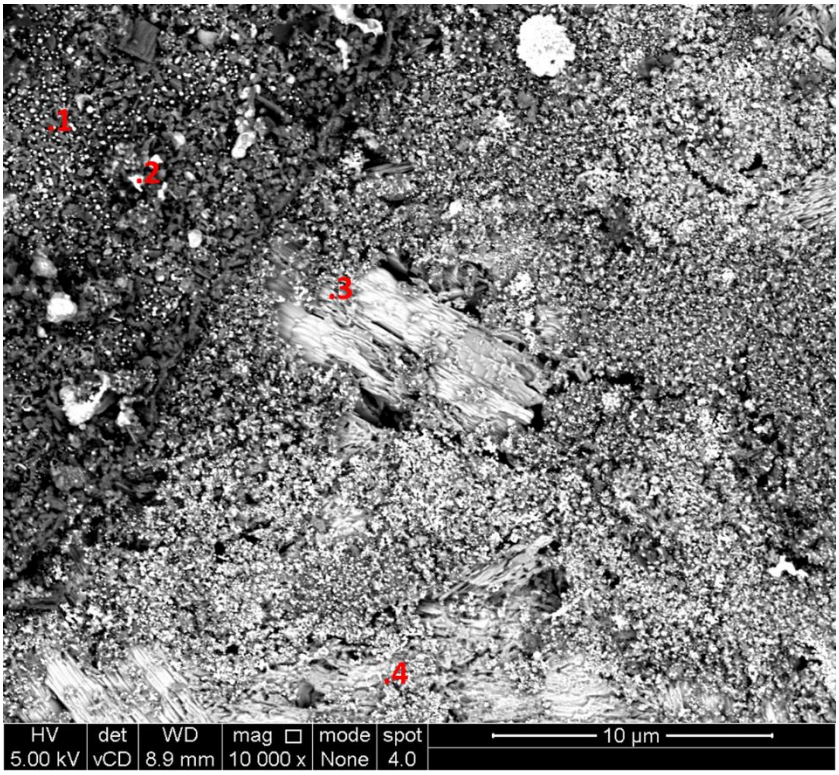

(a) BSE

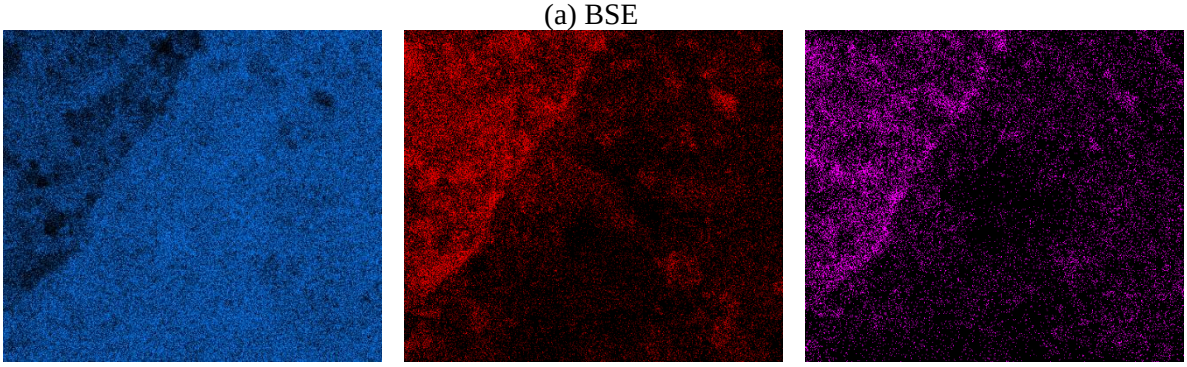

(b) Ti $K_{\alpha1}$ (c) Al $K_{\alpha1}$ (d) O $K_{\alpha1}$

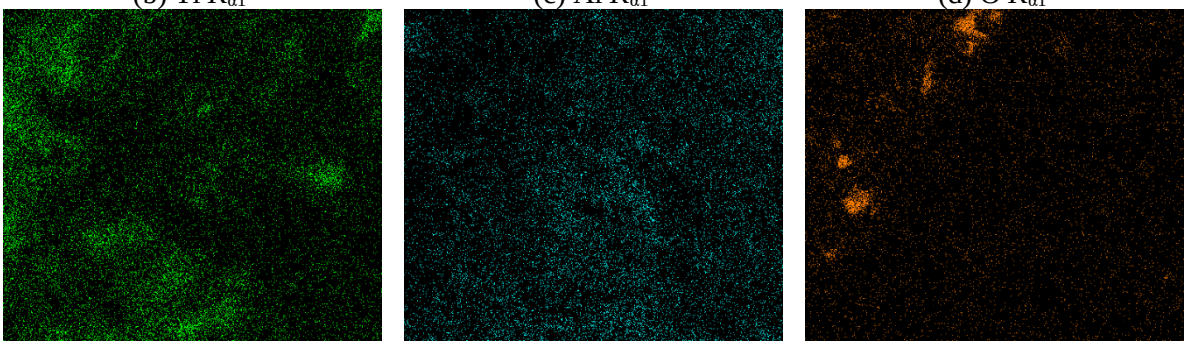

(e) Cl $K_{\alpha1}$ (f) C $K_{\alpha1}$ and $K_{\alpha2}$ (g) Fe $K_{\alpha1}$

Figure 109 – BSE image of the surface of a sample of Ti_3AlC_2 which was exposed to LKE at 850°C for 125 h. The majority of the image shows a pitted region, whereas the top left of the image shows the oxidised surface. The elemental compositions of the map and point spectra are shown in Table 24.

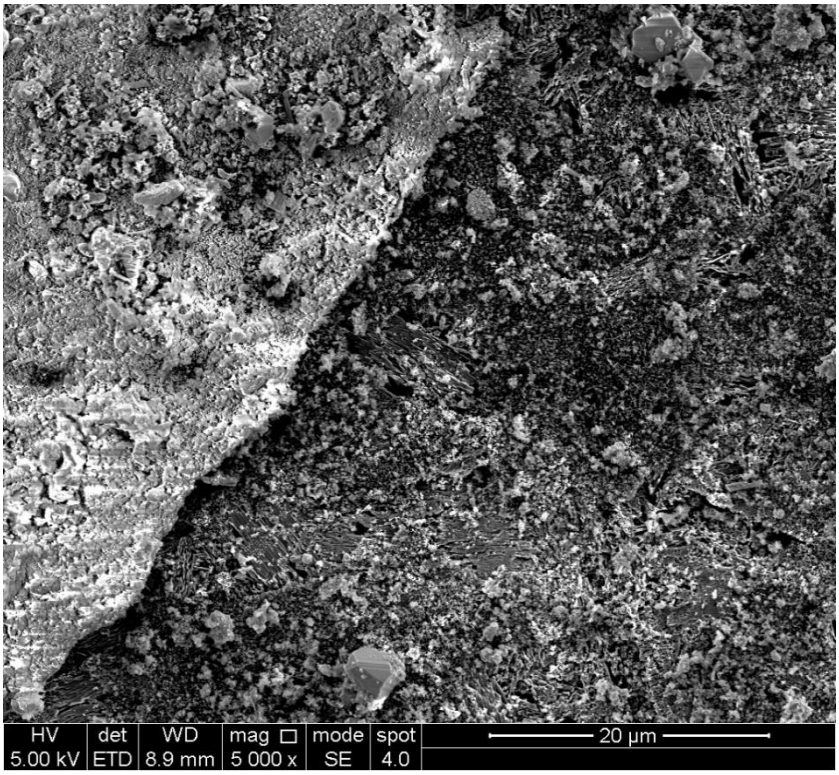

Figure 110 – SE image of the surface of a sample of Ti_3AlC_2 which was exposed to LKE at 850°C for 125 h. The top left of the image shows the oxide layer and the bottom right shows the pitted region.

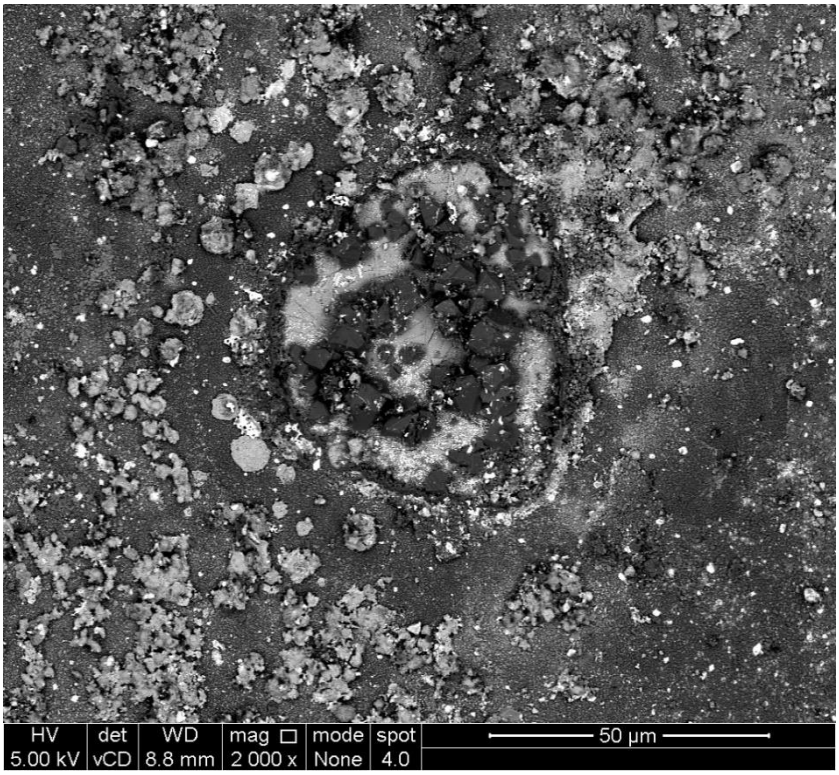

Figure 111 – BSE image of the surface of a sample of Ti_3AlC_2 which was exposed to LKE at 850°C for 125 h. The image appears to show the initial stages of pit formation.

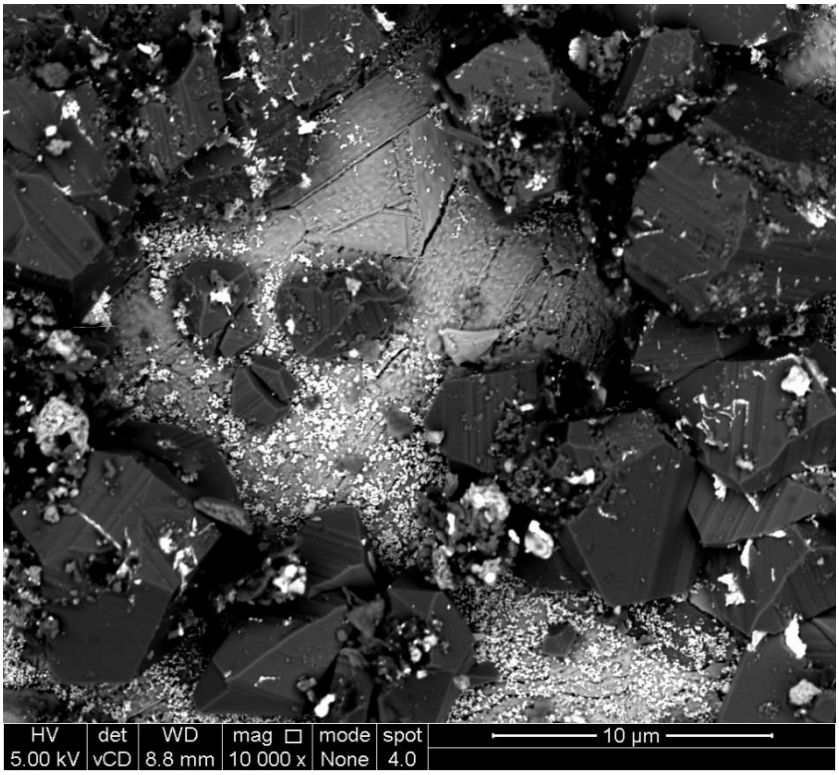

(a) BSE image

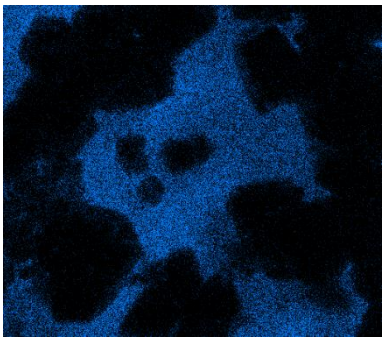

(b) Ti $K_{\alpha1}$

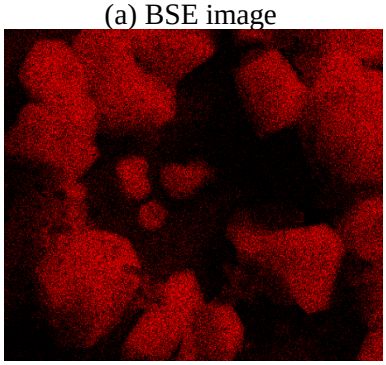

(c) Al $K_{\alpha1}$

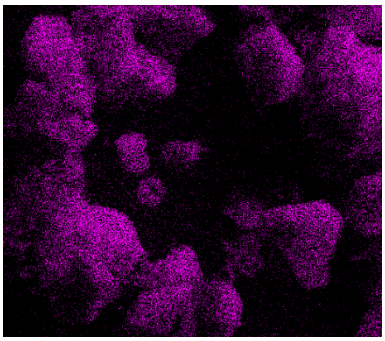

(d) O $K_{\alpha1}$

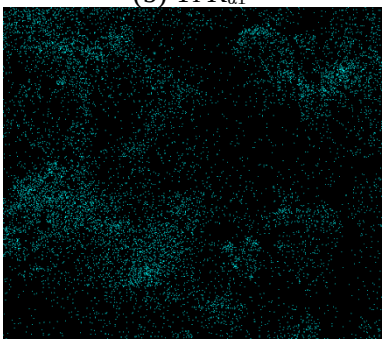

(e) C $K_{\alpha1}$ and $K_{\alpha2}$

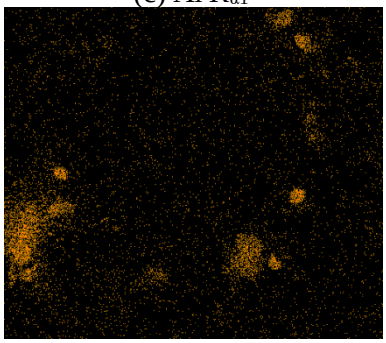

(f) Fe $K_{\alpha1}$

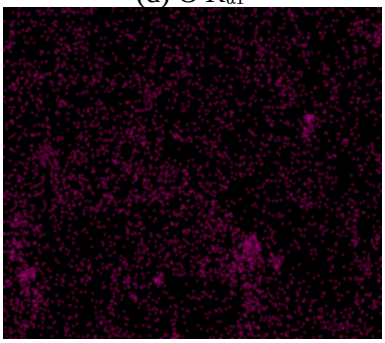

(g) W $L_{\alpha1}$

Figure 112 – BSE image of a sample of Ti_3AlC_2 which was exposed to LKE at 850°C for 125 h. The image appears to show the centre of a pit in its initial stages. The rectangular MAX phase grains can be seen in the centre surrounded by particles of aluminium oxide.

6.1.4.2 Microstructural examination of the cross-section

The orientation of the sample affected the rate of corrosion. The one side of the sample was significantly corroded, whereas the opposite side seemed to form a protective tungsten film. Figure 113 shows a BSE image and EDS analysis of the heavily corroded side of the sample. Iron and copper are visible as impurities. Iron is present at the surface only so is believed to be introduced to the crucible from the corrosion vessel. This suggests that the more heavily corroded side of the sample was facing up. Copper can be seen throughout the bulk of the sample and is therefore believed to have been introduced from the brass tools used during micropreparation. The map sum spectrum shows that a significant fraction of Al has been lost. The carbon fraction is most likely high due to the conductive Bakelite used to mount the sample, visible at the top of the image, and due to adventitious carbon, but may also indicate that a significant fraction of Ti has also been lost. Spectra 9 and 10 were collected in the bulk of the material; the titanium and aluminium ratios seem fairly accurate, whereas the carbon fraction is higher than expected and copper was also detected as an impurity. Spectra 2 and 5 appear to show TiC_x formed by aluminium loss. Spectrum 1 also appears to show this; however, x is approximately 2 which may indicate the presence of TiC_2, where only the titanium atoms sandwiched between carbon atoms remain. Spectra 6, 7 and 8 show mainly Ti and C, but also some Cl. Their morphology reflects the exfoliation of the layers of the MAX phase structure. Spectra 3 and 4 show significant fractions of oxygen, which could indicate the presence of titanium oxide, titanium oxycarbide or lithium titanate.

Figure 114 is a BSE image and EDS maps of the heavily corroded side of the sample, which shows a greater extent of oxide formation. Spectrum 11 indicates that the EDS results are fairly accurate as the composition is approximately equal to Ti_3AlC_2. Spectrum 1 contains mainly Ti and C, with the amount of C much higher than Ti. It is most likely TiC_2 layers from Ti_3AlC_2, potentially with some further loss of Ti to carbide derived carbon. Spectra 2, 3 and 4 contain Ti, C and O in similar ratios. The dark contrast in the BSE image suggests it has a low molecular mass, so could contain lithium titanate, TiC_2 layers from Ti_3AlC_2, or carbide derived carbon. Point 5 contains Al, C and O and is close to the edge of the sample and the Bakelite, so is most likely γ-$Al_{2.67}O_4$ or γ-$LiAlO_2$. Points 6, 8 and 9 appear to be an oxide phase. Point 7 appears to be either titanium carbide or the Ti-C-Cl phase observed in earlier samples. Point 10 seems to be similar but at an earlier stage of reaction.

Figure 115 is a BSE image and EDS maps of the opposite side of the sample. It is clear that this side of the sample is significantly less corroded, with a depth of corrosion up to ~5 μm, with some further reaction up to 7 μm. Near the surface, chlorine has diffused into the material, giving the morphology of exfoliated MAX phase grains, and aluminium has diffused out and deposited at the surface. The morphology beyond the exfoliated grains appears different and may indicate the initial stages of reaction with chlorine.

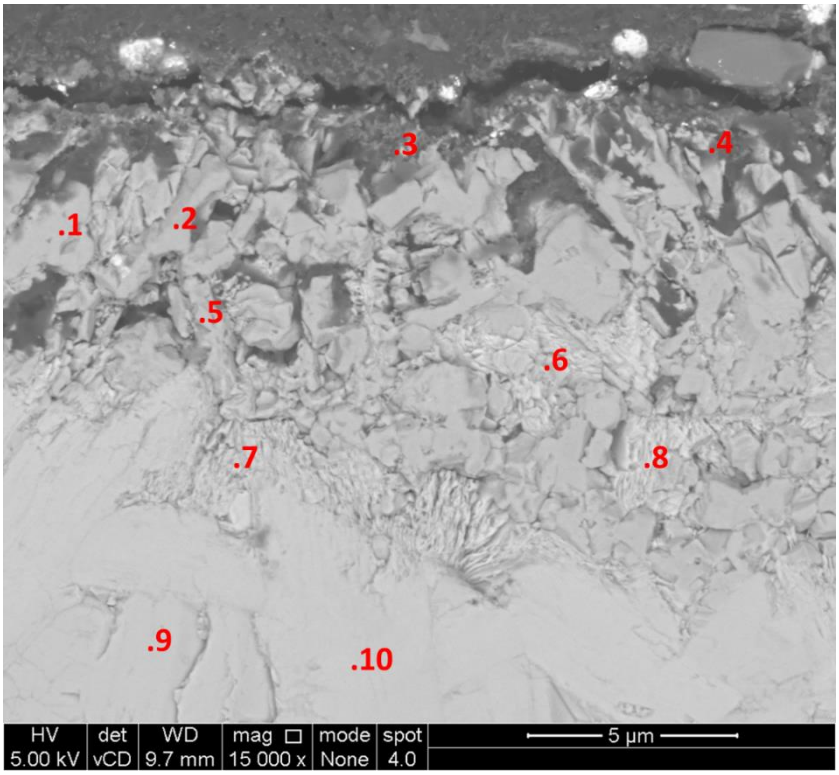

(a) BSE

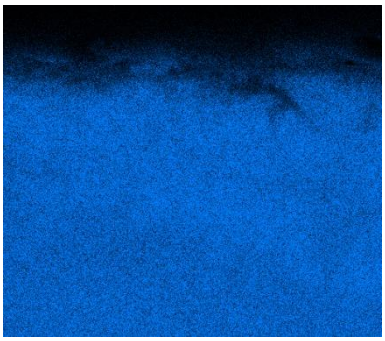

(b) Ti $K_{\alpha1}$

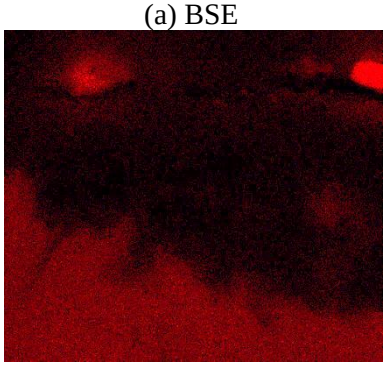

(c) Al $K_{\alpha1}$

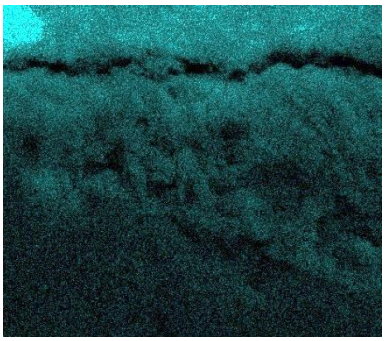

(d) C $K_{\alpha1}$ and $K_{\alpha2}$

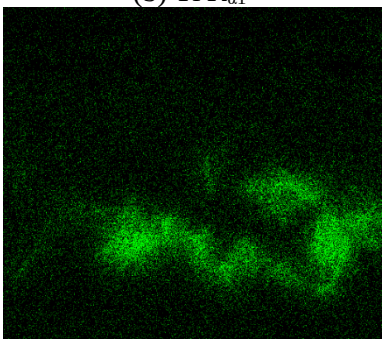

(e) Cl $K_{\alpha1}$

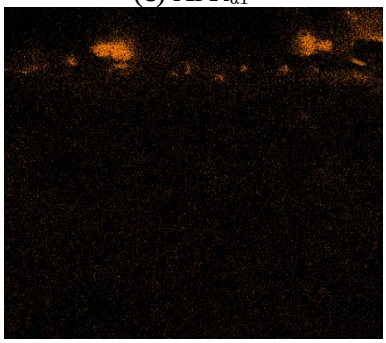

(f) Fe $K_{\alpha1}$

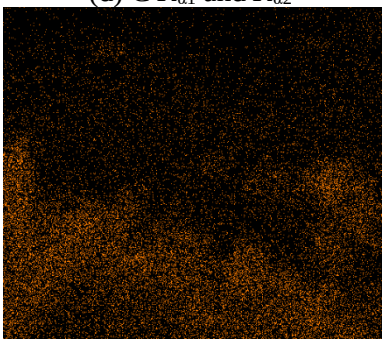

(g) Cu $K_{\alpha1}$

Figure 113 – BSE image and EDS maps of the heavily corroded side of a sample of Ti_3AlC_2 which was exposed to LKE at 850°C for 125 h. The annotations mark the locations of point analyses, and the elemental compositions of EDS spectra can be found in Table **25**.

Table 25 – Elemental compositions (in at.%) of the EDS spectra shown in Figure 113.

Spectrum	Ti	Al	C	Cl	Fe	Cu	O	Other	Other Elements
Map	24.9	2.8	70.3	0.5	0.4	0.5	-	0.5	Si, Ca, W, Mg, Zn, S, K
1	36.8	0.1	62.9	-	-	-	-	0.2	Ca, Si
2	47.2	0.1	52.2	-	0.1	-	-	0.4	Ca, S, W
3	14.3	0.3	73.2	0.1	0.1	-	11.2	0.7	Si, Na, Ca, Zn, Mg, W, S
4	17.8	1.7	64.2	0.0	0.2	-	15.7	0.3	Si, Ca, S, W
5	40.3	0.3	58.8	0.1	0.1	0.1	-	0.3	Ca, Si
6	46.3	0.7	45.1	6.3	0.2	1.1	-	0.3	Ca, Si, Pb
7	38.1	2.3	50.0	8.0	0.2	1.2	-	0.2	Si, Ca
8	36.9	1.6	52.5	7.1	0.1	1.6	-	0.2	Si, Ca
9	46.1	13.7	39.6	-	-	0.6	-	-	-
10	46.2	13.2	38.7	-	-	1.9	-	-	-

Table 26 – Elemental compositions (in at.%) of the EDS maps and point analyses shown in Figure 114.

Spectrum	Ti	Al	C	Cl	O	Cu	Other	Other Elements
Map	23.9	4.3	56.7	0.5	13.2	0.7	0.6	Fe, Si, Ca, W, S, K
1	26.7	1.2	71.8	-	-	-	0.3	Si, Ca, Fe, W
2	28.6	2.4	49.8	0.1	18.3	-	0.9	Si, Na, Ca, Zn, Mg, W
3	31.2	0.5	54.6	-	13.5	-	0.3	Ca, Na, Zn, W
4	26.2	0.1	58.3	0.1	15.1	-	0.3	Zn, Ca, Fe
5	3.7	10.3	43.4	0.1	42.3	-	0.3	Fe, W, Ca, K, Ta
6	15.4	19.7	23.3	0.3	40.9	0.2	0.2	Fe, Ca
7	43.5	2.5	44.6	7.1	-	1.2	1.1	Fe, Pb, Si, Ca
8	23.2	23.3	33.6	0.8	17.6	1.2	0.3	Fe, Si
9	11.4	17.6	10.4	0.3	59.9	0.3	0.0	Ca, Si
10	44.1	5.1	42.5	6.6	-	1.4	0.4	Si, Ca, Fe
11	47.5	13.2	37.4	-	-	1.6	0.3	Si, Ca

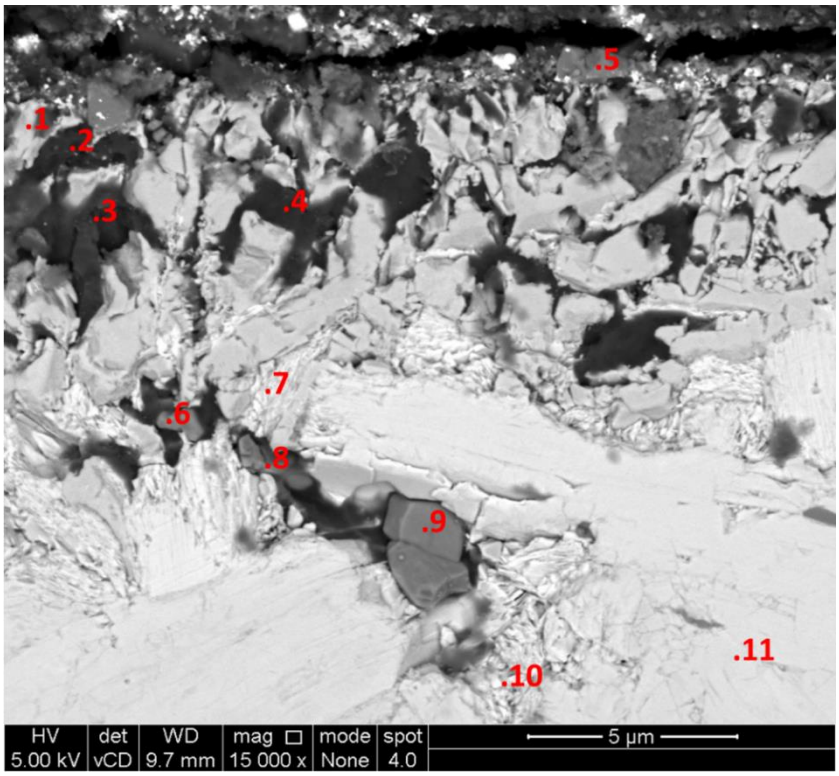

(a) BSE image

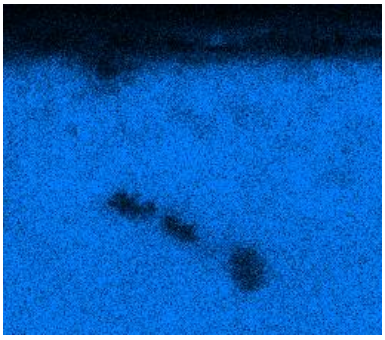

(b) Ti $K_{\alpha 1}$

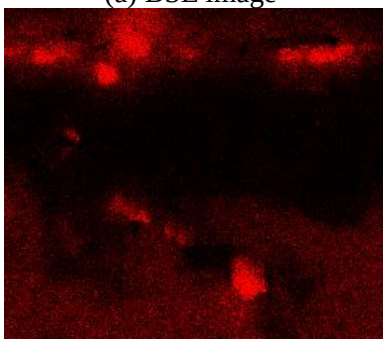

(c) Al $K_{\alpha 1}$

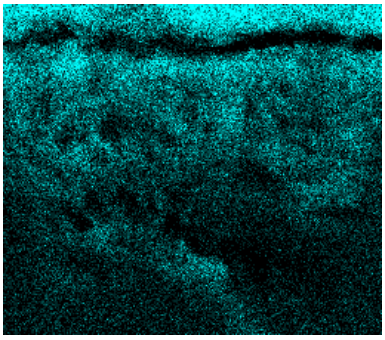

(d) C $K_{\alpha 1}$ and $K_{\alpha 2}$

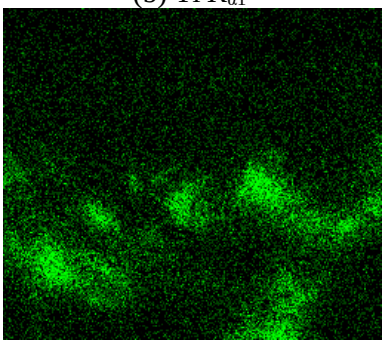

(e) Cl $K_{\alpha 1}$

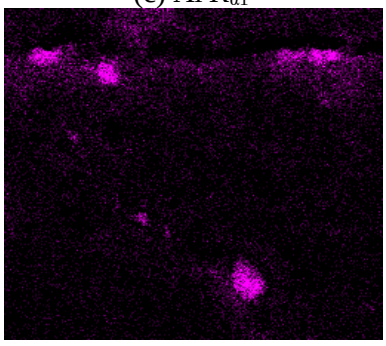

(e) O $K_{\alpha 1}$

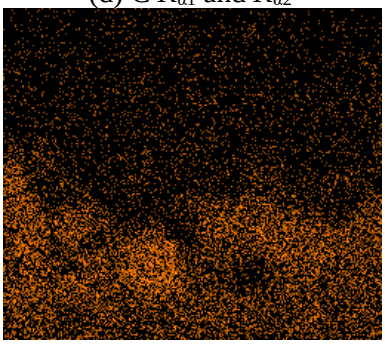

(e) Cu $K_{\alpha 1}$

Figure 114 – BSE image and EDS maps of a sample of Ti_3AlC_2 which was exposed to LKE at 850°C for 125 h. The elemental compositions of the EDS spectra can be found in Table **26**. The image shows a heavily corroded region with significant presence of oxides.

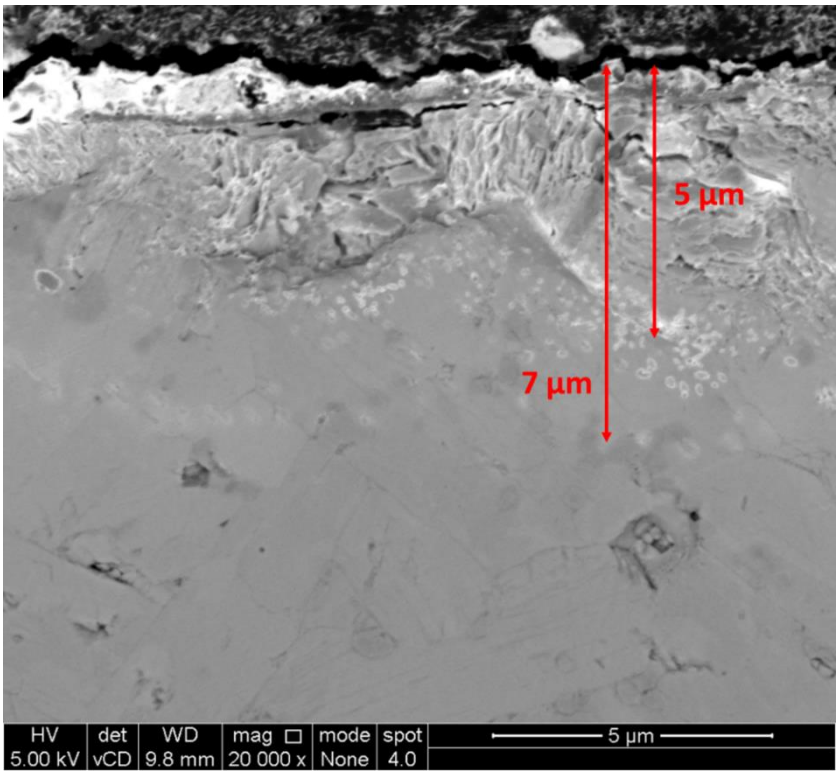

(a) BSE

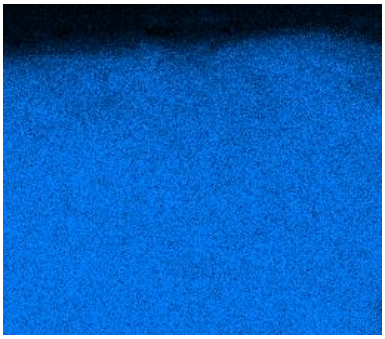

(b) Ti $K_{\alpha1}$

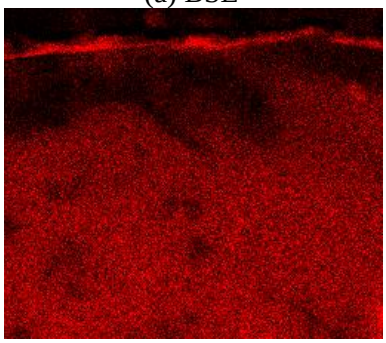

(c) Al $K_{\alpha1}$

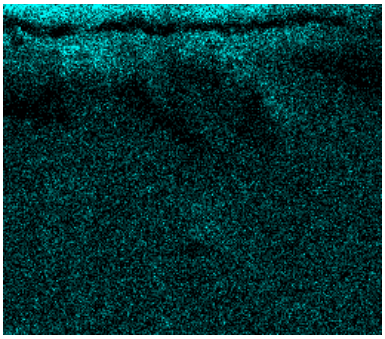

(d) C $K_{\alpha1}$ and $K_{\alpha2}$

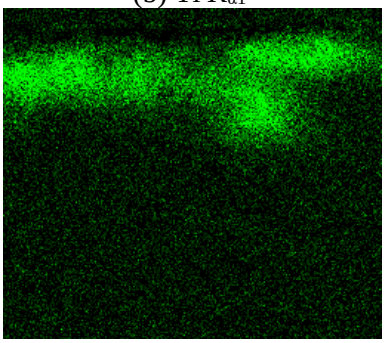

(e) Cl $K_{\alpha1}$

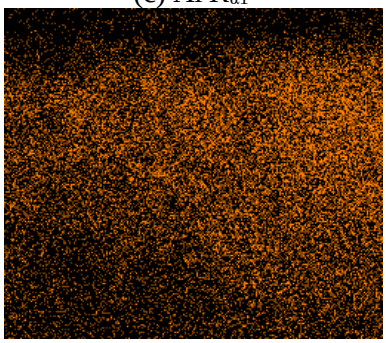

(f) Cu $K_{\alpha1}$

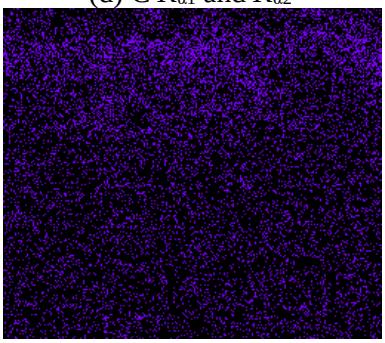

(g) W $L_{\alpha1}$

Figure 115 – BSE image and EDS maps of the cross-section of a sample of Ti_3AlC_2 which was exposed to LKE at 850°C for 125 h. The image shows the less corroded side of the sample.

6.2 Corrosion in KCl-$MgCl_2$ Eutectic

6.2.1 Processed salt, 600°C, 125 h

6.2.1.1 Glancing angle X-ray diffraction

The GAXRD patterns for the sample of Ti_3AlC_2 which was exposed to processed KME at 600°C for 125 h are shown in Figure 116, normalised relative to the W (110) peak [178,179,195,198,199]. This W-based phase could be α-W, a W-based alloy (for example, with Ti or Al alloying elements) or WC_x. β-W and MgO were also observed on the surface after exposure to KME. The peaks for β-W overlap with those of W_2C [197]. Ti_3AlC_2 and TiC_x peaks disappear at < 1° ω.

6.2.1.2 Microstructural examination of the surface

Figure 117 is a BSE image with EDS maps of the surface showing a general overview of the morphology. The morphology of the surface has changed considerably relative to the pristine material due to the formation of oxides, primarily of aluminium and magnesium. The low fraction of titanium observed suggests that it has most likely remained in the bulk material. Some tungsten and iron

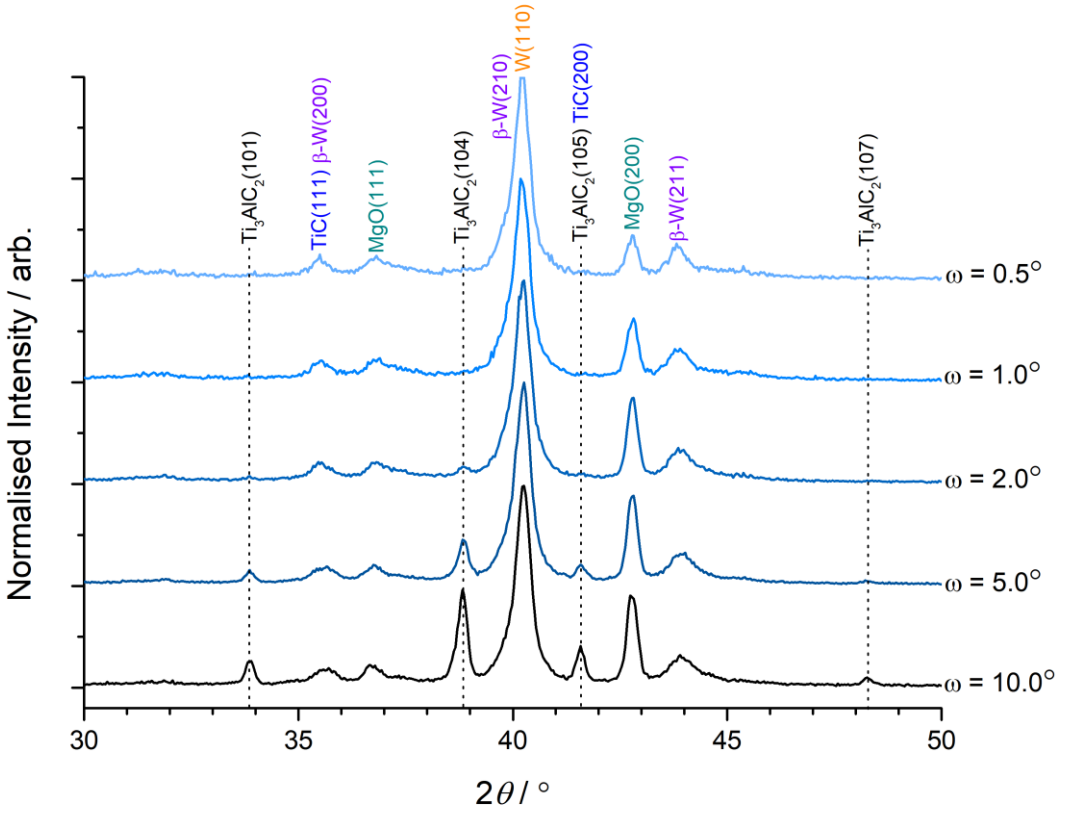

Figure 116 – GAXRD patterns for a sample of Ti_3AlC_2 which was exposed to processed KME at 600°C for 125 h. The patterns were normalised relative to the W (110) peak. The significant presence of W, potentially including W-based alloys, indicates that the salt became contaminated from processing.

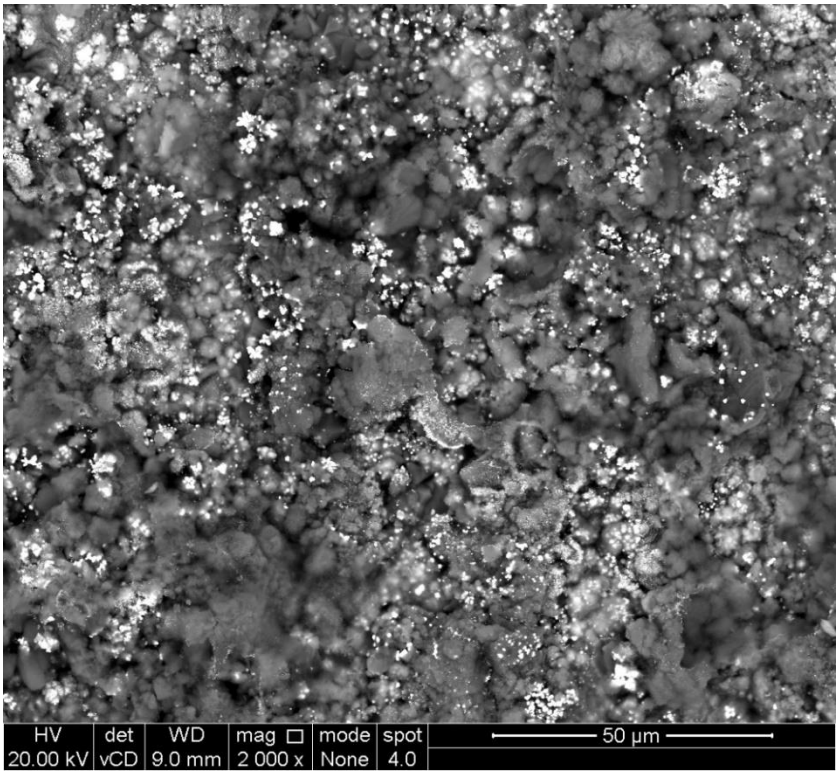

(a) BSE

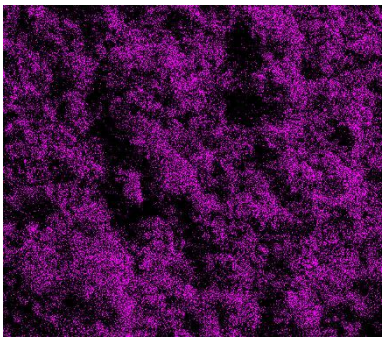

(b) O $K_{\alpha1}$ (59.6at.%)

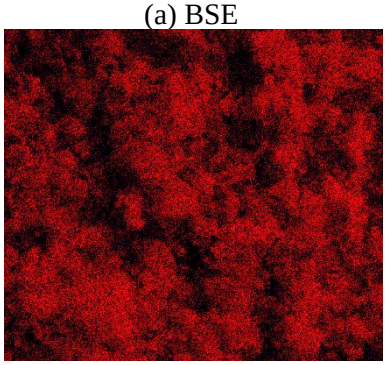

(c) Al $K_{\alpha1}$ (25.6at.%)

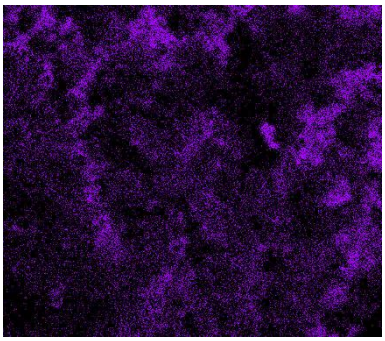

(d) Mg $K_{\alpha1}$ and $K_{\alpha2}$ (9.1at.%)

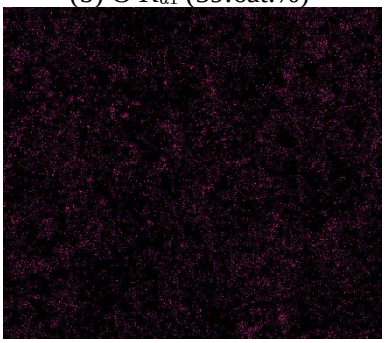

(e) W $L_{\alpha1}$ (2.4at.%)

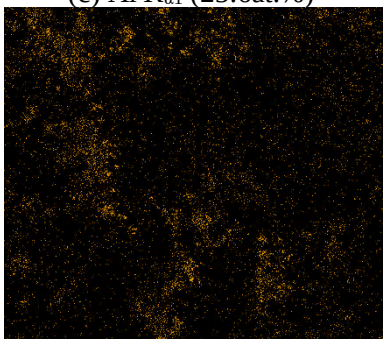

(f) Fe $K_{\alpha1}$ (1.3at.%)

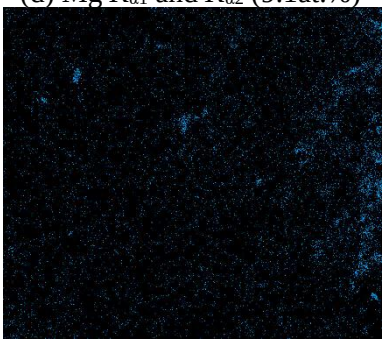

(g) Ti $K_{\alpha1}$ (0.7at.%)

Figure 117 – BSE image and EDS maps of the surface of a sample of Ti_3AlC_2 which was exposed to processed KME at 600°C for 125 h. The EDS maps are ordered by concentration, with the elemental compositions shown in brackets. The image shows a general overview of the surface morphology.

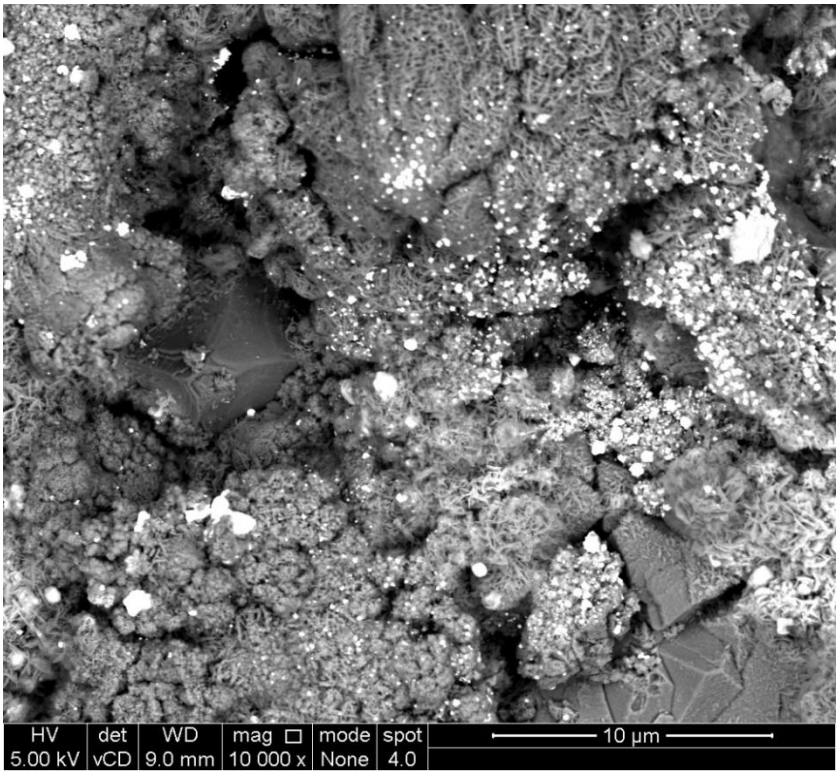

Figure 118 – BSE image of the surface of a sample of Ti_3AlC_2 which was exposed to processed KME at 600°C for 125 h. The magnification used provides a detailed view of the morphology of particles.

impurities are also observed. Chlorine (0.4at.%) was also observed, suggesting the sample may have been insufficiently cleaned.

Figure 118 is a higher magnification BSE image which provides greater detail of the morphology of the surface layer. There appears to be an underlying layer of oxide particles with a network of needle-like particles above.

6.2.1.3 Microstructural examination of the cross-section

Figure 119 shows a general view of the corrosion layer. The thickness varies but is typically 5-8 µm. A deposition layer has formed on the surface of the material, as indicated by the generally smooth underlying surface. There are occasional protrusions in this underlying surface, the presence of which is unclear.

Figure 120 is a BSE image of the opposite side of the sample, where the deposition layer is significantly thicker. Figure 121 is a higher magnification BSE image of the deposits which have formed on the surface. The annotations show the locations of point analyses, the elemental compositions of which are summarised in Table 27. The bright contrast region of location 2 contains significant amounts

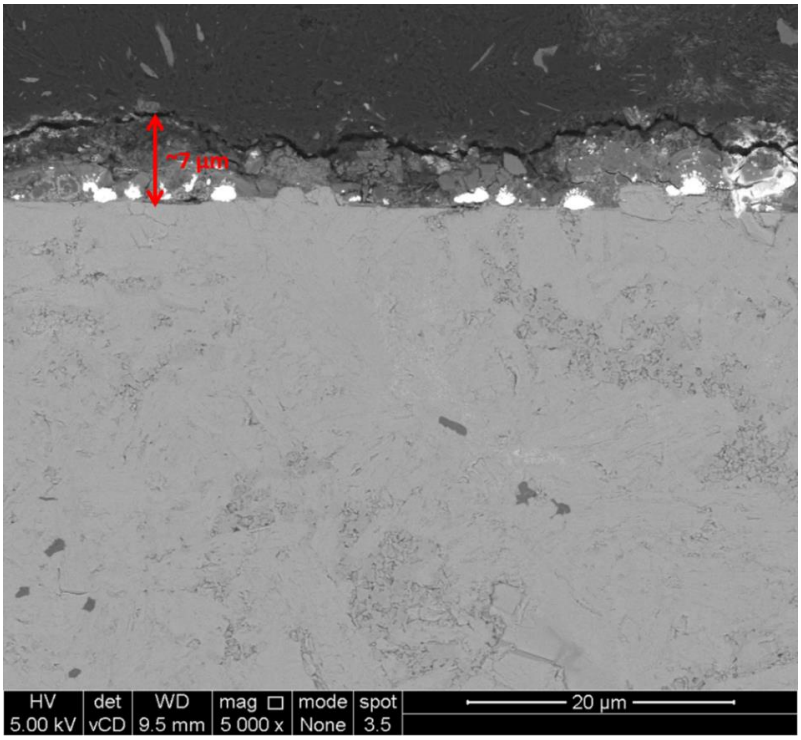

Figure 119 – BSE image of the cross-section of a sample of Ti_3AlC_2 which was exposed to processed KME at 600°C for 125 h. The image provides a general overview of the thickness of the deposition layer.

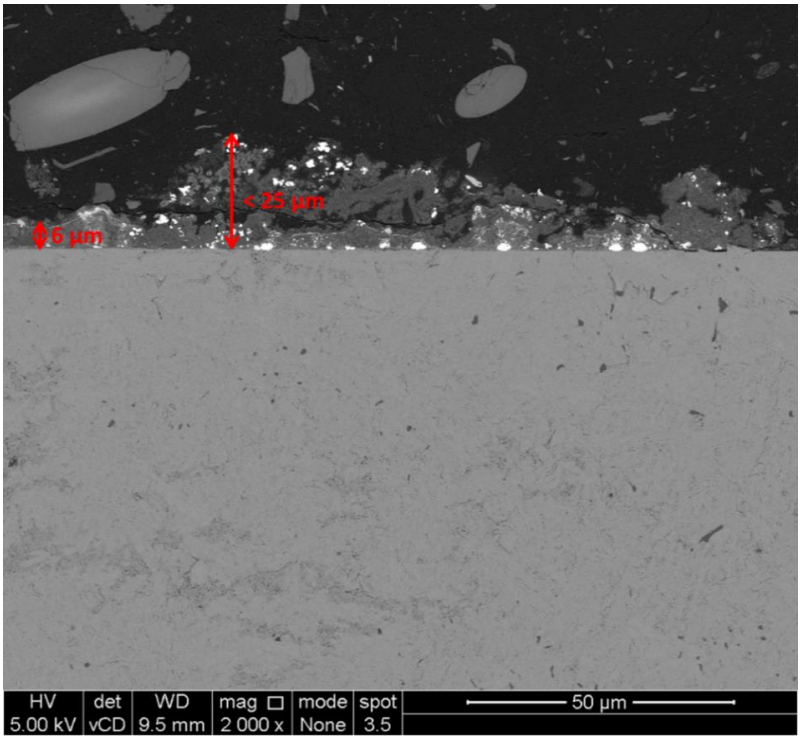

Figure 120 – BSE image of the cross-section of the opposite side of a sample of Ti_3AlC_2 which was exposed to processed KME at 600°C for 125 h. The deposition layer is thicker than that shown in Figure 119.

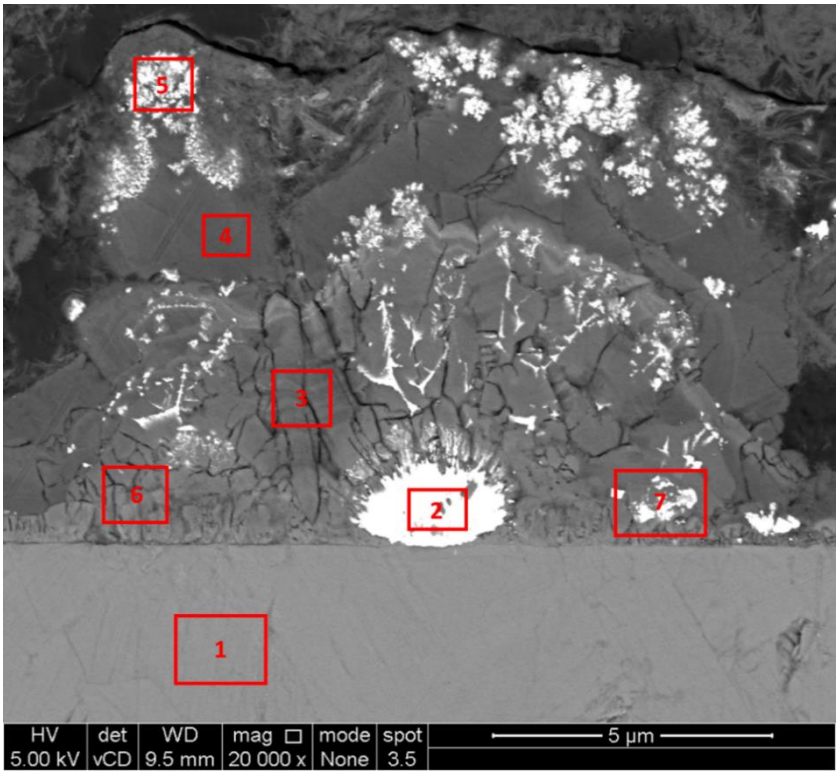

Figure 121 – Higher magnification image of a typical deposit on the surface of a sample of Ti_3AlC_2 which was exposed to KCl-$MgCl_2$ at 600°C for 125 h. The bright centre consists of tungsten and is surrounded by magnesium oxide.

Table 27 – Elemental compositions (in at.%) of the point analyses shown in Figure 121.

Spectrum	Ti	Al	C	W	Mg	O	Cl	Fe	K
1	50.0	35.5	14.5	-	-	-	-	-	-
2	4.4	2.3	39.8	26.9	8.2	16.6	-	-	-
3	0.5	0.8	10.1	1.2	41.0	45.7	0.5	0.1	0.1
4	0.2	1.5	12.0	0.8	40.6	43.6	0.7	0.4	0.2
5	0.4	6.6	34.7	4.0	14.8	35.9	0.5	2.9	0.1
6	4.7	5.0	13.2	5.6	23.3	46.2	0.7	0.4	0.2
7	4.0	3.9	18.4	4.2	25.2	41.9	0.7	0.7	0.2

of tungsten and carbon, suggesting this is a deposit of tungsten carbide. Tungsten carbide typically forms as either WC or W_2C; the uneven ratio of W to C may indicate both phases are present [206]. Some magnesium and oxygen are also present in this region. Points 3-7 also show significant quantities

of Mg and O. It is possible that Mg was deposited and has oxidised during micropreparation of the sample, although only MgO was observed by GAXRD. Point 5 contains a significant amount of Fe, suggesting that the similar dentritically-shaped bright areas may also consist of an Fe impurity. The lids for most of the samples contained holes, and therefore some iron may have been able to deposit in the crucibles from the vessel.

6.2.2 Processed salt, 600°C, 250 h

6.2.2.1 Glancing angle X-ray diffraction

The GAXRD patterns are shown in Figure 122, normalised relative to the MgO (220) peak [178,179,195,198,199]. It should be noted that the MgO peaks could also represent MgO with Fe substitution or Fe_xTi_{1-x}, and the W peaks could represent WC_x and various W-based alloys such as W_xTi_{1-x} [200]. Both MgO and W are intense at all glancing angles, although the W peaks increase slightly in intensity as the glancing angle is decreased. β-W also appears to be present, mainly identified by the presence of its (211) peak, although some of its lower intensity and high angle peaks may be missing. Ti_3AlC_2 and TiC_x peaks decrease in intensity from 5° to 1° ω, and are absent at 0.5° ω. A small peak for KCl can be seen at 0.5° ω, indicating some residual salt is present on the sample surface.

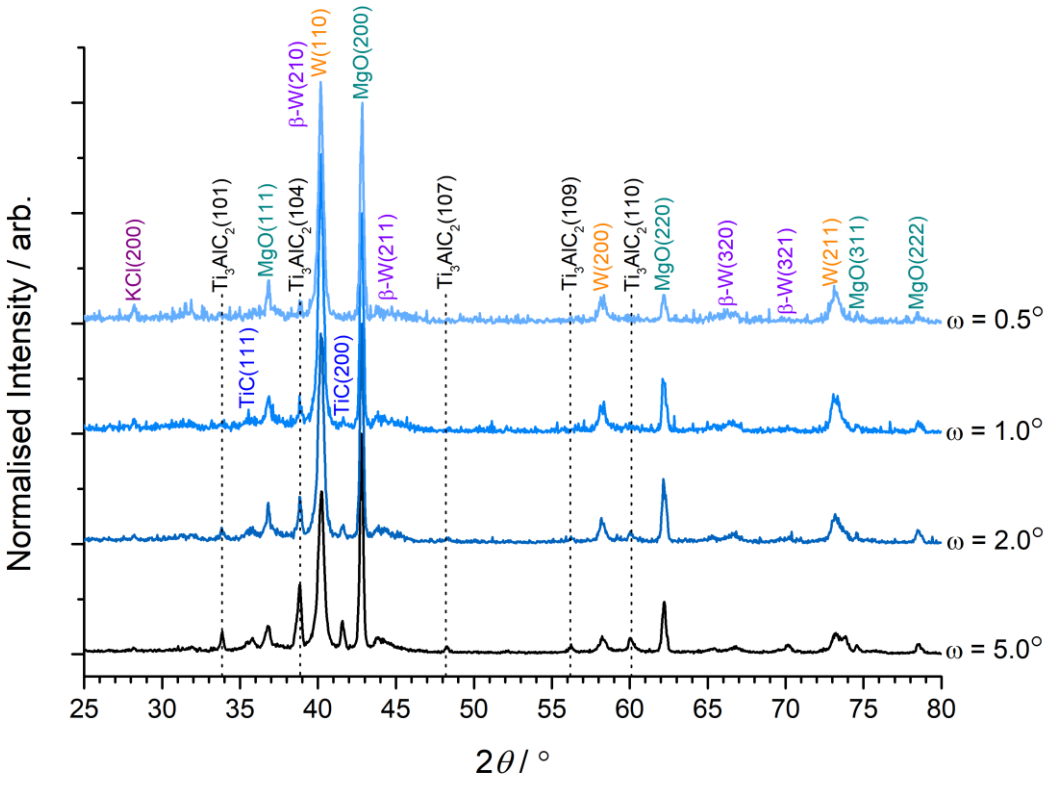

Figure 122 – GAXRD patterns for a sample of Ti_3AlC_2 which was exposed to KME for 250 h. The patterns were normalised relative to the MgO (200) peak.

6.2.2.2 Microstructural examination of the surface

Figure 124 shows a BSE image and EDS maps of the sample. The annotations mark the locations of point analyses, the results of which are summarised in Table 28 along with the overall map composition. The overall map composition indicates that most of the surface has oxidised. A significant fraction of the surface is coated with Mg, which is located in the bright contrast regions of the BSE image. At lower magnifications this morphology is observed across the majority of the surface, and it is appears that the top left of the image is the underlying surface. Ti can only be found in the top left of the image, and point 1 suggests it is most likely present as an oxide. A significant amount of Al is also found in this top left region. Significant fractions of Al and O are present at point 2, which looks as though it may be deposited on the surface. Combined with the greater fraction of Al in the overall image composition, this suggests that Al has leached out of the material and deposited on the surface. However, there is also a significant fraction of C in this region, which may suggest that Ti has diffused out rather than Al. Point 5 shows that some Al is also present in the bright contrast region. The K and Cl maps show that a small fraction of KCl is present over the entire surface but appears to be more concentrated on the underlying surface; this may just be because it is more difficult to remove from this region due to the lower topography. Some Fe can be found dotted on the surface, most likely deposited as an impurity.

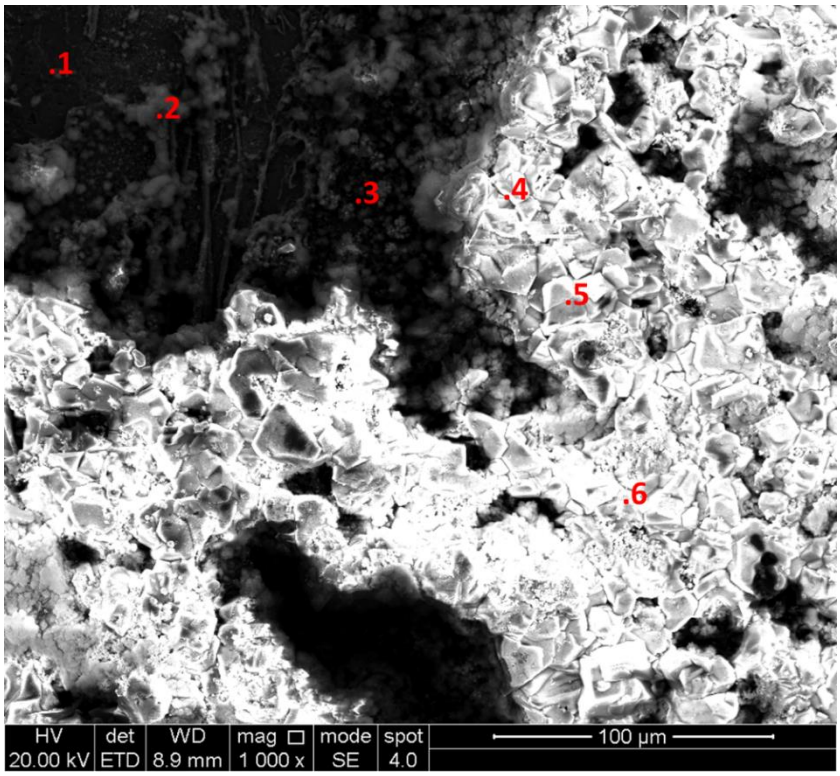

Figure 123 – BSE image of the surface of a sample of Ti_3AlC_2 which was exposed to KME for 250 h at 600°C. The elemental compositions of the map sum spectrum and point analyses are shown in Table 28 and EDS maps are shown in Figure 124.

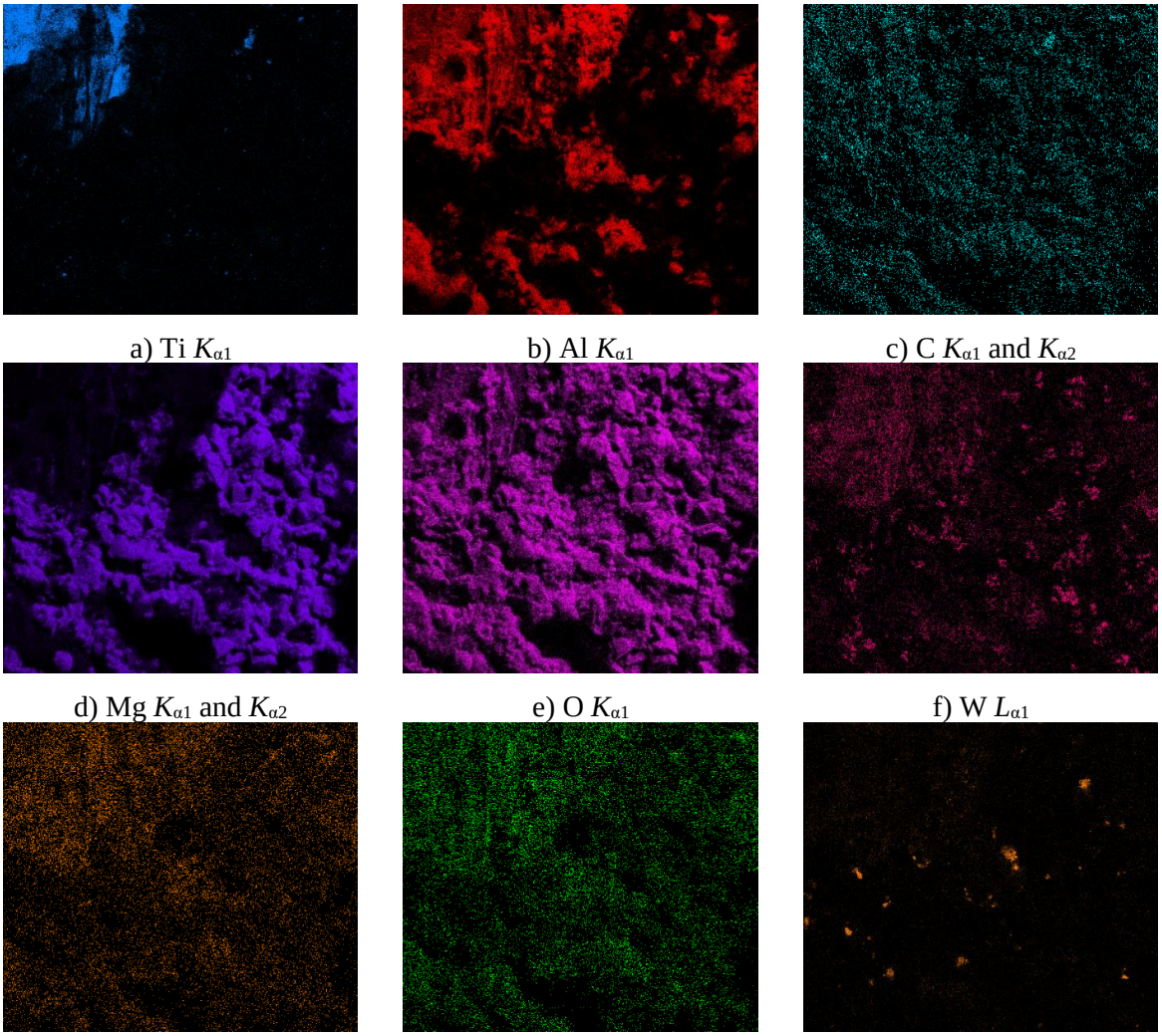

a) Ti $K_{\alpha1}$ b) Al $K_{\alpha1}$ c) C $K_{\alpha1}$ and $K_{\alpha2}$

d) Mg $K_{\alpha1}$ and $K_{\alpha2}$ e) O $K_{\alpha1}$ f) W $L_{\alpha1}$

g) K $K_{\alpha1}$ h) Cl $K_{\alpha1}$ i) Fe $K_{\alpha1}$

Figure 124 – EDS maps (image width ~300 µm) of the surface of a sample of Ti_3AlC_2 which was exposed to KME for 250 h at 600°C. The elemental compositions of the map sum spectrum and point analyses are shown in Table 28.

Table 28 – Elemental compositions (in at.%) of the EDS spectra in Figure 123.

Spectrum	O	Mg	C	Al	Ti	W	Fe	Cl	K
Map	49.6	24.5	12.1	10.0	1.9	1.1	0.4	0.2	0.2
1	30.9	0.5	19.9	13.4	35.1	0.1	-	-	-
2	51.2	4.2	15.6	24.9	0.8	1.6		0.4	0.8
3	45.0	27.9	13.2	11.0	0.4	0.8	0.9	0.5	0.2
4	50.4	38.6	10.6	0.3	-	0.1	-	-	-
5	41.8	26.9	-	27.9	0.5	1.1	0.2	0.6	1.0
6	49.0	40.9	9.9	-	-	0.1	-	-	-

6.2.2.3 Microstructural examination of the cross-section

Figure 125 is a BSE image showing the morphology in the deposition layer. Lower magnification images revealed that the deposition layer was relatively uniform, varying between ~15-25 µm thick. Points 13 and 15 confirm the EDS spectra are relatively accurate, as their morphology and elemental compositions clearly represent Ti_3AlC_2 and TiC_x respectively. It can also be seen in point 14 that the sample contained particles of alumina (or unreacted aluminium) within the bulk. It can be seen from the EDS maps that the locations of Mg and Al do not overlap, indicating that the oxide formed is not a joint oxide such as magnesium aluminate. Points 6 and 10 appear to be MgO, whereas points 4, 7 and 9 appear to be Al_2O_3. W has deposited directly on the surface of the MAX phase grains in a layer ~1-2 µm thick, and the oxide layers have deposited on top of this relatively thin layer. Interestingly, the underlying MAX phase surface appears relatively smooth and there does not appear to be aluminium depletion despite the significant presence of alumina in the deposition layer.

Table 29 – Elemental compositions (in at.%) of the EDS spectra shown in Figure 125.

Spectrum	Ti	Al	C	Mg	O	W	Fe	K	Cl	Other	Other Elements
Map	12.8	5.9	50.0	4.5	25.1	0.2	0.2	0.0	-	1.2	Si, Ca
1	71.1	1.4	9.2	8.4	5.0	1.7	0.3	0.4	0.2	2.6	Si, Ca
2	0.1	5.6	80.3	1.6	11.6	0.3	0.0	0.1	0.0	0.5	Si, Sr, Ca, P, S
3	0.1	10.1	70.2	2.4	16.3	0.3	0.0	0.2	0.1	0.3	Si, Sr, Ca, P
4	0.1	27.1	20.5	1.1	50.0	0.2	-	0.8	0.1	0.2	Na, Zn
5	0.6	4.0	59.5	2.4	26.2	6.9	0.3	0.1	-	0.1	Ca
6	0.1	0.9	6.8	45.7	45.9	-	0.2	0.0	0.3	-	-
7	0.2	29.9	9.2	4.4	55.0	0.6	0.1	0.5	0.2	-	-
8	0.1	1.3	77.5	9.0	11.5	-	0.2	0.1	0.1	0.3	Si, Ca
9	0.2	25.9	17.1	5.2	50.1	0.5	0.3	0.4	0.2	0.1	S
10	0.1	-	7.5	46.7	45.5	0.2	-	-	-	-	-
11	0.9	4.6	17.9	21.6	42.1	8.2	2.1	0.3	0.7	1.6	Sr, P, Ca
12	3.0	5.5	11.0	29.7	46.4	2.7	0.7	0.3	0.8	-	-
13	49.1	14.2	36.8	-	-	-	-	-	-	-	-
14	11.7	22.8	7.8	-	57.7	-	-	-	-	-	-
15	48.9	3.8	47.3	-	-	-	-	-	-	-	-

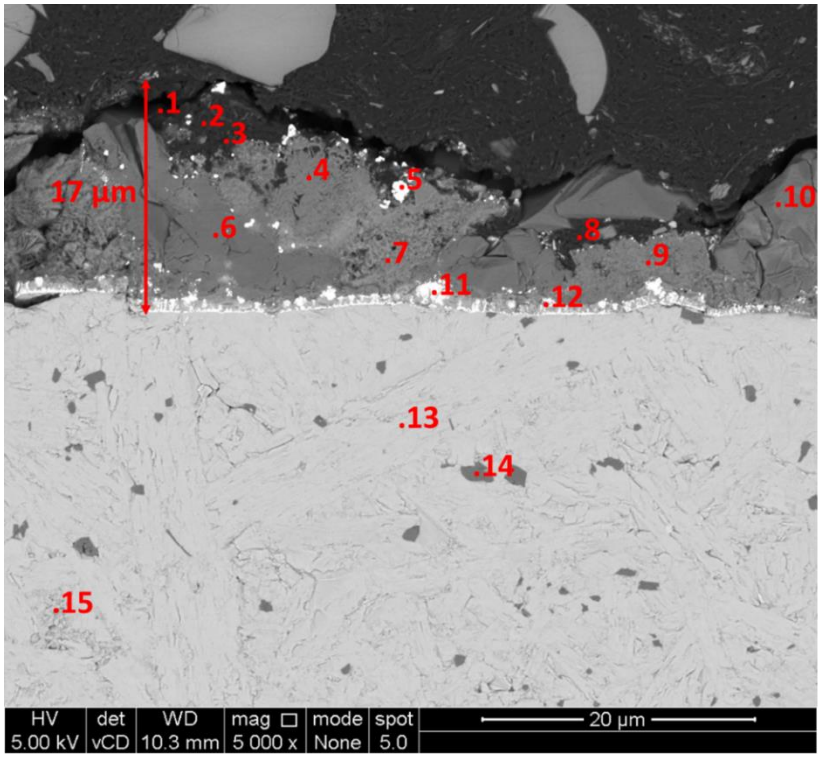

(a) BSE

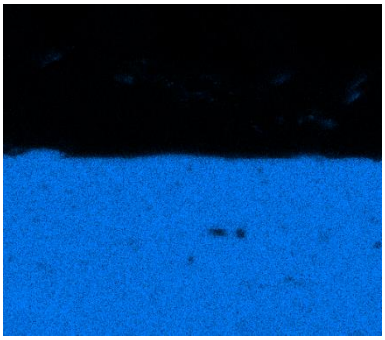

(b) Ti $K_{\alpha1}$

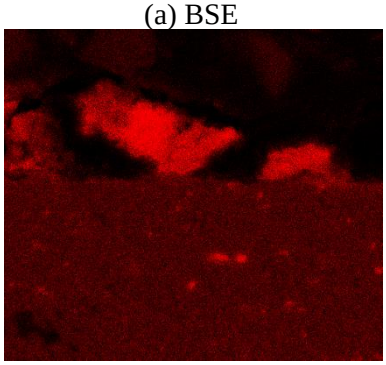

(c) Al $K_{\alpha1}$

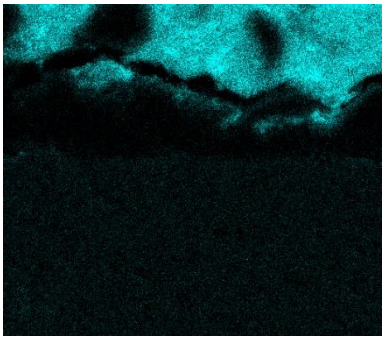

(d) C $K_{\alpha1}$

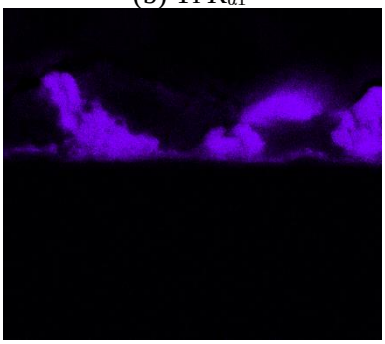

(e) Mg $K_{\alpha1}$ and $K_{\alpha2}$

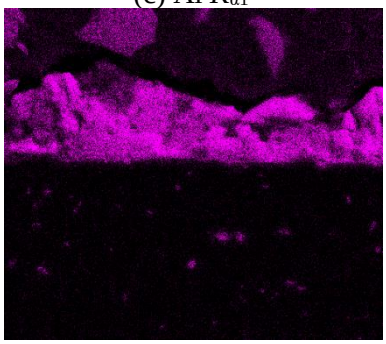

(f) O $K_{\alpha1}$

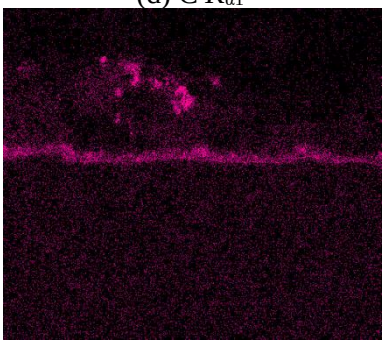

(g) W $L_{\alpha1}$

Figure 125 – BSE image with EDS maps of the cross-section of a sample of Ti_3AlC_2 which was exposed to processed KME at 600°C for 250 h. The annotations mark the locations of point analyses, the elemental compositions of which are summarised in Table 29. The image shows the morphology of the products in the deposition layer.

6.2.3 Processed salt, 850°C, 125 h

6.2.3.1 Glancing angle X-ray diffraction

The GAXRD patterns are shown in Figure 126, normalised relative to the $MgAl_2O_4$ (311) peak [178,179,195,198,199,207]. $MgAl_2O_4$ (spinel) is the dominant phase at all glancing angles. MgO is also present at all glancing angles, with little variation in its intensity. Ti_3AlC_2 and TiC_x in the substrate can be seen at 5° ω, and their concentration decreases with glancing angle. The Im-3m phase is a W-based alloy, but its exact identity is difficult to determine from XRD alone. Its peaks decrease slightly in intensity as the glancing angle is decreased, indicating it is mainly present on the surface of the substrate. The Fm-3m phase is aluminium or an alloy such as $Al_{1-x}Mg_x$, where Al is the dominant species. The Fm-3m (111) peak is most intense at 5° ω and 0.5° ω, which may indicate that metallic aluminium is present at both the surface of the substrate and the surface of the deposition layer. Within the deposition layer, it most likely undergoes reaction to form $MgAl_2O_4$. There is an unidentified peak at ~25.5° 2θ in the pattern at 5° ω which may represent an oxide of aluminium or titanium [208].

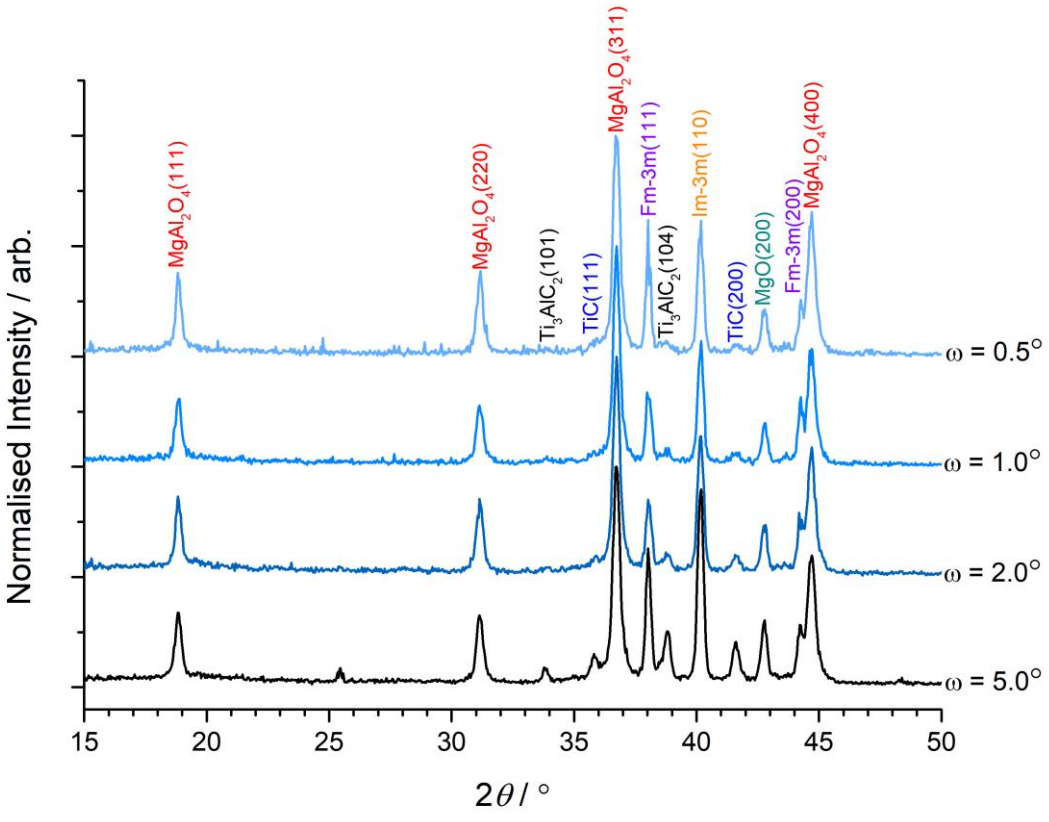

Figure 126 – GAXRD patterns for Ti_3AlC_2 which was exposed to processed KME at 850°C for 125 h. The major phase at all angles was $MgAl_2O_4$, and the patterns were normalised relative to the $MgAl_2O_4$ (311) peak. The Im-3m phase is a W-based phase such as W, WC_x or $W_{1-x}Ti_x$. The Fm-3m is Al or an alloy such as $Al_{1-x}Mg_x$.

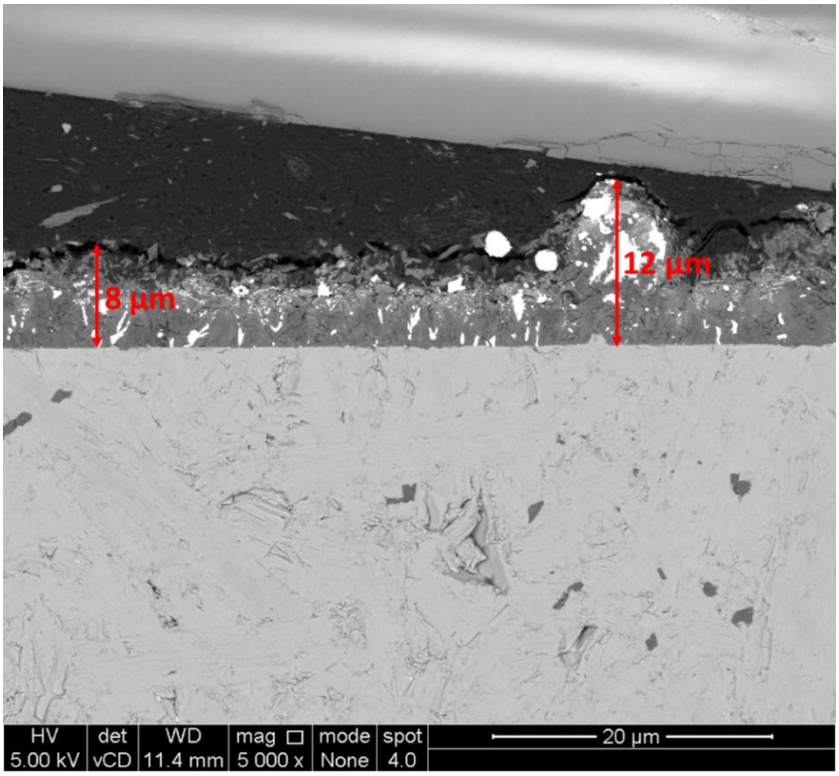

Figure 127 – BSE image of the cross-section of a sample of Ti_3AlC_2 which was exposed to processed KME at 850°C for 125 h. The image provides a general overview of a deposition layer which has formed on the surface of the material.

6.2.3.2 Microstructural examination of the cross-section

Figure 127 is a BSE image which provides a general overview of the cross-section, showing that a deposition has formed. The average thickness of this layer is ~8 µm, but it appears to extend up to ~12 µm in some locations. The underlying surface is relatively smooth.

Figure 128 is a BSE image and EDS maps of a different region of the sample. The deposition layer appears to be typically ~4-5 µm and extends up to 15 µm in some locations. It appears that some of this deposition layer has broken away during sample mounting. The Ti map shows it is only present in the bulk; no Ti is present in the deposition layer. The Al map shows a high concentration in the deposition layer and significant deficiency in clustered regions in the bulk. The morphology of the bulk indicates that these depleted regions are TiC_x. Significant fractions of Mg and O were also found in the deposition layer, indicating that the deposition layer consists of oxides in agreement with the $MgAl_2O_4$ and MgO phases observed by GAXRD. Mg appears to be concentrated close to the surface of the bulk material as opposed to the outer region of the deposition layer, indicating that Mg deposits due to reaction with the MAX phase or surface oxide layers. In addition to the usual impurities of Fe (0.2at.%) and W (0.1at.%), Ag was found as an impurity, concentrated in the bright regions of the BSE image. This suggests that the batch of salt used was contaminated with Ag due to breakage of a reference electrode.

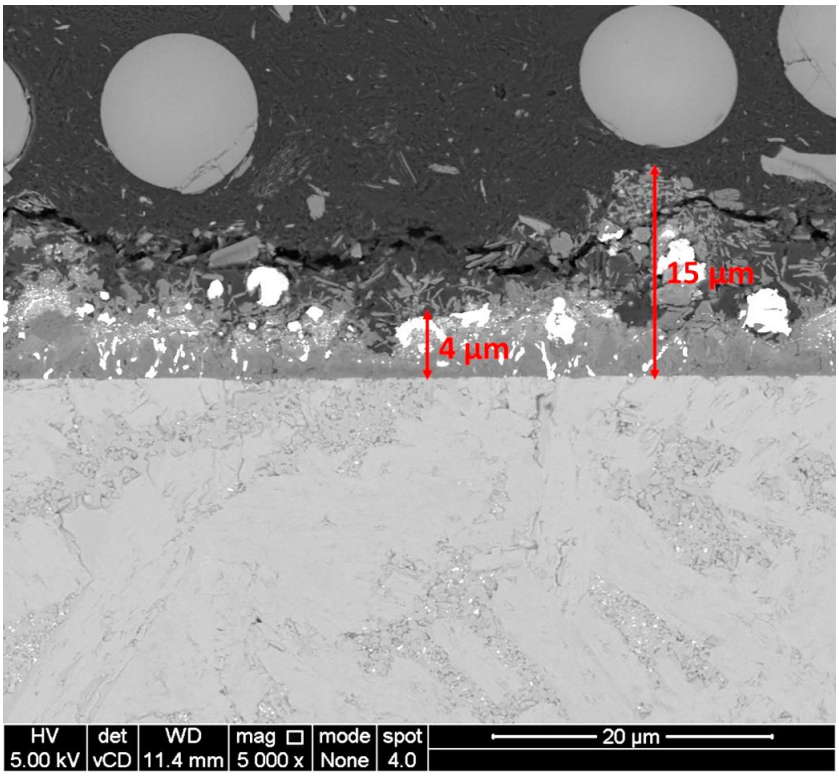

(a) BSE

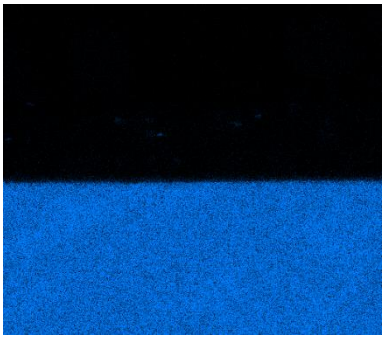

(b) Ti $K_{\alpha1}$(11.2at.%)

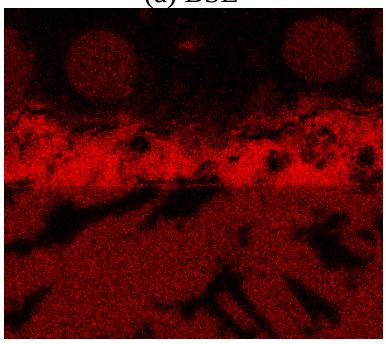

(c) Al $K_{\alpha1}$ (4.7at.%)

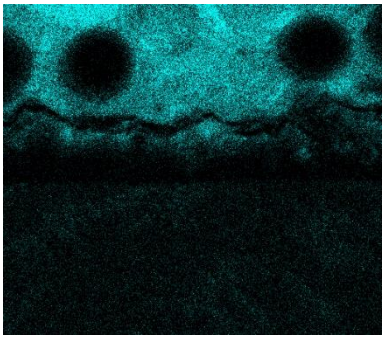

(d) C $K_{\alpha1}$ and $K_{\alpha2}$ (57.4at.%)

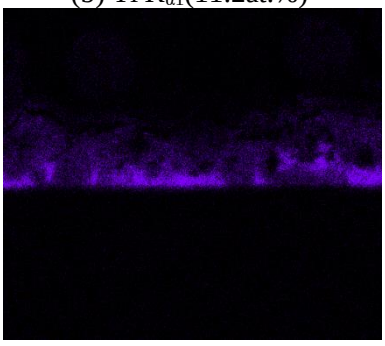

(e) Mg $K_{\alpha1}$ and $K_{\alpha2}$ (1.8at.%)

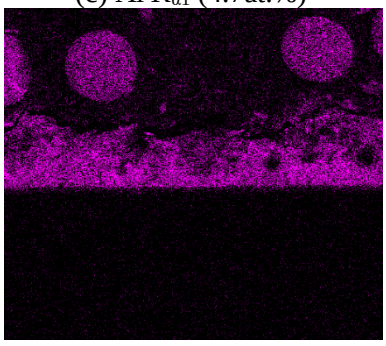

(f) O $K_{\alpha1}$ (22.4at.%)

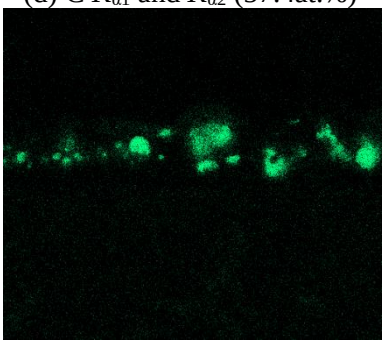

(g) Ag $L_{\alpha1}$ (0.4at.%)

Figure 128 – BSE image and EDS maps showing a general overview of the cross-section of a sample of Ti_3AlC_2 which was exposed to processed KME at 850°C for 125 h.

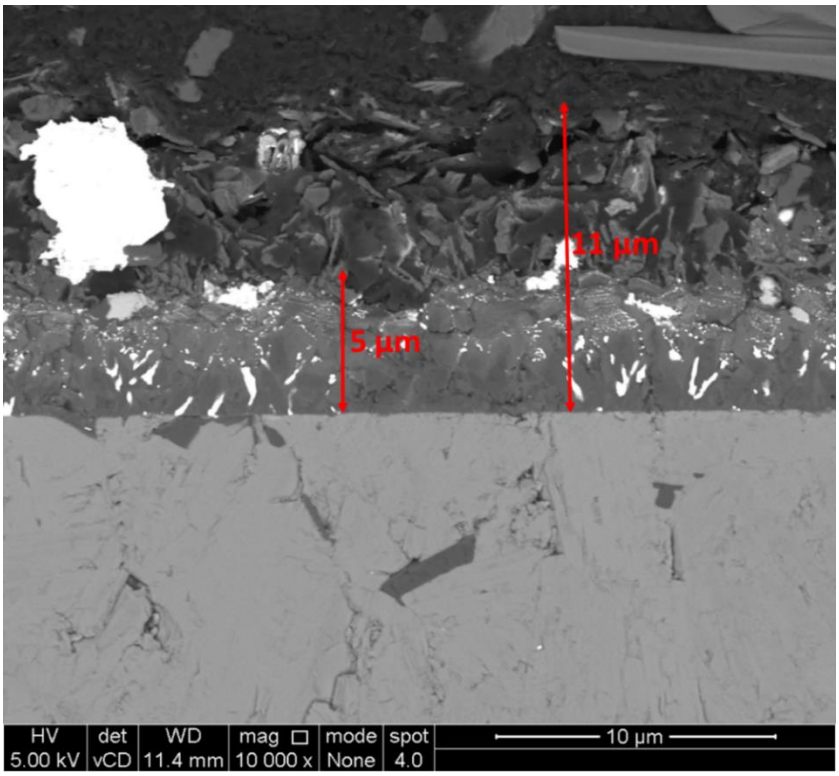

(a) BSE

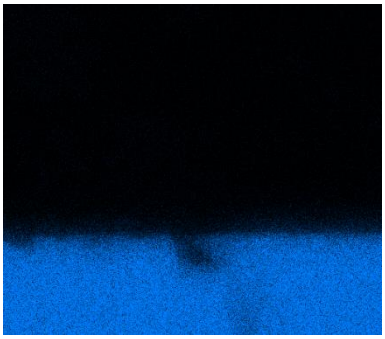

(b) Ti $K_{\alpha1}$(7.6at.%)

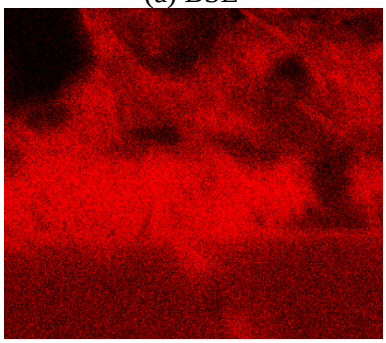

(c) Al $K_{\alpha1}$ (11.0at.%)

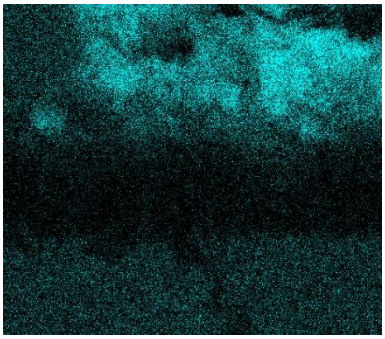

(d) C $K_{\alpha1}$ and $K_{\alpha2}$ (29.6at.%)

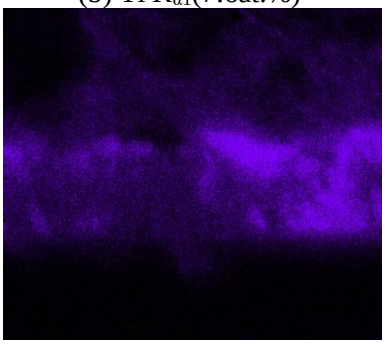

(e) Mg $K_{\alpha1}$ and $K_{\alpha2}$ (7.0at.%)

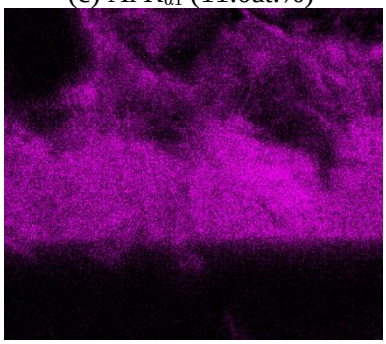

(f) O $K_{\alpha1}$ (41.0at.%)

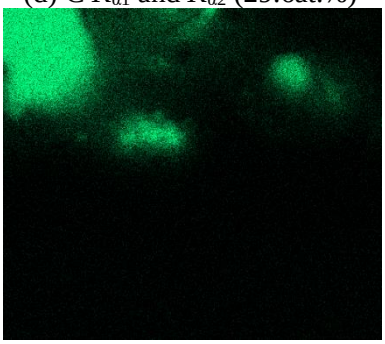

(g) Ag $L_{\alpha1}$ (2.1at.%)

Figure 129 – BSE image and EDS maps showing the morphology of the deposition layer formed on a sample of Ti_3AlC_2 which was exposed to processed KME at 850°C for 125 h.

Figure 129 is a BSE image with EDS maps taken at a higher magnification, showing greater detail of the deposition layer morphology. There appears to be an inner deposition layer ~5 μm thick, with an outer deposition layer formed on top of this for a further ~6 μm. The inner layer appears to consist mainly of Mg, Al and O, and is therefore the $MgAl_2O_4$ phase observed by GAXRD. The outer layer consists mainly of Al, O and C and appears to have a plate-like morphology. The bright contrast in the BSE image is Ag. Fe (0.6at.%) and W (0.6at.%) were also observed as impurities.

6.3 Discussion

Two of the samples exposed to as-received salt were accidentally switched prior to exposure, so two samples of Ti_3AlC_2 were exposed to as-received LKE and none were exposed to as-received KME. Overall, the mechanism of corrosion appears to be similar to that for the sample in the initial static corrosion test (§ 16.1.4). Both samples were suspended by nickel wire and were suspended from a stainless-steel bar, so it is possible that galvanic corrosion occurred despite attempts to limit the formation of a circuit. It is likely that chloride ions were oxidised to chlorine gas which then reacted with Ti_3AlC_2. The reaction of MAX phases with chlorine gas has been investigated by numerous researchers [144–146], and found to result in loss of the A-group element and formation of a layered MX_n compound. This appears to be consistent with the observations in this work. SEM images and EDS of the cross-sections show loss of Al from the MAX phase structure and penetration of chlorine. The reaction layer was thinner for sample A, and peaks for Ti_3AlC_2 could be seen in the GAXRD pattern, but the Ti_3AlC_2 peaks disappeared for sample B which had a thicker reaction layer (see § 0).

The GAXRD patterns contain numerous unidentified peaks, many of which suggest a phase with similar crystal structure to Ti_3AlC_2 with an expanded lattice parameter. Furthermore, it is possible that Ti_xCCl_y forms as an intermediate, similar to the $Ti_3C_2T_2$ compounds (e.g. $Ti_3C_2F_2$ and $Ti_3C_2(OH)_2$) observed by researchers such as Naguib *et al.* [149–151]. It is likely that the XRD pattern of such a phase would overlap with that of Ti_3AlC_2 with different lattice parameters due to presence of Cl^-. The ionic radius of Al^{3+} is 0.54 Å (6 coordinate) whilst that of Cl^- is 1.81 Å, so lattice expansion and a shift in 2θ would be expected [185]. Furthermore, the theoretical lattice parameter of $Ti_3C_2F_2$ has been determined by DFT as 21.541 Å, comparable to the value of 22.3 Å for the T-C-Cl phase in this work. EDS suggests a tentative stoichiometry of Ti_2C_3Cl for this phase. Further reaction with Cl_2 may occur causing loss of Ti, and under extended heating the remaining TiC_x may recrystallise to stoichiometric or near-stoichiometric TiC_x with ordered carbon vacancies.

The sample exposed to processed LKE underwent very little corrosion and negligible mass loss was observed. The surface was slightly rougher after exposure and a bumpy coating of spherical oxide particles could be observed on the surface, as seen in samples exposed to air at high temperatures [38]. Most concerning was the presence of MgO on the surface which was observed by both SEM and GAXRD. The most probable explanation for this is contamination of the batch of salt. The same reference electrode was used for preparing batches of LKE and KME. Li^+ ions enter the mullite sheath in LKE, and Mg^{2+} ions in KME. A separate reference electrode should have been used for each salt to prevent such contamination.

The sample which was exposed for 250 h was absent of oxides, but multiple tungsten-based phases were observed, and some oxygen and magnesium were present in the EDS spectra. There was a small amount of mass loss and the surface was approximately twice as rough as the sample exposed for 125 h.

β-W was observed, which is less stable than α-W and has been observed to form by electrodeposition in molten chloride salts [199].

At 850°C, corrosion was severe on one side of the sample and less severe on the other. The sample was raised on a piece of alumina, so the underside was exposed, and the presence of tungsten on the less corroded side suggests it was the underside as tungsten would be expected to sink to the bottom of the crucible. The morphology on the underside is similar to samples which reacted with chlorine gas, with exfoliation of MAX phase grains visible. Aluminium diffused out of the Ti_3AlC_2 structure and deposited at the surface. It is likely that lithium is deposited at the surface during electrolysis of LiCl, and aluminium, either as $Al_{(s)}$ or $AlCl_{3(g)}$, reacts with lithium and forms an alloy or oxide. The reaction between $AlCl_{3(g)}$ and Li (Equation 33) at 850°C is spontaneous, with a $\Delta_r G$ of -443 kJ mol^{-1} [99].

Equation 33

$$AlCl_{3(g)} + 3Li \rightleftharpoons Al + 3LiCl$$

Pits were observed on the heavily corroded side, and green and pink iridescence could be seen, most likely due to refraction from thin oxide layers. Iron may be involved in the pit formation mechanism, as EDS showed it was present at the edge of the pits. The Ti_3AlC_2 (004) peak decreased in intensity at lower glancing angles, indicating loss of the Al atoms in the basal planes (Figure 130). Similarly, the (002) peak intensity increased, and EDS results indicated the presence of TiC_2. This would be expected to form from Ti_3AlC_2 by loss of Al to form Ti_3C_2 (Equation 34), after which the Ti atoms on the outer sides of the layers would be lost to form TiC_2 (Equation 35). Following this, further loss of Ti could occur to leave a carbide derived carbon (Equation 36) [38,144–146].

Equation 34

$$Ti_3AlC_2 \rightleftharpoons Ti_3C_2 + Al$$

Equation 35

$$Ti_3C_2 \rightleftharpoons TiC_2 + 2Ti$$

Equation 36

$$TiC_2 \rightleftharpoons Ti + 2C$$

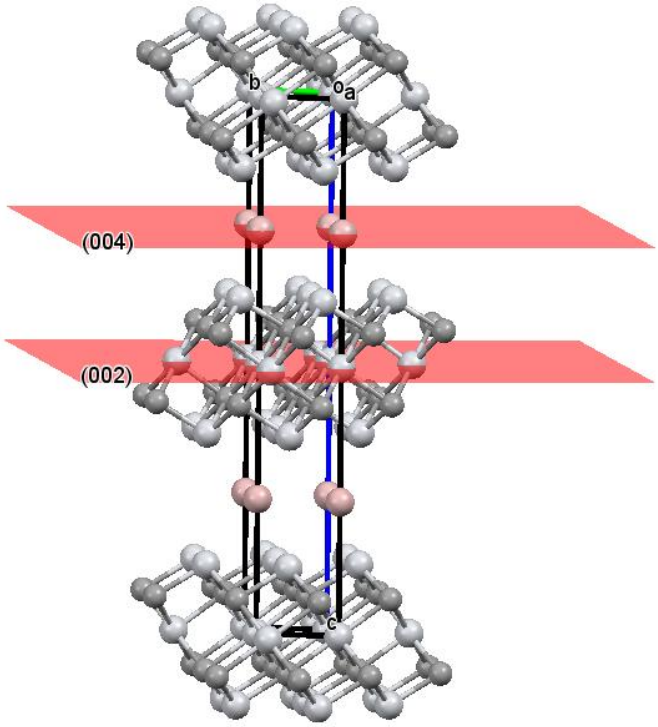

Figure 130 – Crystal structure of Ti_3AlC_2 with the (002) and (004) planes highlighted.

The corrosion mechanism for the samples exposed to processed KME at 600°C seemed to be the same regardless of exposure time. Unfortunately, the sample exposed for 250 h was not weighed prior to micropreparation of the cross-section, so gravimetric data is unavailable. Mass gain was observed for the 125 h sample due to formation of a deposition layer. Consequently, there was an increase in roughness, and the roughness almost doubled with twice the exposure time. The thickness of the deposition also appears to have increased from ~5-8 µm to ~15-25 µm, although thicknesses up to ~25 µm could be seen for the sample exposed for 125 h.

The only phases observed by GAXRD in the deposition layer for both samples were α-W, β-W and MgO. All of these phases may also exist as solid solutions, with W_xTi_{1-x}, W_xAl_{1-x} and WC_x being possible alternatives for the W-based phases. EDS showed a high fraction of C associated with W, suggesting both WC and W_2C as likely alternatives for α-W and β-W respectively. Fe was observed as an impurity for both samples, the most likely source being corrosion of the reaction vessel. Analysis of the surfaces by EDS suggests that a significant fraction of aluminium was also present. It is possible that aluminium oxide or $MgAl_2O_4$ had formed but could not be detected by XRD, or that Al may have substituted for Mg in MgO.

For the sample exposed for 125 h the ratio of Ti:Al:C near the deposition layer was ~3:2:1, which may indicate diffusion of Ti and C towards the deposition layer. Conversely, the sample exposed for 250 h had a ratio of 3:1:2 as per the composition of Ti_3AlC_2. In both cases, W deposited first then oxides

formed on top. For the 125 h sample, the W deposits were spots and MgO was the only oxide clearly observed. For the 250 h sample, W deposited as a thin layer, ~1-2 µm thick, and oxides of Mg and Al deposited separately on the surface. The bulk material did not appear to be depleted in Al so the most likely source would be the oxide layers formed on the surface of Ti_3AlC_2 prior to corrosion. It is worth noting that alumina, as per the crucibles, is stable to reaction with chlorine gas, so deterioration of the crucibles would not be expected (Δ_rG = 320 kJ mol^{-1} at 600°C) [99].

$MgAl_2O_4$ was the dominant corrosion product when Ti_3AlC_2 was exposed to processed KME at 850°C. The original surface was relatively smooth, but a deposition layer formed. Magnesium was mainly present close to the original surface, with aluminium present in the entire deposition layer. Clusters of TiC_x were observed in the bulk material. The proposed mechanism of reaction is as follows: Mg^{2+} deposited on the surface by reaction with surface oxides or oxygen in the melt to form MgO. At 850°C, the Gibbs free energy of formation of Al_2O_3 is -1320 kJ mol^{-1} whereas that of TiO_2 is -741 kJ mol^{-1}. Therefore, the most likely reaction would be with TiO_2 as it is the least stable oxide. This may form titanium metal (redox reaction) or titanium chloride, but there is insufficient evidence to say which. MgO and Al_2O_3 can then undergo reaction at the surface to form $MgAl_2O_4$ (-14 kJ mol^{-1}). Aluminium is more mobile than titanium in the MAX phase so it is drawn to the surface to replace the Al_2O_3 which is lost, enabling further reaction.

As expected, the mechanisms appeared to be the same for both exposure times when the exposure temperature was kept constant. Minimal corrosion occurred at both exposure times in LKE. MgO was present on the sample exposed for 125 h due to contamination of the batch of salt, and W-based phases were present on the sample exposed for 250 h due to contamination from the tungsten working electrode used for salt processing. Both samples in KME formed MgO on their surfaces. Tungsten-based phases also deposited on their surfaces due to impurities from processing. Mass loss was observed in LKE and increased with exposure time, whereas mass gain occurred in KME, although the effect of exposure time was not determined. There was an increase in roughness with exposure time for both samples, and the roughness of the samples exposed to KME was much greater than those exposed to LKE. The thickness of the corrosion layer increased in KME but could not be measured in LKE.

In LKE the corrosion mechanism changed significantly with exposure temperature. At 600°C, corrosion was uniform and relatively low. The main changes observed were due to the presence of impurities. When the temperature was increased to 850°C, the corrosion mechanism appeared to be similar to the samples which suffered dissimilar materials corrosion, *i.e.* reaction with chlorine gas. Aluminium diffused to the surface and formed oxide species. Pitting occurred, possibly due to the iron impurity, causing breakdown of the oxide scale. The mass loss had a similar order of magnitude to samples exposed to as-received salts at 600°C. The change in surface roughness was negligible.

In KME, MgO was observed on the surface at 600°C, whereas $MgAl_2O_4$ became the dominant corrosion product when the temperature was raised to 850°C. This was due to the increased mobility of Al in the MAX phase structure at higher temperature, enabling diffusion of Al to the surface where it could react with MgO. The mass gain and thickness of the deposition layer increased with temperature, although the sample roughness was approximately equal.

Comparison to work by Craig Jantzen suggests that Ti_3AlC_2 (and Maxthal 312, see §7) were clearly less stable than Hastelloy N under the environment in this work [43]. The most comparable experiments are the exposure at 600°C for 250 h and the exposure at 850°C for 125 h. At 600°C for 250 h Hastelloy N underwent limited corrosion in both LKE and KME, although the performance was better in LKE. Respectively, the mass gain was 0.3 mg cm^{-2} and 0.7 mg cm^{-2} and the depth of penetration was 1.6 ± 0.6 µm and 4.8 ± 1.1 µm. Corrosion of Ti_3AlC_2 was significantly greater than these values. At 850°C for 125 h Hastelloy N gained 13.0 mg cm^{-2} and corroded to 20.0 ± 5.5 µm in LKE, and gained 2.6 mg cm^{-2} and corroded to 18.6 ± 5.1 µm in KME. Hastelloy N corroded uniformly in all experiments, whereas many samples of Ti_3AlC_2 underwent intergranular corrosion, indicating a preference for Hastelloy N.

With relation to operation of an MSR, the results are indicative of the extent of corrosion that may be expected with a build-up of fission products, particularly noble or semi-noble metals, and deviation from operating conditions due to an increase in redox potential and ingress of air. Overall, it is unlikely that Ti_3AlC_2 would be sufficiently corrosion resistant for use in molten salt reactors, even with appropriate control of the moisture and oxygen content of the salt. This is due to the high mobility of aluminium which appears to leave the layered MAX phase structure, leaving behind a Ti-C-Cl phase.

7 Corrosion of Maxthal 312

Table 30 summarises the results from corrosion experiments of Maxthal 312. Results for the majority of these samples follow, and additional results can be found in Appendix H. Maxthal 312 was tested because Ti_3SiC_2 is one of the most well studied MAX phase compositions available, it is commercially available, it compares well with Ti_3AlC_2 to show the effect of the A-group element, and there is evidence that it performs well under irradiation damage and has low neutron absorption. Samples were exposed to LiCl-KCl eutectic (LKE) because it is the standard solvent used for pyroprocessing of nuclear waste (there is a wealth of data available for the chemistry of elements in this solvent) and KCl-$MgCl_2$ eutectic (KME) because it has been proposed as a very low-cost solvent for the secondary coolant loop of molten salt reactors. The samples were sintered from Maxthal 312 powder (7.0 g) by SPS. The holding temperature was 1300°C, the dwell time was 10 min, and the ramp rate was 100°C min^{-1}. The uniaxial force was maintained at a constant value of 16 kN. The synthesis and characterisation of these samples is discussed in detail in Appendix D, §15.2.

Oxides were observed as corrosion products in all samples. Possible sources of oxygen include the presence of oxides on the sample surface prior to exposure, insufficient purification of the melt, and insufficient seal during the corrosion test. Unfortunately, this limits the ability to understand how Ti_3SiC_2 reacts with chloride salts, because oxygen is more electronegative than chlorine so would be expected to be the more reactive component [44].

The approximate thicknesses of the reaction layers for all samples are summarised in Table 30. It is clear that minimal reaction occurred in processed salts at 600°C, but the reaction was significant in processed salts at 850°C. Corrosion appears to be more severe in KME than LKE. As-received salts also resulted in significant reaction, although this was mainly due to the samples being in contact with Ni during exposure, resulting in diffusion of Ni into the samples.

The samples exposed to processed LKE appeared to undergo no mass loss. This is consistent with characterisation by other techniques which show very little corrosion. For all other samples, mass gain as opposed to mass loss was observed. This is fairly insignificant for the samples exposed to processed KME at 600°C and processed LKE at 850°C. In the former case, some W was observed on the surface of the sample, and in the latter case some lithium titanium silicates formed. For the samples exposed to as-received KME at 600°C and processed KME at 850°C, significant mass gain was observed. For the samples exposed to as-received KME at 600°C, mass gain was due to the diffusion of Ni into the samples. For the sample exposed to processed KME at 850°C, W deposited on the surface and significant reaction with O and Mg occurred.

The pristine surface perpendicular to the direction of uniaxial pressure during sintering was polished to 1 µm and had a roughness of 0.083 ± 0.002 µm, and the side parallel to the direction of uniaxial

Table 30 – Summary of corrosion results for samples of Maxthal 312.

Experiment	Salt	Temperature / °C	Duration / h	Mass loss / mg cm^{-2}	Reaction Layer Thickness / µm	Roughness / µm	Reaction Products	Type of reactions	Type of corrosion	Main Impurities	Relation to MSR Operation
Static corrosion	LKE, processed	600	125	0.00	Face: 1-2 Side 2-3	0.29 ± 0.02	anatase, rutile, TiC_x	oxidation, TiC_x formation	uniform corrosion	O	Operation in slightly oxidising conditions (e.g. air ingress).
Static corrosion	LKE, processed	850	125	-0.53	Face: 31 Side: 22	5.10 ± 0.88	TiC_x, Li_2SiO_3, $Li_2Ti(SiO_4)O$, Li_2SiO_3, $Li(TiO_2)$, W	oxidation, TiC_x formation, W deposition, Fe diffusion	intergranular and intragranular corrosion	O, W, Fe, Mg	Effect of noble metal fission products with air ingress. Compatibility with steels.
Static corrosion (sample A)	KME, as-received	600	125	-1.00	Face: 10-42 Side: 5-35	Face: 2.10 ± 0.29 Side: 2.58 ± 0.20	$MgTiO_3$, $Mg_2(SiO_4)$, δ-Ni_2Si, Ni	oxidation, reaction with MgO, nickel diffusion	intergranular and intragranular corrosion, spalling	O, Ni	Operation in slightly oxidising conditions (e.g. air ingress). Compatibility with nickel superalloys.
Static corrosion (sample B)	KME, as-received	600	125	-3.02	Face: 95 Side: N/A	N/A	$MgTiO_3$, $Mg_2(SiO_4)$, δ-Ni_2Si, Ni	oxidation, reaction with MgO, nickel diffusion	intergranular and intragranular corrosion, spalling	O, Ni	Operation in slightly oxidising conditions (e.g. air ingress). Compatibility with nickel superalloys.
Static corrosion	KME, processed	600	125	-0.22	Face: 1-5 Side: 2-11	0.26 ± 0.02	TiC_x, anatase, rutile, W	W deposition, oxidation,	uniform corrosion, possibly some intergranular corrosion, deposition	O, W	Effect of noble metal fission products with air ingress.
Static corrosion	KME, processed	850	125	-2.74	Face: 7-47 Side: 7	3.20 ± 1.56	α-W, β-W, MgO, $MgTiO_3$	oxidaiton, reaction with MgO, W deposition, Fe diffusion	intergranular and intragranular corrosion, deposition	O, W, Fe	Effect of noble metal fission products with air ingress. Compatibility with steels.

pressure during sintering was polished to P1200 and had a roughness of 0.25 ± 0.04 μm. In processed LKE and KME at 600°C, the surfaces roughened slightly but not significantly. When the temperature was increased to 850°C the surfaces roughened significantly due to the formation of numerous oxides. The sample exposed to as-received KME, for which the data of sample A is shown, roughened significantly, albeit to a slightly lesser extent than those exposed to processed salts at 850°C. There was little difference between the roughness of the perpendicular and parallel surfaces.

7.1 Corrosion in LiCl-KCl Eutectic

7.1.1 Processed salt, 600°C, 125 h

There was very little corrosion of the sample exposed to processed LKE at 600°C. Titanium oxides were observed by GAXRD, and uniform corrosion to a depth of < 3 µm was observed by SEM. No mass change was observed.

7.1.1.1 Glancing-angle X-ray diffraction

The GAXRD patterns from 0.5-5.0° ω, normalised relative to the peak at 36° 2θ, are shown in Figure 131 [178,179,211–213]. The peak at 36° corresponds to the TiC_x (111) and the rutile (101) peaks. The TiC_x (220) peak shows that the intensity of TiC_x decreases as the glancing angle is decreased, indicating that it is present mainly in the bulk of the material. The TiC_x peaks are less intense than the

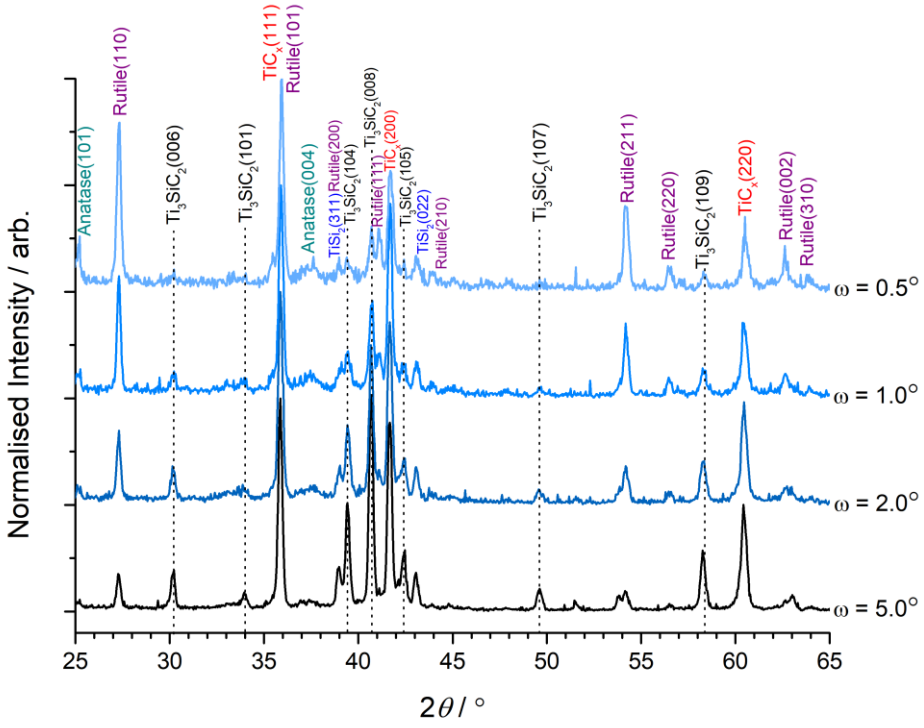

Figure 131 – GAXRD patterns for a sample of Maxthal 312 which was exposed to processed LKE at 600°C for 125 h. The peaks were normalised relative to the peak at ~36°, which corresponds to the TiC_x (111) and rutile (101) peaks.

Ti_3SiC_2 peaks at high glancing angles, but more intense at low glancing angles. This suggests formation of TiC_x by decomposition of Ti_3SiC_2. The increasing intensity of the rutile (110) and anatase (101) peaks as the glancing angle decreases shows that oxidation is occurring at the surface of the sample. However, the presence of rutile at 5.0° ω indicates that oxidation has penetrated relatively deep into the material. It is difficult to tell if there has been a change in the intensity of $TiSi_2$ peaks with glancing angle.

7.1.1.2 Microstructural examination of the cross-section

Figure 132 is a BSE image of the cross-section showing a general overview of the corrosion layer on the surface perpendicular to the direction of pressing during sintering. The surface is relatively rough and there is some alteration to a depth of ~2 µm. The gravimetry results suggest negligible corrosion has occurred, and the morphology shown in the image indicates that minimal uniform corrosion has occurred.

Figure 133 shows the corrosion layer on the side of the sample parallel to the direction of pressing. The depth of alteration is slightly deeper, between 2-3 µm, and the surface is still relatively rough and appears to be uniformly corroded. The greater depth of corrosion is most likely due to the coarser level of micropreparation prior to exposure. However, the grains have some preferred orientation perpendicular to this surface which may have some implication on the corrosion resistance.

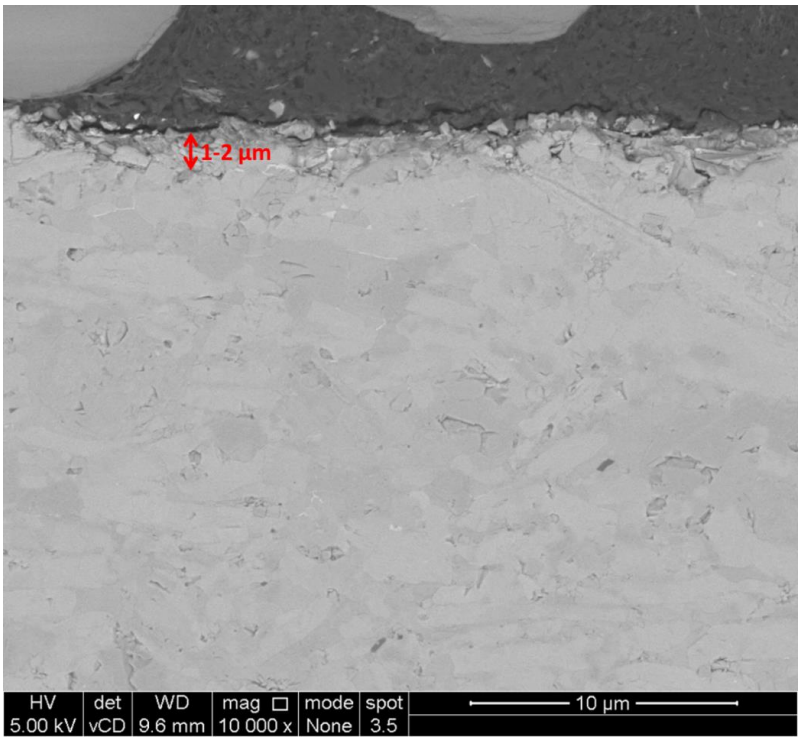

Figure 132 – BSE image showing a general overview of the corrosion layer of a sample of Maxthal 312 which was exposed to processed LKE at 600°C for 125 h.

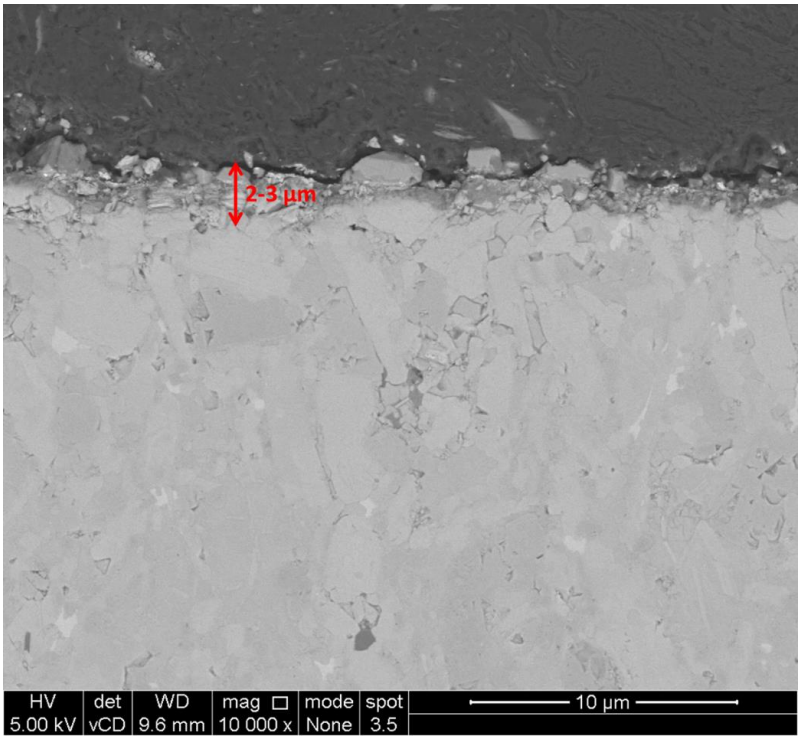

Figure 133 – BSE image showing a general overview of the side of a sample of Maxthal 312 which was parallel to the direction of pressing during SPS, after exposure to processed LKE at 600°C for 125 h.

7.1.2 Processed salt, 850°C, 125 h

In LKE at 850°C, there appears to be a mixture of both intergranular and intragranular corrosion. Close to the original surface, the grain boundaries have been selectively etched and there is partial reaction of Ti_3SiC_2 grains. Further out, there are numerous small particles which have formed by an intragranular corrosion reaction. There are also some larger particles which have elemental compositions consistent with the corrosion products observed by GAXRD, particularly $Li_2Ti(SiO_4)O$, but also Li_2SiO_3 and possibly $Li(TiO_2)$. It appears that Ti_3SiC_2 reacts with Li and O, possibly as Li_2O, to form TiC_x and Li_2SiO_3, which later undergoes further reaction to form $Li_2Ti(SiO_4)O$. Overall, the SEM images and GAXRD patterns show that the corrosion mechanism is particularly complex, and further characterisation with additional techniques is required to fully understand the process.

7.1.2.1 Glancing-angle X-ray diffraction

The GAXRD patterns between the glancing angles, ω, 0.5°-5.0° are shown in Figure 134, normalised relative to the Li_2SiO_3 (020) peak [179,201,214]. At the highest glancing angle used, 5° ω, Li_2SiO_3 was the most intense phase. As the angle decreases, $Li_2Ti(SiO_4)O$ becomes the most intense phase at 1° ω. $Li(TiO_2)$ also fits well; its most intense peak, the (101) peak, overlaps with the $Li_2Ti(SiO_4)O$ (101)

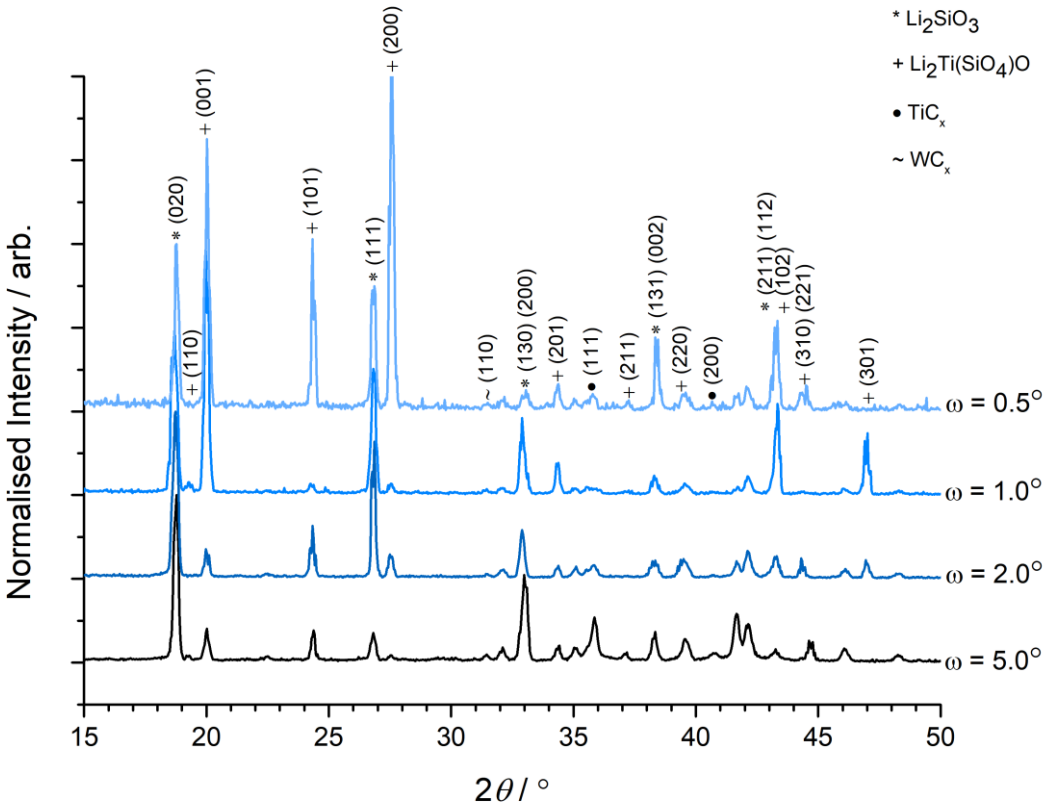

Figure 134 – GAXRD patterns for a sample of Maxthal 312 which was exposed to processed LKE at 850°C for 125 h. The patterns were normalised relative to the Li_2SiO_3 (020) peak. Li_2SiO_3 appears to be the dominant phase at high glancing angles, and $Li_2Ti(SiO_4)O$ appears to be the dominant phase at low glancing angles.

peak. Some peaks of Ti_3SiC_2 may also be present, particularly the (105) peak at ~42.4°, and the (104) peak may overlap with the $Li_2Ti(SiO_4)O$ (220) peak. Like TiC_x, FeO has a space group of Fm-3m so its peaks overlap; however, the SEM images suggest that Fe is associated with Si, indicating that these peaks represent TiC_x. The peaks are broad, which may indicate that the phase has formed by loss of Si from Ti_3SiC_2, forming small crystallites and, if Ti has also been removed, a range of stoichiometries. Fe may be present as a solid solution, substituting Ti or Si in one of the phases. A small quantity of an Im-3m phase was also observed, which corresponds to W, W_xTi_{1-x} or WC_x.

7.1.2.2 Microstructural examination of the cross-section

Figure 135 and Figure 136 show a detailed view of the corrosion layer formed on the surface of the sample which was perpendicular to the uniaxial pressure applied during sintering. The corrosion layer appears to consist primarily of Ti, O and C, with some Mg. The main impurities were Fe and W. Fe appears to have reacted with $TiSi_2$ and the outer surface of the corrosion layer. W appears to have deposited on the surface of the corrosion layer. The morphology at points 8 and 9 appears to show a MAX phase grain which is undergoing decomposition. The elemental compositions indicate loss of Si and possibly Ti, and gain of O. Additionally, the composition of point 10 suggests it is a Ti_3SiC_2 grain,

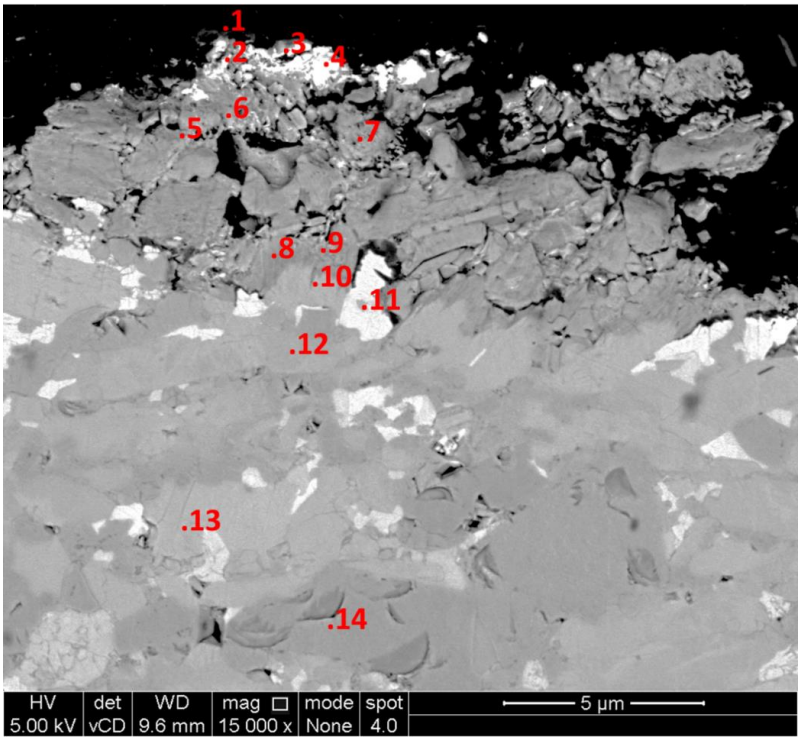

Figure 135 – BSE image showing a detailed view of the corrosion layer formed on a sample of Maxthal 312 which was exposed to processed LKE at 850°C for 125 h. The annotations mark the locations of point analyses, and the elemental compositions of the EDS spectra can be found in Table 31.

along with 12 and 13 in the bulk of the material. Points 5, 6 and 7 may show grains which are at a further stage of decomposition, with greater loss of Ti relative to C, and a larger concentration of O. Point 11 is most likely $TiSi_2$ which has reacted with Fe and O. Point 14 in the bulk clearly shows TiC_x. Overall, it appears that Si has been depleted and the remaining TiC_x has reacted with oxygen to form titanium oxides or oxycarbides.

Figure 137 and Figure 138 show a BSE image and EDS maps of the corner of the sample, where the top surface is the surface perpendicular to the direction of uniaxial pressing during sintering. Points 1, 2 and 6 have similar morphology and contain Ti, O and C, which suggests they are either titanium carbide, titanium oxides, titanium oxycarbide or $Li(TiO_2)$. The particles in this area are relatively small. Point 3 shows titanium carbide. Point 4 contains significant amounts of O, and may be a grain of Ti_3SiC_2 which has lost Si and Ti. Points 5 and 8 have similar contrast, and the ~5 parts O to Ti and Si may indicate that it is $Li_2Ti(SiO_4)O$. Point 7 appears to show WC_x. Point 11 appears to be a grain of $TiSi_2$ which has reacted with Fe at its surface, such as point 10. The morphology at point 12 appears to be a grain of Ti_3SiC_2, but the composition of C is higher than expected and that of Si is lower, which may simply be due to the resolution limit of the EDS system used. The morphology and composition of point 13 is consistent with TiC_x, and suggests that the carbon content in other locations is relatively accurate, albeit slightly high.

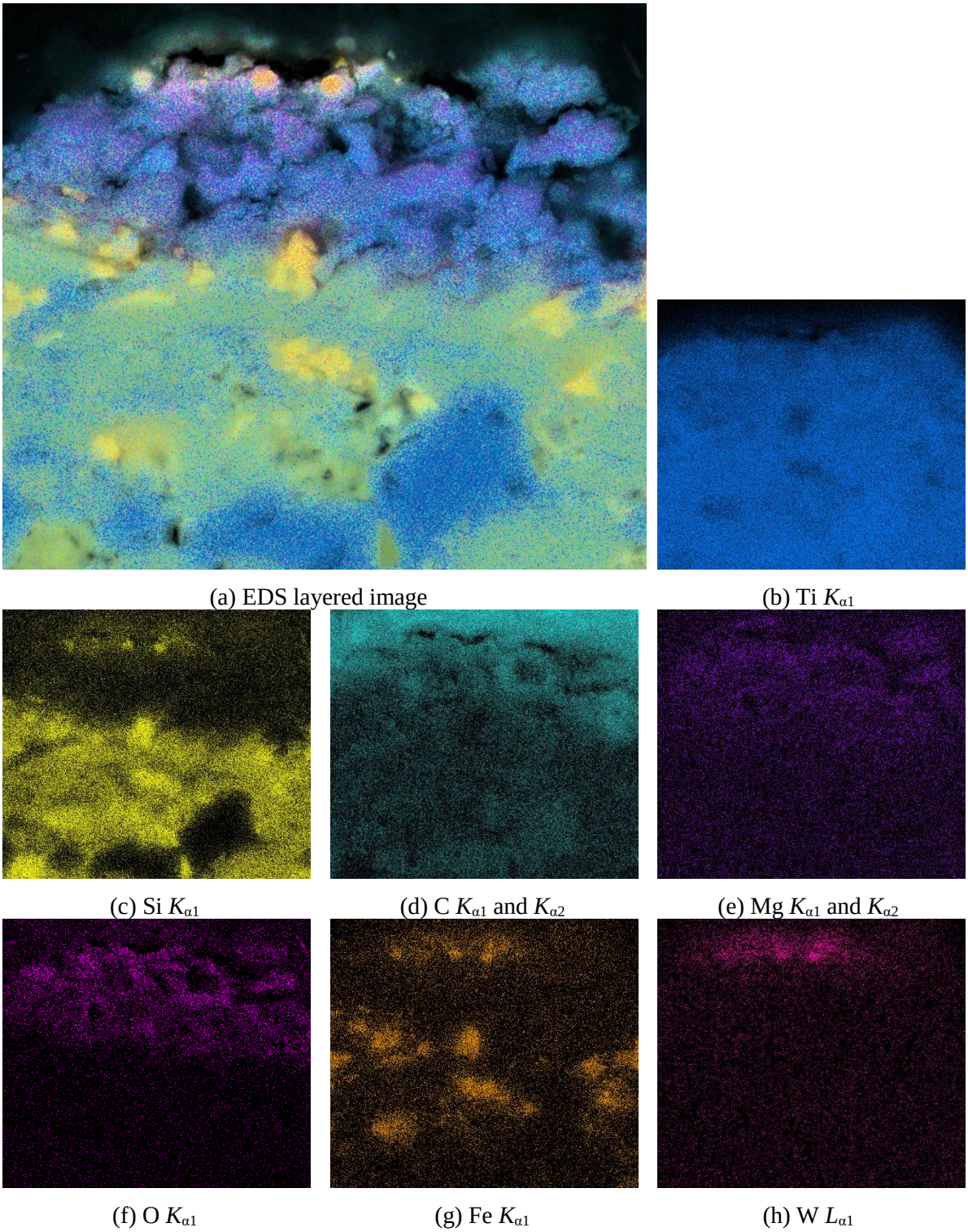

(a) EDS layered image (b) Ti $K_{\alpha1}$

(c) Si $K_{\alpha1}$ (d) C $K_{\alpha1}$ and $K_{\alpha2}$ (e) Mg $K_{\alpha1}$ and $K_{\alpha2}$

(f) O $K_{\alpha1}$ (g) Fe $K_{\alpha1}$ (h) W $L_{\alpha1}$

Figure 136 –EDS maps (image width ~20 µm) showing a detailed view of the corrosion layer formed on a sample of Maxthal 312 which was exposed to processed LKE at 850°C for 125 h. The annotations mark the locations of point analyses, and the elemental compositions of the EDS spectra can be found in Table 31.

Table 31 – The elemental compositions (in at.%) of the EDS spectra shown in Figure 136.

Spectrum	Ti	Si	C	Mg	O	Fe	W	Other	Other Elements
Map	24.2	4.0	58.3	0.2	11.8	0.7	0.2	0.4	Ca, Al, Na, K, Cl, S
1	3.1	0.4	79.9	1.3	9.8	0.7	1.0	3.7	Al, Ca, Sr, Zn, P, Na, S, Cl, K
2	8.8	0.6	66.5	0.5	19.0	1.0	1.5	2.3	Ca, Sr, Al, Na, P, Zn, S, K, Sr
3	4.9	-	71.6	0.3	18.7	1.2	1.8	1.6	Ca, Al, Na, Zn, K
4	1.7	-	73.3	-	15.8	4.0	4.2	0.9	Sr, P, Ca
5	18.4	0.6	52.1	0.6	26.8	0.3	0.3	0.8	Ca, Al, Cl, Na, Sr, K, Zn, P, S
6	16.5	0.8	46.5	0.9	33.2	0.5	0.4	0.9	Ca, Al, Na, Sr, Zn, Cl, K, P, S
7	17.9	0.8	45.3	1.2	33.0	0.4	0.3	0.9	Na, Ca, Zn, Al, Cl, K, S
8	32.2	2.0	37.2	0.7	26.7	0.3	0.1	0.7	K, Cl, Ca, Al, Zn
9	35.1	1.8	39.3	0.4	22.3	0.4	0.1	0.7	Ca, Na, Cl, K, Al
10	41.7	9.9	46.9	-	-	1.0	-	0.3	K, Cl, Ca
11	30.1	25.0	34.2	-	-	20.6	-	0.1	Ca
12	45.6	12.3	41.6	-	-	0.3	-	0.1	Ca
13	34.3	17.5	42.6	-	-	5.3	-	0.3	Cu, Ni
14	48.1	1.0	50.9	-	-	-	-	-	-

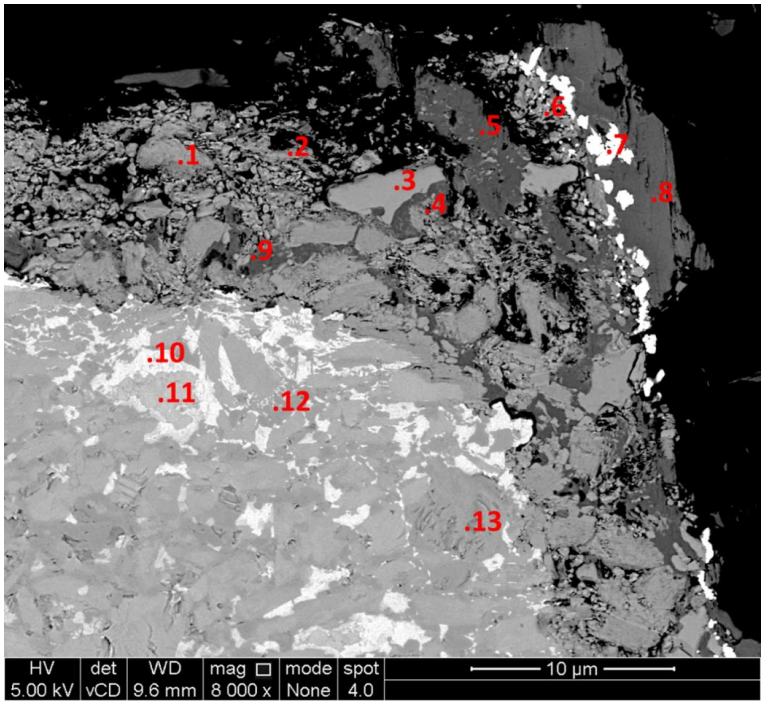

Figure 137 – BSE image of the corner of a sample of Maxthal 312 which was exposed to processed LKE at 850°C for 125 h. The top surface is the direction perpendicular to the uniaxial pressure applied during sintering. The elemental compositions of the EDS spectra are shown in Table 32.

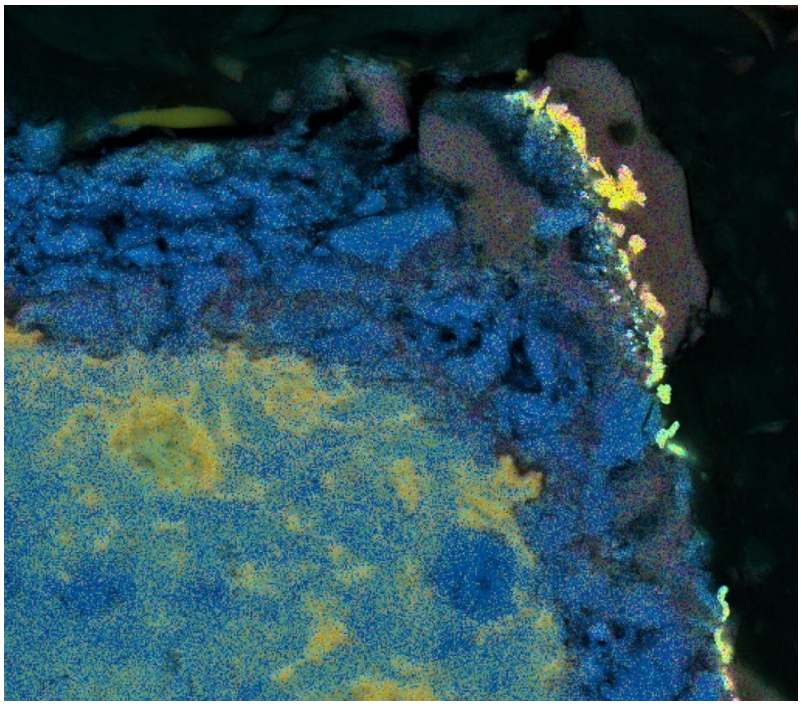

(a) EDS layered image

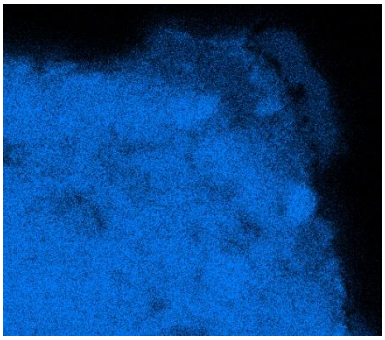

(b) Ti

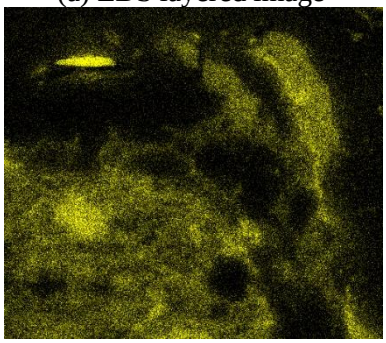

(c) Si

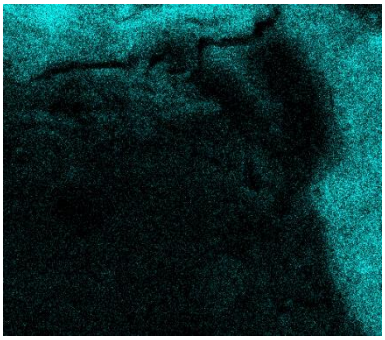

(d) C

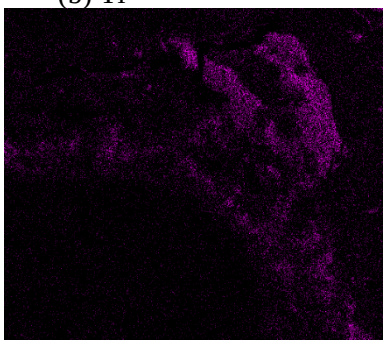

(e) O

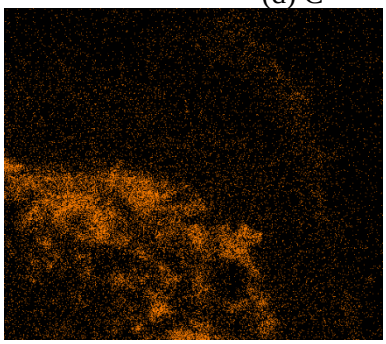

(f) Fe

Figure 138 – EDS maps of the corner of a sample of Maxthal 312 which was exposed to processed LKE at 850°C for 125 h. The top surface is the direction perpendicular to the uniaxial pressure applied during sintering. The elemental composition of the EDS map sum spectra is shown in Table 32.

Table 32 – Elemental compositions (in at.%) of the EDS spectra relevant to Figure 138.

Spectrum	Ti	Si	C	Mg	O	Fe	W	Other	Other Elements
Map	16.3	3.6	63.3	0.1	15.4	0.7	0.2	0.4	Al, Ca, Zn, K, Cl
1	30.5	0.3	47.3	0.6	19.9	0.4	-	0.9	Cl, Ca, K, Na, Zn
2	20.8	0.2	63.4	0.1	14.8	0.1	-	0.5	Ca, Zn
3	44.7	0.6	54.6	-	-	-	-	0.1	Ca
4	26.5	5.4	33.4	0.1	34.0	0.1	-	0.5	Ca, Zn, Cl, K
5	11.6	7.9	29.2	-	51.3	-	-	0.2	Cl, Ca, K
6	25.2	1.3	52.6	0.5	18.1	0.2	1.4	0.5	Ca, Al, Cl, K
7	3.8	2.0	54.3	-	17.3	0.7	21.6	0.4	Ca
8	9.2	9.7	26.7	-	54.3	-	0.1	0.1	Ca
9	24.7	6.8	20.0	-	48.0	0.1	-	0.3	Cl, Ca, K
10	26.1	29.4	29.0	-	-	15.2	-	0.3	Cu, Ca
11	40.9	34.4	21.9	-	-	2.8	-	-	-
12	46.5	7.9	43.6	-	-	-	2.0	-	-
13	48.6	0.2	51.0	-	-	0.1	-	-	-

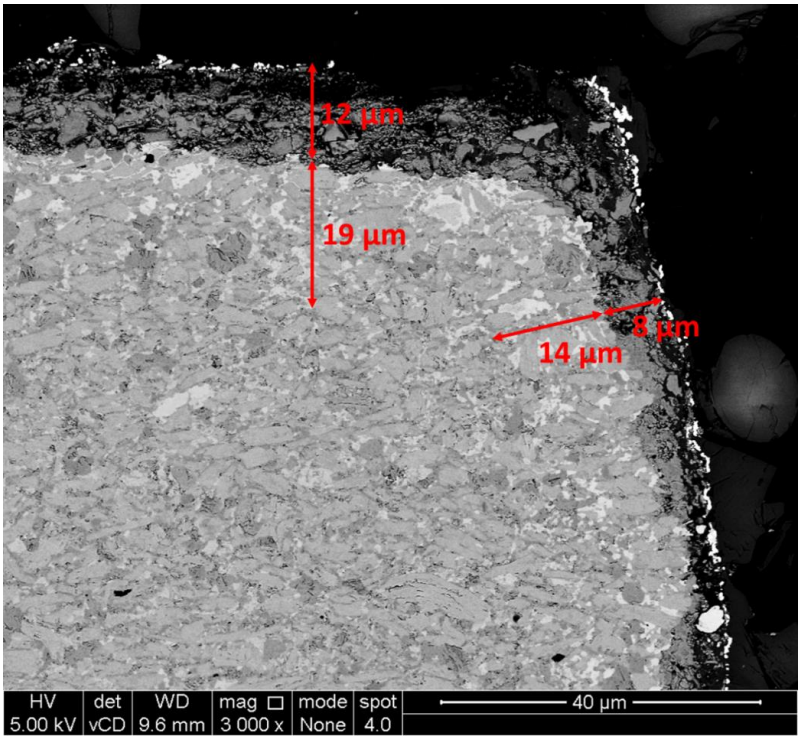

Figure 139 – BSE image of the corner of a cross-section of a sample of Maxthal 312 which was exposed to processed LKE at 850°C for 125 h. The annotations show the approximate depths of the corrosion layer and Fe diffusion layer on the two sides.

Figure 139 is a lower magnification image of the corner shown in Figure 138. The depth of corrosion of the surface perpendicular to the uniaxial pressure applied during sintering has a thicker corrosion layer than the surface which was parallel. The depth of the former was ~12 µm, whilst that of the latter was ~8µm. Furthermore, there appears to be further alteration due to the diffusion of Fe into the material, as noted by the increased concentration of the bright contrast phase near the surface. For the perpendicular surface, this extends to ~19 µm, and for the parallel surface this extends to ~14 µm. However, it is worth noting that these depths are very approximate as the depth is difficult to distinguish; a superior method would be to look at the depth of Fe penetration in the EDS maps.

7.2 Corrosion in KCl-$MgCl_2$ Eutectic

7.2.1 As-received salt, 600°C, 125 h, sample A

Two samples were exposed to as-received KME at 600°C for 125 h. The results for the second sample can be found in Appendix H. The reactions observed were the same for both samples, although the extent of corrosion was greater for the second sample. Oxidation occurred at the surface with incorporation of Mg from KME to form magnesium titanate and magnesium silicate. Additionally, nickel diffused into the samples from the nickel wire used to suspend them in the salt.

7.2.1.1 Glancing Angle X-ray Diffraction

The GAXRD patterns between 0.5-10.0° ω are shown in Figure 140. The peaks were normalised relative to the peak at ~41°, although this peak represents Ti_3SiC_2 at high glancing angles and $MgTiO_3$ at low glancing angles. There is an unidentified peak at 28.0°. Overall, it appears that Ti_3SiC_2 and TiC_x decrease in concentration towards the surface of the sample, whilst $MgTiO_3$, $Mg_2(SiO_4)$, δ-Ni_2Si and Ni increase in concentration. Both Mg and O play a key role in the corrosion mechanism, as evidenced by the formation of $MgTiO_3$ and $Mg_2(SiO_4)$. The presence of δ-Ni_2Si confirms that Ni interacts preferentially with Si, seemingly replacing Ti in $TiSi_2$. However, the Ni containing phase may represent an alloy such as Ni_xTi_{1-x}. Note that $TiSi_2$ is not shown in the GAXRD patterns because it overlaps with a number of peaks from other phases, so its exact presence is difficult to distinguish without pattern fitting.

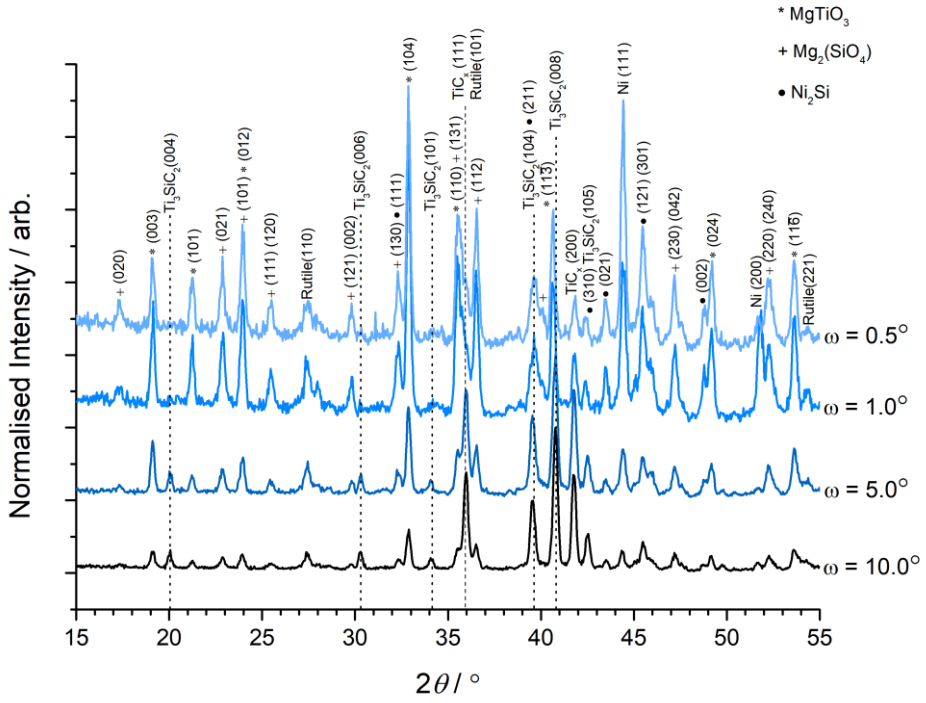

Figure 140 – GAXRD patterns for a sample of Maxthal 312 which was exposed to as-received KME at 600°C for 125 h. The patterns were normalised relative to the peak at ~41°, although this peak represents Ti_3SiC_2 at high glancing angles and $MgTiO_3$ at low glancing angles.

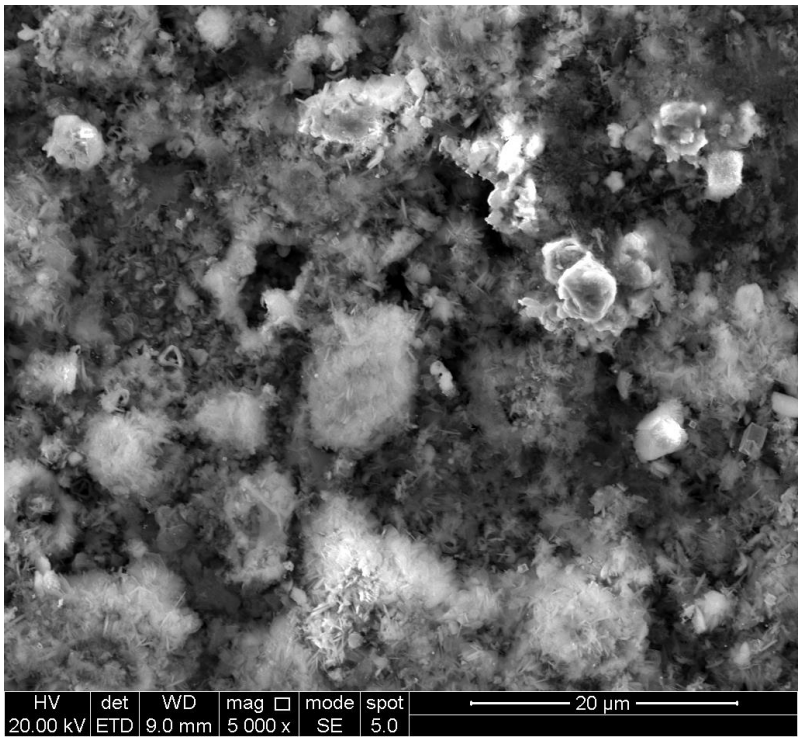

(a) BSE image

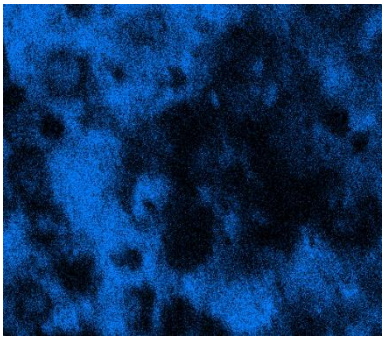

(b) Ti $K_{\alpha1}$

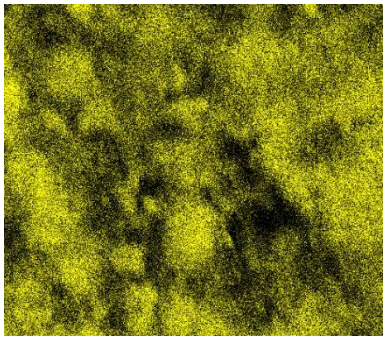

(c) Si $K_{\alpha1}$

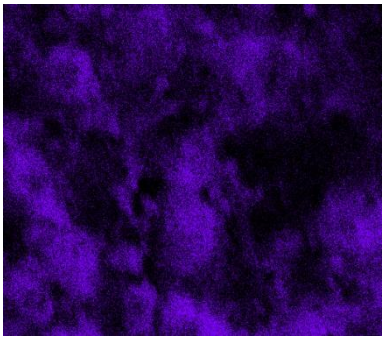

(d) Mg $K_{\alpha1}$ and $K_{\alpha2}$

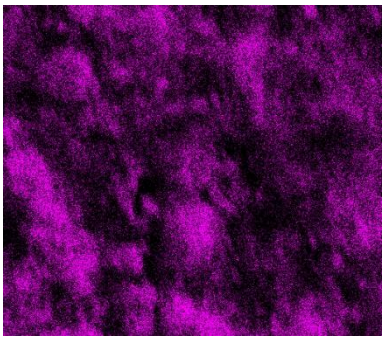

(e) O $K_{\alpha1}$

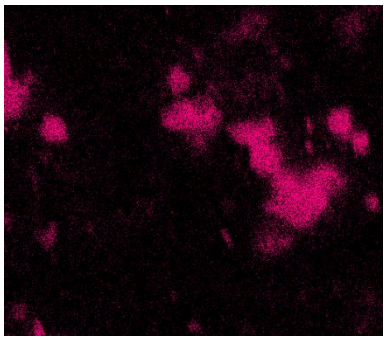

(f) Ni $K_{\alpha1}$

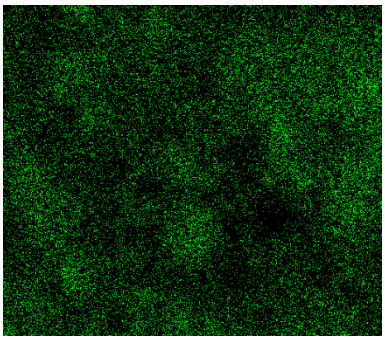

(g) Cl $K_{\alpha1}$

Figure 141 – BSE image and EDS maps for Maxthal 312 after exposure to as-received LKE at 600°C for 125 h.

7.2.1.2 Microstructural Examination of the Surface

Figure 141 is a BSE image and EDS maps of Maxthal 312 prior to cleaning with distilled water in an ultrasonic bath. Si appears to be present in all phases. One phase appears to contain mainly Ti and Si. A second phase contains Si, Mg and O, and is most likely $Mg_2(SiO_4)$. A third phase contains Si and Ni, and is most likely Ni_2Si. C, Fe and K were also detected in minor quantities.

7.2.1.3 Microstructural examination of the cross-section

Figure 142 is a BSE image of the alteration layer showing the morphology of the various phases. EDS maps taken at the same location follow.

Figure 143 shows the EDS maps taken at the same location as Figure 142. The layered image highlights the phases present in the material: the light blue phase is Ti_3SiC_2, the dark blue phase is TiC_x, the yellow phase is $TiSi_2$ and the pink regions show the location of Ni, as Ni_2Si, although some Ti is also present. Mg was detected in the surface deposition layer in association with Si, O and some Ti, indicative of $MgTiO_3$ and $Mg_2(SiO4)$. A small amount (0.2at.%) of Fe was also observed. Figure 145 is a BSE image showing the presence of Ni at the surfaces of the $TiSi_2$ grains. The surface is particularly rough, and it appears that the deposition layer has broken off. Points 3 and 8 show the composition of seemingly fully reacted $TiSi_2$ grains. The amount of Ni is approximately equal to the amount of Si, with

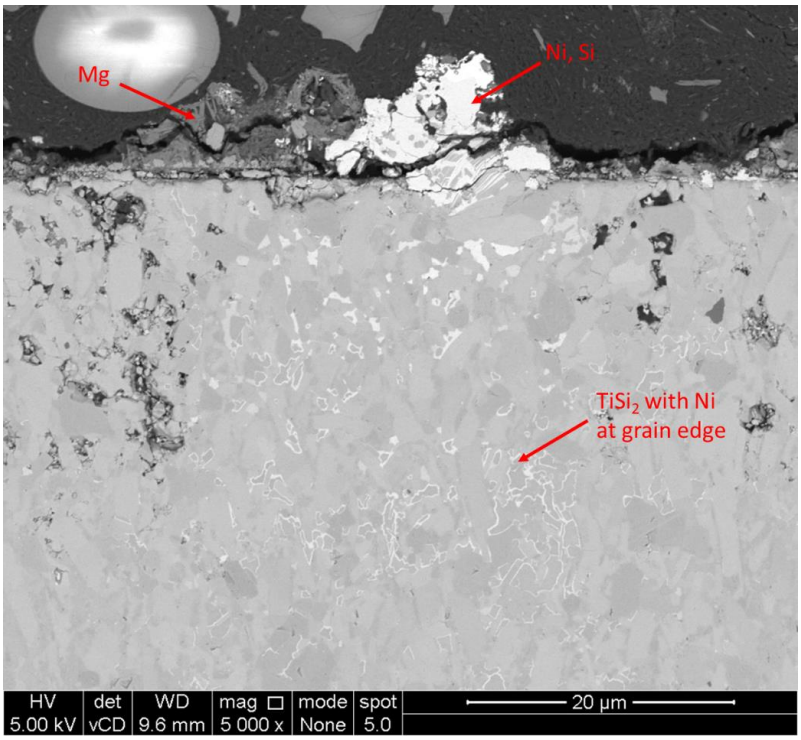

Figure 142 – BSE image showing the cross-section of a sample of Maxthal 312 which was exposed to as-received KME at 600°C for 125 h.

approximately a quarter to a third of the amount of Ti, which is consistent with a mixture of Ni_2Si and $TiSi_2$. The presence of Ni in the bulk of the material with initial reaction at the surface of $TiSi_2$

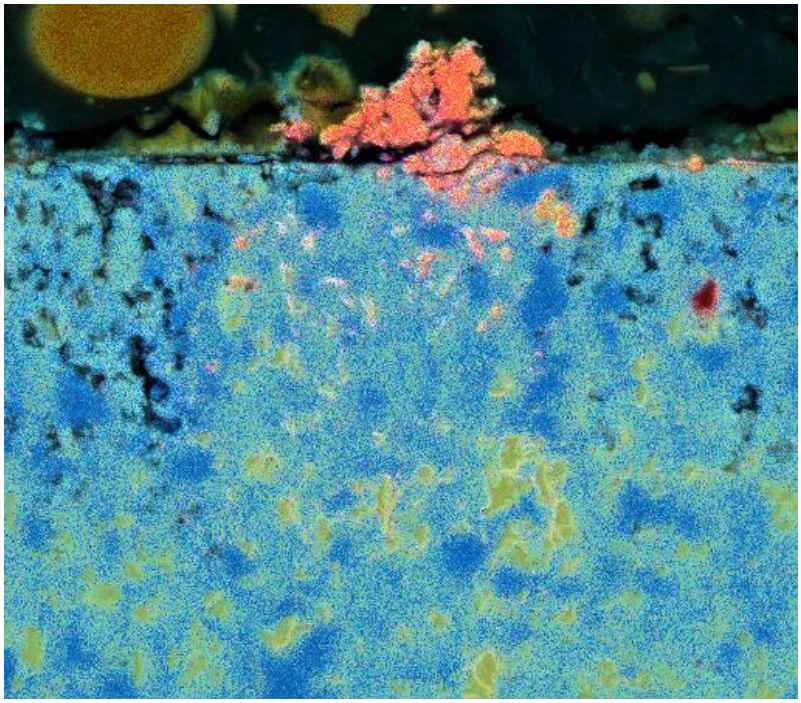

(a) Layered EDS map

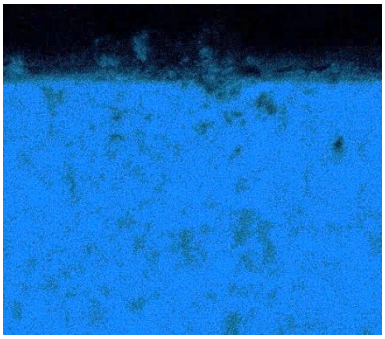

(b) Ti $K_{\alpha1}$ (49.3at.%)

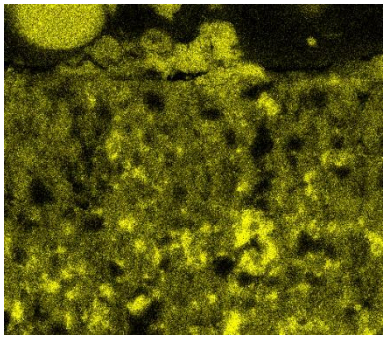

(c) Si $K_{\alpha1}$ (17.3at.%)

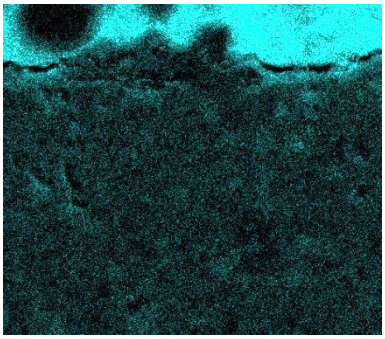

(d) C $K_{\alpha1}$ and $K_{\alpha1}$ (N/A)

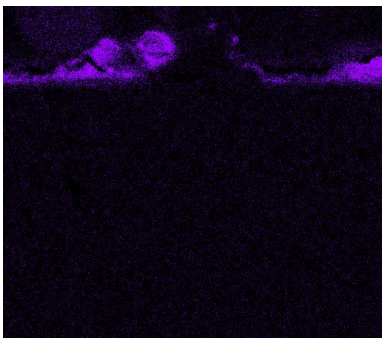

(e) Mg $K_{\alpha1}$ and $K_{\alpha2}$ (1.4at.%)

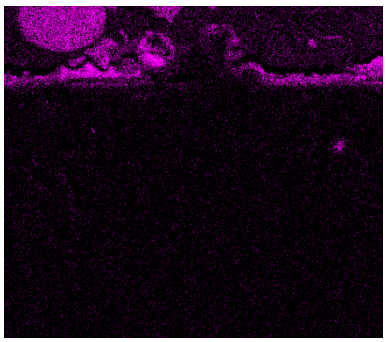

(f) O $K_{\alpha1}$ (28.3at.%)

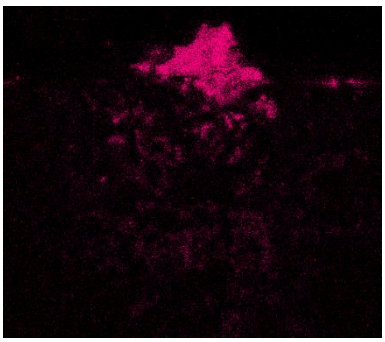

(g) Ni $K_{\alpha1}$ (2.3at.%)

Figure 143 – EDS maps (image width ~60 µm) taken at the same location as Figure 142.

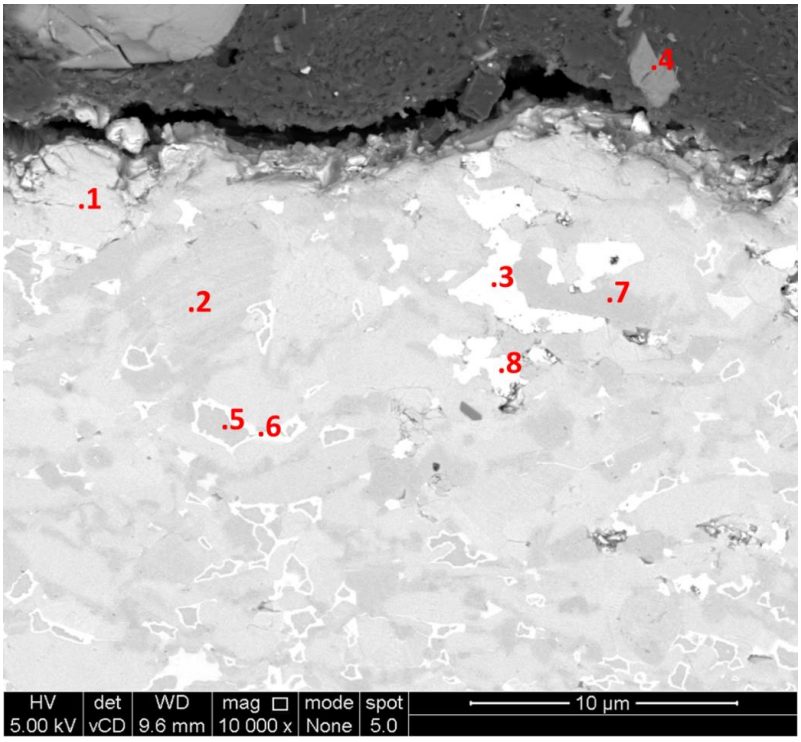

Figure 144 – BSE image showing the presence of Ni around the $TiSi_2$ grains in a sample of Maxthal 312 which was exposed to as-received KME at 600°C for 125 h. The elemental compositions of the EDS spectra are shown in Table 33.

grains indicates that it diffuses through the material intergranularly, suggesting Ti_3SiC_2 is likely to be incompatible for use in combination with Ni-based alloys. Points 5 and 6 show that the original grains consist primarily of Ti and Si. Point 1 appears to show Ti_3SiC_2 as the ratio of Ti/Si is ~3. Points 2 and 7 appear to show TiC_x as the Ti content is high, with a minimal amount of Si.

Table 33 – Elemental compositions (in at.%, excluding C) of the EDS spectra associated with Figure 145.

Spectrum	Ti	Si	Ni	Fe	O	Other	Other Elements
Map	70.8	22.7	4.8	0.2	-	1.6	Al, Ca, K, Cl
1	74.9	24.4	0.4	-	-	0.4	Ca, K
2	87.9	11.8	0.2	-	-	0.2	Ca
3	15.6	42.0	41.6	0.3	-	0.5	Cl, K
4	6.2	13.5	0.6	0.2	65.9	13.7	Al
5	45.5	51.2	3.2	-	-	0.1	Ca
6	60.2	32.7	7.2	-	-	-	-
7	95.7	3.1	1.2	-	-	-	-
8	11.9	45.9	41.1	0.5	-	0.7	Yb, Cl, Ca

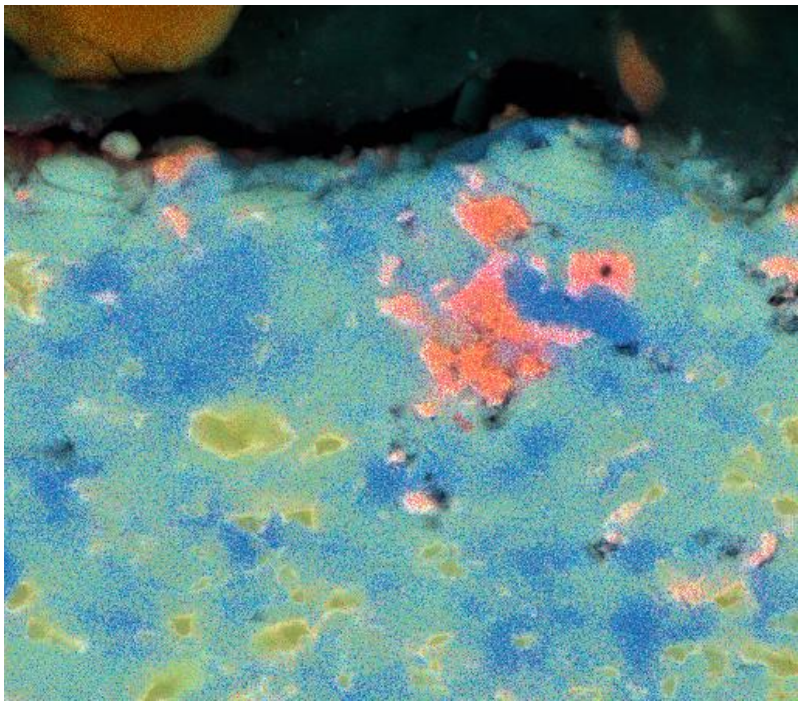

(a) layered EDS map

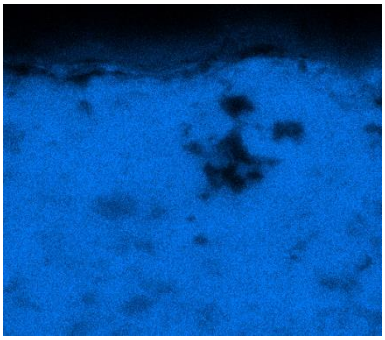

(b) Ti $K_{\alpha 1}$

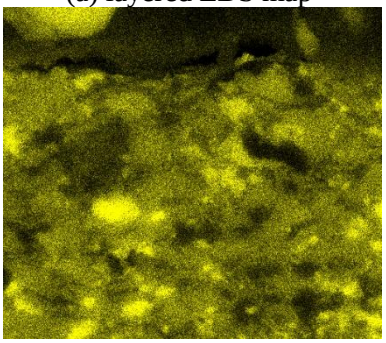

(c) Si $K_{\alpha 1}$

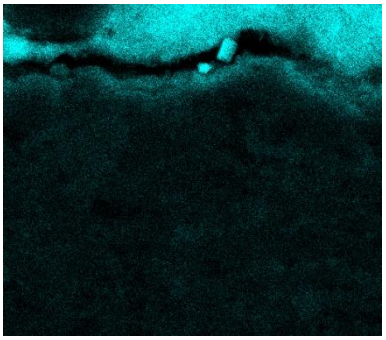

(d) C $K_{\alpha 1}$ and $K_{\alpha 2}$

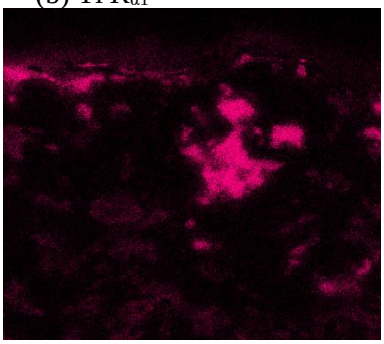

(e) Ni $K_{\alpha 1}$

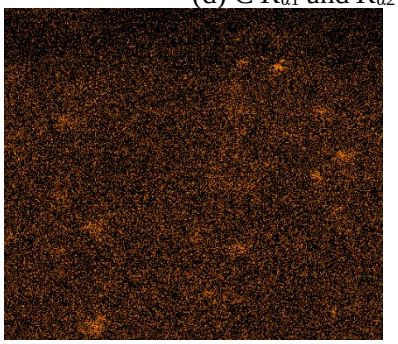

(f) Fe $K_{\alpha 1}$

Figure 145 – EDS maps (image width ~30 µm) showing the presence of Ni around the $TiSi_2$ grains in a sample of Maxthal 312 which was exposed to as-received KME at 600°C for 125 h. The elemental compositions of the EDS spectra are shown in Table 33.

Figure 146 and Figure 147 is a BSE image and EDS maps of the surface of the sample parallel to the direction of pressing. The deposition layer was ~5 µm thick and the alteration layer was ~30 µm thick. Point spectra of the deposition layer indicated the presence of Ti, Si, Mg and O. The morphology suggests that numerous phases are present, which is consistent with the observation of $MgTiO_3$ and $Mg_2(SiO_4)$ by GAXRD.

Figure 148 is a higher magnification BSE image of the deposition layer shown in Figure 147. Numerous phases are clearly visible. The primary phase has elongated grains. Underneath the deposition layer there appear to be some small grains with morphology similar to TiC_x, which may be due to loss of Si from a grain of MAX phase. A gap is clearly visible between the deposition layer and the Bakelite, which may indicate the presence of a soft or water-soluble outer layer which was removed during sample preparation.

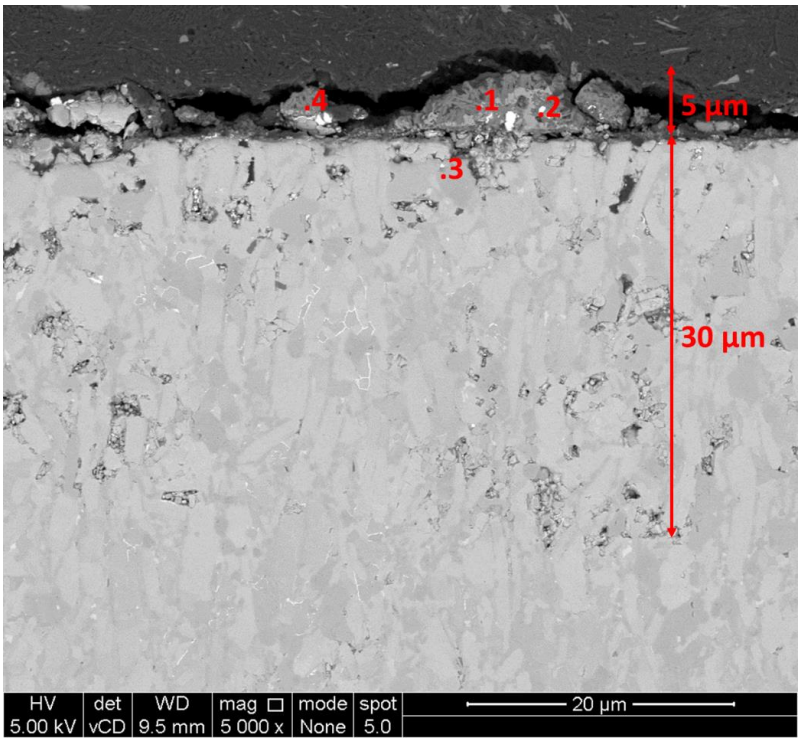

Figure 146 – BSE image of the cross-section of a sample of Maxthal 312 which was exposed to as-received KME at 600°C for 125 h. The elemental compositions of the EDS spectra are shown in Table 34. The surface shown is the side which was parallel to the direction of uniaxial pressure applied during sintering.

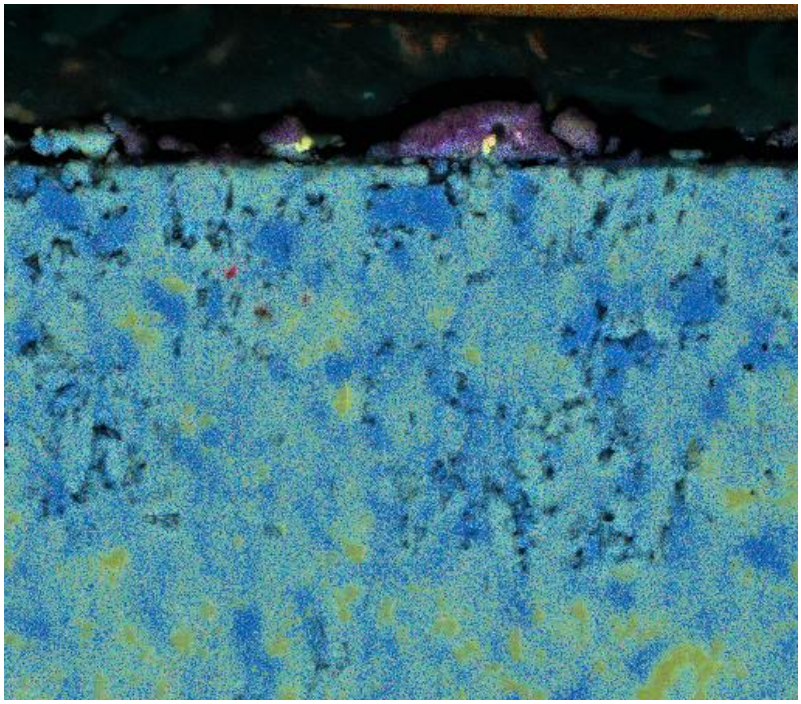

(a) layered EDS map

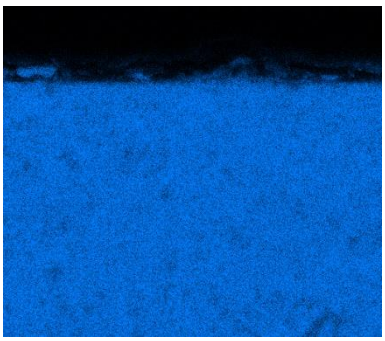

(b) Ti $K_{\alpha1}$

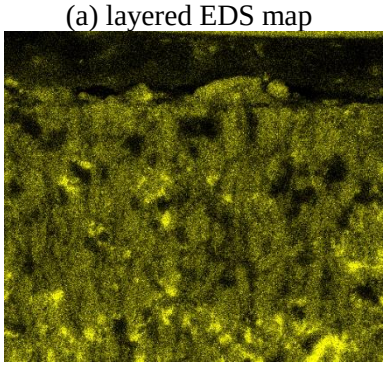

(c) Si $K_{\alpha1}$

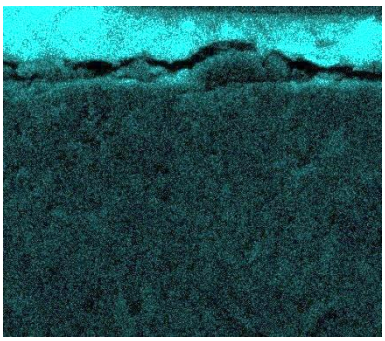

(d) C $K_{\alpha1}$ and $K_{\alpha2}$

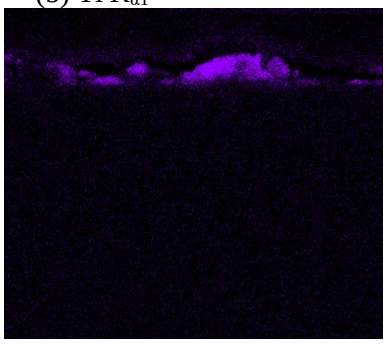

(e) Mg $K_{\alpha1}$ and $K_{\alpha2}$

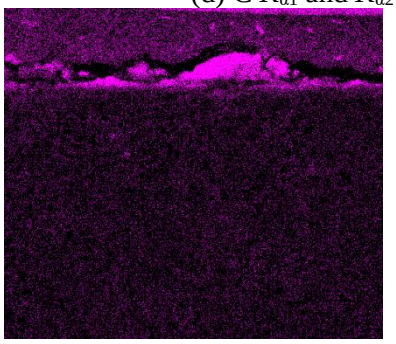

(f) O $K_{\alpha1}$

Figure 147 – EDS maps (image width ~60 µm) of the cross-section of a sample of Maxthal 312 which was exposed to as-received KME at 600°C for 125 h. The elemental composition of the EDS map sum spectrum is shown in Table 34. The surface shown is the side which was parallel to the direction of uniaxial pressure applied during sintering.

Table 34 – Elemental compositions (in at.%, excluding C) for the EDS spectra associated with Figure 146 and Figure 147.

Spectrum	Ti	Si	Mg	O	Ni	Other	Other Elements
Map	55.6	15.0	1.2	27.0	0.3	1.0	Al, Ca, Re, K, Cl
1	7.2	10.3	18.6	62.8	0.2	0.8	Cl, K, Ca, Zn, Fe, Mo
2	13.4	11.6	16.1	57.8	0.3	0.9	Cl, K, Ca, Zn
3	98.9	0.9	-	-	-	0.2	Ca
4	14.8	13.9	12.5	53.8	3.7	1.2	Cl, Fe, Al, K, Ca, Zn

Due to the gaps observed between the conductive Bakelite and the sample, a cross-section of the sample was cut and examined without mounting. The images show that the surface is relatively rough and suggest that in the previous images material from the corrosion layer has most likely been removed during polishing. Figure 149 shows that the straight edge of the underlying material has been maintained, but there is a significant amount of corrosion product on the surface of the sample. Globules which look like deposited metal were also observed on the surface, as shown in Figure 150.

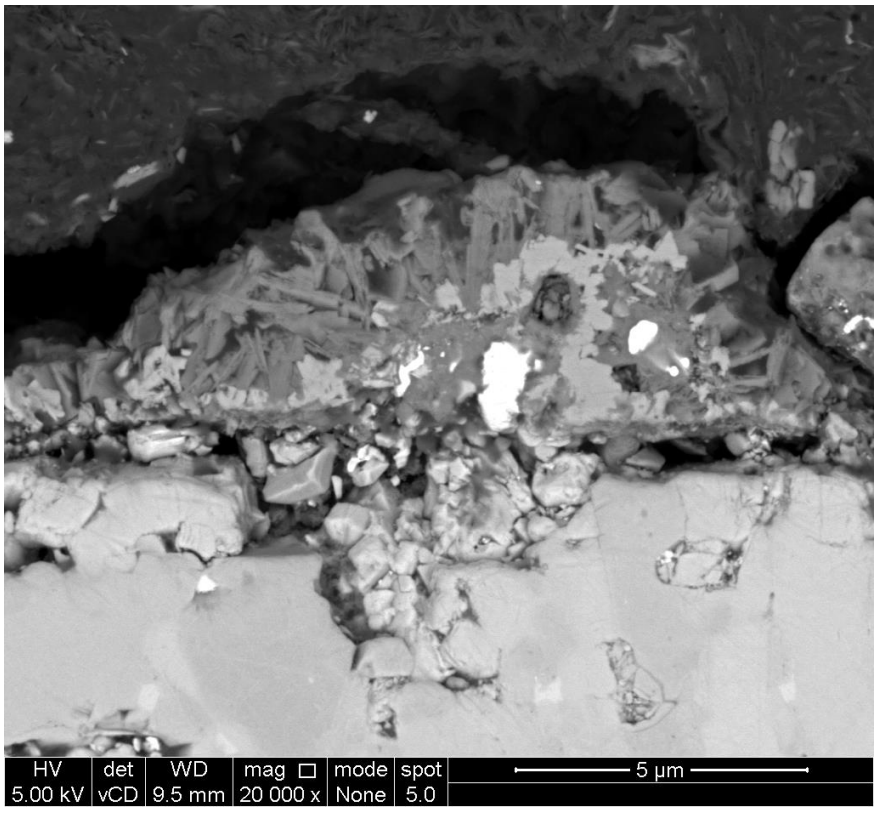

Figure 148 – BSE image of the cross-section of the deposition layer on the side of a sample of Maxthal 312 which was exposed to as-received KME at 600°C for 125 h.

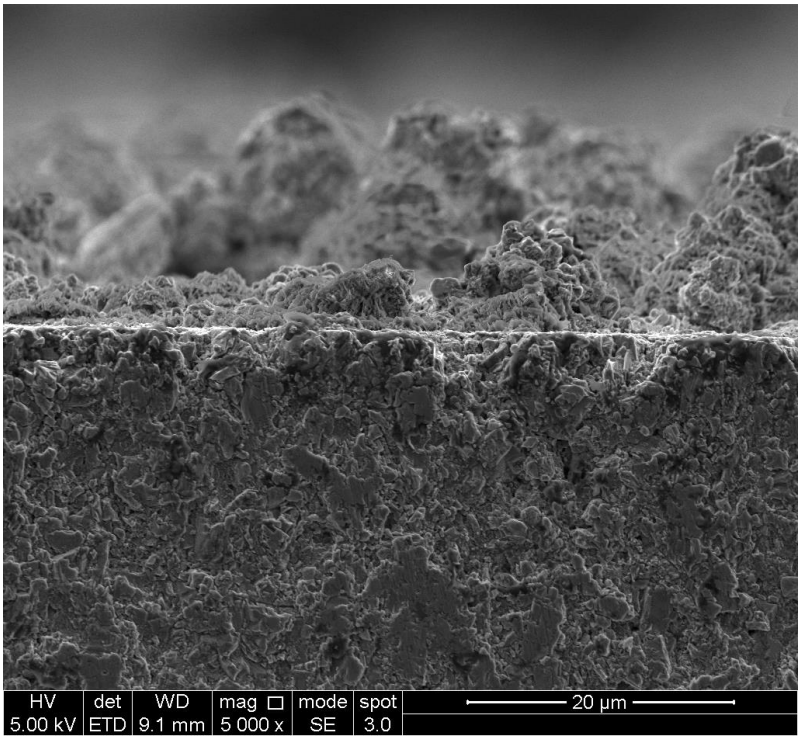

Figure 149 – SE image of a cross-section of an unmounted sample of Maxthal 312 which was exposed to as-received KME at 600°C for 125 h.

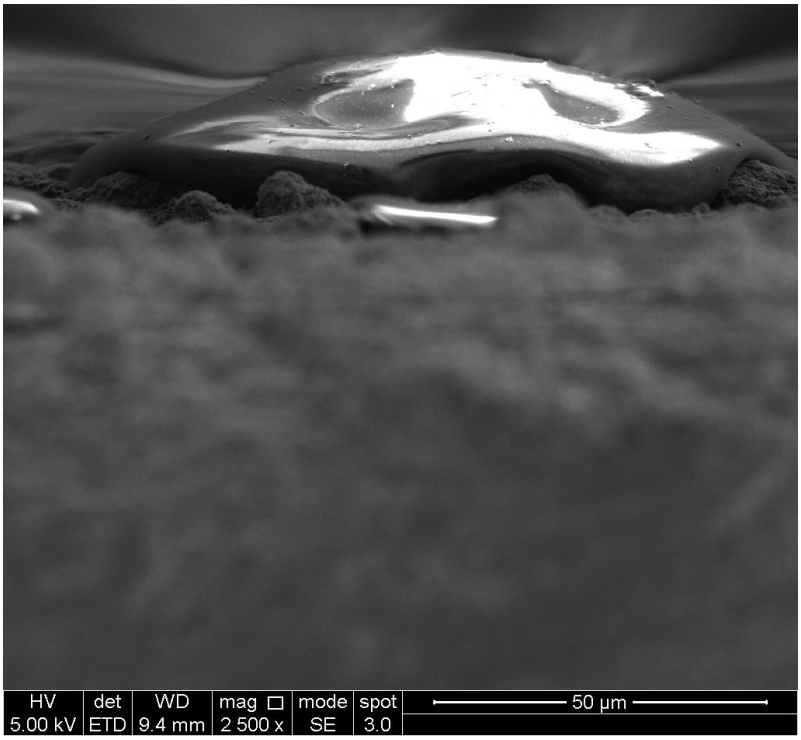

Figure 150 – Globules were observed on the surface of a sample of Maxthal 312 which was exposed to as-received KME at 600°C for 125 h.

7.2.2 Processed salt, 600°C, 125 h

The results for the sample exposed to processed KME at 600°C were similar to those of the sample exposed to LKE at 600°C, although tungsten was observed by both SEM and GAXRD and there was a small amount of mass gain. It appears that tungsten deposited as a thin layer on the original surface, on top of which an oxide layer formed. In general, the corrosion layer was uniform in thickness and relatively thin, but there were locations where alteration appears to have extended below the thin layer of tungsten, which may indicate there is an aspect of intergranular corrosion. This could be interdiffusion of Ti and W along the grain boundaries, although it is difficult to tell without any EDS data.

7.2.2.1 Glancing-angle X-ray diffraction

The GAXRD patterns measured between 0.5-5.0° ω are shown in Figure 151, normalised relative to the Ti_3SiC_2 (104) peak. The other Ti_3SiC_2 peaks appear to decrease in intensity towards the surface, which may indicate that the (104) peak overlaps with another phase. The TiC_x and $TiSi_2$ peaks also reduce in intensity towards the surface. Conversely, the presence of oxides, particularly rutile but also

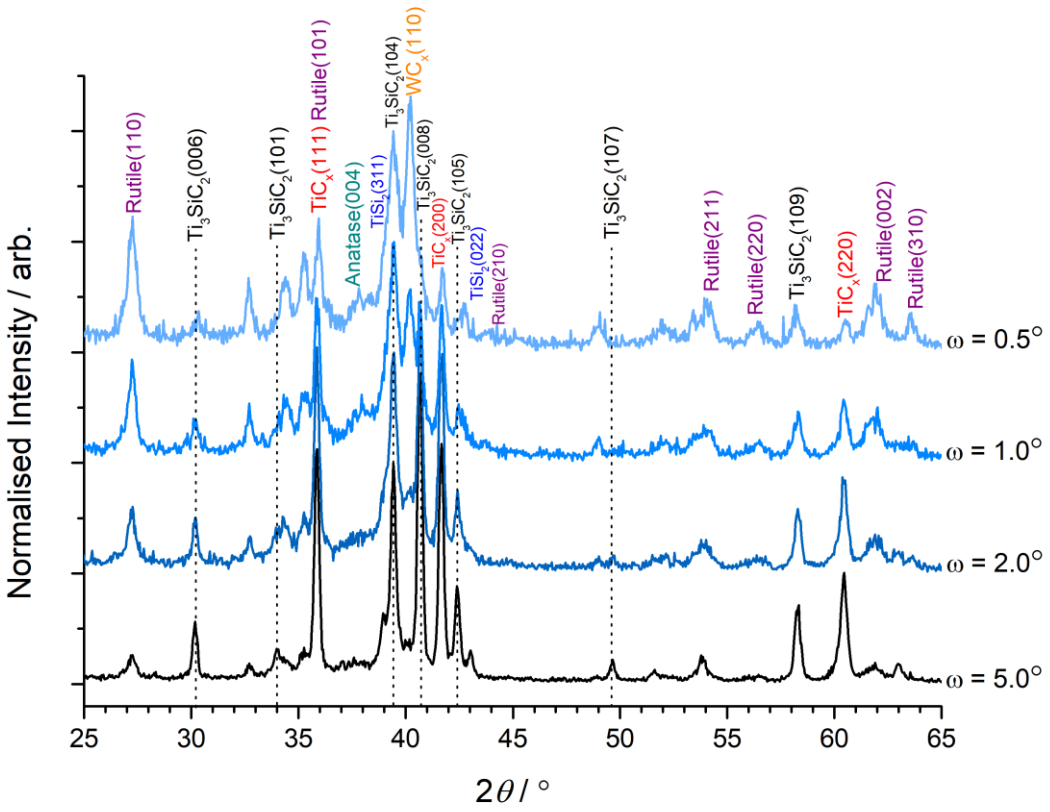

Figure 151 – GAXRD patterns for a sample of Maxthal 312 which was exposed to processed KME at 600°C for 125 h. Oxidation has occurred, indicated by the presence of titanium oxides, and a W-based alloy (W, WC_x, or W_xTi_{1-x}) has deposited on the surface. Unidentified peaks can be seen at 32.7°, 34.4°, 35.2°, 49.0° and ~62°.

some anatase, increases at the surface, but can be seen at all glancing angles. A W-based phase, which may be W, WC_x or an alloy such as W_xTi_{1-x}, can be seen to form towards the surface. It is the most intense phase at the surface of the material, as indicated by its (110) peak. A number of unidentified peaks were observed, increasing in intensity towards the surface of the sample, at 32.7°, 34.4°, 35.2°, 49.0° and ~62° (overlaps with rutile).

7.2.2.2 Microstructural Examination of Cross-Section

Figure 152 is a BSE image showing the morphology of the cross-section. The surface is particularly rough, and grains appears to be breaking away. This alteration layer appears to be between 1-5 µm thick. The bright spots likely indicate the presence of W, which appears to have penetrated below the surface of the material.

Figure 153 shows a BSE image of the surface of the sample which was parallel to the direction of pressing. The grains were partially ordered perpendicular to the surface. The surface received a coarser polish than the surface which was perpendicular to the direction of pressing. The surface is relatively rough, and a layer of W has deposited, < 3 µm thick. The reaction appears to have extended into the bulk of the material in some locations up to a depth of ~11 µm.

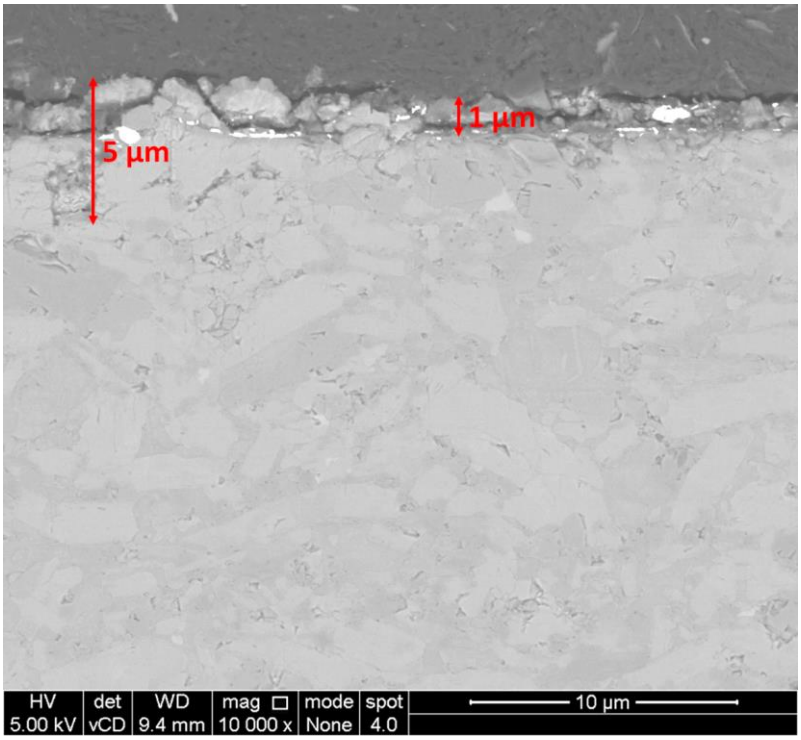

Figure 152 – BSE image showing the morphology of the cross-section of a sample of Maxthal 312 which was exposed to processed KME at 600°C for 125 h.

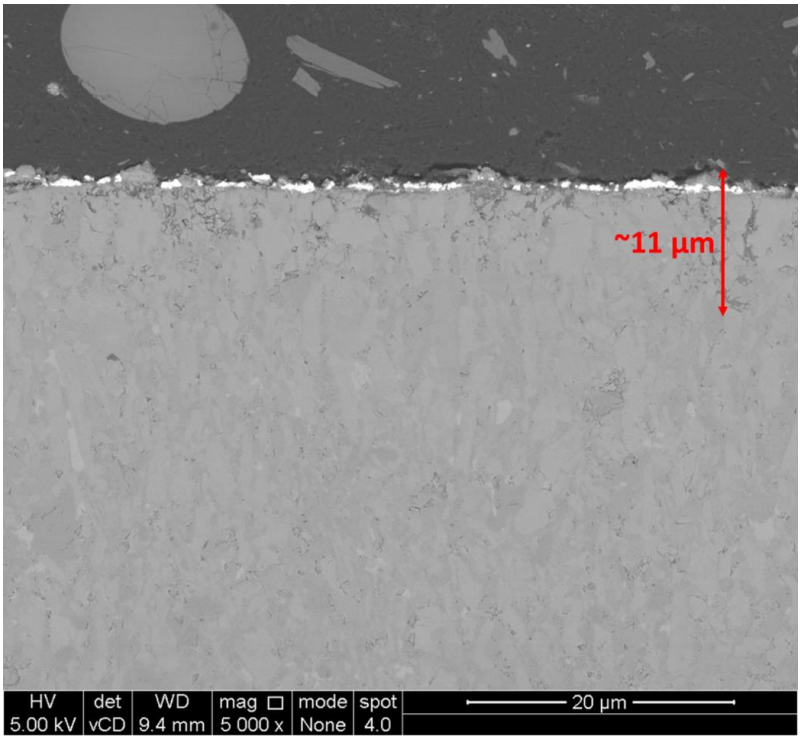

Figure 153 – BSE image showing the cross-section of a sample of Maxthal 312 which was exposed to processed KME at 600°C for 125 h. The grains are slightly ordered perpendicular to the surface.

7.2.3 Processed salt, 850°C, 125 h

In KME at 850°C there appears to be intergranular corrosion at the surface of the sample, and a corrosion layer has deposited on the surface. Many of the phases observed by GAXRD had multiple matches due to the possibility of solid solutions. A phase containing Mg, Si and O was observed by SEM, but no phases with this composition were observed by GAXRD. Overall, numerous oxides have formed and there has been significant reaction with Mg. W and Fe were also observed as impurities.

7.2.3.1 Glancing-Angle X-ray Diffraction

The GAXRD patterns, normalised relative to the (110) peak of the Im-3m phase, are shown in Figure 154. The Im-3m phase appears to be a tungsten-based solid solution such as W, W_xTi_{1-x} or WC_x [201]. The R-3 phase is $MgTiO_3$, but may also be a solid solution with Ti at the Mg sites or Fe at the Ti sites [215]. The Fm-3m phase is MgO, although solid solutions with Ti at the Mg sites are also possible [195]. Furthermore, peaks for an Fe-Ti phase with space group Pm-3m overlap many of the peaks for the Fm-3m phase. There appears to also be a P-3m1 phase which represents W_2C [197]. TiC_x fits the peaks at ~36° (110) and ~42° (200), but the (220) peak should be present at about half the intensity of these peaks at ~60.5° [179].

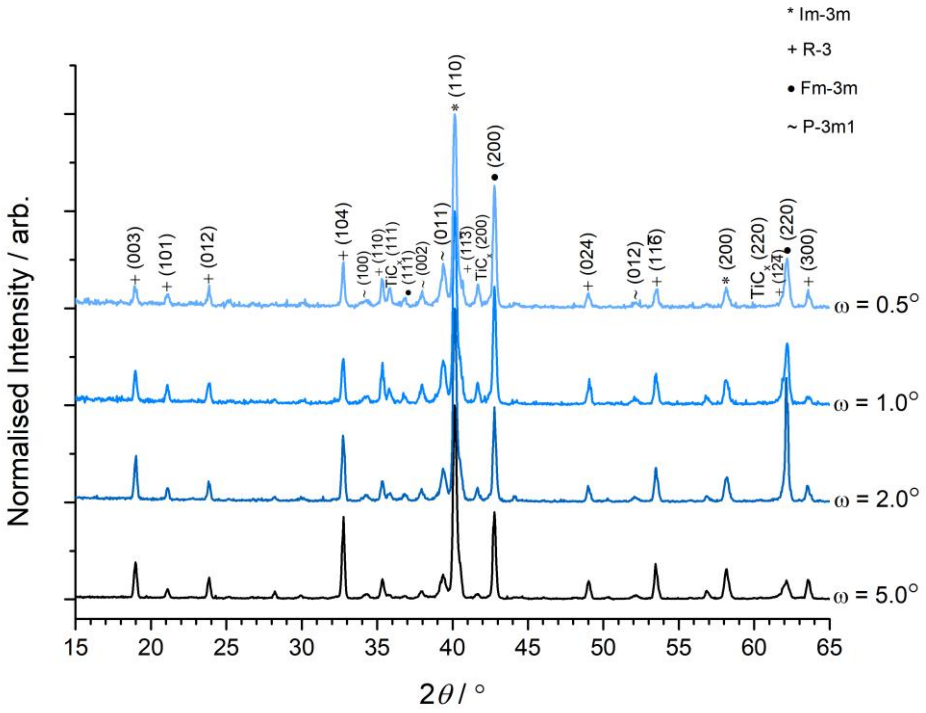

Figure 154 – GAXRD patterns for a sample of Maxthal 312 which was exposed to processed KME at 850°C for 125 h. The peaks were normalised relative to the (110) peak of the Im-3m phase (tungsten alloy).

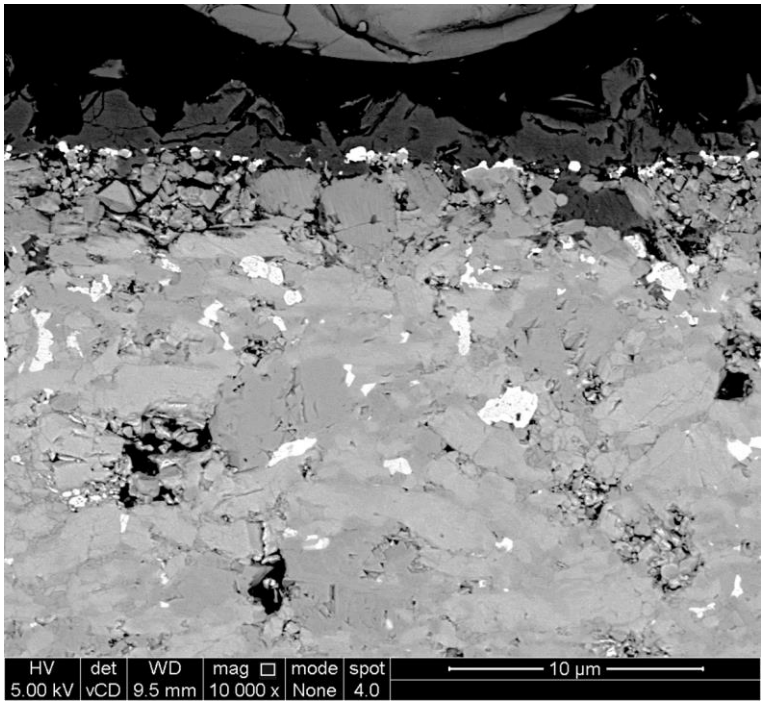

Figure 155 – BSE image of the alteration layer of a sample of Maxthal 312 which was exposed to processed KME at 850°C for 125 h.

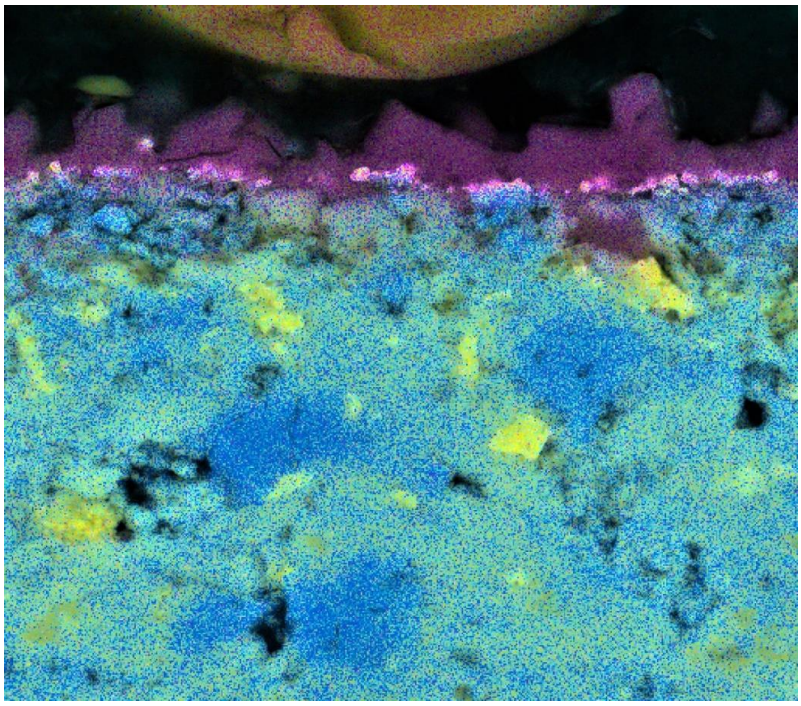

(a) EDS layered image

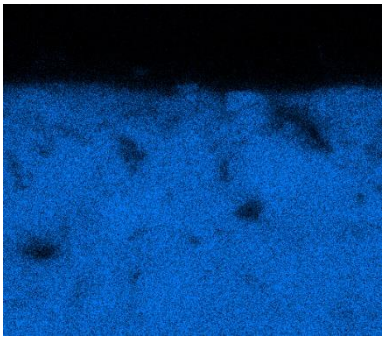

(b) Ti $K_{\alpha 1}$

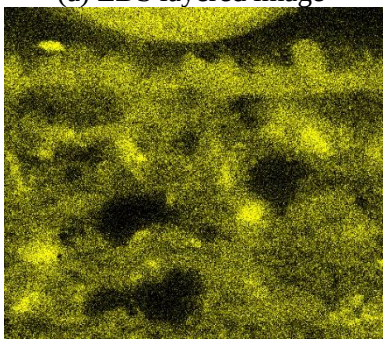

(c) Si $K_{\alpha 1}$

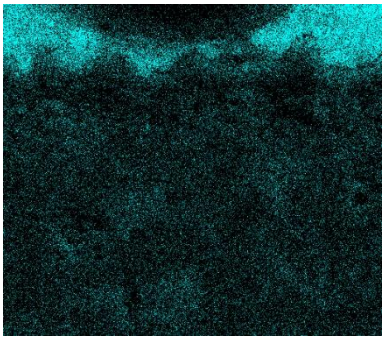

(d) C $K_{\alpha 1}$ and $K_{\alpha 2}$

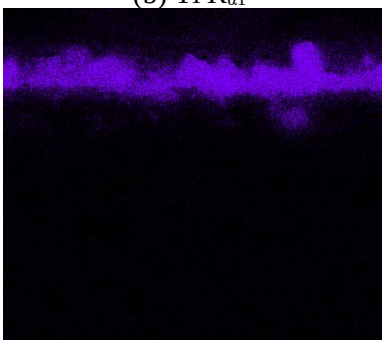

(e) Mg $K_{\alpha 1}$ and $K_{\alpha 2}$

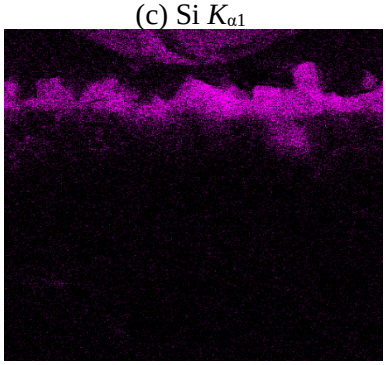

(f) O $K_{\alpha 1}$

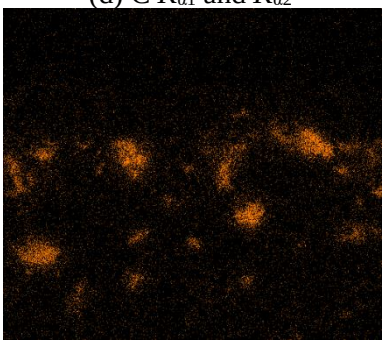

(g) Fe $K_{\alpha 1}$

Figure 156 –EDS maps (image width ~30 µm) of the alteration layer of a sample of Maxthal 312 which was exposed to processed KME at 850°C for 125 h.

7.2.3.1 Microstructural examination of the cross-section

Figure 155 and Figure 156 show a BSE image and EDS maps of the alteration layer. Si, Mg and O can be seen in the deposition layer which has formed on the surface. Fe appears to have reacted with $TiSi_2$.

Figure 157 is a BSE image of the corner, where the top surface is the side perpendicular to the uniaxial pressure applied during sintering. A deposition layer has formed on the surface of both sides, although it is broken off in some places and out of the frame for the side surface. The depth of the deposition layer on the perpendicular surface extends to ~7 µm. Additional alteration in the bulk can be seen to a depth of ~40 µm for the perpendicular surface and ~7 µm for the parallel surface.

Figure 158 is a BSE image showing a detailed view of the deposition layer formed on the surface of the sample parallel to the direction of applied uniaxial pressure during sintering. The thickness of the deposition layer was ~11 µm and was representative of the entire side.

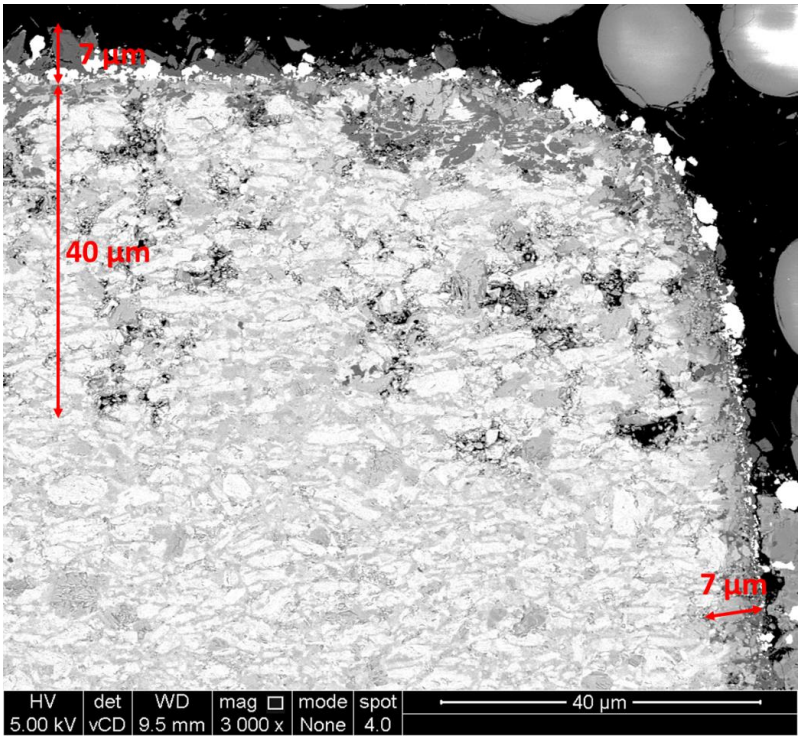

Figure 157 – BSE image showing the corner of the cross-section of a sample of Maxthal 312 which was exposed to processed KME at 850°C for 125 h. The annotations show the approximate depths of the reaction layers at the two sides.

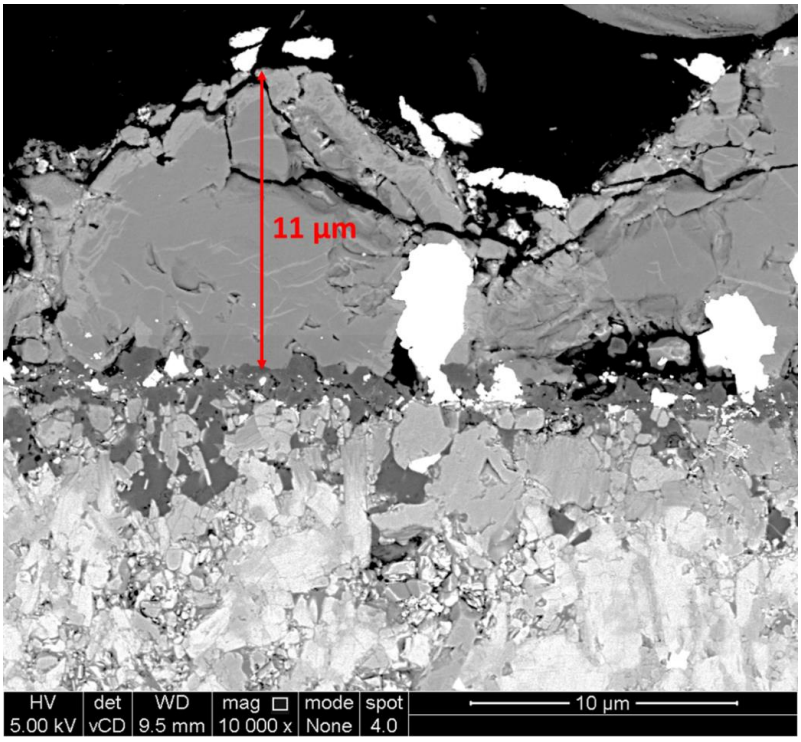

Figure 158 – BSE image of the reaction layer on the side of a sample of Maxthal 312 which was exposed to processed KME at 850°C for 125 h.

7.3 Discussion – Corrosion of Maxthal 312

For both samples exposed to processed salts at 600°C, corrosion seemed more severe at the surface parallel to the direction of pressing during sintering. The grains on this surface were mainly oriented with their A-group planes exposed to the melt, maximising the surface area for diffusion of Si into the melt. The roughness of the surface perpendicular to the direction of pressing during sintering was similar for both samples. Overall, corrosion seemed slightly more severe for the sample exposed to KME.

Iron was observed as an impurity in both samples exposed at 850°C. This was likely due to contamination from the reaction vessel during or prior to the experiment. Tzenov *et al.* observed that small quantities of Fe and V, as low as 1%, can cause decomposition of Ti_3SiC_2 [216]. Fe can react with Ti and Si to form a liquid phase, possibly $Ti_5Si_3Fe_2$, and this pushes the equilibrium between Ti-Si-C to a region of the phase diagram which favours formation of TiC_x and SiC as impurities alongside Ti_3SiC_2. However, it is worth noting that Tzenov *et al.* annealed their samples at 1600°C, significantly higher than the exposure temperature in this work.

The gravimetric results obtained for the samples exposed at 850°C compare favourably with the results obtained by Liu *et al.*, who exposed Ti_3SiC_2 (93wt.%) to as-received NaCl at 850°C in air for 100 h and observed a total mass gain of 2 mg cm^{-2} [135]. The lower mass gain observed in LKE is likely due to better control of impurities in the salt, including oxygen and moisture, whereas the greater mass gain in KME is likely due to the presence of impurities such as tungsten. Differences due to the change in cation are also probable but are difficult to distinguish without improved purification and accuracy.

In the work of Liu *et al.*, for the heavily corroded samples exposed to NaCl containing > 35wt.% Na_2SO_4, the oxide layers which formed consisted of sodium titanates ($Na_{0.23}TiO_2$ and $Na_2Ti_{16}O_{13}$), TiO_2 and Na_2SiO_3, similar to those observed in this work. TiO_2 was observed in regions where the oxide layer had spalled, indicating that TiO_2 is an intermediate in the corrosion mechanism. S was also observed

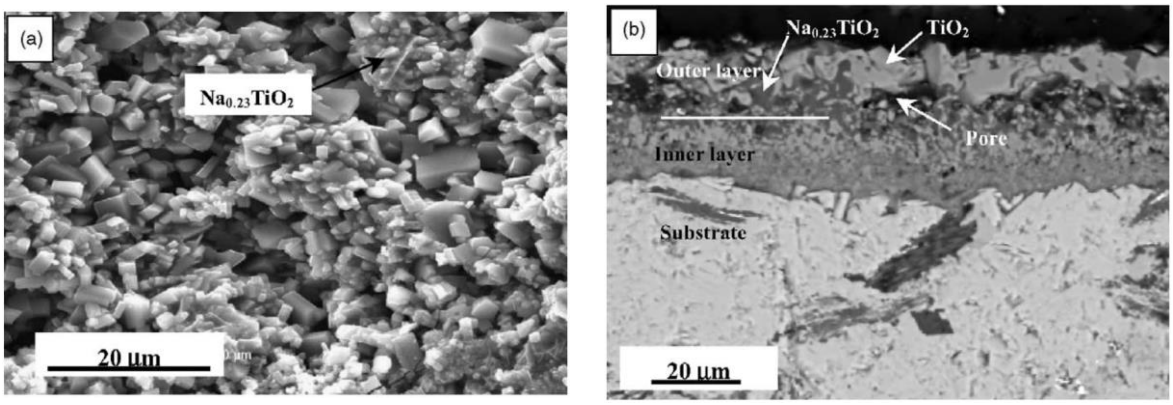

Figure 159 – Morphologies of (a) the surface, and (b) the cross-section, of sample of Ti_3SiC_2 exposed to NaCl in air for 100 h by Liu *et al.*; reproduced from [135].

under the oxide layer and may play a similar role to W, possibly as part of a redox reaction. For the samples exposed to 25wt.% Na_2SO_4-75wt.% NaCl and NaCl, TiO_2 and $Na_{0.23}TiO_2$ were observed as the only corrosion products. SiO_2 may have formed on the inner surface but was not detected by XRD, suggesting it was amorphous. The morphologies observed by Liu *et al.* are shown in Figure 159. The thickness of the corrosion layer was ~35 µm, and is again similar to that obtained for the sample exposed to LKE and KME in this work.

The extent of corrosion was severe for the samples exposed to as-received KME. However, it is probable that corrosion was accelerated by contact with Ni wire. Furthermore, Ni reacts preferentially with Si and was observed to diffuse along the grain boundaries and react with grains of $TiSi_2$ to form Ni_2Si. Yin *et al.* also observed diffusion of Ni along the grain boundaries of Ti_3SiC_2 during investigation of diffusion bonding of the two materials (Figure 160) [119]. The experiments conducted by Yin *et al.* were conducted between 800°C and 1100°C, higher than the 600°C used here, but the exposure times were shorter, between 10-90 min. They observed $Ni_{31}Si_{12}$, $Ni_{16}Ti_6Si_7$ and TiC_x near the Ni, and Ti_2Ni and TiC_x near the Ti_3SiC_2. They found that the reaction layer formed by nickel diffusing into Ti_3SiC_2, and Ni-Si solid solutions formed by diffusion of Si towards Ni; these observations are consistent with this work. Essentially, Ni travels along the grain boundaries and provides a path for Si transport, resulting in the decomposition of Ti_3SiC_2 to TiC_x and the formation of Ni-Ti, Ni-Si and Ni-Ti-Si species. The extent of reaction observed for the two samples differed, with sample B having greater mass gain. This is attributed to a much greater depth of diffusion of Ni into the sample, which may have been due to greater contact surface area with the Ni wire.

Magnesium titanate and magnesium silicate were observed as corrosion products. This indicates the presence of significant quantities of oxygen in the melt. It is likely that the presence of oxygen and

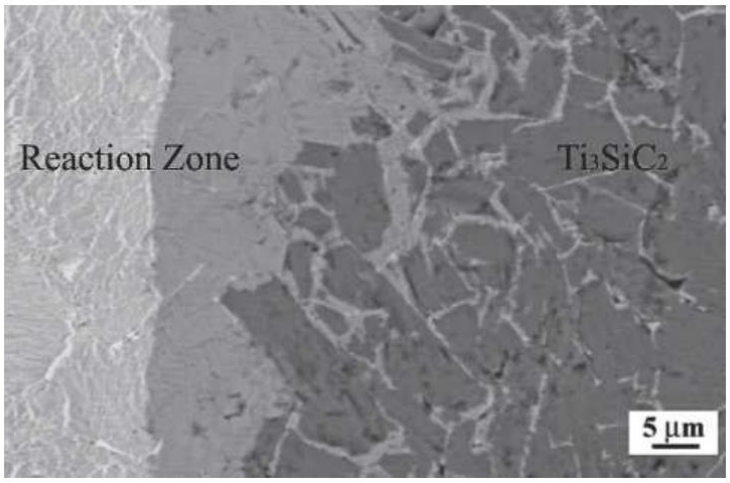

Figure 160 – Cross-section of a sample of Ti_3SiC_2 which was diffusion bonded to Ni at 1100°C for 30 min under 20 MPa uniaxial pressure by Yin *et al.*; reproduced from [119].

water in the melt caused formation of MgO, which preferentially deposited on the surface of the material, whereupon it underwent reaction with TiO_2 and SiO_2 to form $MgTiO_3$ and Mg_2SiO_4 respectively, as per Equation 37 and Equation 38. At 600°C, $\Delta_r G$ is equal to -24.1 kJ mol^{-1} for formation of $MgTiO_3$ and -62.4 kJ mol^{-1} for formation of Mg_2SiO_4. The fact that the latter is more negative suggests its reaction was more favourable, which may explain why there was some residual TiO_2 observed but no SiO_2, although SiO_2 could be present but amorphous. It would be interesting to see if the material reacts substantially with Mg^{2+} in the absence of O-containing species.

Equation 37

$$MgO_{(s)} + TiO_{2(s)} \rightleftharpoons MgTiO_3$$

Equation 38

$$2MgO_{(s)} + SiO_{2(s)} \rightleftharpoons Mg_2SiO_4$$

Liu *et al.* studied the corrosion of Ti_3SiC_2 in carbonate and sulfate melts [131,133,136]. In carbonate melts, they observed Li_2TiO_3 and $TiO_{1.04}$ as the main corrosion products [131]. They argued that corrosion most likely occurred by the reaction of Ti_3SiC_2 with oxygen dissolved in the melt to form TiO_2 and SiO_2, which then react with the salt to form Li_2TiO_3 and Li_2SiO_3. They assumed that SiO_2 may have been amorphous or present in insufficient quantities to be detected by XRD. Therefore, it is likely that SiO_2 forms as an intermediate in the formation of silicates in this work, despite not being detected by GAXRD.

The formation of oxides as opposed to chlorides is consistent with the greater electronegativity of oxygen and the lower Gibbs free energy of formation of the oxides [44,99]. Measurement and control of the oxide concentration in the melt is certainly required. Exposure at more times and temperatures would be useful to determine the rate of reaction and activation energy of the process. Furthermore, exposure for times longer than 125 h would help determine the applicability of using MAX phases in pure and oxygen-containing chloride salts; greater spalling may occur at longer exposure times. Consequently, the mechanical integrity of the oxide scales should also be investigated.

Overall, the presence of impurities including oxygen, tungsten and nickel limits the ability to conclude whether Maxthal 312 is resistant to corrosion in molten chloride salts. However, the fact that only a relatively thin (< 3 µm) corrosion layer was observed on the sample exposed to processed LKE at 600°C, arguably the experiment with the least number of impurities, shows there is some promise for the corrosion resistance of Ti_3SiC_2 in molten chloride salts.

8 Corrosion of TiC

Table 35 summarises the results from corrosion experiments of TiC. TiC was tested because it aids understanding of the effect on corrosion of the TiC_x impurity observed in most of the samples produced. Furthermore, it has low neutron absorption and likely performs well under irradiation damage, and may be possible to use as a coating or as a component of a composite material. Samples were exposed to LiCl-KCl eutectic (LKE) because it is the standard solvent used for pyroprocessing of nuclear waste (there is a wealth of data available for the chemistry of elements in this solvent) and KCl-$MgCl_2$ eutectic (KME) because it has been proposed as a very low-cost solvent for the secondary coolant loop of molten salt reactors. The samples were prepared by sintering TiC powder (2 µm, 7.5 g) by SPS. The powder was heated to 2000°C at a rate of 200°C min^{-1} then held for 15 min at 16 kN force. The on/off pulse time was 15/5 s. The synthesis and characterisation of these samples is discussed in detail in Appendix E, § 15.

The performance of TiC enabled further understanding of corrosion of Ti_3AlC_2 and Ti_3SiC_2. Both MAX phase materials contained TiC_x as an impurity, so by understanding the corrosion performance of TiC the influence of this impurity on the extent of corrosion could be understood in greater detail. Overall, TiC exhibited very little corrosion in the molten chloride salts used. The fact that less corrosion was observed for TiC relative to the samples of Ti_3AlC_2 and Ti_3SiC_2 indicates that TiC impurities are cathodic relative to the MAX phases and should not have caused dissimilar materials corrosion because the volume fraction was relatively small.

In LKE, the mass loss increased when the sample was exposed to processed salt rather than as-received salt. The GAXRD data shows that oxidation occurred at the surface in both cases but was more severe in the processed salt. The mass loss in processed KME at 600°C was lower than that of processed LKE at 600°C. LiCl is more hygroscopic than $MgCl_2$, so it is possible that the oxidation observed in LKE was due to moisture absorbed when setting up the corrosion test.

Mass gain was observed for the sample exposed to as-received KME at 600°C and both samples exposed to processed salts at 850°C. The mass gain at 850°C was due to the formation of lithium titanate in LKE and magnesium titanate in KME. The molecular mass of Li_2TiO_3 is 110 g mol^{-1} and that of $MgTiO_3$ is 120 g mol^{-1}, both of which are similar, which indicates that either a greater amount of titanate formed in KME, or more impurities were deposited on its surface. Small quantities of iron were found on the surface of the sample exposed to LKE, whereas a layer of W, which has a relatively high molecular mass of 184 g mol^{-1}, was deposited in a layer on the surface of the sample exposed to KME. It is likely that iron entered the system by spalling of the corrosion vessel or contamination of the batch of LKE. Tungsten was present in the batches of KME due to dissolution of the working electrode during processing.

Table 35 – Summary of corrosion results for samples of TiC.

Experiment	Salt	Temperature / °C	Duration / h	Mass loss / mg cm^{-2}	Reaction Layer Thickness / µm	Roughness / µm	Reaction Products	Type of reaction	Type of corrosion	Main Impurities	Relation to MSR Operation
Static corrosion	LKE, as-received	600	125	0.13	N/A	N/A	anatase, rutile, WO_3	oxidation, tungsten deposition	uniform corrosion	W, O	Corrosion in the presence of semi-noble fission products and air ingress.
Static corrosion	LKE, processed	600	125	0.22	< 3	0.25 ± 0.02	anatase, rutile, WO_3	oxidation, tungsten deposition	uniform corrosion	W, O, S	Corrosion in the presence of semi-noble fission products and air ingress. Effect of sulfur from Cl transmutation.
Static corrosion	LKE, processed	850	125	-0.66	Intergranular corrosion: ~20-25 Deposition layer: < 10	1.38 ± 0.26	$LiTiO_3$, WC_x	tungsten deposition, oxidation, reaction with lithium to form titanate	intergranular and intragranular corrosion	W, O, Fe, Ni	Corrosion in presence of Fe, Ni, W impurities. Fission products, and Fe and Ni would be present if carbides used in combination with nickel superalloys or steels. Intergranular corrosion may indicate not suitable for use at higher tempeatures.
Static corrosion	KME, processed	600	125	0.09	0	0.11 ± 0.01	nothing	none	uniform corrosion	none	Suggests no significant corrosion would be expected under redox and oxoacidity control, *i.e.* standard operating conditions.
Static corrosion	KME, processed	850	125	-1.84	Intergranular corrosion: < 10 Deposition layer: < 12	3.01 ± 0.28	$MgTiO_3$, MgO, WC_x	tungsten deposition, oxidation, reaction with magnesium to form titanate	intergranular and intragranular corrosion	W, O	Corrosion in the presence of semi-noble fission products and air ingress.

In both salts, the roughness increased substantially when the exposure temperature was increased from 600°C to 850°C. Comparing the two salts, the roughness was lower in KME than LKE at 600°C, but higher in KME than LKE at 850°C. At 600°C, this difference is explained by oxidation at the surface in LKE, which did not occur in KME. At 850°C, the difference in roughness is most likely due to differences in morphology of the two titanate phases, lithium titanate and magnesium titanate.

A brief comparison to work by Craig Jantzen suggests that titanium carbide may be more stable than Hastelloy N [43]. The most comparable experiment is the exposure at 850°C for 125 h, where Hastelloy N gained 13.0 mg cm^{-2} and corroded to 20.0 ± 5.5 µm in LKE, and gained 2.6 mg cm^{-2} and corroded to 18.6 ± 5.1 µm in KME. The mass gain of TiC was certainly lower, but the depth of penetration was similar. However, Hastelloy N corroded uniformly in all experiments, whereas TiC underwent partial intergranular corrosion at higher temperatures, which suggests Hastelloy N may be preferable. The corrosion of TiC should be investigated further, and if intergranular attack persists then its cause must be investigated further for successful use of TiC.

8.1 Corrosion in LiCl-KCl eutectic

8.1.1 As-received salt, 600°C, 125 h

Figure 161 shows the GAXRD patterns with glancing angles, ω, between 0.5° and 2°, normalised relative to the TiC (200) peak [179,211,212,217]. At all glancing angles, peaks of low intensity were observed which correspond to oxide phases. The titanium oxides, rutile and anatase, were observed at all glancing angles, indicating oxidation of the sample. Oxidation has likely occurred due to absorption of moisture by the LKE during the experimental set-up. The best match for the peak at 14.3° 2θ was WO_3 (100), which fits with the fact that a small amount of WC was present in the pristine material, and with the microstructural examination results of the sample exposed to processed LKE at 600°C which oxidised similarly.

8.1.2 Processed salt, 600°C, 125 h

8.1.2.1 Glancing angle X-ray diffraction

Figure 162 shows the GAXRD patterns between glancing angles, ω, of 0.5° and 2.0°, normalised relative to the TiC (200) peak [179,211,212,217]. TiC gave the most intense peaks at all angles, indicating corrosion was not severe. The lattice parameter of TiC was 4.333 ± 0.003 Å (calculated from

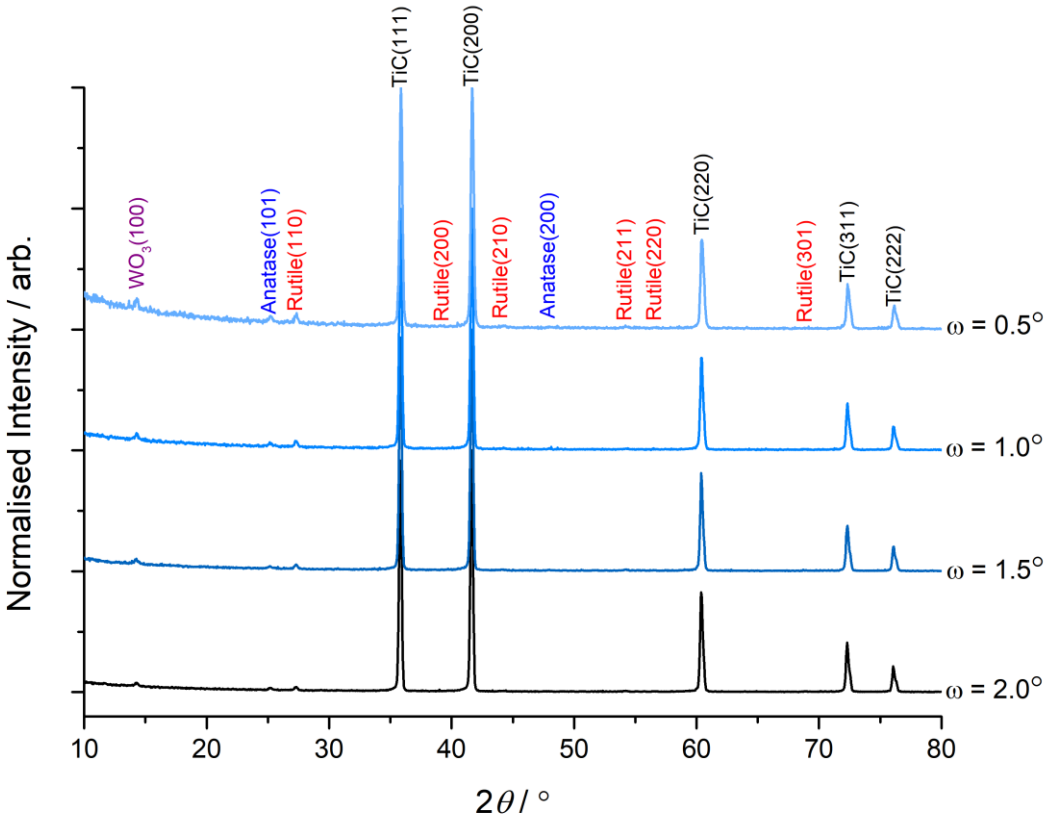

Figure 161 – GAXRD patterns of TiC exposed to as-received LKE for 5 days at 650°C. TiC was the major phase at all glancing angles, but oxides of titanium and tungsten have formed on the surface.

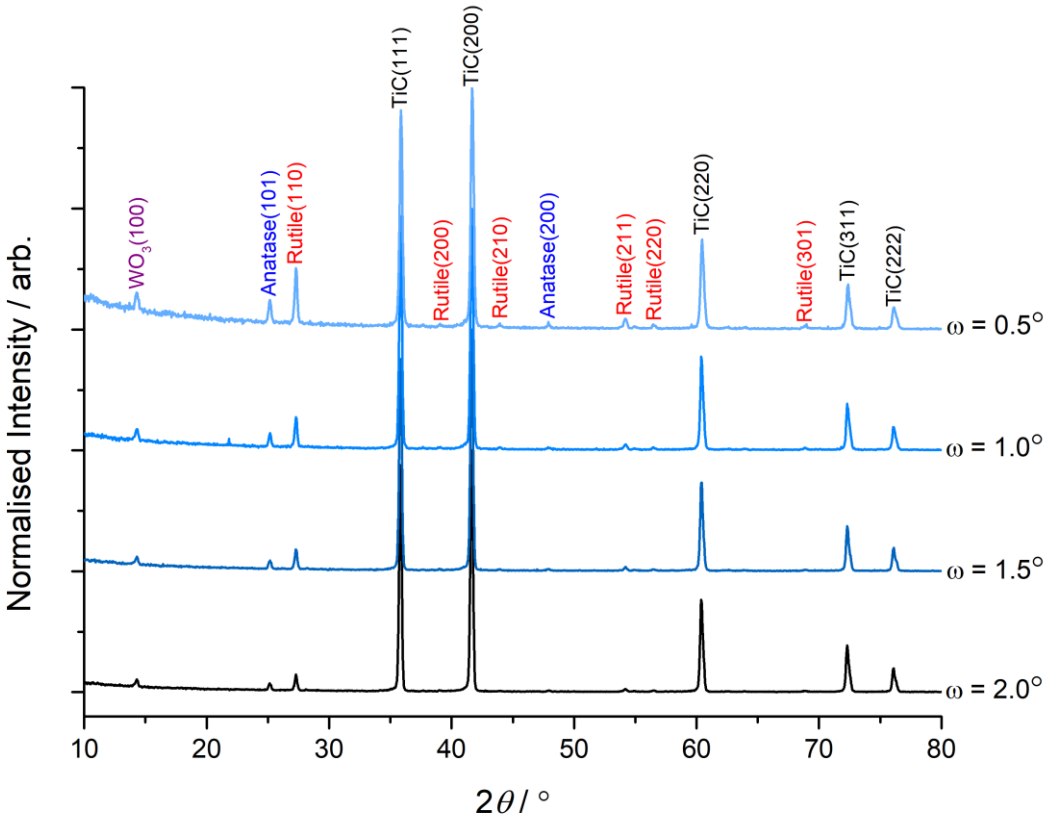

Figure 162 – GAXRD patterns of a sample of TiC which was exposed to processed LKE at 600°C for 125 h. TiC was the major phase at all glancing angles, but oxides of titanium and tungsten have formed on the surface.

the first four peaks of the 1° pattern). Rutile and anatase were the next most intense phases. As with the sample exposed to as-received LKE, the peak at 14.3° 2θ was difficult to identify but may be a tungsten oxide such as WO_3.

8.1.2.2 Microstructural examination

An image of the cross-section is shown in Figure 163. The surface has some slight roughness but overall is quite smooth. The grain boundaries are faint but visible, and the bright contrast WC phase identified in the pristine sample can be seen at some of the grain boundaries. WC clusters such as this can be seen distributed throughout the bulk of the material. The EDS maps do not indicate any diffusion of material towards the surface.

Figure 164 is an SE image showing a general overview of the surface of the sample. There appears to be a lot of material deposited on the surface, but the underlying surface is still visible. Figure 165 is a BSE image at the same magnification.

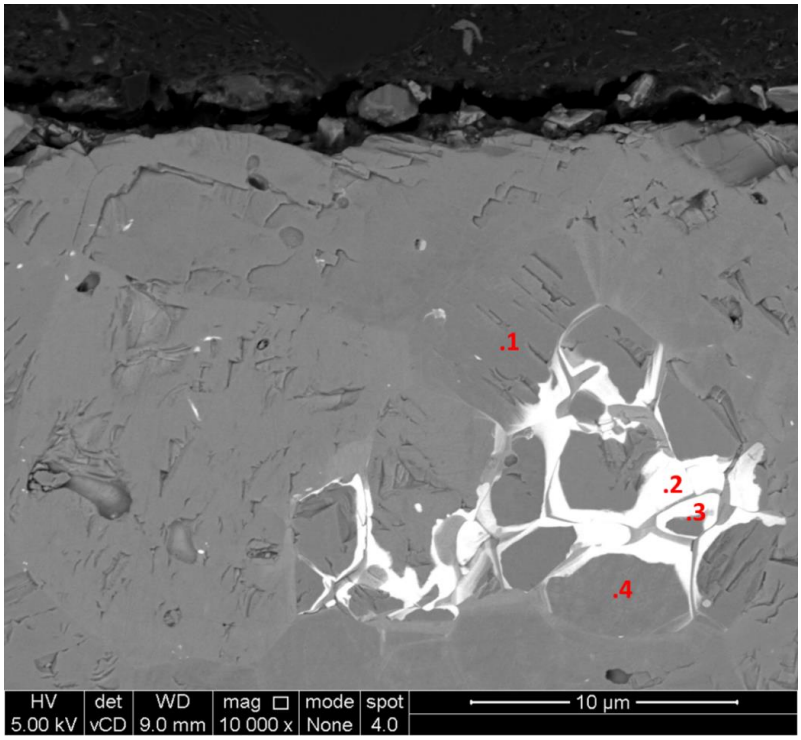

(a) BSE image annotated with locations of point analyses

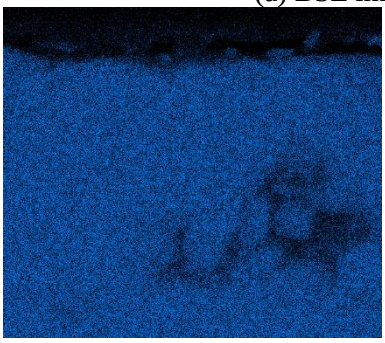

(b) Ti $K_{\alpha 1}$

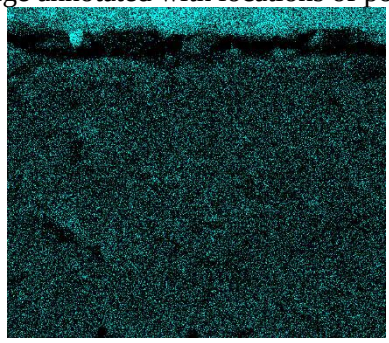

(c) C $K_{\alpha 1}$ and $K_{\alpha 2}$

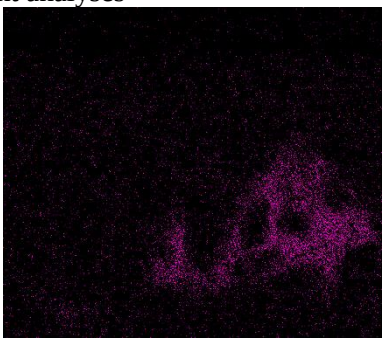

(d) W $L_{\alpha 1}$

Figure 163 – A BSE image and EDS maps of the cross-section of a sample of TiC which was exposed to processed LKE for 125 h at 600°C. The annotations mark the locations of point analyses, the compositions of which are summarised in Table 36.

Table 36 – Elemental compositions (in at.%) of the point analyses shown in Figure 163.

Point	Ti	C	W
1	51.0	49.0	0
2	20.9	65.8	13.0
3	21.7	68.8	9.1
4	44.9	54.4	0.7

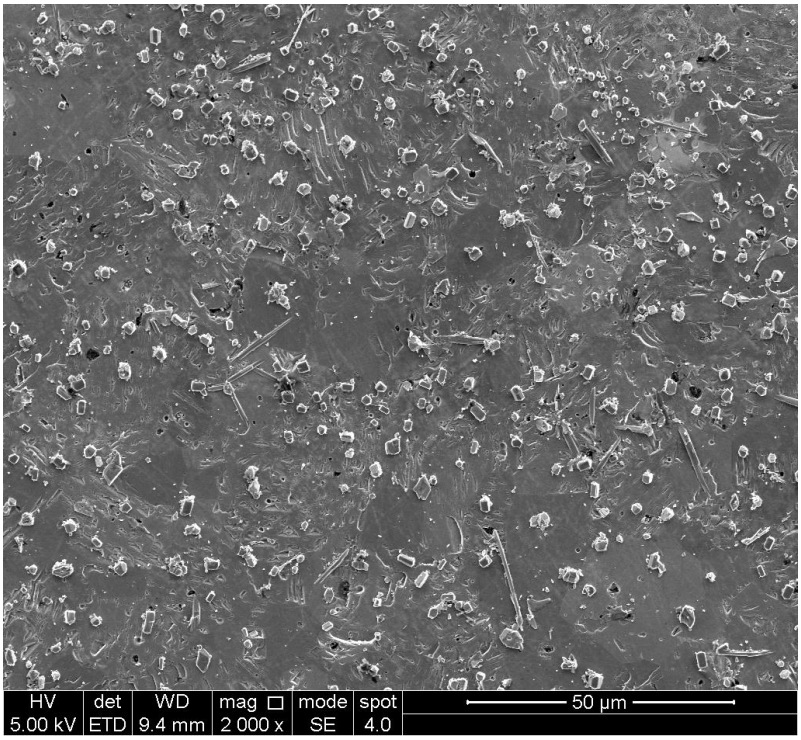

Figure 164 – SE image showing the corrosion products on the surface of a sample of TiC which was exposed to processed LKE at 600°C for 125 h.

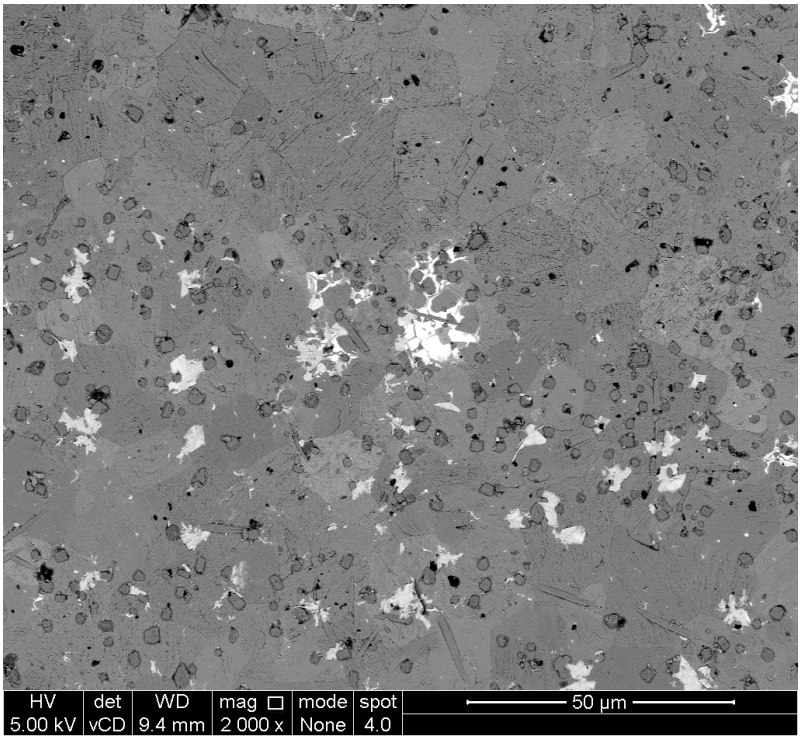

Figure 165 – BSE image showing a general overview of the surface of a sample of TiC which was exposed to LKE at 600° for 125 h.

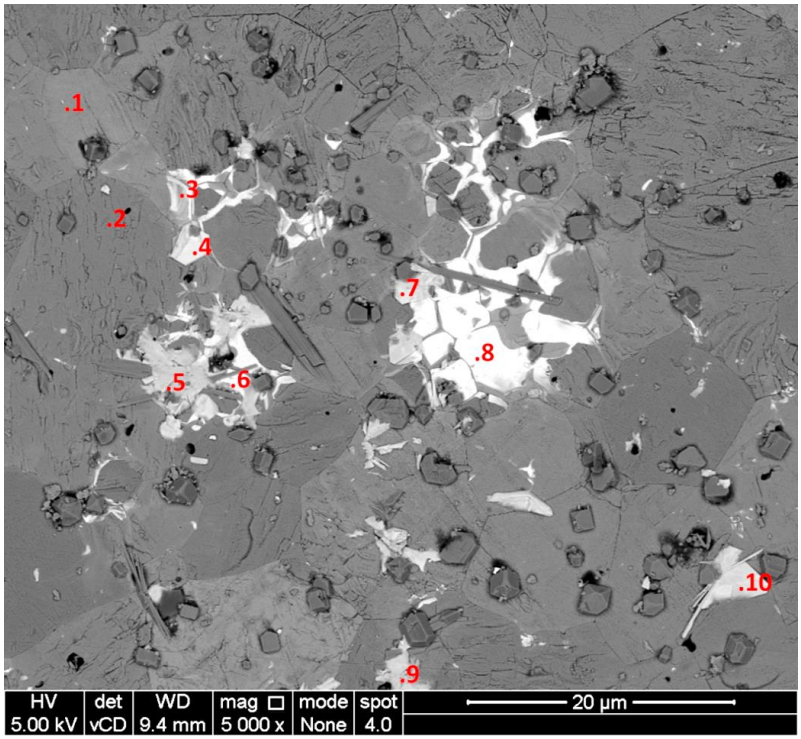

(a) Backscattered electron image

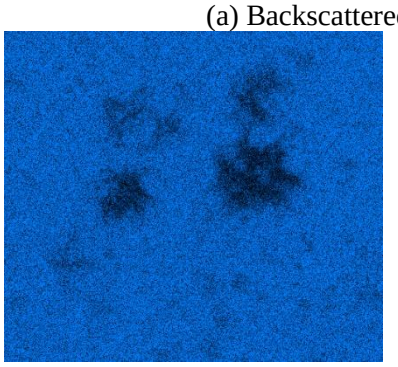

(b) Ti $K_{\alpha 1}$

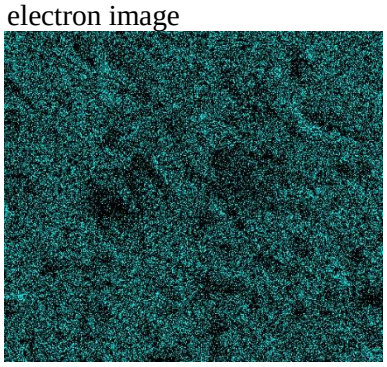

(c) C $K_{\alpha 1}$ and $K_{\alpha 2}$

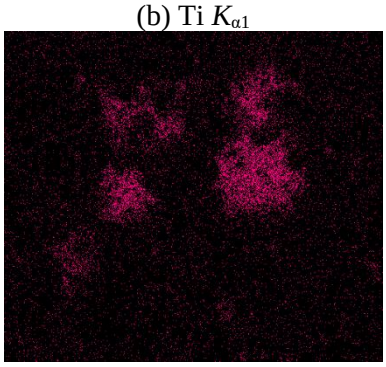

(d) W $L_{\alpha 1}$

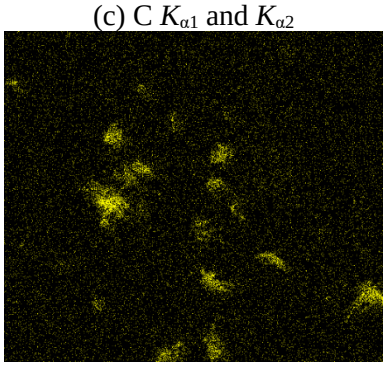

(e) S $K_{\alpha 1}$

Figure 166 – BSE image and EDS maps of the surface of a sample of TiC which was exposed to LKE at 600°C for 125 h. The annotations mark the locations of point analyses, the compositions of which are summarised in Table 37.

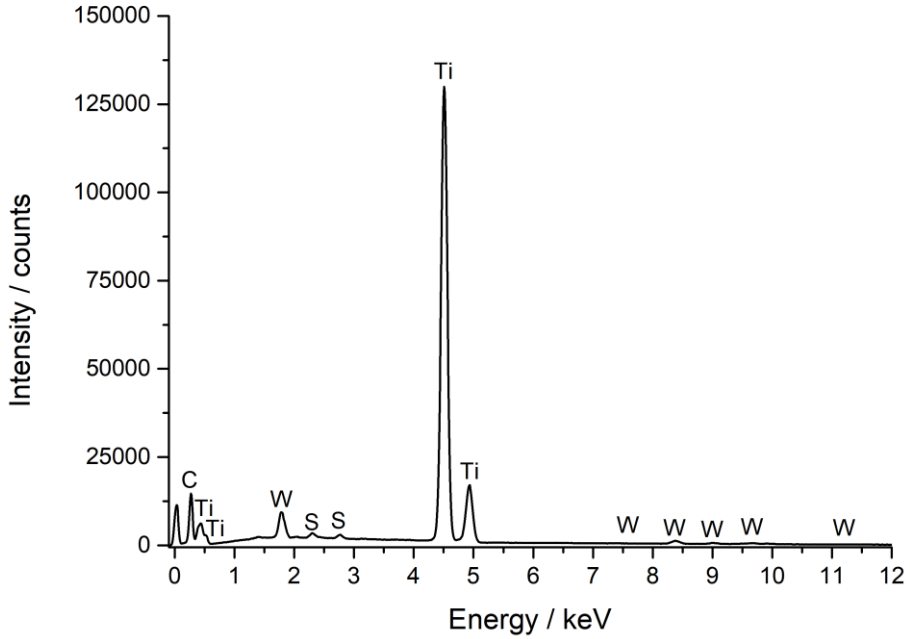

Figure 167 – Map sum spectrum for the EDS maps shown in Figure 166.

Table 37 – Elemental compositions (in at.%) of the point analyses shown in Figure 166.

Point	Ti	W	Mo	S	O
Map	97.6	1.8	-	0.6	-
1	100.	0.0	-	-	-
2	99.7	0.3	-	-	-
3	86.0	14.0	-	-	-
4	75.3	3.7	7.1	13.0	-
5	47.2	2.7	11.9	21.5	16.7
6	54.1	26.8	-	-	19.2
7	59.8	6.9	6.8	13.0	12.4
8	61.5	33.7	-	-	-
9	88.1	-	4.4	7.5	-
10	82.7	0.1	5.9	11.3	

Figure 166 is a BSE image and EDS map of the surface of the sample, showing its typical morphology. Point analyses were taken at the annotated locations, the results of which (excluding carbon) are summarised in Table 37. The morphology of the tungsten phase is the same as that observed in the pristine sample and the cross-section. Sulfur and molybdenum, the peaks of which overlap, were also detected; the lack of higher energy molybdenum peaks in the spectrum (Figure 167) indicate it is sulfur.

8.1.3 Processed salt, 850°C, 125 h

8.1.3.1 Glancing angle X-ray diffraction

The GAXRD patterns at glancing angles between 0.5° to 5° are shown in Figure 168, normalised relative to the Li_2TiO_3 (1,3,-3) peak [179,201,218]. Li_2TiO_3 was observed at all glancing angles, whereas the intensity of WC and TiC peaks decreased as the glancing angle decreased, indicating they were present in lower quantities at the surface of the sample. There is an unidentified peak at 44.6° 2θ which also follows this trend; possible candidates for this peak include graphite, lithium tungsten oxide, and iron (possibly as an alloy). In the reference pattern, the Li_2TiO_3 (002) peak is the most intense peak, followed by the (1,3,-3) peak then the (202) peak. The high intensity of the (1,3,-3) peak may simply be due to the (1,3,-3) and (202) peaks overlapping because the step size was too large.

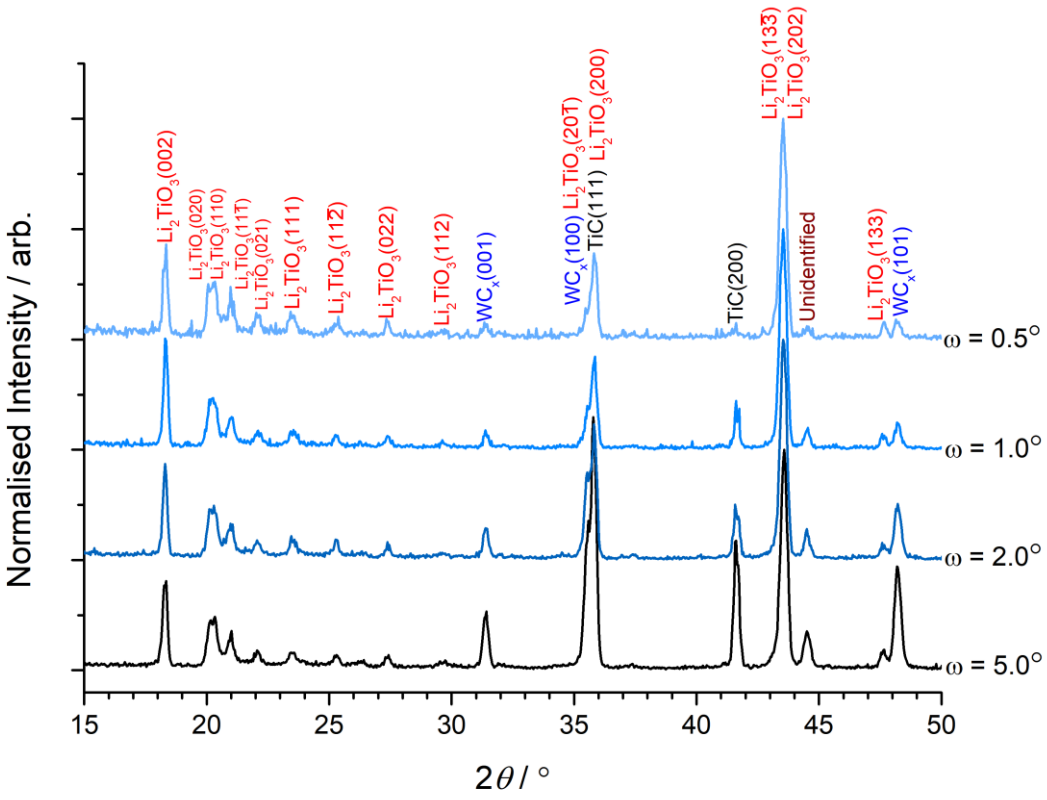

Figure 168 – GAXRD patterns for a sample of TiC which was exposed to LKE at 850°C for 125 h. The patterns were normalised relative to the Li_2TiO_3 (1,3,-3) peak.

8.1.3.1 Microstructural examination of the cross-section

Figure 169 is a BSE and associated EDS maps showing the general corrosion products. The annotations mark the locations of point analyses, the compositions of which are shown in Table 38.

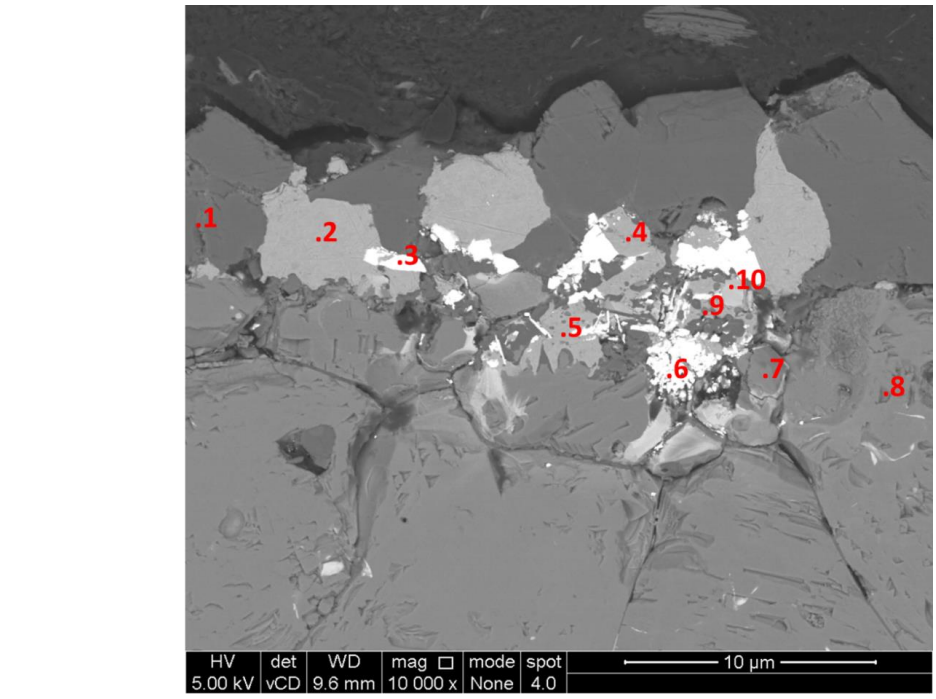

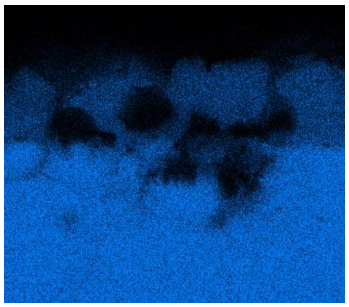

(b) Ti $K_{\alpha1}$

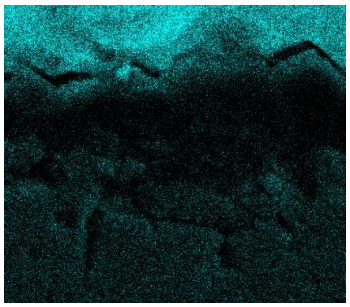

(c) C $K_{\alpha1}$ and $K_{\alpha2}$

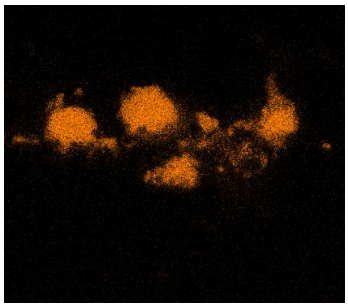

(d) Fe $K_{\alpha1}$

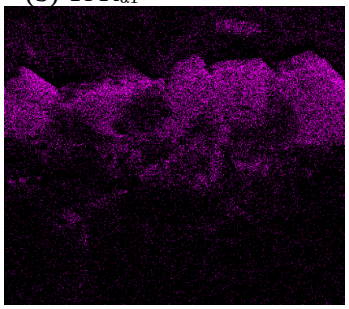

(e) O $K_{\alpha1}$

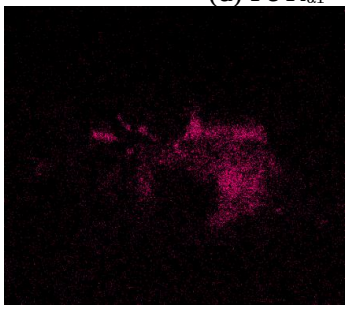

(f) W $L_{\alpha1}$

Figure 169 – BSE image and EDS maps showing the general corrosion products on a sample of TiC which was exposed to LKE at 850°C for 125 h.

Table 38 – Elemental compositions (in at.%) of the point analyses shown in Figure 169.

Point	Ti	C	Fe	O	W	Mg	Ni	Other	Other Elements
1	20.9	10.4	0.3	67.1	-	0.8	-	0.6	Zn, Ca, Si, P
2	3.4	27.9	66.4	-	-	-	2.1	0.2	Ca
3	3.5	60.9	2.6	12.4	19.8	-	-	0.8	Mo, Ca
4	5.1	33.2	46.8	9.0	2.8	0.5	1.5	1.2	Sr, P, Ca, S
5	6.4	26.1	56.3	7.4	0.6	-	1.8	1.4	Co*
6	4.0	66.2	2.0	4.6	23.2	-	-	-	-
7	31.8	67.2	0.2	-	0.7	-	-	-	-
8	53.0	46.8	-	-	0.1	-	-	0.1	Ca
9	14.2	21.6	5.6	49.1	8.4	0.9	-	0.2	Ca
10	27.1	45.8	6.1	14.6	5.5	0.6	-	0.2	Ca

The grain boundaries at the edge of the bulk material have been partially etched, and the TiC grains at the surface have reacted to form an oxide layer at the surface. The darker contrast regions such as point 1 contain Ti and O in an approximate ratio of 1:3, while the lighter contrast regions such as

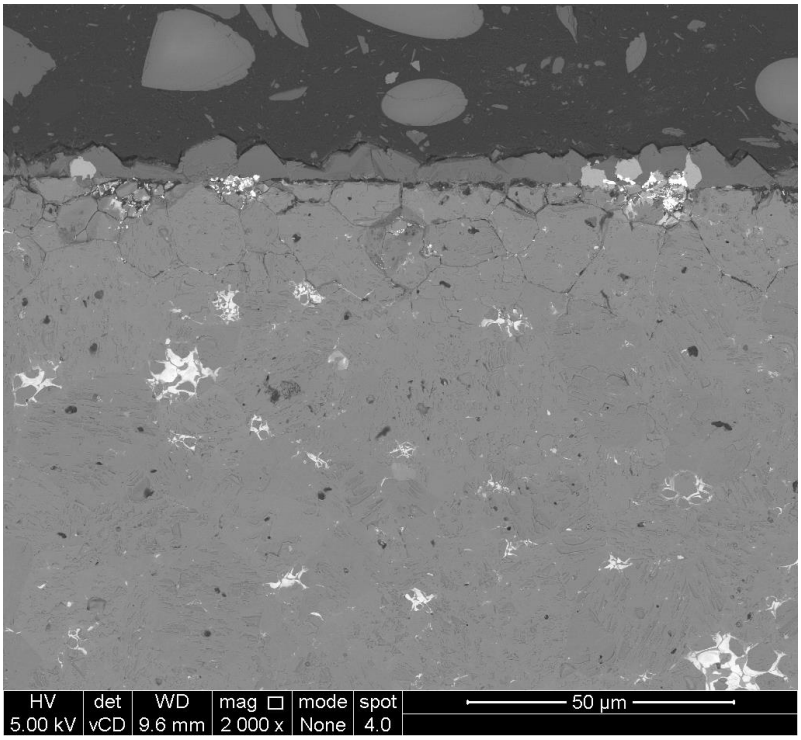

Figure 170 – BSE image showing a general overview of the corrosion layer of a sample of TiC which was exposed to LKE at 850°C for 125 h. An oxide layer has formed on the surface. The underlying surface is relatively smooth, but intergranular corrosion is visible.

point 2 appear to consist primarily of Fe and C. Note that Li cannot be detected by EDS because it emits low energy X-rays which are not easily detected. Therefore, based on the GAXRD results, the darker contrast phase appears to be $LiTiO_3$. The amount of titanium in the corrosion layer is lower than that present in the bulk material, as can be seen in the EDS map for titanium. A significant amount of W is present in the region penetrating the bulk (point 6), which may indicate that the WC clusters are prone to attack.

Figure 170 is a lower magnification BSE image showing a general overview of the corrosion layer. The intergranular corrosion is much clearer in this image. The oxide layer extends to approximately 8 µm thick, and the depth of intergranular attack reaches approximately 38 µm. The surface appears to be relatively smooth, but there are some locations where chemical attack has penetrated the bulk, similar to that observed in Figure 169.

8.2 Corrosion in KCl-$MgCl_2$ eutectic

8.2.1 Processed salt, 600°C, 125 h

8.2.1.1 Glancing angle X-ray diffraction

Figure 171 shows the GAXRD patterns collected at glancing angles between 0.5° and 2.0° and normalised relative to the TiC (200) peak [179]. The phase observed was TiC with a lattice parameter 4.333 ± 0.003 Å (calculated from the first four peaks of the 1° pattern). An additional unidentified peak was observed at approximately 18.8°; the very low intensity of this peak indicates that it is present in very low quantities.

8.2.1.2 Microstructural examination of the surface

Figure 172 is a BSE image which provides a general overview of the surface of the sample. The surface seems similar to that observed for the pristine sample, indicating a lack of corrosion consistent with the GAXRD data.

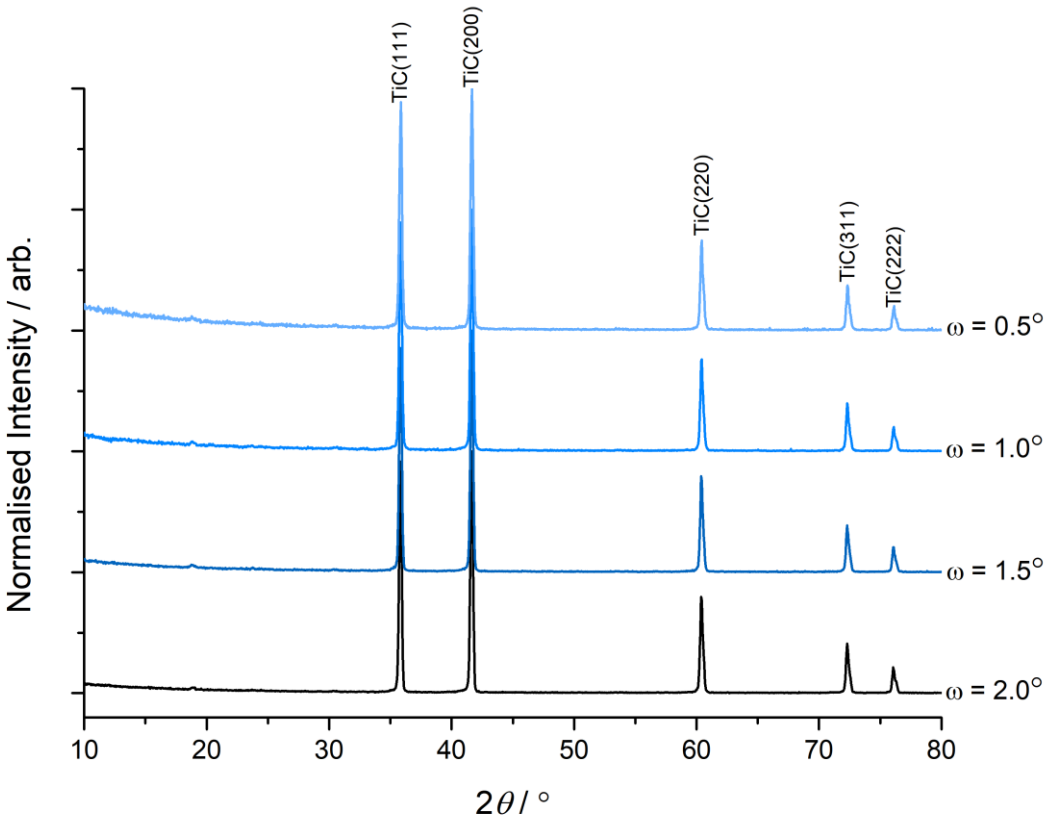

Figure 171 – GAXRD patterns of a sample of TiC which was exposed to processed KME at 600°C for 125 h.

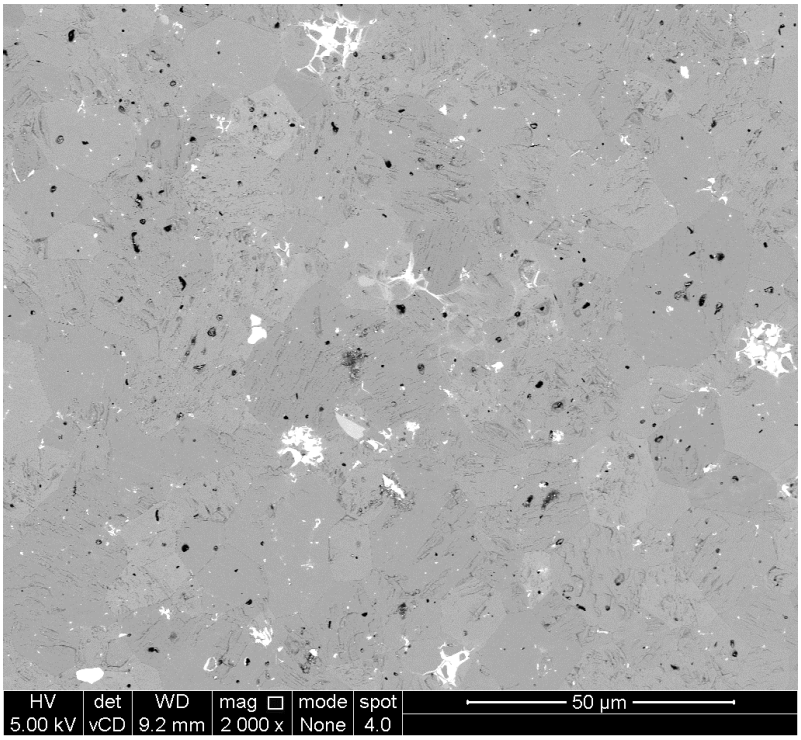

Figure 172 – BSE image showing a general overview of a sample of TiC which was exposed to KME at 600°C for 125 h. The dark spots are pores and the bright contrast regions are clusters of WC_x.

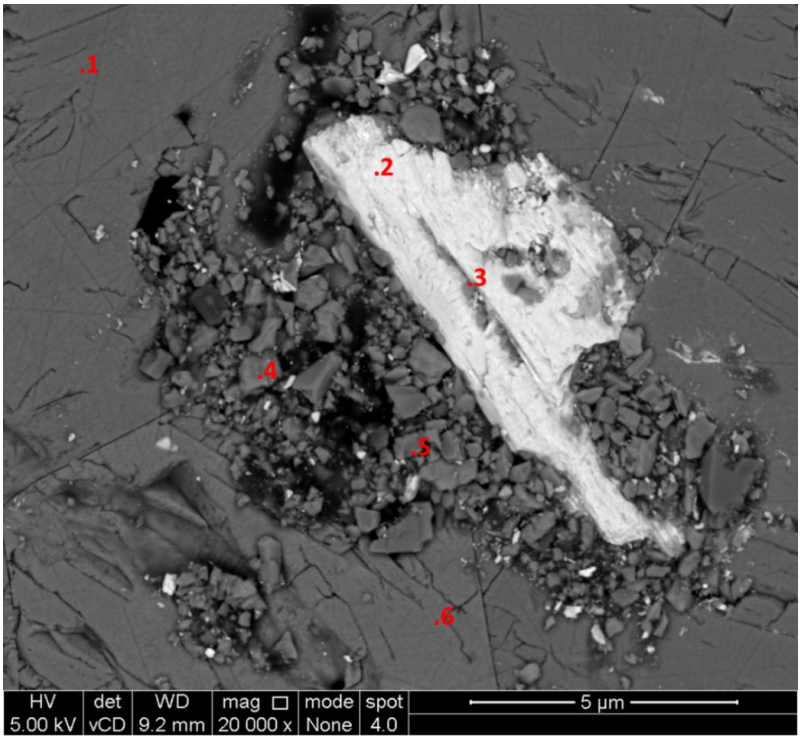

Figure 173 – BSE image showing the morphology of an additional phase observed in a sample of TiC which was exposed to processed KME at 600°C for 125 h. The annotations mark the locations of point analyses, the elemental compositions of which are summarised in Table 39.

Table 39 – Elemental compositions (in at.%) of the point analyses marked in Figure 173.

Point	Ti	O	Mg	W	Si	Al	Other
1	100.0	-	-	-	-	-	-
2	17.2	60.5	12.0	9.8	-	-	0.5
3	16.4	59.8	12.0	9.7	-	-	2.2
4	90.3	-	1.3	-	6.6	1.0	0.8
5	95.7	-	1..3	0.3	1.1	1.0	0.5
6	99.9	-	-	0.1			

Figure 173 shows the presence of an additional phase which was present in small amounts. The results shown are excluding carbon, and the "other" elements present included Cu, Sr, Cl and K. Points 1 and 6 confirm the surrounding material contains titanium. Points 2 and 3 show that the bright contrast particle is an oxide consisting of titanium, tungsten, magnesium and oxygen, although some carbide may also be present. This particle appears to be embedded within the TiC matrix. Points 4 and 5 indicate the surrounding particles consist mainly of titanium, with some magnesium, aluminium and silicon. These particles are relatively small, < 2 µm. Figure 174 is a secondary electron image taken at the same location. It suggests that all particles are raised relative to the underlying TiC substrate.

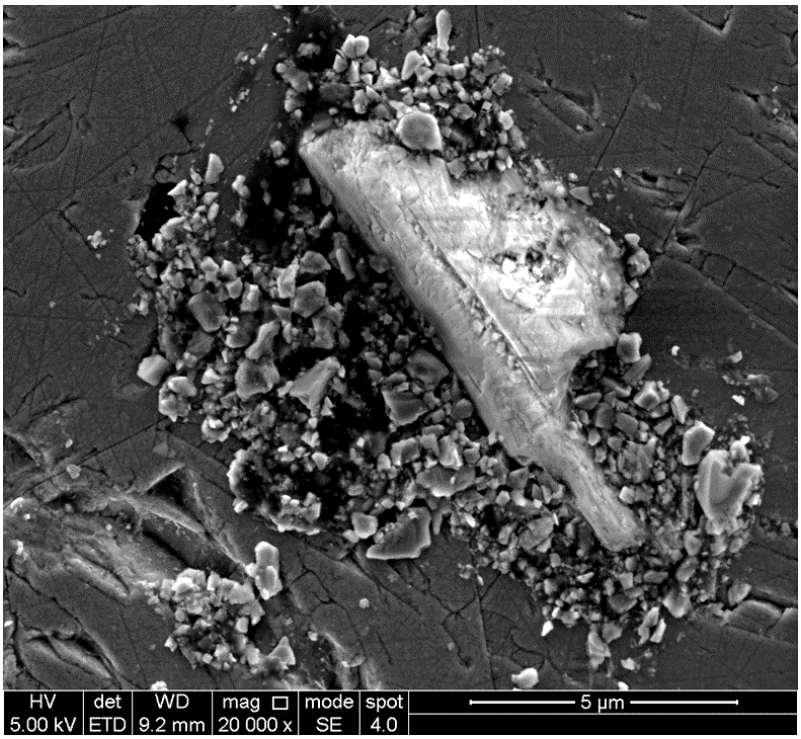

Figure 174 – SE image taken at the same location as Figure 173.

8.2.2 Processed salt, 850°C, 125 h

8.2.2.1 Glancing angle X-ray diffraction

Figure 175 shows the GAXRD patterns measured at glancing angles from 0.5° to 5°, normalised relative to the $MgTiO_3$ (003) peak [179,195,201,215]. The underlying TiC can only be seen at 5° indicating a relatively thick alteration layer. WC_x decreases in intensity at lower angles showing that it is present in greater quantities closer to the underlying TiC. This is consistent with the cross-sectional SEM images, which show a layer of WC_x deposited on the surface of TiC. Above this layer is a deposition layer of $MgTiO_3$, the peaks of which become more intense at lower glancing angles. Peaks for MgO are observed at all angles but are most intense at a glancing angle of 1°.

8.2.2.2 Microstructural examination of the cross-section

Figure 174 gives a general overview of the corrosion layer at relatively low magnification. Tungsten has deposited at the surface, which remains relatively smooth. However, a deposition layer has formed above this layer of tungsten up to a thickness of ~10 µm. Some intergranular attack is also observed near to the surface to a depth of ~12 µm.

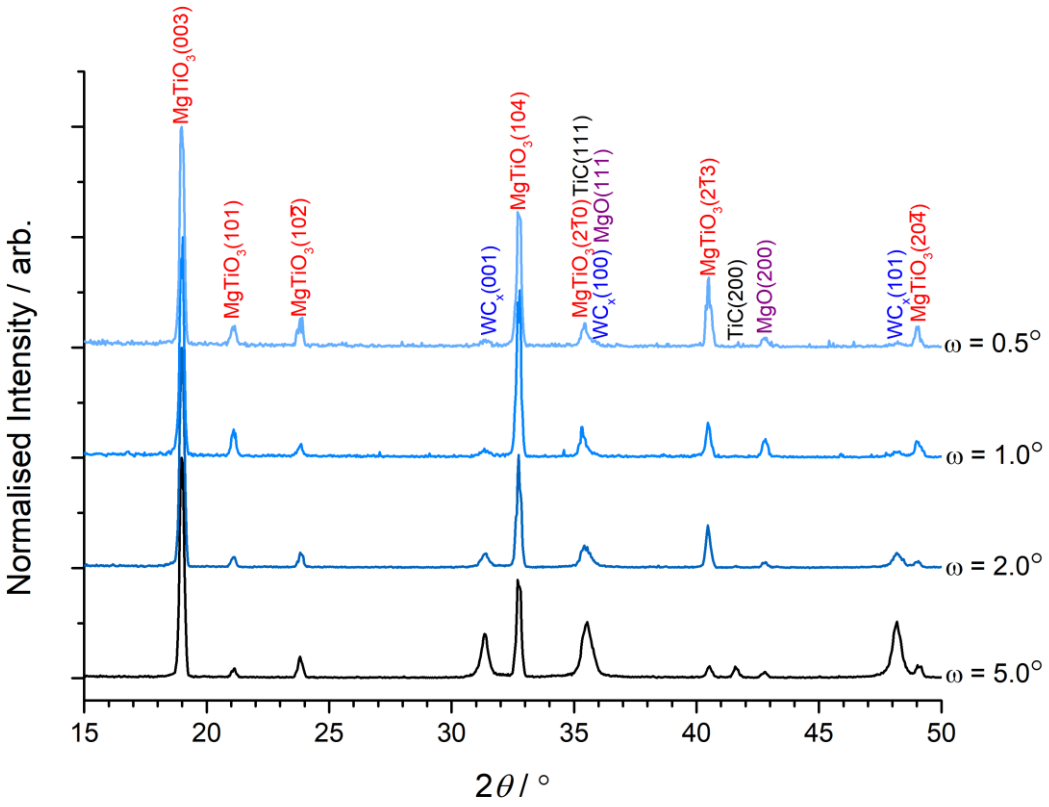

Figure 175 – GAXRD patterns for a sample of TiC which was exposed to KME at 850°C for 125 h. The patterns were normalised relative to the $MgTiO_3$ (003) peak.

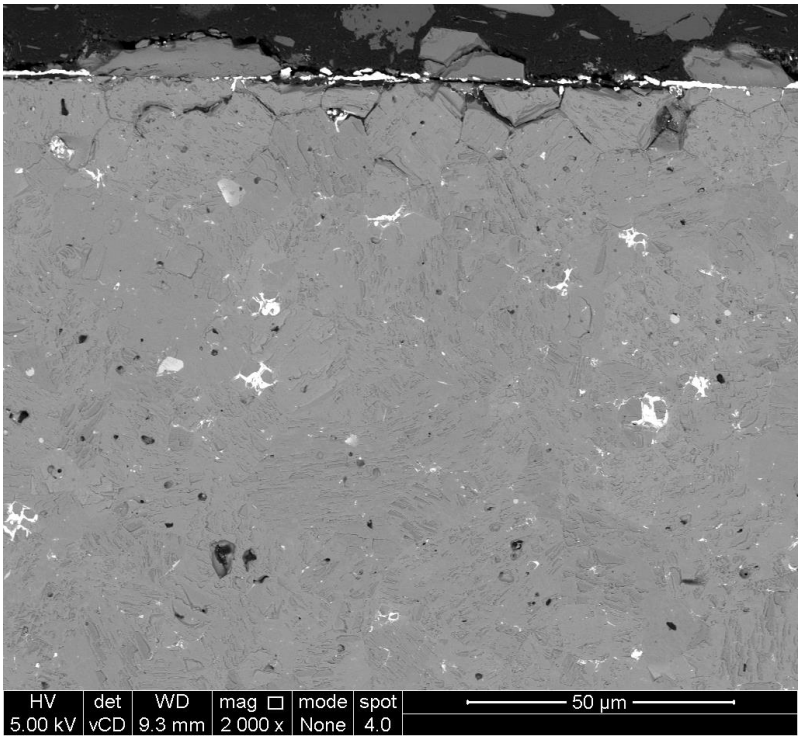

Figure 176 – BSE image which gives a general overview of the corrosion observed for a sample of TiC which was exposed to KME at 850°C for 125 h.

Figure 177 is a higher magnification image with elemental compositions from EDS. A layer of tungsten has deposited on the surface. Magnesium had then deposited on top of this and formed magnesium titanate, as shown by the GAXRD data and the presence of titanium and oxygen in the EDS data. However, points 1 and 2 show varying ratios of Ti to Mg, and carbon is also present, suggesting that a mixture of oxides and potentially oxycarbides are present; oxycarbides have overlapping peaks with carbides in XRD data. The morphology and contrast observed at point 5 indicates the deterioration of titanium carbide grains.

Table 40 – Elemental compositions (in at.%) of the points analyses shown in Figure 177.

Point	Ti	C	W	O	Mg	Other	Other Elements
1	7.5	17.8	-	35.8	38.4	0.4	Cl, K
2	13.9	17.5	-	53.1	15.3	0.1	Zr, Ca
3	3.3	66.7	23.9	5.6	-	0.6	Fe, Ca
4	26.6	59.9	13.5	-	-	-	-
5	33.6	15.1	0.1	46.5	4.6	-	-
6	28.1	62.9	8.7	-	-	0.4	P, Ca
7	47.4	52.6	-	-	-	-	-
8	6.2	56.4	29.0	6.9	1.0	0.7	Fe, Ca

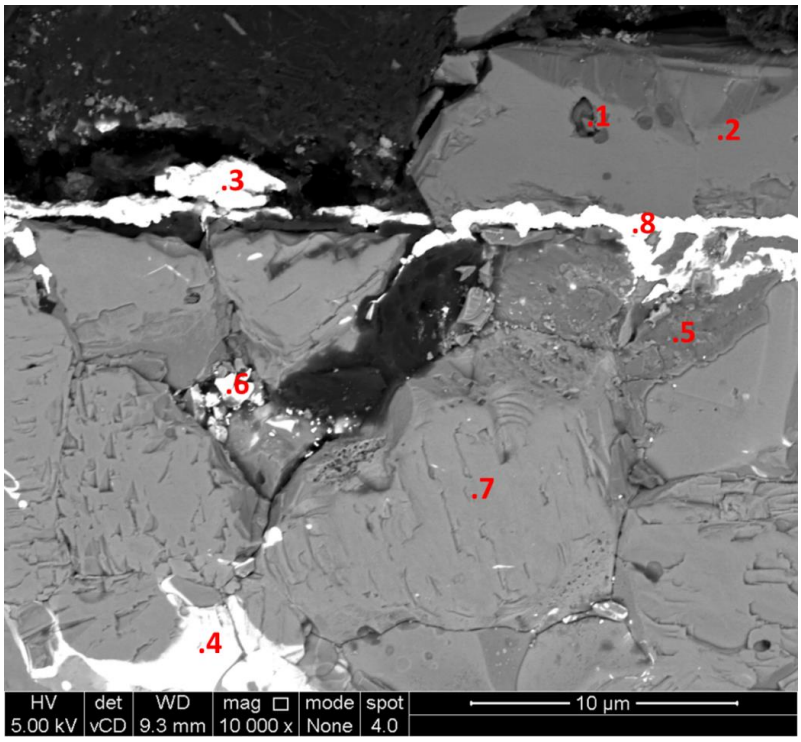

(a) BSE image

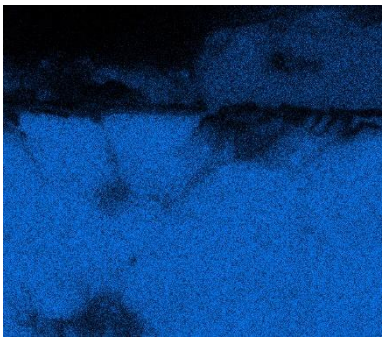

(b) Ti $K_{\alpha1}$

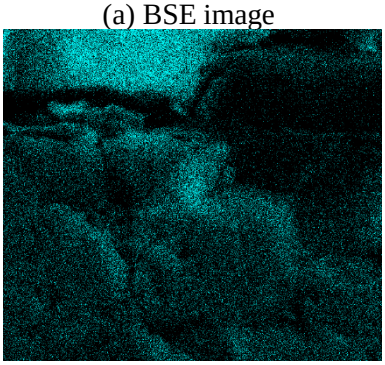

(c) C $K_{\alpha1}$ and $K_{\alpha2}$

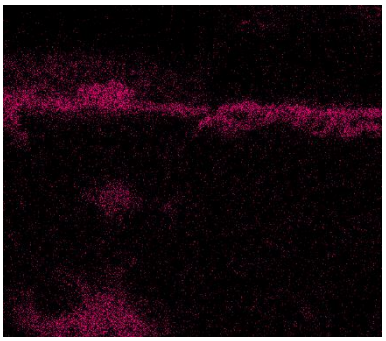

(d) W $L_{\alpha1}$

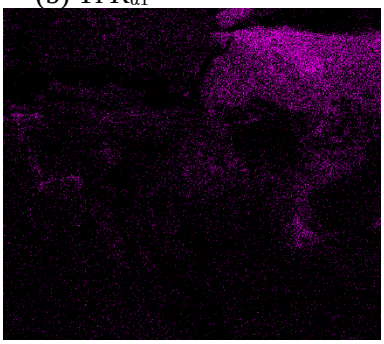

(e) O $K_{\alpha1}$

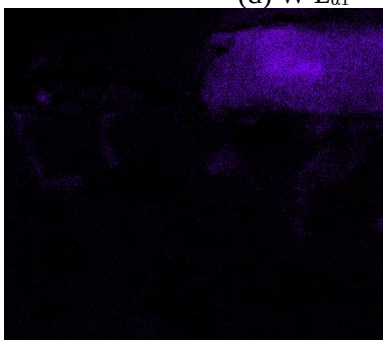

(f) Mg $K_{\alpha1}$ and $K_{\alpha2}$

Figure 177 – BSE image and EDS maps showing the corrosion products formed on a sample of TiC which was exposed to KCl-$MgCl_2$ at 850°C for 125 h.

Figure 178 shows another region of the sample. The dark contrast regions around the grains near the surface are believed to be oxide based on earlier images. This suggests that oxidation is occurring at the grain boundaries and may ultimately lead to grains breaking away at the surface.

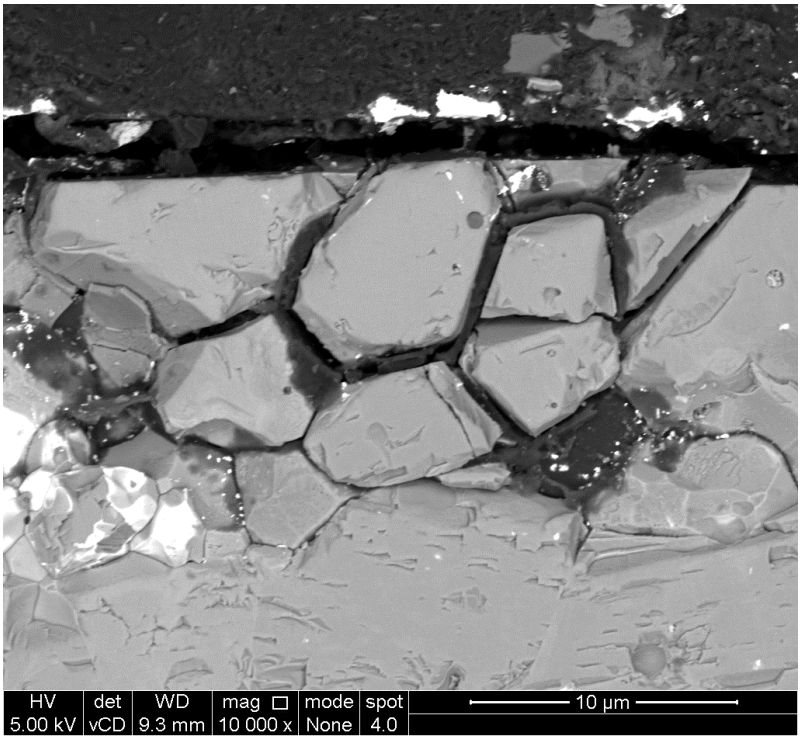

Figure 178 – BSE image showing intergranular oxidation of TiC grains.

8.3 Discussion – Corrosion of TiC

Minimal corrosion was observed in all samples exposed at 600°C. Oxidation occurred on the surface of samples exposed to both as-received and processed LKE, as indicated by peaks of anatase and rutile, and possibly WO_3, in the GAXRD patterns. The mass loss observed in the sample exposed to processed LKE was slightly greater than that of the sample exposed to as-received LKE, which suggests that the salt cleaning method may have introduced impurities which increased corrosion, or the salt may have been exposed to atmosphere longer prior to the experiment.

The sample exposed to processed KME corroded less than the samples exposed to both processed and as-received LKE. LiCl is particularly hygroscopic, so it is possible that water was introduced into the system during preparation of the apparatus. The surface of the sample exposed to KME contained some particles consisting of Ti, Mg, W and O, and there was an unidentified peak at 18.8° in the GAXRD patterns. The experiment in as-received KME failed due to spillage of the salt after approximately 24 h (observed by failure of a thermocouple in close proximity to the crucible) and the sample was not characterised.

Temperature plays a significant role in the corrosion of materials in molten salts. At 600°C there was very little corrosion, regardless of salt processing. However, titanates formed in both salts when the temperature was raised to 850°C; Li_2TiO_3 formed in LKE and $MgTiO_3$ formed in KME. Furthermore, both intergranular and intragranular corrosion were observed in both cases.

The sample exposed to LKE at 850°C shows two corrosion regions: an alteration layer, and intergranular corrosion penetrating the bulk of the material. The intergranular corrosion is likely caused by migration of Ti to the surface, as observed by Gu *et al.* [160], but is difficult to confirm without further microstructural analysis, including the use of techniques such as TEM. The grains of TiC at the surface have clearly undergone intragranular reaction. The primary product is Li_2TiO_3, as confirmed by GAXRD and the ~3:1 ratio of Ti:O in the EDS results. However, there is also a significant amount of Fe present in association with C. Fe is more stable than Ti in chloride salts [99]. Therefore, it is possible that Fe was present in the salt as a chloride species and underwent a redox reaction with Ti at the surface of the sample, depositing as iron oxide or Fe_xTi_yC and causing dissolution of Ti. The dissolved titanium species, most likely $[TiCl_4]^{2-}$, could then have undergone reaction with O^{2-} and Li^+ to deposit on the surface as Li_2TiO_3. It would be useful to repeat this experiment with a purer batch of salt to see if the same reaction occurs, performing chemical analysis on the salt before and after corrosion. It may also be useful to polish samples immediately prior to their exposure to the salt to remove any oxide layers from the surface, preferably carrying out as much work as possible in an inert atmosphere.

The sample exposed to KME shows approximately four different reaction zones. Intergranular corrosion can be seen within the bulk material. At the edge of the bulk material, grains of TiC which are partially decomposed can be observed, possibly through reaction with oxygen, indicating

intragranular corrosion. A layer of W has deposited on top of the bulk material as WC_x. Magnesium titanate has then deposited on top of this WC_x layer. W was present as a contaminant in the salt due to dissolution of the W working electrode used during salt processing. Like Fe, W is more stable than Ti in molten chloride salts [99]. The combination of W and O impurities in the salt appears to have caused oxidation and dissolution of Ti from the bulk material. Magnesium titanate was then most likely formed by a reaction between $[TiCl_4]^{2-}$, Mg^{2+} and O^{2-}.

Gu *et al*. found that the corrosion of TiC in molten FLiNaK at 800°C was also intergranular, although no intragranular corrosion was observed [160]. Ti was selectively removed from the grain boundaries, and the dominant corrosion product was K_2TiF_6. The mass loss observed by Gu *et al*. was ~2-3 mg cm^{-2} at 125 h (interpolated). The mass loss of the samples exposed to chloride salts at 600°C was around an order of magnitude lower than this. However, mass gain was observed in both LKE and KME at 850°C due to the formation of titanates. This mass gain was greater in KME and is partly attributed to the layer of WC which formed between the bulk TiC and the layer of $MgTiO_3$.

Overall, the results suggest that titanium carbide is highly suited to use in a molten salt reactor which uses molten chloride salts at 600°C, but its applicability at higher temperatures requires further investigation. The samples exposed to LKE at 600°C underwent very little reaction despite the presence of oxygen-containing species in the salts, and no reaction was observed for the sample exposed to KME. This suggests titanium carbide should retain stability if air ingress into the reactor occurs, although further investigation is required to confirm the stability of the oxide layers with regards to fluxing or spalling. Additionally, the stability of the sample exposed to processed LKE at 600°C, whilst worse than that for the as-received salt, was relatively high despite the presence of molybdenum and sulfur, the latter of which would form as a transmutation product for chlorine and could be particularly reactive.

The suitability at 850°C is less clear. Intergranular corrosion is a concern as it suggests the material would spall, leading to build-up of crud in the reactor during operation. However, it is clear that a significant amount of oxygen-containing species were present, and that tungsten was introduced into the salts during processing. Consequently, the salts were oxoacidic due to the presence of oxide, and highly oxidising due to the lower stability of tungsten chloride or oxychloride relative to titanium chloride, departing significantly from reactor operation conditions. Conversely, if tungsten was present in the salt as a metallic species, it may indicate the plating out of semi-noble species could be a particular concern if titanium carbide were to be used.

9 Conclusions

Considering the aims of the thesis:

1. Determine a synthesis method to produce pure Ti_3AlC_2.

   Relatively pure Ti_3AlC_2 was produced consistently with greater purity than commercially available MAX phases such as Maxthal 312. However, TiC_x was present as an impurity up to 5 wt.%. High purity samples containing > 98wt.% Ti_3AlC_2 with < 2wt.% Al_2O_3 were also produced but could not be consistently reproduced due to equipment issues. The main purpose of producing pure Ti_3AlC_2 was to limit the effect of impurities on its corrosion. However, as the corrosion performance of TiC was also tested and it was found to be more cathodic relative to Ti_3AlC_2, the presence of TiC_x does not hinder analysis of the performance of Ti_3AlC_2.

2. Perform corrosion tests in purified molten chloride salts.

   Samples were exposed to two different salt compositions, LiCl-KCl eutectic and KCl-$MgCl_2$ eutectic, with and without implementation of a purification method, and with variation of the exposure duration and exposure temperature. Impurities were observed in the corrosion products, primarily oxygen and tungsten, as well as iron and nickel in some samples. Whilst this indicates purification was not as successful as desired, the results are comparable to various reactor operation scenarios such as extended burn-up, lack of redox control, and air ingress, and consequently still achieve the overall aim of determining the feasibility of using MAX phases in molten salt reactors.

3. Compare the corrosion of Ti_3AlC_2 to other materials.

   Samples of Maxthal 312 (primarily Ti_3SiC_2 with some TiC_x and $TiSi_2$ impurities) and TiC underwent concurrent corrosion performance analysis. Samples of nickel superalloys, including Hastelloy N, and molybdenum alloys were also tested under identical conditions by Craig Jantzen at the University of Manchester [43]. As such, the corrosion performance of Ti_3AlC_2 with respect to use in a molten salt reactor has been compared to that of numerous other candidate materials.

Fully dense, almost single-phase samples of Ti_3AlC_2 (~98wt.%) were successfully produced using a two-step process whereby titanium and graphite powders were milled for 240 min in the first step then mixed with aluminium and reactively sintered by SPS in a second step. A small amount of Al_2O_3 was observed by SEM-EDS, Raman microspectroscopy and XRD. However, the Retsch Cryomill used to prepare the sample was unsuitable for further sample preparation due to powder leakage.

The method was adapted for use in a SPEX 8000M Mixer/Mill by varying the milling time, sintering temperature and aluminium stoichiometry. The best results were obtained when titanium and graphite were milled for 2 h then mixed with 1.0 parts aluminium and sintered at 1350°C for 15 min, consistently producing high purity Ti_3AlC_2 (95wt.%) with a TiC_x (5wt.%) impurity phase. SEM of the surface revealed the TiC_x impurity phase was heterogeneously distributed in clusters throughout the material. Analysis of the cross-section of a sintered sample by SEM indicated that aluminium diffused out of the sample at the edges during sintering and reacted with the graphite paper lining the die and punches. This left a layer of TiC_x > 100μm thick around the sample.

The following reaction mechanism has been proposed under these synthesis parameters. Milling titanium and graphite caused diffusion of graphite into the titanium structure without spontaneous, exothermic recrystallisation to titanium carbide. In the presence of aluminium, when the temperature was raised above 642°C, titanium and aluminium reacted exothermically to form Ti_3Al. Further temperature rise caused Al and Ti_3Al to melt, quickly followed by formation of TiC_x and intercalation of Al into the non-stoichiometric titanium carbide structure. The molten Ti-Al continued to fill gaps between particles, aiding densification and mass transport and enabling any remaining Ti-C to dissolve in the melt and recrystallise in the presence of aluminium to TiC_x, followed by vacancy ordering and intercalation of aluminium to form Ti_3AlC_2.

Samples of Ti_3AlC_2, Ti_3SiC_2 (Maxthal 312) and TiC were exposed to molten LiCl-KCl eutectic (LKE) and KCl-$MgCl_2$ eutectic (KME) with variation of the salt processing, exposure temperature and exposure time. The samples were characterised by GAXRD, SEM with EDS, gravimetry and profilometry. The least corrosion was observed for TiC, and Ti_3SiC_2 also performed favourably. The corrosion of Ti_3AlC_2 varied significantly depending on the reaction conditions, showing minimal corrosion for some samples but severe corrosion for others.

The presence of oxygen in many of the experiments limited the ability to accurately determine the effects of chloride. Oxygen is more electronegative than chlorine and reacts preferentially, forming stable oxides which do not break down easily in chloride salts. However, it is unclear whether continued oxide formation and spalling would occur over longer periods of time.

A salt processing method was implemented to minimise the presence of oxygen. However, it is believed that oxygen and moisture were mainly introduced by insufficient sealing or damage to the corrosion vessel, and the presence of oxide layers on the surface of pristine samples. Salt processing was achieved by electrolysing the salt with a tungsten electrode, resulting in formation of chlorine gas which then reacted with any oxides to liberate oxygen gas. Tungsten was a significant impurity in the majority of experiments in processed salts due to unsuccessful separation of dissolved tungsten from the purified salt. Iron was also a significant impurity in many experiments and was introduced by corrosion of the vessel used to maintain an inert atmosphere. Consequently, many of the results are

representative of the environment expected after operating a molten salt reactor for a long period of time, particularly with poor redox and oxoacidity control and with limited removal of fission products.

The samples of Ti_3AlC_2 underwent two types of reaction depending on the exposure conditions. The initial experiments underwent corrosion which can be categorised as reaction with chlorine gas, and the latter samples can be categorised as oxidation in the presence of lithium or magnesium. Chlorine gas was formed in the initial experiments due to electrolysis of the melt, reducing lithium or magnesium onto the surface of the sample whilst producing chlorine gas. Chlorine reacted selectively with aluminium, stripping it from the Ti_3AlC_2 structure to leave behind a Ti-C-Cl phase. The reaction was similar to that between Ti_3AlC_2 and HF, which produces $Ti_3C_2F_2$ with fluoride ions interleaved between Ti_3C_2 layers. The experiments in processed salts typically resulted in oxidation at the surface of the samples. Minimal corrosion of Ti_3AlC_2 was observed in processed LKE at 600°C, regardless of the exposure time. Lithium aluminate and lithium titanate were observed in LKE at 850°C. Corrosion was severe, with pitting of the oxide layer visible by eye. Corrosion of the underlying surface was reminiscent of the samples which reacted with chlorine gas formed by electrolysis. The experiments in processed KME at 600°C had deposits of magnesium oxide on their surface. When the temperature was raised to 850°C, MgO was replaced by $MgAl_2O_4$ which formed by diffusion of aluminium from Ti_3AlC_2 to the oxidised surface.

The samples of Ti_3SiC_2 all formed surface oxides. At 600°C in processed salts, TiO_2 was observed as both rutile and anatase. The reaction layer was relatively thin. The mass loss was negligible in LKE and slight mass gain was observed in KME due to the presence of tungsten in the melt. In as-received salt at 600°C and processed salt 850°C, more complicated oxide phases formed which incorporated the most reducible metal in each salt eutectic. In LKE at 850°C, Li_2SiO_3 and $Li_2Ti(SiO_4)O$ were the dominant oxidation products. In KME, $MgTiO_3$ was the dominant oxidation product in both as-received salt at 600°C and processed salt at 850°C. In as-received KME, Mg_2SiO_4 was also a dominant oxidation product. Furthermore, the samples reacted significantly with the nickel wire used to suspend them, forming Ni_2Si by diffusion of nickel along the grain boundaries and causing silicon to diffuse from Ti_3SiC_2 and $TiSi_2$. These results suggest the compatibility of Ti_3SiC_2 with nickel-based superalloys could be limited due to intergranular corrosion.

The samples of TiC showed very limited corrosion. At 600°C, oxidation occurred in processed and as-received LKE, and negligible change was observed in processed KME. At 850°C, both intergranular and intragranular corrosion was observed in both salts. Titanates were the dominant oxidation products in both salts: lithium titanate formed in LKE and magnesium titanate formed in KME. Mass gain was observed in both cases. The intergranular corrosion observed is postulated to be due to diffusion of titanium along the grain boundaries to the surface.

Comparison to samples of Hastelloy N exposed to the same conditions indicated that Ti_3AlC_2 performed worse, whereas TiC may have performed better. The lack of clarity with TiC was due to some intergranular corrosion being observed at 850°C, suggesting spalling may occur under prolonged exposure.

Overall, the feasibility of using Ti_3AlC_2 or Ti_3SiC_2 MAX phases in molten salt reactors seems limited. However, there is some promise for using textured MAX phases with the MX_n layers facing the molten salt, imparting the same corrosion resistance as binary interstitial carbides whilst retaining the favourable mechanical properties and irradiation damage resistance of MAX phases.

10 Further Work

The effect of milling parameters on the composition of TiC_x formed and the synthesis of MAX phase materials requires further study. Numerous milling parameters were changed when switching from the Retsch Cryomill to the SPEX 8000M Mixer/Mill, including the ball-to-powder ratio, number of balls and milling frequency. Further variation of these parameters, along with characterisation of the milled powders and the sintered samples, should help define the reaction mechanism. In particular, greater understanding of the ignition reaction between titanium and carbon is required.

Sintering should be attempted at temperatures slightly below 1350°C and with shorter hold times because the titanium carbide impurity is suspected to form by decomposition of Ti_3AlC_2 grains. Furthermore, an argon atmosphere should be used rather than vacuum to lower the vapour pressure of aluminium and prevent its evaporation. Additionally, there has been mention in the literature that a slightly lower than stoichiometric carbon content should be combined with a slightly higher than stoichiometric aluminium content to produce a purer product. Such studies should be combined with thorough analysis of the Ti-Al-C ternary phase diagram.

Further characterisation techniques could be used to better understand the reaction mechanism. Raman spectroscopy of both the milled powders and the bulk samples could confirm whether titanium carbide is non-stoichiometric [90]. In particular, Raman spectroscopy of the milled powders may reveal the presence of titanium carbide despite its absence by X-ray diffraction [91]. Electron microscopy would also provide useful information about the powder morphology. In-situ X-ray or neutron diffraction during sintering should provide better understanding of the reaction mechanism and reveal any similarities and differences to the work of Riley and Kisi, although spark plasma sintering may be challenging to study in-situ [77,85]. However, any characterisation of milled powders must account for appropriate powder handling due to their pyrophoricity and affinity for oxygen.

The samples produced in this work were not etched, which made characterisation of the grain size difficult. Most mentions of etching in the literature used solutions containing hydrofluoric acid, the safety implications of which make it difficult to work with. Therefore, it would be useful to investigate alternative etching methods for use with MAX phases. This would also help with understanding the effect of grain size on their corrosion properties. Based on the corrosion studies in this work, it is likely that electro-etching could be a very appropriate technique.

The grain structure of MAX phases often results in formation of textured materials. It is important to understand such texture by accounting for preferred orientation in XRD data. Some preferred orientation was observed in the samples produced in this work, so the Rietveld refinement results should be re-checked. In particular, the samples of Maxthal 312 had severe preferred orientation, so determination of their weight fractions was not possible. It would be particularly useful to further

investigate the effects of texture on the chemical properties of MAX phases, especially considering the relatively high corrosion resistance of titanium carbide. Initial investigation of the effect of anisotropy on the corrosion of MAX phases has been conducted by Du *et al.*, but it is an area of the literature which is lacking [155].

Further investigation of the corrosion of MAX phases in molten salts is required to determine if they can be used in a molten salt reactor. In particular, it is important to ensure the salt is completely clean and not exposed to atmosphere; tungsten was a significant impurity in this work, and the formation of oxides indicates insufficient removal of oxygen-containing species. Whilst the results can be related to expected molten salt reactor operating conditions, adding controlled quantities of impurities would be better from a fundamental science perspective. Conducting experiments in a dedicated glovebox equipped with a furnace would eliminate any exposure to air.

The compositions of many of the corroded samples are complex. Therefore, further characterisation is required to better understand the corrosion mechanism, combined with characterisation after different exposure times. Some XPS was performed, and the results were useful, but the thickness of the corrosion layer highlights that depth profiling is required to obtain any meaningful results. Transmission electron microscopy, particularly combined with techniques such as electron diffraction and electron energy loss spectroscopy (EELS), would provide much greater characterisation of any unknown or ambiguous phases. In particular, the identity of the Ti-C-Cl phase could be determined, providing significant insight into the corrosion mechanism. This data could be combined with XRD data for greater clarity, either by GAXRD or powder XRD of material removed from the corrosion layer. Raman spectroscopy may also be useful if issues with high background counts can be resolved and the peaks can be identified.

More accurate determination of the extent of corrosion is required in order to obtain any meaningful kinetic data. Provided the extent of corrosion can be determined more accurately, more exposure times would enable the rate of reaction to be discerned and more exposure temperatures would enable the activation energy of the rate limiting reaction to be ascertained. A standardised cleaning method should be implemented to obtain more accurate gravimetric data; in this work, removal of corrosion products was avoided in order to better identify reaction products. The thickness of the corrosion layer could be established from multiple measurements using image analysis software, yielding a statistical error. The thickness of samples before and after corrosion could be used to deduce whether any spalling occurred. Elemental analysis of the salt would be another method to verify the extent of corrosion and would also highlight the presence of any impurities. The composition of the bubble trap should also be characterised to determine whether gases such as $TiCl_4$, $AlCl_3$ or $SiCl_4$ are produced. If so, the dissolved species formed from these gases may provide another method to discern the extent of corrosion.

Some initial electrochemical data was collected in this work, but the interpretation was limited. Electrochemical experiments have the potential to provide vast insight into the reaction mechanisms in molten salts. Measurement of the corrosion potential and comparison to that of other materials, including pure metals and Hastelloy N, would enable the formation of a galvanic series under particular exposure conditions. The use of cyclic voltammetry combined with comparison to reference materials would provide greater understanding of the reaction mechanisms, particularly if combined with static corrosion tests where the potential is measured. Tafel analysis could provide useful kinetic data which could be compared to that obtained from static corrosion tests. Electrochemical impedance spectroscopy would be very powerful if the corrosion mechanism is well understood and could provide very accurate kinetic data.

The formation of oxide layers on many of the samples indicates that an oxide coating may be beneficial to prevent corrosion in molten chloride salts, although it is likely that such coatings would not be stable in fluoride salts. Oxide-coated nickel alloys, steels and MAX phases should be exposed to pure molten chlorides to determine their stability. In particular, any pitting at higher temperatures should be ruled out in order for oxide coatings to be deemed stable.

The compatibility of MAX phases, particularly Ti_3SiC_2, with nickel-based superalloys should be investigated. Samples of Maxthal 312 which were suspended with nickel wire showed diffusion of nickel along the grain boundaries and interdiffusion with $TiSi_2$ precipitates. This may indicate that Ti_3SiC_2 would bind strongly to nickel-based superalloys. This may enable its use as a coating, or with successful diffusion bonding would enable the use of low neutron absorbing Ti_3SiC_2 in the reactor core connected to intricate piping constructed from nickel-based superalloys. However, the intergranular nature of this diffusion requires further investigation of the mechanical integrity of the intermediate phases and understanding of their corrosion and radiation damage tolerance.

MAX phases with alternative compositions should be investigated. Based on thermodynamic data, titanium and aluminium are more reactive with chlorine and fluorine than nickel and may be expected to perform poorly. Niobium and molybdenum are much more stable metals and have relatively low neutron capture cross-sections, so may perform more favourably [95,99,221]. Investigation of the effect of the A-group element is required, as Ti_3SiC_2 performed better than Ti_3AlC_2. If silicon-based MAX phases are found to be stable, it is possible that silicides may also be stable to corrosion in molten salts. It is unknown whether nitrides would be preferable to carbides, but boron nitride is known to be particularly stable in molten fluoride salts, so the performance of nitride materials should certainly be investigated.

Based on the favourable performance of TiC, the molten salt corrosion of binary carbide composites should be investigated. Initial investigations of such materials have been presented in the literature, but it is an area which has seen limited study. Such materials include composites such as SiC-SiC, SiC-

TiC, SiC-ZrC and carbide dispersion strengthened alloys [114,160,222]. Binary carbide coatings of materials such as titanium, molybdenum or niobium carbide may also be favourable. In addition, the use of nitrides must not be ruled out; boron nitride is particularly stable in molten fluorides and indicates nitrides may be stable, although boron itself cannot be used for nuclear applications without enrichment to ^{11}B.

With regards to the use of such materials in molten salt reactors, an extensive program of research and development would be required. Once the compatibility with pure chloride or fluoride salts is known, the compatibility with fission products must be understood. Corrosion should be minimal provided the electrochemical potential is controlled (*i.e.* sufficiently reducing), but certain species may react preferentially with the material as per the reaction of tellurium with alloying components of nickel superalloys. In the case of MAX phases, the A-group element can be particularly reactive and may react preferentially with certain fission products. Other than corrosion, the ability to withstand neutron and gamma radiation should be investigated. Whilst MAX phases appear to be relatively resistant to irradiation damage, the effects of radiation-induced corrosion must be investigated. Furthermore, an extensive review of the mechanical properties of such materials is required with regards to their suitability for use in molten salt reactors, particularly their post irradiation creep resistance and their susceptibility to stress corrosion cracking in molten salts. All these performance properties must be measured over extensive periods of time in order to qualify the materials for use in molten salt reactors at high temperatures. It is also necessary to determine the most appropriate method of implementing such materials. Joining components could prove difficult, so it may be preferable to use them in specialised applications such as pump components or as coatings for a cheaper material such as a stainless steel qualified for use in high temperature nuclear reactors.

11 Appendix A – Methodological Theory

11.1 Density

The buoyant force acting on an object which is immersed in a fluid is equal to the weight of fluid which is displaced by the object. Thus, by measuring the mass of an object in both air and a liquid, the buoyant force can be determined. Provided the density of the liquid is known, the volume of liquid which is displaced can be calculated, after which the density of the object can be found from its mass and volume.

The density of a material is given by Equation 39, where ρ (in g cm^{-3}) is the density of the sample, m_{air} (in g) is the mass of the sample when weighed in air, and V (in cm^3) is the volume of the sample.

Equation 39

$$\rho = \frac{m_{air}}{V}$$

The volume of the sample is given by Equation 40, where m_{liquid} (in g) is the mass of the sample in the liquid and ρ_{liquid} (in g cm^{-3}) is the density of the liquid. In this work, water was used as the liquid. The density of the liquid is dependent on the temperature.

Equation 40

$$V = \frac{m_{air} - m_{liquid}}{\rho_{liquid}}$$

Combining the two equations, the density can be determined using Equation 41.

Equation 41

$$\rho = \frac{m_{air} \times \rho_{liquid}}{m_{air} - m_{liquid}}$$

11.2 X-ray Diffraction

When waves encounter regularly spaced obstacles similar in size to their wavelength they undergo constructive and destructive interference dependent upon the positions of the obstacles [223]. X-ray diffraction (XRD) is a technique whereby monochromatic, collimated X-rays, of wavelength close to atomic spacings, are passed through a material and are scattered by the electron cloud within the atoms, as illustrated in Figure 179. The beam and detector are varied through a diffraction angle θ and the intensity of the diffracted beam is measured.

Constructive interference of scattered X-rays occurs at specific angles according to Bragg's law, Equation 42, revealing the spacing size (d_{hkl}) between adjacent, parallel planes of atoms. This is related to the lattice parameters (a, b, and c) and the Miller indices (h, k and l), enabling determination of the crystal structure of the material. The symmetry of the unit cell affects the number of peaks observed

and the lattice parameters determine the location of such peaks. Thus, the diffraction pattern of intensity plotted against θ is unique for each material. Powdered samples are typically used for accurate identification of a material as they minimise distortion of peak intensities from preferred orientation.

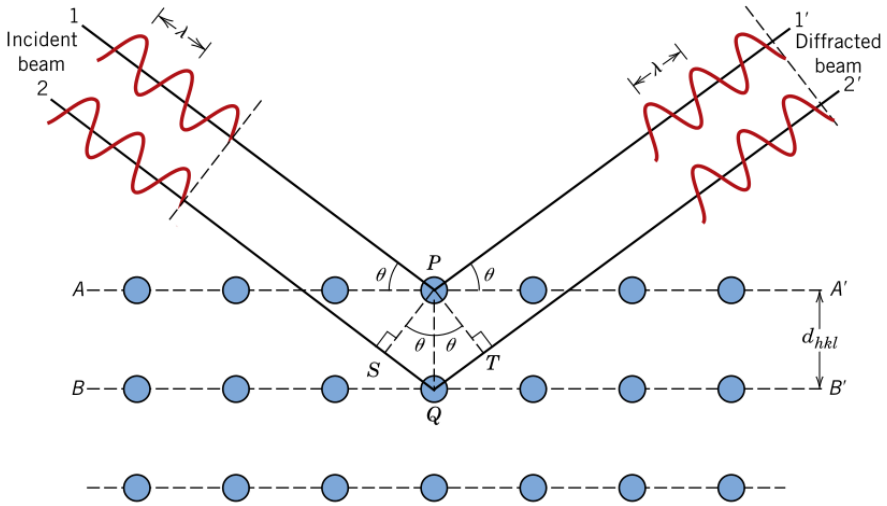

Figure 179 – Diagram depicting the diffraction of X-rays by planes of atoms; reproduced from [223].

Equation 42

$$n\lambda = 2d_{hkl}sin\theta$$

There are various instrument geometries used for X-ray diffraction experiments. The two geometries significant to this work are reflection and glancing angle (or grazing incidence). Reflection geometry is commonly referred to as the Bragg-Brentano focusing method, which is depicted in Figure 180 [165]. This geometry was used for characterisation of bulk pristine samples and powders. The sample is mounted horizontally and remains stationary while the X-ray source and detector move together (the θ-θ condition) through increasing values of the angle θ, in order to collect diffraction intensities in the range 2θ. The beam is referred to as self-focusing because wherever it hits the sample and diffracts, it will be reflected directly into the detector. The sample can be rotated around its vertical axis in order to minimise the effects of preferred orientation. Powdered samples were covered with Kapton film to prevent exposure to atmosphere; the powders were handled in a glove box (< 0.1 ppm O_2 and < 0.1 ppm H_2O) and prepared on a zero-background sample holder.

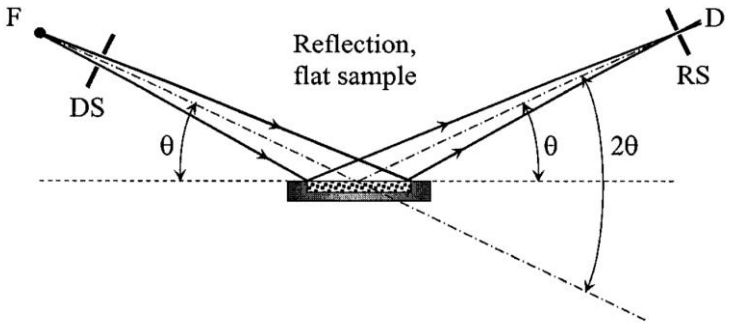

Figure 180 – Diagram of reflection geometry (the Bragg-Brentano focusing method) for X-ray diffraction experiments; reproduced from [165]. The flat sample is mounted horizontally, enabling self-focusing of the diffracted beam after reflection from the sample. F is the focus of the X-ray source, DS is the divergence slit, RS is the receiving slit, D is the detector, and θ is the Bragg angle.

Glancing angle geometry was used to characterise the corrosion layers formed after exposure to molten salts. The X-ray source is kept at a constant angle ω (in °) relative to the surface of the sample, whilst the detector is moved through 2θ whilst collecting the diffracted intensities. In this way, the depth of penetration of the X-rays into the sample is kept constant (along with irradiated volume and irradiated sample length) whilst the various diffraction angles are measured. Consequently, the greatest diffraction intensity is obtained when θ is equal to ω and decreases linearly as θ increases.

The irradiation length of the incidence beam is particularly important for collecting accurate X-ray diffraction of the sample only. Irradiation of the sample support, commonly referred to as beam spill, will lead to unwanted background effects and incorrect relative peak intensities [224]. Figure 181 illustrates the concept of the irradiation length and irradiation volume [225]. At higher angles of 2θ, the irradiation length decreases whilst the irradiation volume remains constant (assuming the sample is sufficiently thick). The intensity of the diffracted beam will begin to decrease when the irradiation length is longer than the length of the sample. The size of the irradiation length can be decreased by using a smaller divergence slit.

A larger goniometer radius increases the resolution of the diffractometer, but this is at the expense of lower intensity of the diffracted beam due to beam divergence [165]. The divergence of the beam can be quantified as the irradiated sample length. Equation 43 can be used to calculate the irradiated sample length, L (in mm), for a given combination of diffractometer goniometer radius, R (in mm), divergence slit angular opening, α (in °), and incidence beam angle, θ (in °) [224]. It is important to select a divergence slit which will give a reasonable compromise between irradiated sample length (to avoid beam spill) and intensity of the diffracted beam.

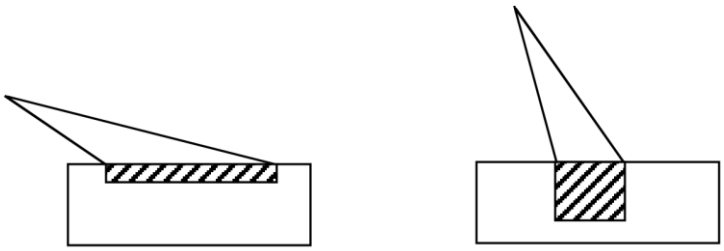

Figure 181 – Diagram illustrating the concept of irradiation length and irradiation volume; reproduced from [225]. For reflection geometry, as the diffraction angle 2θ increases the irradiation length decreases but the irradiation volume stays constant, provided the sample is sufficiently thick.

Equation 43

$$L = \frac{R\tan(\alpha)}{\sin(\theta)}$$

The Bruker D2 diffractometer has a goniometer radius of 141 mm: the variation of irradiated sample length with incidence beam angle is depicted in Figure 182 for a variety of divergence slit widths. The divergence slit angular opening is equal to the divergence slit width multiplied by (° / 2 mm), therefore 1 mm is equivalent to 0.5° and 0.6 mm is equivalent to 0.3°. For a 20 mm diameter sample, a 0.6 mm divergence slit is fine at all angles, and a 1.0 mm divergence slit is appropriate above ~10° 2θ.

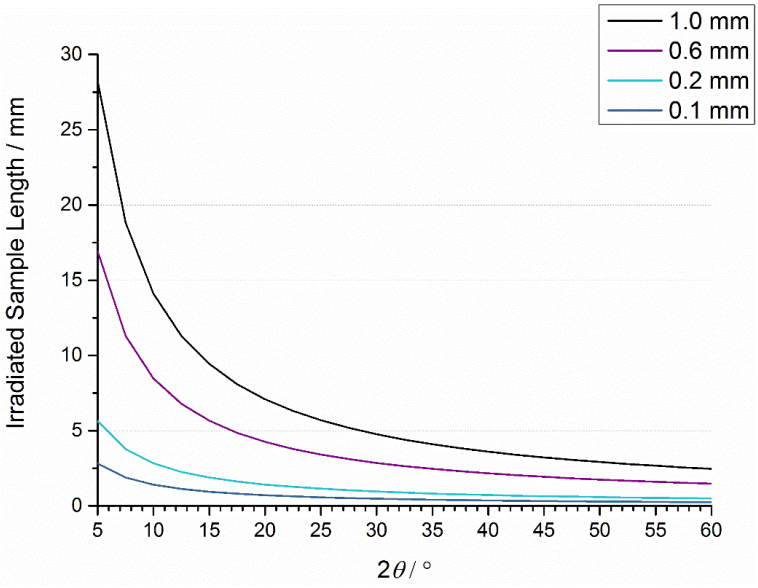

Figure 182 – The variation of irradiated sample length with 2θ for different divergence slit widths on the Bruker D2 Phaser diffractometer.

The Panalytical X'Pert 3 diffractometer has a goniometer radius of 240 mm: the variation of irradiated sample length with incidence beam angle is depicted in Figure 183 for a variety of divergence

slit angular openings. For a 20 mm diameter sample, a 0.25° divergence slit is fine above ~7° 2θ, whereas a 0.5° divergence slit should only be used for angles above ~14° 2θ.

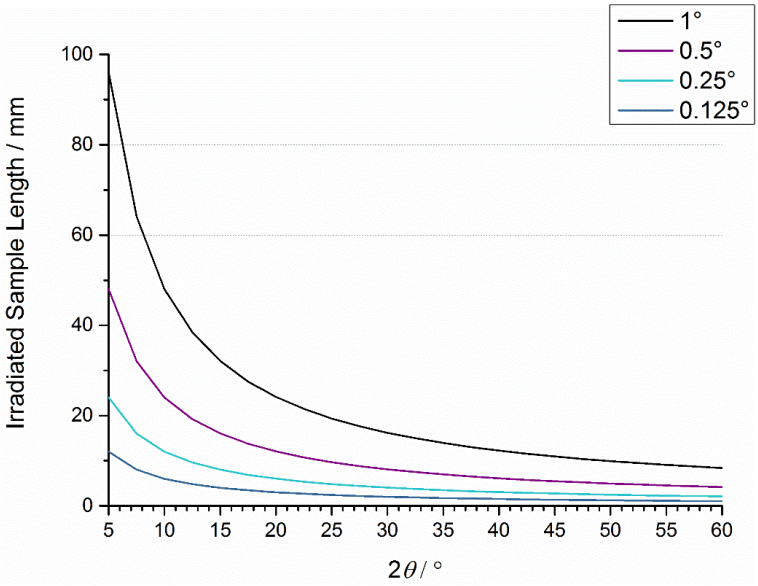

Figure 183 – The variation of irradiated sample length with 2θ for different divergence slit angular openings on the Panalytical X'Pert^3 Powder diffractometer.

11.2.1 Crystallite Size

A crystallite is an individual perfect crystal within a material. Crystallites are commonly referred to as grains; however, grains can contain defects and be split further into domains. Consequently, the crystallite size may differ from the grain size, as grains can consist of multiple crystallites. The size of crystallites between 100-500 nm can be determined from the breadth of peaks in an X-ray diffraction pattern [226].

The breadths of peaks in an X-ray diffraction pattern are affected by instrumental broadening, crystallite size, and lattice strain. Instrumental broadening can be accounted for by measuring the breadths of peaks for an annealed material (to remove lattice strain) with a large grain size (*e.g.* 10 µm). The peak breadth, B (in radians 2θ), is equivalent to the full width half maximum of the peaks. The breadth remaining, B_r, after subtracting the instrumental broadening, B_i, from the observed breadth, B_o, can be calculated in various ways depending on the observed peak shape.

The broadening due to crystallite size, $B_{crystallite}$, can be calculated from the Scherrer equation, shown by Equation 44, where λ (in nm) is the wavelength of the X-rays used, θ (in radians) is the Bragg angle, L (in nm) is the crystallite size, and k is a constant (which can often be assumed to be equal to 1.0).

Equation 44

$$B_{crystallite} = \frac{k\lambda}{L\cos\theta}$$

The broadening due to lattice strain, $B_{lattice}$, can be calculated from Equation 45, where η (in nm) is the lattice strain.

Equation 45

$$B_{strain} = \eta \tan\theta$$

By combining Equation 44 and Equation 45 and multiplying by cosθ, we get Equation 46. By plotting $B_r\cos\theta$ against sinθ, a straight line is obtained, where the gradient is equal to η and L can be determined from the y-intercept. This is illustrated by the diagram in Figure 184.

Equation 46

$$B_r \cos\theta = \frac{k\lambda}{L} + \eta \sin\theta$$

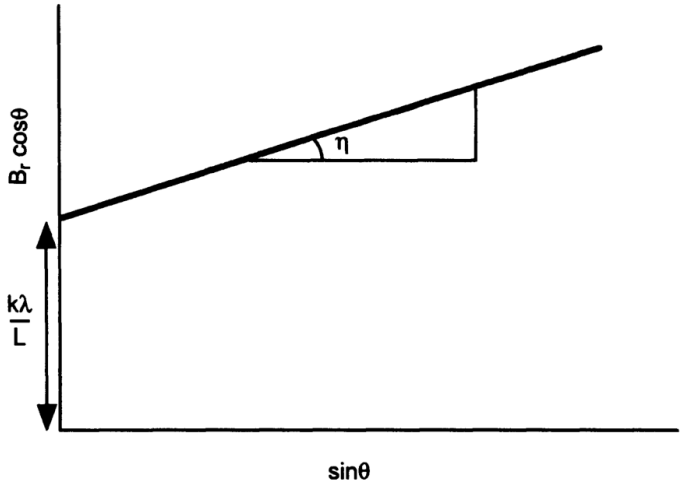

Figure 184 – Diagram showing the linear relationship between $B_r\cos\theta$ aand sinθ, which can be used to calculate the crystallite size and lattice strain; reproduced from [226].

11.3 Scanning Electron Microscopy and Energy Dispersive X-ray Spectroscopy

The use of accelerated electrons for imaging enables microscale and nanoscale observations of materials at high resolution [223]. The de Broglie relationship shows that the wavelength of an accelerated particle is inversely proportional to its mass and velocity. Thus, large velocities of electrons can produce wavelengths smaller than visible light leading to a higher resolution limit as the electrons can distinguish smaller features. The electrons are fired at the surface of a material to produce several signals that can be detected to form an image. These signals are illustrated in Figure 185 [227]. The beam is typically rastered across an area to build up an image but may be focused on a particular point for techniques such as X-ray spectroscopy.

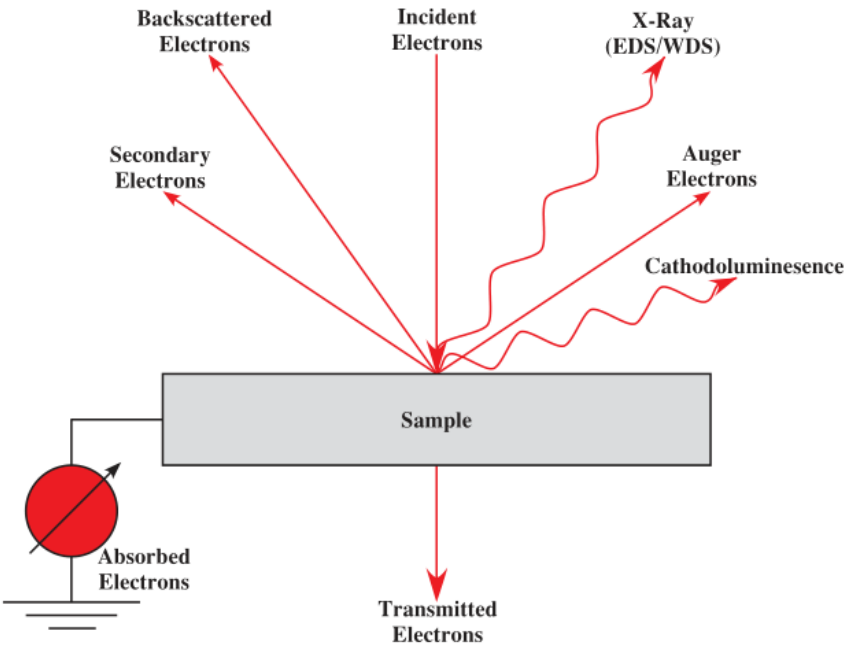

Figure 185 – Diagram of the signals produced by interaction of accelerated electrons with a sample; reproduced from [227].

The most common detection method uses secondary electrons to give a topographical image of the surface. These are low energy electrons released by ionisation of the sample due to inelastic collision of the primary electron beam. The contrast of the image shows the topography of the surface, with bright regions showing higher areas and dark regions showing lower areas.

Backscattered electrons are a result of elastic collisions of the primary electron beam with the sample. Absorption of electrons results in less reflection of the beam, thus providing qualitative information regarding chemical composition. The contrast of the image varies with the atomic mass of the species observed and is therefore affected by chemical composition. Phases with a low average atomic number have lower brightness due to greater electron absorption, whereas phases with a higher average atomic number have greater brightness due to greater reflection.

X-rays enable quantitative chemical characterisation of the sample, providing quantities of elements present at a point or area. An X-ray photon is emitted when an electron removes an internal electron from an atom, causing an outer electron to lose energy as a photon and fill the hole [226]. Energy-dispersive X-ray spectroscopy (EDS) uses an efficient, multi-energy detector whereas wavelength-dispersive X-ray spectroscopy (WDS) directly correlates intensity at individual wavelengths, which is more accurate but time-consuming.

Different photon energies are possible depending upon the transition involved [226]. The most common transition is from a 2p orbital to a 1s orbital; the X-ray observed is referred to as a *K*α emission. The *K*α emission is a doublet due to a shift caused by the interaction of the electron's spin with the

magnetic field produced by its orbit around the nucleus. The most intense of these is the transition from the $2p_{3/2}$ energy level to the 1s energy level, termed $K_{\alpha 1}$, and the least intense is the transition from the $2p_{1/2}$ energy level to the 1s energy level, termed $K_{\alpha 2}$.

11.4 X-ray Photoelectron Spectroscopy

X-ray photoelectron spectroscopy (XPS) is a method of electron spectroscopy [228]. X-rays, typically produced by K_{α} emission from an aluminium anode, are directed at the surface of a sample causing ejection of electrons via the photoelectric effect. The kinetic energies of the resultant electrons are measured, and the difference in energy relative to the incident X-ray photon is characteristic of the electron binding energy and consequently the elements present in the sample. Furthermore, the local environment of an atom will cause small shifts in the energy required for electron emission, indicative of the oxidation states and bonding in the sample. The XPS process is illustrated in Figure 186.

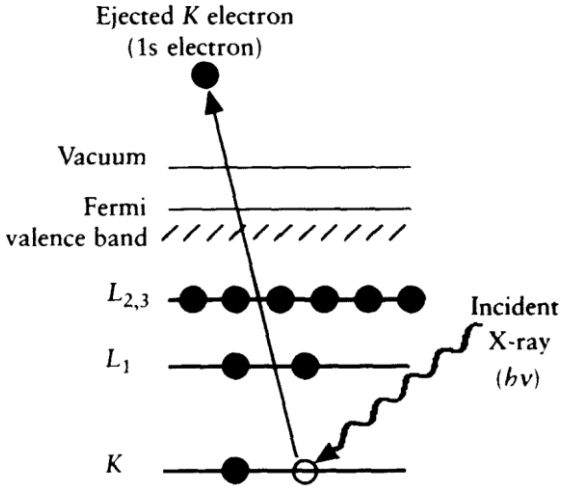

Figure 186 – Diagram of XPS process, showing the X-ray induced ejection of an electron from the 1s orbital of an atom; reproduced from [228].

11.5 Raman Spectroscopy

Raman spectroscopy enables identification of chemical bonds by inelastic scattering of light [229]. Laser excitation of chemical bonds leads to vibration of atoms, causing a loss of energy dependent on the bond strength and atomic masses. The photon emitted when the atoms relax has a longer wavelength than the incident photon and can be observed by a detector. Not all vibrational modes are Raman active as they must involve a change in polarisability upon excitation, which is dependent upon the symmetry of the chemical species. Varying wavelength, a spectrum of vibrational modes is obtained enabling identification of chemical species (Figure 187).

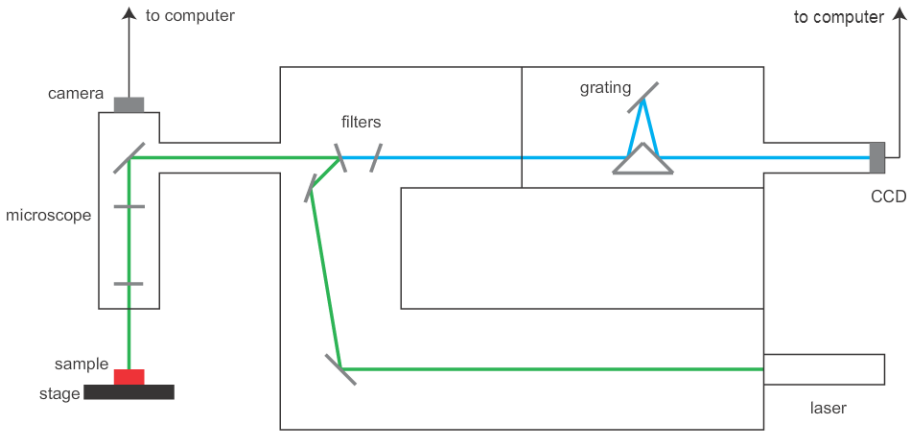

Figure 187 – Diagram of the Raman microspectroscopy apparatus; reproduced from [229].

11.6 Thermal Analysis

Differential thermal analysis, thermogravimetry and mass spectroscopy were conducted on milled powders to improve understanding of the reactions which occur as the powders are heated during SPS. Differential thermal analysis compares the heat taken in or given out as a sample is heated to that of an inert reference. The changes at which endothermic and exothermic transitions occur can then be identified. Thermogravimetric analysis is the process of measuring changes to the mass of a sample as it is heated. Gases may evolve during heating, or the sample may react with gases in the chosen atmosphere, and the temperature at which such reactions occur can be identified from the change in mass. A mass spectrometer can be used with a simultaneous thermal analyser to identify any changes to the composition of gas stream as the sample is heated.

11.7 Indentation Hardness Testing

Hardness measures the resistance to deformation of a material by a scratch or an indent [223]. Indentation hardness testing is a technique whereby a sharp tip made of a hard material, typically diamond, is pressed into the surface of a polished sample with increasing force up to a defined maximum. The size of the indent is measured and used to calculate the hardness. There are numerous hardness testing methods which vary mainly by the geometry and size of the indentation tip.

Vickers microhardness testing uses a tip which is on the micrometer scale in size [223]. It uses a square-based pyramidal diamond tip where the angle between opposite corners of the base and the point is equal to 136°. The hardness measurement it provides is dependent on the microstructure as both grains and grain boundaries will be incorporated in hardness measurements.

Nanoindentation hardness testing uses a much smaller tip with nanoscale dimensions [230,231]. The small size allows grain boundaries to be avoided. Consequently, the result obtained should be comparable to a single crystal of the material. The sample must be polished as flat as possible.

During nanoindentation hardness testing, the depth of penetration is measured as the force is increased and plotted as a load-displacement curve, such as Figure 188, where P_{max} (in GPa) is the maximum applied load, h_{max} (in nm) is the displacement measured at the maximum applied load, h_f (in nm) is the final displacement measured after the load is removed, and S (in N m^{-1}) is the stiffness. The material only partially recovers from the displacement, and the amount by which it recovers is related to the elastic modulus and the size of the indent. The initial gradient of the curve upon unloading is proportional to the stiffness of the material, which is also proportional to the reduced Young's modulus, E_r (in GPa), as per Equation 47, where A is the area of the indentor (in nm^2) [230]. The reduced Young's modulus accounts for the effects of non-rigid indenters, and can be used to calculate the Young's modulus of the materials provided the Poisson's ratios of the sample and the indenter are known in addition to the Young's modulus of the indenter [230].

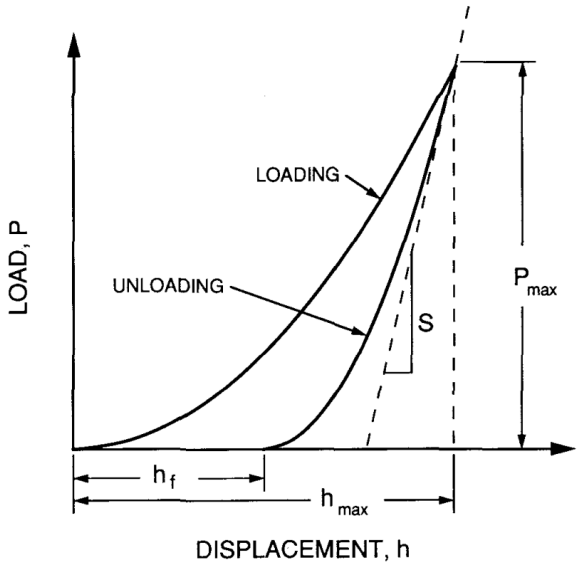

Figure 188 – Diagram of a load-displacement curve measured by nanoindentation hardness testing; reproduced from [230].

Equation 47

$$S = \frac{dP}{dh} = \frac{2}{\sqrt{\pi}} E_r \sqrt{A}$$

The hardness, H (in GPa), measured by nanoindentation can be calculated using Equation 48 [230].

Equation 48

$$H = \frac{P_{max}}{A}$$

11.8 Profilometry

Profilometry is the process of measuring the surface topography of a material, the results of which can be used to calculate the surface roughness. Profilometers can be split broadly into contact

profilometers and optical profilometers. Contact profilometers use a stylus, typically a diamond tip, which is dragged across the surface whilst measuring its displacement. Optical, or non-contact, profilometers use light to obtain a 3-dimensional image of the sample surface. There are various methods of measuring the roughness from the surface profile, but the most common method is to use the arithmetical mean deviation of the profile, the value of which is referred to as the average roughness, R_a (in µm), and is calculated via Equation 49, where y_i (in µm) is the deviation from the centre line through the profile along the measured length [232].

Equation 49

$$R_a = \frac{1}{n}\sum_{i=1}^{n}|y_i|$$

11.9 Electrochemical Techniques

11.9.1 Chrono Potentiometry

Chrono potentiometry measures the voltage over time as a current is applied to the system. If no current is applied, then the technique can be used to measure the open circuit potential of the system (*i.e.* the potential of the overall reaction which spontaneously occurs, proportional to the Gibbs free energy of reaction). Application of a positive current will cause anodic dissolution of a sample.

11.9.2 Cyclic Voltammetry

Cyclic voltammetry is used to determine the potentials at which redox reactions occur within a system. A potential is applied and scanned within the potential window whilst the current is measured. The peaks observed represent redox reactions within the system: the potential is proportional to the Gibbs free energy change of the process and the current is proportional to the extent of reaction.

12 Appendix B – Synthesis of Ti_3AlC_2: Additional Results

12.1 Additional data for previously presented samples

12.1.1 Sintering profiles

The sintering profiles for all the samples of Ti_3AlC_2 prepared from a precursor milled in a SPEX 8000M Mixer/Mill all had the same profile shape but slightly different onset temperatures for changes in piston movement. The additional profiles are summarised here in Figure 189 to Figure 195.

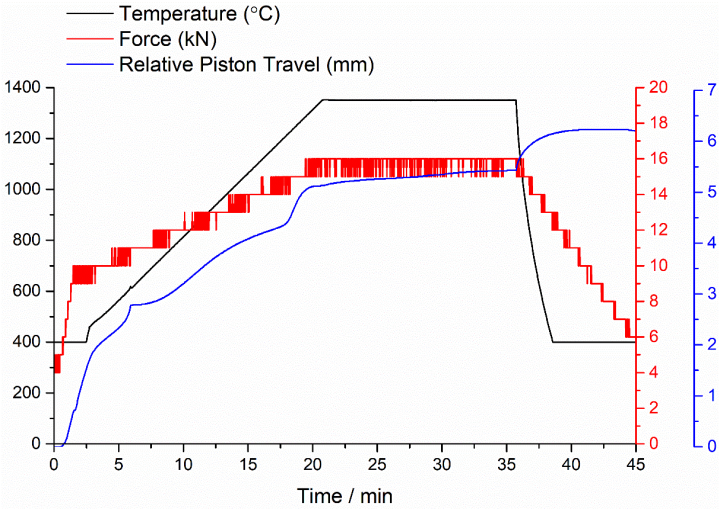

Figure 189 – Sintering profile for a sample prepared from TiC_x which was milled for 3 h.

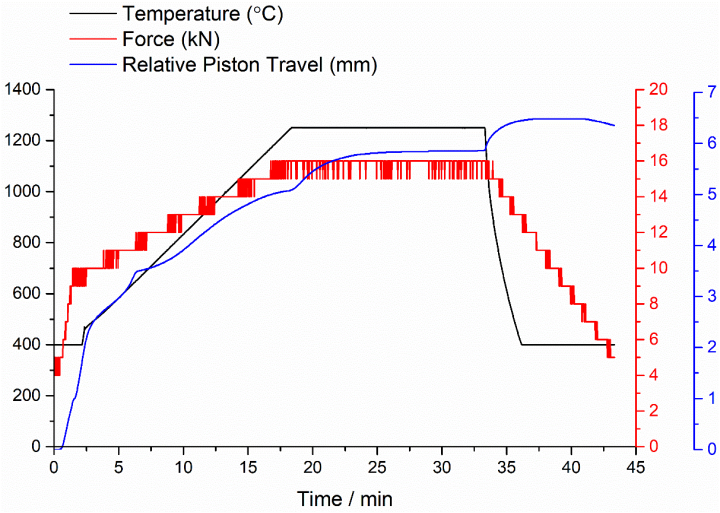

Figure 190 – Sintering profile for a sample prepared at a holding temperature of 1250°C.

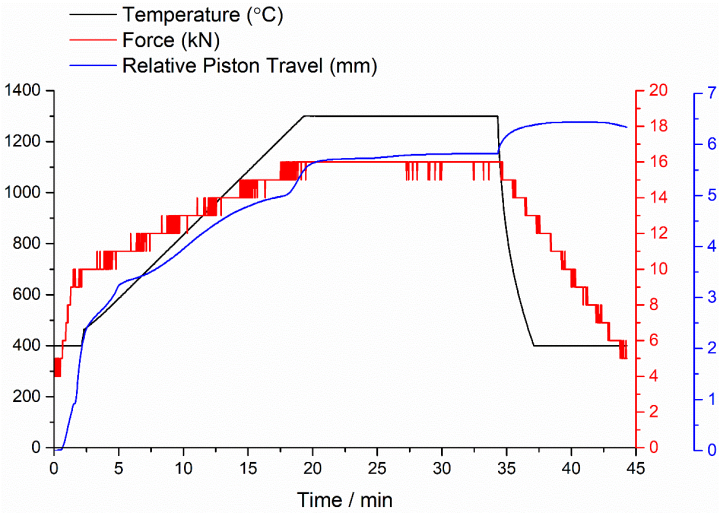

Figure 191 – Sintering profile for a sample prepared at a holding temperature of 1300°C.

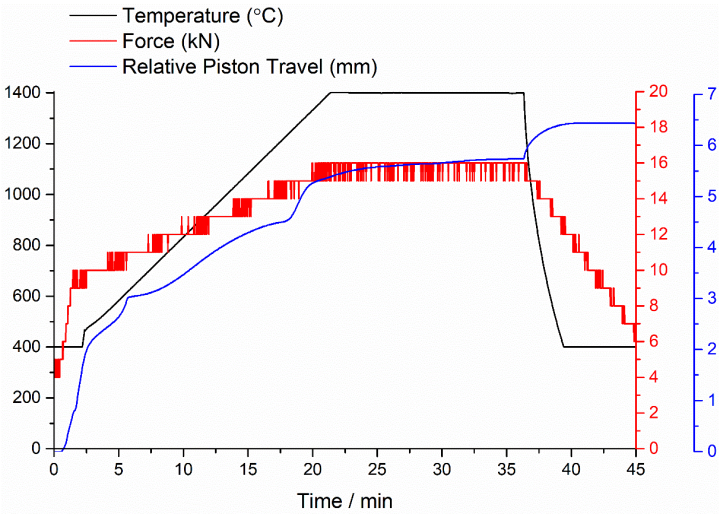

Figure 192 – Sintering profile for a sample prepared at a holding temperature of 1400°C.

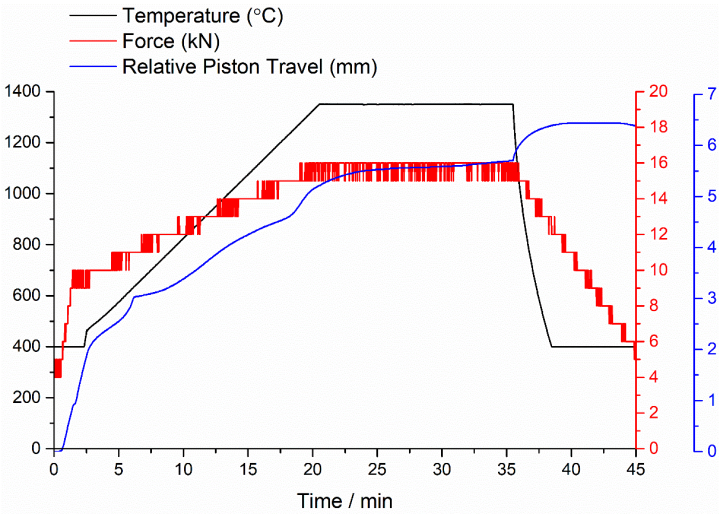

Figure 193 – Sintering profile for a sample prepared using 1.2 parts Al.

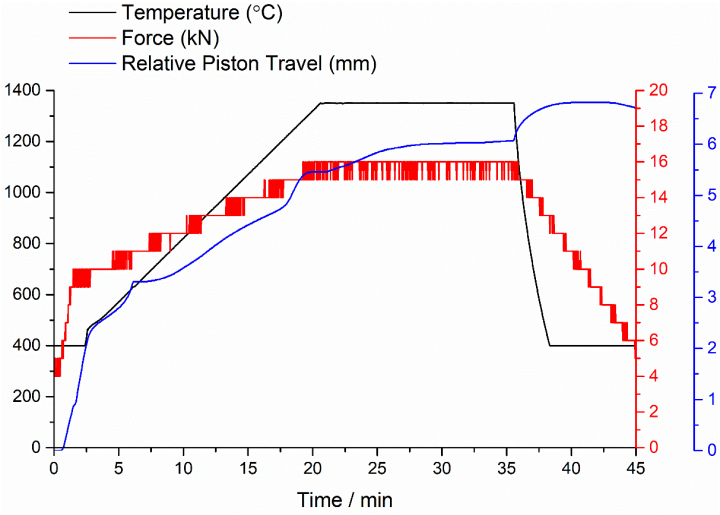

Figure 194 – Sintering profile of a sample which was prepared using 1.3 parts Al.

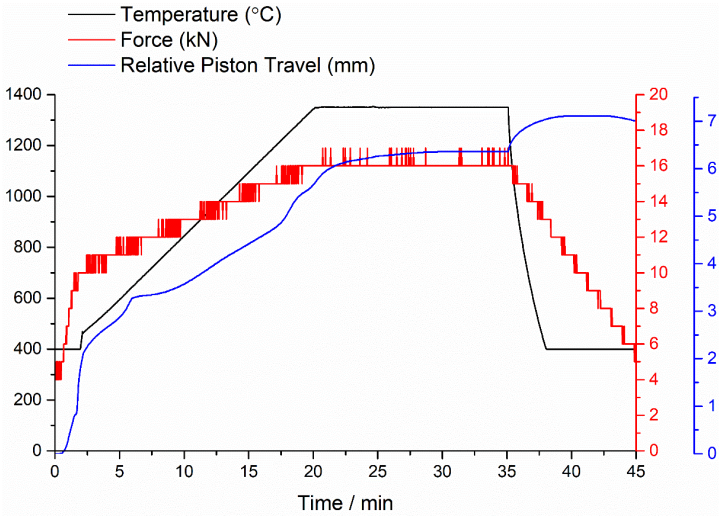

Figure 195 – Sintering profile of a sample which was prepared using 1.4 parts Al.

12.2 Synthesis from Ti, Al and TiC mixed using a Retsch Cryomill

Four samples were prepared from titanium, aluminium and titanium carbide. The first three samples were mixed without milling media in a Retsch Cryomill at liquid nitrogen temperature for 30 min in 5 min intervals. These samples were sintered at holding temperatures of 1300°C and 1350°C and dwell times of 15 min and 30 min. A fourth sample was prepared by including a 25 mm diameter hardened steel ball during milling, then sintered at 1350°C for 15 min.

A Retsch Cryomill was used to mill the initial samples due to the ability to seal the milling vessel in a glovebox under an argon atmosphere. Titanium and aluminium powders are pyrophoric and therefore should be handled in an inert atmosphere. The first samples were prepared without milling media to test the quality of the seal. No oxides were found in the as-sintered products, suggesting the seal was reasonable.

The sample sintered at 1300°C for 15 min followed synthesis parameters reported by Zou *et al.*, who found the ideal sintering conditions using Ti, Al and TiC were 1300°C and 15 min [74]. Zou *et al.* carried out synthesis using numerous combinations of reagents [56,58,73–75]. In this work, Ti, Al and TiC were used initially under the assumption that Ti and C would react to form TiC during the reaction process. Hence, it was believed that using TiC would decrease the required steps in the mechanism and thus produce better results. SPS pulse times were not presented by Zou *et al.*, so 12/2 s on/off pulse times used by Gao *et al.* in the synthesis of Ti_3SiC_2 were used [233].

Qualitative phase analysis by XRD showed the sample was multiphase, containing Ti_3AlC_2, Ti_2AlC and TiC. A fourth, minor phase was visible in the EDS maps. The high proportion of Ti_2AlC suggested the reaction was incomplete, so the effects of sintering for a longer dwell time of 30 min and a higher temperature of 1350°C were investigated. Analysis of these additional samples showed both samples were again multiphase. Doubling the dwell time reduced the intensity of Ti_2AlC peaks and increased the intensity of Ti_3AlC_2 peaks but was accompanied by an increase in intensity of TiC peaks, most likely due to evaporation of Al [54,76,187,192]. Sintering at 50°C higher temperature gave optimum conditions; the Ti_3AlC_2 peaks were most intense of the three samples while the TiC peaks were least intense. The density of this sample was also closest to the theoretical density of Ti_3AlC_2.

The low purity of these initial samples was likely due to the lack of milling media used when mixing. Zou *et al.* milled powders for 24 h in a Turbula shaker mixer under an argon atmosphere but did not specify the milling media used [74]. Therefore, the difference relative to Zou *et al.* was most likely due to the difference in milling conditions and consequently particle size reduction and extent of mixing. A 25 mm diameter hardened steel ball was included during milling (BPR ~8.4) and a sample was prepared by sintering for 15 min at 1350°C. Results improved significantly, albeit Ti_2AlC was still present as a major impurity alongside a minor impurity of TiC. The density was closest of all four samples to the theoretical density of Ti_3AlC_2.

12.2.1 X-ray diffraction

The XRD patterns for the samples produced without using milling media are shown in Figure 196. Data were collected on a Bruker D2 phaser with a step size of 0.02° 2θ. The major peaks were labelled using reference patterns for Ti_3AlC_2, Ti_2AlC and TiC from the ICSD database [178,234–237]. The Ti_3AlC_2 (002) peak showed a clear increase for the sample produced at 1350°C for 15 min, while the TiC (111) peak was also significantly less intense. Therefore, a holding time of 1350°C and dwell time of 15 min was used for subsequent samples.

Figure 197 shows an indexed XRD pattern for a sample prepared from Ti, Al and TiC powders which were milled for 30 min at liquid nitrogen temperature in a Retsch cryomill. Sintering was performed at 1350°C for 15 min. The XRD pattern was collected on a Bruker D2 Phaser with a step

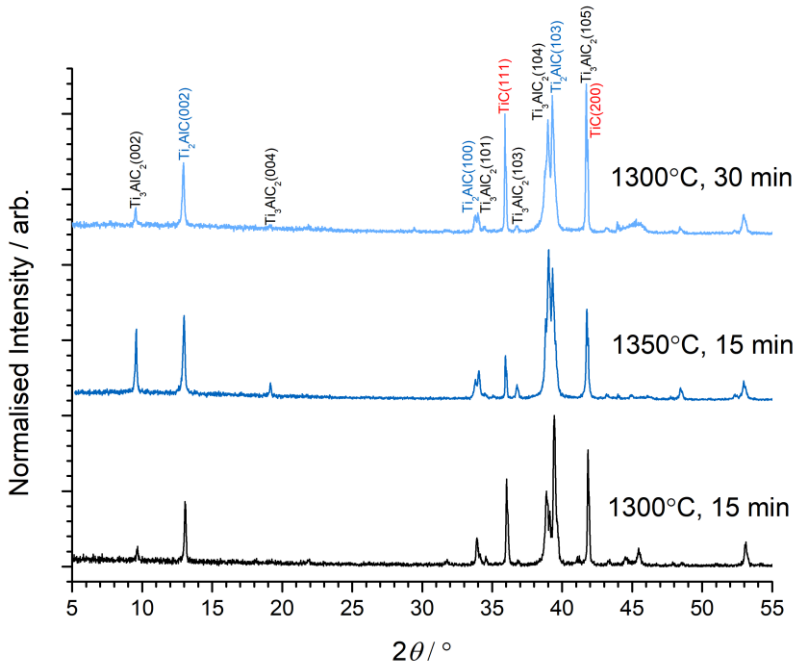

Figure 196 – XRD patterns of samples prepared from Ti, Al and TiC without using milling media.

size of 0.02° 2θ. In comparison to the sample produced without milling media, the Ti_3AlC_2 (002) peak has increased in intensity relative to the Ti_2AlC (002) peak indicating that the product was purer.

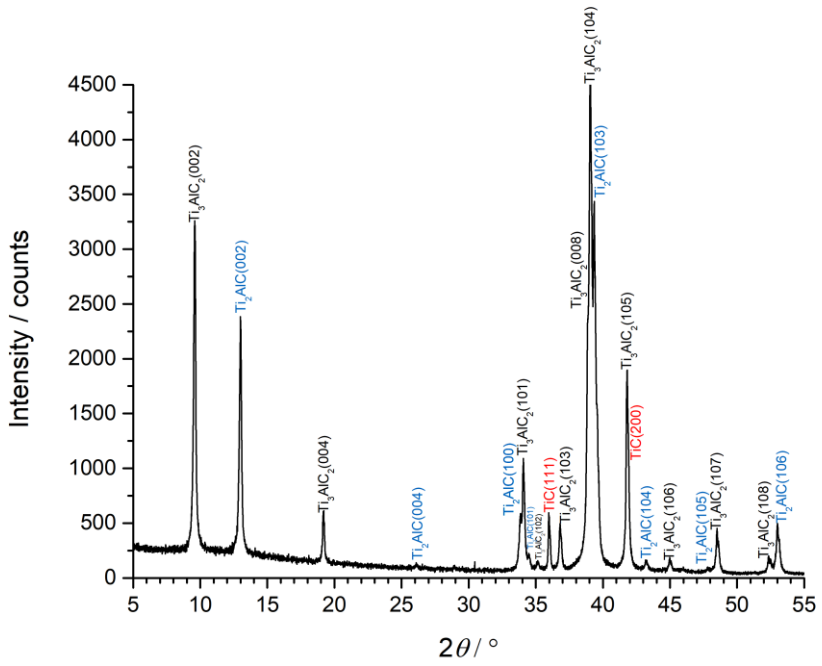

Figure 197 – XRD pattern of a sample prepared from Ti, Al and TiC powders which were milled for 30 min at liquid nitrogen temperature in a Retsch cryomill.

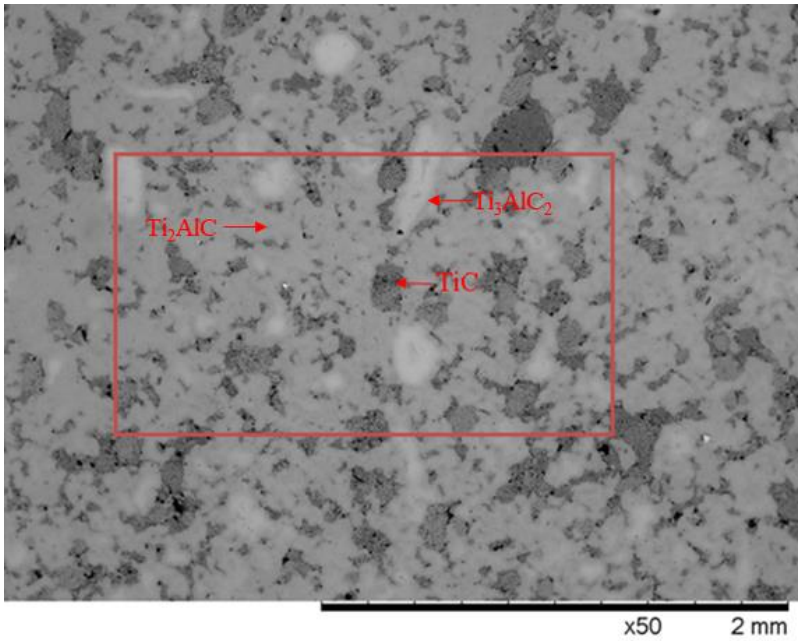

(a) BSE image at x50 original magnification

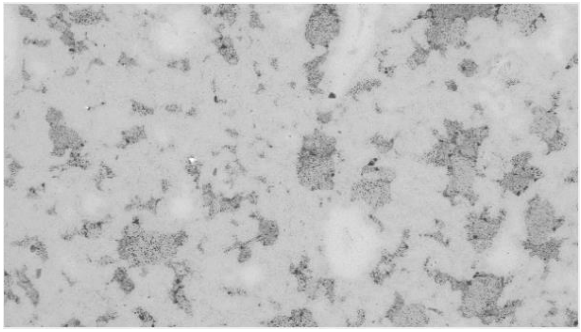

(b) Section of the BSE image

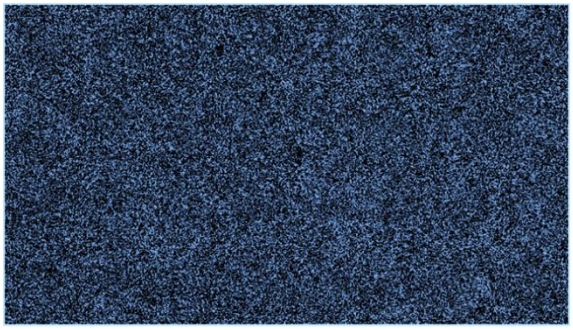

(c) Ti $K_{\alpha 1}$

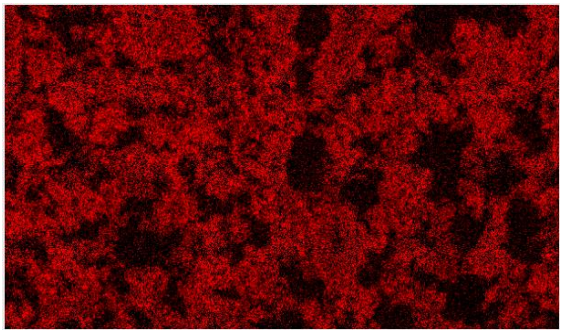

(d) Al $K_{\alpha 1}$

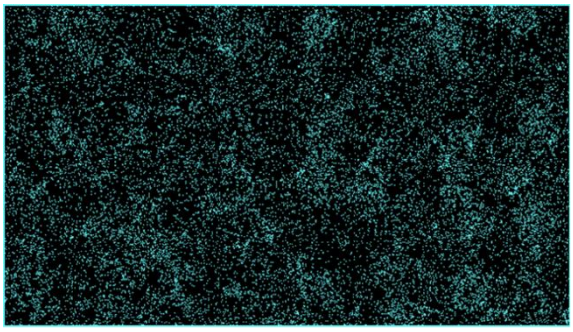

(e) C $K_{\alpha 1}$ and $K_{\alpha 2}$

Figure 198 – BSE image and EDS maps of a sample produced from Ti, Al and TiC by sintering at 1300°C for 15 min.

12.2.2 Density

Table 41 contains the densities of samples prepared from Ti, Al and TiC [74]. When submerged in water each sample formed bubbles on its surface, indicating porosity. Thus, the standard deviations

were relatively large, and the densities shown are the first measurements only. Among the samples prepared without milling media, the density of the sample sintered at 1350°C for 15 min was closest to the theoretical density of Ti_3AlC_2, 4.25 g cm^{-3}. The sample prepared using a 25 mm hardened steel ball while milling had the greatest density.

Table 41 – Densities of all samples produced from Ti, Al and TiC.

Sintering Temperature / °C	Dwell Time / min	Milling Media	Density / g cm^{-3}
1300	15	None	3.27
1350	15	None	4.01
1300	30	None	3.88
1350	15	25 mm hardened steel ball	4.11

12.2.3 Microstructural examination

Figure 198 is a representative BSE image at low original magnification with an EDS map of the sample sintered at 1300°C for 15 min. The image was collected on a Hitachi TM3030. Four levels of contrast are present, although the XRD pattern shows only three phases. At the magnification used it is difficult to distinguish the composition of the darkest spots; they may be pores, although Raman spectroscopy on a later sample suggests they are likely α-Al_2O_3 (§ 12.3.3). The large sections of dark grey contrast are TiC, as shown from the lack of Al in the EDS map. The medium grey and light grey contrast represent Ti_2AlC and Ti_3AlC_2 respectively.

12.3 Synthesis via a TiC_x precursor using a Restch Cryomill at ambient-temperature

A sample of ~98% pure Ti_3AlC_2 was produced from a TiC_x precursor which was mixed with aluminium and reactively sintered by SPS. The precursor was formed by milling titanium (6.4 g) and graphite (1.1 g) continuously for 4 h at ambient temperature in a Retsch cryomill, with a ball-to-powder mass ratio of 8.4. The vessel was loose after milling and material had been lost. The resultant 6.2 g was mixed with 1.0 g aluminium and reactively sintered. The sintering parameters were determined from earlier synthesis attempts using Ti, Al and TiC as reagents. An additional sample prepared with slight error in the quantities (+0.1 g Ti and -0.1 g C) contained a similarly high quantity of Ti_3AlC_2.

12.3.1 X-ray diffraction and density

Figure 199 shows the indexed XRD pattern and Rietveld refinement fit of the bulk sample (χ^2 4.716, R_p 0.1143, R_{wp} 0.1455). The data was collected between 5-80° 2θ on a Bruker D2 Phaser with a step size of 0.01° 2θ and a time per step of 0.6 s. Most peaks correspond to Ti_3AlC_2, but there are some very low-intensity peaks visible which correspond to Al_2O_3. The lattice parameters, volumes and weight fractions of the two phases are summarised in Table 42. The density was 4.227 ± 0.087 g cm^{-3}, which corresponds a relative density of 99.7% based on the weight fractions from Rietveld refinement.

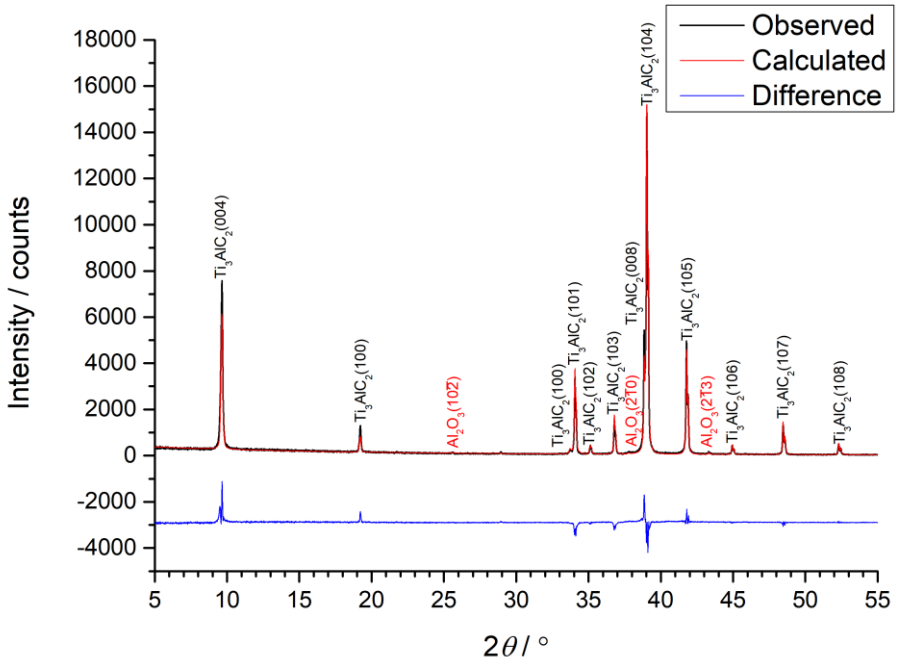

Figure 199 – Indexed XRD pattern and Rietveld refinement fit of a bulk sample of Ti_3AlC_2. Ti and C were milled for 4 h at ambient temperature in a Retsch cryomill then reactively sintered with Al by SPS.

Table 42 – Crystal properties from Rietveld refinement of a bulk sample of Ti_3AlC_2. Ti and C were milled for 4 h at ambient temperature in a Retsch cryomill then reactively sintered with Al by SPS.

Phase	a / Å	c / Å	Volume / Å^3	Weight Fraction / wt.%
Ti_3AlC_2	3.077	18.575	152.265	98.2
Al_2O_3	4.773	13.034	257.115	1.8

Initially, a sample was milled for 2 h but XRD showed Ti peaks only. The work of Riley and Kisi stated that ignition occurred after milling for 109 min (~2 h) and produced non-stoichiometric TiC_x [77,85]. Riley and Kisi used a SPEX 8000M Mixer/Mill with three 10 mm diameter and six 5 mm diameter hardened steel balls with ~6.3 g reagent, giving a BPR of ~10:1 [72]. Therefore, the difference was likely due to less efficient mixing with a single hardened steel ball and possibly a lower milling energy in the Retsch Cryomill, so it was decided to mill in further 1 h periods and perform XRD until TiC_x was observed. At 3 h, the powder was still Ti. At 4 h, the powder ignited during preparation of the XRD sample, which indicated the temperature of the powder was at the critical point of ignition. The powder was then milled for a further hour and XRD using a controlled atmosphere sample holder showed peaks of TiC_x. A sample was prepared from this powder by sintering at 1000°C, the temperature used by Riley and Kisi [77,85], but the purity was terrible and multiple phases were present. It is worth noting that it is not clear from Riley and Kisi's work what the purities of their products were, although they do suggest the product was very pure [77,85].

12.3.2 Microstructural examination

Figure 200 is a BSE image which is representative of the surface of the sample. The image was taken after polishing with colloidal silica, using a lower accelerating voltage on the SEM and maximising the contrast to reveal the grain boundaries. Most of the material is a lighter contrast phase, and darker contrast particles are distributed throughout. XRD indicates the lighter contrast phase is Ti_3AlC_2 while the darker contrast spots are Al_2O_3. The rectangular grain shape and laminar structure typical of MAX phase materials can be observed [73,74].

Image analysis was used to obtain the grain size of the material from four images taken at an original magnification of x5000, as per the image which is shown in Figure 200. The distributions of length, width and aspect ratio are shown in Figure 201. The mean length, width and aspect ratio of all 114 measurements (including outliers) were 9.6 ± 4.6 µm, 2.5 ± 1.3 µm and 4.0 ± 1.6 respectively. Overall, there appears to be a bimodal distribution of length and width, whereas the aspect ratio is unimodal. Unfortunately, at the magnification used most of the larger grains did not fit entirely in the image and were not measured, so the distribution is skewed towards smaller grain sizes. The values of the median and the mean in the box plots, which exclude the outliers, are therefore representative of the grain size of smaller grains.

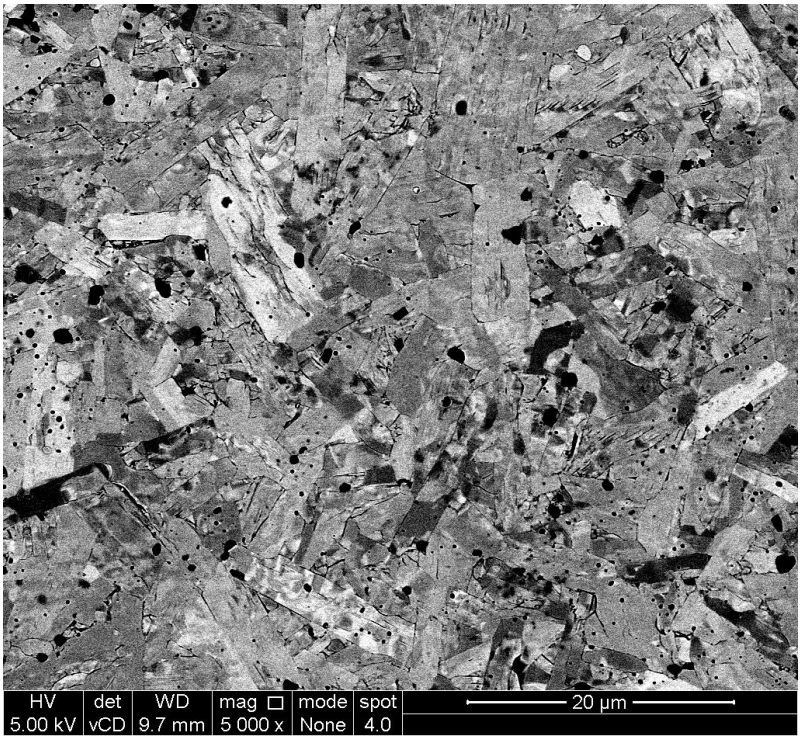

Figure 200 – BSE image showing a general view of a sample of Ti_3AlC_2; a TiC_x precursor was produced using a Retsch cryomill then reactively sintered with Al by SPS. The sample was polished using colloidal silica, and the contrast was maximised to reveal the grain boundaries.

Figure 202 shows a BSE image and EDS maps of the sample obtained using a Hitachi TM3030. The EDS maps confirm that the lighter contrast phase consists of Ti, Al and C, and is therefore Ti_3AlC_2. The regions of darker contrast lack Ti and C but contain Al and O, confirming the presence of aluminium oxide as an impurity. The round shape of these regions suggests they may be due to unreacted aluminium during processing, likely due to it being present in excess; conversely, oxidation of the aluminium layers of MAX phase grains at the surface would likely lead to rectangular aluminium oxide grains, and the maps would not lack titanium and carbon in these regions.

Image analysis was used to determine the volume fraction of the alumina spots . Figure 203, taken at an original magnification of x1000, contained a volume fraction of < 2vol.% Al_2O_3, in agreement with the fraction determined by Rietveld refinement.

12.3.3 Raman spectroscopy

A representative Raman spectrum, collected over ten accumulations with an exposure time of 60 s, is shown in Figure 204. The peak locations were determined by curve fitting using a Voigt peak profile, and the peak centres are listed in Table 43. The peak centres were compared to those found by Presser *et al.* for Ti_3AlC_2 [238] and Gallas *et al.* for α-Al_2O_3 [239]. The presence of α-Al_2O_3 peaks confirms the chemical structure of the spots of darker contrast observed by microstructural examination.

12.3.4 Indentation hardness testing

Indentation hardness testing was used to non-destructively obtain basic mechanical properties of the material. The Vickers hardness obtained from 12 measurements at 10 kN force was 4.0 ± 0.3 GPa. This value agrees with that from Tzenov and Barsoum, who obtained a value of ~3.5 GPa for a sample with a grain size of ~25 µm [187].

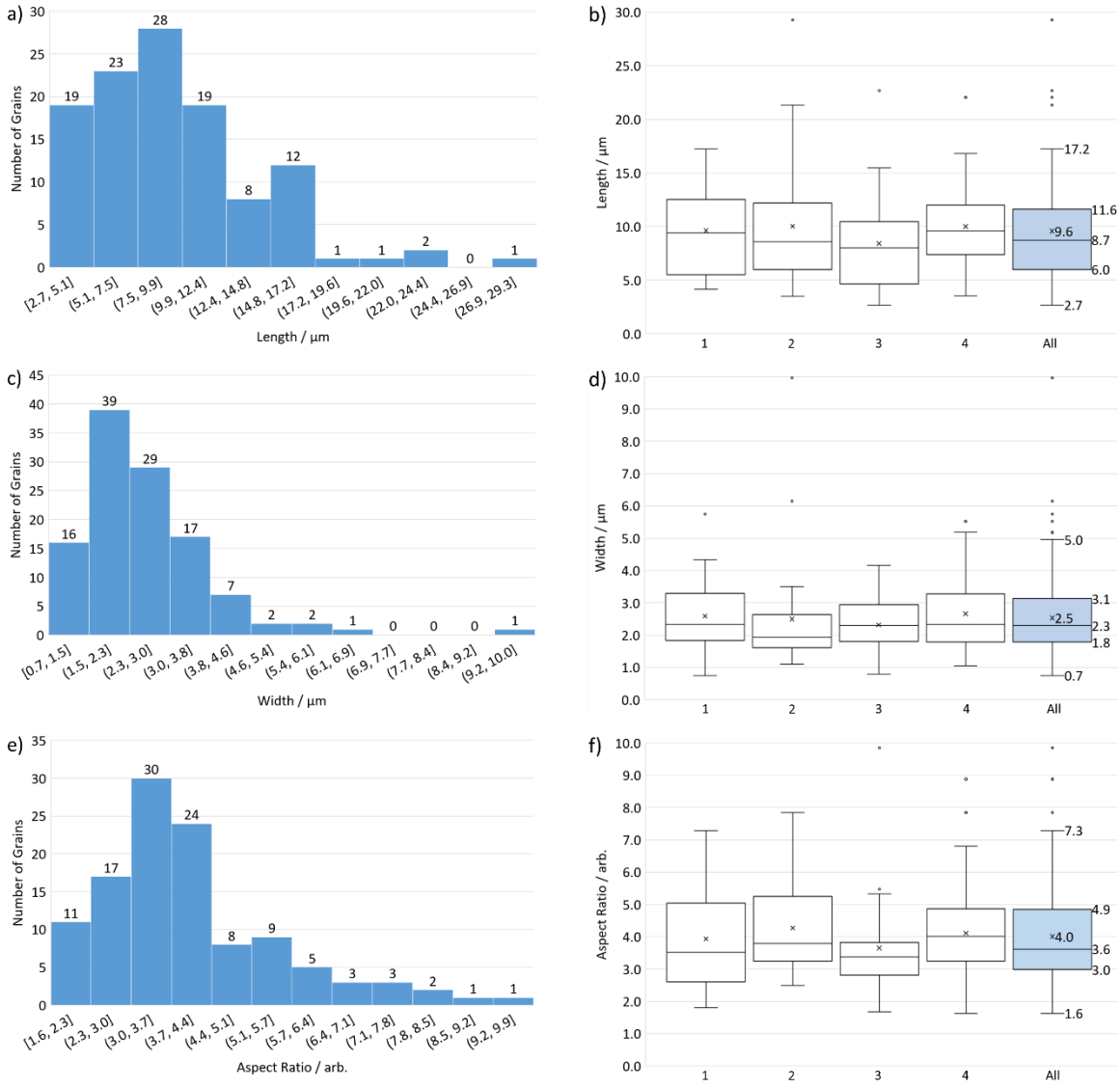

Figure 201 – Histograms and box plots of the length, width and aspect ratio of grains measured from four images. The lines in the box plots, from bottom to top, show the minimum, first quartile, median, third quartile and maximum. The X shows the mean, and the circles mark the outliers.

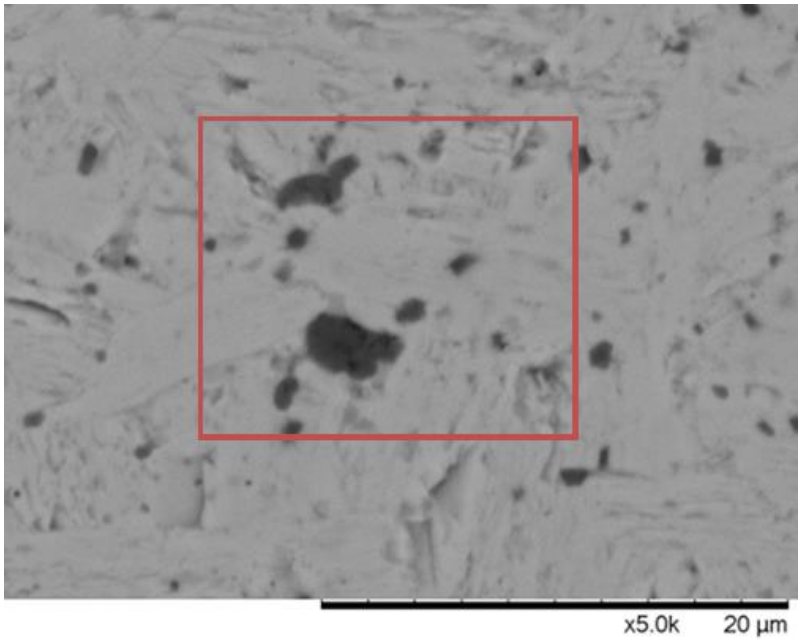

a) BSE image

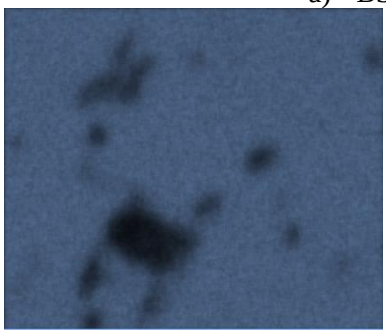

b) Ti $K_{\alpha 1}$

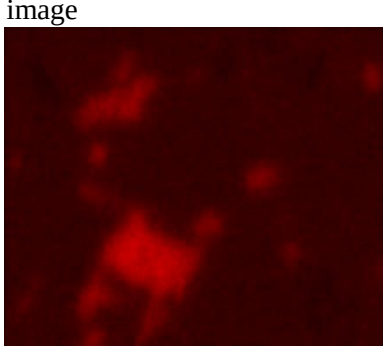

c) Al $K_{\alpha 1}$

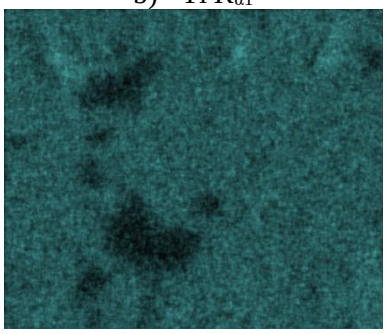

d) C $K_{\alpha 1}$ and $K_{\alpha 1}$

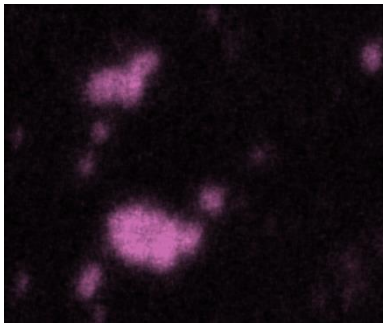

e) O $K_{\alpha 1}$

Figure 202 – BSE image and EDS maps of a bulk sample of Ti_3AlC_2, prepared from Ti and C milled for 4 h at ambient temperature in a Retsch cryomill then reactively sintered with Al by SPS. The images show the presence of aluminium and oxygen at the dark contrast spots, suggesting the presence of particles of aluminium oxide.

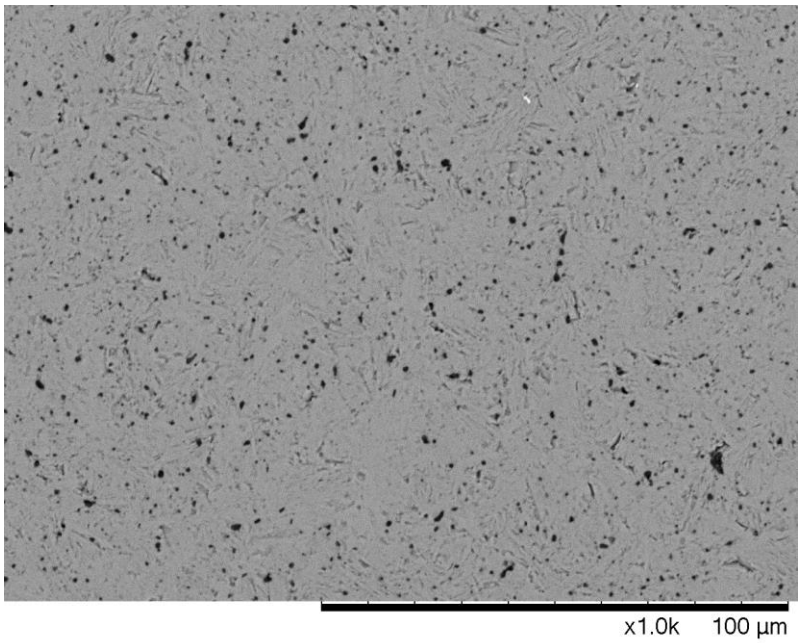

Figure 203 – BSE image representative of a bulk sample of Ti_3AlC_2; Ti and C were milled for 4 h at ambient temperature in a Retsch cryomill, then reactively sintered with aluminium by SPS.

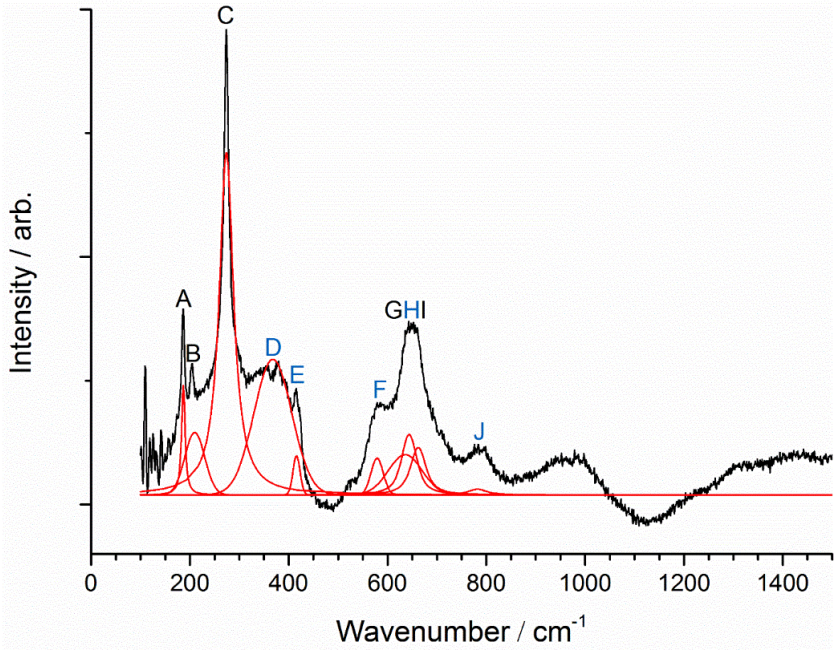

Figure 204 – Raman spectrum of a bulk sample of Ti_3AlC_2; Ti and C were milled for 4 h in a Retsch cryomill at ambient temperature then reactively sintered with Al by SPS. The red peaks were fit using a Voigt fitting profile.

Table 43 – Wavenumbers of peaks observed in Figure 204 and corresponding references for Ti_3AlC_2 [238] and α-Al_2O_3 [239].

Peak	Wavenumber (Observed) / cm^{-1}	Wavenumber (Ti_3AlC_2) / cm^{-1}	Wavenumber (α-Al_2O_3) / cm^{-1}
A	187	183.4	-
B	210	201.5	-
C	274	270.2	-
D	368	-	379
E	416	-	418
F	579	-	578
G	636	632.2	-
H	644	-	645
I	662	663.2	-
J	782	-	760

Nanoindentation hardness testing was performed on a sample which was mounted in conductive Bakelite and polished with colloidal silica. Nanoindentation was performed in four locations with nine measurements per location in a 3 x 3 grid. Five measurements were discarded as erroneous. The mean contact depth was 131.0 ± 10.7 nm, the mean hardness was 12.9 ± 1.5 GPa, and the mean reduced Young's modulus was 208.1 ± 22.6 GPa. The hardness and modulus of each indent are shown in Figure 205a and Figure 205b respectively. A typical load-displacement curve is shown in Figure 205c. Due to the layered nature of the materials, several "pop-ins" were observed in the load-displacement curves, an example of which is shown in Figure 205d. Hence, the range of both the hardness and reduced modulus was broad.

The mean hardness obtained from nanoindentation was higher than the Vicker's hardness value; this is typically the case for nanoindentation methods, and the difference is due to an indentation size effect, where the hardness value increases with decreasing load and penetration depth [86,187]. Bei *et al.* performed nanoindentation at eight different loads between 1-250 mN and observed that the hardness decreased as the applied load increased [86]. Therefore, they fit the hardness values using a model proposed by Nix and Gao [240], obtaining a value of intrinsic hardness of 11.4 ± 0.7 GPa [86]. The hardness value in this work was obtained at a load of 10 mN and is slightly higher than the intrinsic hardness measured by Bei *et al.*, but it fits within the error for the value they obtained at a load of 10 mN. Bei *et al.* observed that the Young's modulus did not change with load and had an average value of 260 ± 10 GPa. The reduced Young's modulus obtained in this work was lower than the value obtained by Bei *et al.* The pop-ins observed are typical of MAX phase materials and are due to movement of the kink bands after sufficient force is applied [38].

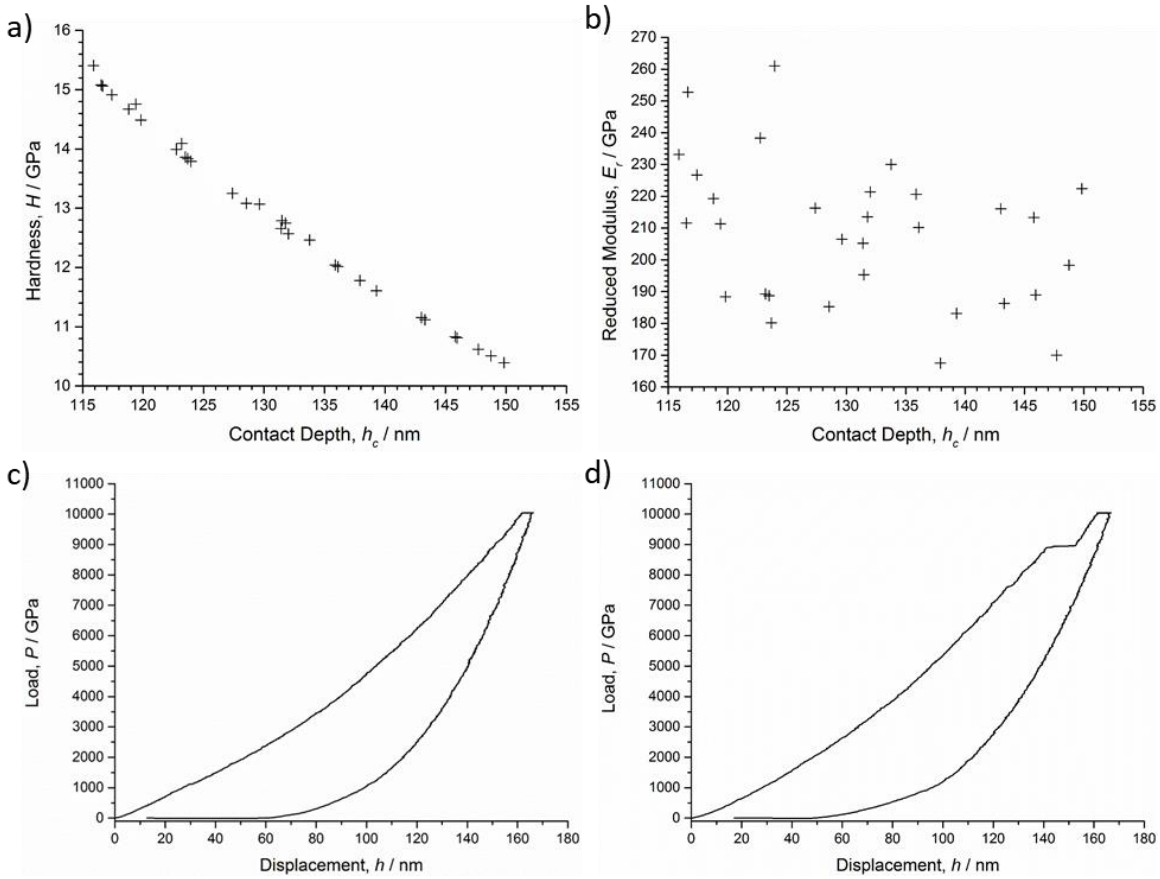

Figure 205 – Nanoindentation measurements for Ti_3AlC_2: a) hardness measurements from 31 indents; b) reduced Young's modulus measurements from 31 indents; c) typical load-displacement curve; d) load-displacement curve with "pop-in" due to the layered nature of the material.

Unfortunately, this synthesis method proved unsuitable for preparing additional samples because the vial loosened when milling and material was lost. Furthermore, the powder used to prepare this sample was not characterised. The pyrophoric nature of the powder meant that closed system methods were required for characterisation, and it was assumed at the time that the sample could be repeated later if it worked. Therefore, it is not certain whether stoichiometric or non-stoichiometric TiC_x was formed by milling, or if the powder was simply a mixture of Ti and C with very small particle size.

12.4 Syntheis via a TiC_x precursor using a hardened steel vial and milling media

A sample of Ti_3AlC_2 was prepared by the precursor method using a hardened steel vial and milling media to prepare the TiC_x precursor in a SPEX 8000M Mixer/Mill. The molar ratio of reagents was Ti:Al:C 3:1:2 with a total mass of 7.5 g. Consequently, the mass of Ti was 5.53 g and the mass of C was 0.93 g. The two 12.7 mm diameter hardened steel balls weighed 16.6 g, resulting in a BPR of 2.6 (*c.f.* 3.3 for the WC milling media). The sample was sintered at 1350°C for 15 min.

The indexed XRD pattern, fitted by Rietveld refinement, is shown in Figure 206 (χ^2 3.260, Rp 0.0789, wRp 0.1033). The major phase was Ti_3AlC_2 (92wt.%), and the minor phase was TiC_x (8wt.%). The lattice parameters were as follows: *a*(Ti_3AlC_2) 3.080 Å, *c*(Ti_3AlC_2) 18.615 Å, and *a*(TiC) 4.333 Å. The measured density was 4.183 ± 0.005 g cm^{-3}, giving a relative density of 97%. Based on the ball-to-powder mass ratio, the milling time, and the subsequent weight fractions of phases, the sample is essentially intermediate of the 1 h and 2 h milled samples.

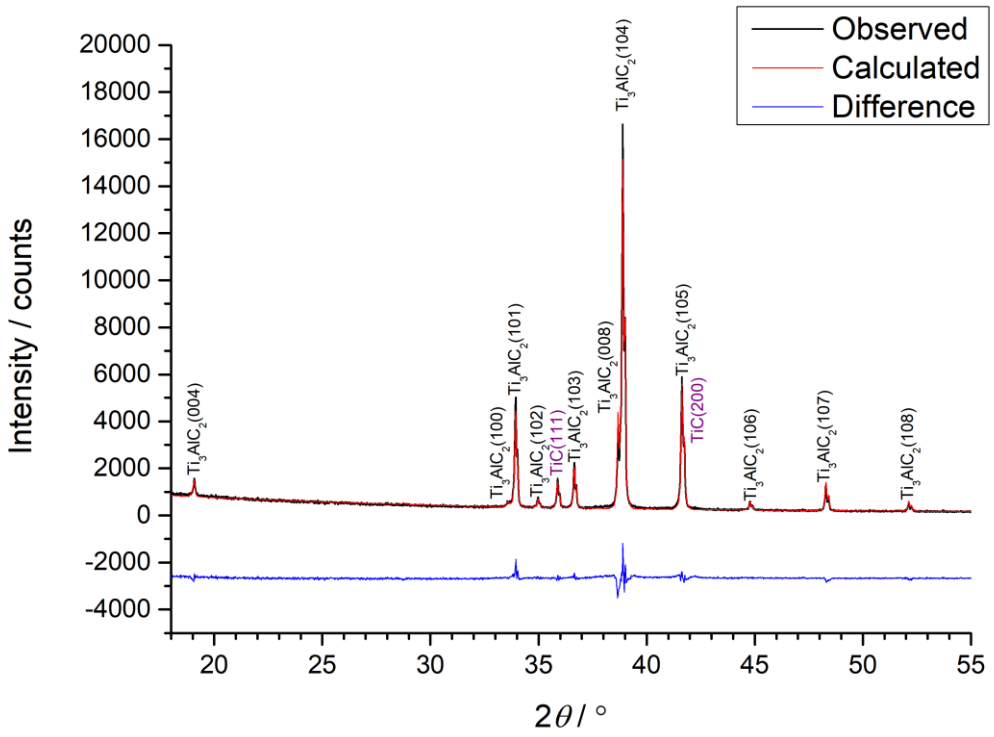

Figure 206 – Indexed XRD pattern fitted by Rietveld refinement for a sample which was prepared by milling Ti and C for 2 h in a hardened steel vial set, then sintering with Al at 1350°C for 15 min.

12.5 Synthesis via a TiC_x precursor using a SPEX 8000M Mixer/Mill: minor variations of synthesis parameters

Multiple parameters were changed when switching from the Retsch Cryomill to the SPEX 8000M Mixer/Mill. Firstly, the mass of milling media for the SPEX 8000M Mixer/Mill was much lower, so the mass of powder used in the SPS was reduced from 7.5 g to 6 g to increase the BPR when milling. Secondly, the boron nitride spray coating was unavailable when preparing the first few samples. Thirdly, a less accurate one decimal point balance was used when preparing samples on the Retsch Cryomill, so it was suspected that the mass of aluminium may have been slightly higher than stoichiometric. Consequently, the effect of sintering mass, use of a boron nitride coating, and use of a slight excess of aluminium were investigated.

Several samples were prepared by milling titanium and graphite powders for 2 h then sintering at 1350°C for 15 min with a variation of additional synthesis parameters. The following samples were prepared to compare the use of a boron nitride coating during SPS, the powder mass used during SPS, and a slight excess of aluminium stoichiometry. The seven samples are summarised in Table 44. Very little difference was observed in the compositions and densities of most of the samples, except for those prepared from 6 g of powder with 1.0 parts aluminium. Further discussion of the effects of using excess aluminium can be found in § 5.3.

Table 44 – Summary of variables for samples prepared with minor variations of synthesis parameters, including the mass of powders used for SPS, the use of a boron nitride coating on the graphite paper used for SPS, and the stoichiometry of aluminium.

Mass / g	Boron Nitride	Aluminium Stoichiometry / mol	Ti_3AlC_2 / wt.%	TiC / wt.%	Density / g cm^{-3}	Relative Density / %
6.0	No	1.0	92	8	4.285 ± 0.005	99
7.5	No	1.0	94	6	4.268 ± 0.010	99
6.0	Yes	1.0	90	10	4.163 ± 0.005	96
7.5	Yes	1.0	95	5	4.276 ± 0.002	100
6.0	No	1.1	94	6	4.268 ± 0.011	99
7.5	Yes	1.1	94	6	4.158 ± 0.006	97

12.5.1 Effect of mass used for SPS

The samples sintered from 6 g of powder were prepared by milling 5.14 g titanium with 0.86 g graphite (BPR of 3.3) then replacing the relevant amount of powder with aluminium to maintain stoichiometry.

The samples sintered from 7.5 g of powder with 1.0 parts aluminium were prepared by milling 5.53 g titanium and 0.93 g graphite (BPR 3.3) then mixed with 1.04 g aluminium. The samples sintered from 7.5 g of powder with 1.1 parts aluminium were prepared by milling 5.46 g titanium and 0.91 g graphite (BPR 3.4) then mixed with 1.13 g aluminium. Thus, in addition to changes in the sintering mass, there were also minor changes in the BPRs

When no boron nitride coating was used with aluminium stoichiometry of 1.0, the purity was greater with 7.5 g of powder, but there was minimal variation in density. When a boron nitride coating was used with aluminium stoichiometry of 1.0, a greater mass of powder and lower BPR resulted in a purer product. The difference in purity was greater between these two samples than the ones without boron nitride. Additionally, the density varied significantly, and the product was fully dense when using 7.5 g of powder.

The comparisons suggest that use of a greater mass of powder and slightly lower BPR resulted in purer, denser products. This may be due to a more intense effect from the direct current due to the shorter path length and resistance. Alternatively, it is possible that the higher BPR for the 6 g powder led to the greater formation of stoichiometric titanium carbide before sintering or formation at a lower temperature during sintering and hindered product purity.

12.5.2 Effect of boron nitride coated sintering apparatus

When 6 g of reagent was used with an aluminium stoichiometry of 1.0, the product purity decreased slightly when a boron nitride coating was used, and the density decreased significantly. Both samples had the lowest purity of all the samples produced. When 7.5 g of reagent was used with an aluminium stoichiometry of 1.0, both the product purity and density increased slightly when a boron nitride coating was used. It is therefore inconclusive as to whether the use of a boron nitride coating improves or hinders the formation of a pure, dense product.

12.5.3 Effect of aluminium stoichiometry

When 6 g of reagent and no boron nitride coating were used, product purity increased with an increase in aluminium content, with insignificant variation in density. When 7.5 g of reagent and a boron nitride coating were used, both product purity and density decreased slightly with an increase in aluminium content. The former samples did not use a boron nitride coating, so it is likely that the increase in aluminium content accounted for the loss of aluminium to the surrounding graphite and gave superior results. Conversely, the latter samples did use a boron nitride coating, which likely hindered the loss of aluminium, so greater purity was obtained with a stoichiometric amount of aluminium.

The best results were obtained when 7.5 g of powder were used with a boron nitride coating and an aluminium stoichiometry of 1.0. Hence, these parameters were used to produce all subsequent samples. The variation with sintering mass may be that a lower mass resulted in the current passed through the

material being more intense due to the lower path of resistance, which may have caused greater decomposition of Ti_3AlC_2 to TiC_x. The benefit of a boron nitride coating was ambiguous, but overall it was decided that it was worth using based on the argument that it may help prevent reaction of aluminium with the outer graphite paper. The use of an excess of aluminium resulted in only a slight decrease in Ti_3AlC_2 content, indicating there is reasonable tolerance for the quantity of aluminium used. Overall, the fact that four of the six samples had very similar compositions and densities indicates the method was consistent.

12.6 Synthesis via a TiC_x precursor using a SPEX 8000M Mixer/Mill and a transient holding temperature during sintering

A sample was sintered with a transient holding temperature, rising from 1250°C to 1350°C over 15 min. The sintering profile is shown in Figure 207.

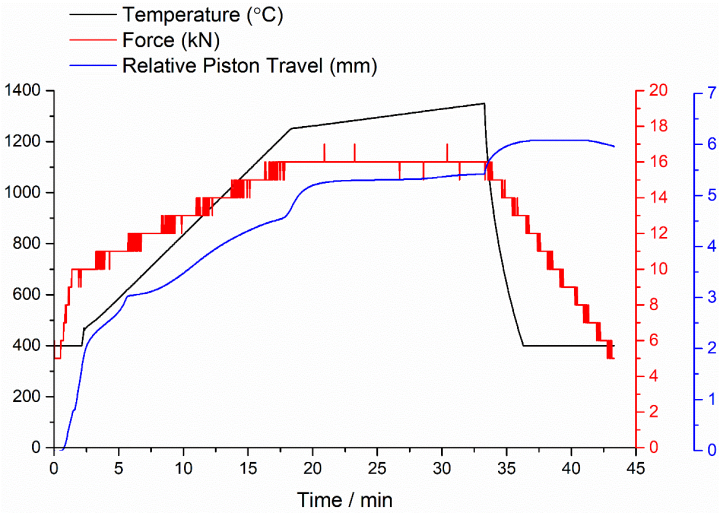

Figure 207 – Heating profile measured during sintering for a sample of Ti_3AlC_2 which was prepared using a transient holding temperature.

The XRD pattern is shown in Figure 208. The phase fractions were determined by Rietveld refinement as 87wt.% Ti_3AlC_2 and 13wt.% TiC (χ^2 2.331, R_p 0.0699, R_{wp} 0.0910). The lattice parameters were similar to those observed previously: *a*(Ti_3AlC_2) 3.080 Å, *c*(Ti_3AlC_2) 18.611 Å, and *a*(TiC) 4.333 Å. No $TiAl_3$ was present, but the fraction of TiC_x was higher than for the sample produced at 1350°C. This highlights that temperature is important for reaction of $TiAl_3$, but also that the holding time at 1350°C is important. Therefore, it would be useful to investigate the effect of holding temperatures between 1300°C and 1350°C and holding times.

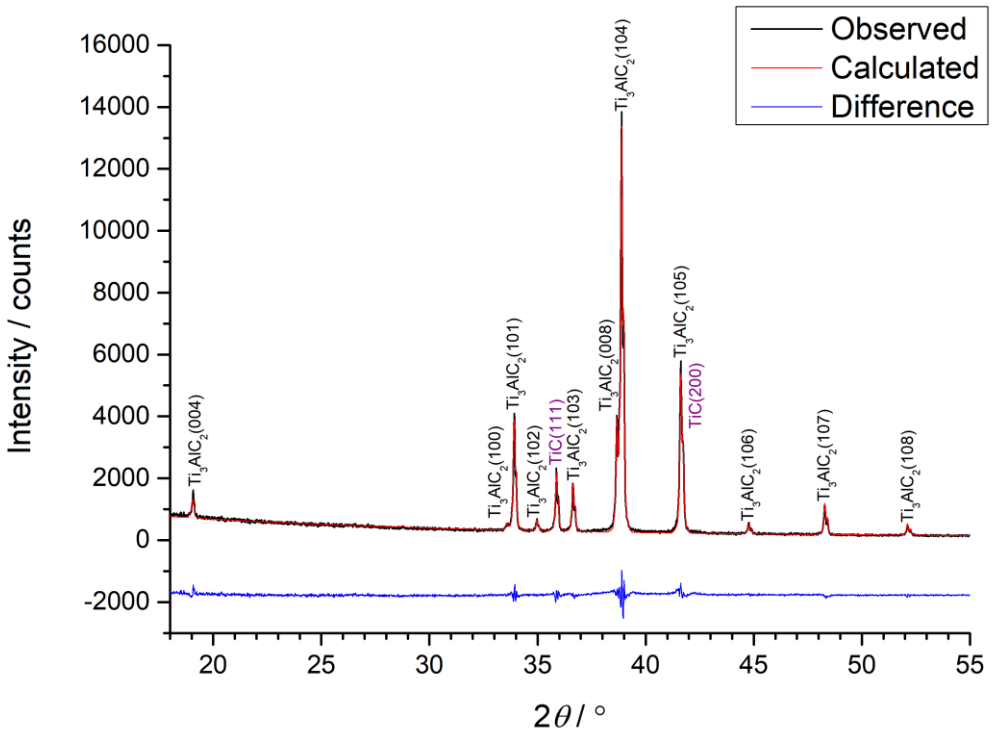

Figure 208 – XRD pattern of a sample produced by transient heating between 1250°C and 1350°C.

13 Appendix C – Synthesis of Ti_2AlC from Ti, Al and C

An attempt was made to reproduce the synthesis of Ti_2AlC from the method used by Zhou *et al.* [241]. Ti (5.17 g), Al (1.68 g) and C (0.65 g) were weighed in the ratio 2:1.15:1 then milled for 10 min in a SPEX 8000M Mixer/Mill. The powder was transferred to a 20 mm diameter graphite die then reactively sintered by SPS by heating at 80°C min^{-1} to a holding temperature of 1100°C for a dwell time of 8 min under 30 MPa uniaxial pressure. The on/off pulse time was 12/2 s.

13.1.1 X-ray diffraction

The indexed XRD pattern after Rietveld refinement is shown in Figure 209 [178,235]. The phase fractions were determined as 68wt.% Ti_3AlC_2 and 32wt.% Ti_2AlC (χ^2 4.498, R_p 0.0805, R_{wp} 0.1147). The density was determined as 4.16 ± 0.04 g cm^{-3}, with a relative density of 99%.

13.1.2 Indentation hardness testing

The hardness of the sample was measured using a DuraScan-70 hardness tester at 4.9 N with a dwell of 10 s. The Vickers hardness was 4.1 ± 0.5 GPa. This value is slightly lower than that for the 95wt.% Ti_3AlC_2 sample prepared from powder milled for 2 h due to the lack of TiC_x.

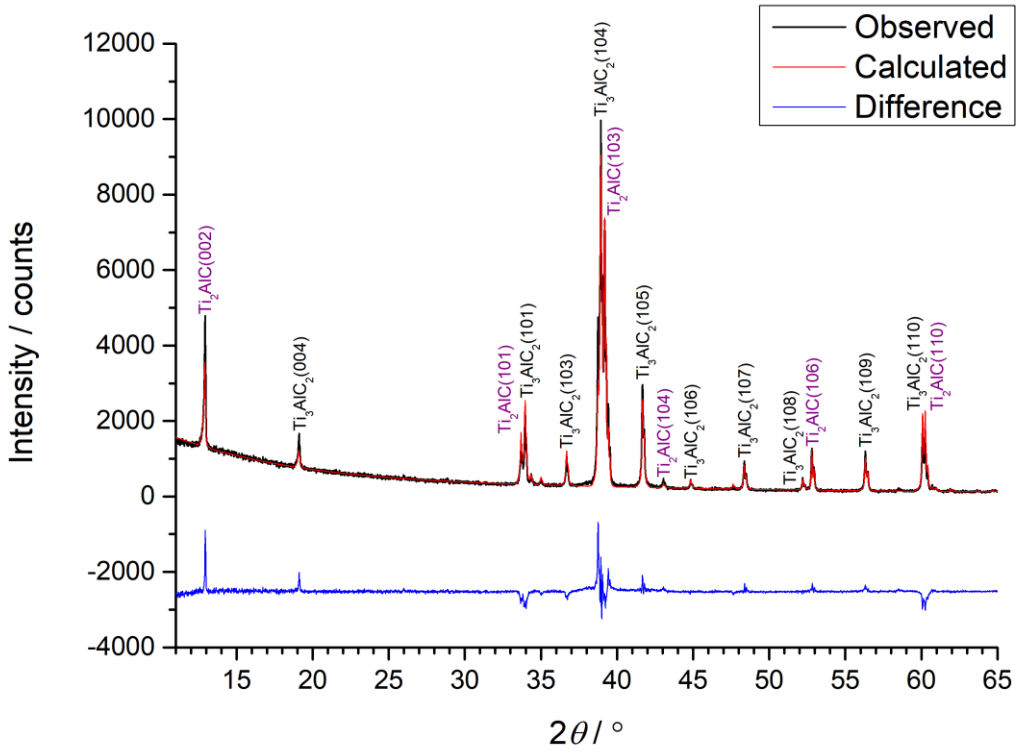

Figure 209 – XRD pattern and Rietveld refinement difference plot of a sample for which the target composition was Ti_2AlC.

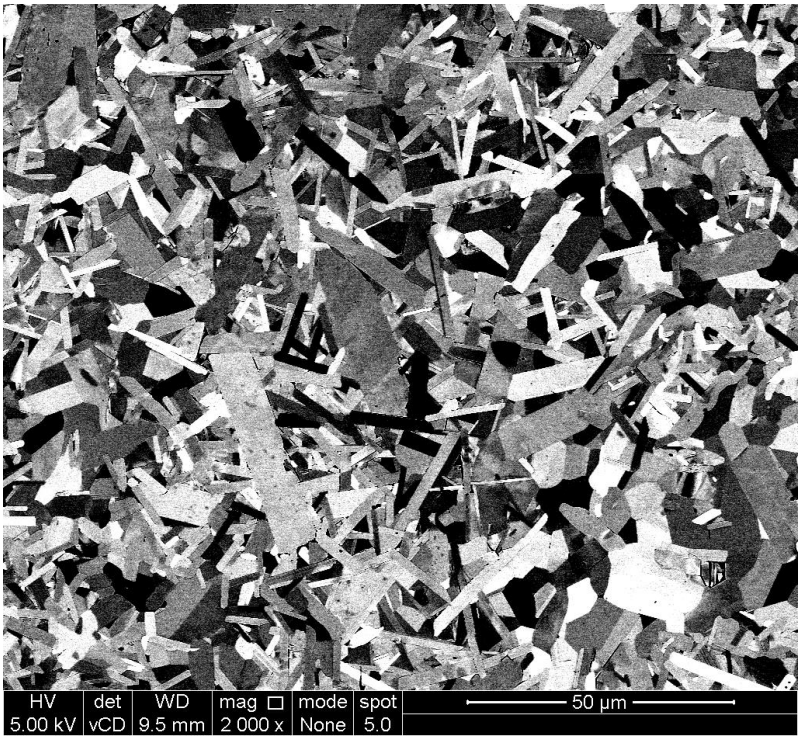

Figure 210 – BSE image showing a general overview of a sample for which the target composition was Ti_2AlC. The contrast was maximised to reveal grain boundaries.

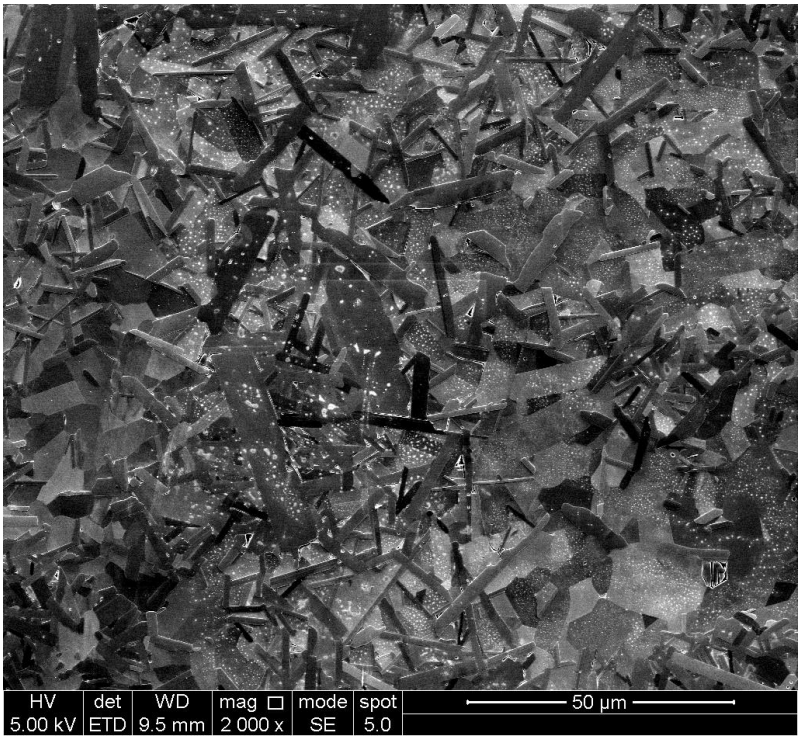

Figure 211 – SE image showing a general overview of a sample for which the target composition was Ti_2AlC. The image was taken at the same location as Figure 210.

13.1.3 Microstructural examination

A BSE image providing a general overview of the sample is shown in Figure 210. The sample was polished with colloidal silica, and the contrast and brightness were manipulated to maximise the contrast and reveal the grain boundaries. Numerous levels of contrast can be observed, so it is difficult to identify grain compositions. The size of the grains varies significantly, with a mixture of large and small grains.

Figure 211 is a secondary electron image taken at the same location as the BSE image in Figure 210. The white spots appear to be residual particles of colloidal silica. One phase appears to have been removed preferentially by micropreparation.

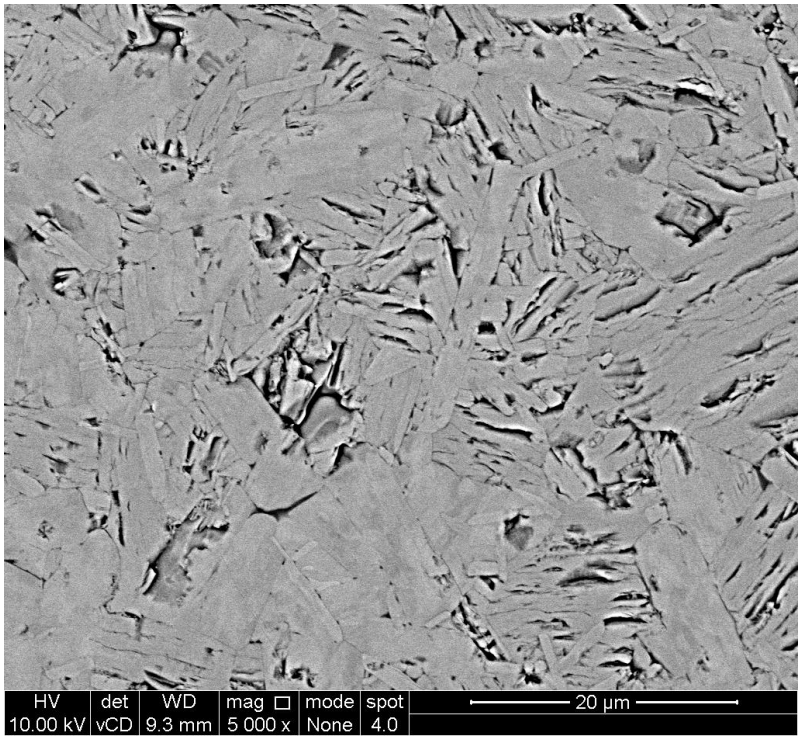

(a) BSE image

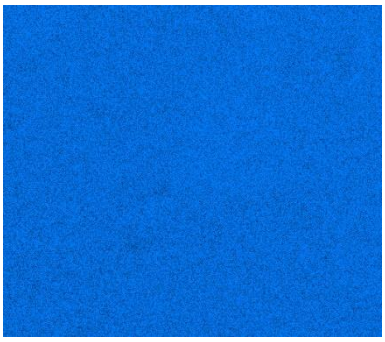

(c) Ti $K_{\alpha1}$

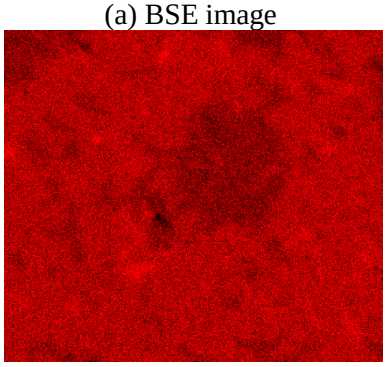

(d) Al $K_{\alpha1}$

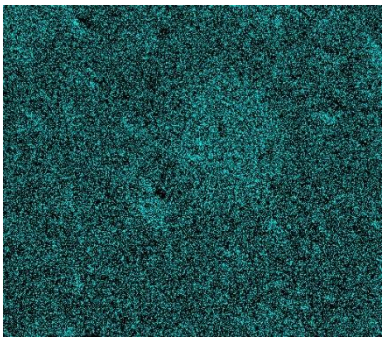

(e) C $K_{\alpha1}$ and $K_{\alpha2}$

Figure 212 – BSE image and EDS maps showing the morphology of phases in a sample for which the target composition was Ti_2AlC. The relative intensities of the Al and C maps suggest that the slightly lighter phase with smaller grains is Ti_3AlC_2 and the slightly darker phase with larger grains is Ti_2AlC.

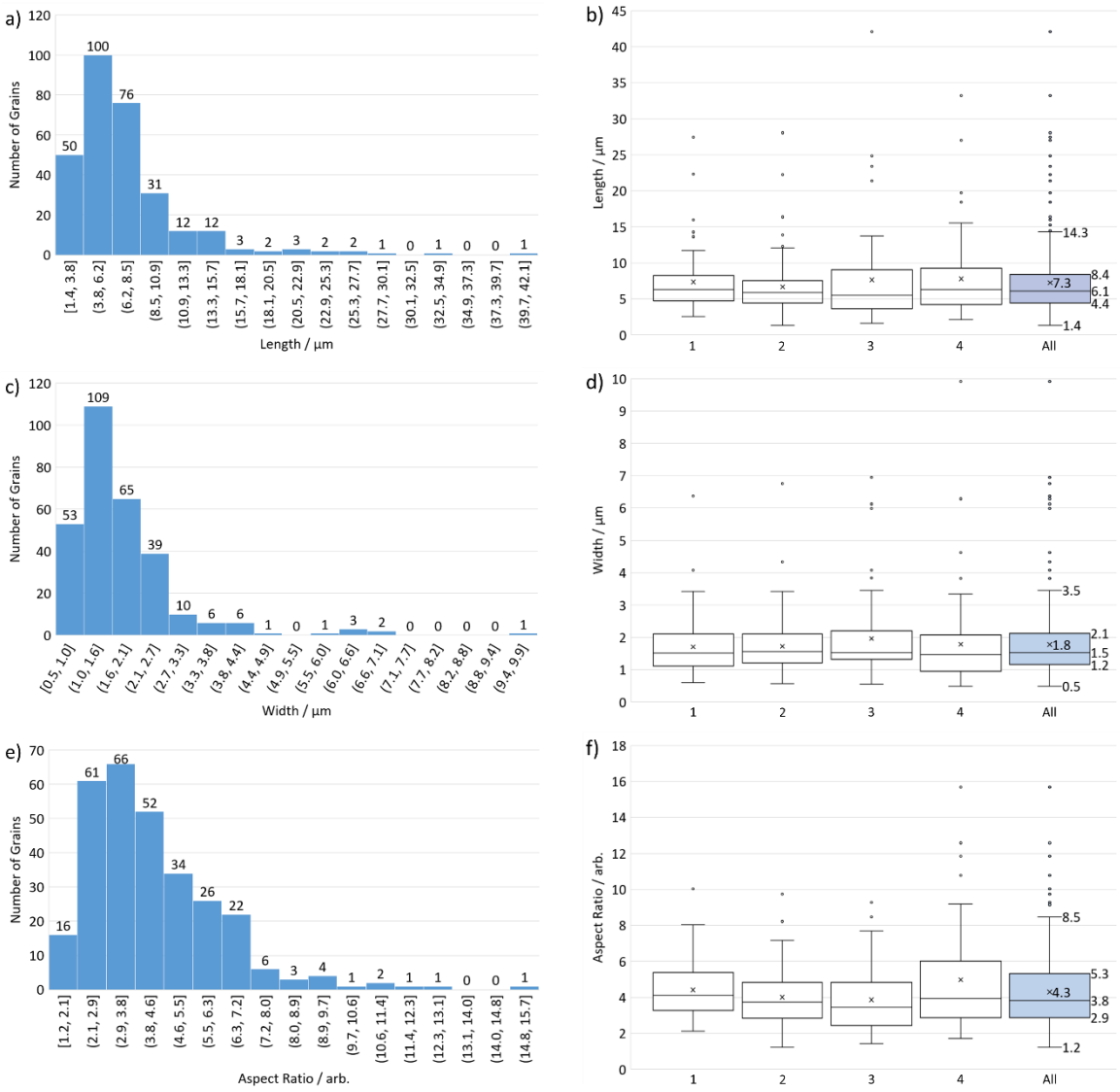

Figure 213 – Histograms and boxplots showing the distributions of length, width and aspect ratio from 296 measurements.

Figure 212 is a BSE image and EDS maps which helps reveal the morphology of the two phases. By comparing the relative intensities from the Al map and the C map, it appears that the phase with the slightly lighter contrast and smaller grains is Ti_3AlC_2, due to the increased ratio of C relative to Al. Conversely, the slightly darker contrast and larger grained phase appears to be Ti_2AlC due to the lower ratio of C relative to Al. Furthermore, it appears that the Ti_3AlC_2 phase forms clusters distributed within a matrix of Ti_2AlC, other than some randomly distributed grains, which is surprising considering the higher weight fraction of Ti_3AlC_2 from the Rietveld refinement results. However, the Ti_2AlC grains appear to have a larger grain size, and the Ti_3AlC_2 phase appears to be filling all the gaps, which may explain this discrepancy. To confirm the Rietveld refinement results, the map sum spectrum of an image

taken at 5x lower magnification (*i.e.* 1000x original magnification) gave 50.2at.% Ti, 19.7at.% Al, and 30.1at.% C. From this, the weight fractions of the two phases were determined as 72wt.% Ti_3AlC_2 and 28wt.% Ti_2AlC, which is consistent with the results from Rietveld refinement.

The grain size was determined by measuring the lengths and widths of individual grains using ImageJ, the distributions of which are shown in Figure 213. In total, 296 measurements were made across four images taken at an original magnification of x5000. However, there is a lack of distinction between the two phases, so the results are averaged for the entire material. The mean length, width and aspect ratio for all measurements were 7.3 ± 5.0 μm, 1.8 ± 1.1 μm and 4.3 ± 2.0 respectively.

13.1.4 Discussion

The synthesis of Ti_2AlC did produce a pure MAX phase material but it was a mixture of two different MAX phases, Ti_3AlC_2 and Ti_2AlC. This is unusual as Zhou *et al.* reported a relatively pure material consisting of Ti_2AlC as the major phase with minor impurities of TiC and TiAl [241]. The sintering parameters were approximately the same as those used by Zhou *et al.*, although the instrument used was different.

There may be some difference in the reagents used, mainly particle size, but the key difference is likely the milling step. Zhou *et al.* state that they mixed the powders in ethanol for 24 h, although it is not clear by what method and whether milling media were used. The SPEX 8000M Mixer/Mill used in this work is a high energy ball mill, so even just 10 min of milling should achieve good mixing and significant particle size reduction. This may have facilitated diffusion during SPS, enabling TiAl and TiC to react together to form Ti_2AlC, and Ti_2AlC to react with TiC to form Ti_3AlC_2, and allowing the latter to occur at lower temperature. This formation of Ti_3AlC_2 is surprising considering Zou *et al.* and Yoshida *et al.* observed formation of Ti_3AlC_2 at higher temperatures than 1100°C, typically ~1300°C [73,74,76], although Riley and Kisi observed its formation at 1000°C or lower [85].

It is also possible that there was more evaporation of Al in this work, which would explain preferential formation of Ti_3AlC_2 [54,76,187,192]. In this work, synthesis was performed under vacuum, which aids evaporation of Al.

The material was not used for corrosion tests as the purity of Ti_3AlC_2 produced by other methods was significantly greater. However, in hindsight the corrosion of this material would have been interesting to study as it represents a pure MAX phase material despite being multiphase, and the corrosion potential of Ti_2AlC is likely closer to that of Ti_3AlC_2 than that of TiC_x, minimising the possibility of dissimilar corrosion driven by the potential difference between the two phases. The synthesis method was not repeated, so it would be interesting to see if the same material can be reproduced consistently.

14 Appendix D – Synthesis of Ti_3SiC_2

14.1 Synthesis of Ti_3SiC_2 via a TiC_x precursor using a SPEX 8000M Mixer/Mill

Due to the low melting point of aluminium and its significant loss at the edge of the pellet, it was decided to investigate the effect of using silicon. Additionally, Riley and Kisi showed that the same method worked for both Ti_3AlC_2 and Ti_3SiC_2, so the method was expected to work without changes. A sample was produced by milling titanium and graphite for 2 h, which was then mixed with 1.0 parts silicon powder and sintered at 1350°C for 15 min.

14.1.1 Sintering profile

The heating profile measured during sintering is shown in Figure 214. The profile shape is similar to that for samples produced with aluminium, indicating little change in the reaction mechanism. The rate of piston movement is relatively uniform between 500-900°C, slows slightly between 900-1250°C, then increases again from 1250-1350°C. Further movement is observed at the dwell temperature and force indicating further densification and reaction. There is a small amount of piston movement due to thermal contraction as the temperature and force are relieved.

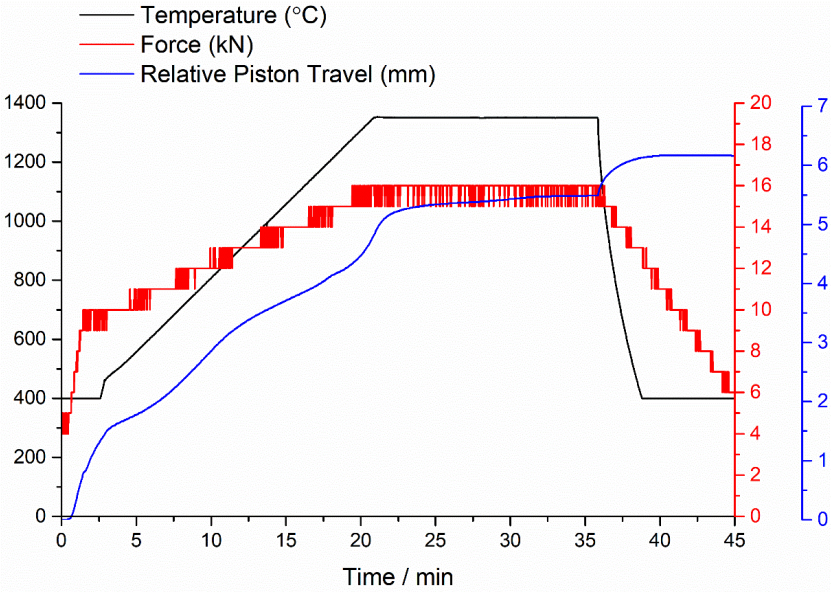

Figure 214 – Heating profile measured during sintering for a sample of Ti_3SiC_2 produced from a TiC_x precursor.

14.1.2 X-ray diffraction

The XRD pattern of the bulk sample, between 5° and 55° 2θ, is shown in Figure 215 (χ^2 2.504, R_p 0.0732, R_{wp} 0.0942) [179,213,242]. The lattice parameters for Ti_3SiC_2 were a = 3.072 Å and c = 17.706 Å. Both values are smaller than those observed for Ti_3AlC_2 and are a consequence of the smaller size and stronger bonding with Si rather than Al. The lattice parameter, a, for TiC_x was 4.327 Å, which is smaller than that observed in all of the Ti_3AlC_2-based samples. The lattice parameters for $TiSi_2$ were

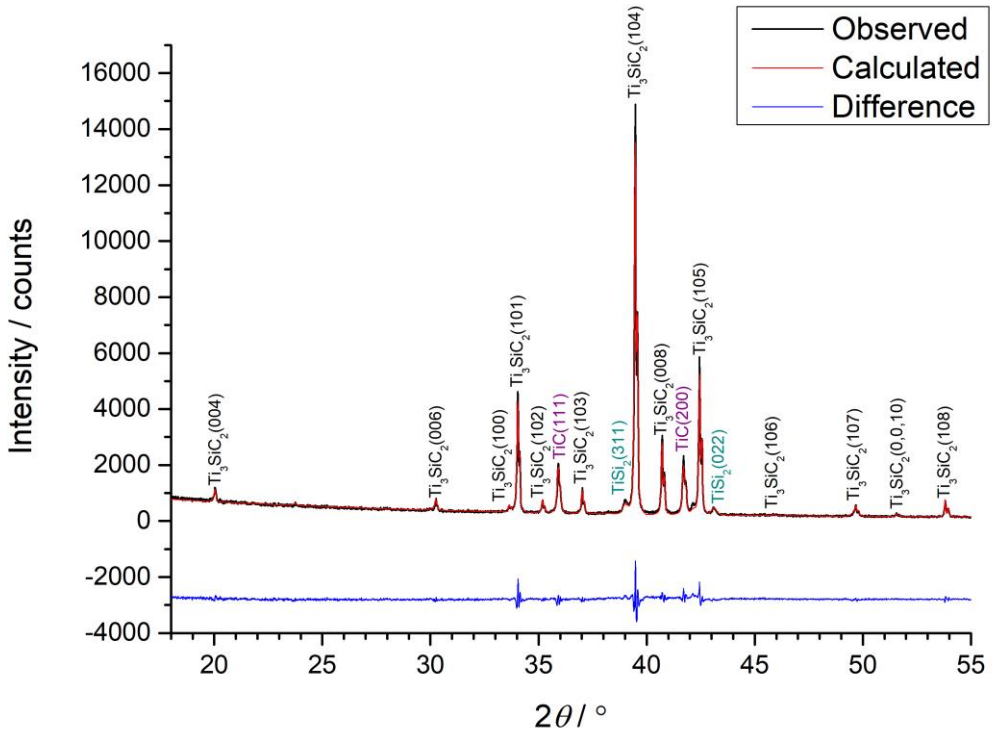

Figure 215 – The indexed XRD pattern of a sample prepared from titanium and graphite milled for 2 h then mixed with 1.0 parts silicon and sintered at 1350°C.

a = 8.287 Å, *b* = 4.809 Å, and c = 8.569 Å. The density was 4.437 ± 0.005 g $cm^{-3,}$ and the relative density was 98%, indicating the sample was almost fully dense.

The phase fractions determined by Rietveld refinement indicated 80wt.% Ti_3SiC_2, 14wt.% TiC and 6wt.% $TiSi_2$. The amount of MAX phase present is significantly lower than in the Ti_3AlC_2 sample produced with the same synthesis variables. Thus, the hypothesis that Si will give a purer product because it has a higher melting point so is likely to be less mobile, seems invalid. On the other hand, if Si is less mobile, it may not distribute sufficiently throughout the sample during sintering, forming the impurities TiC_x and $TiSi_2$. Alternatively, these results may suggest that different sintering parameters are required to produce Ti_3SiC_2, although many researchers, including Riley and Kisi upon which the precursor synthesis method is based, have found similar results with the same sintering parameters for both Ti_3AlC_2 and Ti3SiC2 [77,85].

14.1.3 Indentation hardness testing

The hardness of the sample was measured using a DuraScan-70 hardness tester at 4.9 N with a dwell of 10 s. The Vickers hardness was 7.7 ± 0.9 GPa. This value is larger than for the 95wt.% Ti_3AlC_2 sample which was milled for 2 h, but less than the 70wt.% TiC_x sample which was milled for 4 h.

14.1.4 Microstructural examination

Figure 216 is a BSE image of the sample of Ti_3SiC_2 taken at a low original magnification. The image provides a general overview of the distribution of phases within the material. The lightest contrast phase is Ti_3SiC_2. The medium contrast is TiC_x; this phase is relatively evenly distributed among the Ti_3SiC_2 phase. The dark contrast regions are $TiSi_2$. The morphology of these $TiSi_2$ regions resembles that of the Al_3Ti regions in the sample produced with a sintering temperature of 1250°C (§ 5.2.3.1).

Figure 217 and the associated EDS maps indicate that the medium grey contrast regions are titanium carbide. Titanium is present evenly throughout the image, but the medium grey contrast regions are deficient in silicon and abundant in carbon, indicating the presence of titanium carbide.

Figure 218 is a higher magnification image showing the morphology of the titanium carbide phase. The grain boundaries are difficult to distinguish, but the grains appear to be equiaxed.

Figure 219 shows the morphology of a region of $TiSi_2$. The EDS maps show titanium is diminished in this region and carbon is hardly present at all, whereas silicon is abundant. Secondary phases are visible, the morphology of which are consistent with TiC_x and Ti_3SiC_2; the TiC_x phase has the same

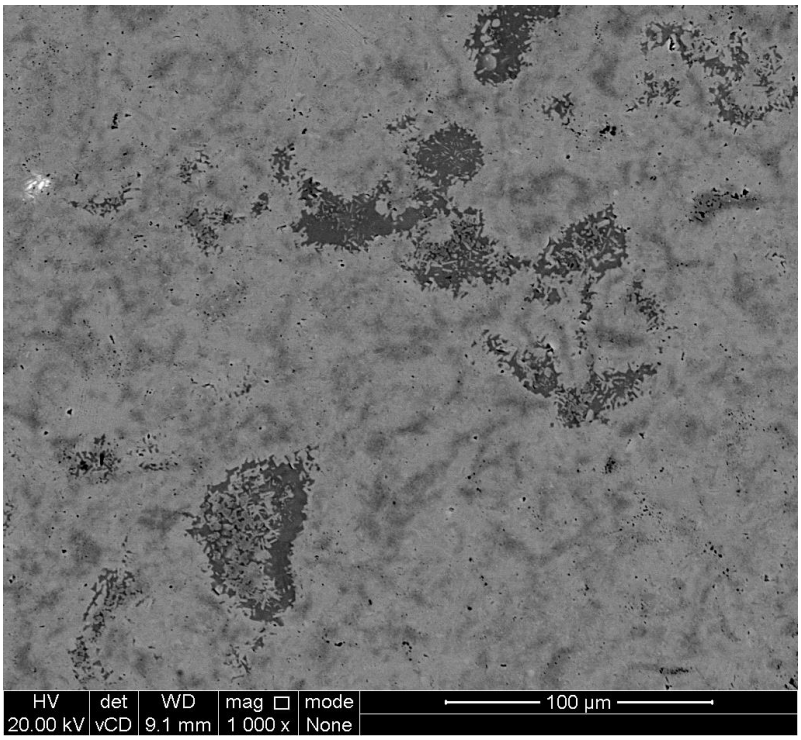

Figure 216 – BSE image at a low original magnification of a sample produced using Si rather than Al. This image provides a general overview of the microstructure of the material. Three distinct levels of contrast are visible, consistent with the three phases observed by XRD: light grey - Ti_3SiC_2, medium grey - TiC_x and dark grey - $TiSi_2$.

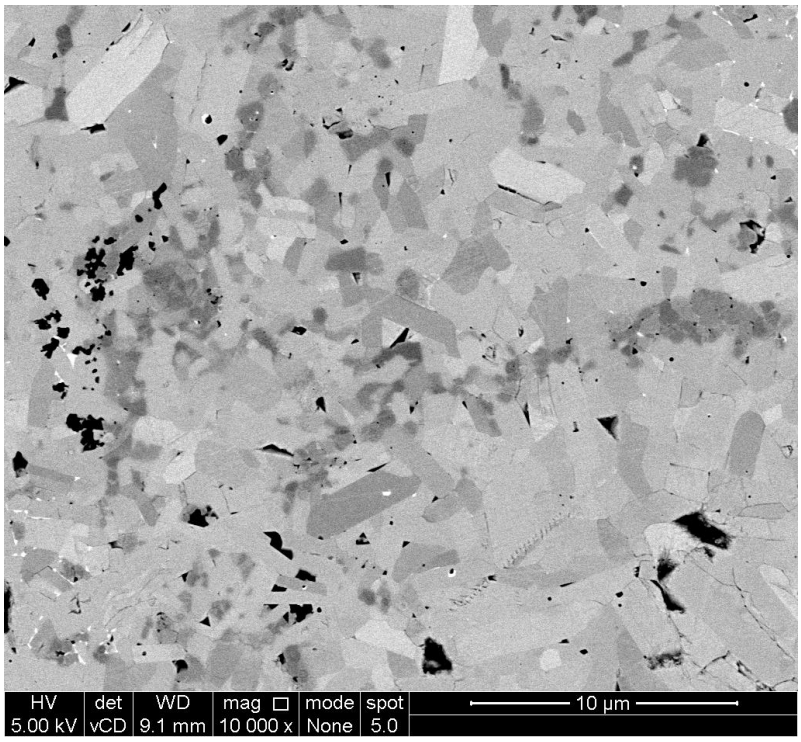

(a) BSE image

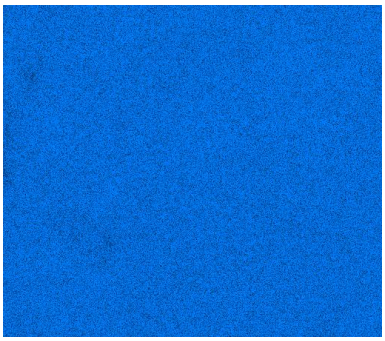

(b) Ti $K_{\alpha 1}$

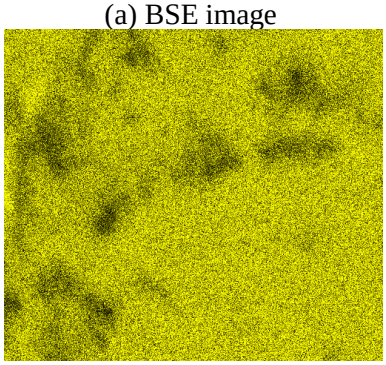

(c) Si $K_{\alpha 1}$

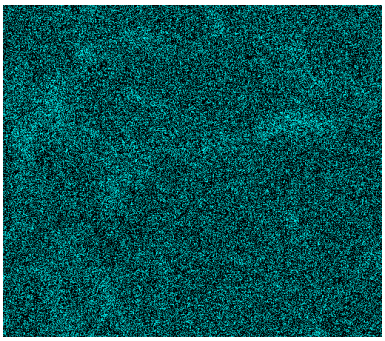

(d) C $K_{\alpha 1}$ and $K_{\alpha 2}$

Figure 217 – BSE image and EDS maps showing the presence of a titanium carbide phase located where Si is deficient, and C is abundant.

morphology as Figure 217, and the rectangular grains are consistent with morphology observed for MAX phases. The small grain size of the Ti_3SiC_2 grains suggests that these grains are undergoing growth and the presence of these $TiSi_2$ regions is due to insufficient time or temperature for reaction to occur fully. Overall, it appears that $TiSi_2$ has acted as a liquid medium for the formation of Ti_3SiC_2 from TiC_x because the morphology of these regions corresponds to that observed for the sample of Ti_3AlC_2 which was sintered at 1250°C. In comparison to the Al_3Ti phase observed for the Ti_3AlC_2 samples, some grain structure can be observed in the $TiSi_2$ phase, and the contrast is lighter. In the

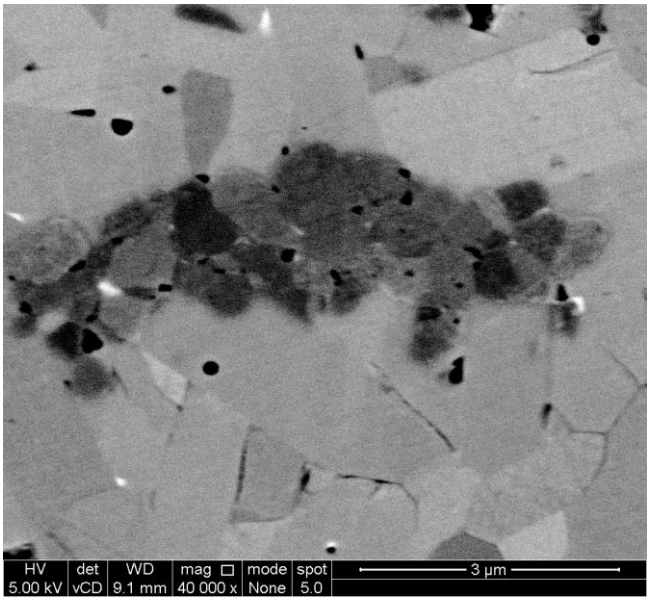

Figure 218 – BSE image showing the morphology of the titanium carbide phase in a sample of Ti_3SiC_2.

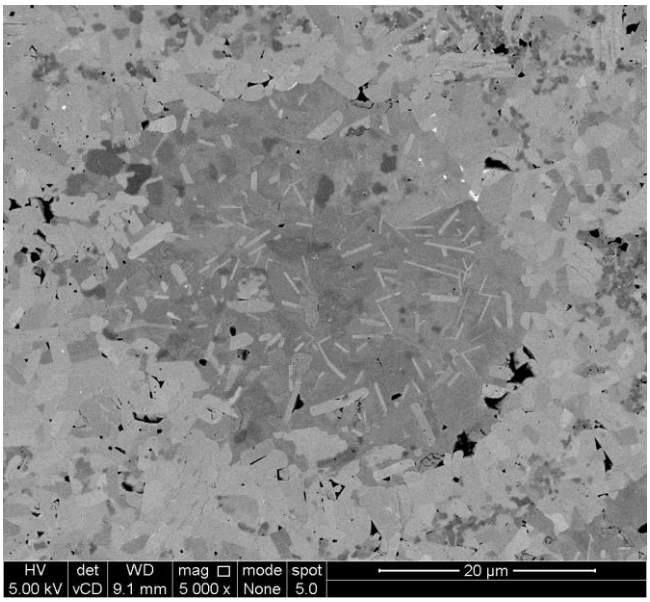

(a) BSE image

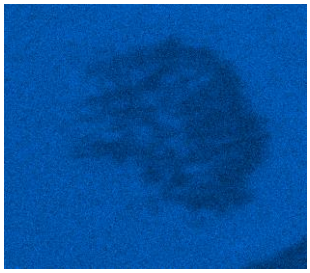

(b) Ti $K_{\alpha 1}$

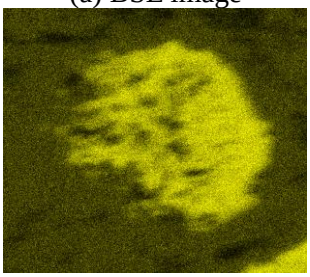

(c) Si $K_{\alpha 1}$

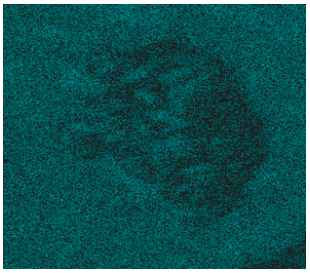

(d) C $K_{\alpha 1}$ and $K_{\alpha 2}$

Figure 219 – BSE image and EDS maps showing the morphology of a cluster of $TiSi_2$. Small rectangular grains of partially formed Ti_3SiC_2 are visible within the cluster.

aluminium-based samples an increase in temperature removed the Al_3Ti phase, indicating it was a reaction intermediate. Therefore, it is likely that a further increase in sintering temperature, or potentially an increase in hold time, would remove the $TiSi_2$ impurity and result in a purer product.

Numerous regions of black contrast were observed in the BSE images. Comparison with SE images, as per Figure 220 and Figure 221, suggest that these are regions with depressions, likely due to the loss of a particular phase during micropreparation, most likely TiC_x due to its high relative hardness.

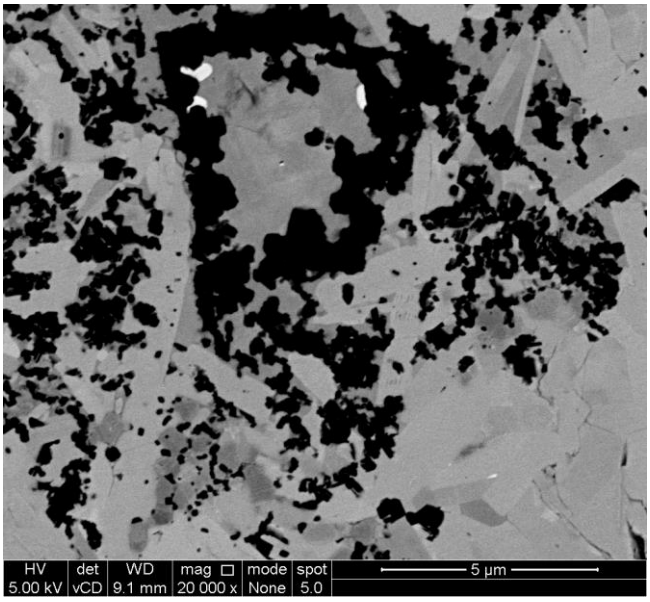

Figure 220 – BSE image of a region with significant depressions in the surface.

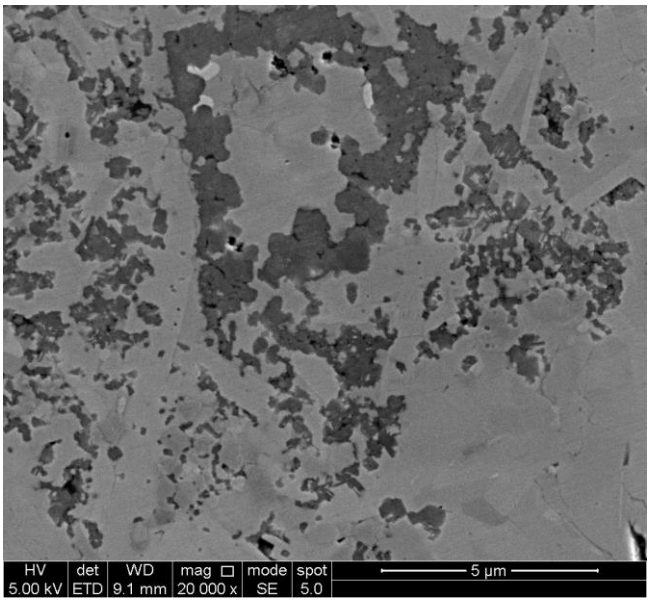

Figure 221 – SE image of a region with significant depressions in the surface.

14.2 Preparation of Maxthal 312 (Ti_3SiC_2) by SPS

Samples of Ti_3SiC_2 were prepared using Maxthal 312 powder (Kanthal). Various sintering parameters were investigated by Carl Magnus (University of Sheffield), and the samples used for corrosion tests were made according to the best parameters for the highest fraction of Ti_3SiC_2 found at the time [190]. SPS was performed using 7 g of powder per sample. The holding temperature was 1300°C, the dwell time was 10 min, and the ramp rate was 100°C min^{-1}. The uniaxial force was maintained at a constant value of 16 kN. The on/off pulse times were 12/2 s.

A typical sintering profile is shown in Figure 222. The initial increase in piston travel is due to densification as the uniaxial pressure of 16 kN is applied. The majority of densification occurs from ~1000°C approaching the dwell temperature of 1300°C. The piston movement as the sample is cooled is due to thermal contraction.

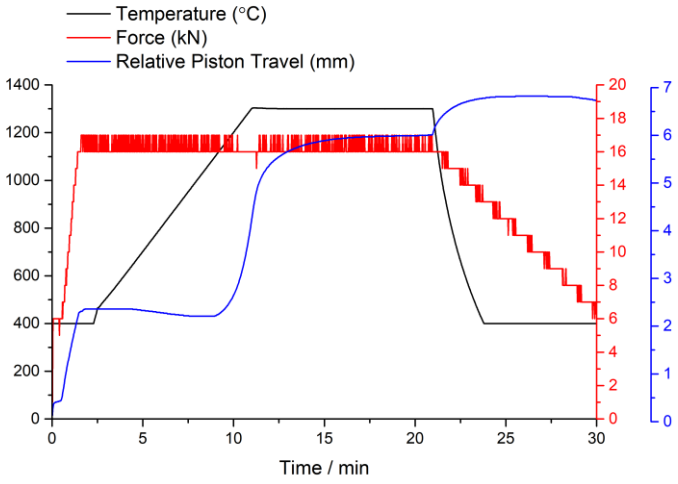

Figure 222 – Typical sintering profile for Maxthal 312 samples.

14.2.1 X-ray diffraction and density

The XRD pattern for a typical sample is shown in Figure 223. Attempts to fit the data by Rietveld refinement were not possible without accounting for the significant preferred orientation in the sample, with increased intensities observed on the (00*l*) plane. The TiC_x peaks are relatively intense, indicating the sample contains a significant fraction of TiC_x. The density was measured as 4.556 ± 0.003 g cm^{-3}.

XRD was also performed on the reagent Maxthal 312 powder. The XRD pattern and Rietveld refinement fit (full profile 18-120° 2θ) are shown in Figure 224 (χ^2 2.248, Rp 0.0684, wRp 0.0897) [179,213,242]. The phase fractions were 91wt.% Ti_3SiC_2 and 9wt.% TiC_x. The lattice parameters of Ti_3SiC_2 were a = 3.075 Å and c = 17.710 Å, and that of TiC_x was a = 4.334 Å.

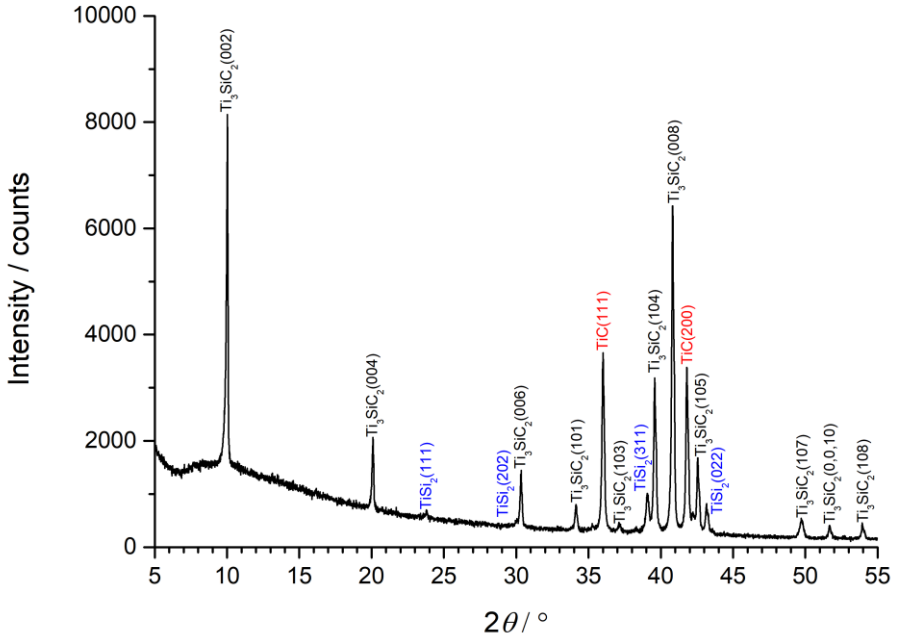

Figure 223 – Indexed XRD pattern of a bulk sample of Maxthal 312.

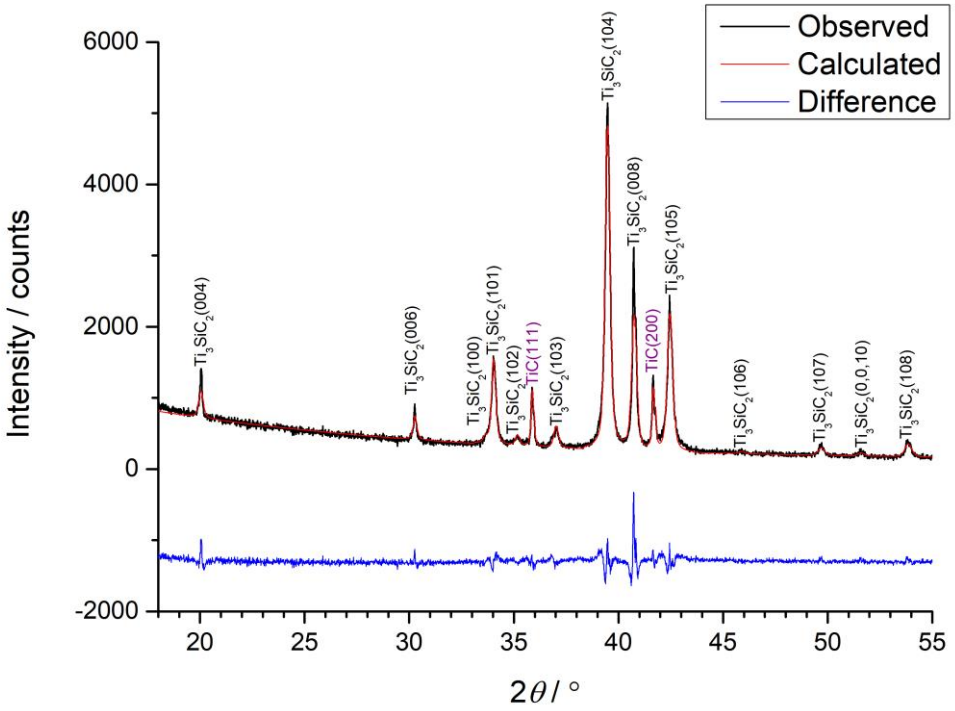

Figure 224 – XRD pattern fitted by Rietveld refinement for Maxthal 312 powder. Fitting was performed on data between 18-120° 2θ.

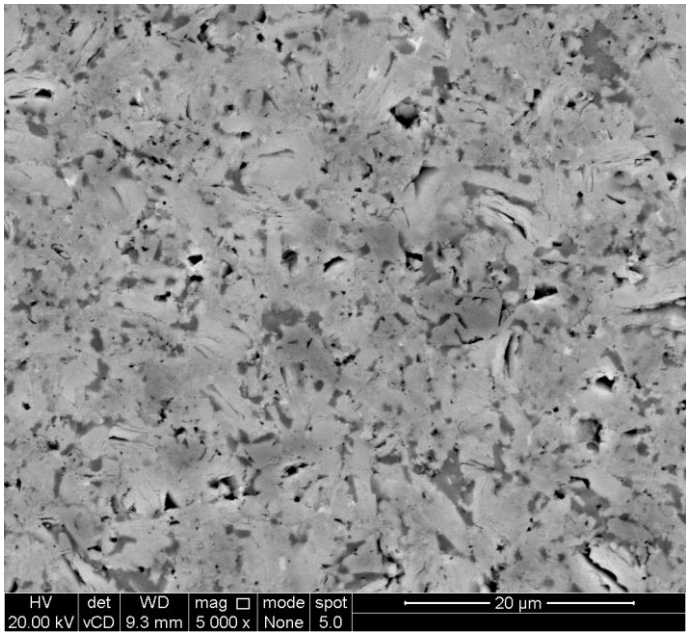

(a) BSE image

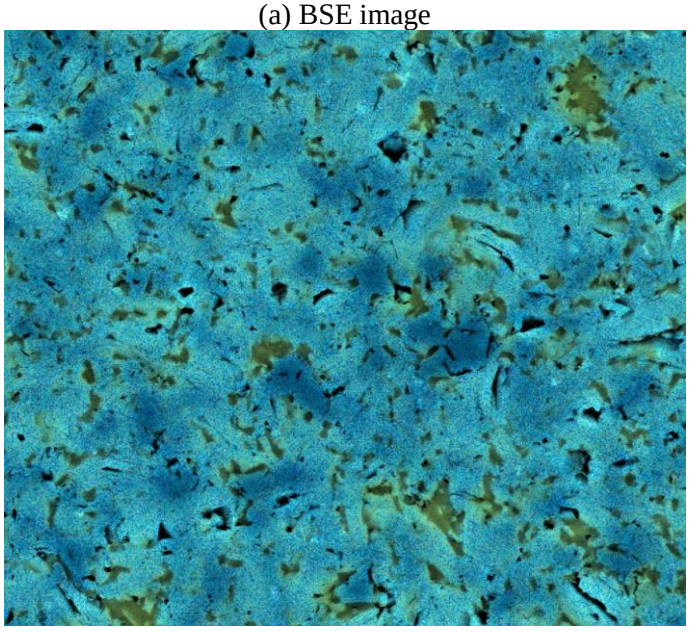

(b) EDS layered image

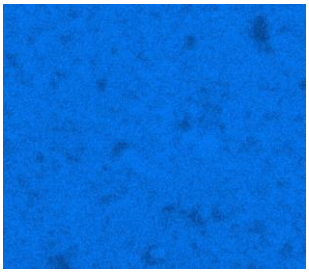

(c) Ti $K_{\alpha 1}$

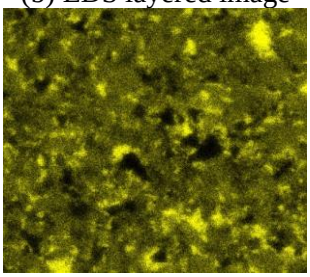

(d) Si $K_{\alpha 1}$

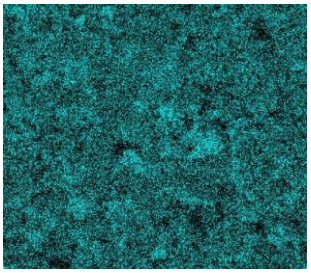

(e) C $K_{\alpha 1}$ and $K_{\alpha 2}$

Figure 225 – BSE image and EDS maps (Image width ~60 µm) showing the phase distribution of a sample of Ti_3SiC_2 (Maxthal 312).

14.2.2 Microstructural examination

Figure 225 shows a BSE image and EDS maps of the distribution of phases. Excluding carbon, the EDS spectrum showed 76.4at.% Ti and 23.6at.% Si, indicating an approximately 3:1 ratio of Ti:Si. The three phases shown by XRD are most easily distinguished in the Si map. The phase with the brightest Si is $TiSi_2$, the darkest Si is TiC and the medium contrast Si is Ti_3SiC_2. Consequently, in the BSE image the brightest contrast phase is Ti_3SiC_2, the darkest contrast phase is $TiSi_2$, and the medium contrast phase is TiC_x.

Figure 226 is a BSE image showing a general overview of the surface morphology. In the brightest contrast phase, the rectangular, layered structure of the MAX phase grains can be distinguished. The aspect ratios of these grains seem smaller than for the sample produced by from a TiC_x precursor.

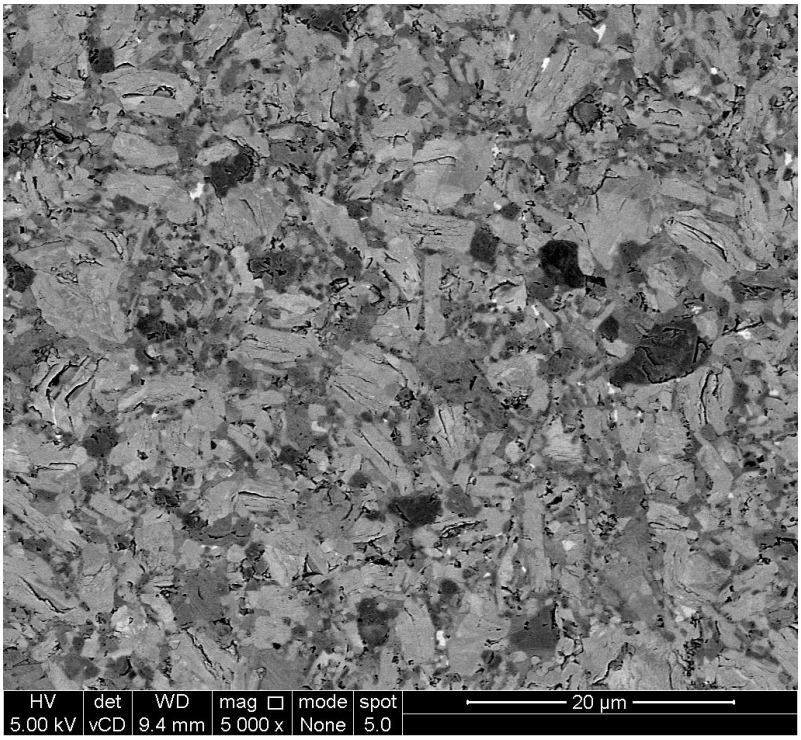

Figure 226 – BSE image of Ti_3SiC_2 (Maxthal 312) taken at 5 kV, showing morphology of the phases in greater detail.

14.3 Discussion

The preparation of Maxthal 312 by SPS from powder supplied by Kanthal was investigated by Carl Magnus at the University of Sheffield [190]. The effects of a variety of parameters was investigated, including temperature ramp rate, holding temperature, holding time, uniaxial pressure applied, and quantity of powder used.

There are two key differences relative to the sample of Ti_3SiC_2 produced from a TiC_x precursor: the grain shape, and the relative intensities of peaks in the XRD pattern. Further differences were observed in the sintering profile, highlighting a difference in reaction mechanism, and in the morphology of the $TiSi_2$ and TiC_x phases.

The grain size was not measured for either material because the grain boundaries were difficult to distinguish without etching. However, the grains of Ti_3SiC_2 in the Maxthal 312 samples appeared to have a smaller aspect ratio, and in many cases were almost square, whereas the aspect ratio of Ti_3SiC_2 in the sample produced from TiC_x were more elongated, with an aspect ratio similar to MAX phase grains observed in the Ti_3AlC_2 samples.

The variation of peak intensities in the XRD pattern of the Maxthal 312 sample was due to preferred orientation along the (00*l*) plane. This plane is parallel to the Si layers in the material and is depicted for a number of planes in Figure 227. There also appears to be some preferred orientation for both the Maxthal 312 powder and the Ti_3SiC_2 produced from a TiC_x precursor, with less preferred orientation observed in the latter. All three samples had polymorphism consistent with α-Ti_3SiC_2, which is most easily distinguished from the peaks in the (10*l*) plane.

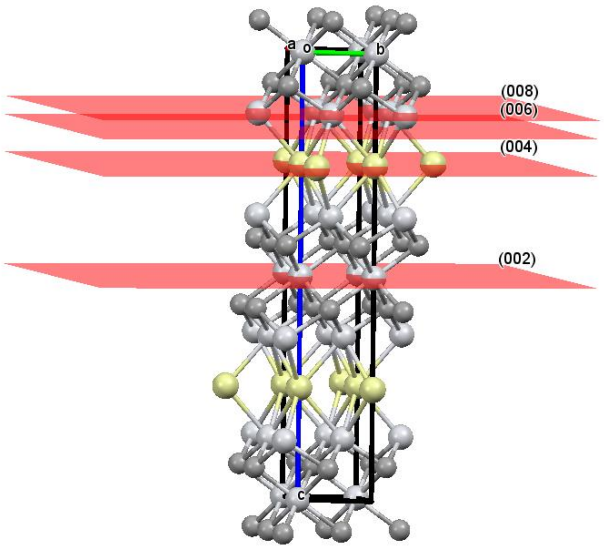

Figure 227 – Diagram showing the (00*l*) planes in α-Ti_3SiC_2 and α-M_3AC_2 isostructures.

Preferred orientation was not accounted for in the Rietveld refinement, which may limit the accuracy of the weight fractions of phases obtained. Furthermore, fitting the bulk Maxthal 312 sample was not possible without accounting for preferred orientation. However, the relative intensities of TiC_x peaks in the bulk Maxthal 312 sample were much greater than for the TiC_x precursor sample, indicating that the Ti_3SiC_2 samples produced in this work were purer. However, the Maxthal 312 powder contained 91wt.% Ti_3SiC_2, which shows that the Ti_3SiC_2 produced from the precursor was less pure than commercially available reagent powder, but the Ti_3AlC_2 samples were purer.

The sintering profile of Maxthal 312 was very simple. Initial piston movement was due to powder compaction as force was applied. Further piston movement was observed from ~1000°C up to the dwell temperature of 1350°C, and the absence of changes suggests this was due to compaction and sintering of the powder. However, the difference in composition of the reagent powder and the bulk sample does suggest decomposition of Ti_3SiC_2. This decomposition may not have resulted in a change in overall density of the sample and was therefore not observed during sintering.

$TiSi_2$ was observed in clusters, as with the sample produced from the TiC_x precursor, but these clusters were much smaller in the Maxthal 312 sample. From the micrographs obtained it is not possible to determine if there are any smaller MAX phase grains visible within the cluster, as was observed with the sample produced from the TiC_x precursor. TiC_x appears to be distributed relatively homogeneously throughout the material, particularly among grain boundaries, and in shapes similar to MAX phase grains. This suggests formation of TiC_x by decomposition of Ti_3SiC_2.

Ultimately, bulk samples of Maxthal 312 were used for corrosion tests due to the ease of fabricability and the potential to compare the Ti_3AlC_2 samples to a commercial MAX phase material. Further details of the material's characterisation and performance, including its mechanical properties and wear behaviour, can be found in work by Carl Magnus [190].

15 Appendix E – Synthesis of TiC

The parameters used for sintering TiC by SPS were investigated by Tanagorn Kwamman (University of Sheffield) [189]. Parameters which gave the highest density of TiC were used for sample preparation. Samples of were prepared from 7.5 g TiC (2 µm, 99.5%, Alfa Aesar) per sample.

15.1 Sintering profile

The powder was heated to 2000°C at a rate of 200°C min^{-1} then held for 15 min with 16 kN force. The on/off pulse time was 15/5 s. The sintering profile for a typical sample is shown in Figure 228. The piston movement increased initially as the powder was compressed by the piston force. There was then some negative movement as the force reached 10 kN. Extrapolating the temperature suggests this occurred at ~200°C. The negative movement is likely due to thermal expansion of the material. Further piston movement was observed from ~1100°C and 13 kN up to the dwell temperature and force. During this time a small amount of piston movement was observed, suggesting the majority of densification occurred during the temperature and force ramp. Significant piston movement was observed as the temperature and force were relieved.

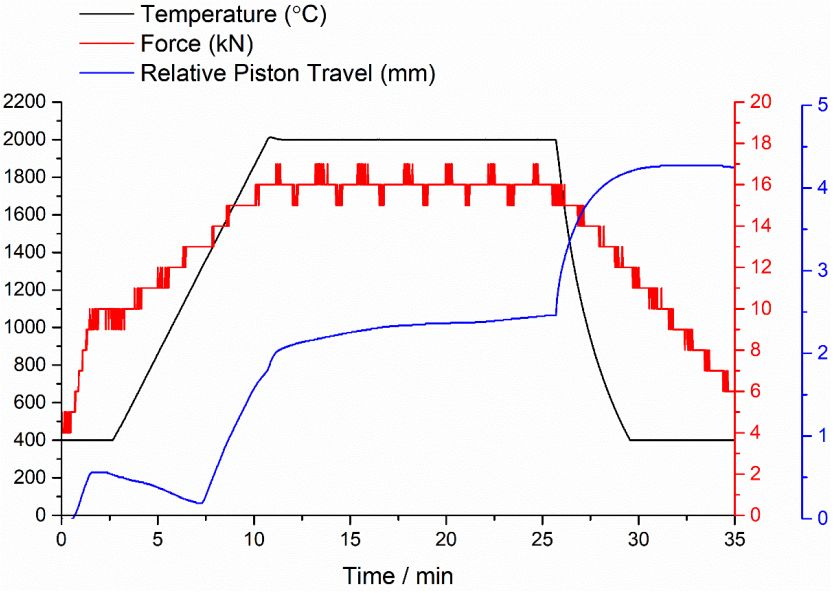

Figure 228 – Typical sintering profile for a sample of TiC, showing the temperature, applied force and relative piston movement.

15.2 X-ray diffraction

The XRD pattern is shown in Figure 229. The data were fitted to TiC by Rietveld refinement (χ^2 3.522, R_p 0.0957, R_{wp} 0.1267) [179]. The lattice parameter, *a*, was 4.333 Å and the cell volume was 81.345 $Å^3$. The density was measured as 4.802 ± 0.011 g cm^{-3}, giving a density relative to the calculated density of TiC of 98%.

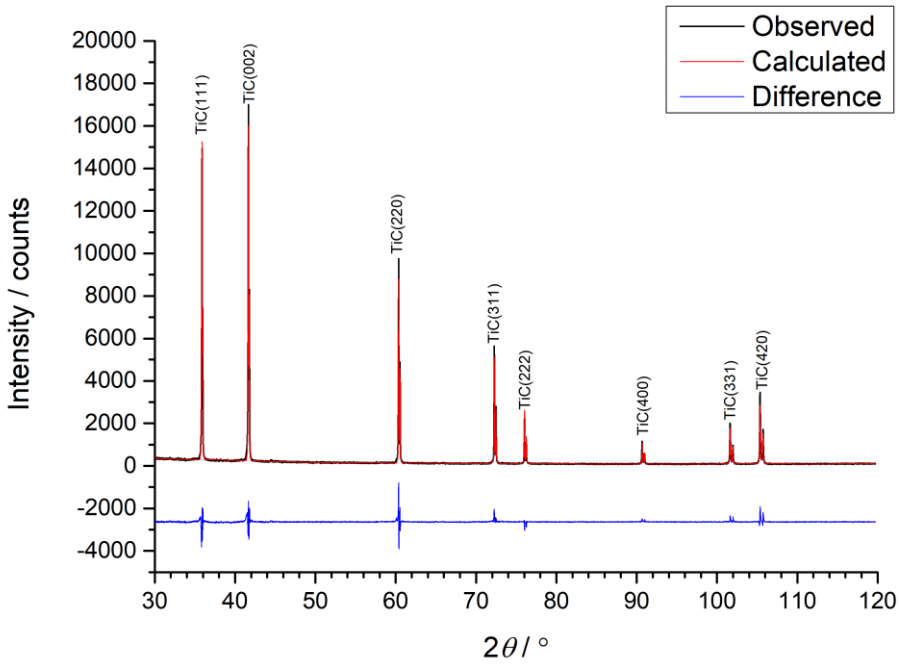

Figure 229 – Indexed XRD pattern fitted by Rietveld refinement for a typical sample of bulk TiC.

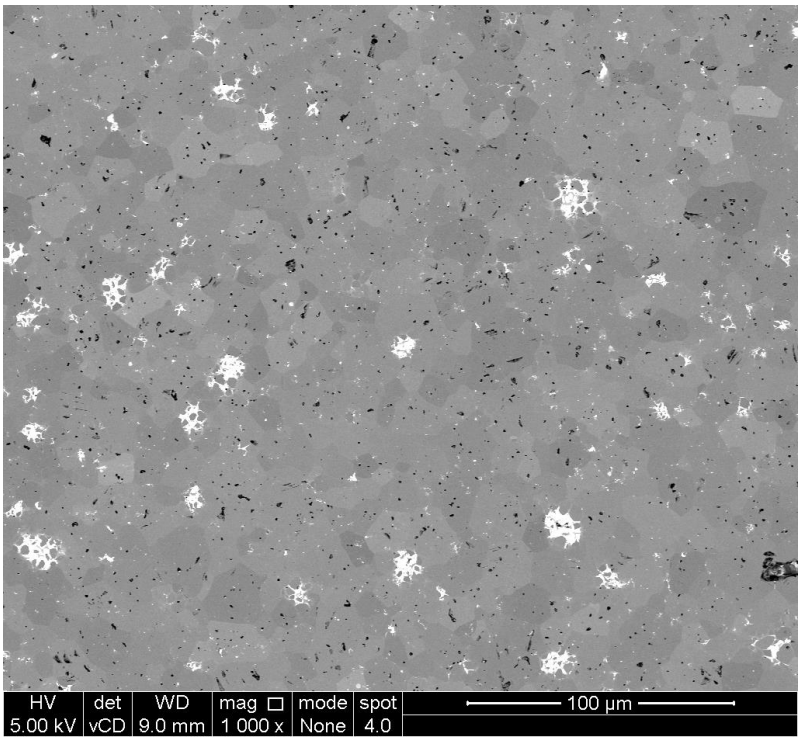

Figure 230 – BSE image showing a general overview of the morphology at the surface of a bulk sample of TiC. The bright contrast regions show the presence of WC_x.

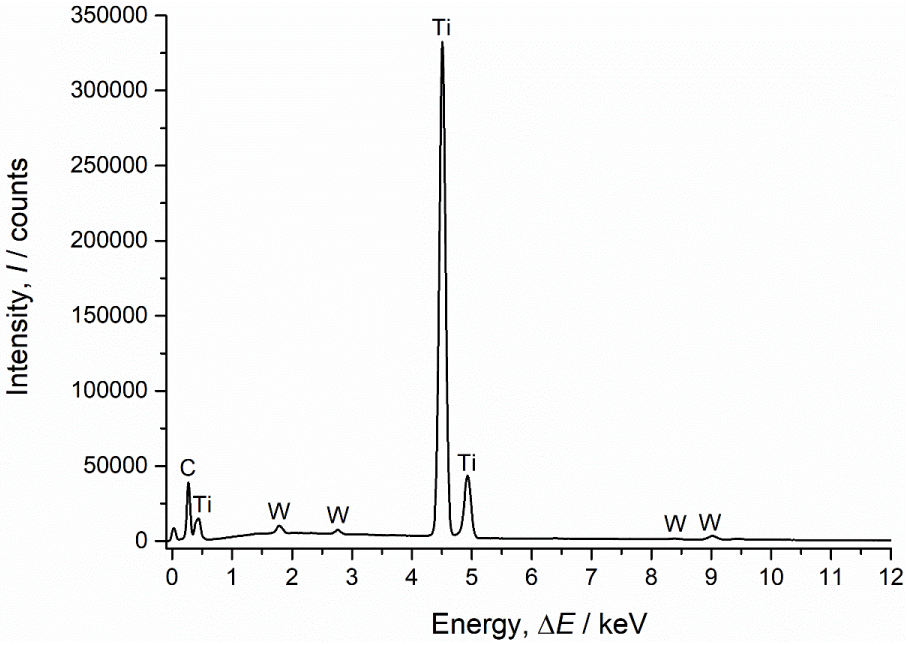

Figure 231 – Map sum spectrum for the EDS map of Figure 230. The composition calculated by the Aztec software, excluding carbon, was 99.5at.% Ti and 0.5at.% W.

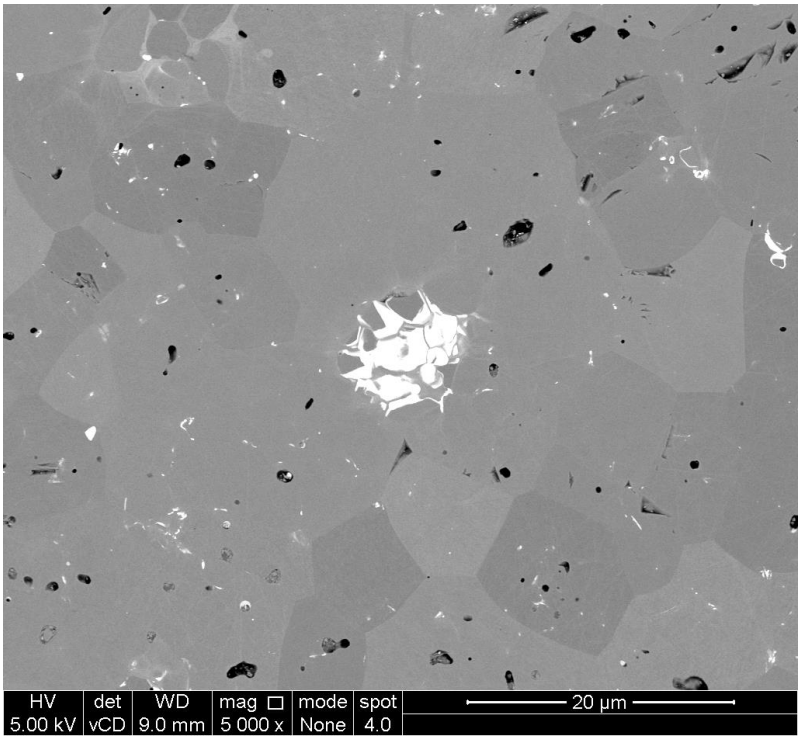

Figure 232 – BSE image taken at a higher magnification, showing the general morphology of a cluster of WC_x in the middle of the image. In the top left corner of the image, some W can be observed surrounding TiC grains. The dark contrast spots are pores.

15.3 Microstructural examination

Further characterisation was performed by SEM. Figure 230 is a BSE image giving a general overview of the sample morphology. EDS mapping revealed that the bright regions are WC_x. The map sum spectrum is shown in Figure 231. The fraction of W present was found to be 0.5at.%; this was consistent with the stated reagent purity of 99.5% TiC. Some porosity is also visible as dark spots. The pores appear relatively small and unconnected, which is consistent with the high relative density. The grain size from simple measurements is ~2 µm.

Figure 232 is a higher magnification image showing the general morphology of the WC_x clusters. The grain size of the WC_x particles appears to be smaller than TiC. In the top left of the image, it appears that W has distributed around TiC grains in some locations, reducing their grain size in such locations.

15.4 Discussion

The samples of TiC produced were of decent quality. They were not fully dense, but the relative density of 97.4% was sufficiently high for corrosion testing. The grains were relatively fine, with a grain size of ~2 µm. This grain size is the same as the initial particle size of the reagent.

A significant quantity of tungsten carbide, ~0.5mol.%, was observed in the bulk samples. Neither the powder nor bulk samples were exposed to WC during processing, so the impurity must have been present from the supplier. The purity of powder used was 99.5% which is approximately consistent with the mole fraction determined from EDXS. It is likely that the manufacturer prepared the powder as a sintered material then milled with WC milling media and sieved to obtain the TiC powder with relatively small particle size.

The densities and XRD patterns of all samples of TiC used for corrosion testing were consistent. Further details of the material's characterisation, including its mechanical properties, can be found in work by Tanagorn Kwamman [189].

16 Appendix F – Corrosion of Ti_3AlC_2: Additional Results

16.1 Preliminary Experiments

Preliminary experiments were performed on a sample polished to 1 µm on both sides then cut into quarters. The graphite was not ground from the edge of the sample under the assumption that it would be unreactive and act as a mask [193] (the curved edge was discounted when calculating the surface area). One sample was used to measure the open circuit potential, otherwise known as the corrosion potential. Another sample was used to obtain a cyclic voltammogram with Ti_3AlC_2 as the working electrode, after which a positive current was applied to anodically dissolve the sample. A third sample underwent a preliminary static corrosion test which was accelerated by a galvanic circuit. The results obtained from these preliminary experiments aid the interpretation of results obtained in later static corrosion tests.

Following these experiments, all samples were characterised by GAXRD and SEM with EDS. Raman spectroscopy was also attempted. The counts were high, but the peaks were obscured by background; a lower laser power did not resolve the issue. Consequently, Raman spectroscopy was abandoned as a testing method for later samples.

After 16 h exposure to LKE at 550°C, uniform corrosion was observed with migration of aluminium to the surface and penetration of chlorine. Aluminium and oxygen were present on the surface of the sample, but it is difficult to determine whether oxidation occurred in-situ or post-corrosion. The GAXRD data may indicate that this is lithium aluminium oxide. The presence of lithium metal, which could subsequently react with alumina, would be consistent with electrolysis of LiCl at the surface of Ti_3AlC_2 followed by reaction of $Cl_{2(g)}$ with the MAX phase.

Significant reaction was observed for the sample which underwent anodic dissolution with 50 mA for 1 h in LKE at 550°C. Multiple phases were visible in the microstructure and require further characterisation to fully ascertain the reaction mechanism. Large regions of TiC_x with small grain size formed, which appears to be a final corrosion product.

16.1.1 Open circuit potential

The open circuit potential (OCP) for a sample of Ti_3AlC_2 as the working electrode was measured over 16 h at 550°C (measured by temperature controller), as shown by Figure 233. A rapid reaction occurred in the first hour, reaching equilibrium in the latter stages of the experiment. The potential at 16 h was -0.968 V, at which point it had been stable to three significant figures for 37 min. Cyclic voltammetry with a tungsten electrode indicated no significant impurities were present in the salt after measurement of the OCP. The microstructure of this sample is representative of the early stages of corrosion in relatively pure LKE.

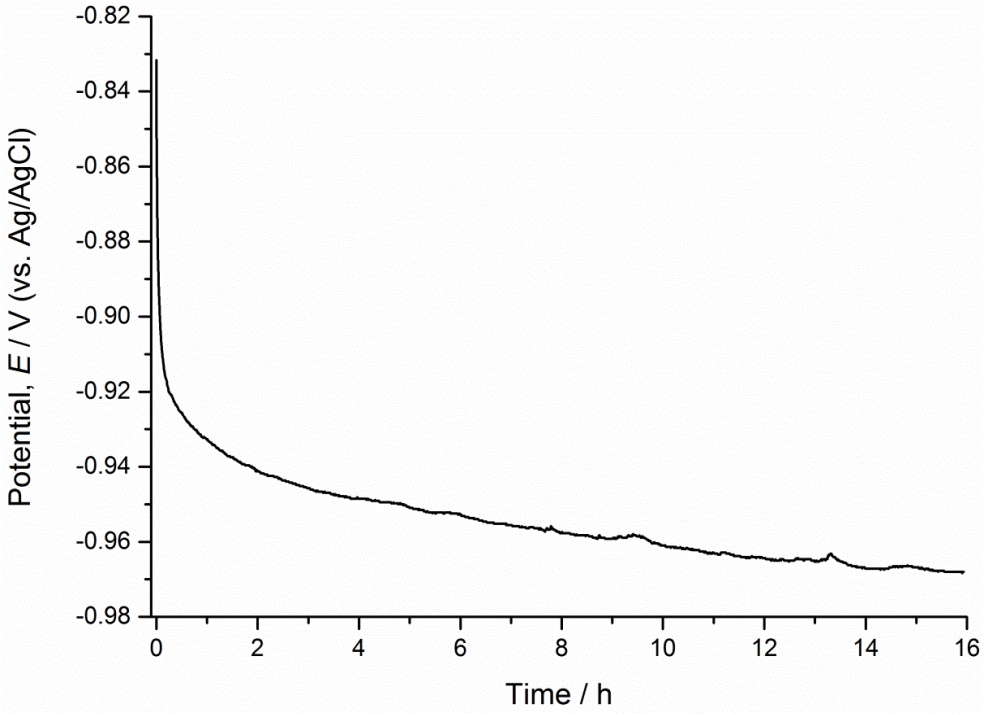

Figure 233 – Measurement of the open circuit potential vs. Ag/AgCl (1.5 wt.%) for a Ti_3AlC_2 working electrode.

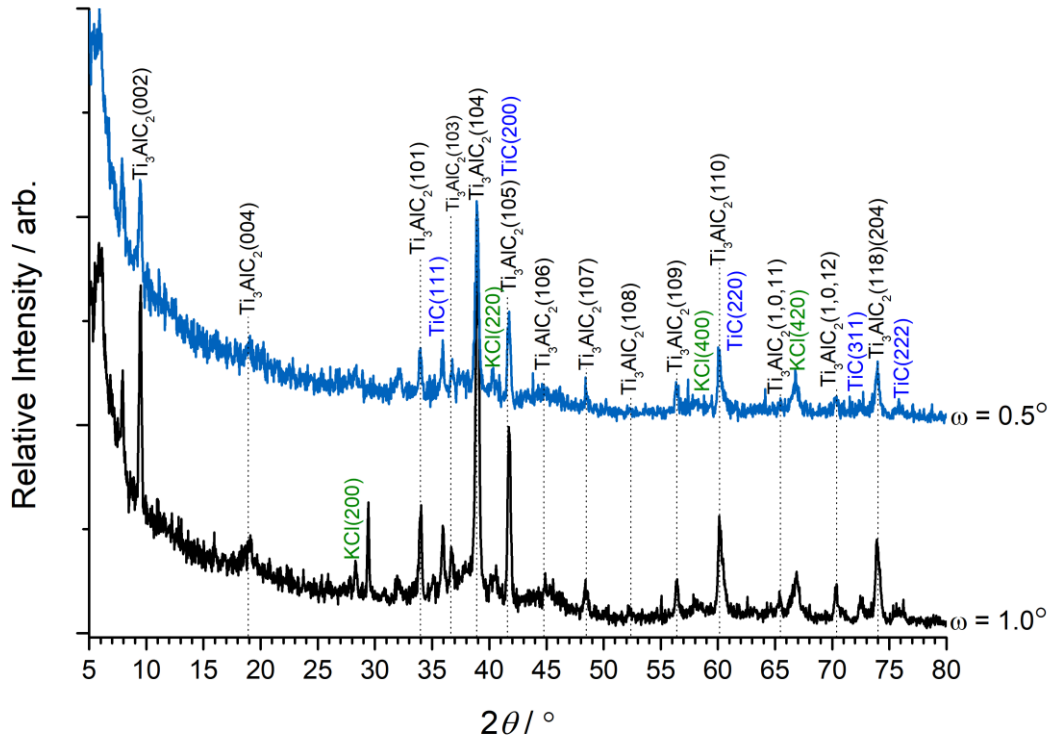

Figure 234 – GAXRD patterns for a sample of Ti_3AlC_2 which was exposed to LKE for 16 h whilst measuring the OCP. The patterns were normalised relative to the most intense peak in each pattern.

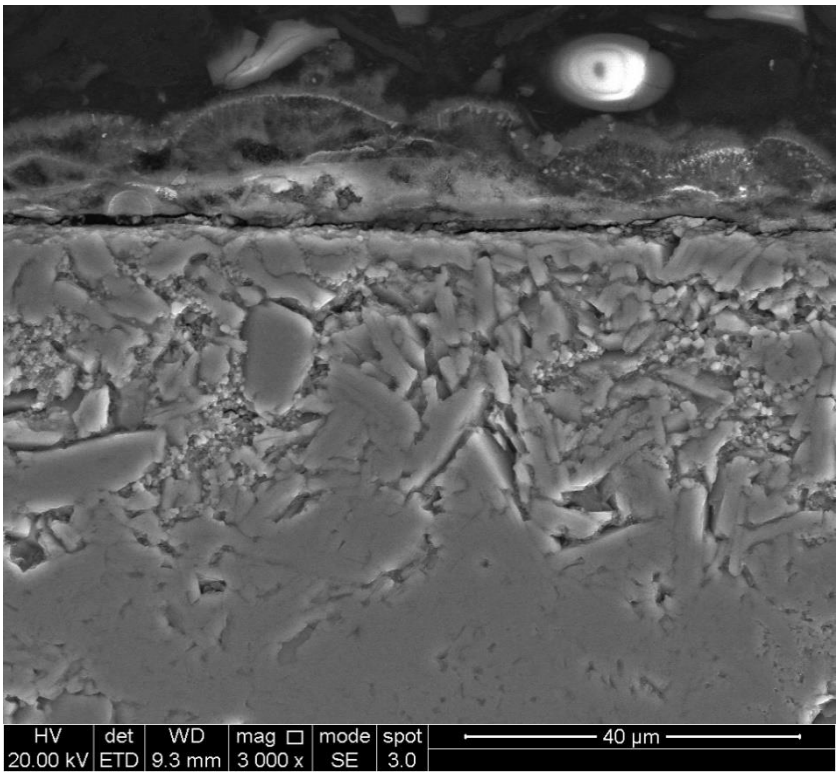

(a) SE image

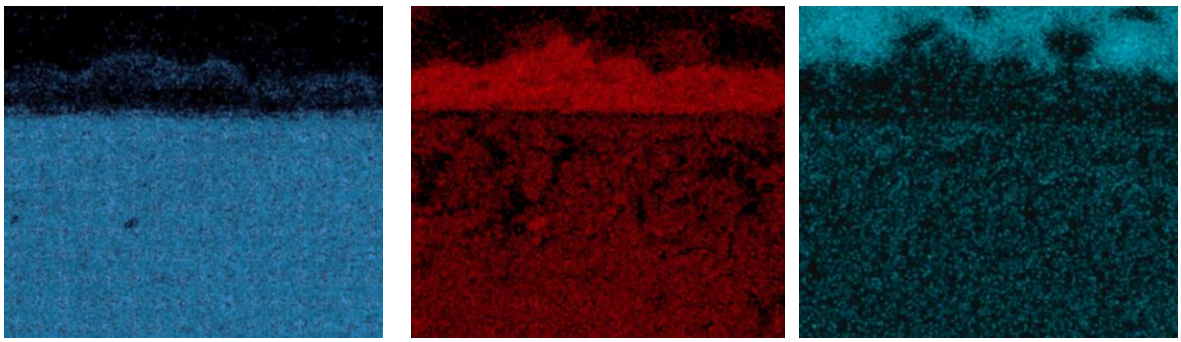

(b) Ti $K_{\alpha1}$ (c) Al $K_{\alpha1}$ (d) C $K_{\alpha1}$ and $K_{\alpha2}$

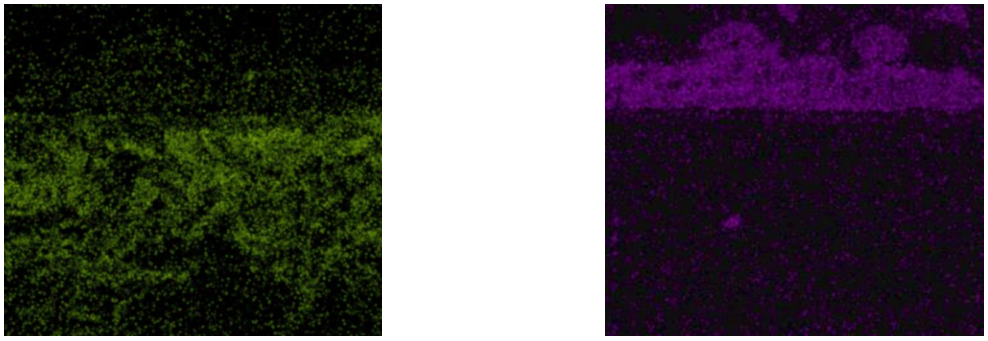

(e) Cl $K_{\alpha1}$ (f) O $K_{\alpha1}$

Figure 235 – SE image and EDS maps of the corrosion layer of a sample of Ti_3AlC_2 which was exposed to LKE at 550°C for 16 h whilst measuring the open-circuit potential.

The GAXRD patterns for the sample exposed to LKE for 16 h whilst measuring the OCP are shown in Figure 234 [178,179]. Ti_3AlC_2, TiC_x and KCl are the main phases identified, but there are some additional peaks which remain undetermined. Lithium aluminium oxide, either $LiAl_5O_8$ or $LiAl_2O_{3.5}$, appears to be a good match for a number of these peaks [209,210]. Furthermore, such a phase is consistent with EDS of the cross-section which shows Al and O present on the surface of the material. There are additional unidentified peaks at 6.1° and 7.9° 2θ.

Figure 235 is a BSE image of the cross-section which shows the corrosion layer of the sample. The thickness of the corrosion layer is ~40 µm and the morphology appears similar to the general morphology observed after the initial static corrosion test (§ 16.1.4) and exposure to as-received salts (§ 6.1.1 and 0). A deposit of aluminium oxide is visible on top of the underlying surface. This may have been present as aluminium and oxidised upon exposure to the atmosphere. Such deposits were not observed in the static corrosion tests which suggests that aluminium dissolves in the molten salt after migrating to the surface. The underlying surface has relatively low roughness, which suggests spalling may have occurred in the more severe corrosion tests. Chlorine has penetrated the corrosion layer, as per previous experiments.

16.1.2 Cyclic voltammetry

Cyclic voltammetry was performed with a Ti_3AlC_2 working electrode. The cyclic voltammogram, with a scan rate 2 mV s^{-1}, is shown in Figure 236. It is clear from the current response that numerous reduction reactions occurred at the surface of the sample.

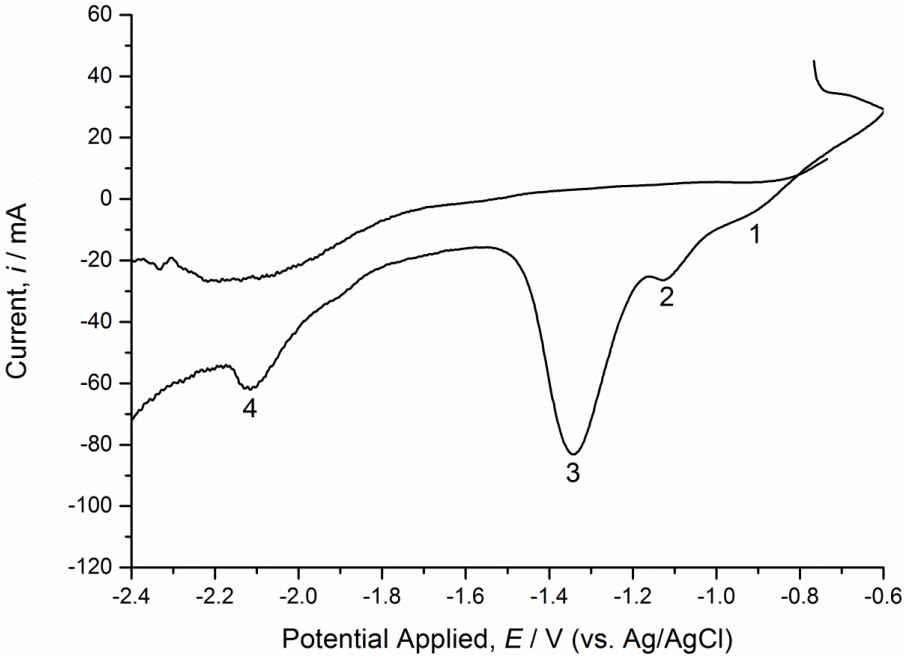

Figure 236 – Cyclic voltammogram measured using a Ti_3AlC_2 electrode.

16.1.3 Anodic dissolution

A current of 50 mA was applied for 1 h to a sample exposed to LKE at 550°C as an accelerated corrosion test, after which the sample was characterised by GAXRD and SEM. However, the sample essentially represents corrosion of Ti_3AlC_2 by $Cl_{2(g)}$ formed via the electrolysis of LiCl at the electrode surface when a current is applied. The microstructure observed is similar to that of the sample B exposed to as-received LKE at 600°C for 125 h (§ 0).

The GAXRD patterns are shown in Figure 237, normalised relative to the Ti_3AlC_2 (104) peak. The intensity of TiC_x peaks increase as the glancing angle is decreased, indicating that TiC_x is a corrosion product. The greater intensity of the TiC_x (200) peak relative to the (111) peak may indicate that any carbon vacancies are randomised; however, the Ti_3AlC_2 (105) peak overlaps with the TiC (200) peak [129]. KCl is present at all glancing angles and its peaks are most intense at 10° ω. A graphite peak is present at 10° ω due to graphite on the edge of the sample from the synthesis process, rather than as a corrosion product.

An overview of the corrosion layer is shown in Figure 238. The morphology is relatively complex and appears to contain multiple species. The corrosion layer is approximately 125-185 µm thick. Some

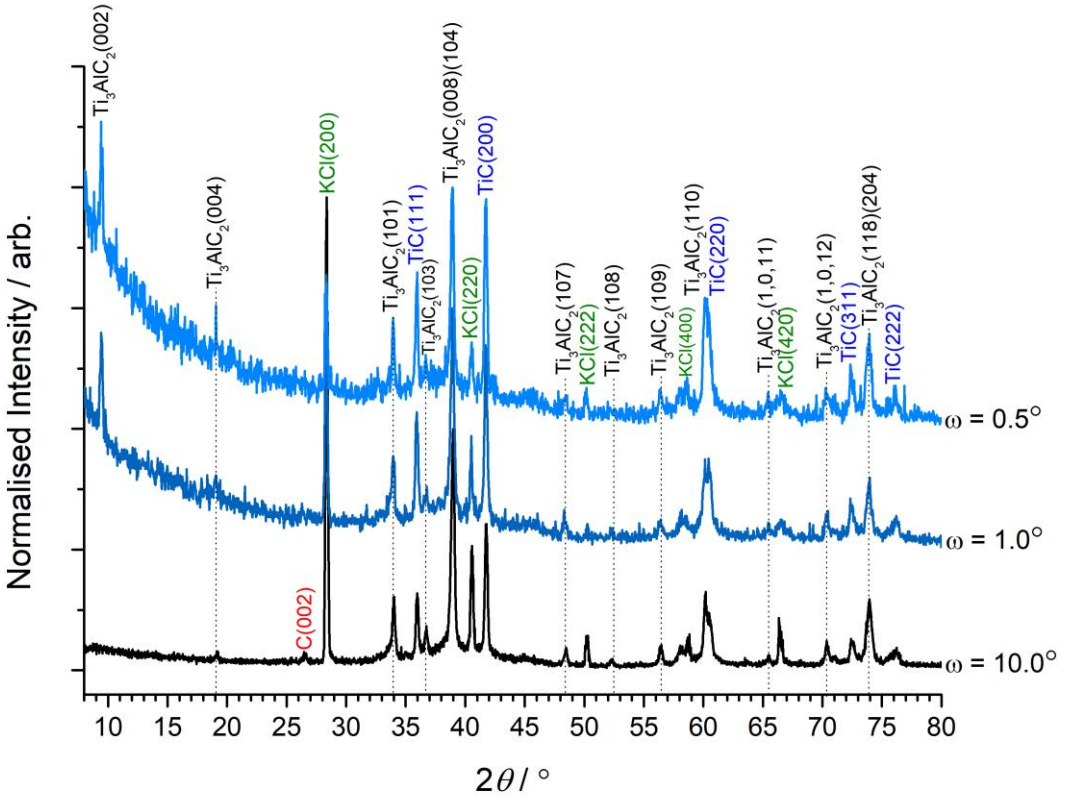

Figure 237 – GAXRD patterns for a sample of Ti_3AlC_2 which underwent anodic dissolution by a 50 mA current for 1 h in LKE at 550°C. The patterns were normalised relative to the Ti_3AlC_2 (104) peak.

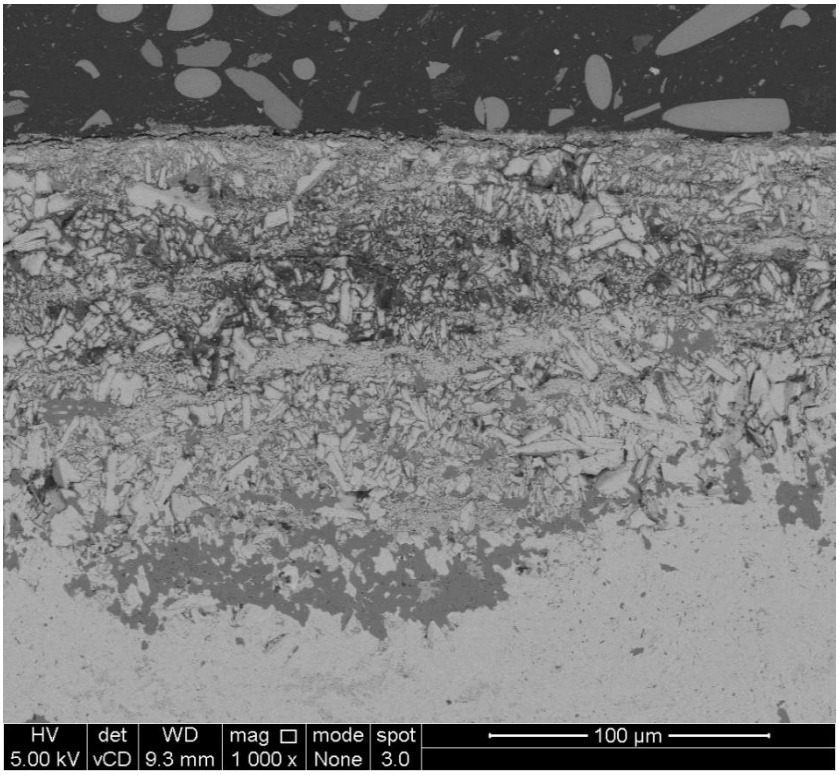

Figure 238 – BSE image showing an overview of the corrosion layer in a cross-section of a sample of Ti_3AlC_2 which was subject to anodic dissolution.

spalling can be seen at the sample surface. Overall, the sample morphology is most comparable to sample B of the two samples which were exposed to as-received LKE at 600°C for 125 h (§ 0).

Figure 239 is representative of the morphology observed at the corrosion front. A dark contrast phase can be seen, with similar morphology to that observed for sample B exposed to as-received LKE at 600°C for 125 h.

The particles with a very small grain size are indicative of titanium carbide and are shown further in Figure 240. Here it can be seen that the grain size is typically < 1 µm. The large volume of this phase in comparison to the titanium carbide impurity phased observed in the synthesis chapter suggests that this is a corrosion product formed by the decomposition of Ti_3AlC_2.

Furthermore, there are regions within the corrosion layer where large clusters of TiC_x dispersed amongst what appear to be former grains of MAX phase (Figure 241).

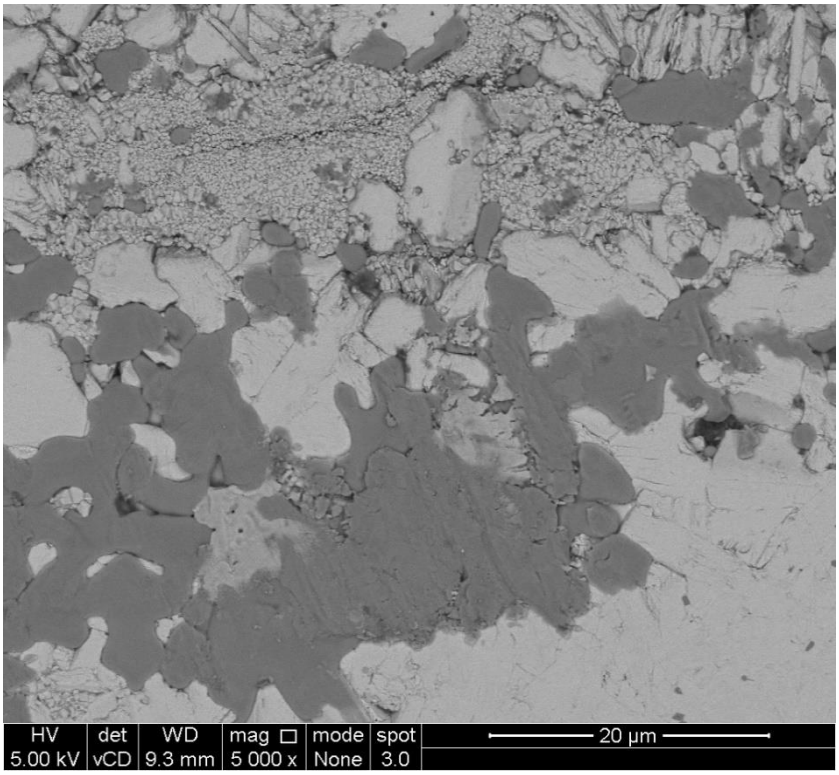

Figure 239 – BSE image showing the morphology of phases at the corrosion front of a sample of Ti_3AlC_2 which underwent anodic dissolution.

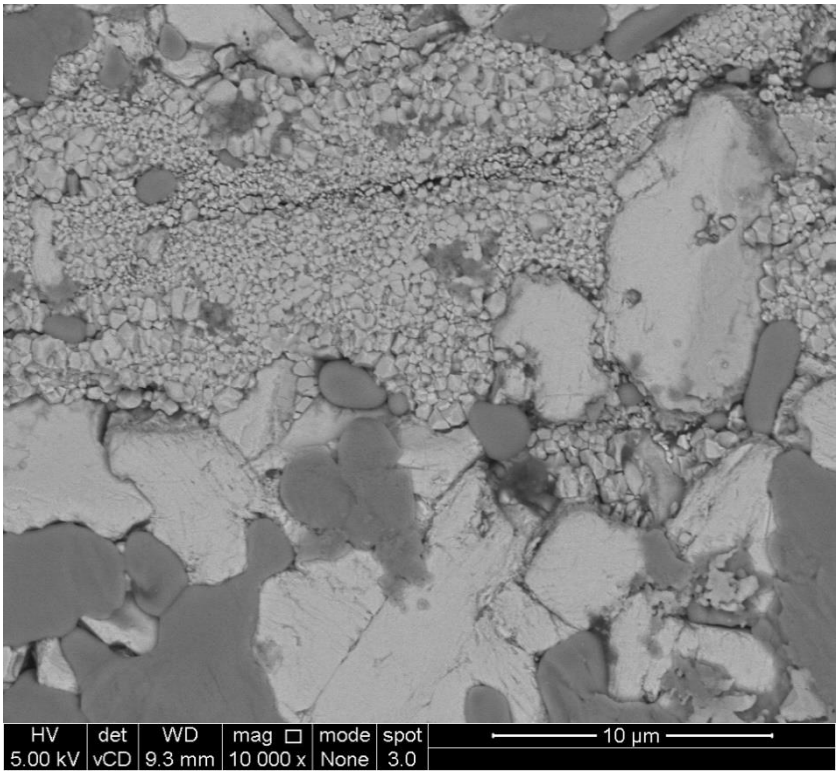

Figure 240 – Morphology of a TiC_x phase observed in the corrosion layer of a sample of Ti_3AlC_2 which underwent anodic dissolution.

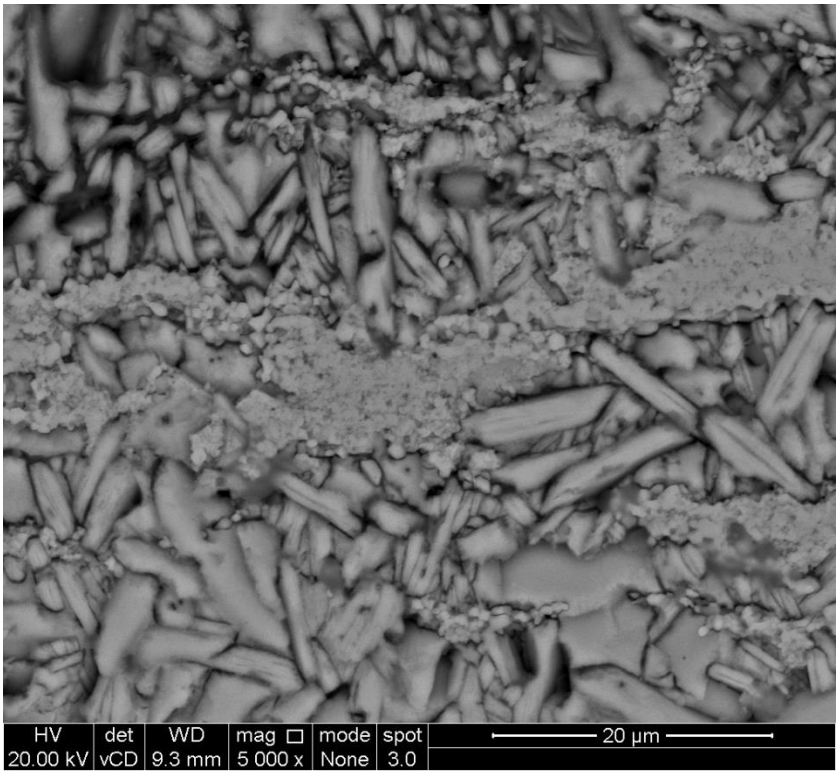

Figure 241 – BSE image of a sample of Ti_3AlC_2 which underwent anodic dissolution, showing a region within the corrosion layer where large clusters of TiC_x are dispersed amongst former grains of MAX phase.

16.1.4 Initial corrosion test

The sample was weighed then wrapped in 0.5 mm diameter molybdenum wire and suspended from the lid of the vessel. The nickel crucible, containing 11.9 g of processed LKE, was placed in the vessel and the lid of the vessel was suspended above the base so that the samples were suspended in their respective crucibles. The furnace was heated at a rate of 5°C min^{-1}. The temperature was held at 150°C for 12 h to flush any residual air or moisture from the vessel. The temperature was then raised to 500°C, at which point the samples were submerged and the vessel fully sealed. The furnace temperature was then raised further to 650°C (actual temperature in vessel ~600°C) where it was held for 112 h. The cooling rate was also 5°C min^{-1}.

The effects of dissimilar material corrosion were not considered at the time; a circuit was formed, and the sample represents an accelerated corrosion test. This circuit, consisting of the sample, the salt, the nickel crucible, the stainless-steel vessel and the molybdenum wire, is shown in Figure 242. This certainly exacerbated the rate of corrosion as illustrated by the significant mass loss of 5.54 mg cm^{-2} and the corrosion depth between 170-270 µm. Chloride ions were oxidised to chlorine gas which then reacted with Ti_3AlC_2. With regards to performance in a molten salt reactor, this sample represents the expected corrosion in a very oxidising salt which has departed from standard operating conditions.

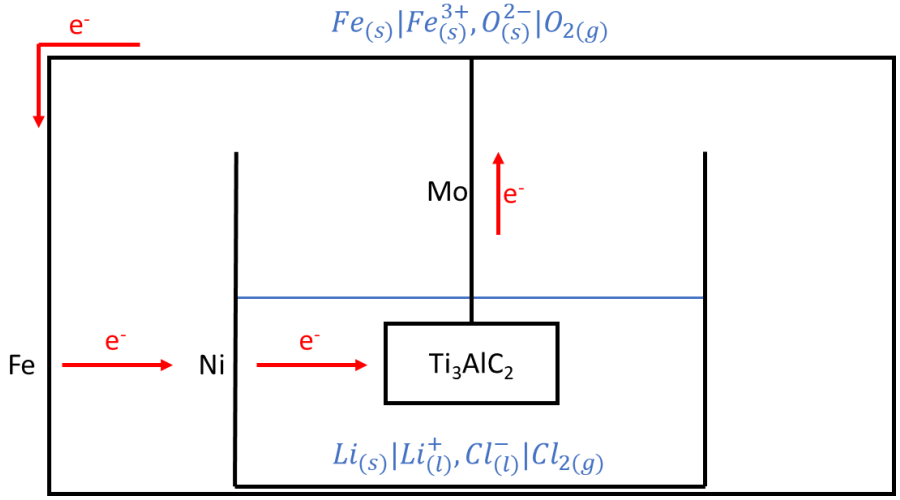

Figure 242 – Diagram of the electrochemical circuit formed in the initial corrosion test.

The experiment was the first use of the stainless-steel vessel and high purity salt prepared by Hugues Lambert was used. No oxygen was detected in the corrosion layers by EDS, confirming that air and moisture were excluded. As such, it appears that this sample shows the effect of chlorine on Ti_3AlC_2 in the absence of oxygen.

The mass loss per unit area of the sample was high relative to samples of nickel-based superalloys exposed to the same conditions. The mass loss per unit area of Hastelloy-N was 0.01 mg cm^{-2} and that of Haynes-214 was 0.90 mg cm^{-2} [43].

16.1.4.1 Glancing angle X-ray diffraction

Figure 243 shows the GAXRD patterns of the initial static corrosion test sample collected at glancing angles, ω, of 0.5°, 1°, 5° and 10° [177–179]. The major peaks at all angles belong to titanium carbide. The peaks are very broad, likely due to the presence of carbon vacancies. The peaks at approximately 34° and 39° 2θ agree with the peak locations for Ti_3AlC_2. Additionally, these peaks decrease in intensity as the glancing angle is decreased, indicating that the peaks are due to the underlying substrate. The (101) and (104) peaks of Ti_3AlC_2 are the most intense which explains why the other peaks for Ti_3AlC_2 were not detected. The fact that TiC_x is the dominant phase even at 10° ω indicates significant corrosion. There also appears to be unidentified peaks at approximately 28° and 58° 2θ. The peak at approximately 26° 2θ is due to the graphite on the edge of the sample from sample preparation, which had been removed prior to data collection at the other glancing angles.

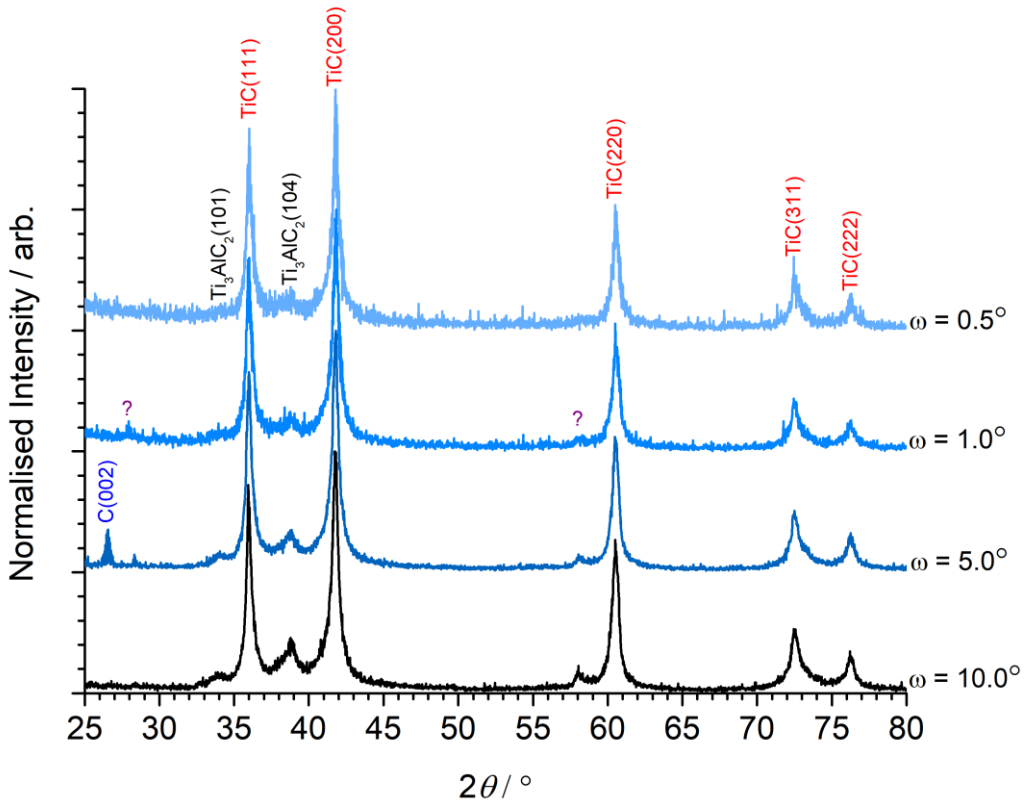

Figure 243 - GAXRD pattern of the initial static corrosion test sample. TiC_x was the major phase at all glancing angles.

The lattice parameter, a, of TiC_x was calculated from the 2θ value of the (200) peak as 4.324 Å. From the graph of TiC_x stoichiometry *vs.* lattice parameter produced by Rudy, this corresponds to a carbon content of ~0.67 [89]. Hence, the corrosion product appears to be non-stoichiometric $TiC_{0.67}$. The relative intensity of the (111) and (200) peaks indicate randomisation of the carbon vacancies, which would be expected to occur over the exposure time used [129].

16.1.4.2 Microstructural analysis of the surface

Figure 244 is a BSE image taken of the corroded surface which provides a general overview of the surface microstructure after corrosion. Preferential attack of the grain boundaries has occurred. Additionally, there appears to be two distinct regions, one with heavily etched grains and one where the grains have either only have been lightly etched or have sintered.

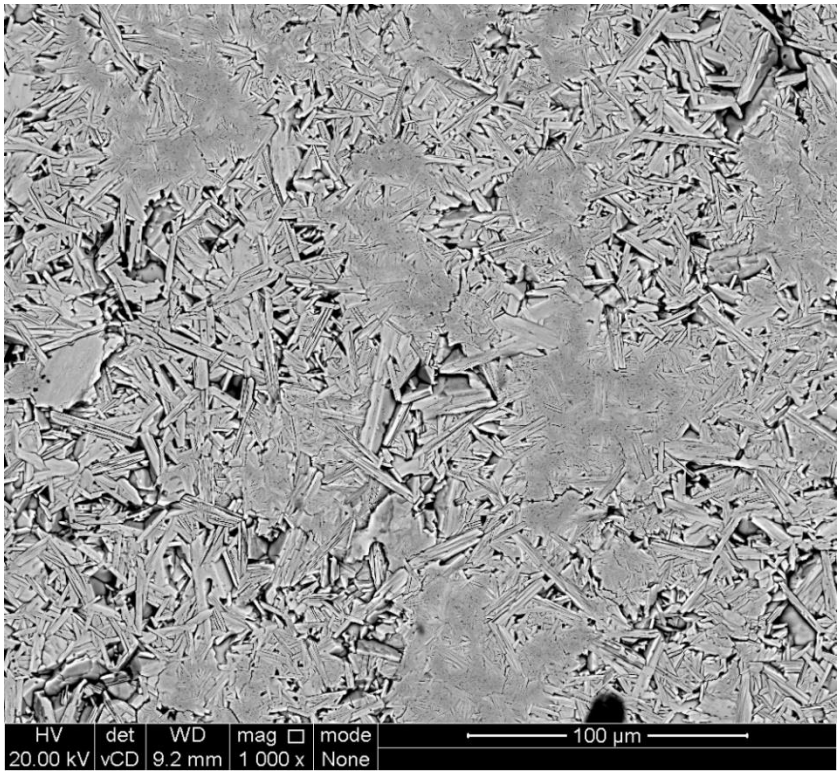

Figure 244 – BSE image of the corroded surface.

Figure 245 is a BSE image taken at a greater magnification. The annotations are the locations of point analyses, the compositions of which can be found in Table 45. It appears that Al has been almost completely removed from the surface of the material. Delamination of the layers within the MAX phase-like grains is consistent with the loss of aluminium. Additionally, the amount of C is mostly lower than Ti, suggesting the GAXRD data represents non-stoichiometric TiC_x. Both the rectangular MAX phase-like grains and the smaller TiC-like grains have very similar compositions. Additionally, the TiC_x clusters appear larger than in the pristine sample. This suggests that as the MAX phase loses aluminium, the grains recrystallize over time.

16.1.4.3 Microstructural examination of the cross-section

Figure 246 is a BSE image and EDS maps of the cross-section of the initial static corrosion test sample. The magnification used highlights the depth of the reaction layer. Most of the layer extends to ~170 µm deep but there are some bulges such as the lower half of the image which extend up to ~270 µm deep. Aluminium has been lost throughout the entire corrosion layer and chlorine has

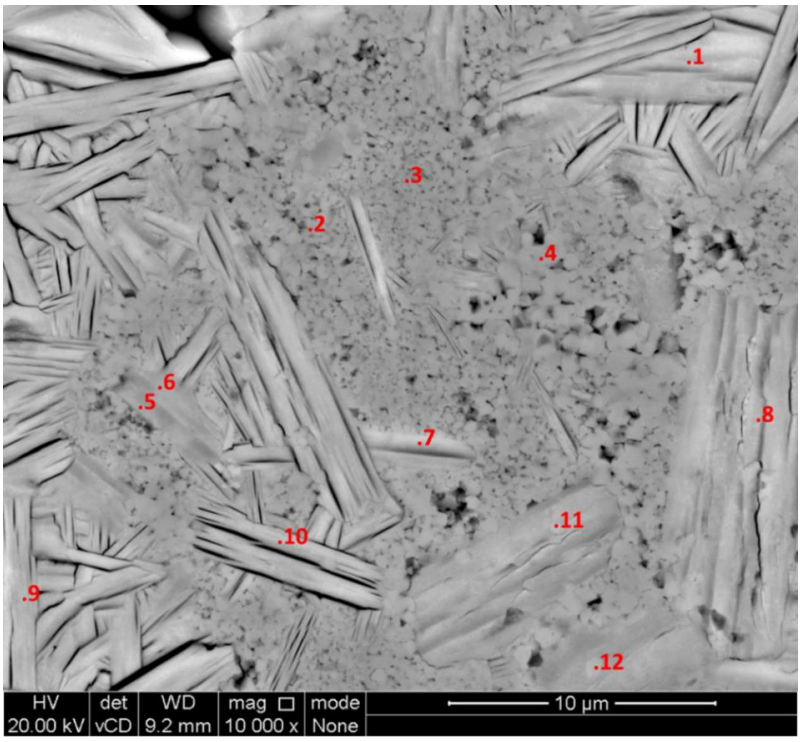

Figure 245 – BSE image of corroded sample annotated with the locations of point analyses (Table 45).

Table 45 – Elemental compositions (in at.%) of the point analyses shown in Figure 245.

Point	Ti	C	Cl	Fe	Ni	Al	O	Other	Other Elements
1	53.6	40.3	2.2	1.4	1.2	0.6	-	0.6	S, K, Si, W
2	53.2	45.1	0.8	0.4	0.1	0.2	-	0.1	Si
3	55.7	43.8	0.2	-	0.1	0.1	-	-	-
4	56.3	43.7	0.1	-	-	-	-	-	-
5	42.4	54.1	2.0	0.6	0.4	0.2	-	0.3	K, Si, S, W
6	45.1	49.6	3.5	0.6	0.5	0.2	-	0.5	K, Si, S
7	52.1	43.9	1.2	0.9	0.9	0.7	-	0.4	S, Si, K
8	34.7	45.0	6.9	0.7	0.7	0.5	10.9	0.5	K, Si, S
9	35.0	56.9	5.3	0.9	0.9	0.6	-	0.5	K, Si, S
10	49.1	46.2	1.8	1.2	0.6	0.5	-	0.7	Si, Cu, K, S
11	44.1	48.1	5.2	0.9	0.7	0.4	-	0.6	K, Cu, Si, S
12	48.9	45.2	3.6	0.8	0.6	0.5	-	0.4	K, Si, S

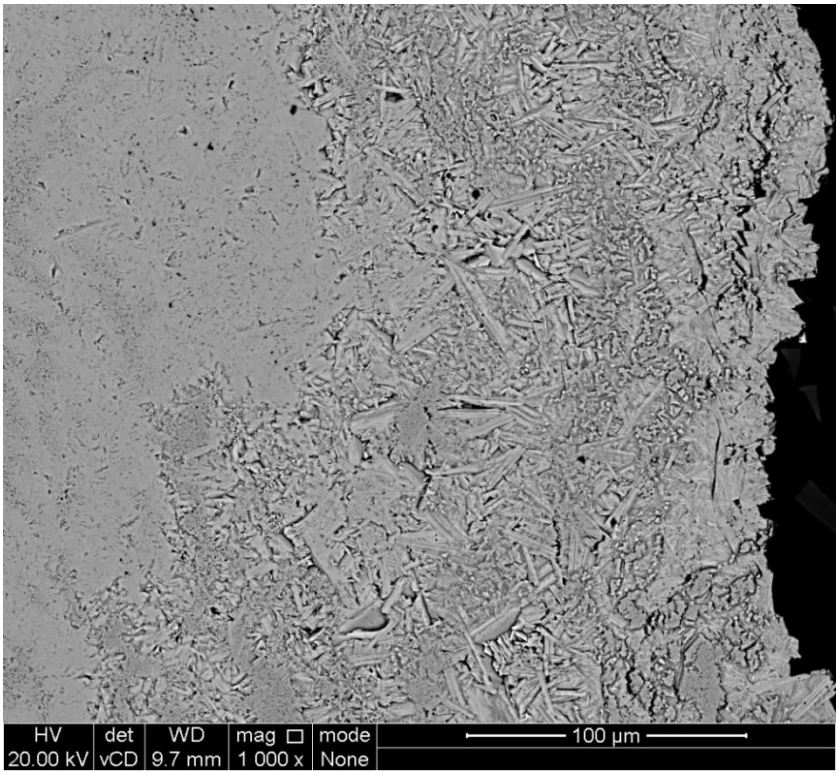

a) BSE image

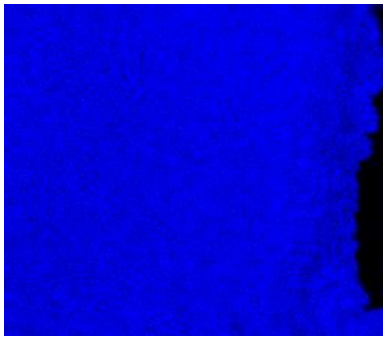

b) Ti $K_{\alpha1}$

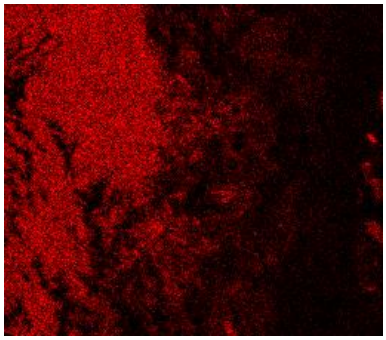

c) Al $K_{\alpha1}$

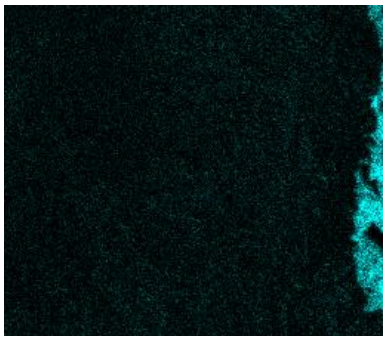

d) C $K_{\alpha1}$ and $K_{\alpha2}$

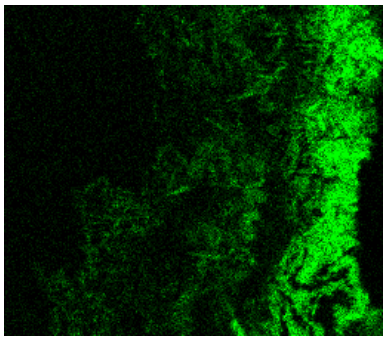

e) Cl $K_{\alpha1}$

Figure 246 – BSE image and EDS maps of the cross-section of the initial static corrosion test sample showing the depth of the reaction layer.

penetrated to the underlying substrate. There are two particular regions of the corrosion layer. There is an outer region ~50 µm thick where chlorine has penetrated significantly, aluminium is completely

absent and there is a slight absence of titanium, and an inner region where chlorine has penetrated less significantly, and some aluminium remains. The morphology in the BSE image differs in the two regions.

Figure 247 is a BSE image of the outermost region of the reaction layer. The annotations show the locations of point analyses, with the corresponding compositions found in

Table 46. The regions with morphology similar to location 1 have the composition of titanium carbide. The particles with morphology similar to location 4 contain chlorine, as well as carbon and titanium. The carbon content is ~50at.% for all of these points, but the titanium content seems to decrease as the chlorine content increases, suggesting that titanium reacts or interdiffuses with chlorine. From their morphology, these grains appear to be former Ti_3AlC_2 grains which have lost all their aluminium and some of their titanium. The presence of chlorine suggests it plays a key role in the dissolution of these elements. Chlorine appears to migrate through the layers of the former MAX phase grains to penetrate to the corrosion front. After complete removal of aluminium and partial removal of titanium, the grains likely recrystallise as titanium carbide.

Figure 248 is a BSE image of the innermost region of the reaction layer. The compositions of the point analyses at the annotated locations are shown in Table 47. The compositions of these locations are consistent with Ti_3AlC_2 with a small proportion of chlorine. The morphology of these particles is

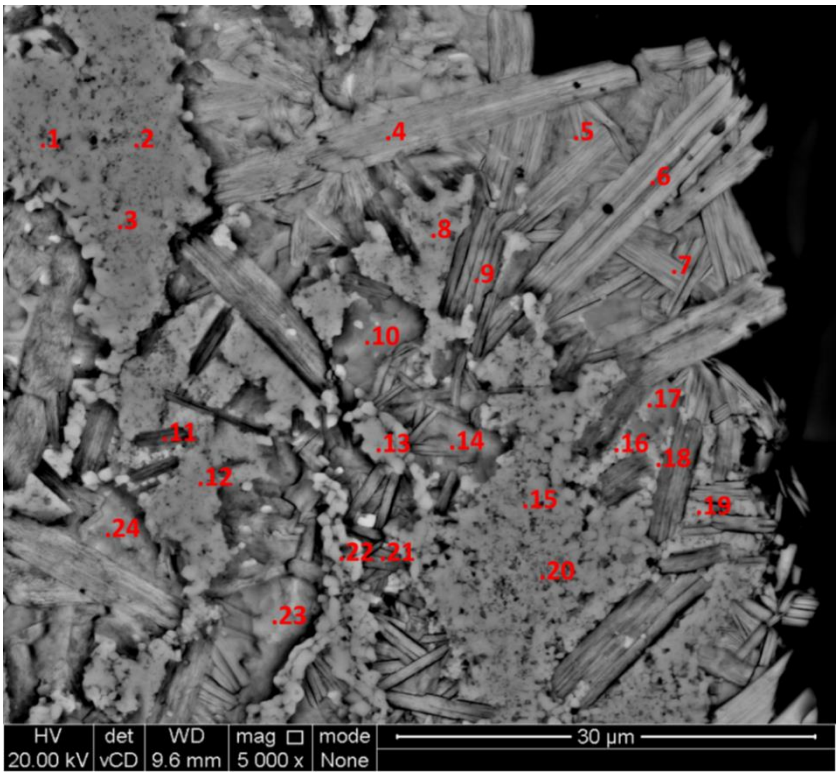

Figure 247 – BSE image of the outermost region of the reaction layer of the initial static corrosion test. The compositions of the point analyses are shown in Table **46**.

Table 46 – Elemental compositions (in at.%) of point analyses shown in Figure 247.

Location	Ti	C	Cl	Other	Other Elements
1	52.4	47.3	0.2	0.1	Al
2	53.0	46.5	0.2	0.2	Al, Si, Rh
3	50.4	49.0	0.5	0.2	Al, Si
4	33.8	50.5	15.3	0.4	Al, Si, K
5	41.5	50.4	7.2	0.8	Fe, Al, Si, K, Ca
6	42.0	50.8	6.3	1.0	Fe, Al, Si, K, Ca, Cu
7	46.7	48.8	3.6	0.9	Fe, Al, Si, K, Ca
8	57.5	39.2	2.9	0.4	Al, Si, K, Fe
9	54.2	41.8	3.3	0.6	Al. Fe. Si, K
10	52.5	47.0	0.2	0.3	Al, Si
11	39.8	50.0	9.4	0.8	Al, Si, K, Ca, Fe, Cu
12	39.7	47.6	11.6	1.1	Al, Cu, Si, K, Fe
13	50.7	45.9	2.9	0.5	Al, Si, K, Fe
14	75.2	23.1	1.4	0.3	Al, Si, Fe
15	56.3	40.0	3.0	0.6	Fe, Al, Si, K, Ca
16	49.9	49.8	0.1	0.2	Al, Si
17	55.0	44.6	0.2	0.2	Al, Si
18	54.5	45.2	0.2	0.1	Al,
19	51.9	47.8	0.1	0.2	Al, Fe
20	44.0	55.3	0.4	0.3	Al, Si, K, Fe
21	46.9	49.1	3.3	0.8	Al, Si, Fe, K, Ca
22	45.4	54.0	0.4	0.2	Al, Si
23	45.9	46.6	7.0	0.6	Al, Si, K, Ca, Fe
24	46.2	53.3	0.3	0.2	Al, Si

Table 47 – Elemental compositions (in at.%) of the point analyses shown in Figure 248.

Location	Ti	C	Al	Cl
1	48.7	36.7	13.8	0.7
2	49.5	37.3	12.4	0.8
3	48.7	37.4	12.5	1.3
4	44.9	40.4	14.4	0.3

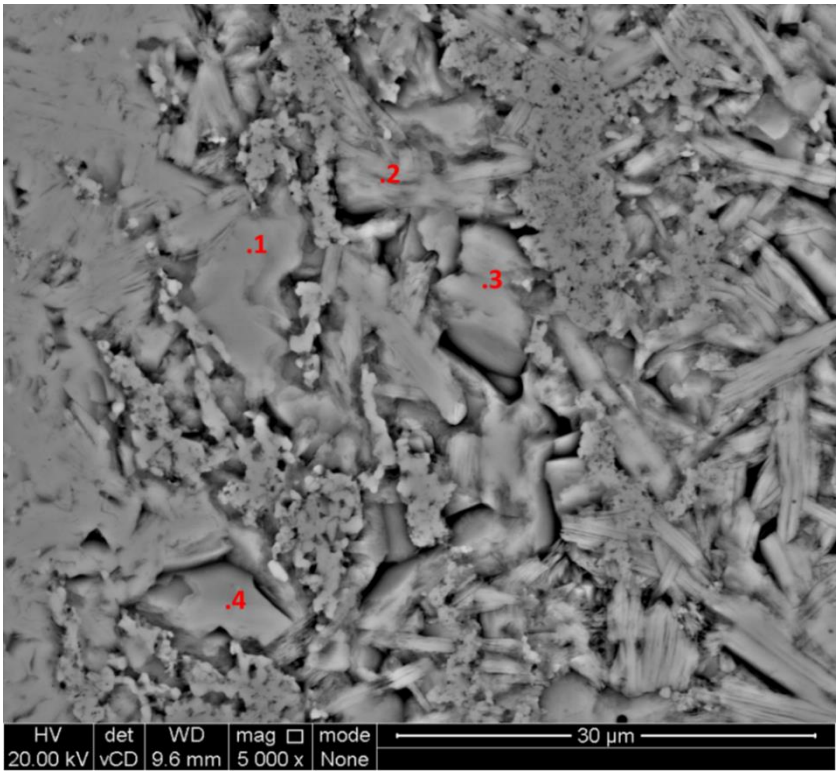

Figure 248 – BSE image of the innermost region of the reaction layer of the initial static corrosion test sample. The compositions of the point analyses can be found in Table 47.

indicative of the initial stages of corrosion, showing partial reaction of the grains. Both the TiC_x and Ti-C-Cl morphologies observed in Figure 247 can also be observed in this image.

16.2 As-received salt, 600°C, 125 h, sample B

An additional sample was exposed to as-received salt at 600°C for 125 h (§ 6.1.1). The reaction observed was generally the sample, with loss of Al and formation of both TiC_x and Ti-C-Cl phases. However, the results suggest that some spalling occurred with sample A, as the corrosion layer thickness was greater for sample B but the mass loss was lower. The GAXRD pattern agrees with that obtained for sample A, with the same peaks and *c*-axis lattice parameter for a proposed Ti-C-Cl phase. The complex morphology observed in the relatively thick reaction layer is reminiscent of the sample which was subjected to anodic dissolution (§ 16.1.3)

16.2.1 Glancing angle X-ray diffraction

The GAXRD patterns for sample B are shown in Figure 249, with the intensity of the most intense peak in each pattern set to 100% [179]. TiC_x was clearly identified at every glancing angle but there were no clear matches for the remaining peaks. Based on the images obtained by SEM, it is proposed that the remaining peaks are based on the original Ti_3AlC_2 structure (*i.e.* the same or similar crystal system), but consist of Ti-C-Cl. The same observation was made for sample A, although the peaks for

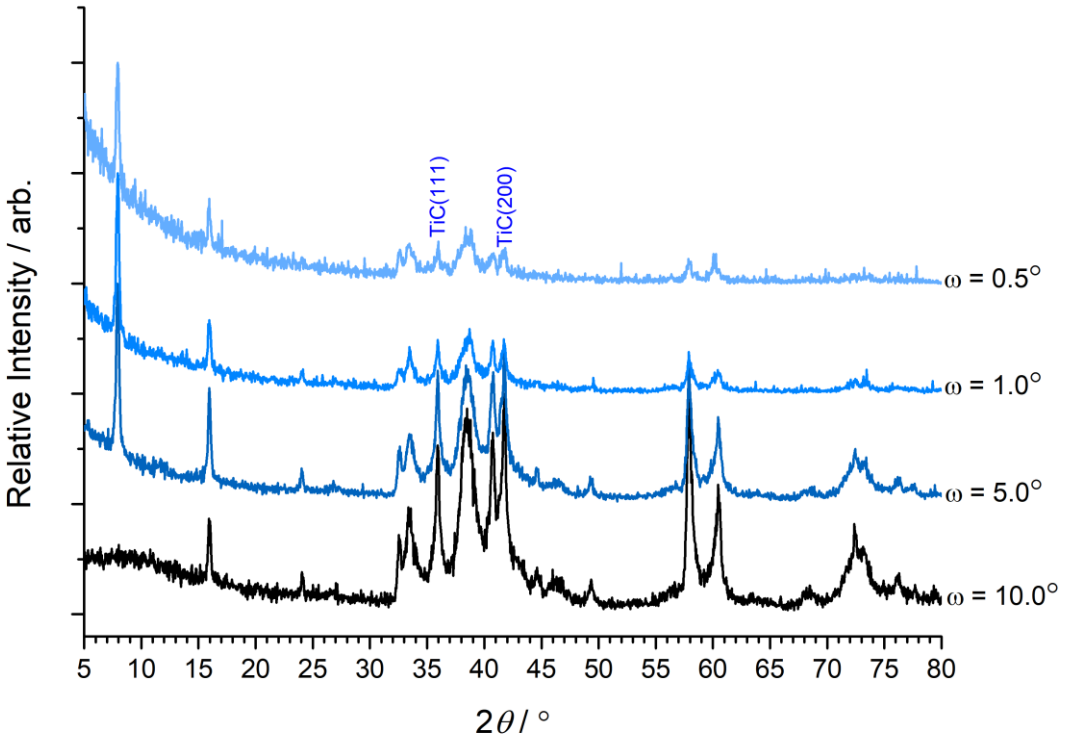

Figure 249 – GAXRD patterns for the second of two samples of Ti_3AlC_2 which were exposed to as-received LKE at 600°C for 125 h. The patterns were normalised such that the highest peak in each pattern was set to 100% intensity. TiC_x was clearly identified in the patterns, and the remaining peaks appear to be based on the 312 MAX phase structure.

the unidentified phase are much more intense here. If it is assumed that the peaks at 7.9°, 16.0° and 24.0° 2θ correspond to the (002), (004) and (006) planes respectively, the *c*-axis lattice parameter has expanded to 22.3 ± 0.1 Å (*c.f.* 18.557 Å for Ti_3AlC_2) [178].

16.2.2 Microstructural examination of the cross-section

The four edges of the cross-section were examined, and corrosion appeared to be more severe than sample A. However, the mass loss was lower than sample A, which may indicate removal of material from sample A. The longer sides, the faces of which were polished to 1 µm prior to corrosion, showed significant corrosion to depths between 300-400 µm for one of the faces and 160-240 µm at the opposite face. The shorter sides, the faces of which were polished to 3 µm, showed less corrosion to depths between 60-120 µm on the one face and 80-160 µm on the opposite face.

The less corroded longer side is shown in Figure 250. The morphology is similar to that observed for sample A, but the thickness of the reaction layer is greater. At higher magnification, the same layered structure and exfoliation of planes could be seen. The surface appears to be less rough, which further suggests that some spalling occurred with sample A.

The cross-section of the more heavily corroded longer side is shown in Figure 251. An additional phase with darker grey contrast can be seen between the bulk material and the outer corrosion layer.

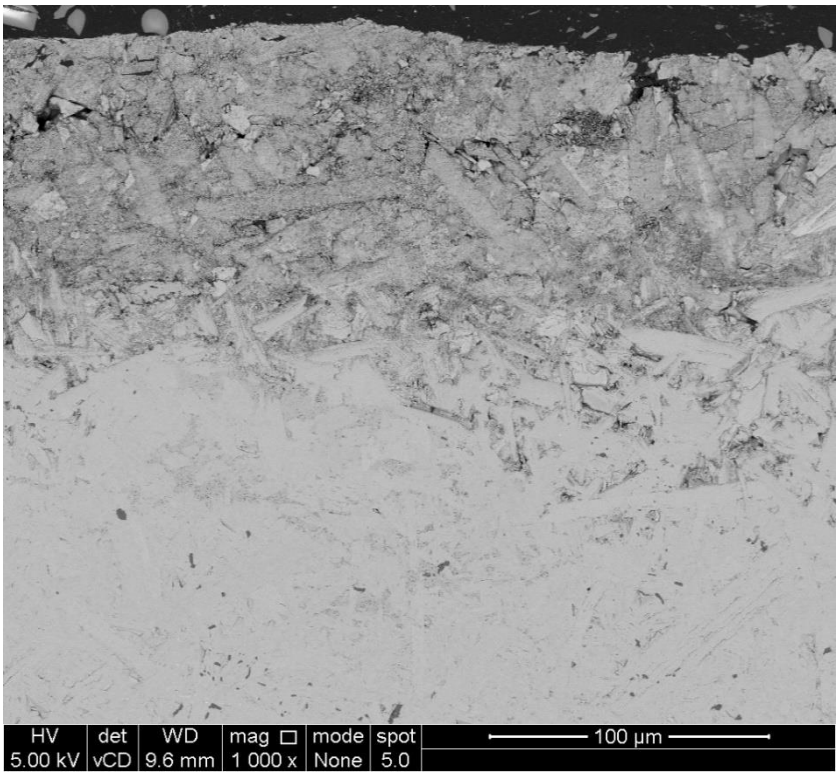

Figure 250 – BSE image showing a general overview of the cross-section of the less corroded longer side of sample B, which was polished to 1 µm prior to corrosion.

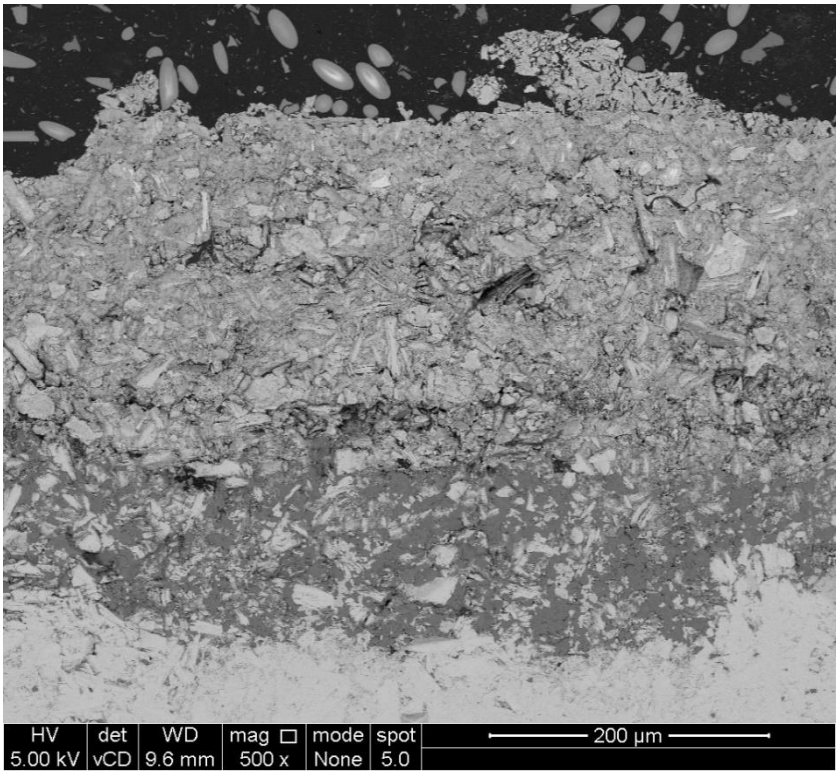

Figure 251 – BSE image showing a general overview of the cross-section of the more heavily corroded longer side of sample B, which was polished to 1 µm prior to corrosion.

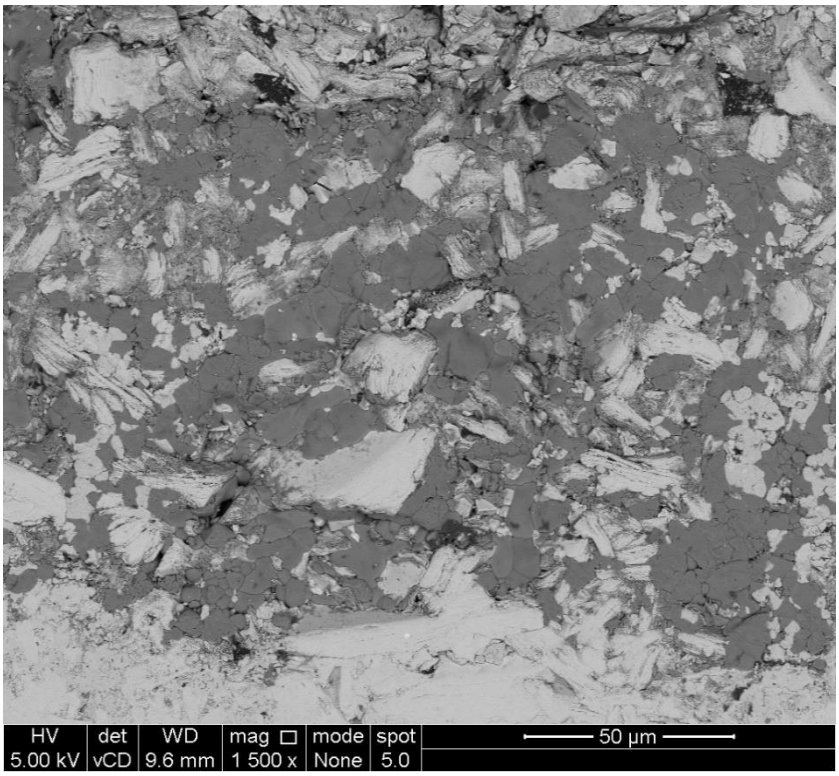

Figure 252 – Higher magnification BSE image of the inner corrosion layer observed in Figure 251.

The outer corrosion layer has the same morphology of the corrosion layers observed previously for samples A and B. The surface has clearly roughened significantly.

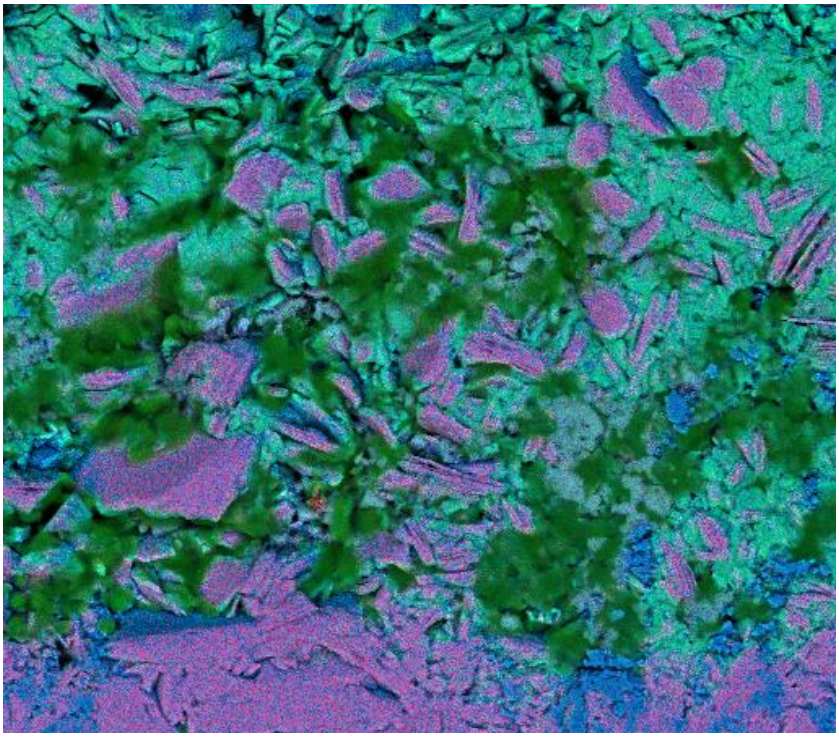

(a) EDS layered image

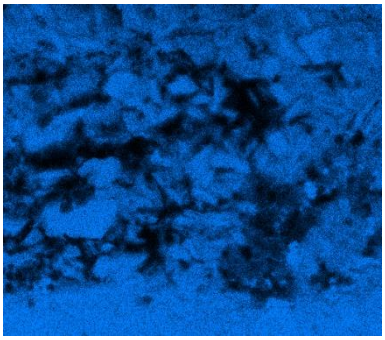

(b) Ti $K_{\alpha1}$

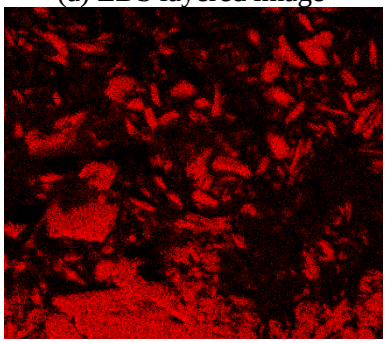

(c) Al $K_{\alpha1}$

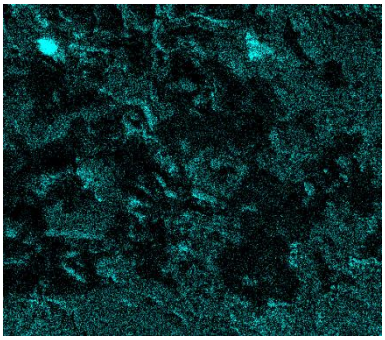

(d) C $K_{\alpha1}$ and $K_{\alpha2}$

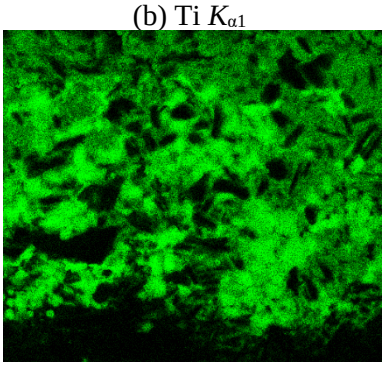

(e) Cl $K_{\alpha1}$

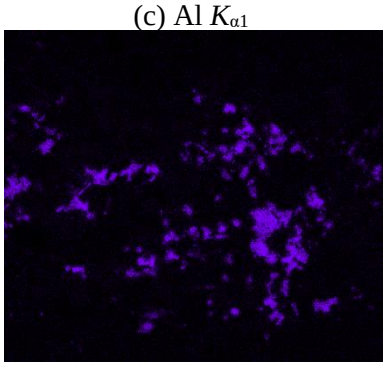

(f) K $K_{\alpha1}$

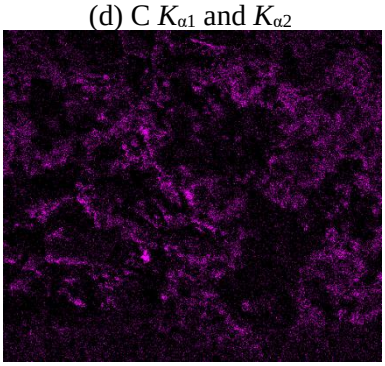

(g) O $K_{\alpha1}$

Figure 253 – EDS maps (image width ~200 µm) showing the location of elements in Figure 252.

A higher magnification image of the inner corrosion layer is shown in Figure 252, and corresponding EDS maps are shown in Figure 253. Chlorine is present in significant quantities in the dark grey phase and does not overlap well with the maps of titanium, aluminium, carbon and oxygen. Potassium appears to overlap in some locations, but not all. Considering lithium is not detected by EDS, it is possible that this phase contains lithium. However, the sample was polished in water, so it is unlikely that this phase is simply LiCl and KCl. The point analysis at location 3 shows that a significant fraction of titanium is still present in this phase, despite its lower intensity in the EDS maps. The morphology could therefore be indicative of titanium metal which has been removed from the MAX phase and is undergoing reaction with the chloride salts.

17 Appendix G – X-ray photoelectron spectroscopy

XPS was performed on the pristine material and sample A exposed to as-received salt at 600°C for 125 h (§ 6.1.1). Depth profiling was achieved by ion beam etching. The pristine material contained oxide layers on the surface which mostly disappeared after etching. The survey scan of the corrosion layer indicated numerous contaminants were present. The extent of depth profiling was limited but revealed interesting results. A single 150 µm diameter point was examined for the pristine material, and four 700 µm by 300 µm rectangles were examined for the corrosion layer.

17.1 Analysis of pristine material

Table 48 shows the surface composition measured for a cross-section of the sample before and after ion beam etching, which was used to better understand the bonding environment of the pristine MAX phase material. The sample was initially etched for three hours, then etched for a further two hours due to the continued presence of oxygen and adventitious carbon, despite using the most aggressive ion beam available with 5 keV Ar^+ ions. In the unetched material, Ti(IV) and Al(III) were observed which disappeared after etching, indicating the presence of oxides which form as a passive film when Ti_3AlC_2 is exposed to air. After etching, the data shows that titanium and aluminium in Ti_3AlC_2 are metallic (oxidation state 0); however, there is a significant quantity of Ti(II). It is possible that Ti(II) is formed

Table 48 – Surface composition of a cross-section of a sample of Ti_3AlC_2, showing the bonding environments of a pristine MAX phase.

	Unetched		After 3 hours etching		After 5 hours etching	
Component	**Binding Energy / eV**	**Composition / at.%**	**Binding Energy / eV**	**Composition / at.%**	**Binding Energy / eV**	**Composition / at.%**
O	530.4 532.5 534.3	22.4	530.7	19.3	530.7	18.2
Ti(0)	454.4	2.4	454.4	15.4	454.3	16.9
Ti(II)	455.6	3.4	455.6	15.7	455.5	16.4
Ti(IV)	458.7	0.6	N/A	N/A	N/A	N/A
C-C, C-O	286.0 289.3	59.1	285	16.8	285	11.1
Carbide	281.7	5.1	281.6	22.7	281.6	26.1
Al(0)	72.1	5.1	73.1	10.1	73.2	11.3
Al(III)	74.6	1.9	N/A	N/A	N/A	N/A

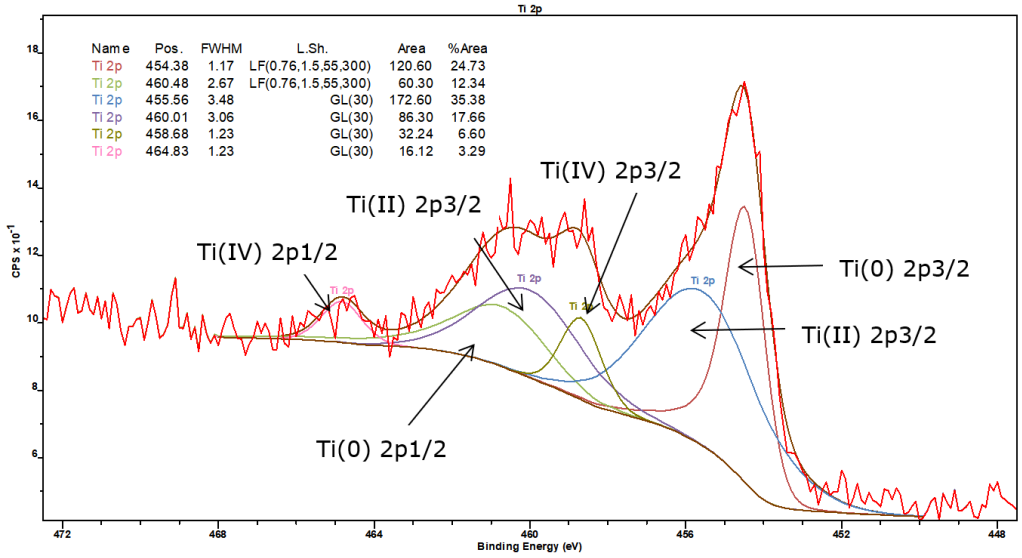

Figure 254 – X-ray photoelectron spectrum of titanium in the unetched bulk of a sample of Ti_3AlC_2.

by ionisation due to the high energy of the ion beam, although this would lead to a charge imbalance. Alternatively, TiO may be present on the surface because the levels of oxygen were still high. None of this oxygen appeared to be associated with the remaining adventitious carbon.

The spectrum for titanium in the unetched material is shown in Figure 254. Three bonding environments are observed, corresponding to Ti(0), Ti(II) and Ti(IV). The asymmetry of the Ti(0) $2p_{3/2}$ peak is indicative of its metallic properties. After etching, the Ti(IV) peaks disappeared.

The spectrum for aluminium in the unetched material is shown in Figure 255. Two peaks are visible in the expected locations for aluminium metal (usually ~72.6 eV [194]) and aluminium oxide (usually ~74.6 eV [194]). The aluminium oxide peaks disappeared after etching. Whilst the peak intensities are

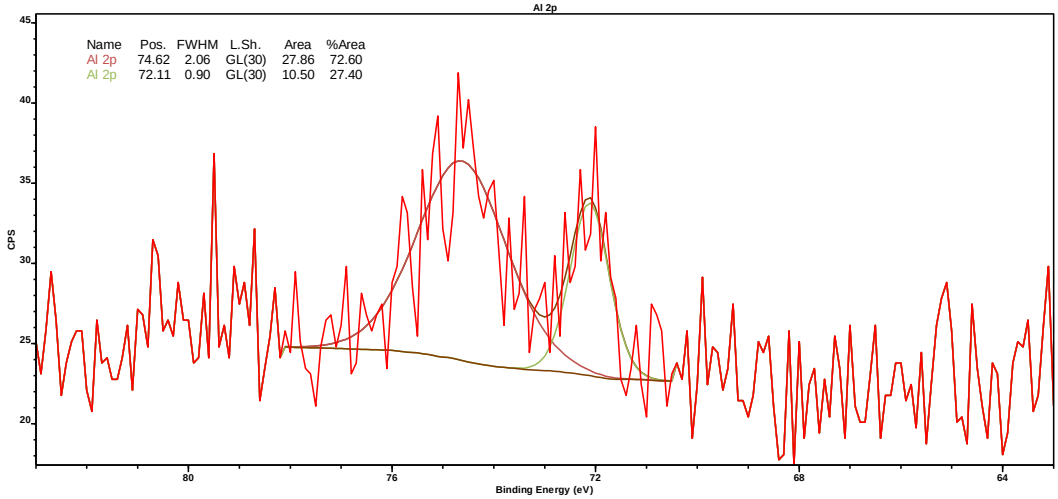

Figure 255 – X-ray photoelectron spectrum of aluminium in the unetched bulk of a sample of Ti_3AlC_2.

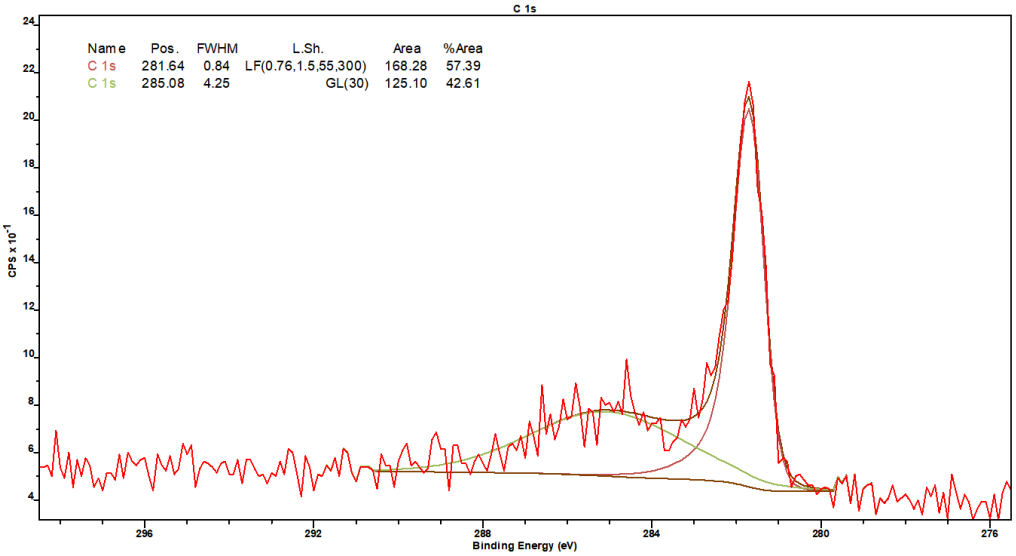

Figure 256 – X-ray photoelectron spectrum of carbon in the bulk of a sample of Ti_3AlC_2 after etching for 3 h.

low relative to the background, their locations in the expected positions combined with the expected chemistry of the material confirms their presence.

The spectrum for carbon after 3 h etching is shown in Table 29. The sharp, asymmetric peak is characteristic of carbide. The presence of C-C bonds after etching is unusual as all adventitious carbon should have been removed, although it may be carbide derived carbon [153].

The spectrum for oxygen in the unetched material is shown in Figure 257. The two higher binding energy peaks disappeared after etching, leaving just the metal oxide peak.

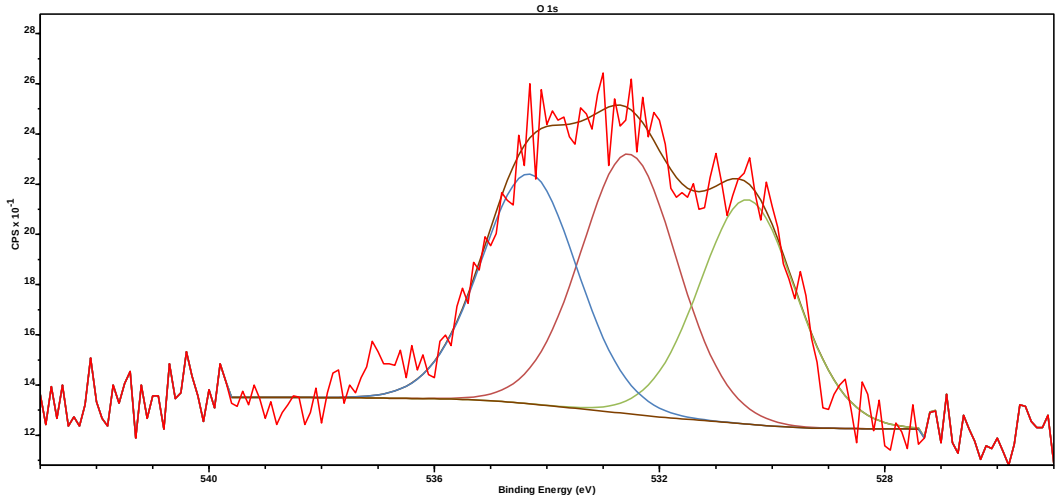

Figure 257 – X-ray photoelectron spectrum of oxygen in the unetched bulk of a sample of Ti_3AlC_2

17.2 Survey scans of the corrosion layer

The surface composition of each of the four points is summarised in Table 49. Sulfur and phosphorus were present as sulfate and phosphate respectively. Nitrogen, iron and copper were also unexpected elements. However, the elements detected agree well with those detected by EDS. High resolution scans were conducted for all elements except P, S and Cu and are discussed in the following section.

Table 49 – Elemental compositions (in at.%) from survey scans of four areas of the corroded sample.

Area	C	N	O	Al	P	S	Cl	Ti	Fe	Cu
1	55.7	1.3	32.1	1.3	1.0	0.2	1.8	3.0	3.6	<0.1
2	39.2	0.8	46.5	1.1	1.3	0.4	2.5	2.5	5.8	<0.1
3	49.5	1.2	38.4	1.1	1.0	0.3	1.8	2.1	4.6	0.2
4	55.5	1.1	32.9	1.1	0.8	0.3	1.9	2.4	3.7	0.2

17.3 High resolution scans of the corrosion layer

The binding energy and elemental compositions for the titanium 2p spectra are summarised in Table 50. The Ti(0) peak belongs to the pristine MAX phase and the Ti(IV) peak most likely represents TiO_2. TiO_2 is known to form on the surface of Ti_3AlC_2 [38], so the high fraction of Ti(IV), despite the absence of TiO_2 in the GAXRD patterns, is attributed to the surface sensitivity of XPS. The Ti(II) peak is most likely due to TiO, as postulated for the pristine sample. However, there is a possibility it belongs to a Ti-C-Cl phase, as observed by EDS of the cross-section.

Table 50 – Binding energy (in eV) and elemental composition (in at.%) of the bonding environments for Ti 2p in the corrosion layer. The first binding energy for each pair is the $2p_{3/2}$ peak, and the second is the $2p_{1/2}$ peak.

Area	Ti(0)		Ti(II)		Ti(IV)	
	eV	at.%	eV	at.%	eV	at.%
1	454.8 460.9	22.9	456.1 460.9	31.8	458.5 464.2	45.3
2	454.7 460.8	15.9	455.7 461.7	32.5	458.5 464.2	51.6
3	454.7 460.8	13.2	455.7 461.7	45.1	458.4 464.1	41.7
4	454.9 461.0	24.3	456.1 462.1	29.1	458.5 464.2	46.6

The Al 2p spectra represented aluminium oxide, with no aluminium metal observed. As for titanium, aluminium at the surface of Ti_3AlC_2 is known to oxidise to Al_2O_3 [38], so the sole presence of aluminium oxide is attributed to the surface sensitivity of XPS. The binding energies of the $2p_{3/2}$ peaks were 74.4, 74.2, 74.1 and 74.2 eV, and those of the $2p_{1/2}$ peaks were 74.8, 74.7, 74.6 and 74.6 eV.

The position of the chlorine peaks was consistent with a metal chloride. The $2p_{3/2}$ peaks were located at 198.6, 198.4, 198.4 and 198.4 eV, and the $2p_{1/2}$ peaks were located at 200.2, 200.0, 200.0 and 200.0 eV. Neither lithium nor potassium were detected in the survey scan, although lithium may be difficult to detect. Aluminium and titanium chlorides would be unlikely to be present after exposure to air at room temperature; $AlCl_3$ and $TiCl_4$ are gaseous at the exposure temperature, and $TiCl_3$ readily reacts with oxygen and moisture to form oxide and hydrochloric acid [44]. Therefore, the peaks may be consistent with a stable Ti-C-Cl phase with Ti-Cl bonds.

The binding energy and elemental compositions for the carbon 1s spectra are summarised in Table 51. Only a small fraction of the carbon peaks represent carbide; the majority is adventitious carbon.

Table 51 – Binding energy (in eV) and elemental composition (in at.%) of the bonding environments for C 1s in the corrosion layer.

Area	Carbide		C-C/C-H		C-O		$C=O/CO_3^{2-}$	
	eV	at.%	eV	at.%	eV	at.%	eV	at.%
1	282.0	2.7	285.0	85.3	286.5	7.8	288.8	4.1
2	281.9	3.3	285.0	74.4	286.7	13.1	288.7	9.3
3	281.9	2.9	285.0	79.0	286.7	11.1	288.8	7.0
4	282.2	2.7	285.0	85.7	286.5	7.5	288.8	4.2

The binding energy and elemental compositions for the oxygen 1s spectra are summarised in Table 52. The high concentration of metal oxide is expected from the titanium and aluminium spectra. The amount of C-O carbon is insufficient to account for amount of C-O oxygen, suggesting that carbonate or metal hydroxide is also present. The spectra for iron suggest that iron hydroxide is present, fitting well with this observation. It is also possible that carbonate may have formed in the molten salt by reaction of metal oxide with dissolved carbon dioxide if air was able to enter the system.

Table 52 – Binding energy (in eV) and elemental composition (in at.%) of the bonding environments for O 1s in the corrosion layer.

Area	Metal Oxide		C-O/ CO_3^{2-}/M-OH		C=O/H_2O	
	eV	at.%	eV	at.%	eV	at.%
1	530.0	40.4	531.5	46.6	533.0	13.1
2	530.0	41.6	531.5	46.2	532.9	12.2
3	530.0	41.1	531.5	45.9	533.0	13.1
4	530.0	41.3	531.5	47.2	533.0	11.5

The binding energy and elemental compositions for the iron 2p spectra are summarised in Table 53. Neither Fe(0) nor Fe(II) were observed, and the peak positions matched those for Fe(III) but were slightly shifted relative to Fe_2O_3. Based on the oxygen 1s spectra, it is likely that a hydrated iron oxide is present, *i.e.* FeO(OH). There is a possibility that $FeCl_3$ was present, although the amount of chlorine was not sufficient to account for all the iron.

Table 53– Binding energy (in eV) and elemental composition (in at.%) of the bonding environments for Fe 2p in the corrosion layer.

Area	Fe(III)		Fe(III) split		Fe(III) satellite	
	eV	at.%	eV	at.%	eV	at.%
1	710.6 724.1	35.1	712.0 726.1	54.5	719.2 733.2	10.4
2	711.2 724.6	67.9	714.2 727.8	15.3	718.8 733.3	16.9
3	711.2 724.7	65.8	714.4 727.9	18.0	719.4 733.2	16.2
4	710.9 724.6	72.2	713.2 727.3	15.8	719.4 732.8	11.9

The nitrogen 1s spectra indicated both C-N bonds and metal nitride were present. The binding energies and compositions are shown in Table 54. Nitrogen can substitute into many carbide and nitride structures with minimal change to the XRD patterns, so it is difficult to know which metals have formed nitrides. The C-N environments are components of the adventitious carbon.

Table 54 – Binding energy (in eV) and elemental composition (in at.%) of the bonding environments for O 1s in the corrosion layer.

Area	Nitride		C-N	
	eV	at.%	eV	at.%
1	396.8	47.9	400.3	52.1
2	396.5	45.8	400.0	54.2
3	396.7	63.7	399.9	36.4
4	396.6	67.9	400.2	32.1

17.4 Depth profiling of the corrosion layer

Ion beam etching was used to collect spectra of the corrosion layer at different depths. The filament failed after two etches so limited data was collected. The elemental compositions at the three depths are summarised in Table 55. The amount of carbide and nitride increased whilst the amount of adventitious carbon decreased as the depth increased, with the C-X peaks decreasing in area for the carbon, oxygen and nitrogen spectra. The decrease in the C-O oxygen 1s peak may also indicate a decrease in hydroxide concentration. Additionally, the Ti(II) peaks disappeared and Fe(II) peaks started to appear. Overall, this shows a loss of the species which formed or deposited at the surface of the sample after exposure to air.

Table 55 – Elemental compositions (in at.%) for the X-ray photoelectron spectra obtained by etching the corrosion layer with an ion beam.

Depth	C	N	O	Al	P	Cl	Ti	Fe
0	43.1	1.1	41.2	3.2	0.9	3.1	2.0	5.4
1	24.9	1.6	45.7	2.4	2.0	4.6	4.2	14.7
2	22.8	1.8	47.3	2.7	2.0	4.7	2.3	16.4

18 Appendix H – Corrosion of Maxthal 312: Additional Results

18.1 As-received salt, 600°C, 125 h, sample B

18.1.1 Glancing Angle X-ray Diffraction

The GAXRD patterns between 0.5-10.0° ω are shown in Figure 258, normalised relative to the (121) and (301) peaks of δ-Ni_2Si. The phases identified are the same as those observed for sample A, although there is an unidentified peak at 47.2° and no peak at 28.0°. This peak may represent Si but was difficult to identify. The SEM images of the cross-section show that Ni has penetrated fairly deep into the material. The stoichiometric ratio of transition metal to silicon in Ni_2Si is four times greater than that of $TiSi_2$, so replacement of Ti with Ni may have led to significant amounts of free Si. There are various other phases which have peaks in locations which overlap with those of the phases identified, including MgO and Mg_2C_3.

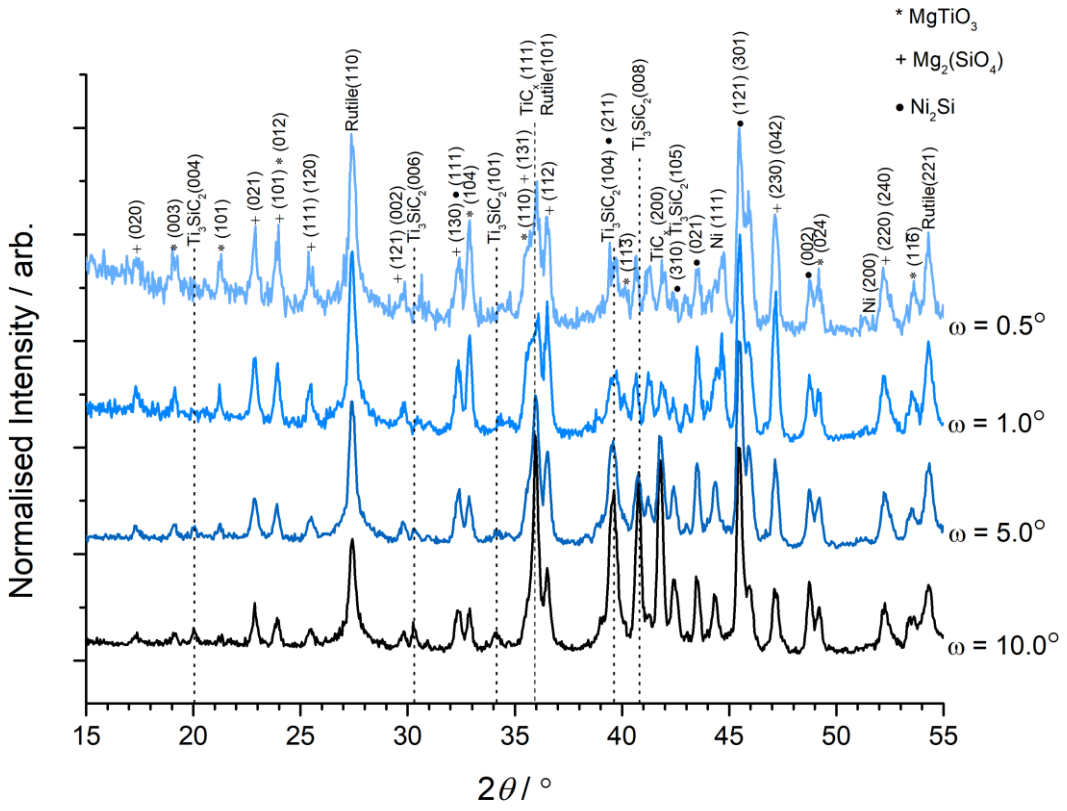

Figure 258 – GAXRD patterns for a sample of Maxthal 312 which was exposed to as-received KME at 600°C for 125 h. The patterns were normalised relative to the (121) and (301) peaks of Ni_2Si. The Ti_3SiC_2 and TiC_x peaks decrease in intensity towards the surface of the sample, whereas the $MgTiO_3$ and $Mg_2(SiO_4)$ peaks increase in intensity. There is an unidentified peak at 47.2° which may be due to Si.

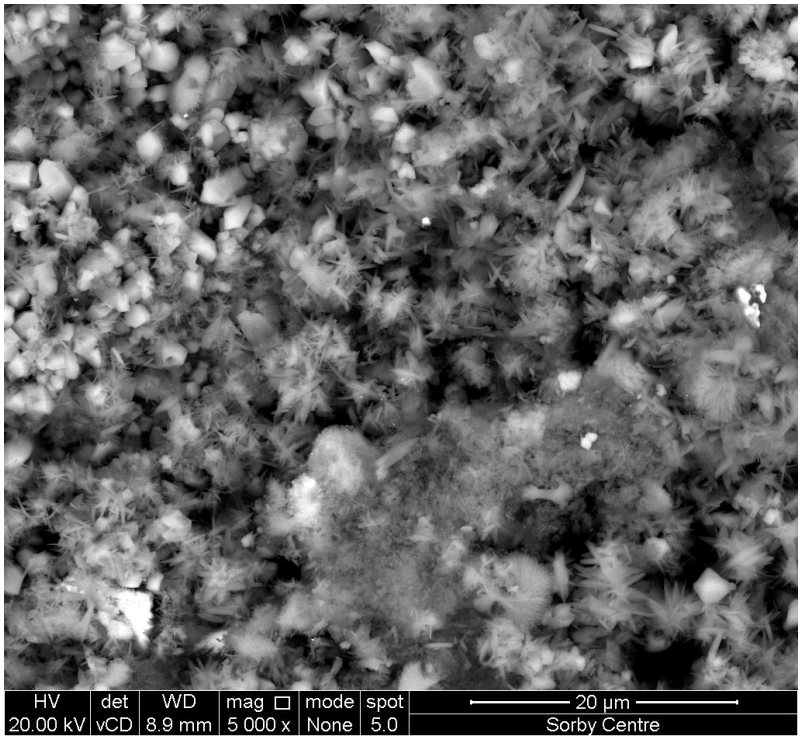

(a) backscattered electron image

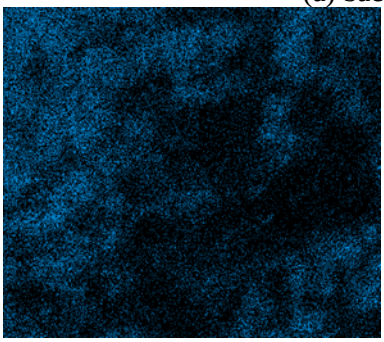

(b) Ti $K_{\alpha 1}$ (19.3at.%)

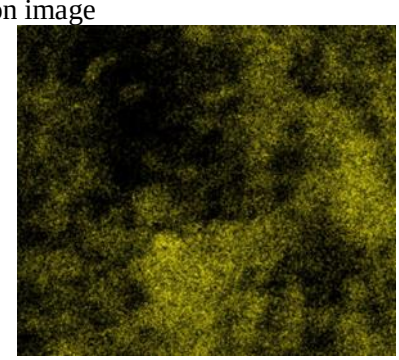

(c) Si $K_{\alpha 1}$ (5.7at.%)

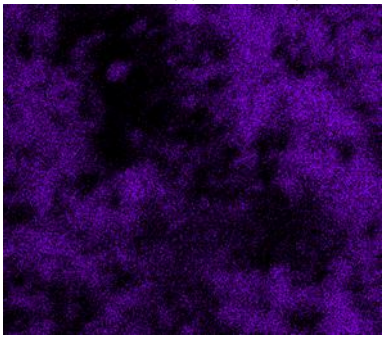

(d) Mg $K_{\alpha 1}$ and $K_{\alpha 2}$ (13.0at.%)

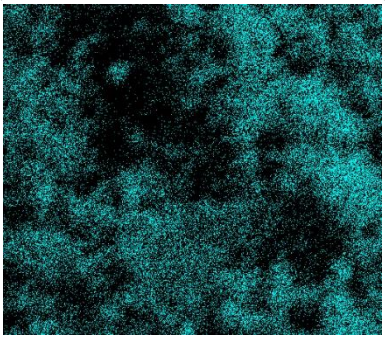

(e) O $K_{\alpha 1}$ (61.1at.%)

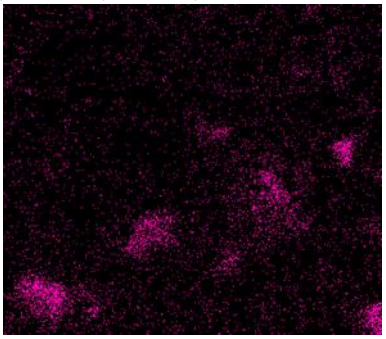

(f) Ni $K_{\alpha 1}$ (0.6at.%)

Figure 259 – BSE image and EDS maps showing a general overview of the surface morphology of a sample of Maxthal 312 which was exposed to as-received KME at 600°C for 125 h.

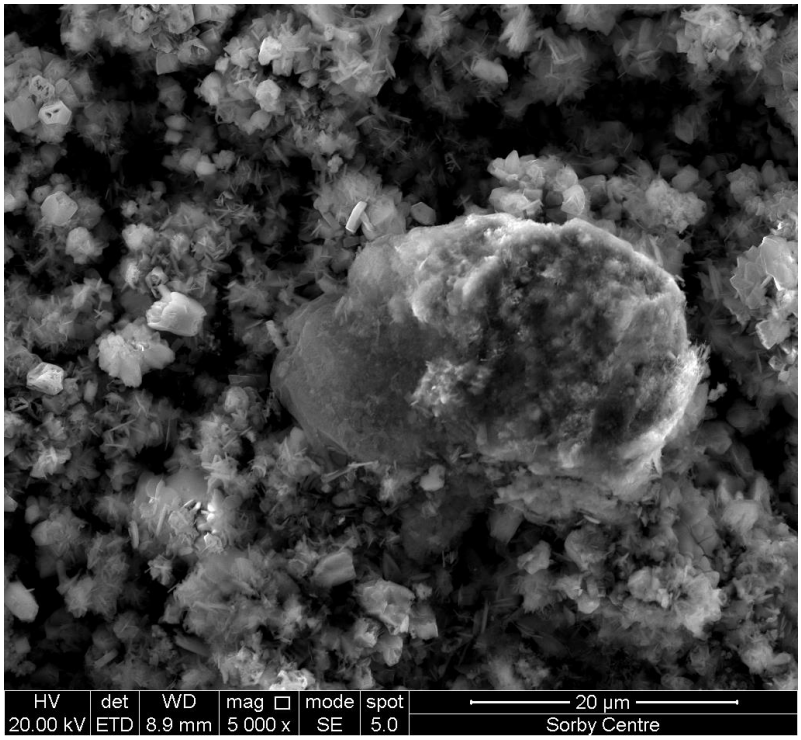

(a) BSE image

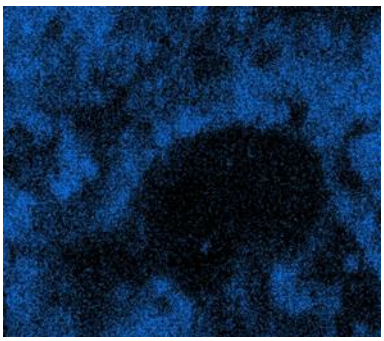

(b) Ti $K_{\alpha1}$ (28.1at.%)

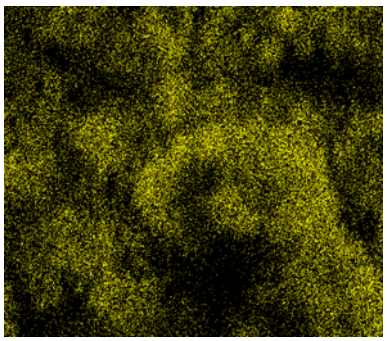

(c) Si $K_{\alpha1}$ (5.0at.%)

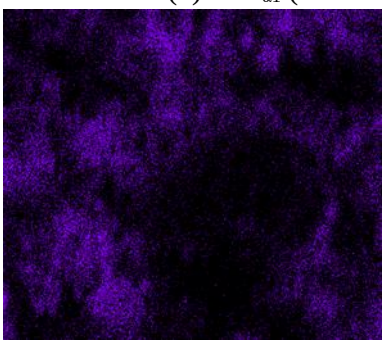

(d) Mg $K_{\alpha1}$ and $K_{\alpha2}$ (7.1at.%)

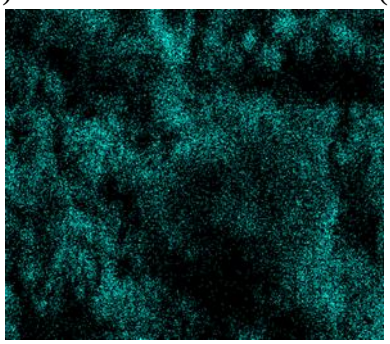

(e) O $K_{\alpha1}$ (50.8at.%)

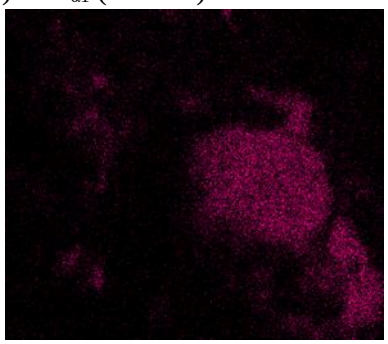

(f) Ni $K_{\alpha1}$ (3.6at.%)

Figure 260 – BSE image and EDS maps of a large nickel silicide particle on the surface of a sample of Maxthal 312 which was exposed to as-received KME at 600°C for 125 h.

18.1.2 Microstructural examination of the surface

Figure 259 provides a general overview of the surface morphology. Numerous phases are visible, and individual phases are difficult to distinguish. The elemental composition of the EDS map indicates that there is a very high fraction of O at the surface. Figure 260 is a BSE image of a particle of nickel silicide.

18.1.3 Microstructural examination of the cross-section

Figure 261 provides a general overview of the surface layer. Again, Ni has reacted with the Si in the sample. Compared to sample A, Ni appears to have diffused to a much greater depth, ~95 µm, and the surface is much rougher.

Figure 262 is a BSE image showing a more detailed view of the edge of the sample. Ni has diffused along the grain boundaries and reacted with the $TiSi_2$ phase. Additionally, the surface has roughened significantly, and grains appear to be breaking away. The morphology of the smaller grains may indicate the formation of titanium carbide.

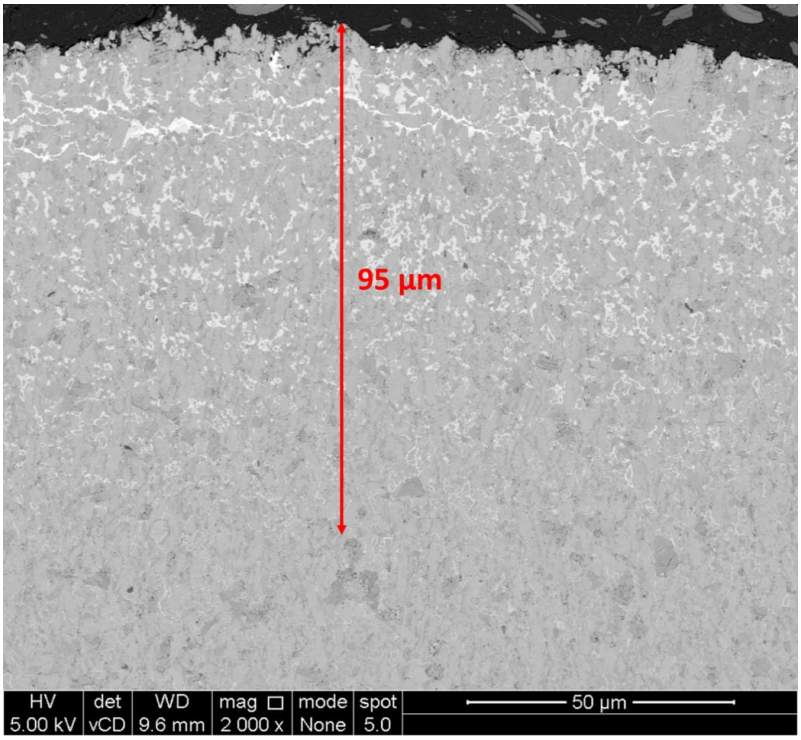

Figure 261 – BSE image showing a general overview of the alteration layer of a sample of Maxthal 312 which was exposed to as-received KME at 600°C for 125 h.

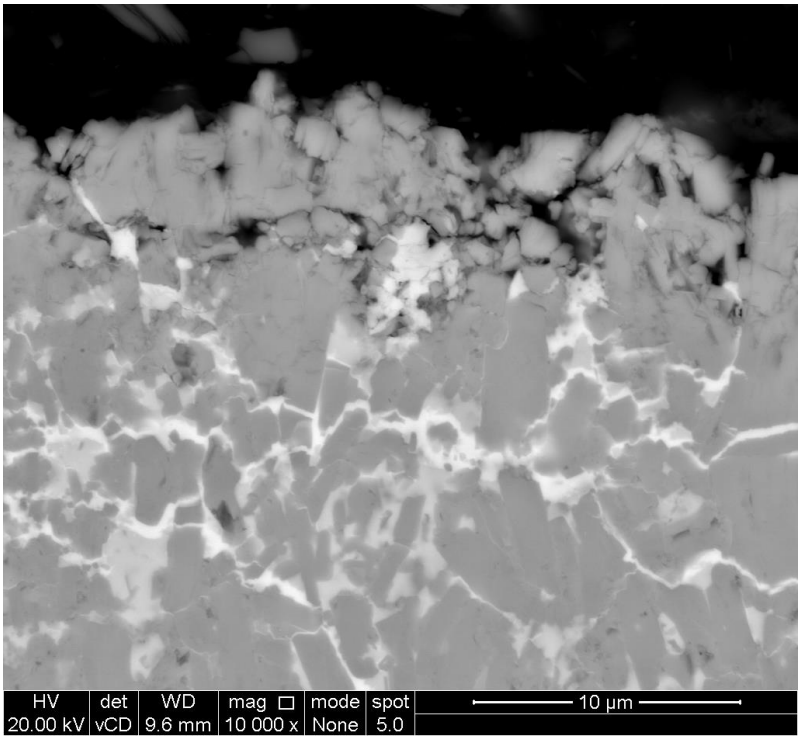

Figure 262 – BSE image showing a detailed view of the outer edge of the corrosion layer of a sample of Maxthal 312 which was exposed to as-received KME at 600°C for 125 h.

19 References

[1] GIF-002-00, A Technology Roadmap for Generation IV Nuclear Energy Systems, 2002. doi:10.2172/859029.

[2] R.B. Hargraves, Thorium: Energy, Cheaper Than Than Coal, CreateSpace Independent Publishing Platform, 2012.

[3] S. Delpech, C. Cabet, C. Slim, G.S. Picard, Molten fluorides for nuclear applications, Mater. Today. 13 (2010) 34–41. doi:10.1016/S1369-7021(10)70222-4.

[4] O. Beneš, R.J.M. Konings, Molten Salt Reactor Fuel and Coolant, in: Compr. Nucl. Mater., 1st ed., Elsevier Inc., Karlsruhe, Germany, 2012: pp. 359–389. doi:10.1016/B978-0-08-056033-5.00062-8.

[5] V. Ignatiev, A. Surenkov, Material Performance in Molten Salts, in: Compr. Nucl. Mater., Elsevier Inc., Karlsruhe, Germany, 2012: pp. 221–250.

[6] M.W. Rosenthal, P.R. Kasten, R.B. Briggs, Molten-Salt Reactors - History, Status and Potential, Nucl. Appl. Technol. 8 (1970) 107–117.

[7] J. Serp, M. Allibert, O. Beneš, S. Delpech, O. Feynberg, V. Ghetta, D. Heuer, D. Holcomb, V. Ignatiev, J.L. Kloosterman, L. Luzzi, E. Merle-Lucotte, J. Uhlíř, R. Yoshioka, D. Zhimin, The molten salt reactor (MSR) in generation IV: Overview and perspectives, Prog. Nucl. Energ. 77 (2014) 308–319. doi:10.1016/j.pnucene.2014.02.014.

[8] Transatomic Power Technical White Paper, Boston, USA, 2014.

[9] T. Griffiths, J. Tomlinson, R. O'Sullivan, MSR Review: Feasibility of Developing a Pilot Scale Molten Salt Reactor in the UK, London, 2015.

[10] W.C. May, W.E. Simmons, AEEW-R 1059: Conceptual Design and Assessment of a He Cooled 2500 MWe Molten Salt Fast Reactor with Integrated Gas Turbine Plant, Atomic Energy Establishment, Winfrith, Dorchester, Dorset, 1976.

[11] J. Smith, W.E. Simmons, R.C. Asher, G. Long, H.A.C. McKay, D.L. Reed, AEEW - R 956: An Assessment of a 2500 MWe Molten Chloride Salt Fast Reactor, Atomic Energy Establishment, Winrith, Dorchester, Dorset, 1974.

[12] A. Mourogov, P.M. Bokov, Potentialities of the fast spectrum molten salt reactor concept: REBUS-3700, Energy Convers. Manag. 47 (2006) 2761–2771. doi:10.1016/j.enconman.2006.02.013.

[13] P. Yvon, F. Carré, Structural materials challenges for advanced reactor systems, J. Nucl. Mater. 385 (2009) 217–222. doi:10.1016/j.jnucmat.2008.11.026.

[14] S.J. Zinkle, J.T. Busby, Structural materials for fission & fusion energy, Mater. Today. 12 (2009) 12–19. doi:10.1016/S1369-7021(09)70294-9.

[15] T. Allen, J. Busby, M. Meyer, D. Petti, Materials challenges for nuclear systems, Mater. Today. 13 (2010) 14–23. doi:10.1016/S1369-7021(10)70220-0.

[16] K.L. Murty, I. Charit, Structural materials for Gen-IV nuclear reactors: Challenges and opportunities, J. Nucl. Mater. 383 (2008) 189–195. doi:10.1016/j.jnucmat.2008.08.044.

[17] H.G. Macpherson, The Molten Salt Reactor Adventure, Nucl. Sci. Eng. 90 (1985) 374–380.

[18] D. LeBlanc, Denatured Molten Salt Reactors (DMSR): An Idea Whose Time Has Finally Come?, 2010.

[19] J.A. Lane, H.G. MacPherson, F. Maslan, Fluid Fuel Reactors, Addison-Wesley Publishing Company, Inc., Reading, Massachusetts, USA, 1958.

[20] F. Lantelme, H. Groult, Molten Salts Chemistry: from lab to applications, Elsevier, 2013. doi:10.1017/CBO9781107415324.004.

[21] L. Guo, J.M. Calo, E. Dicocco, E.J. Bain, Development of a low temperature, molten hydroxide direct carbon fuel cell, Energy and Fuels. 27 (2013) 1712–1719. doi:10.1021/ef302100h.

[22] D. LeBlanc, Molten salt reactors: A new beginning for an old idea, Nucl. Eng. Des. 240 (2010) 1644–1656. doi:10.1016/j.nucengdes.2009.12.033.

[23] R. Elder, R. Allen, Nuclear heat for hydrogen production: Coupling a very high/high temperature reactor to a hydrogen production plant, Prog. Nucl. Energy. 51 (2009) 500–525.

doi:10.1016/j.pnucene.2008.11.001.
[24] X.L. Yan, H. Sato, Y. Tachibana, K. Kunitomi, R. Hino, Evaluation of high temperature gas reactor for demanding cogeneration load follow, J. Nucl. Sci. Technol. 49 (2012) 121–131. doi:10.1080/18811248.2011.636564.
[25] C.W. Forsberg, P.F. Peterson, P.S. Pickard, Molten-Salt-Cooled Advanced High-Temperature Reactor for Production of Hydrogen and Electricity, Nucl. Technol. (2008) 1–25.
[26] T.J. Dolan, Molten Salt Reactors and Thorium Energy, Woodhead Publishing, Cambridge, UK, 2017.
[27] D. LeBlanc, Integral Molten Salt Reactor, US2015/0036779 A1, 2014.
[28] R. Mccracken, The SSR - a new path for nuclear energy?, Energy Econ. April (2015).
[29] H. Xu, X. Cai, W. Guo, Thorium Energy R&D in China, in: Thorium Energy Conf. 2013, 2013.
[30] I. Scott, 21 – Stable salt fast reactor, in: Molten Salt React. Thorium Energy, 2017: pp. 571–580. doi:10.1016/B978-0-08-101126-3.00021-X.
[31] D. LeBlanc, C. Rodenburg, 18 – Integral molten salt reactor, in: Molten Salt React. Thorium Energy, 2017: pp. 541–556. doi:10.1016/B978-0-08-101126-3.00018-X.
[32] Z. Dai, 17 – Thorium molten salt reactor nuclear energy system (TMSR), in: Molten Salt React. Thorium Energy, 2017: pp. 531–540. doi:10.1016/B978-0-08-101126-3.00017-8.
[33] M.A. Fütterer, L. Fu, C. Sink, S. de Groot, M. Pouchon, Y.W. Kim, F. Carré, Y. Tachibana, Status of the very high temperature reactor system, Prog. Nucl. Energy. (2014) 1–16. doi:10.1016/j.pnucene.2014.01.013.
[34] S. McKevitt, T. Ryan, Project Sunshine: How science can use the sun to fuel and feed the world, 1st ed., Icon Books Ltd, London, United Kingdom, 2013.
[35] IAEA, Hydrogen as an Energy Carrier and Its Production by Nuclear Power, Vienna, Austria, 1999.
[36] B.C.R. Ewan, R.W.K. Allen, A figure of merit assessment of the routes to hydrogen, Int. J. Hydrogen Energy. 30 (2005) 809–819.
[37] J.E. O'Brien, M.G. McKellar, E.A. Harvego, C.M. Stoots, High-temperature electrolysis for large-scale hydrogen and syngas production from nuclear energy--summary of system simulation and economic analyses, Int. J. Hydrogen Energy. 35 (2010) 4808–4819.
[38] M.W. Barsoum, MAX Phases - Properties of Machinable Ternary Carbides and Nitrides, Wiley-VCH, Weinheim, Germany, 2013.
[39] M.W. Barsoum, The MAX Phases: Unique New Carbide and Nitride Materials, Am. Sci. 89 (2013) 334–343.
[40] M.W. Barsoum, T. El-Raghy, Synthesis and Characterization of a Remarkable Ceramic: Ti_3SiC_2, J. Am. Ceram. Soc. 79 (1996) 1953–1956. doi:10.1111/j.1151-2916.1996.tb08018.x.
[41] M. Naguib, V. Presser, D. Tallman, J. Lu, L. Hultman, Y. Gogotsi, M.W. Barsoum, On the Topotactic Transformation of Ti_2AlC into a Ti-C-O-F Cubic Phase by Heating in Molten Lithium Fluoride in Air, J. Am. Ceram. Soc. 94 (2011) 4556–4561. doi:10.1111/j.1551-2916.2011.04896.x.
[42] H. Lambert, Molten salt spectroscopy and electrochemistry for spent nuclear fuel treatment, University of Manchester, 2017.
[43] C.A. Jantzen, An Investigation of Primary Circuit Materials in Molten Chloride Salts with the Design of High Temperature Corrosion Vessels, University of Manchester, 2017.
[44] D.M.P. Mingos, Essential Trends in Inorganic Chemistry, Oxford University Press, Oxford, United Kingdom, 1998.
[45] M.W. Barsourn, B. Houng, Transient Plastic Phase Processing of Titanium-Boron-Carbon Composites, J. Am. Ceram. Soc. 76 (1993) 1445–1451.
[46] L. Farber, I. Levin, M.W. Barsoum, T. El-Raghy, T. Tzenov, High-resolution transmission electron microscopy of some $Ti_{n+1}AX_n$ compounds (n=1, 2; A=Al or Si; X=C or N), J. Appl. Phys. 86 (1999) 2540–2543. doi:10.1063/1.371089.
[47] B. Garcia-Diaz, MAX phase coatings for accident tolerant nuclear fuel, Trans. Am. Nucl. Soc. 110 (2014) 994–996.
[48] A. Heinzel, A. Weisenburger, G. Müller, Long-term corrosion tests of Ti_3SiC_2 and Ti_2AlC in

oxygen containing LBE at temperatures up to 700°C, J. Nucl. Mater. 482 (2016) 114–123. doi:10.1016/j.jnucmat.2016.10.007.
[49] A. Heinzel, G. Müller, A. Weisenburger, Compatibility of Ti_3SiC_2 with liquid Pb and PbBi containing oxygen, J. Nucl. Mater. 392 (2009) 255–258. doi:10.1016/j.jnucmat.2009.03.004.
[50] A.K. Rivai, M. Takahashi, Compatibility of surface-coated steels, refractory metals and ceramics to high temperature lead-bismuth eutectic, Prog. Nucl. Energy. 50 (2008) 560–566. doi:10.1016/j.pnucene.2007.11.081.
[51] L.A. Barnes, N.L. Dietz Rago, L. Leibowitz, Corrosion of ternary carbides by molten lead, J. Nucl. Mater. 373 (2008) 424–428. doi:10.1016/j.jnucmat.2007.04.054.
[52] K. Lambrinou, T. Lapauw, A. Jianu, A. Weisenburger, J. Ejenstam, P. Szakálos, J. Wallenius, E. Ström, K. Vanmeensel, J. Vleugels, Corrosion-resistant ternary carbides for use in heavy liquid metal coolants, in: Ceram. Mater. Energy Appl. V, 2016: pp. 19–34.
[53] M. Utili, M. Agostini, G. Coccoluto, E. Lorenzini, Ti_3SiC_2 as a candidate material for lead cooled fast reactor, Nucl. Eng. Des. 241 (2011) 1295–1300. doi:10.1016/j.nucengdes.2010.07.038.
[54] L. Cornish, G. Cacciamani, D.M. Cupid, J. De Keyzer, Refractory Metal Systems: Aluminium - Carbon - Titanium, in: G. Effenberg, S. Ilyenko (Eds.), Ternary Alloy Syst. Phase Diagrams, Crystallogr. Thermodyn. Data - Gr. IV Phys. Chem. - Vol. 11, Subvolume E, Part 1, Springer-Verlag Berlin Heidelberg, 2006. doi:10.1007/978-3-540-88053-0_6.
[55] J.M. Low, S. Goumri-Said, S.P. Harimkar, M. Le Flem, C. Li, Y. Medkour, W.K. Pang, X. Qian, G. Song, W.-H. Tuan, E. Wu, M. Yoshida, H. Zhang, A. Zhou, Y.-L. Chin, Advances in science and technology of $M_{n+1}AX_n$ phases, Woodhead Publishing Limited, 2012.
[56] Y. Zou, Z.M. Sun, H. Hashimoto, L. Cheng, Synthesis reactions for Ti_3AlC_2 through pulse discharge sintering TiH_2/Al/C powder mixture, J. Alloys Compd. 468 (2009) 217–221. doi:10.1016/j.jallcom.2008.01.062.
[57] Y. Zou, Z.M. Sun, S. Tada, H. Hashimoto, Synthesis reactions for Ti_3SiC_2 through pulse discharge sintering TiH_2/Si/TiC powder mixture, Mater. Res. Bull. 43 (2008) 968–975. doi:10.1016/j.materresbull.2007.04.028.
[58] Y. Zou, Z. Sun, S. Tada, H. Hashimoto, Rapid synthesis of single-phase Ti_3AlC_2 through pulse discharge sintering a TiH_2/Al/TiC powder mixture, Scr. Mater. 56 (2007) 725–728. doi:10.1016/j.scriptamat.2007.01.026.
[59] M. Peng, X. Shi, Z. Zhu, M. Wang, Q. Zhang, Facile synthesis of Ti_3SiC_2 powder by high energy ball-milling and vacuum pressureless heat-treating process from Ti–TiC–SiC–Al powder mixtures, Ceram. Int. 38 (2012) 2027–2033. doi:10.1016/j.ceramint.2011.10.038.
[60] Z.M. Sun, H. Hashimoto, Z.F. Zhang, S.L. Yang, S. Tada, Synthesis and Characterization of a Metallic Ceramic Material – Ti_3SiC_2, Mater. Trans. 47 (2006) 170–174.
[61] Z. Sun, Z. Zhang, H. Hashimoto, T. Abe, Ternary Compound Ti_3SiC_2: Part I. Pulse Discharge Sintering Synthesis, Mater. Trans. 43 (2002) 428–431.
[62] Z.F. Zhang, Z.M. Sun, H. Hashimoto, Rapid Synthesis of Ternary Carbide Ti_3SiC_2 through Pulse-Discharge Sintering Technique from Ti/Si/TiC Powders, Metall. Mater. Trans. A. 33 (2002) 3321–3328.
[63] Z.F. Zhang, Z.M. Sun, H. Hashimoto, T. Abe, Application of pulse discharge sintering (PDS) technique to rapid synthesis of Ti_3SiC_2 from Ti/Si/C powders, J. Eur. Ceram. Soc. 22 (2002) 2957–2961.
[64] Z.F. Zhang, Z.M. Sun, H. Hashimoto, Low temperature synthesis of Ti_3SiC_2 from Ti/SiC/C powders, Mater. Sci. Technol. 20 (2004) 1252–1256. doi:10.1179/026708304X6103.
[65] Z.F. Zhang, Z.M. Sun, H. Hashimoto, T. Abe, Effects of sintering temperature and Si content on the purity of Ti3SiC2 synthesized from Ti/Si/TiC powders, J. Alloys Compd. 352 (2003) 283–289. doi:10.1016/S0925-8388(02)01171-4.
[66] Z.. Zhang, Z.. Sun, H. Hashimoto, T. Abe, A new synthesis reaction of Ti_3SiC_2 through pulse discharge sintering Ti/SiC/TiC powder, Scr. Mater. 45 (2001) 1461–1467. doi:10.1016/S1359-6462(01)01184-8.
[67] Y. Zou, Z.M. Sun, H. Hashimoto, S. Tada, Synthesis of Ti_3SiC_2 through Pulse Discharge Sintering Powder Mixture Containing Coarse Ti, Mater. Trans. 47 (2006) 1910–1913.

doi:10.2320/matertrans.47.1910.
[68] P.R. Soni, Mechanical Alloying: Fundamentals and Applications, Cambridge International Science Publishing, Cambridge, United Kingdom, 1998.
[69] C. Suryanarayana, Mechanical Alloying and Milling, Marcel Dekker, New York, 2004. doi:10.1016/S0079-6425(99)00010-9.
[70] C. Suryanarayana, E. Ivanov, V.. Boldyrev, The science and technology of mechanical alloying, Mater. Sci. Eng. A. 304–306 (2001) 151–158. doi:10.1016/S0921-5093(00)01465-9.
[71] C. Suryanarayana, Mechanical alloying and milling, CRC Press, 2004.
[72] D.P. Riley, E.H. Kisi, D. Phelan, SHS of Ti_3SiC_2: ignition temperature depression by mechanical activation, J. Eur. Ceram. Soc. 26 (2006) 1051–1058. doi:10.1016/j.jeurceramsoc.2004.11.021.
[73] Y. Zou, Z. Sun, H. Hashimoto, S. Tada, Low temperature synthesis of single-phase Ti_3AlC_2 through reactive sintering Ti/Al/C powders, Mater. Sci. Eng. A. 473 (2008) 90–95. doi:10.1016/j.msea.2007.04.009.
[74] Y. Zou, Z. Sun, H. Hashimoto, S. Tada, Synthesis of high-purity polycrystalline Ti_3AlC_2 through pulse discharge sintering Ti/Al/TiC powders, J. Alloy. Compd. 456 (2008) 456–460. doi:10.1016/j.jallcom.2007.02.105.
[75] Y. Zou, Z. Sun, S. Tada, H. Hashimoto, Synthesis reactions for Ti_3AlC_2 through pulse discharge sintering $Ti/Al_4C_3/TiC$ powder mixture, Scr. Mater. 55 (2006) 767–770. doi:10.1016/j.scriptamat.2006.07.018.
[76] M. Yoshida, Y. Hoshiyama, J. Ommyoji, A. Yamaguchi, Reaction mechanism for the synthesis of Ti_3AlC_2 through an intermediate carbide of Ti_3AlC from elemental Ti, Al, and C powder mixture, J. Ceram. Soc. Japan. 118 (2010) 37–42.
[77] D.P. Riley, E.H. Kisi, A New Solid State Synthesis Methodology for Ternary and Higher Order Compounds, Mater. Forum. 32 (2008) 1–8.
[78] D.P. Riley, E.H. Kisi, T.C. Hansen, A.W. Hewat, I.M.V.L. Langevin, Self-Propagating High-Temperature Synthesis of Ti_3SiC_2: I, Ultra-High-Speed Neutron Diffraction Study of the Reaction Mechanism, J. Am. Ceram. Soc. 85 (2002) 2417–2424.
[79] E. Wu, E.H. Kisi, D.P. Riley, R.I. Smith, Intermediate Phases in Ti_3SiC_2 Synthesis from Ti/SiC/C Mixtures Studied by Time-Resolved Neutron Diffraction, J. Am. Ceram. Soc. 85 (2002) 3084–3086.
[80] E. Wu, E.H. Kisi, S.J. Kennedy, A.J. Studer, In Situ Neutron Powder Diffraction Study of Ti_3SiC_2 Synthesis, J. Am. Ceram. Soc. 84 (2001) 2281–2288.
[81] Z. Ge, K. Chen, J. Guo, H. Zhou, J.M.F. Ferreira, Combustion synthesis of ternary carbide Ti_3AlC_2 in Ti-Al-C system, J. Eur. Ceram. Soc. 23 (2003) 567–574. doi:10.1016/S0955-2219(02)00098-5.
[82] W.C. Lee, S.L. Chung, Ignition phenomena and reaction mechanisms of the self-propagating high-temperature synthesis reaction in the titanium-carbon-aluminum system, J. Am. Ceram. Soc. 80 (1997) 53–61. doi:10.1111/j.1151-2916.1997.tb02790.x.
[83] S.-B. Li, H.-X. Zhai, G.P. Bei, Y. Zhou, Z.L. Zhang, Formation of Ti_3AlC_2 by mechanically induced self-propagating reaction in Ti–Al–C system at room temperature, Mater. Sci. Technol. 22 (2006) 667–672. doi:10.1179/174328406X91050.
[84] E.H. Kisi, D.P. Riley, Crystalline ternary ceramic precursors, 12/279,710, 2009.
[85] D.P. Riley, E.H. Kisi, The Design of Crystalline Precursors For the Synthesis of $M_{n+1}AX_n$ Phases and Their Application to Ti_3AlC_2, J. Am. Ceram. Soc. 90 (2007) 2231–2235. doi:10.1111/j.1551-2916.2007.01728.x.
[86] G.P. Bei, V. Gauthier-Brunet, C. Tromas, S. Dubois, Synthesis, Characterization, and Intrinsic Hardness of Layered Nanolaminate Ti_3AlC_2 and $Ti_3Al_{0.8}Sn_{0.2}C_2$ Solid Solution, J. Am. Ceram. Soc. 95 (2012) 102–107. doi:10.1111/j.1551-2916.2011.04846.x.
[87] Z.G. Liu, J.T. Guo, L.L. Ye, G.S. Li, Z.Q. Hu, Formation mechanism of TiC by mechanical alloying, Appl. Phys. Lett. 65 (1994) 2666–2668. doi:10.1063/1.112596.
[88] H.O. Pierson, Handbook of Refractory Carbides & Nitrides: Properties, Characteristics, Processing and Apps., William Andrew, Westwood, New Jersey, USA, 1996.
[89] E. Rudy, Ternary phase equilibria in transition metal-boron-carbon-silicon systems. Part 5.

Compendium of phase diagram data, 1969.
[90] B.H. Lohse, A. Calka, D. Wexler, Raman spectroscopy as a tool to study TiC formation during controlled ball milling, J. Appl. Phys. 97 (2005) 114912. doi:10.1063/1.1927282.
[91] B.H. Lohse, A. Calka, D. Wexler, Raman spectroscopy sheds new light on TiC formation during the controlled milling of titanium and carbon, J. Alloy. Compd. 434–435 (2007) 405–409. doi:10.1016/j.jallcom.2006.08.216.
[92] L.L. Ye, M.X. Quan, Synthesis of nanocrystalline TiC powders by mechanical alloying, Nanostructured Mater. 5 (1995) 25–31. doi:10.1016/0965-9773(95)00012-4.
[93] K.R. Trethewey, J. Chamberlain, Corrosion for science and engineering, NACE International, Houston, Texas, USA, 1995.
[94] M. Taube, J. Ligou, Molten plutonium chlorides fast breeder reactor cooled by molten uranium chloride, Ann. Nucl. Sci. Eng. 1 (1974) 277–281. doi:10.1016/0302-2927(74)90045-2.
[95] V.F. Sears, Neutron scattering lengths and cross sections, Neutron News. 3 (1992) 26–37. https://www.ncnr.nist.gov/resources/n-lengths/.
[96] D.F. Williams, Assessment of Candidate Molten Salt Coolants for the NGNP/NHI Heat-Transfer Loop, Oak Ridge, Tennessee, USA, 2006.
[97] D.F. Williams, L.M. Toth, K.T. Clarno, Assessment of Candidate Molten Salt Coolants for the Advanced High-Temperature Reactor (AHTR), Oak Ridge, Tennessee, USA, 2006.
[98] C.F. Baes, Jr., The chemistry and thermodynamics of molten salt reactor fuels, J. Nucl. Mater. 51 (1974) 149–162. doi:10.1016/0022-3115(74)90124-X.
[99] Outokumpu, HSC Chemistry 5.1, Finland, 2002.
[100] P.E. Osborne, A.S. Icenhour, G.D. Del Cul, Hydrofluoric Acid Corrosion Study of High-Alloy Materials, ORNL. TM (2002).
[101] H.E. McCoy Jr, Status of materials development for molten salt reactors, Oak Ridge, Tennessee, USA, 1978.
[102] J.R. Keiser, ORNL/TM-6002 Status of Tellurium-Hastelloy N Studies in Molten Fluoride Salts, Oak Ridge, Tennessee, 1977.
[103] S. Delpech, E. Merle-Lucotte, D. Heuer, M. Allibert, V. Ghetta, C. Le-Brun, X. Doligez, G. Picard, Reactor physic and reprocessing scheme for innovative molten salt reactor system, J. Fluor. Chem. 130 (2009) 11–17. doi:10.1016/j.jfluchem.2008.07.009.
[104] X. Doligez, D. Heuer, E. Merle-Lucotte, M. Allibert, V. Ghetta, Coupled study of the Molten Salt Fast Reactor core physics and its associated reprocessing unit, Ann. Nucl. Energy. 64 (2014) 430–440. doi:10.1016/j.anucene.2013.09.009.
[105] V.M. Novikov, The results of the investigations of Russian Research Center - “Kurchatov Institute” on molten salt applications to problems of nuclear energy systems, in: AIP Conf. Proc. 346, 1995. doi:10.1063/1.49148.
[106] V.L. Chernigets, T.P. Rebrova, Studies of some acid-base equilibria in the molten eutectic mixture KCl-LiCl at 700°C, Electrochim. Acta. 45 (1999) 469–476. doi:10.1016/S0013-4686(99)00274-1.
[107] M. Lébl, J. Trnka, Entfernung von sauerstoffhaltigen Anionen aus Alkalihalogeniden, Zeitschrift Für Phys. 186 (1965) 128–136. doi:10.1007/BF01380730.
[108] J.W. Koger, ONRL-TM-4286 Alloy compatibility with LiF--BeF 2 salts containing ThF 4 and UF 4, 1972.
[109] T.M. Pollock, S. Tin, Nickel-Based Superalloys for Advanced Turbine Engines: Chemistry, Microstructure and Properties, J. Propuls. Power. 22 (2006) 361–374. doi:10.2514/1.18239.
[110] Heat Resistant Materials, in: ASM Handb., 1997: pp. 219–335.
[111] V. Ignatiev, A. Surenkov, Alloys compatibility in molten salt fluorides: Kurchatov Institute related experience, J. Nucl. Mater. 441 (2013) 592–603. doi:10.1016/j.jnucmat.2013.05.007.
[112] S. Delpech, E. Merle-Lucotte, T. Auger, X. Doligez, D. Heuer, G. Picard, MSFR: Material issues and the effect of chemistry control, Paris, Fr. (2009) 9–10.
[113] B. El-Dasher, J. Farmer, J. Ferreira, M.S. De Caro, A. Rubenchik, A. Kimura, Corrosion of oxide dispersion strengthened iron-chromium steels and tantalum in fluoride salt coolant: An in situ compatibility study for fusion and fusion-fission hybrid reactor concepts, J. Nucl. Mater.

419 (2011) 15–23. doi:10.1016/j.jnucmat.2011.07.036.
[114] C. Yang, O. Muránsky, H. Zhu, G.J. Thorogood, M. Avdeev, H. Huang, X. Zhou, The effect of milling time on the microstructural characteristics and strengthening mechanisms of NiMo-SiC Alloys prepared via powder metallurgy, Materials (Basel). 10 (2017) 389. doi:10.3390/ma10040389.
[115] C. Yang, H. Huang, X. Zhou, Z. Li, X. Zhou, T. Xia, D. Zhang, High-temperature stability of Ni-3 wt.% SiCNP composite and the effect of milling time, J. Nucl. Mater. 467 (2015) 635–643. doi:10.1016/j.jnucmat.2015.10.044.
[116] D.C. Topor, J.R. Selman, Molten Salt Electrodeposition of Refractory Metal Carbide - II. Mechanism and Nucleation Studies, J. Electrochem. Soc. 140 (1993) 352–361.
[117] D.C. Topor, J.R. Selman, Molybdenum Carbide Coatings Electrodeposited from Molten Fluoride Bath - Preparation of a Coherent Coating, J. Electrochem. Soc. 135 (1988) 384–387. doi:10.1149/1.2095621.
[118] A. Ganguly, M.W. Barsoum, R.D. Doherty, Interdiffusion between Ti_3SiC_2-Ti_3GeC_2 and Ti_2AlC-Nb_2AlC diffusion couples, J. Am. Ceram. Soc. 90 (2007) 2200–2204. doi:10.1111/j.1551-2916.2007.01680.x.
[119] X.H. Yin, M.S. Li, Y.C. Zhou, Microstructure and mechanical strength of diffusion-bonded Ti_3SiC_2/Ni joints, J. Mater. Res. 21 (2006) 2415–2421. doi:10.1557/jmr.2006.0290.
[120] C. Lu, J. Zhang, T. Duan, C. Liu, Microstructure evolution and brazing mechanisms of the Ti_2AlC/Ni joints using nickel based filler alloy, J. Eur. Ceram. Soc. 36 (2016) 3319–3327. doi:10.1016/j.jeurceramsoc.2016.05.024.
[121] W. Hu, Z. Huang, L. Cai, C. Lei, H. Zhai, S. Hao, W. Yu, Y. Zhou, Preparation and mechanical properties of TiC_x-Ni_3(Al,Ti)/Ni composites synthesized from Ni alloy and Ti_3AlC_2 powders, Mater. Sci. Eng. A. 697 (2017) 48–54. doi:10.1016/j.msea.2017.04.113.
[122] W. Wang, H. Zhai, L. Chen, Z. Huang, G. Bei, C. Baumgärtner, P. Greil, Preparation and mechanical properties of in situ TiC_x-Ni (Si, Ti) alloy composites, Mater. Sci. Eng. A. 616 (2014) 214–218. doi:10.1016/j.msea.2014.08.020.
[123] S. Basu, M.F. Ozaydin, A. Kothalkar, I. Karaman, M. Radovic, Phase and morphology evolution in high-temperature Ti_3SiC_2-NiTi diffusion-bonded joints, Scr. Mater. 65 (2011) 237–240. doi:10.1016/j.scriptamat.2011.04.015.
[124] L. Hu, A. Kothalkar, G. Proust, I. Karaman, M. Radovic, Fabrication and characterization of NiTi/Ti_3SiC_2 and NiTi/Ti_2AlC composites, J. Alloys Compd. 610 (2014) 635–644. doi:10.1016/j.jallcom.2014.04.224.
[125] A. Kothalkar, A. Cerit, G. Proust, S. Basu, M. Radovic, I. Karaman, Interfacial study of NiTi-Ti_3SiC_2 solid state diffusion bonded joints, Mater. Sci. Eng. A. 622 (2015) 168–177. doi:10.1016/j.msea.2014.10.033.
[126] T. El-Raghy, M.W. Barsoum, M. Sika, Reaction of Al with Ti_3SiC_2 in the 800 – 1000°C temperature range, Mater. Sci. Eng. A. 298 (2001) 174–178.
[127] J.J. Sienicki, A. Moisseytsev, G. Aliberti, S. Bortot, Q. Lu, SUPERSTAR: an improved natural circulation, lead-cooled, small modular fast reactor for international deployment, in: Proc. ICAPP 2011, 2011.
[128] T. Mroz, Evaluating a New Material for Hall-Héroult Cell Cathodes, JOM. (1997) 24–26.
[129] M.W. Barsoum, T. El-Raghy, L. Farber, M. Amer, R. Christini, A. Adams, The Topotactic Transformation of Ti_3SiC_2 into a Partially Ordered Cubic Ti($C_{0.67}Si_{0.06}$) Phase by the Diffusion of Si into Molten Cryolite, J. Electrochem. Soc. 146 (1999) 3919. doi:10.1149/1.1392573.
[130] L. Li, G. Yu, X. Zhou, Corrosion behaviour of Ti_3SiC_2 and Ti_3AlC_2 with LiF-NaF-KF molten salt, Nucl. Tech. 37 (2014).
[131] G. Liu, M. Li, Y. Zou, Y. Zhang, Corrosion behaviour and strength degradation of Ti_3SiC_2 exposed to a eutectic K_2CO_3 and Li_2CO_3 mixture, J. Eur. Ceram. Soc. 23 (2003) 1957–1962.
[132] D. Sun, A. Zhou, Z. Li, L. Wang, Corrosion behavior of Ti_3AlC_2 in molten KOH at 700°C, J. Adv. Ceram. 2 (2013) 313–317. doi:10.1007/s40145-013-0077-6.
[133] G. Liu, M. Li, Y. Zhou, Effect of Na_2SO_4 and Water Vapor on the Corrosion of Ti_3SiC_2, Oxid. Met. 66 (2006) 115–125. doi:10.1007/s11085-006-9027-9.

[134] Y. Qian, X. Li, M. Li, J. Xu, B. Lu, Hot corrosion of modified Ti_3Al-based alloy coated with thin Na_2SO_4 film at 910 and 950°C in air, Trans. Nonferrous Met. Soc. China. 27 (2017) 954–961. doi:10.1016/S1003-6326(17)60111-0.
[135] G. Liu, M. Li, Y. Zhou, Y. Zhang, Hot corrosion behavior of Ti_3SiC_2 in the mixture of Na_2SO_4-NaCl melts, J. Eur. Ceram. Soc. 25 (2005) 1033–1039. doi:10.1016/j.jeurceramsoc.2004.04.013.
[136] G. Liu, M. Li, Y. Zhou, Y. Zhang, Influence of pre-oxidation on the hot corrosion of Ti_3SiC_2 in the mixture of Na_2SO_4-NaCl melts, Corros. Sci. 48 (2006) 650–661. doi:10.1016/j.corsci.2005.02.002.
[137] A.M. Abdelkader, Molten salts electrochemical synthesis of Cr_2AlC, J. Eur. Ceram. Soc. 36 (2016) 33–42. doi:10.1016/j.jeurceramsoc.2015.09.003.
[138] W.B. Tian, P.L. Wang, Y.M. Kan, G.J. Zhang, Cr_2AlC powders prepared by molten salt method, J. Alloys Compd. 461 (2008) 6–11. doi:10.1016/j.jallcom.2007.06.094.
[139] B. Wang, A. Zhou, Q. Hu, L. Wang, Synthesis and oxidation resistance of V_2AlC powders by molten salt method, Int. J. Appl. Ceram. Technol. 14 (2017) 873–879. doi:10.1111/ijac.12723.
[140] T. Galvin, N.C. Hyatt, W.M. Rainforth, I.M. Reaney, D. Shepherd, Molten salt synthesis of MAX phases in the Ti-Al-C system, Press. (2018).
[141] T. Galvin, I. Reaney, N.C. Hyatt, W.M. Rainforth, D. Shepherd, Second Year Report: Use of MAX phases in accident tolerant fuel cladding, 2016.
[142] X. Guo, J. Wang, S. Yang, L. Gao, B. Qian, Preparation of Ti_3SiC_2 powders by the molten salt method, Mater. Lett. 111 (2013) 211–213. doi:10.1016/j.matlet.2013.08.077.
[143] W.R. Grimes, Chemical Basis for Molten-Salt Reactors, Oak Ridge, Tennessee, USA, 1964.
[144] Y. Gogotsi, A. Nikitin, H. Ye, W. Zhou, J.E. Fischer, B. Yi, H.C. Foley, M.W. Barsoum, Nanoporous carbide-derived carbon with tunable pore size, Nat. Mater. 2 (2003) 591–594. doi:10.1038/nmat957.
[145] G.N. Yushin, E.N. Hoffman, A. Nikitin, H. Ye, M.W. Barsoum, Y. Gogotsi, Synthesis of nanoporous carbide-derived carbon by chlorination of titanium silicon carbide, Carbon N. Y. 43 (2005) 2075–2082. doi:10.1016/j.carbon.2005.03.014.
[146] E.N. Hoffman, G. Yushin, M.W. Barsoum, Y. Gogotsi, Synthesis of Carbide-Derived Carbon by Chlorination of Ti_2AlC, Chem. Mater. 17 (2005) 2317–2322.
[147] M. Naguib, V. Presser, N. Lane, D. Tallman, Y. Gogotsi, J. Lu, L. Hultman, M.W. Barsoum, Synthesis of a new nanocrystalline titanium aluminum fluoride phase by reaction of Ti_2AlC with hydrofluoric acid, RSC Adv. 1 (2011) 1493. doi:10.1039/c1ra00390a.
[148] J. Travaglini, M.W. Barsoum, V. Jovic, T. El-Raghy, The corrosion behavior of Ti_3SiC_2 in common acids and dilute NaOH, Corros. Sci. 45 (2003) 1313–1327. doi:10.1016/S0010-938X(02)00227-5.
[149] M. Naguib, M. Kurtoglu, V. Presser, J. Lu, J. Niu, M. Heon, L. Hultman, Y. Gogotsi, M.W. Barsoum, Two-dimensional nanocrystals produced by exfoliation of Ti_3AlC_2, Adv. Mater. 23 (2011) 4248–53. doi:10.1002/adma.201102306.
[150] M. Naguib, O. Mashtalir, J. Carle, V. Presser, J. Lu, L. Hultman, Y. Gogotsi, M.W. Barsoum, Two-dimensional transition metal carbides., ACS Nano. 6 (2012) 1322–1331. doi:10.1021/nn204153h.
[151] L. Wang, H. Zhang, B. Wang, C. Shen, C. Zhang, Q. Hu, A. Zhou, B. Liu, Synthesis and electrochemical performance of $Ti_3C_2T_x$ with hydrothermal process, Electron. Mater. Lett. 12 (2016) 702–710. doi:10.1007/s13391-016-6088-z.
[152] M. Alhabeb, K. Maleski, B. Anasori, P. Lelyukh, L. Clark, S. Sin, Y. Gogotsi, Guidelines for Synthesis and Processing of Two-Dimensional Titanium Carbide ($Ti_3C_2T_x$ MXene), Chem. Mater. 29 (2017) 7633–7644. doi:10.1021/acs.chemmater.7b02847.
[153] M.R. Lukatskaya, J. Halim, B. Dyatkin, M. Naguib, Y.S. Buranova, M.W. Barsoum, Y. Gogotsi, Room-temperature carbide-derived carbon synthesis by electrochemical etching of MAX phases, Angew. Chemie - Int. Ed. 53 (2014) 4877–4880. doi:10.1002/anie.201402513.
[154] D. Li, Y. Liang, X. Liu, Y. Zhou, Corrosion behavior of Ti_3AlC_2 in NaOH and H_2SO_4, J. Eur. Ceram. Soc. 30 (2010) 3227–3234. doi:10.1016/j.jeurceramsoc.2010.07.002.
[155] Y. Du, J.-X. Liu, Y. Gu, X.-G. Wang, F. Xu, G.-J. Zhang, Anisotropic corrosion of Ti_2AlC and

Ti_3AlC_2 in supercritical water at 500ºC, Ceram. Int. (2017). doi:10.1016/j.ceramint.2017.02.153.
[156] X. Li, Z. Dong, A. Westwood, A. Brown, S. Zhang, R. Brydson, N. Li, B. Rand, Preparation of a titanium carbide coating on carbon fibre using a molten salt method, Carbon N. Y. 46 (2008) 305–309.
[157] J. Ding, W.J. Yuan, C.J. Deng, H.X. Zhu, Novel synthesis and characterization of titanium carbide coatings on graphite flakes, in: Adv. Mater. Res., 2013: pp. 3052–3055.
[158] J. Ye, R.P. Thackray, W.E. Lee, S. Zhang, Microstructure and rheological properties of titanium carbide-coated carbon black particles synthesised from molten salt, J. Mater. Sci. 48 (2013) 6269–6275. doi:10.1007/s10853-013-7424-4.
[159] B. Popov, M. Kimble, R. White, H. Wendt, Electrochemical behaviour of titanium(II) and titanium(III) compounds in molten lithium chloride/potassium chloride eutectic melts, J. Appl. Electrochem. 21 (1991) 351–357. http://link.springer.com/article/10.1007/BF01020221.
[160] Y. Gu, J.X. Liu, Y. Wang, J.X. Xue, X.G. Wang, H. Zhang, F. Xu, G.J. Zhang, Corrosion behavior of TiC–SiC composite ceramics in molten FLiNaK salt, J. Eur. Ceram. Soc. 37 (2017) 2575–2582. doi:10.1016/j.jeurceramsoc.2017.02.020.
[161] Y. Wang, Z.F. Tang, Y. Fu, S.R. Huang, S.F. Zhao, P. Zhang, L.D. Xie, X.G. Wang, G.J. Zhang, Corrosion behavior of ZrC-SiC composite ceramics in LiF-NaF-KF molten salt at high temperatures, Ceram. Int. 41 (2015) 12996–13005. doi:10.1016/j.ceramint.2015.06.143.
[162] R.E. Chinn, Ceramography, 1st ed., ASM International, Ohio, USA, 2002.
[163] L.B. McCusker, R.B. Von Dreele, D.E. Cox, D. Louër, P. Scardi, Rietveld refinement guidelines, J. Appl. Crystallogr. 32 (1999) 36–50. doi:10.1107/S0021889898009856.
[164] R.A. Young, The Rietveld Method, Oxford University Press, Oxford, United Kingdom, 1993.
[165] V. Pecharsky, P.Y. Zavalij, Fundamentals of Powder Diffraction and Structural Characterization of Materials, 2005. doi:10.1007/978-0-387-09579-0.
[166] A. Clearfield, J. Reibenspies, N. Bhuvanesh, Principles and Applications of Powder Diffraction, Blackwell Publishing Ltd., 2008.
[167] B.H. Toby, EXPGUI, a graphical user interface for GSAS, J. Appl. Crystallogr. 34 (2001) 210–213.
[168] A.C. Larson, R.B. Von Dreele, Gsas, Gen. Struct. Anal. Syst. LANSCE, MS-H805, Los Alamos, New Mex. (1994).
[169] B.H. Toby, R factors in Rietveld analysis: How good is good enough ?, Powder Diffr. 21 (2006) 67–70. doi:10.1154/1.2179804.
[170] C. a Schneider, W.S. Rasband, K.W. Eliceiri, NIH Image to ImageJ: 25 years of image analysis, Nat. Methods. 9 (2012) 671–675. doi:10.1038/nmeth.2089.
[171] ASTM International, ASTM E112-13 Standard Test Methods for Determining Average Grain Size, (2013) 1–28. doi:https://doi.org/10.1520/E0112.
[172] Vickers Hardness Test, (n.d.). https://www.gordonengland.co.uk/hardness/vickers.htm (accessed February 20, 2018).
[173] K. Davies, S.X. Li, Simplified Reference Electrode for Electrorefining of Spent Nuclear Fuel in High Temperature Molten Salt, in: Glob. 2007, 2007: pp. 1099–1103.
[174] S.P. Fusselman, Thermodynamic Properties for Rare Earths and Americium in Pyropartitioning Process Solvents, J. Electrochem. Soc. 146 (1999) 2573. doi:10.1149/1.1391974.
[175] R. Sailer, G. McCarthy, ICDD grant-in-aid, Fargo, North Dakota, USA North Dakota State Univ. (1993).
[176] N. Muts, R. Gladyshevskii, E. Gladyshevskii, Crystal structures of the compounds $PrAl_2Si_2$, $Pr_3Al_4Si_6$ and $PrAlSi_2$, J. Alloys Compd. 402 (2005) 66–69.
[177] J.Y. Howe, C.J. Rawn, L.E. Jones, H. Ow, Improved crystallographic data for graphite, Powder Diffr. 18 (2003) 150–154.
[178] E. Wu, J. Wang, H. Zhang, Y. Zhou, K. Sun, Y. Xue, Neutron diffraction studies of $Ti3Si_{0.9}Al_{0.1}C_2$ compound, Mater. Lett. 59 (2005) 2715–2719. doi:10.1016/j.matlet.2005.03.063.
[179] K. Nakamura, M. Yashima, Crystal structure of NaCl-type transition metal monocarbides MC (M=V, Ti, Nb, Ta, Hf, Zr), a neutron powder diffraction study, Mater. Sci. Eng. B. 148 (2008) 69–72. doi:10.1016/j.mseb.2007.09.040.

[180] H. Goretzki, Neutron Diffraction Studies on Titanium-Carbon and Zirconium-Carbon Alloys, Phys. Stat. Sol. 20 (1967) K141.
[181] V. Moisy-Maurice, N. Lorenzelli, C.H. De Novion, P. Convert, High temperature neutron diffraction study of the order-disorder transition in TiC_{1-x}, Acta Metall. 30 (1982) 1769–1779. doi:10.1016/0001-6160(82)90093-1.
[182] M.Y. Tashmetov, V.T. Em, C.H. Lee, H.S. Shim, Y.N. Choi, J.S. Lee, Neutron diffraction study of the ordered structures of nonstoichiometric titanium carbide, Phys. B Condens. Matter. 311 (2002) 318–325. doi:10.1016/S0921-4526(01)01033-X.
[183] P. Stecher, F. Benesovsky, A. Neckel, H. Nowotny, Untersuchungen in den Systemen Titan (Zirkonium, Hafnium)-Niob-Kohlenstoff, Monatshefte Für Chemie Und Verwandte Teile Anderer Wissenschaften. 95 (1964) 1630–1645.
[184] Y. Choi, S.W. Rhee, Effect of aluminium addition on the combustion reaction of titanium and carbon to form TiC, J. Mater. Sci. 28 (1993) 6669–6675. doi:10.1007/BF00356413.
[185] W.M. Haynes, CRC Handbook of Chemistry and Physics, CRC press, 2014.
[186] N. Pessall, R.E. Gold, H.A. Johansen, A study of superconductivity in interstitial compounds, J. Phys. Chem. Solids. 29 (1968) 19–38. doi:http://dx.doi.org/10.1016/0022-3697(68)90251-5.
[187] N. V Tzenov, M.W. Barsoum, Synthesis and Characterization of Ti_3AlC_2, J. Am. Ceram. Soc. 83 (2000) 825–832.
[188] T. Lapauw, D. Tytko, K. Vanmeensel, S. Huang, P. Choi, D. Raabe, E.N. Caspi, O. Ozeri, M. Baben, J.M. Schneider, K. Lambrinou, J. Vleugels, $(Nb_x,Zr_{1-x})_4AlC_3$ MAX Phase Solid Solutions: Processing, Mechanical Properties, and Density Functional Theory Calculations, Inorg. Chem. 55 (2016) 5445–5452. doi:10.1021/acs.inorgchem.6b00484.
[189] T. Kwamman, W.M. Rainforth, Study of carbide composites and their interfaces for Generation IV nuclear reactors: PhD 2nd Year Progress Report, Sheffield, 2016.
[190] C. Magnus, W.M. Rainforth, I.M. Reaney, Tribological Behaviour of MAX Phases: 1st Year Confirmation Report, Sheffield, 2017.
[191] I. Barin, F. Sauert, E. Shultze-Rhonhof, W.S. Sheng, Thermochemical Data of Pure Substances, Wiley VCH, New York, 1989.
[192] W. Zhou, B. Mei, J. Zhu, X. Hong, Synthesis of high-purity Ti_3SiC_2 and Ti_3AlC_2 by spark plasma sintering (SPS) technique, J. Mater. Sci. 40 (2005) 2099–2100. doi:10.1007/s10853-005-1245-z.
[193] L.C. Olsen, Materials Corrosion in Molten LiF-NaF-KF Eutectic Salt, University of Wisconsin-Madison, 2009. doi:10.1007/s13398-014-0173-7.2.
[194] C.D. Wagner, W.M. Riggs, L.E. Davis, J.F. Moulder, G.E. Muilenberg, Handbook of X-ray Photoelectron Spectroscopy, Perkin-Elmer Corporation, 1979.
[195] S. Sasaki, K. Fujino, Y. Takeuchi, X-ray Determination of Electron-Density Distributions in Oxides, MgO, MnO, CoO, and NiO, and Atomic Scattering Factors o f their Constituent Atoms, Proc. Jpn. Acad. 55 (1979) 43–48. doi:10.2183/pjab.55.43.
[196] B.A. Wechsler, R.B. Von Dreele, Structure refinements of Mg_2TiO_4, $MgTiO_3$ and $MgTi_2O_5$ by time-of-flight neutron powder diffraction, Acta Crystallogr. Sect. B. 45 (1989) 542–549. doi:10.1107/S010876818900786X.
[197] A.S. Kurlov, A.I. Gusev, Neutron and X-ray diffraction study and symmetry analysis of phase transformations in lower tungsten carbide W_2C, Phys. Rev. B. 76 (2007) 1–16. doi:10.1103/PhysRevB.76.174115.
[198] H.E. Swanson, E. Tatge, X. Standard, R.D.P. Patterns, National Bureau of Standards, Washington, DC, Circ. 539 (1953) 37.
[199] A. Katagiri, M. Suzuki, Z. Takehara, Electrodeposition of Tungsten in $ZnBr_2$-NaBr and $ZnCl_2$-NaCl Melts, J. Electrochem. Soc. 138 (1991) 767–773.
[200] E. Rudy, S. Windisch, Revision of the titanium-tungsten system, 1968.
[201] K. Page, J. Li, R. Savinelli, H.N. Szumila, J. Zhang, J.K. Stalick, T. Proffen, S.L. Scott, R. Seshadri, Reciprocal-space and real-space neutron investigation of nanostructured Mo_2C and WC, Solid State Sci. 10 (2008) 1499–1510. doi:10.1016/j.solidstatesciences.2008.03.018.
[202] W. Wong-Ng, H. McMurdie, B. Paretzkin, C. Hubbard, A. Dragoo, JCPDS Grant-in-Aid Report,

(1986).
[203] J. Braun, M. Ellner, B. Predel, Experimental investigations of the structure and stability of the TiAl phase, Zeitschrift Fur Met. 86 (1995) 870–876.
[204] W. Guse, H. Saalfeld, X-ray characterization and structure refinement of a new cubic alumina phase (α-Al_2O_3) with spinel-type structure, Neues Jahrb. Für Mineral. Monatshefte. (1990) 217–226.
[205] Q. Zhang, M.G. Verde, J.K. Seo, X. Li, Y.S. Meng, Structural and electrochemical properties of Gd-doped $Li_4Ti_5O_{12}$ as anode material with improved rate capability for lithium-ion batteries, J. Power Sources. 280 (2015) 355–362.
[206] H.O. Pierson, Handbook of Refractory Carbides & Nitrides: Properties, Characteristics, Processing and Apps., William Andrew, 1996.
[207] T. Yamanaka, Y. Takéuchi, Order-disorder transition in $MgAl_2O_4$ spinel at high temperatures up to 1700°C, Zeitschrift Für Krist. Mater. 165 (1983) 65–78.
[208] I.E. Grey, C. Li, I.C. Madsen, G. Braunshausen, TiO_2-II. Ambient pressure preparation and structure refinement, Mater. Res. Bull. 23 (1988) 743–753.
[209] M. Kriens, G. Adiwidjaja, W. Guse, K.H. Klaska, C. Lathe, H. Saalfeld, The crystal structures of $LiAl_5O_8$ and $Li_2Al_4O_7$, Neues Jahrb. Fur Mineral. (1996) 344–350.
[210] W. Wong-Ng, H.F. McMurdie, B. Paretzkin, Y. Zhang, K.L. Davis, C.R. Hubbard, A.L. Dragoo, J.M. Stewart, Standard X-ray diffraction powder patterns of sixteen ceramic phases, Powder Diffr. 2 (1987) 191–202.
[211] P. Groth, E. Kaiser, Zeitschrift für Kristallographie, Kristallgeometrie, Kristallphysik, Kristallchemie, Akademische Verlagsgesellschaft., 1877.
[212] W.H. Baur, A.A. Khan, Rutile-type compounds. IV. SiO_2, GeO_2 and a comparison with other rutile-type structures, Acta Crystallogr. Sect. B Struct. Crystallogr. Cryst. Chem. 27 (1971) 2133–2139.
[213] W. Jeitschko, Refinement of the crystal structure of $TiSi_2$ and some comments on bonding in $TiSi_2$ and related compounds, Acta Crystallogr. Sect. B Struct. Crystallogr. Cryst. Chem. 33 (1977) 2347–2348. doi:10.1163/003925995X00233.
[214] A. Ziadi, G. Thiele, B. Elouadi, The crystal structure of Li_2TiSiO_5, J. Solid State Chem. 109 (1994) 112–115.
[215] R.P. Liferovich, R.H. Mitchell, Geikielite-ecandrewsite solid solutions: Synthesis and crystal structures of the $Mg_{1-x}Zn_xTiO_3$ ($0 \leq x \leq 0.8$) series, Acta Crystallogr. Sect. B Struct. Sci. 60 (2004) 496–501. doi:10.1107/S0108768104017963.
[216] N. Tzenov, M.W. Barsoum, Infuence of small amounts of Fe and V on the synthesis and stability of Ti_3SiC_2, J. Eur. Ceram. Soc. 20 (2000) 801–806.
[217] B. Gerand, G. Nowogrocki, J. Guenot, M. Figlarz, Structural study of a new hexagonal form of tungsten trioxide, J. Solid State Chem. 29 (1979) 429–434.
[218] J.F. Dorrian, R.E. Newnham, Refinement of the Structure of Li_2TiO_3, Mater. Res. Bull. 4 (1969) 179–183.
[219] G.E. Lloyd, Atomic Number and Crystallographic Contrast Images with the SEM: A Review of Backscattered Electron Techniques, Mineral. Mag. 51 (1987) 3–19. doi:10.1180/minmag.1987.051.359.02.
[220] S.S. Hwang, J. Han, D. Lee, S.W. Park, Synthesis of Ti_3SiC_2 by infiltration of molten Si, J. Alloys Compd. 509 (2011) L336–L339. doi:10.1016/j.jallcom.2011.06.074.
[221] Thermal Neutron Capture Cross-sections, (2007). https://environmentalchemistry.com/yogi/periodic/crosssection.html (accessed November 2, 2017).
[222] X. Yang, D. Zhang, M. Liu, S. Feng, W. Xue, H. Liu, G. Yu, X. Zhou, H. Xia, P. Huai, Z. Li, Y. Lu, H. Zhou, S. Dong, Corrosion of SiC induced by Hastelloy N alloy and its corrosion products in LiF-NaF-KF molten salt, Corros. Sci. 109 (2016) 62–67. doi:10.1016/j.corsci.2016.03.029.
[223] W.D. Callister, D.G. Rethwisch, Materials Science and Engineering: An Introduction, 9th ed., Wiley Global Education, 2013.

[224] S. Krumm, The art of slit setting, Www.Ccp14.Ac.Uk. (1997). http://www.ccp14.ac.uk/ccp/web-mirrors/krumm/html/xray/slits.html (accessed August 31, 2016).
[225] S.A. Speakman, Basics of X-Ray Powder Diffraction, (n.d.). http://prism.mit.edu/xray/Basics of X-Ray Powder Diffraction.pdf (accessed January 16, 2018).
[226] C. Suryanarayana, M.G. Norton, X-Ray Diffraction - A practical Approach, Springer Science & Business Media, 1998. doi:10.1007/978-1-4899-0148-4.
[227] D. Brandon, W.D. Kaplan, Microstructural Characterization of Materials, 2nd ed., John Wiley & Sons, Ltd, Chichester, UK, 2008. doi:10.1002/9780470727133.
[228] J.F. Watts, J. Wolstenholme, An Introduction to Surface Analysis by XPS and AES, John Wiley & Sons Ltd., 2003.
[229] Raman Spectroscopy, DoITPoMS, Univ. Cambridge. (2015). http://www.doitpoms.ac.uk/tlplib/raman/index.php (accessed May 7, 2015).
[230] W.C. Oliver, G.M. Pharr, An improved technique for determining hardness and elastic modulus using load and displacement sensing indentation experiments, J. Mater. Res. 7 (1992) 1564–1583.
[231] W.C. Oliver, G.M. Pharr, Measurement of hardness and elastic modulus by instrumented indentation: Advances in understanding and refinements to methodology, J. Mater. Res. 19 (2004) 3–20. doi:10.1557/jmr.2004.19.1.3.
[232] E.P. DeGarmo, J.T. Black, R.A. Kohser, DeGarmo's Materials and Processes in Engineering, 10th Ed., John Wiley & Sons, 2007.
[233] N.F. Gao, J.T. Li, D. Zhang, Y. Miyamoto, Rapid synthesis of dense Ti_3SiC_2 by spark plasma sintering, J. Eur. Ceram. Soc. 22 (2002) 2365–2370.
[234] G. Bergerhoff, I.D. Brown, F.H. Allen, others, Crystallographic databases, Int. Union Crystallogr. Chester. (1987) 77–95.
[235] T. Cabioc'h, P. Eklund, V. Mauchamp, M. Jaouen, Structural investigation of substoichiometry and solid solution effects in $Ti_2Al(C_x,N_{1-x})_y$ compounds, J. Eur. Ceram. Soc. 32 (2012) 1803–1811. doi:10.1016/j.jeurceramsoc.2011.12.011.
[236] I.I. Ivanova, A.N. Demidik, M. V. Karpets, N.A. Krylova, A.P. Polushko, S. a. Firstov, Synthesis of Binary Titanium Compounds Ti_3AlC_2 and Ti_4AlN_3 by Isothermal Sintering, Powder Metall. Met. Ceram. 53 (2014) 377–385. doi:10.1007/s11106-014-9627-x.
[237] A. Belkly, M. Helderman, V.L. Karen, P. Ulkch, New developments in the Inorganic Crystal Structure Database (ICSD): Accessibility in support of materials research and design, Acta Crystallogr. Sect. B Struct. Sci. 58 (2002) 364–369. doi:10.1107/S0108768102006948.
[238] V. Presser, M. Naguib, L. Chaput, A. Togo, G. Hug, M.W. Barsoum, First-order Raman scattering of the MAX phases, J. Raman Spectrosc. 43 (2012) 168–172. doi:10.1002/jrs.3036.
[239] M.R. Gallas, Y.C. Chu, G.J. Piermarini, Calibration of the Raman effect in α–Al_2O_3 ceramic for residual stress measurements, J. Mater. Res. 10 (1995) 2817–2822. doi:10.1557/JMR.1995.2817.
[240] W.D. Nix, H.J. Gao, Indentation size effects in crystalline materials: A law for strain gradient plasticity, J. Mech. Phys. Solids. 46 (1998) 411–425. doi:10.1016/s0022-5096(97)00086-0.
[241] W.B. Zhou, B.C. Mei, J.Q. Zhu, X.L. Hong, Rapid synthesis of Ti_2AlC by spark plasma sintering technique, Mater. Lett. 59 (2005) 131–134. doi:10.1016/j.matlet.2004.07.052.
[242] E.H. Kisi, J.A.A. Crossley, S. Myhra, M.W. Barsoum, Structure and Crystal Chemistry of Ti_3SiC_2, J. Phys. Chem Solids. 59 (1998) 1437–1443.
[243] M.A. Stopher, The effects of neutron radiation on nickel-based alloys, Mater. Sci. Technol. (United Kingdom). 33 (2017) 518–536. doi:10.1080/02670836.2016.1187334.